

Transactions of the ASME®

FLUIDS ENGINEERING DIVISION

Technical Editor
DEMETRI P. TELIONIS (1999)

Executive Secretary
PAT WHITE (1999)

Assistant to the Editor
N. W. SCHAEFFLER

Calendar Editor
M. F. ACKERSON

Associate Technical Editors

S. BANERJEE (1999)
P. W. BEARMAN (2001)
P. BRADSHAW (2000)
M. N. DHAUBHADEL (1999)
J. K. EATON (1999)
G. ERLEBACHER (2000)
U. GHIA (2001)
M. HAJJ (2001)
J. KATZ (2001)
C. L. MERKLE (2000)
P. RAAD (2001)
B. SCHIAVELLO (1999)
M. SOMMERFELD (1999)
F. K. WARDEN (2000)
D. R. WILLIAMS (2000)
K. ZAMAN (2001)

BOARD ON COMMUNICATIONS

Chairman and Vice-President
R. K. SHAH

OFFICERS OF THE ASME

President, **R. E. NICKELL**

Exec. Director
D. L. BELDEN

Treasurer
J. A. MASON

PUBLISHING STAFF

Managing Director, Engineering
CHARLES W. BEARDSLEY

Director, Technical Publishing
PHILIP DI VIETRO

Managing Editor, Technical Publishing
CYNTHIA B. CLARK

Managing Editor, Transactions
CORNELIA MONAHAN

Production Assistant
MARISOL ANDINO

Transactions of the ASME, Journal of Fluids Engineering (ISSN 0098-2202) is published quarterly (Mar., June, Sept., Dec.) for \$215.00 per year by The American Society of Mechanical Engineers, Three Park Avenue, New York, NY 10016. Periodicals postage paid at New York, NY and additional mailing offices.

POSTMASTER: Send address changes to Transactions of the ASME, Journal of Fluids Engineering, c/o THE AMERICAN SOCIETY OF MECHANICAL ENGINEERS, 22 Law Drive, Box 2300, Fairfield, NJ 07007-2300.

CHANGES OF ADDRESS must be received at Society headquarters seven weeks before they are to be effective. Please send old label and new address.

PRICES: To members, \$40.00, annually; to nonmembers, \$215.00. Add \$40.00 for postage to countries outside the United States and Canada.

STATEMENT from By-Laws. The Society shall not be responsible for statements or opinions advanced in papers or printed in its publications (B7.1, Par. 3).

COPYRIGHT © 1999 by The American Society of Mechanical Engineers. For authorization to photocopy material for internal or personal use under those circumstances not falling within the fair use provisions of the Copyright Act, contact the Copyright Clearance Center (CCC), 222 Rosewood Drive, Danvers, MA 01923, tel: 978-750-8400, www.copyright.com.

Request for special permission or bulk copying should be addressed to Reprints/Permission Department.

INDEXED by Applied Mechanics Reviews and Engineering Information, Inc. Canadian Goods & Services Tax Registration #126148048.

Journal of Fluids Engineering

Published Quarterly by The American Society of Mechanical Engineers

VOLUME 121 • NUMBER 4 • DECEMBER 1999

Technical Papers

- 713 Numerical Study of Developing Flow and Heat Transfer in a Wavy Passage
K. Stone and S. P. Vanka
- 720 Cinema PIV and Its Application to Impinging Vortex Systems
J.-C. Lin and D. Rockwell
- 725 Turbulent Flow in a Rotating Two Pass Smooth Channel
Shou-Shing Hsieh, Ping-Ju Chen, and Hsiang-Jung Chin
- 735 Comparison and Scaling of the Bursting Period in Rough and Smooth Walls Channel Flows
S. Demare, L. Labraga, and C. Tournier
- 747 A Modified Model for Diffusion in Second-Moment Turbulence Closures
Anthony G. Straatman
- 757 Analytical and Experimental Investigation of Laminar Channel Flow With Respect to Flow Metering
Franz Peters
- 762 Single Jet Mixing at Arbitrary Angle in Turbulent Tube Flow
Zhigang Feng, Xiaodong Wang, and Larry J. Forney
- 766 Effect of Injected Longitudinal Vorticity on Particle Dispersion in a Swirling, Coaxial Jet
Ryan B. Wicker and John K. Eaton
- 773 Re-Entrant Jet Modeling of Partial Cavity Flow on Two-Dimensional Hydrofoils
J. Dang and G. Kuiper
- 781 Re-Entrant Jet Modeling of Partial Cavity Flow on Three-Dimensional Hydrofoils
J. Dang and G. Kuiper
- 788 Experimental Investigation of the Flow Field in an Automotive Torque Converter Stator
Y. Dong and B. Lakshminarayana
- 798 Field Study on Pump Vibration and ISO's New Criteria
Toshiyuki Osada, Takashi Kawakami, Tadashi Yokoi, and Yoshinobu Tsujimoto
- 804 Three-Dimensional Numerical Analysis of Flow-Induced Vibration in Turbomachinery
Chen Zuoyi, Wang Jihong, and Liu Hong
- 808 Study of Several Jets Impinging on a Plane Wall: Visualizations and Laser Velocimetry Investigations
A. Bernard, L.-E. Brizzi, and J.-L. Bousgarbiès
- 813 Experimental Investigation of Blade Loading Effects at Design Flow in Rotating Passages of Centrifugal Impellers (Data Bank Contribution)
Nicholas H. Hesse and J. H. G. Howard
- 824 Turbulence Modeling and Computation of Viscous Transitional Flows for Low Pressure Turbines
A. Chernobrovkin and B. Lakshminarayana
- 834 Analysis of Rotating Cavitation in a Finite Pitch Cascade Using a Closed Cavity Model and a Singularity Method
Satoshi Watanabe, Kotaro Sato, Yoshinobu Tsujimoto, and Kenjiro Kamijo
- 841 Cavitating Centrifugal Pump at Rapid Change in Operating Conditions—Part 1: Transient Phenomena at Opening/Closure of Discharge Valve
T. Tanaka and H. Tsukamoto
- 850 Transient Behavior of a Cavitating Centrifugal Pump at Rapid Change in Operating Conditions—Part 2: Transient Phenomena at Pump Startup/Shutdown
T. Tanaka and H. Tsukamoto
- 857 Transient Behavior of a Cavitating Centrifugal Pump at Rapid Change in Operating Conditions—Part 3: Classifications of Transient Phenomena
T. Tanaka and H. Tsukamoto

(Contents continued on p. 746)

This journal is printed on acid-free paper, which exceeds the ANSI Z39.48-1992 specification for permanence of paper and library materials. ♻️™
♻️ 85% recycled content, including 10% post-consumer fibers.

(Contents continued)

- 866 **Three-Dimensional Linear Analysis of Rotating Cavitation in Inducers Using an Annular Cascade Model**
Satoshi Watanabe, Kazuhiko Yokota, Yoshinobu Tsujimoto, and Kenjiro Kamiyo
- 872 **Numerical Computation of Shock Waves in a Spherical Cloud of Cavitation Bubbles**
Yi-Chun Wang and Christopher E. Brennen
- 881 **Effects of Nuclei Size Distribution on the Dynamics of a Spherical Cloud of Cavitation Bubbles**
Yi-Chun Wang
- 887 **Monitoring Fluidization Dynamics for Detection of Changes in Fluidized Bed Composition and Operating Conditions**
J. Ruud van Ommen, Jaap C. Schouten, and Cor M. van den Bleek
- 895 **Flow Pattern Transition During Gas Liquid Upflow Through Vertical Concentric Annuli—Part I: Experimental Investigations**
G. Das, P. K. Das, N. K. Purohit, and A. K. Mitra
- 902 **Flow Pattern Transition During Gas Liquid Upflow Through Vertical Concentric Annuli—Part II: Mechanistic Models**
G. Das, P. K. Das, N. K. Purohit, and A. K. Mitra
- 908 **Dusty Gas Flow in a Converging-Diverging Nozzle**
O. Igra, I. Elperin, and G. Ben-Dor

Technical Briefs

- 914 **Aerodynamic Torque Acting on a Butterfly Valve. Comparison and Choice of a Torque Coefficient**
C. Solliec and F. Danbon
- 917 **A Model for Flows With Massive Separation**
K. Sanjeev Rao
- 920 **Fluids Engineering Calendar**

Announcements

- 924 **First Forum Call for Papers—2000 IMECE**
- 926 **Statement of Numerical Accuracy**
- 926 **Statement of Experimental Uncertainty**
- 926 **Access to the Electronic JFE**
- 926 **Submission of Papers**

Numerical Study of Developing Flow and Heat Transfer in a Wavy Passage

K. Stone
Graduate Student.

S. P. Vanka
Professor.

Department of Mechanical
and Industrial Engineering,
University of Illinois at Urbana-Champaign,
1206 W Green Street, Urbana, IL 61801

Developing flow and heat transfer in a wavy passage are studied using a numerical scheme that solves the two-dimensional unsteady flow and energy equations. Calculations are presented for a wavy channel consisting of 14 waves. Time-dependent simulations have been performed for several Reynolds numbers. At low Reynolds numbers, the flow is steady in the complete channel. As the Reynolds number is progressively increased, the flow becomes unsteady. As a result of the unsteadiness, there is increased mixing between the core and the wall fluids, thereby increasing the heat transfer rate. With further increase in Reynolds number, the flow becomes unsteady at a much earlier spatial location.

1 Introduction

In a previous numerical study, Wang and Vanka (1995) presented fully developed flow and heat transfer characteristics for a spatially periodic converging-diverging passage. The periodic regime represents an infinitely long passage for which the velocity and temperature profiles entering any wave are the same as the exit profiles of a previous wave. Thus, the analysis could be restricted to a single wave. Wang and Vanka (1995) performed several numerical calculations to study the effect of the inflow Reynolds number on the transition from a steady flow to an unsteady flow. The geometry of the wave had the same parameters as that studied experimentally by Nishimura et al. (1984). Wang and Vanka (1995) observed that at low Reynolds numbers, the flow consists of steady, separation bubbles in the top and bottom troughs. As the Reynolds number is progressively increased, the flow becomes unsteady, and periodic self-sustained oscillations are generated. Such unsteadiness results in complex interactions between the core fluid and the boundary layers formed on the channel walls, thereby producing increased mixing and near-wall temperature gradients. The rates of heat transfer are consequently increased by significant amounts. Typically, increases of a factor of two or three have been observed both experimentally and through numerical solution of the governing fluid flow equations.

A detailed review of previous works on wavy channels is given by Wang and Vanka (1995), and by Stone (1997). A number of experimental, as well as computational, studies have been previously reported. Goldstein and Sparrow (1977) were probably the first to study the local and average heat/mass transfer characteristics for laminar, transitional, and low Reynolds number turbulent flows in a corrugated wall channel. It was shown experimentally that, in the laminar regime up to a Reynolds number of 1200, the transfer coefficients were only moderately larger than those for a parallel-plate channel. However, for low Reynolds number turbulent flow ($Re = 6000-8000$), the rates of heat transfer exceeded those for a straight channel by nearly a factor of three. Their corrugated channel had only two corrugation cycles, therefore, the results were influenced by entrance effects. O'Brien and Sparrow (1982) studied heat transfer characteristics for a fully developed periodic channel in the turbulent Reynolds number range and obtained heat transfer enhancement by a factor of 2.5 over a conventional straight channel, resulting from a highly complex

flow pattern. Sparrow and Comb (1983) studied the effect of spacing of the corrugated walls. Ali and Ramadhyani (1992) conducted an experimental study in corrugated channels of planar cross-section in steady and transitional Reynolds number regimes. Flow visualization studies indicated the appearance of longitudinal vortices, as the Reynolds number was progressively increased. Furthermore, it was observed that in the transitional regime, spanwise vortical structures rolled up from the shear layers at a regular frequency. These vortical structures transfer the near-wall fluid to the core region, and enhance the rate of heat transfer. It was observed that corrugated channels operated at transitional Reynolds numbers provide superior rates of heat transfer.

Flow characteristics in a channel with a symmetric sinusoidal wavy wall were investigated experimentally by Nishimura et al. (1984). In the laminar flow regime, the pressure coefficient was observed to be inversely proportional to the Reynolds number, but in the transitional and turbulent regimes, it was independent of Reynolds number. Nishimura et al. (1985) also studied the mass transfer coefficients for the same channel. For steady flow, no enhancement in transport properties relative to a plane channel was observed; however, substantial increase in mass transfer was seen, once the flow became unsteady. Enhancement in heat and mass transfer due to pulsatile in-flow in wavy channel geometry has been studied by a number of researchers (Sobey, 1982; Stephanoff et al., 1980, 1986; Ralph, 1986 and a few others). However, in the present study we are concerned with heat transfer and fluid flow characteristics when the inflow is uniform and steady.

Studies on fully developed flow in periodic converging-diverging passages with uniform in-flow report a Hopf bifurcation at $Re \approx 130$, followed by a series of bifurcations leading to chaos (Guzmán and Amon, 1994; Amon, Guzmán and Morel, 1996). The flow was observed to be quasi-periodic with up to three fundamental frequencies and multiple sub- and super-harmonics in the Reynolds number range of 130–800. At 850, the flow became aperiodic with broad band frequency spectra of the velocity signals. Schatz et al. (1991) introduced periodic disturbances in a channel by asymmetric placement of cylindrical bodies and observed supercritical transition due to convective instabilities. They identified a Hopf bifurcation at Reynolds number of 130. Greiner, Spencer and Fischer (1996) studied a fully developed triangular grooved channel configuration in a Reynolds number range of 140–2000. They found that, compared to smoothly curved geometry, the triangular grooves cause early unsteadiness and three-dimensionality in the flow. The spanwise flow turns irregular around a Reynolds number of 748. There is also related work on flow through grooved channels with square cross-section (Ghaddar et al., 1986a, 1986b), communicating channels (Majumdar and

Contributed by the Fluids Engineering Division for publication in the JOURNAL OF FLUIDS ENGINEERING. Manuscript received by the Fluids Engineering Division April 3, 1998; revised manuscript received June 22, 1999. Associate Technical Editor: P. M. Sockol.

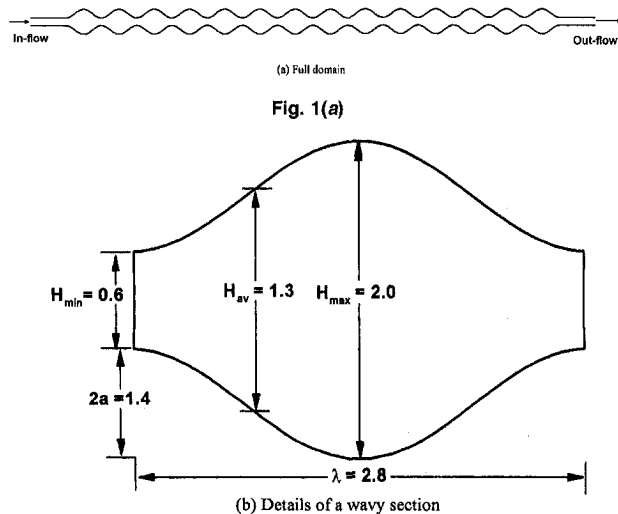


Fig. 1 Geometry considered

Amon, 1993), and channels with periodic array of cylinders (Karniadakis et al., 1988). In these geometries as well, improved mixing is achieved due to unsteady shear layers that interact with the near-wall fluid.

The present numerical study considers flow and heat transfer in the developing flow region of a furrowed channel. The Prandtl number of the fluid is taken to be 0.7. At a Reynolds number less than the Hopf bifurcation value (~ 130), the flow in the entire domain is characterized by vortices in the troughs and a steady core flow. At a Reynolds number above the Hopf bifurcation point, flow begins to become unsteady in the downstream sections. As the Reynolds number is increased, the location of unsteadiness moves upstream from the exit. Thus, the flow consists of mixed steady/unsteady regimes with low mixing in the steady regime, and enhanced mixing in the unsteady flow region. In this study, we numerically investigate the characteristics of such a developing flow in a channel with a series of wavy sections. In the present study, the flow is assumed to be two-dimensional. This is because three-dimensional computations are much more expensive and at the Reynolds numbers considered, the major effects of unsteadiness can be captured by two-dimensional simulations. Temporal development of the flow for a number of Reynolds numbers has been computed and the corresponding unsteady behavior and associated heat transfer rates have also been studied.

2 Numerical Procedure

A detailed description of the equations and the numerical procedure followed in this study is available in Wang and Vanka

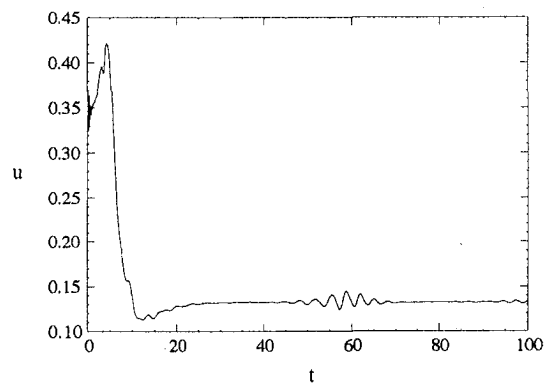


Fig. 2 Time signal of u -velocity at $Re = 180$ in the 14th wavy section

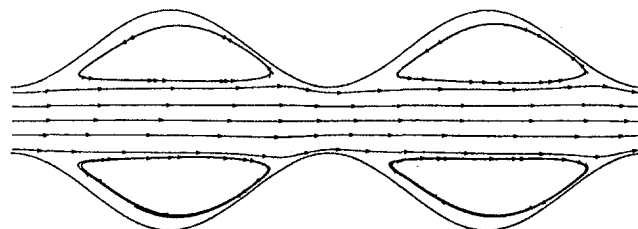


Fig. 3 Instantaneous streamline plot in the 13th and 14th wavy sections at $Re = 180$

(1995). In the present work an incompressible fluid with constant physical properties has been considered. The spatial discretization uses a cell-centered collocated arrangement of velocities (Cartesian components) and pressure. The two-dimensional transient conservation equations are solved on a curvilinear orthogonal grid. The orthogonal mesh is generated through the solution of a pair of elliptic partial-differential equations. A pair of boundary values of x and y is computed from the orthogonality constraint and the given shape of the boundary. For the entire channel consisting of fourteen wavy sections, each wavy section is discretized by an orthogonal mesh. At the two ends, straight sections of lengths each equal to that of one wavy section are attached.

Numerical integration of the above equations is based on a two-stage fractional step procedure with backward Euler differencing of the time derivative and Adams-Bashforth explicit differencing of the convection terms. Diffusion terms are discretized with an explicit central difference scheme. The equations are written in conservative form and due to the differencing schemes used, an overall second order accuracy is established. The Poisson equation for pressure is solved using conjugate gradient (CG) algorithm. Typically, 200 iterations of the CG were necessary to reduce the residue norms by at least five orders of magnitude.

Nomenclature

C_p = pressure coefficient
 D_h = hydraulic diameter ($H_{\min} + H_{\max}$)
 h = heat transfer coefficient
 H = inter-wall spacing
 k = thermal conductivity
 Nu = Nusselt number
 p = pressure
 Pr = Prandtl number
 Q = volumetric flow rate per unit width of the channel
 Re = Reynolds number (Q/ν)
 t = time

u = Cartesian velocity component in the x direction
 v = Cartesian velocity component in the y direction
 x = Cartesian coordinate
 y = Cartesian coordinate
 ξ, η = transformed co-ordinates
 λ = wavelength of the wavy wall
 ν = kinematic viscosity
 θ = dimensionless temperature
 ρ = density

Subscripts and Superscripts

avg = spatially averaged quantity
 in = inlet condition
 m = bulk mean quantity
 max = quantity evaluated at maximum cross section
 min = quantity evaluated at minimum cross section
 n = number of the wavy section
 w = wall value

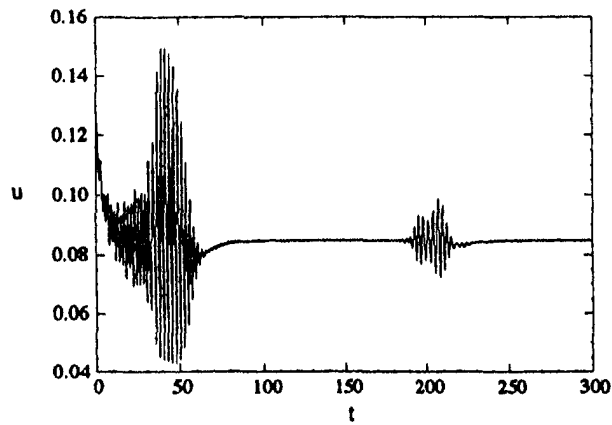


Fig. 4(a)

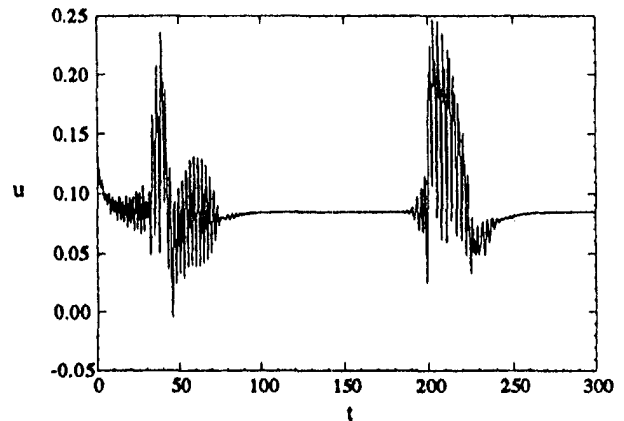


Fig. 4(b)

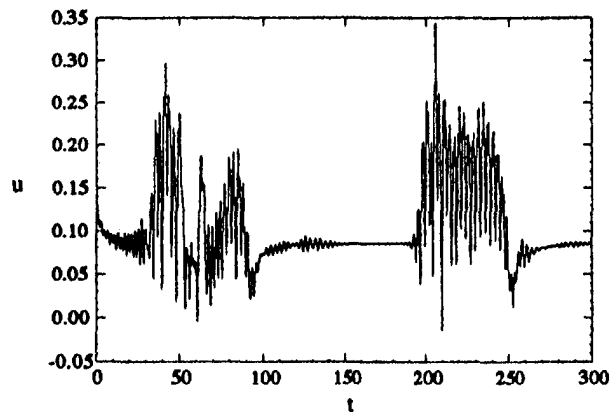


Fig. 4(c)

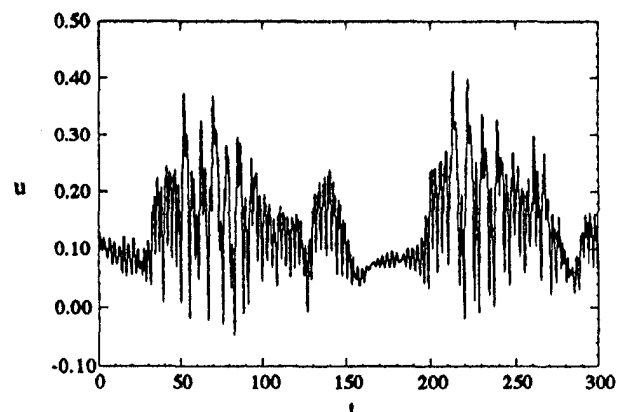


Fig. 4(d)

Fig. 4 Time signals for u -velocity at $Re = 300$: (a) wavy section 8; (b) wavy section 10; (c) wavy section 12; (d) wavy section 14

3 Computational Details

In the present study, a long wavy channel consisting of fourteen wavy sections and a pair of inlet and outlet straight sections has been considered (Fig. 1(a)). Dimensions of each wavy section of the passage were chosen to correspond exactly with those used in the experiments of Nishimura et al. (1984) (Fig. 1(b)). The Reynolds number is defined as

$$Re = \frac{u_{in} H_{in}}{\nu} = \frac{Q}{\nu}$$

where Q is the volume flow rate per unit width of the channel, ν is the fluid viscosity; u_{in} and H_{in} are the velocity and height at the channel inlet respectively. On the channel walls, no-slip and constant temperature are prescribed. At the inlet, uniform axial flow (with zero cross-flow) and uniform temperature are prescribed. The dimensionless temperatures at the inlet and on the wall are unity and zero respectively. A convective outflow condition is used at the channel exit.

For fully developed flow in the periodic domain, Wang and Vanka (1995) reported a systematic study on effects of grid refinement. A wide range of grid sizes were used (64×32 to 256×128). For steady flow, even the 64×32 grid gave good accuracy compared to other finer grids. However, it was observed that higher grid resolution in the cross-flow direction was required for the unsteady flow. Present computations are carried out using the same code as Wang and Vanka (1995). Considering the much larger size of the computational domain for the present study on developing flow, an overall 1024×64 grid was used which corresponds to 64×64 nodes in each wavy or straight section. A time step of 0.0025 units, which is

much smaller than the convective and diffusive limits, has been used for all the simulations.

The initial computation was performed for $Re = 120$ ($<$ Hopf bifurcation value, 130). The problem was impulsively started with a guessed initial condition ($u = 1.0$) everywhere in the domain. The computation was continued until a stationary state (steady in this case) was reached. This steady-state field was then used as

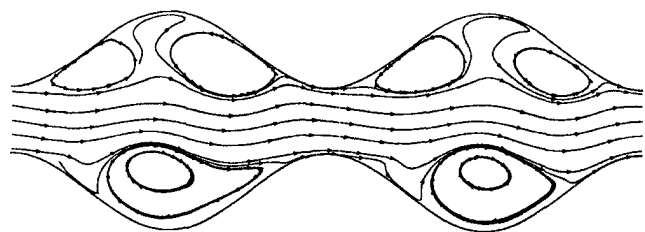


Fig. 5 Instantaneous streamline plot in the 13th and 14th wavy sections at $Re = 300$ (unsteady flow)

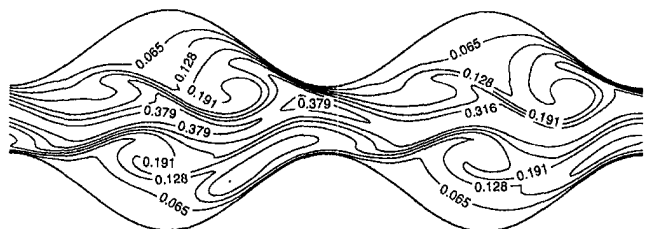


Fig. 6 Instantaneous isotherm plot in the 13th and 14th wavy sections at $Re = 300$ (unsteady flow)

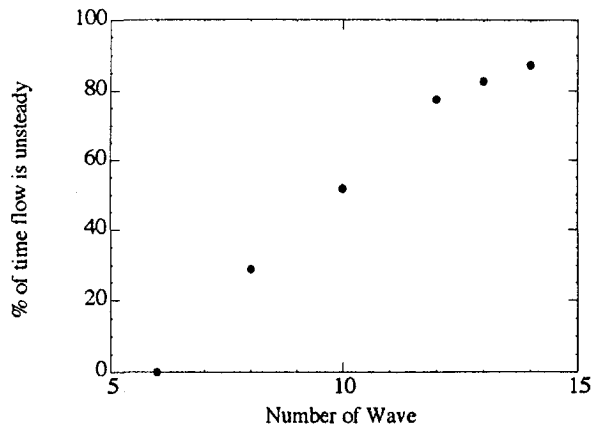


Fig. 7 Percentage of time flow is unsteady as a function of location at $Re = 300$

initial condition for the case of $Re = 180$. Subsequent calculations at higher Reynolds numbers were started from the field values obtained at the lower Reynolds number. In each case, further time integration was continued for more than 200 non-dimensional time units. This was much greater than the average time required for a disturbance to be convected from inlet to the exit. During each simulation, axial velocity (u) has been monitored in each wavy section at points with local co-ordinates of $(\lambda/2, 0.75H_{max})$. The surface area averaged pressure coefficient and Nusselt number for each wavy section are also calculated at each time instant and further averaged in time.

Computations were performed on a Silicon Graphics Power Challenge Array (PCA). The computer code took around 12 CPU hours for 5000 time steps on the 1024×64 grid using four PCA processors (i.e., $17.5 \mu s/node/time$ step).

4 Results

Calculations were performed for several Reynolds numbers from a low value up to 600. Here we present results for $Re = 180, 300, 360$ and 420 . This set provides a representative sampling of the developing flow in a wavy passage in the regime where transition to an oscillatory state takes place. Figure 2 shows the u -velocity time signal in wave 14 for $Re = 180$. At $Re = 180$, it is evident from the time signals that the flow becomes steady throughout the entire passage immediately after the initial conditions are convected out of the channel. A number of locations within each cavity of a wavy section were monitored. Flow unsteadiness is observed to be identical at all the monitoring points outside the core of the channel. The streamline plot in Fig. 3 shows single trapped vortices in the cavities and almost perfectly straight core flow. These are expected patterns for steady flow in a wavy passage. As a result, the warm core fluid passes straight through the center of the passage, without significantly mixing with the cooler fluid near the walls. This shows that when the flow is steady, only minimal increases in heat transfer rates can be expected, due to the fact that the cooler fluid becomes isolated in the large recirculating vortices that fill the two furrows of each wave.

The flow field at $Re = 240$ is also observed to be steady. The observed results are not discussed here, as they are very similar to those at $Re = 180$. At $Re = 300$, however, the flow behavior

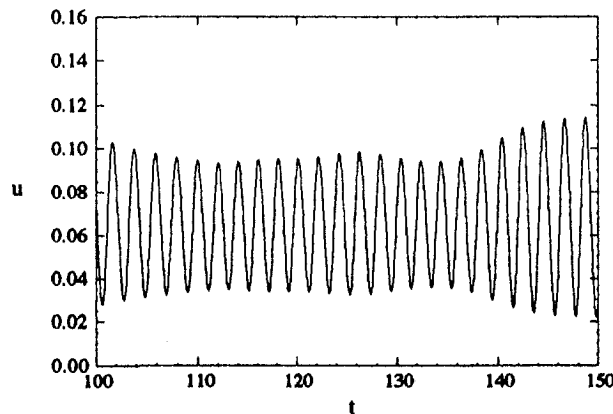


Fig. 8(a)

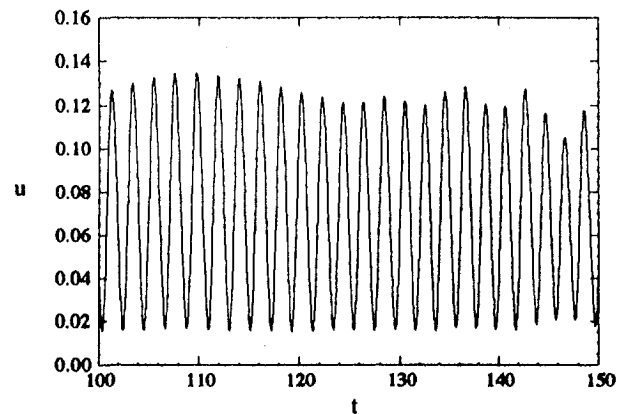


Fig. 8(b)

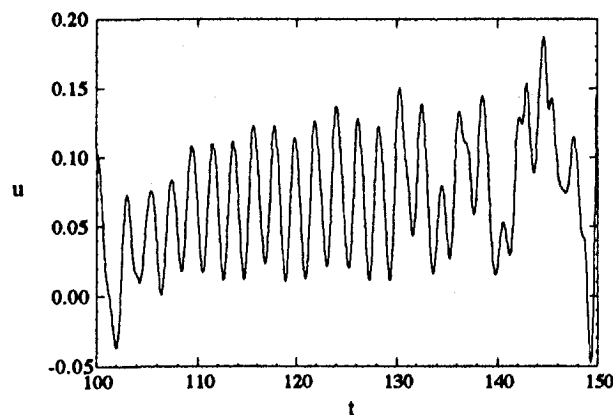


Fig. 8(c)

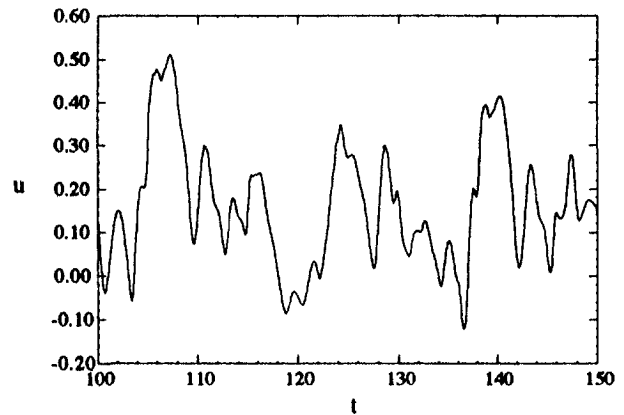


Fig. 8(d)

Fig. 8 Time signals for u -velocity at $Re = 360$: (a) wavy section 8; (b) wavy section 10; (c) wavy section 12; (d) wavy section 14

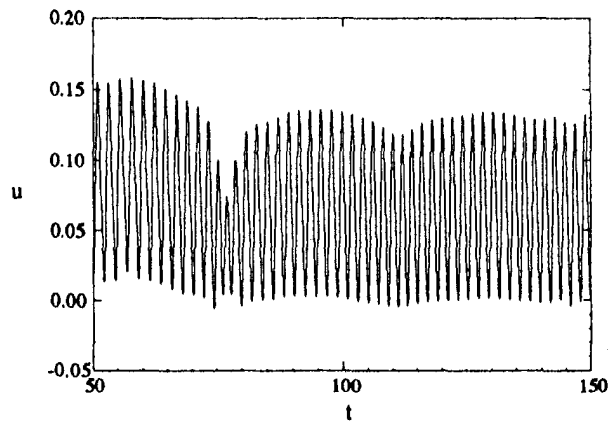


Fig. 9(a)

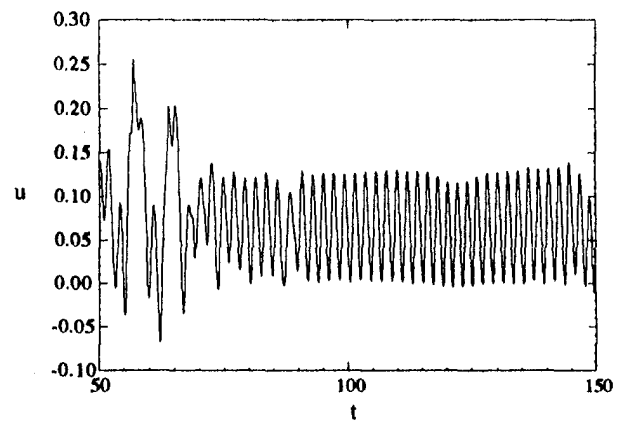


Fig. 9(b)

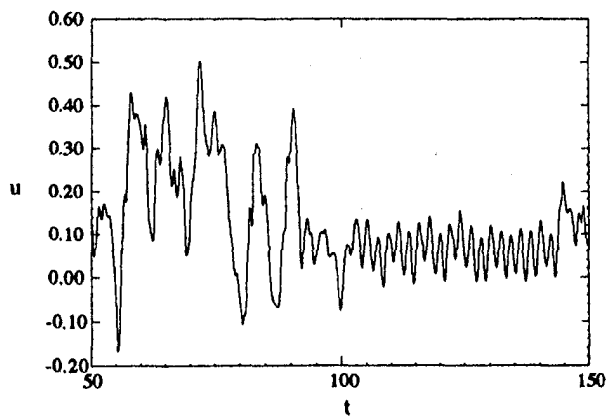


Fig. 9(c)

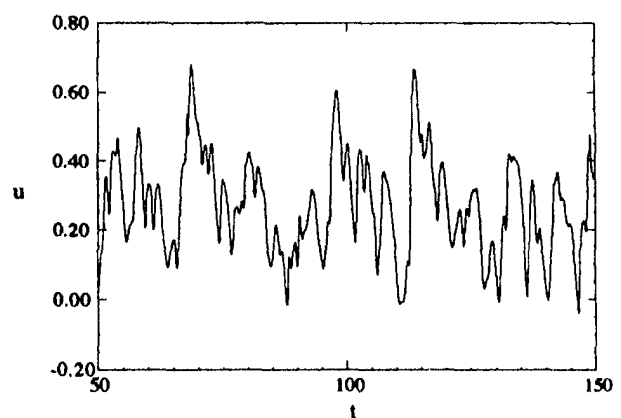


Fig. 9(d)

Fig. 9 Time signals for u -velocity at $Re = 420$: (a) wavy section 8; (b) wavy section 10; (c) wavy section 12; (d) wavy section 14

becomes more interesting. Figure 4 shows signals of u -velocity in waves 8, 10, 12, and 14. We observe that an interesting pattern develops at this Reynolds number. We see that for certain periods of time, the time signal does not fluctuate significantly, and the flow appears to be steady, leading to flow and temperature profiles similar to those at $Re = 180$. However, suddenly, large oscillations appear in the time signals. The resulting flow pattern contains multiple vortices and divergent core flow, especially in the last two waves of the passage, as shown in Fig. 5. The temperature profile in Fig. 6 shows enhanced mixing of the core and near-wall fluids. This unsteady flow lasts for a certain amount of time, until the oscillations quickly die out, and the flow becomes steady again. After awhile, the cycle repeats itself. Thus, beginning eight waves downstream and continuing at least through the fourteenth wave, the flow is "intermittently" unsteady. It is unsteady for a certain period of time, and steady for the rest of the time. It can be also seen that the time extents over which the flow is unsteady increase with downstream position. In the fourteenth wave, the flow is unsteady at all times.

From these results of intermittent unsteadiness, we can compute a fraction of time the flow is unsteady in each wave. The flow was considered to be unsteady when the fluctuations were greater than 3–4 percent of the steady value. Figure 7 shows such a percentage of time at $Re = 300$, plotted as a function of streamwise location. It can be seen that the flow is completely steady through the sixth wave but the percentage of unsteady period increases to 80% by the 12th wave. This is an interesting phenomenon, as the heat transfer enhancement is directly related to the unsteadiness and no enhancement is observed when the flow is steady. Such an intermittent phenomenon was also observed by Greiner et al. (1990) for flow in a channel with a triangular grooved wall at a comparable

Reynolds number. Further, the intermittency only existed for a small range of Reynolds number.

At $Re = 360$, the flow was observed to be oscillatory, beginning at the fifth wave. The time signals, shown in Figure 8, do not display the intermittent behavior seen in the $Re = 300$ case. As before, the amplitude of the oscillations increases as the flow progresses downstream. Through the tenth wave, the oscillations are fundamentally periodic with a single dominant frequency, but further downstream, multiple frequencies are present in the signals. The instantaneous streamlines and isotherms are similar to those shown in Figures 5 and 6. The Strouhal number corresponding to the dominating frequency (from wave 8 downstream) is 0.433. This compares well with the range of value of 0.428–0.436 reported by Guzman and Amon (1994) for Re range of 180–750.

Finally, at $Re = 420$, the flow is unsteady beginning at the third wave. And once again, the oscillations are completely self-sustaining downstream of this point with their amplitude increasing as the flow proceeds downstream. The time signals in Fig. 9 exhibit patterns similar to those of the $Re = 360$ case. The flow is basically periodic with a single frequency until the eighth wave, but multiple frequencies exist downstream of this point. As before, the instantaneous streamline plots (not shown here) exhibit multiple vortices and divergent core flow that result from the unsteady nature of the flow. This instability is absolute, as it is self-sustaining, and does not convect out of the flow domain.

The time-averaged values for the pressure coefficient and Nusselt number averaged across each wavelength are plotted in Figs. 10 and 11, respectively, as a function of the number of the wave counted from the inlet, for all four Reynolds numbers investigated. The local Nusselt number is defined as:

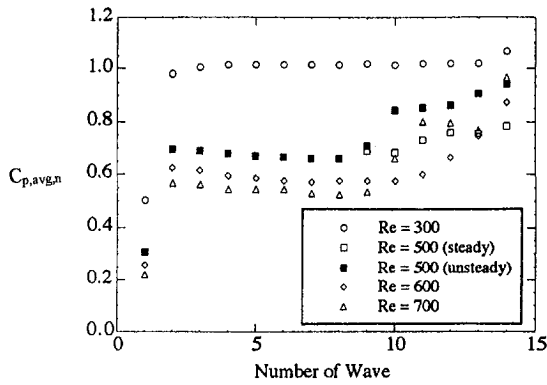


Fig. 10 Time-averaged pressure coefficient averaged across each wavelength as a function of location

$$\text{Nu}(\xi) = \frac{hD_h}{k} = \frac{D_h(\partial\theta/\partial\eta)_w}{\theta_m(\xi)} \quad (1)$$

where, $D_h = (H_{\min} + H_{\max})$ is taken to be the hydraulic diameter. The average Nusselt number over a single wavelength is calculated by integrating the local values:

$$\text{Nu}_{\text{avg}} = \frac{\int_{C_n} \text{Nu}(\xi) d\xi}{\int_{C_n} d\xi} \quad (2)$$

where C_n represents the curve length of the n th wave after the inlet section. The pressure coefficient ($C_{p,\text{avg},n}$) is calculated from the cross-sectional averaged pressure drop across a single wavelength. Thus,

$$C_{p,\text{avg},n} = \frac{\overline{P_{\text{upstream},n}} - \overline{P_{\text{downstream},n}}}{(1/2)\rho u_{\text{avg},in}^2} \quad (3)$$

where the overbars on the pressure imply averaging over the cross-sectional area of the flow at the respective locations of the wave, n . Note that two sets of data are presented for $\text{Re} = 300$. One set of quantities was tabulated during the time the flow was steady, and the other set was obtained while it was unsteady. In Fig. 10 $C_{p,\text{avg},n}$ is very low in the first wave of the channel. Because the boundary layers have developed through the straight section, the velocity profile entering the first wave is more parabolic than the flow entering the subsequent waves. By the second wave, the pressure coefficient has reached a value that remains constant for

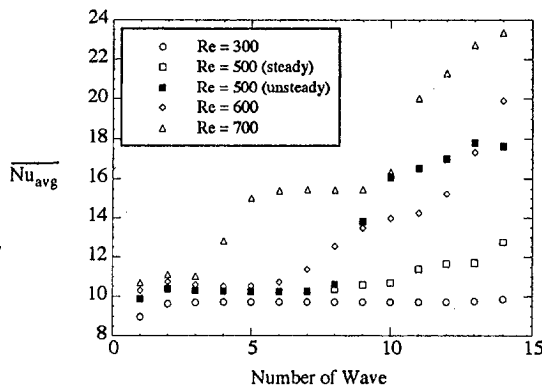


Fig. 11 Time averaged Nusselt number averaged across each wavelength as a function of location

Table 1 Location of onset of unsteadiness as a function of Reynolds number

Reynolds number	First wave of unsteadiness
180	>14
240	>14
300	8
360	5
420	3

all downstream waves, as long as the flow is steady. Thus, for $\text{Re} = 180$, $C_{p,\text{avg},n}$ is basically the same for each wave from wave 2 through the final wave of the passage. As expected in the steady regime, $C_{p,\text{avg},n}$ decreases with increase of Reynolds number. For higher Re , however, there is a noticeable increase in the pressure coefficient once the flow becomes unsteady.

Figure 11 reveals how unsteady flow in a wavy channel can enhance heat transfer, while steady flow in the same geometry produces only minimal increase. For $\text{Re} = 180$, and the steady case at $\text{Re} = 300$, the Nusselt number remains virtually constant throughout the passage, beginning at the second wave from the inlet. The slight increases in the last few waves for the $\text{Re} = 300$ steady case is due to the fact that in these locations, the flow is still slightly unsteady even during the time when the flow is considered "steady." However, the fluctuations are small compared to those occurring when the flow is fully unsteady. For steady flow at $\text{Re} = 180$ and 300, the values of Nu_{avg} are not substantially greater than the $\text{Nu} = 7.54$ value corresponding to a straight channel. When the flow is unsteady at $\text{Re} = 300$, the Nusselt number increases significantly starting from the eighth wave, which is the onset location for unsteady flow. At $\text{Re} = 360$, in the portion of the passage where the flow is steady, the Nusselt number remains constant from wave to wave, and is only slightly higher than for steady flow at $\text{Re} = 300$. However, once the flow becomes unsteady, beginning around the sixth wave, the value of Nu_{avg} increases with downstream distance. This rate of increase becomes larger around the twelfth wave as the oscillations exhibit markedly increased amplitudes, accompanied by multiple frequencies. By the end of the wavy passage, the time-averaged Nusselt number is almost twice as large as the value in the waves near the inlet where the flow is completely steady. At $\text{Re} = 420$, the Nu variation is similar to that for $\text{Re} = 360$, but now the unsteadiness is onset in the third wave. Thus, the Nusselt number increases from wave 4. The values of Nu_{avg} are higher throughout the passage, exceeding a value of 23 by the fourteenth wave. This is in good agreement with the value obtained by Wang and Vanka (1995) for fully developed flow in a periodic domain.

Comparing the Nusselt number plot in Fig. 11 with Table 1, which gives the onset location for each Re examined here, one can see that the initial increases in Nu_{avg} coincide exactly with the point where the flow becomes unsteady.

5 Summary

In this paper, we have presented numerical results on developing flow and heat transfer characteristics in a furrowed wavy channel. The wavy passage consisted of 14 waves with one inlet and one outlet section. The flow was assumed to be two-dimensional, and the Navier-Stokes equations governing a time-dependent flow were numerically solved. At low Reynolds numbers, the flow in the wavy passage is steady, characterized by steady separation bubbles in the troughs of the waves. However, as the Reynolds number is increased beyond a modest value, the flow becomes unsteady, with the rolling up of the shear layers on the channel walls. When the flow becomes unsteady, there is increased mixing between the core and near-wall fluids, resulting in enhanced heat transfer rates and pressure drops. The current simulations have assumed the flow to be two-dimensional. However, the flow will indeed become three-dimensional at some of the high Reynolds

numbers considered here. We are of the opinion that the relative magnitudes of the three-dimensional effects over and above the effects of unsteadiness will be small. Nevertheless, such three-dimensional studies must be considered in future.

Acknowledgments

This research was supported in part by the Air-Conditioning and Refrigeration Center at University of Illinois, Urbana-Champaign. Computations were performed at NCSA, Illinois.

References

- Ali, M. M., and Ramadhyani, S., 1992, "Experiments on Convective Heat Transfer in Corrugated Channels," *Experimental Heat Transfer*, Vol. 5, pp. 175-193.
- Amon, C. H., Guzmán, A. M., and Morel, B., 1996, "Lagrangian Chaos, Eulerian Chaos, and Mixing Enhancement in Converging-Diverging Channel Flows," *Physics of Fluids*, Vol. 8, pp. 1192-1206.
- Ghaddar, N., Korczak, K. Z., Mikic, B. B., and Patera, A. T., 1986, "Numerical Investigation of Incompressible Flow in Grooved Channels, Part 1. Stability of Self-Sustained Oscillations," *Journal of Fluid Mechanics*, Vol. 163, pp. 99-127.
- Ghaddar, N., Magen, M., Mikic, B. B., and Patera, A. T., 1986, "Numerical Investigation of Incompressible Flow in Grooved Channels, Part 2. Resonance and Oscillatory Heat Transfer Enhancement," *Journal of Fluid Mechanics*, Vol. 168, pp. 541-567.
- Goldstein, J. L., and Sparrow, E. M., 1977, "Heat Mass Transfer Characteristics for Flow in a Corrugated Wall Channel," *ASME Journal of Heat Transfer*, Vol. 99, pp. 187-195.
- Greiner, M., Chen, R. F., and Wirtz, R. A., 1990, "Heat Transfer Augmentation Through Wall-Shape-Induced Flow Destabilization," *ASME Journal of Heat Transfer*, Vol. 112, pp. 336-341.
- Greiner, M., Spencer, G., and Fischer, P. F., 1996, "Direct Numerical Simulation of Three-Dimensional Flow and Augmented Heat Transfer in a Grooved Channel," National Heat Transfer Conference, ASME, HTD-Vol. 330, Vol. 8, pp. 125-131.
- Guzmán, A. M., and Amon, C. H., 1994, "Transition to Chaos in Converging-Diverging Channel Flows: Ruelle-Takens-Newhouse Scenario," *Physics of Fluids*, Vol. 6, pp. 1994-2002.
- Karniadakis, G. E., Mikic, B. B., and Patera, A. T., 1988, "Minimum-Dissipation Transport Enhancement by Flow Destabilization: Reynolds Analogy Revisited," *Journal of Fluid Mechanics*, Vol. 192, pp. 365-391.
- Majumdar, D., and Amon, C. H., 1993, "Physics of Heat and Momentum Transfer in Transitional Flows in Complex Geometries," in *Heat Transfer in Turbulent Flows*, R. S. Amano, ed., ASME-HTD Vol. 246, pp. 75-83.
- Nishimura, T., Ohori, Y., and Kawamura, Y., 1984, "Flow Characteristics in a Channel with Symmetric Wavy Wall for Steady Flow," *Journal of Chemical Engineering Japan*, Vol. 17, pp. 466-471.
- Nishimura, T., Murakami, S., Arakawa, S., and Kawamura, Y., 1985, "Mass Transfer Characteristics in a Channel with Symmetric Wavy Wall for Steady Flow," *Journal of Chemical Engineering Japan*, Vol. 18, pp. 550-555.
- Nishimura, T., Kajimoto, Y., and Kawamura, Y., 1986, "Mass Transfer Enhancement in Channels with a Wavy Wall," *Journal of Chemical Engineering Japan*, Vol. 19, pp. 142-144.
- O'Brien, J. E., and Sparrow, E. M., 1982, "Corrugated-duct Heat Transfer, Pressure Drop, and Flow Visualization," *ASME Journal of Heat Transfer*, Vol. 104, pp. 410-416.
- Ralph, M. E., 1986, "Oscillatory Flows in Wavy-walled Tubes," *Journal of Fluid Mechanics*, Vol. 168, pp. 515-540.
- Schatz, M. F., Tagg, R. P., Swinney, H. L., Fischer, P. F., and Patera, A. T., 1991, "Supercritical Transition in Plane Channel Flow with Spatially Periodic Perturbations," *Physical Review Letters*, Vol. 66, No. 12, pp. 1579-1582.
- Sobey, I. J., 1980, "On Flow Through Furrowed Channels, Part 1: Calculated Flow Patterns," *Journal of Fluid Mechanics*, Vol. 96, No. 1, pp. 1-26.
- Sobey, I. J., 1982, "The Occurrence of Separation in Oscillatory Flow," *Journal of Fluid Mechanics*, Vol. 134, pp. 247-257.
- Sparrow, E. M., and Comb, J. W., 1983, "Effect of Interwall Spacing and Fluid Flow Inlet Conditions on Corrugated-wall Heat Exchanger," *International Journal of Heat and Mass Transfer*, Vol. 26, pp. 993-1005.
- Stephanoff, K. D., Sobey, I. J., and Bellhouse, B. J., 1980, "On Flow through Furrowed Channels, Part 2. Observed Flow Patterns," *Journal of Fluid Mechanics*, Vol. 96, pp. 27-32.
- Stephanoff, K. D., 1986, "Self-excited Shear Layer Oscillations in a Multi-Cavity Channel with a Steady Mean Velocity," *ASME JOURNAL OF FLUIDS ENGINEERING*, Vol. 108, pp. 338-342.
- Stone, K. M., 1997, *Numerical Study of Flow and Heat Transfer in Wavy Passages*, M.S. thesis, University of Illinois at Urbana-Champaign, IL.
- Wang, G., and Vanka, S. P., 1995, "Convective Heat Transfer in Periodic Wavy Passages," *International Journal of Heat and Mass Transfer*, Vol. 18, No. 17, pp. 3219-3230.

J.-C. Lin
Research Associate.

D. Rockwell
Paul B. Reinhold Professor.

Department of Mechanical Engineering
and Mechanics,
354 Packard Laboratory,
19 Memorial Drive West,
Lehigh University,
Bethlehem, PA 18015
e-mail: dor0@lehigh.edu

Cinema PIV and Its Application to Impinging Vortex Systems¹

An integrated cinema PIV-pressure measurement system allows detailed insight into impinging vortex systems. It employs a high framing rate camera in conjunction with a scanning-laser version of high-image-density particle image velocimetry, thereby generating space-time representations of the flow. Simultaneously, instantaneous surface pressures are acquired. This approach allows the instantaneous velocity and vorticity fields to be related to the induced loading. The instantaneous structure of vortex systems arising from an initially turbulent jet impinging upon an edge and an initially turbulent shear layer past a cavity are quantitatively characterized for the first time. In addition, distinctive mechanisms of vortex-wedge and vortex-corner interactions are related to the occurrence of peak values of instantaneous surface pressure.

Introduction

Rapid development of particle image velocimetry has led to techniques for imaging instantaneous velocity distributions over an entire plane of the flow. These approaches are summarized by Adrian (1991), who addresses the major concepts and parameters that dictate the effectiveness of particle imaging techniques. Lin and Rockwell (1994) describe a cinema technique of high-image-density particle image velocimetry (PIV), which was applied to the turbulent near-wake of a circular cylinder. The flow speed was sufficiently high that a framing camera, operating at sixty frames per second, was required to attain adequate temporal resolution. At this framing rate, a laser scanning technique, described by Rockwell et al. (1993), is particularly effective for illumination of the seeding particles. As demonstrated in the subsequent work of Lin et al. (1995, 1996), use of this cinema technique, which provides projections of streamwise vorticity in the near-wake, leads to a three-dimensional space-time volume representation of the near-wake of a cylinder. Using an analogous approach, Brede et al. (1996) demonstrated that pseudo three-dimensional space-time images of the instantaneous streamwise vorticity, similar to those of the foregoing, could be obtained from cinema PIV based on a standard 35 mm motor-drive camera. This simplification was possible because the flow speed was low, and thereby the characteristic time scales of the near-wake were relatively long. Further studies using cinema PIV are described by Oakley et al. (1996) and Loth and Stedl (1999), who employed an approach similar to that of Lin and Rockwell (1994) to characterize the turbulent structure of a planar mixing layer.

A cinema technique of particle image velocimetry provides knowledge of the space-time evolution of flow patterns over a given plane in the flow, thereby yielding insight into the physical origin of unsteadiness of flow-structure interactions. For example, it is possible to determine the variation of unsteady events that produce fluctuations of surface pressure or forces on a body such as a circular cylinder. These characterizations can be linked to theoretical concepts, in order to provide a means of identifying contributions of vorticity concentrations to the unsteady forces. For example, it is known from the theoretical frameworks described by Wu (1981) and Lighthill (1986) that the loading on a body is directly linked to the time rate of change of the vorticity field surrounding the body, e.g., an airfoil or a circular cylinder. In

fact, Lin and Rockwell (1996), Noca et al. (1997), Noca (1997), and Unal et al. (1997) show how quantitative knowledge of the flow patterns can lead to approximation of the unsteady forces acting on a circular cylinder via either vorticity- or momentum-based formulations.

In contrast to classical bluff-body configurations, very little effort has been devoted to quantitative imaging of vortex interactions with a sharp leading-edge, such as a wedge or corner, as reviewed by Rockwell (1998). Typical experimental approaches have involved smoke or dye visualization leading to qualitative representations of the complex vortex-edge interactions; in some cases, time-dependent measurements of the surface pressure or force have been undertaken. Quantitative characterization, via laser-Doppler anemometry, of the distortion of vorticity fields incident upon, and along, surfaces of elliptically-shaped leading-edges and airfoils are described by Gursul and Rockwell (1990) and Wilder (1992). A similar approach that characterizes the incident and shed vorticity from a thin, short plate aligned with the direction of the flow is described by Swiryczuk et al. (1993). In all of the foregoing approaches, concepts of phase-referencing/averaging were employed. The focus herein is on the global instantaneous features of the flow patterns.

The objectives of the present investigation are two-fold. The first is to provide full details of a cinema PIV technique integrated with a pressure measurement technique, with the aim of yielding direct correlation of instantaneous surface pressure and instantaneous patterns of velocity and vorticity. Second, it is intended to provide the first instantaneous insight, in terms of images of vortex patterns, for initially-turbulent, impinging shear layers in jet-edge and cavity configurations; correlation with instantaneous surface pressures will allow definition of the origin of peak values of the surface pressure fluctuations.

Experimental System and Techniques

All experiments were performed in one of the large-scale water channels in the fluid mechanics laboratories at Lehigh University. These water channels have a settling reservoir, honeycomb-screen arrangements, and a planar contraction preceding the main test section of the channel, in order to maintain the turbulence intensity below 0.1%. The cross-sectional dimensions of the main test sections are 2 ft \times 2 ft for the jet-edge system and 3 ft \times 2 ft for the cavity system. In the following, the essential features of the test section inserts for the jet-edge and cavity systems are briefly described.

Jet-Edge System. A planar jet was generated from a channel, which had a length of 125 inches and a height of 1 in., correspond-

¹ An abbreviated version of this manuscript appears in Proceedings of ASME Fluids Engineering Division Summer Meeting, June 21–25, 1998, Washington, D.C.; manuscript number FEDSM 98-5270.

Contributed by the Fluids Engineering Division for publication in the JOURNAL OF FLUIDS ENGINEERING. Manuscript received by the Fluids Engineering Division October 28, 1998; revised manuscript received July 27, 1999. Associate Technical Editor: D. R. Williams.

ing to a channel length to height ratio of 125:1; the channel span to height ratio was 18:1. It was located in the main test section described in the foregoing. Boundary layer tripping was employed at the inlet of the channel. Extensive evaluation of the turbulence statistics, including the rms values of velocity fluctuation components and the Reynolds stresses, showed that the turbulent channel flow was fully developed at the Reynolds number of interest in this investigation, $Re = 5,472$, based on the half-channel height.

Cavity System. The cavity test section, which was inserted into the main test section of the large-scale water channel, has an internal width of 18 in. and an overall length of 130 in. It housed a rectangular cavity 8 in. long and 4 in. deep along its bottom surface, and was bounded on either side by vertical false walls extending from the floor of the water channel to a height equal to the upper edge of the channel test section. This arrangement was preceded by two sequential contractions that optimize the inlet flow to the cavity test section. Operation of the system at a free-stream velocity of $U_o = 10.5$ in/s gave a Reynolds number based on momentum thickness θ , i.e., $Re_\theta = 1,371$. Extensive characterization of the rms velocity fluctuations and the Reynolds stresses across the boundary layer, using PIV image averaging, showed excellent agreement with previous documentation.

High-Image-Density PIV Technique. A laser-scanning version of high-image-density PIV, described in detail by Rockwell et al. (1993) involved use of a continuous wave Argon-ion laser having a maximum output of 25 watts. The laser beam was transmitted through an optical train, then reflected from a multi-faceted (48 or 72) rotating mirror, thereby producing a scanning laser beam at a frequency that optimizes the distances between particle images for the PIV technique. The water was seeded with metallic-coated particles having a diameter of 12 microns.

Cinema PIV images were acquired using two approaches. The first involves use of a Hulcher cinema camera, framing at rates up to forty frames per second. Images were recorded on one hundred foot spools of 35 mm film; special high resolution (300 lines/mm) film was employed. Alternately, in cases where high temporal resolution was not essential, a Canon motor-driven system was employed with high-resolution 35 mm film; the maximum framing rate attainable was nine frames per second. A central feature of the high framing rate Hulcher-based camera system employed in this investigation is its integration with simultaneous acquisition of the pressure fluctuations on the sharp leading-edge of the jet-edge system and the impingement corner of the cavity system. In both cases, high sensitivity PCB pressure transducers were employed at critical locations along the impingement surface.

An overview of the integrated system is shown in Fig. 1(a). The jet-edge system is employed for illustration; a very similar technique is employed for the cavity system. As indicated, the output from the pressure transducers is transmitted to an A/D converter, which transforms the analog pressure signals to digitized form in the central microcomputer. This host computer provides a trigger signal to the A/D converter, which transforms the analog pressure signals to digitized form in the central microcomputer. This host computer provides a trigger signal to the A/D converter and to the synchronizer. In total, three signals are transmitted from the computer to the synchronizer: the trigger signal; a start mark signal; and a stop signal. The camera on-off signal is transmitted from the synchronizer. In addition, a marker signal is also transmitted. The output from the Hulcher framing camera is a strobe signal, which passes through a pulsed delay, thereby providing a delayed trigger

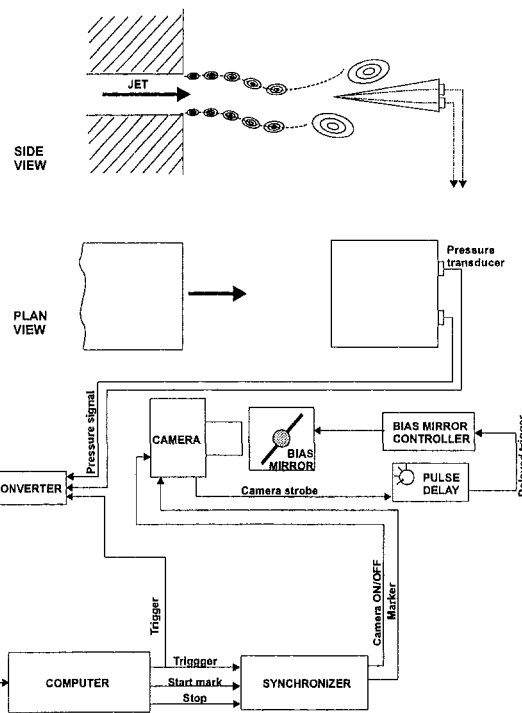


Fig. 1(a) Schematic illustrating overall system for high-image-density cinema PIV. The illustrated case of jet-edge oscillation represents a generic example of a vortex-body interaction.

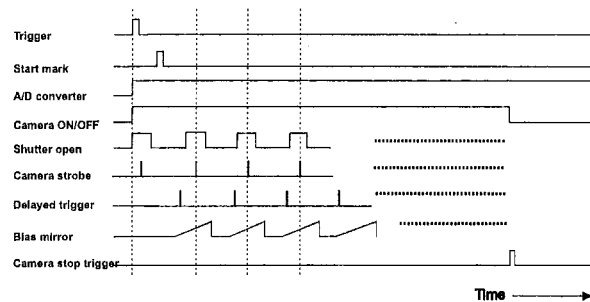


Fig. 1(b) Time histories of signals illustrated in Fig. 1(a)

signal to the bias mirror controller, which in turn drives the oscillating bias mirror, employed in front of the camera lens. This bias mirror provides a constant displacement shift to the entire particle image pattern, and thereby precludes directional ambiguity in regions of local instantaneous reverse flow.

The timing of all of the aforementioned signals between the A/D converter, the computer, the synchronizer, the camera and the bias mirror controller are shown schematically in Fig. 1(b).

The images of particle patterns obtained using either of the foregoing cinema techniques were digitized using a Nikon digitizing system at a resolution of 125 pixels per millimeter. The velocity field was calculated using a single-frame, cross-correlation technique. A standard, fifty percent overlap of the interrogation area was employed. Interrogation windows ranging from 84×84 pixels to 90×90 pixels were employed to yield a given velocity vector. With the range of lens magnification from

Nomenclature

U_o = free-stream velocity

Re_θ = Reynolds number based on θ

θ = momentum thickness

δt = time increment

T = period of oscillation

\bar{U}_m = time-averaged maximum (centerline) velocity

M = magnification factor

A/D = analog to digital

$M = 1:7.75$ to $1:5.78$, this yielded effective grid sizes Δ in the plane of the laser sheet ranging from 1.92 to 2.79 mm. The seeding density was sufficiently high that the high-image-density criterion was satisfied for the sizes of interrogation windows employed herein. Typically, a total of approximately 60 particle images were contained within each interrogation window. This number of particle images well exceeds the dimensionless criterion for high image density (Adrian, 1991); moreover, it optimizes the sharpness of correlation peaks.

Cinema Imaging of Jet-Edge Oscillations

Representative excerpts from the cinema sequence of the jet-edge oscillation are illustrated in the form of velocity and vorticity fields in Figs. 2(a) and 2(b). In this case, the framing rate of the image acquisition was forty frames per second, corresponding to a time resolution between images of $\delta t/T = 0.03$, in which T is the period of the jet oscillation. This sequence of images corresponds to the occurrence of maximum-negative pressure p_u on the upper surface and maximum-positive pressure p_l on the lower surface of the impingement edge. In image 171 of Fig. 2(a), large-scale swirl patterns of velocity vectors are evident on the lower side of the jet at a streamwise position upstream of the impingement edge, and on the upper side of the jet at a location directly above the impingement edge. Temporal development of these swirl patterns in images 172 through 174 shows their downstream progression. Simultaneously, the central portion of the jet impinges upon the tip of the leading-edge in image 171, and deflects downwards in subsequent images through image 174. Close inspection of the patterns of velocity vectors at the edges of the jet, especially in the vicinity of the nozzle exit, indicates small-scale, nevertheless periodic, irregularities, which suggest the existence of small-scale concentrations of vorticity.

Indeed, as shown in the corresponding patterns of instantaneous vorticity in Fig. 2(b), ordered patterns of small-scale vorticity are evident in the shear layers emanating from the channel exit. Their identity is preserved along the entire extent of the jet. Moreover, large-scale clusters of vorticity are evident, approximately in accord with the location of the large-scale swirl patterns of velocity vectors shown in Fig. 2(a). These large-scale structures are comprised of the small-scale concentrations of vorticity evident immediately downstream of the channel exit. With increasing time, corresponding to the development of the flow in images 171 through 174, the large-scale cluster of negative (dashed line) vorticity on the lower side of the jet moves downstream beneath the impingement edge. Simultaneously, the positive cluster of vorticity above the impingement edge is severed from the positive layer of vorticity on the upper side of the jet.

Figure 3 shows an excerpt from another portion of the oscillation cycle. It compares: the instantaneous vorticity (top image); the velocity field in the laboratory reference frame (middle image); and the velocity field in a frame moving at $0.5 \bar{U}_m$ (bottom image), where \bar{U}_m is the averaged centerline velocity at the nozzle exit. The instantaneous pressure signals at this instant are indicated by the solid dots. In addition, the locations of the pressure taps on the impingement edge are designated. It is evident that, at this instant, the pressure on the top surface is at its maximum-negative value, while that on the bottom surface is maximum-positive. This maximum-negative pressure on the top surface of the edge corresponds to passage of the large-scale concentration of vorticity and deflection of the upstream region of the vorticity layer immediately beneath the tip of the edge. The corresponding distributions of instantaneous velocity in the laboratory and moving reference frames show indications of the small-scale concentrations of vorticity in the region immediately downstream of the channel exit.

Cinema Imaging of Cavity Oscillations

Instantaneous patterns of velocity in the laboratory frame and the corresponding instantaneous distribution of vorticity are given

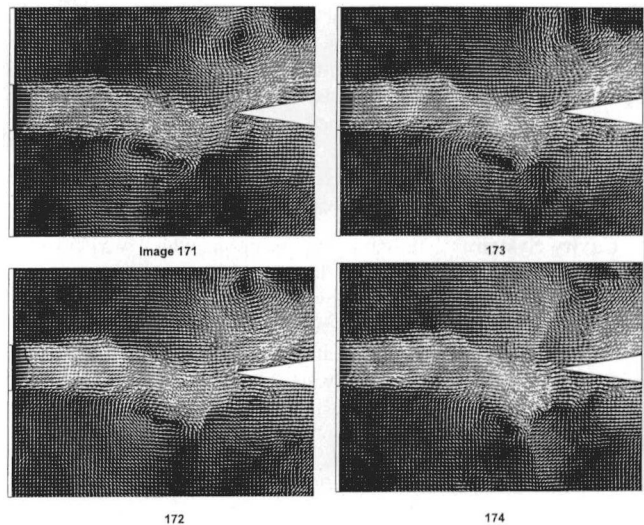


Fig. 2(a) Excerpts from a highly time-resolved cinema sequence of a jet-edge oscillation showing the instantaneous velocity field leading to occurrence of maximum negative pressure p_u on the upper surface and maximum positive pressure p_l on the lower surface of the edge. Time resolution between images is $\delta t/T = 0.03$, in which T is the period of the jet oscillation. Fully developed turbulent flow exists at the exit of the channel, from which the jet is formed.

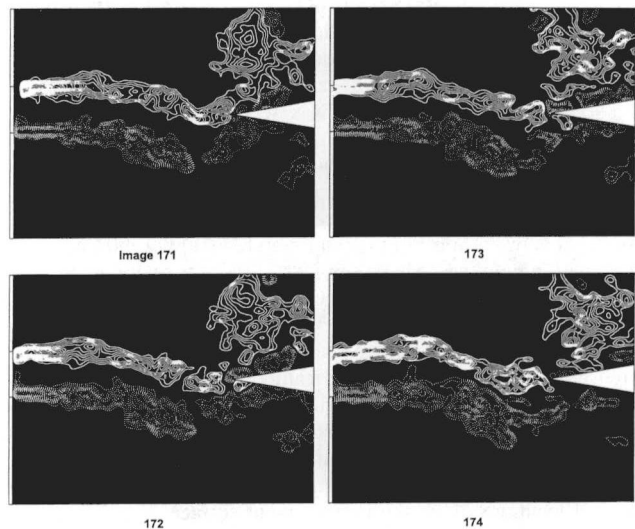


Fig. 2(b) Same as Fig. 2(a), except patterns of instantaneous positive (red) and negative (yellow) vorticity are shown. Minimum and incremental values of vorticity are $\omega_{\min} = 10 \text{ sec}^{-1}$ and $\Delta\omega = 5 \text{ s}^{-1}$.

in Fig. 4(a) for the case of self-excited oscillations arising from turbulent inflow past a cavity. The pattern of instantaneous velocity vectors shows a jet-like flow, oriented in the upward direction immediately upstream of the corner of the cavity. In the corresponding distribution of instantaneous vorticity, this region represents a large-scale concentration of vorticity that has been distorted by its impingement upon the corner and is moving up and out of the cavity. At this instant, maximum-negative pressure occurs at the cavity corner, as indicated by the dot on the instantaneous pressure trace shown in the inset.

Upstream of this large-scale concentration of vorticity at the corner, a number of small-scale concentrations are evident. These small-scale concentrations are also suggested by the local swirl patterns of velocity vectors in the top velocity image. Within the cavity, the vorticity patterns show very little, if any, indication of pronounced vorticity concentrations, suggesting that the recirculation region is nearly vorticity free. In contrast, the pattern of velocity vectors shows a very large-scale swirl emanating from the

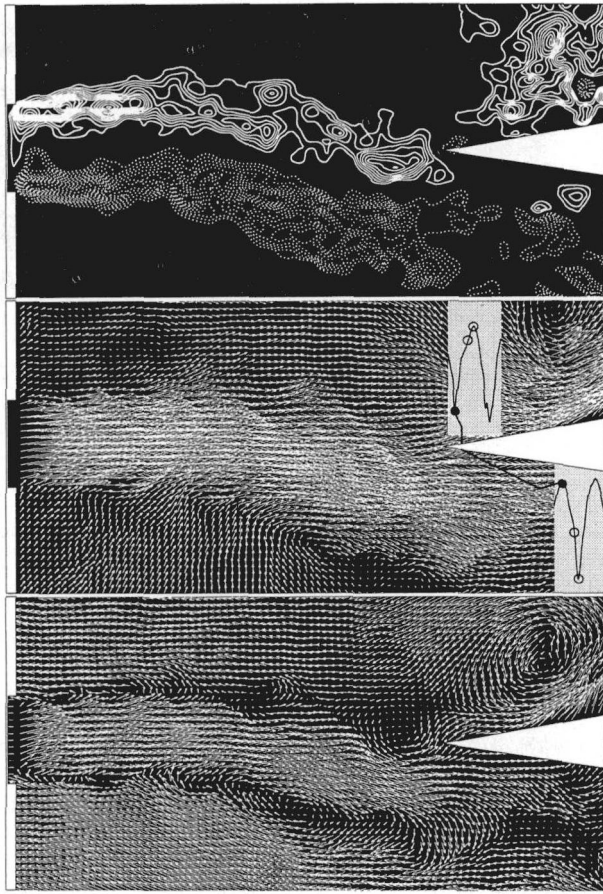


Fig. 3 Comparison of vorticity, velocity in the laboratory frame and velocity in a frame moving at $0.50 U_m$ excerpted from cinema sequence of the jet-edge oscillation. Minimum and incremental values of vorticity are $\omega_{\min} = 10 \text{ s}^{-1}$ and $\Delta\omega = 5 \text{ s}^{-1}$. Also shown are the instantaneous pressure signals on the upper and lower surfaces of the edge. The instant corresponding to this set of images is indicated by the solid circle.

corner region of the cavity; it progresses along the vertical, then horizontal walls, of the cavity, and finally feeds back to and modulates the sensitive region of the cavity shear layer immediately downstream of separation.

The detailed structure of the velocity field along the mouth of the cavity, extending from the leading- to the trailing-corner, is indicated in Fig. 4(b). The three images of velocity correspond respectively to reference frames moving at $0, 0.25$ and $0.50 U_\infty$, in which U_∞ is the freestream velocity. The small-scale vortical structures, in the initially-developing region of the shear layer downstream of the leading-corner, are particularly evident in the moving reference frames. Moreover, the vortical, or swirl nature of the large-scale concentration of vorticity immediately upstream of the corner, already shown in the pattern of large-scale vorticity in Fig. 4(a), is represented as a large-scale swirl pattern of velocity vectors in the pattern of velocity in the frame at $0.5 U_\infty$.

Concluding Remarks

A cinema version of high-image-density particle image velocimetry, integrated with a technique for measuring unsteady surface pressure, is described in detail. This approach allows acquisition of a series of instantaneous images, adequately resolved in time, to provide insight into the origin of the instantaneous surface pressure on an impingement edge or corner. It is demonstrated that organized, large-scale vortical structures can emerge from an initially turbulent shear flow in presence of upstream influence arising from impingement upon

a wedge or corner. In addition, it is possible to define the mechanisms giving rise to peak values of surface pressure fluctuations. They are distinctly different for jet-edge and shear layer-corner interactions. For the former, a combination of passage of a large-scale cluster of vorticity, in conjunction with

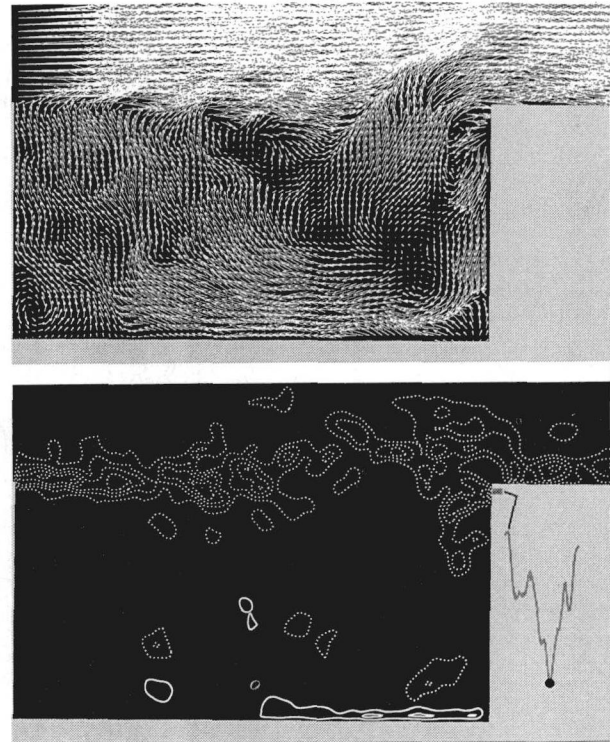


Fig. 4(a) Instantaneous distributions of velocity and vorticity during cavity oscillation in a mode corresponding approximately to the subharmonic frequency $\beta/2$ of the most amplified component β of the cavity shear layer. At the instant shown, the pressure at the corner has its maximum negative value. Minimum and incremental values of vorticity is $\omega_{\min} = 10 \text{ s}^{-1}$ and $\Delta\omega = 5 \text{ s}^{-1}$.

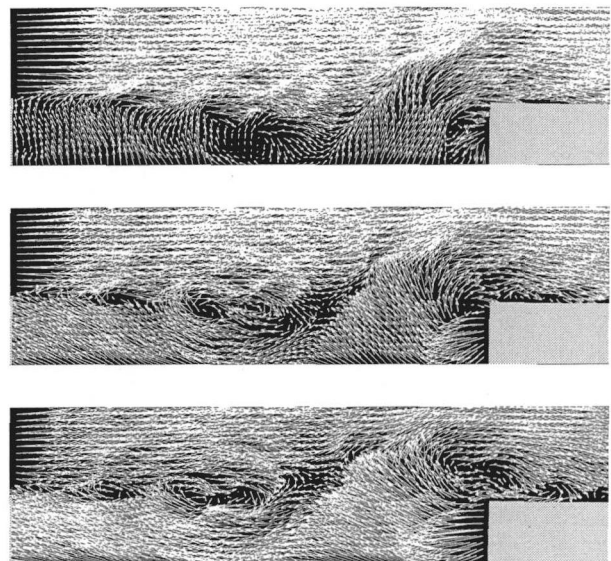


Fig. 4(b) Instantaneous distributions of velocity and vorticity during cavity oscillation in a mode corresponding approximately to the subharmonic frequency $\beta/2$ of the most amplified frequency β of the cavity shear layer. At the instant shown, the instantaneous pressure at the corner has its maximum negative value. The velocity field is shown in reference frames moving at 0.25 and $0.50 U_\infty$, in which U_∞ is the freestream velocity. These images correspond to Fig. 4(a).

transverse deflection of the jet toward the opposite side of the edge, induces a negative spike of the instantaneous pressure. On the other hand, for the latter, coincidence of the approximate center of a large-scale concentration of vorticity with the impingement corner of the cavity, while the shear layer deflects away from the corner, induces the negative spike. For both the jet-edge and cavity configurations, the flow conditions and geometry lead to generation of single, large-scale clusters of vorticity that interact with the edge or corner. It is possible, however, that for longer geometries, multiple, rather than single, vortical structures may evolve. As a consequence, the interrelationship between incident patterns of vorticity and induced surface pressure may become more complex.

Another issue concerns the degree of repetitiveness and statistical significance of the vortex-edge/corner interactions in relation to the surface pressure signatures. Whereas the jet-edge system exhibited highly repetitive vortex formation and pressure signatures, those of the cavity system were modulated, yet organized. The instantaneous relationships between distortions of concentrations of vorticity incident upon an edge or corner and the induced surface pressure are addressed using theoretical/numerical concepts and qualitative flow visualization in the works summarized by Rockwell (1983). The present observations based on quantitative visualization are in accord with these investigations. Among the possibilities for further characterizing the statistical significance of the instantaneous vortical structures is determination of the conditional average using linear stochastic estimation, as suggested by a referee. This approach, as well as others that exploit the space-time features of the cinema images, are currently under consideration.

Acknowledgments

The authors gratefully acknowledge the support of the National Science Foundation, the Office of Naval Research, NASA-Langley Research Center and the Volkswagen Foundation of Hanover, Germany.

References

- Adrian, R. J., 1991, "Particle Imaging Techniques for Experimental Fluid Mechanics," *Annual Review of Fluid Mechanics*, Vol. 23, pp. 261–304.
- Brede, M., Eckelmann, H., and Rockwell, D., 1996, "On Secondary Vortices in the Cylinder Wake," *Physics of Fluids*, Vol. 8, No. 8, pp. 2117–2124.
- Gursul, I., and Rockwell, D., 1990, "Vortex Street Impinging Upon an Elliptical Leading-Edge," *Journal of Fluid Mechanics*, Vol. 211, pp. 211–242.
- Lighthill, J., 1986, "Fundamentals Concerning Wave Loading on Offshore Structures," *Journal of Fluid Mechanics*, Vol. 173, pp. 667–681.
- Lin, J.-C., and Rockwell, D., 1994, "Cinematographic System for High-Image-Density Particle Image Velocimetry," *Experiments in Fluids*, Vol. 17, pp. 110–118.
- Lin, J.-C., and Rockwell, D., 1996, "Force Identification by Vorticity Fields: Techniques Based on Flow Imaging," *Journal of Fluids and Structures*, Vol. 10, No. 6, August, pp. 663–668.
- Lin, J.-C., Vorobieff, P., and Rockwell, D., 1995, "Three-Dimensional Patterns of Streamwise Vorticity in the Turbulent Near-Wake of a Cylinder," *Journal of Fluids and Structures*, Vol. 9, pp. 231–234.
- Lin, J.-C., Vorobieff, P., and Rockwell, D., 1996, "Space-Time Imaging of a Turbulent Near-Wake by High-Image-Density Particle Image Cinematography," *Physics of Fluids*, Vol. 8, No. 2, pp. 555–564.
- Loth, E., and Stedl, J., 1999, "Taylor and Lagrangian Correlations in a Turbulent Free Shear Layer," *Experiments in Fluids*, Vol. 26, No. 1, pp. 1–15.
- Noca, F., 1997, "On the Evaluation of Time-Dependent, Fluid-Dynamic Forces on Bluff-Bodies," Ph.D. dissertation, California Institute of Technology.
- Noca, F., Shiels, D., and Jeon, D., 1997, "Measuring Instantaneous Fluid Dynamic Forces on Bodies Using Only Velocity Field and Their Derivatives," *Journal of Fluids and Structures*, Vol. 11, No. 3, April, pp. 345–350.
- Rockwell, D., 1983, "Invited Lecture: Oscillations of Impinging Shear Layers," *AIAA Journal*, Vol. 21, No. 5, pp. 645–664, 1983.
- Rockwell, D., 1998, "Vortex Body Interactions," *Annual Review of Fluid Mechanics*, Vol. 30, pp. 199–229.
- Rockwell, D., Magness, C., Towfighi, J., Akin, O., and Corcoran, T., 1993, "High-Image-Density Particle Image Velocimetry Using Laser Scanning Techniques," *Experiments in Fluids*, Vol. 14, pp. 181–192.
- Swirydzuk, J., Wilder, M. C., and Telionis, D. P., 1993, "The Interaction of Coherent Vortices with Short Plates," *ASME JOURNAL OF FLUIDS ENGINEERING*, Vol. 115, pp. 590–596.
- Unal, M. F., Lin, J.-C., and Rockwell, D., 1997, "Force Prediction by PIV Imaging: A Momentum-Based Approach," *Journal of Fluids and Structures*, Vol. 11, pp. 965–971.
- Wilder, M. C., 1992, "Airfoil-Vortex Interaction in the Wake of an Oscillating Airfoil," Ph.D. dissertation, Virginia Polytechnic Institute and State University, Blacksburg, VA.
- Wu, J. C., 1981, "Theory for Aerodynamic Force and Moment in Viscous Flows," *AIAA Journal*, Vol. 19, No. 4, Apr., pp. 432–441.

Shou-Shing Hsieh

Sun Yat-Sen Professor
of Mechanical Engineering,
Dean of Engineering,
Fellow ASME

Ping-Ju Chen
Hsiang-Jung Chin

Graduate Students.

Department of Mechanical Engineering,
National Sun Yat-Sen University,
Kaohsiung, Taiwan 80424

Turbulent Flow in a Rotating Two Pass Smooth Channel

Laser-Doppler anemometry has been applied to approximately 2-D turbulent air flow in a rotating 2 pass channel of square cross section. The axis of rotation is normal to the axis of the duct, and the flow is radially outward/inward. The duct is of finite length and the walls are isothermal. Smooth channels are experimentally conducted with rotational speeds of 100, 200, and 300 rpm with $Re_H = 5000$ and 10,000. The main features of the flow, flow separation and mean velocity as well as turbulent intensity at particular location along the downstream are presented. The measured flow field is found to be quite complex, consisting of secondary cross-stream and radially outward flows due to the Coriolis effects and centrifugal forces.

1 Introduction

Owing to the increase in the turbine inlet temperature of gas turbine engines, there is an urgent need today to obtain a higher efficiency in the engines of aircraft, ships, and many other industrial applications. Parallel with the evolution of metal working at high temperatures, several methods of cooling rotor blades have been tried and developed. Cooled blades are widely used in modern engines. Radial channel cooling is a commonly used method. These channels are often designed with two artificially roughened and two smooth walls, and the designer must know the heat transfer coefficient on each of the walls in order to predict the turbine airfoil's life correctly. Naturally, it is also necessary to know the pressure loss for such a channel. Highly sophisticated cooling techniques such as augmented internal convective cooling have been employed for turbine blades in order to maintain acceptable safety requirements under extreme operating conditions. However, it is important to understand the effect of blade rotation on local heat transfer coefficient distribution inside the serpentine coolant passages and the surface heating conditions. Furthermore, rotation of turbine blade cooling passages gives rise to Coriolis and buoyancy (centrifugal buoyancy) forces that can significantly alter the local heat transfer in the inward coolant passage from the development of cross stream (Coriolis), as well as radial (buoyant) secondary flows. Consequently, the flow, in these rotating passages is quite different as compared to that in stationary channels. It is therefore recognized that comprehensive data as well as accurate methods for predicting flow and heat transfer are important.

1.1 The Problem Setup. The present work conducts an experimental study of turbulent flow in a rotating two pass duct of square cross section. The problem schematics are shown in Fig. 1. The axis of rotation is normal to the axis of the duct and the flow is radially outward/inward. The duct walls are isothermal.

1.2 Motivation (Prakash and Zerkle, 1992). As stated earlier, effective turbine blade internal cooling is necessary to enhance the efficiency of advanced aircraft engines. In general, film cooling is imposed on the external surface of the blades, while forced-convection cooling is used inside the blades by means of a cooling passage which is also shown in Fig. 1. The internal cooling passages are connected at the ends, which lead to a serpentine flow path consisting of alternate channels of radial outflow and inflow. To promote turbulence and enhance heat transfer, ribbed type turbulators are frequently used on the walls of internal passages. In addition, since the turbine undergoes high rotation, the flow in the

internal blade cooling passage is strongly affected by the Coriolis and centrifugal forces. Consequently, the flow in these rotating passages is quite different and complex as compared to that in stationary ducts which are usually used as a stator.

Obviously, a comprehensive data base, and accurate methods (e.g., LDV, nonintrusive) for measuring flow in rotating ducts are essentially necessary for turbine cooling design.

1.3 General Physical Feature of the Problem. Flow in a radially rotating duct is characterized by the following physical features:

(a) Coriolis forces produce a secondary flow in the cross stream plane, which alters the distribution of the radial velocity. Consequently, the friction at the walls is modified as compared to a stationary channel. For radial outward (inward) flow in a square duct, the Coriolis force leads to two symmetric cross-stream vortices, which are directed from the leading (trailing) to the trailing (leading) face near the center and vice versa near the side walls. Since such a crossflow transports high momentum fluid from the center to the trailing (leading) face, the wall friction increases over the trailing (leading) face and decreases over the leading (trailing) face. However, since the present experiments are operated adiabatically, the centrifugal force only affects the pressure.

(b) Rotation modifies the turbulent characteristic of the flow by two major factors (i) The Coriolis generated secondary flow field significantly alters the generation and distribution of turbulent kinetic energy, (ii) The Coriolis force influences the basic stability of the turbulent boundary layers. Therefore, for square ducts, turbulence is suppressed.

1.4 Previous Studies. A number of investigators have studied the phenomena of the Coriolis force induced secondary flow. These include the analytical works by Hart (1971), Moore (1967), and Rothe and Johnston (1979), and the experimental works by Wagner and Velkoff (1972), Johnston et al. (1972). They all came to the same conclusion that, when a channel is being rotated, there would be strong secondary flows and have identified aspects of flow stability that produce streamwise-oriented vortex-like structures in the flow of rotating radial passage. However, the effect of centrifugal buoyancy force seems never mentioned until the report from Morris and Ayhan (1979, 1982). Based on their results, the buoyancy force would make a significant change in heat transfer and strongly depend on the flow direction (radially inward or radially outward flow).

Meanwhile, studies of the combined effects of Coriolis and buoyancy forces in smooth rotating channels started to emerge by such investigators as Mori et al. (1971), Johnson (1978), Morris and Ayhan (1979), Lokai and Gunchenko (1979), Morris and Ayhan (1982), Clifford et al. (1984), Iskakov and Trushin (1983), and Guidez (1989) etc. Several of them found that the combined effects would increase

Contributed by the Fluids Engineering Division for publication in the JOURNAL OF FLUIDS ENGINEERING. Manuscript received by the Fluids Engineering Division July 6, 1998; revised manuscript received September 10, 1999. Associate Technical Editor: D. R. Williams.

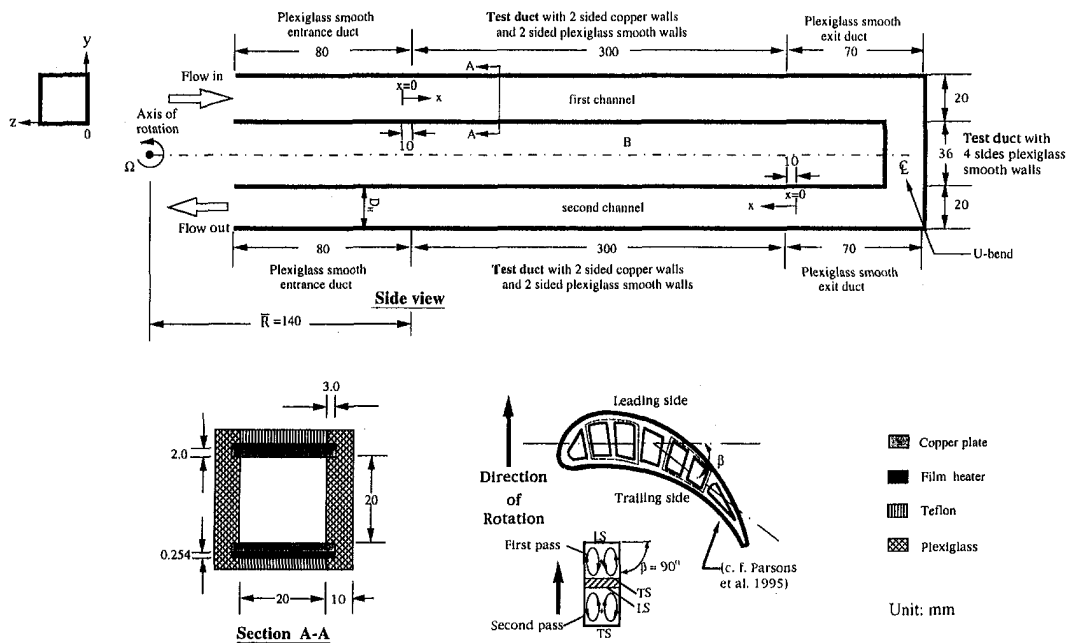


Fig. 1 Dimensions of the test section

the heat transfer coefficient, but others found the opposite results. This may be caused by the different experimental techniques used and different test conditions. These differences have been further confirmed by Wagner et al. (1992). They experimentally determined the influences of heat transfer in rotating multipass by the buoyancy and Coriolis forces. It was found that, for radially outward flow, the heat transfer coefficient on the trailing wall increases with the rotating speed. On the other hand, it decreases with rotating speed on the leading surface. During their experiments, the angle of attack of the ribs was 90 degrees. Later, they did the same experiments but with the angle of attack of 45 degrees. The same results were found except for smaller buoyancy effects. For velocity measurements, it seems there are only a few papers related to this topic. Several papers were found which are Guidez (1989) and, for numerical study, Prakash and Zerkle (1992) reported a numerical prediction of turbulent flow and heat transfer in a radially rotating square duct. Hsieh et al. (1994) presented a 3-D laminar forced convection in a rotating duct with a rib on leading wall. Recently, Dutta et al. (1996) numerically studied turbulent heat transfer in rotating smooth square ducts. Cheah et al. (1996) experimentally studied the flow development through rotating U-ducts using LDV to measure the mean and fluctuating flow field. It is found that the stationary U-bend flow is dominated by the entry and exit plane streamwise pressure gradients. Rotation is found to exert a strong influence in the development of the mean and also the fluctuation motion. Table 1 summarizes the relevant studies regarding the present study.

1.5 Scope and Objectives. This paper is a continuation of work by Hsieh and Hong (1995) on a single passage with isoflux

heating and Hsieh et al. (1997) in two pass rib channel with uneven heat flux. The test section is expanded to two passages compared to Hsieh and Hong (1995) on flow characteristics. The objectives for the study are further examination of Coriolis and centrifugal forces induced by inward and outward flow using LDV techniques for the mean velocity as well as turbulent intensity distribution during the rotation in smooth channel.

It is hoped that after LDV velocity measurements and analysis one may get more clear picture regarding flow phenomena than before. The main controlled parameters are rotational Reynolds number and channel flow Reynolds number.

2 Experimental Apparatus and Procedure

2.1 Rotating Facility. The present test facility initially was followed by Hsieh and Hong (1995) with a slight modification in flow passage. It is almost the same as that of Hsieh et al. (1996) and the extension for LDV measurements. It was comprised of a blower, a motor, a heat source, two slip ring assemblies, a LDV and a datalogger which are shown in Fig. 2.

Experimental data were taken on the leading and trailing surface of the test section in both rotating and stationary channels. Rotational speeds of 100, 200, and 300 rpm and the corresponding $Re_n = 267, 534, \text{ and } 801$ were set either in the counterclockwise or clockwise direction. The test channel geometry and operating conditions for velocity measurements are listed in Table 2. Figure 2 illustrates a stereographic view of the present experimental setup schematic.

Nomenclature

AR = aspect ratio, H/W
 D_H = hydraulic diameter, $2WH/(W + H)$
 H = height of channel
 L = test channel length
 \bar{R} = mean rotation radius
 Re_H = Reynolds number, UD_H/ν
 Re_n = rotation Reynolds number, $\Omega D_H^2/\nu$

u = streamwise velocity
 u_{max} = maximum streamwise mean velocity
 u_o = inlet mean velocity
 v = transverse velocity
 W = width of channel
 x, y, z = x, y and z ordinate

Superscript

' = fluctuation
 $+$ = dimensionless
 β = model orientation
 λ = wavelength
 θ = intersection angle of laser beams
 φ = stream function
 Ω = rotational speed

Table 1 Relevant data for experimental investigations on rotating cooling channels

Investigators	Physical Geometry	Boundary Condition	Rotation Number	Reynolds Number	Smooth/Roughened Channel	Developing/ Fully Developed	Parameters Investigated	Flow Direction	Local/Mean Nu
Guidez (1989)	Triangular Duct	UHF	$0 \leq Ro \leq 0.2$	15,000 50,000	Smooth Channel (two pass/horizontally rotating)	D/FD	Re, Ro, Ra and velocity distribution	Radially Inward/Outward Flow	Local
Wagner et al. (1991a)	Square Duct	UWT	$0 \leq Ro \leq 0.48$	12,500 50,000	Smooth Channel (single pass/orthogonally rotating)	FD	Re, Ro, $\Delta p / \rho$ $R/D, Gr / Re^2$	Radially Outward Flow	Local
Wagner et al. (1991b)	Square Duct	UWT	$0 \leq Ro \leq 0.48$	25,000	Smooth Serpentine Channel (three pass/orthogonally rotating)	D/FD	Re, Ro, $\Delta p / \rho$ $R/D, Gr / Re^2$	Radially Inward/Outward Flow	Local
Prakash and Zerkle (1992)	Square Duct	UWT	$0 \leq Ro \leq 0.48$	25,000	Smooth Channel (single pass/orthogonally rotating)	FD	Re, Ro, $\Delta p / \rho$ and velocity distribution	Radially Outward Flow	Local
Wagner et al. (1992)	Square Duct	UWT	$0 \leq Ro \leq 0.35$	25,000	Roughened Channel (three pass/orthogonally rotating)	D/FD	Re, Ro, $\Delta p / \rho$ $R/D, Gr / Re^2$	Radially Inward/Outward Flow	Local
Han and Zhang (1992)	Square Duct	UWT (uneven)	$0 \leq Ro \leq 0.352$	2,500 25,000	Smooth Channel (single pass/horizontally rotating)	FD	Re, Ro, $\Delta p / \rho$	Radially Outward Flow	Local
Ilan et al. (1993)	Square Duct	UWT (uneven)	$0 \leq Ro \leq 0.352$	2,500 25,000	Smooth Channel (two pass/horizontally rotating)	D/FD	Re, Ro, $\Delta p / \rho$	Radially Inward/Outward Flow	Local
Parsons et al. (1994)	Square Duct	UWT (uneven) /UHF	$0 \leq Ro \leq 0.352$	2,500 25,000	Roughened Channel (two pass/horizontally rotating)	D/FD	Re, Ro, $\Delta p / \rho$	Radially Inward/Outward Flow	Local
Johnson et al. (1994)	Square Duct	UWT	$0 \leq Ro \leq 0.35$	25,000	Smooth (skew) Serpentine Channel (orthogonally rotating)	D/FD	Re, Ro, $\Delta p / \rho$ $R/D, Gr / Re^2$	Radially Inward/Outward Flow	Local
Hsieh and Hong (1995)	Square Duct	UHF	$0 \leq Ro \leq 0.50$	5,000 25,000	Roughened Channel (single pass/orthogonally rotating)	D/FD	Re, Ro, Re_u Ra_u	Radially Outward Flow	Local
Parsons et al. (1995)	Square Duct	UWT/UHF	$0 \leq Ro \leq 0.352$	2,500 25,000	Roughened Channel (two pass/horizontally rotating)	D/FD	Re, Ro, $\Delta p / \rho$	Radially Inward/Outward Flow	Local
Zhang et al. (1995)	Square Duct	UWT (uneven) /UHF	$0 \leq Ro \leq 0.352$	2,500 25,000	Roughened Channel (two pass/horizontally rotating)	D/FD	Re, Ro, $\Delta p / \rho$	Radially Inward/Outward Flow	Local
Dutta et al. (1996)	Square Duct	UWT/UHF	$0 \leq Ro \leq 0.24$	5,000 25,000	Smooth Channel (single pass/horizontally rotating)	D/FD	Re, Ro, $\Delta p / \rho$	Radially Outward Flow	Local
Hsieh and Liu (1996)	Rectangular and Square Duct	UHF (uneven)	$0 \leq Ro \leq 0.615$	5,000 25,000	Roughened Channel (two pass/orthogonally rotating)	D/FD	Re, Ro, $\Delta p / \rho$	Radially Inward/Outward Flow	Local (regionally averaged)
Cheah et al. (1996)	Square Duct	UWT	$-0.2 \leq Ro \leq 0.2$	100,000	Smooth Channel (two pass/orthogonally rotating)	D/FD	Ro and LDV velocity (nonheating) measurements	Radially Inward/Outward Flow	none
Hsieh et al. (1997)	Square Duct	UWT (uneven)	$0 \leq Ro \leq 0.4274$	5,000 25,000	Roughened Channel (two pass/orthogonally rotating)	D/FD	Re, Ro, $\Delta p / \rho$ and LDV velocity (nonheating) measurements	Radially Inward/Outward Flow	Local (regionally averaged)
Present Study	Square Duct	UWT	$0 \leq Ro \leq 0.1602$	5,000 10,000	Roughened Channel (two pass/orthogonally rotating)	D/FD	LDV (nonheating) measurements	Radially Inward/Outward Flow	Local (regionally averaged)

Note: UHF: uniform heat flux, UWT: uniform wall temperature, and uneven: stands for uneven heat flux or temperature.

2.2 LDV Measurements. The present system is a commercial two color, four beam DANTEC fringe-type LDV system, operated in the backward scatter mode, with the general layout also shown in Fig. 2 which is similar to that of Hsieh et al. (1997). The

relevant optical system parameters are listed in Table 3. Standard DANTEC 55x modular optics and a model Stabilite 2016 4W Spectral Physics Ar⁺ laser are mounted on a 2D, traversing system. Two separate LDV channels are formed by use of color

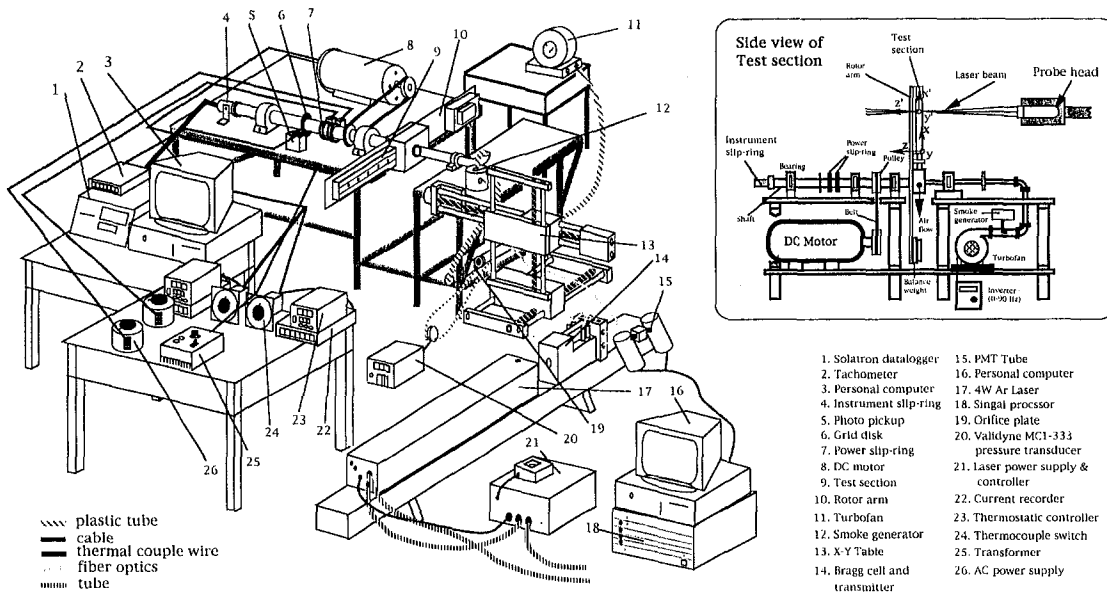
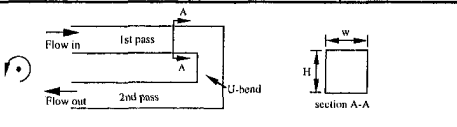


Fig. 2 Stereographic and side view of the experimental setup schematics

Table 2 Geometries and operating conditions in the channel

geometries	W (mm)	H (mm)	D _H (mm)	AR
	20	20	20	1
relevant parameters	Re _H		Re _n	
	5000 - 10000		0 - 801	
boundary conditions	First pass	Second pass	U-bend	
	isothermal	isothermal	isothermal	



separation. They are 514.5 nm (green light) and 488.0 nm (blue light) wavelength beams. These two beams form orthogonal fringes by means of a standard DANTEC two channel optical train. These two set of fringes allow the simultaneous measurement of two orthogonal components. The transverse velocity component is measured using 488.0 nm beam, while the 514.5 nm beam measures a streamwise velocity component. A combined counter-type signal processor (Dantec model 57H00) with functions of counter, buffer interface and coincidence filter, which is interfaced with a LEO (Intel-486) PC in the direct access mode, was employed for data processing. Statistical data were based on a sample size of 320,000 measurements with a sampling frequency of approximately 400 samples/s, from which the time-averaged values were determined.

For the present system, the link consisted of four fiber manipulators and four single mode fibers. Each fiber manipulator was used as a launch unit to couple the beam onto the fiber. The single mode polarization preserving fiber produced a beam diameter 1.35 mm, and beam divergence angle of 0.5 ~ 0.6 mrad. It was fitted

Table 3 Laser-Doppler velocimeter optical parameter

Laser power	4W
Laser wavelength	
green beam	514.5 nm
blue beam	488.0 nm
Beam-diameter at e ⁻² (major and minor axes of ellipsoid)	
green	3.98 mmx0.189 mm
blue	3.98 mmx0.189 mm
Beam half angle	
green	2.72°
blue	2.72°
Focal length	
green	400 mm
blue	400 mm
Fringe opening	
green	5.27 μm
blue	5.27 μm
Number of fringes	36

with two plugs at each end, which included the microlens for focusing (at the receiving end) and/or resetting the divergence angle of the beam (at the probe end).

The selection of seed particles for laser Doppler measurements represents a compromise between large particles (diameter > 10 μm), which are good light scatterers, and small particles (diameter < 1 μm), which follow the air flow very accurately. A satisfactory compromise could be obtained by 4-5 μm diameter soot droplets from a straw smoke generator. Since the flow was forced convection dominated, velocity measurements were made without heating.

3 Data Reduction and Uncertainty Analysis

The laser-Doppler signal from the photomultiplier was fed to a signal processor and, then, measured with a frequency counter. The digital value of the Doppler frequency shift *f_D*, the characteristic wavelength of the laser λ, and the half-angle between the beams θ/2 are translated to streamwise *u* and transverse *v* velocity components, respectively, by the equation

$$u/ \text{ or } v = \frac{\lambda_{u/\text{or } v} f_D}{2 \sin(\theta/2)} \tag{1}$$

Once a valid laser velocimeter signal is generated, the test section angular position is recorded with a shaft encoder. The encoder divides each revolution into 3600 parts. The two velocity signal and the shaft position are simultaneously recorded onto floppy disks by a PC. A typical test had 40 data points in each measured downstream station. This gives two-dimensional velocity and angular position data for the measured point, which were analyzed after the test.

In addition, various sources of uncertainty contribute to the random and system errors in the mean velocity measurements. These include index of refraction effects that alter the half-angle between the beams and the optical probe volume location; velocity bias, filter bias, and velocity gradient broadening; particle seeding and particle deposition considerations; finite size of the data samples; rotating channel wobble and vibrations in rotational speeds of the channel. The visual optical probe volume positioning uncertainty was kept less than ±0.01 mm by the careful determination of an initial reference location and using stepping motors with incremental steps equal to 50 μm.

The nonuniform axial deposition of soot droplets on the glass windows contributed to the random uncertainty of all the velocity measurements as well as to the symmetric uncertainty of these measurements made along axial traverses. Of the uncertainties specifically attributable to the LDA technique, filter bias, velocity bias, and gradient broadening were carefully examined. Filter bias

Table 4 Maximum possible measurement errors

Quantity	Systematic error	Random error
x	±0.5 mm	±0.01 mm
y	±0.5 mm	±0.01 mm
z	±0.5 mm	±0.01 mm
u ₀	±2.5%	±0.25%
u/u ₀	±9%	±8%
u'/u	±12%	±10%
Ω	±1 rpm	±0.5 rpm

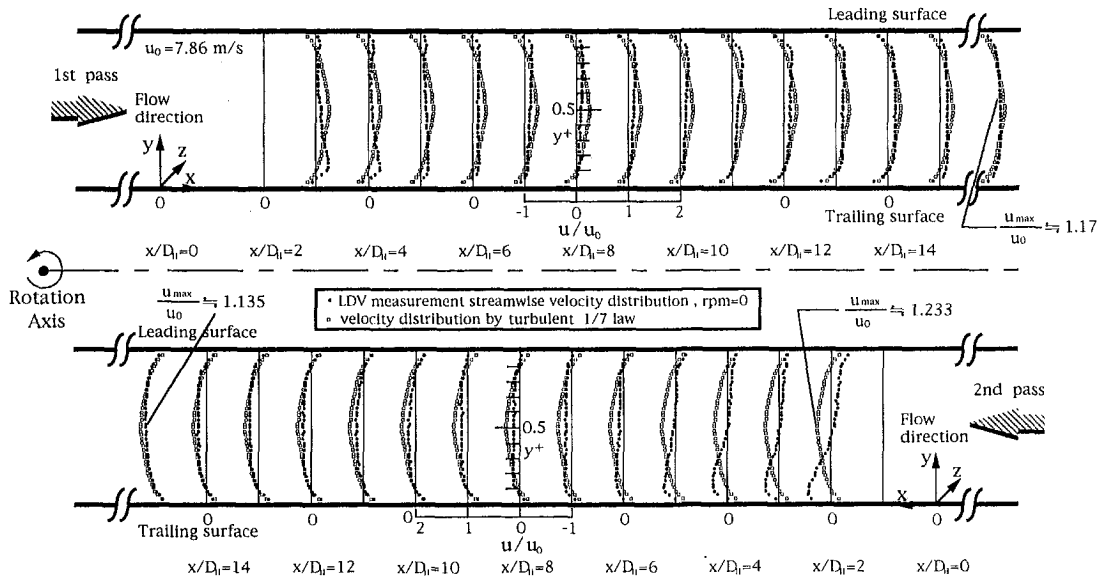


Fig. 3 Verification testing for smooth duct without rotation ($Re_H = 10000$) at $z^+ = 0.5$ (uncertainty in $u/u_0 \pm 0.12$, in $\Omega \pm 0.011$, in $x \pm 0.5$ mm)

was avoided. The maximum velocity bias was estimated to be less than 10 percent but typically, it was about 10 percent. The effect of gradient broadening seems negligible. As mentioned before, the small size ($4\text{--}5 \mu\text{m}$) of the soot droplets used guaranteed the tracking of velocity fluctuation higher than 1 kHz to better than 1 percent speed accuracy. Similarly, particle drift velocity due to the centrifugal force can be shown to be negligibly small. Calculation of the mean and turbulent intensity results in statistical uncertainties of $\pm 12\%$ for mean velocity and $\pm 15\%$ for turbulent intensity at the maximum rotational speed. In this study, channel rotation was maintained constant to within $\pm 0.6\%$. This had a negligible effect on the precision of the data. Table 4 summarizes the estimates of maximum inaccuracy (systematic error) and imprecision (random error) associated with each measurements to take account finite transit time, mean velocity gradient, and instrument noise broadening.

4 Results and Discussion

The forced flow mechanism present in the rotating channel is mainly by the presence of Coriolis and centrifugal forces. The parameters apparent for this type of flow in rotating smooth channels are the flow rates (Re_H) and rotational speeds. The time average, u , circumferential velocity (streamwise/axial direction in the test channel) was measured along a radial line at midplane ($z = 10$ mm) and downstream distance (shown in Fig. 1) at rotational speeds of 100, 200, and 300 rpm. The temperature of the air was maintained at $25 \pm 1^\circ\text{C}$ for all the experiments.

4.1 Qualification Test and Assessment. Verification of the experimental procedure and its accuracy for the mean velocity were made for a smooth duct without rotation at various streamwise locations, and the results were also compared with the known one-seventh law for turbulent flow velocity profile. It was found as

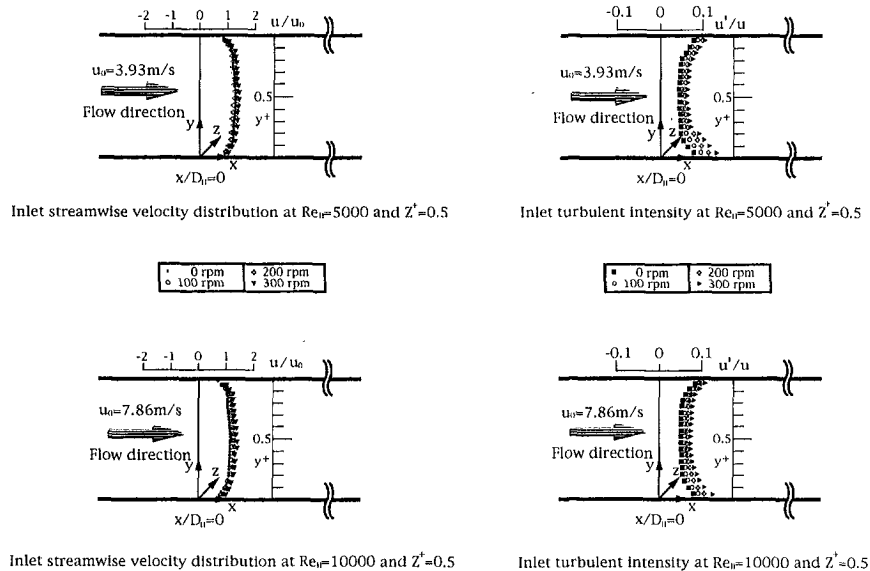


Fig. 4 Streamwise velocity and turbulent intensity distribution at entrance (uncertainty in $u/u_0 \pm 0.12$, in $\Omega \pm 0.011$, in $x \pm 0.5$ mm)

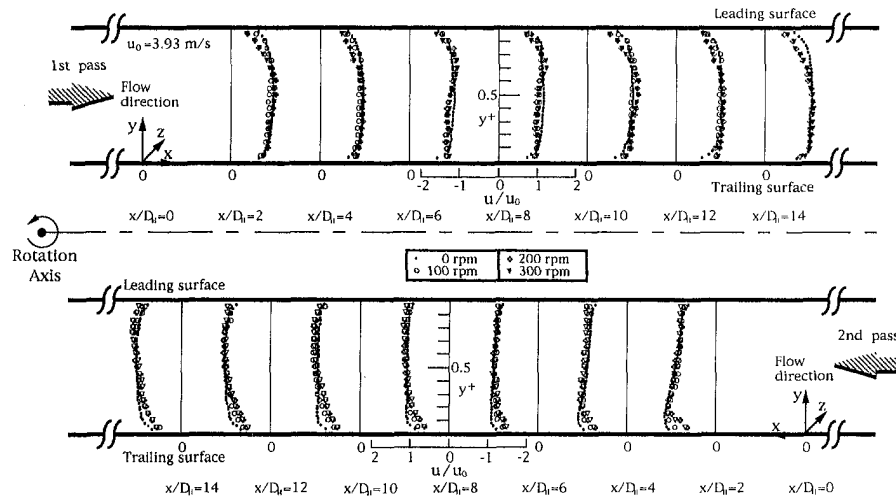


Fig. 5 LDV measurements for streamwise velocity at $Re_H = 5000$ at $z^+ = 0.5$ (uncertainty in $u/u_0 \pm 0.12$, in $\Omega \pm 0.011$, in $x \pm 0.5$ mm)

shown in Fig. 3 that the rms deviations over all points were less than $\pm 1.5\%$ and 2% at $x/D_H \geq 14$ in the first and second channel, respectively. To examine the conservation of the mean flow rate, the mean streamwise velocities were also integrated over each cross section at specified stations. The results showed that the mass continuity was valid within $\pm 3\%$ in entire two channels. The ratios of u_{max}/u_0 for this particular case ($Re_H = 10000$) downstream of the first channel and the second channel were found to be about 1.17 and 1.14, respectively. This coincided adequately with the conventional one-seventh result ($=1.233$). This good agreement served to establish the validity of the measurements and data reduction method, although the present flow seems not fully developed yet at the end of the first straight channel. However, the symmetric nature in the mean velocity distribution still holds except for a short distance shortly after the flow passed through the U-bend.

4.2 Mean Velocity Distribution. At a given location the mean velocity profile is predominantly a function of the applied streamwise pressure and shear stress gradients. In this way the rotational speed and U-bend directly affects the velocity profile through the static pressure field, and indirectly through the modified turbulent structure. Figure 4 indicates that the velocity distribution as well as the turbulent intensity profiles along vertical

duct centerlines at the duct inlet at $Re_H = 5000$ and $10,000$, respectively, for the stationary as well as rotation cases which demonstrate the degree of uniformity and symmetry produced by the entry arrangements. The spatial average velocity for the channel is $u_0 = 3.93$ m/s ($Re_H = 5000$) and 7.36 m/s ($Re_H = 10000$) as shown in Figs. 5 and 6, respectively, and this is used as a reference value for nondimensionalizing the mean velocity data at subsequent transverse stations. With reference to these figures, the details of flow development in the present two pass rotating channel are discussed in the following. The axial velocity profiles obtained for fourteen downstream stations with rotation show the distortion in both figures. Generally, the flow pattern with rotation is skewed continuously from the conventional turbulent velocity profile. The mean velocity profiles show the presence of a nearly uniform velocity core region in which the velocity gradient is small, along the entire length of the duct which isolates the boundary layers adjacent to the duct wall except for the region in the U-bend. In spite of this, the flow structure redistributes slightly with rotation due to Coriolis force. The Coriolis force acts toward the trailing (leading) wall, while it is in the first (second) channel as the channel rotates. Since the present flow is isothermal, rotational (centrifugal) buoyancy is not present. The axial velocity distributions shown in Figs. 5 and 6 are nearly flat (uniform flow)

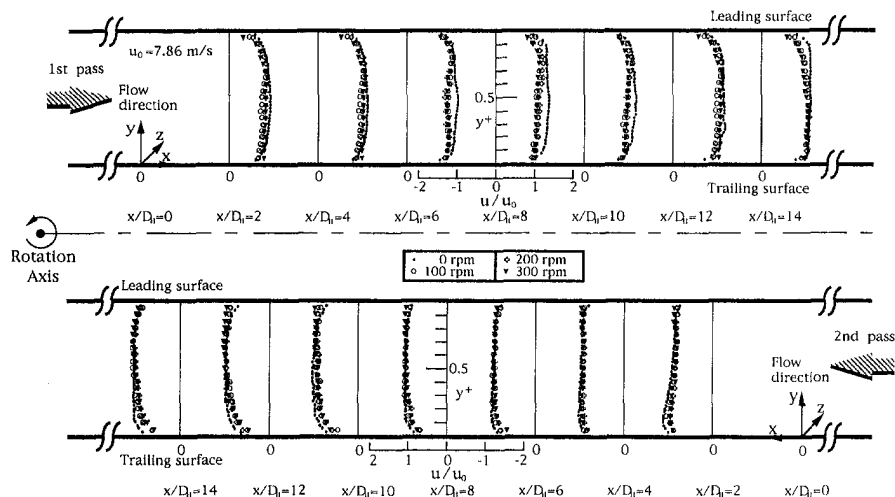


Fig. 6 LDV measurements for streamwise velocity at $Re_H = 10000$ at $z^+ = 0.5$ (uncertainty in $u/u_0 \pm 0.12$, in $\Omega \pm 0.011$, in $x \pm 0.5$ mm)

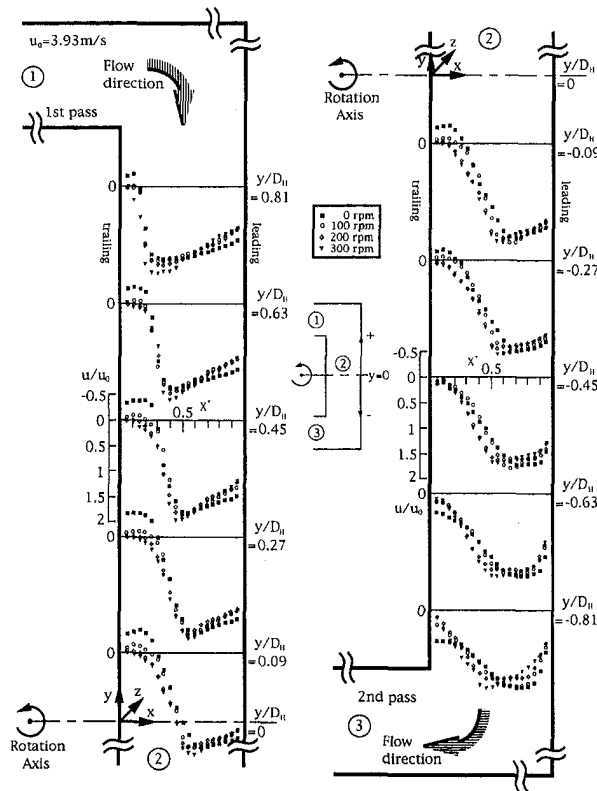


Fig. 7 LDV measurements for the streamwise velocity distribution in U-bend at $Re_H = 5000$ and $z^+ = 0.5$ (uncertainty in $u/u_0 \pm 0.12$, in $\Omega \pm 0.011$, in $y \pm 0.5$ mm)

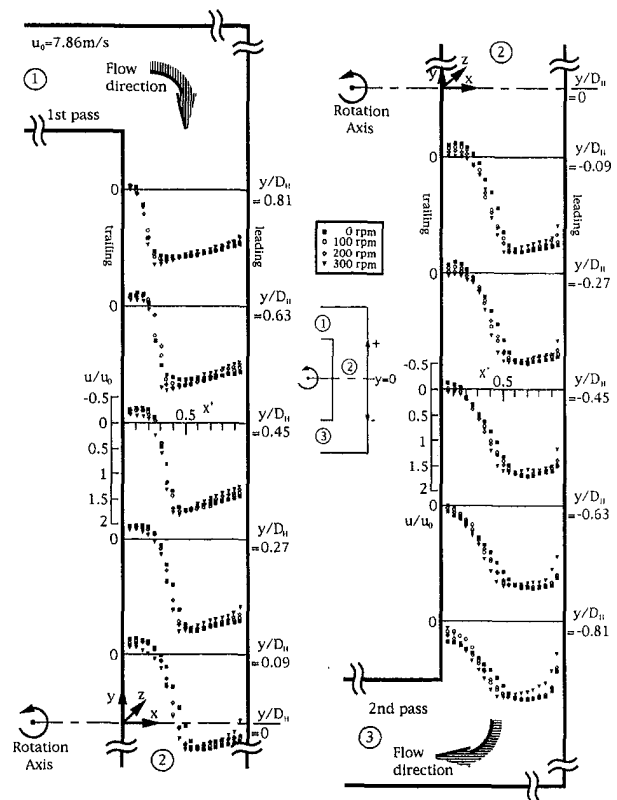


Fig. 8 LDV measurements for the streamwise velocity distribution in U-bend at $Re_H = 10000$ and $z^+ = 0.5$ (uncertainty in $u/u_0 \pm 0.12$, in $\Omega \pm 0.011$, in $y \pm 0.5$ mm)

especially without rotation. This is because the hydrodynamic centrifugal force acts toward radially outward direction in both straight channels which should be balanced by a pressure gradient. Furthermore, both figures illustrate the developing mean flow distribution at various streamwise stations for $Re_H = 5000$ and 10000 , respectively under various rotational speeds. A weak dependence of velocity profiles on rotating speed was found. However, the rotation effect is clearly noted as compared to Fig. 3 without rotation. In spite of this, flow separation may not occur in the first/second channel.

To quantify flow development and downstream behavior in turbulent flow, velocity measurements were taken for the region of 180° U-bend. In Figs. 7 and 8, the streamwise velocity profiles at the midplane are shown in the 180° U-bend channels for Reynolds number of $Re_H = 5000$ and $10,000$, respectively. How the flow evolves in the streamwise region downstream can be observed. As stated earlier, the flow at the U-bend entry is still developing and the boundary layers are thin. These thin boundary layers lead to a nearly uniform flow situation in which the flow is seen to accelerate on the trailing wall side, to balance the slower flow on the leading wall side as a result of higher pressure there. It is found, also by the Kutta condition that, the separation should occur at the 90° sharp corner, although the measurement was not easy. As the flow proceeds through the bend, the fluid begins to move faster over the leading wall. According to the present experiments, at a typical rotational speed (≈ 300 rpm) at $Re_H = 5000$, the flow is reattached on the wall of the second half of the channel at $y/D_H = -0.27$ (-0.09 for $Re_H = 10000$), which creates a recirculating region (the reattachment length $\approx 1.27D_H$) along the wall on the trailing side. This feature is represented by a peak velocity at $y/D_H = 0.81$ and negative velocity on the trailing wall just downstream from $y/D_H = 0.81$. The separated flow at $y/D_H = 0.81$ will also cause a flow deflection toward the opposite side of channel (leading) wall. As a result, the velocity reaches its peak at the position close to $y/D_H = -0.09$ for both $Re_H = 5000$

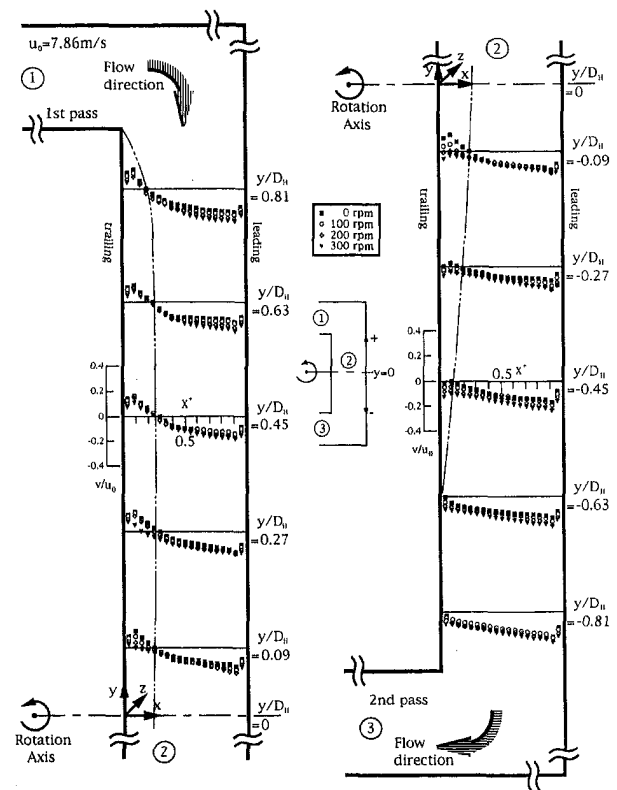


Fig. 9 Velocity (v component) distribution diagram in U-bend at $Re_H = 10000$ (uncertainty in $v/v_0 \pm 0.072$, in $\Omega \pm 0.011$, in $y \pm 0.5$ mm)

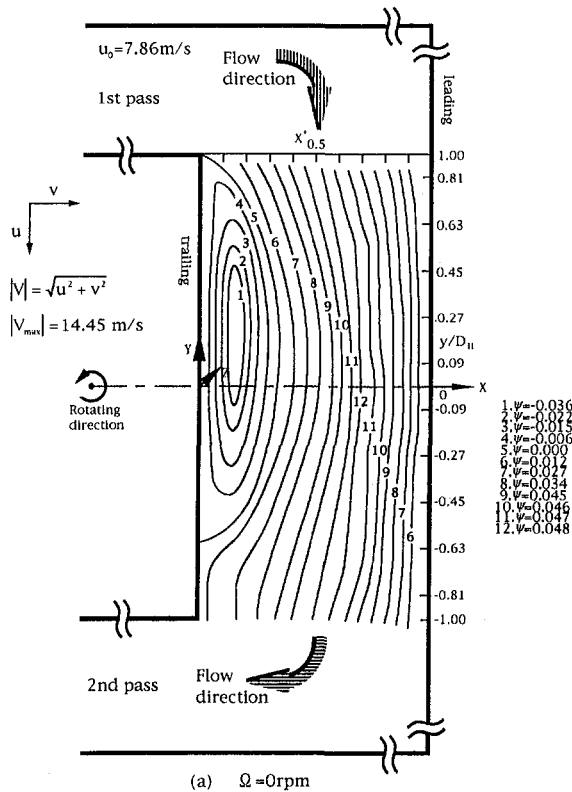


Fig. 10(a)

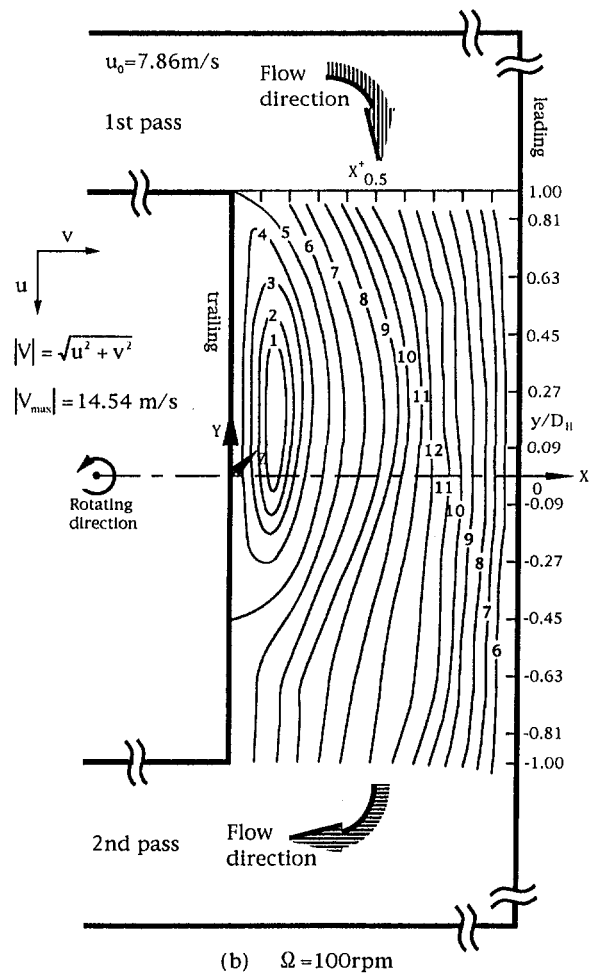


Fig. 10(b)

and 10000. As the flow proceeds through the bend, the fluid begins to move faster over the leading wall. The fluid consequently begins to move across the duct toward trailing wall due to the counter balance of centrifugal and Coriolis forces with rotation within the U-bend. Furthermore, the velocity peak in the streamwise direction increases and is being well displaced toward the leading wall until $y/D_H = -0.09$ as the flow proceeds downstream. Thus the leading wall causes the development of shear layer in such a way that the shear layer was converged and accelerated. The location of zero u moves away from the trailing wall before flow reaches the station at $y/D_H = -0.09$. The rotation effect was noted at $Re_H = 5000$ based on the onset of flow separated and reattachment. This is due to the combined influence of the sustained adverse pressure gradient and 90 deg sharp turn effects on the boundary layer development, as well as the Coriolis force acting toward the trailing (leading) wall. However, the third factor due to Coriolis forces would counter balance the effect due to two former factors. This situation becomes clearly noted as the rotational speed increases. Because of the development of secondary motions, the flow has become strongly three-dimensional.

Figure 9 shows the corresponding plot of the v -velocity components of the streamwise (axial) flow at different rotational speeds of 0, 100, 200, and 300 rpm at $Re_H = 10000$, which provide a picture of the transverse flow development within the U-bend. The figure again indicates that in rotation, the core flow shifts toward the trailing side. It is conjectured that higher turbulence near the trailing wall was found. The vortex due to the flow separation converges fluid from the center of passage to the trailing wall adjacent to the upstream front corner. The boundary layer development is influenced by the 180 deg U-turn and rotational speed, which modify the flows turbulent structure as Re_D increases. Inflection points appear in the profiles of the transverse velocities. The dashed line (e.g., $\Omega = 0$ rpm) on Fig. 9, constructed by joining points where the second derivative is zero, shows the locus of the curved mixing layer between the recirculating region and the main stream. It thus approximates the dividing stream line, which quite coincided with the results of Fig. 10. It shows the

mean stream line (calculated by integration of the mean velocity distribution) plot at $Re_H = 10,000$ at different rotational speeds. Slight differences in the patterns evolve as the rotational speeds increase. Again, no matter what the rotational speed is, the separation shown in Fig. 10 all uniformly occurred (started) at the 90 deg sharp corner. The size of recirculation bubble becomes small as Re_D increases. For instance, in terms of dimensionless reattachment length, y/D_H from 1.63 at $\Omega = 0$ rpm decreases to 1.09 at $\Omega = 300$ rpm for $Re_H = 10000$. This is because in the downstream region the Coriolis force leads to the development of a secondary motion opposite that caused by the U-bend. This counter balance becomes bigger as the flow proceeds further and, consequently, the fluid begins to move across the duct toward the trailing wall and, in turn, results in a shorter reattachment length to occur. Basically, there are several competing mechanisms which affect flow redistribution within the U-bend, namely, Coriolis and centrifugal forces driven secondary flow, pressure-driven secondary flow, stress-driven secondary flow, and growing boundary layers. At a given location in the U-bend, one or more of these factors may dominate, complement or counter each other to give the resultant flow. At the inlet of the U-bend, the pressure-driven secondary flow is still not large enough, and the nearly uniform flow as well as Coriolis and centrifugal forces cause the movement of the fluid towards the trailing wall. It again indicates, as shown in Fig. 10(a) without rotation, pressure-driven secondary flows are setup in this U-bend channel because of an imbalance between the centrifugal force and the spanwise pressure gradient. Fluid from the leading wall side is transported to the trailing wall side along the top and bottom walls and, to maintain continuity, a corresponding amount of fluid moves in the reverse direction in the region

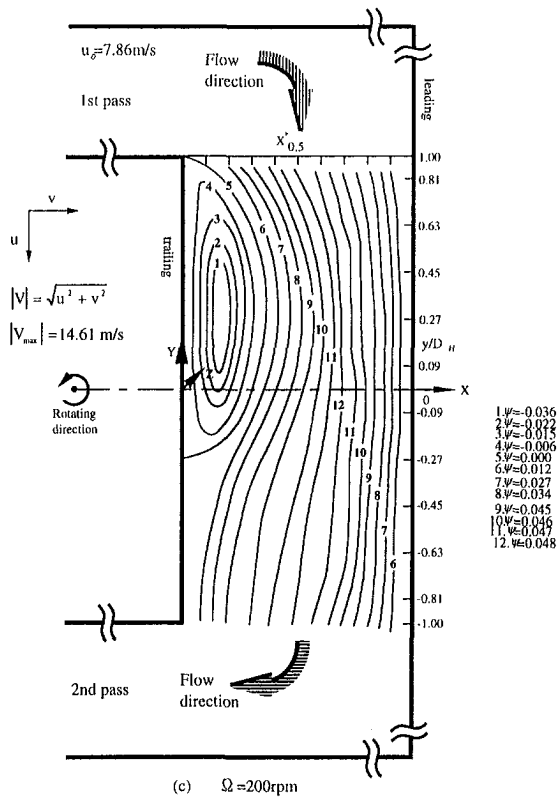


Fig. 10(c)

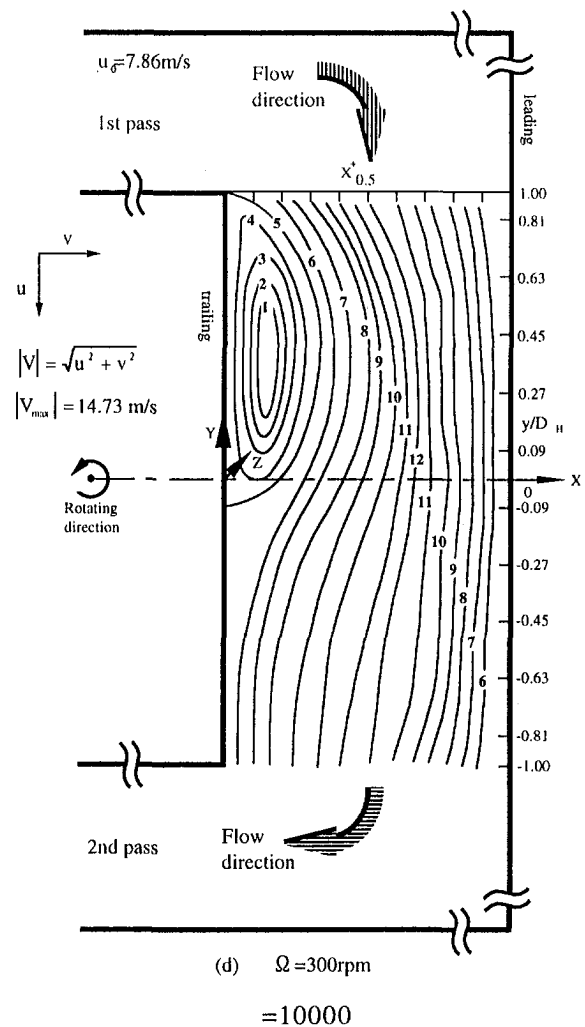


Fig. 10(d)

Fig. 10 Mean streamline distribution diagram in U-bend at $Re_H = 10000$ (uncertainty in $\psi \pm 0.001$, in $\Omega \pm 0.011$, in $y \pm 0.5$ mm)

away from the bottom/top walls. Thus the recirculation zone is generated as shown in Fig. 10(a). This situation would persist as the rotational speed increases as evidenced by Figs. 10(b)–(d). However, the recirculation zone becomes smaller as the rotational speed increases.

4.3 Turbulent Intensity Distribution. The root-mean squares of the velocity fluctuation measurements in the axial direction are presented in Figs. 11 and 12 for $Re_H = 5000$ and $10,000$, respectively, for the same location as the mean velocity profiles of Figs. 5 and 6 at $y = 1$ mm (trailing wall), as well as $y = 19$ mm (leading wall) and $z = 10$ mm. The values are normalized by u , the streamwise time mean velocity. It is expected that the intensity profiles will decrease slightly as Re_H increases. In spite of this, the intensity profiles are approximately constant for $x/D_H = 4(6)$ – $6(10)$ in the first (second) channel, respectively. The peak occurs at the entrance of the second channel due to the U-bend and the exit of the first channel due to the flow deceleration. As the flow develops downstream, the measurements show, for example, a gradual and slight increase to a value of 12% at 100 rpm. In the first channel at $Re_H = 5000$ and 10000 , the turbulent level along trailing and leading wall is nearly the same as one would expect while the channel is stationary. However, after the flow pass through the U-bend, the situation was changed. Moreover, it is found that a higher turbulence level along the leading wall and a corresponding lower value along the trailing wall occur at the same Re_H . The trailing wall turbulence levels are slightly suppressed (~ 6 – 8%) over both channels at $Re_H = 5000$ as compared to these shown in Fig. 12 at $Re_H = 10000$. This is perhaps due to the strong flow acceleration as Re_H increases as shown in Fig. 11. The discrepancies between the rotating channel and stationary cases seem to have little influence on turbulent intensity. Moreover, the influences of the Coriolis force of the basic stability of the turbulent boundary layers (i.e. suppressing capability) as stated before seems not found in the present study. This is perhaps because the rotational speeds under study are not high enough to observe such effect.

5 Conclusions

Flow velocity and turbulent intensity measurements have been made in a rotating two pass flow channel of square cross section for Re_H ranged from 267 to 801 at $Re_H = 5000$ and $10,000$. The following specific features are observed.

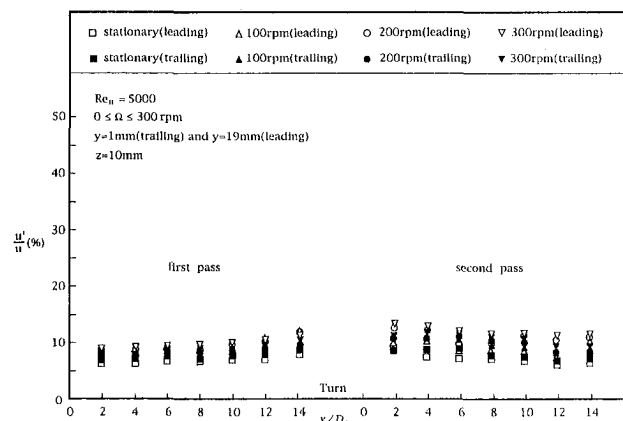


Fig. 11 $Re_H = 5000$, $0 \leq \Omega \leq 300$ rpm, rotating effect on turbulent intensity (uncertainty in $u'/u_0 \pm 0.16$, in $\Omega \pm 0.011$, in $y \pm 0.5$ mm)

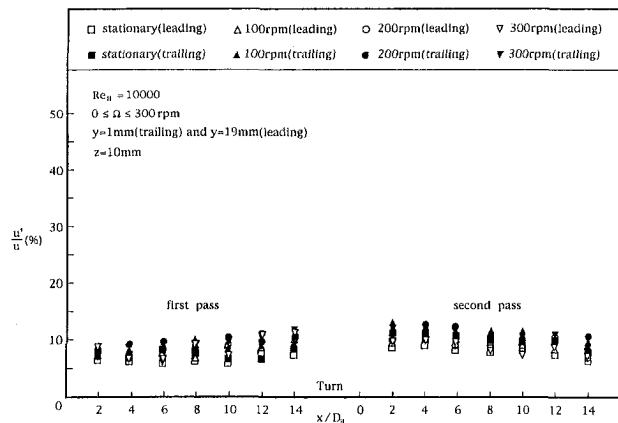


Fig. 12 $Re_H = 10000$, $0 \leq \Omega \leq 300$ rpm, rotating effect on turbulent intensity (uncertainty in $u/u_0 \pm 0.16$, in $\Omega \pm 0.011$, in $y \pm 0.5$ mm)

(1) No separation is observed in both the first and second channels except for a certain size pocket of separation on the inner wall in the U-bend region just immediately after 90 deg sharp turn at the exit of the first channel. But, nevertheless, the skewed streamwise velocity profile was still found.

(2) The influence of the U-bend and rotation on the mean velocity field was apparent throughout the U-bend passage. While, in the both straight channels, the effect seems not clearly noted.

(3) The separation should occur at the 90 deg sharp corner no matter whether the channel rotates or not. Secondary flow observed due to Coriolis force in the first (second) channel and Coriolis as well as centrifugal force in the U-bend are not very strong. The strength of the vortex would increase (based on $|V_{max}|$ increases as shown in Fig. 10) as Re_{Ω} increases, while the rotating effect on the size of separation bubble shows the opposite trend.

It is seen from the present study that rotation can alter the development of the mean and also fluctuating motion within the sharp U-bends. This conclusion is consistent with the findings of Cheah et al. (1996). Further study should include up/downstream vicinity region of the U-bend.

Acknowledgments

This work was supported by a research grant (NSC 86-2212-E-110-018) from the National Science Council, Taiwan, R.O.C.

References

- Cheah, S. C., Iacovides, H., Jackson, D. C., Ji, H., and Launder, B. E., 1996, "LDA Investigation of the Flow Development Through Rotating U-ducts," *ASME Journal of Turbomachinery*, Vol. 118, pp. 590–596.
- Clifford, R. J., Morris, W. D., and Harasgama, S. P., 1984, "An Experimental Study of Local and Mean Heat Transfer in a Triangular-Sectioned Duct Rotating the Orthogonal Mode," *ASME Journal of Engineering for Gas Turbines and Power*, Vol. 106, pp. 661–667.
- Dring, R. P., 1982, "Sizing Criteria for Laser Anemometry Particles," *ASME JOURNAL OF FLUIDS ENGINEERING*, Vol. 104, pp. 15–17.
- Dutta, S., Andrews, M. J., and Han, J. C., 1996, "Prediction of Turbulent Heat Transfer in Rotating Smooth Square Ducts," *International Journal of Heat & Mass Transfer*, Vol. 39, pp. 2505–2514.
- Guidex, J., 1989, "Study of the Convective Heat Transfer in Rotating Coolant Channel," *ASME Journal of Turbomachinery*, Vol. 111, pp. 43–50.
- Han, J. C., and Zhang, Y. M., 1992, "Effect of Uneven Wall Temperature on Local Heat Transfer in a Rotating Square Channel With Smooth Walls and Radial Outward Flow," *ASME Journal of Heat Transfer*, Vol. 114, pp. 850–858.

- Han, J. C., Zhang, Y. M., and Kalkuehler, K., 1993, "Uneven Wall Temperature Effect on Local Heat Transfer in a Rotating Two-Pass Square Channel With Smooth Walls," *ASME Journal of Heat Transfer*, Vol. 115, pp. 912–920.
- Hart, J. E., 1971, "Instability and Secondary Motion in a Rotating Channel Flow," *Journal of Fluid Mechanics*, Vol. 45, pp. 341–351.
- Hong, Y. J., and Hsieh, S. S., 1993, "Heat Transfer and Friction Factor Measurements in Ducts With Staggered and in-Line Ribs," *ASME Journal of Heat Transfer*, Vol. 115, pp. 58–65.
- Hsieh, S. S., Hong, Y. J., and Jeng, S. R., 1994, "3-D Laminar Forced Convection in a Rotating Square Duct With a Rib on Leading Wall," *International Journal of Heat & Mass Transfer*, Vol. 37, pp. 2273–2285.
- Hsieh, S. S., and Hong, Y. J., 1995, "Heat Transfer Coefficients in an Orthogonally Rotating Duct With Turbulators," *ASME Journal of Heat Transfer*, Vol. 117, pp. 69–78.
- Hsieh, S. S., and Liu, W. J., 1996, "Uneven Wall Heat Flux Effect on Local Heat Transfer in Rotating Two-Pass Channels With Two Oppositely Ribbed Walls," *ASME Journal of Heat Transfer*, Vol. 118, pp. 864–876.
- Hsieh, S. S., Wang, Y. S., and Chiang, M. H., 1997, "Local Heat Transfer and Velocity Measurements in a Rotating Ribbed Two-Pass Square Channel With Uneven Wall Temperatures," *ASME Journal of Heat Transfer*, Vol. 119, pp. 843–848.
- Iskakov, K. M., and Trushin, V. A., 1983, "Influence of Rotation on Heat Transfer in Turbine-Blade Radial Slot Channel," *Izvestiya VUZ. Aviatzionnaya Tekhnika*, Vol. 26, No. 1, pp. 97–99.
- Johnson, B. V., 1978, "Heat Transfer Experiments in Rotating Radial Passages With Supercritical Water," *ASME Heat Transfer* (bound proceedings from 1978 ASME Winter Annual Meeting).
- Johnson, B. V., Wagner, J. H., Steuber, G. D., and Yeh, F. C., 1994, "Heat Transfer in Rotating Serpentine Passages With Trips Skewed to the Flow," *ASME Journal of Turbomachinery*, Vol. 116, pp. 112–123.
- Johnston, J. P., Halleen, R. M., and Lezius, D. K., 1972, "Effects of Spanwise Rotation on the Structure of Two-Dimensional Fully Developed Turbulent Channel Flow," *Journal of Fluid Mechanics*, Vol. 56, Part 3, pp. 533–557.
- Lokai, V. I., and Gunchenko, E. I., 1979, "Heat Transfer Over the Initial Section of Turbine Blade Cooling Channels Under Conditions of Rotation," *Thermal Engineering*, Vol. 26, pp. 92–95.
- Moore, J., 1967, "Effects of Coriolis on Turbulent Flow in Rotating Rectangular Channels," MIT Gas Turbine Laboratory Report, No. 89.
- Mori, Y., Fukada, T., and Nakayama, W., 1971, "Convective Heat Transfer in a Rotating Radial Circular Pipe (2nd Report)," *International Journal of Heat & Mass Transfer*, Vol. 14, pp. 1807–1824.
- Morris, W. D., and Ayhan, T., 1979, "Observations on the Influence of Rotation on Heat Transfer in the Coolant Channels of Gas Turbine Rotor Blades," *Proceedings of Institute of Mechanical Engineers*, Vol. 193, pp. 303–311.
- Morris, W. D., and Ayhan, T., 1982, "An Experimental Study of Turbulent Heat Transfer in the Tube Which Rotates About an Orthogonal Axis," *Proc. XIV ICHMT Symposium on Heat and Mass Transfer in Rotating Machinery*, Dubrovnik, Yugoslavia, Aug. 30–Sept. 3.
- Parsons, J. A., Han, J. C., and Zhang, Y. M., 1994, "Wall Heating Effect on Local Heat Transfer in a Rotating Two-Pass Square Channel With 90° Rib Turbulators," *International Journal of Heat and Mass Transfer*, Vol. 37, pp. 1411–1420.
- Parsons, J. A., Han, J. C., and Zhang, Y. M., 1995, "Effect of Model Orientation and Wall Heating Condition on Local Heat Transfer in a Rotating Two-Pass Square Channel With Rib Turbulators," *International Journal of Heat and Mass Transfer*, Vol. 38, pp. 1151–1159.
- Prakash, C., and Zerkle, R., 1992, "Prediction of Turbulent Flow and Heat Transfer in a Radially Rotating Square Duct," *ASME Journal of Turbomachinery*, Vol. 114, pp. 835–846.
- Rothe, P. H., and Johnston, J. P., 1979, "Free Shear Layer Behavior in Rotating Systems," *ASME JOURNAL OF FLUIDS ENGINEERING*, Vol. 101, pp. 117–120.
- Wagner, J. H., Johnson, B. V., and Hajek, T. J., 1991, "Heat Transfer in Rotating Passages With Smooth Walls and Radial Outward Flow," *ASME Journal of Turbomachinery*, Vol. 113, pp. 42–51.
- Wagner, J. H., Johnson, B. V., and Kopper, F. C., 1991b, "Heat Transfer in Rotating Serpentine Passages With Smooth Walls," *ASME Journal of Turbomachinery*, Vol. 113, pp. 321–330.
- Wagner, J. H., Johnson, B. V., Graziani, R. A., and Yeh, F. C., 1992, "Heat Transfer in Rotating Serpentine Passages With Trips Normal to the Flow," *ASME Journal of Turbomachinery*, Vol. 114, pp. 847–857.
- Wagner, R. E., and Velkoff, H. R., 1972, "Measurements of Secondary Flows in a Rotating Duct," *Journal of Engineering for Power*, Vol. 94, pp. 261–270.
- Zhang, Y. M., Han, J. C., Parsons, J. A., and Lee, C. P., 1995, "Surface Heating Effect on Local Heat Transfer in a Rotating Two-Pass Square Channel With 60 deg Rib Turbulators," *ASME Journal of Turbomachinery*, Vol. 117, pp. 272–280.

S. Demare

Doctor.

L. Labraga

Professor.

C. Tournier

Professor.

Laboratoire de Mécanique et d'Energétique,
Université de Valenciennes et du Hainaut
Cambrésis,
le Mont Houy, B.P. 311, 59304 Valenciennes,
Cedex France

Comparison and Scaling of the Bursting Period in Rough and Smooth Walls Channel Flows

The structure of smooth and k -type rough wall turbulent channel flows was examined over a Reynolds number range of 12,700–55,000 using a few of the most common detection techniques (Modified U_Level (MODUL), TERA, Quadrant analysis) and conditional averages. When grouping time is used and a threshold-independent range could be found, all of the above techniques yield approximately the same time between bursts in the major part of the turbulent flow. In the range of Reynolds numbers studied, the bursting frequency is best scaled on mixed variables. The conditional averaged patterns give a representation of the bursting process and show some differences between turbulent flows which develop on smooth and rough walls, in both inner and outer regions.

1 Introduction

In the last three decades, intensive research on two-dimensional turbulent flow has led to the recognition of the existence of a certain order or structure in the turbulent boundary layer (Hussain, 1986). One of the structures consists of streaks of low momentum fluid which appear randomly in time and space. These streaks lift away from the wall, oscillate and then suddenly break up with the ejection of a sizeable quantity of low momentum fluid into the outer portion of a turbulent wall layer. This sequence of events is often referred to as the "bursting process" during which 70% of the total turbulence production takes place. Because of its importance in the production of turbulent energy, a large number of studies of the bursting process have been reported. However, there is considerable disagreement concerning the frequency of occurrence and the scaling of the bursting structure in bounded turbulent shear flow. Before 1981, the general consensus, e.g., Willmarth (1975) and Cantwell (1981), was that the average bursting period, regardless of its precise definition and determination, was more likely to scale on outer variables (the channel half-width or pipe radius h and the centreline velocity U_0) than on inner—sometimes wall—variables (the kinematic viscosity ν and the friction velocity u_*) (Willmarth, 1975; Cantwell, 1981). However, several investigations (Blackwelder and Haritonidis, 1983; Luchik and Tiederman, 1987; Kim and Spalart, 1987; Tiederman, 1989) have suggested that inner scaling was more appropriate. Alfredsson and Johansson (1984) found that neither inner nor outer scaling was appropriate and proposed a mixed scaling (ν/u_*^2) and (h/U_0) obtained by the geometric average of the inner and outer scales. This scaling, defined by $\sqrt{U_0 u_*^2 / h \nu}$, emphasises the likely interaction between the wall flow and the outer flow. Shah and Antonia (1989) who made measurements in fully developed turbulent duct and boundary layer flows, showed that at high Reynolds numbers, scaling on mixed variables provides the best agreement with the data, although scaling on outer variables cannot be ruled out, whereas measurements on smooth wall turbulent boundary layer performed by Kaspersen (1996) showed that the average bursting period is constant when mixed scaling is used. Measurements in rough wall turbulent boundary layer performed by Antonia and Krogstad (1993) showed that this average period is independent of the Reynolds number when it is scaled on outer variables. Clearly, more investigations are needed to resolve these discrepancies. If

we assume that the bursts are solely triggered by large scale motions in the outer region, the outer scaling must be used to make dimensionless the bursting frequency. Hence, the mean time between bursts made dimensionless with outer variables must be independent of the Reynolds-number since the bursting mechanism is supposed to be outer-layer dominated. It is shown in the present study that the bursting period is Reynolds-number dependent when outer scaling is used. For the same reasons, inner scaling is not valid. In the range of Reynolds-numbers investigated, we show that the mixed scaling is the best candidate. This scaling behavior could possibly be due to an interaction process between the outer flow and the flow in the near wall region, as it was underlined by Alfredsson and Johansson (1984). The lack of consensus is most frequently ascribed to the different detection algorithms used. By 1980, a wider variety of methods had been used to detect bursts which gave a wide range of results for the average burst period in all the standard turbulent flows (Bandyopadhyay, 1982; Bogard and Tiederman, 1986). Bogard and Tiederman (1986) showed that the average bursting period from four flow visualization studies and nine probe detection studies in fully developed pipe and channel flows varied from about 2 to $50h/U_0$ at a momentum Reynolds number of 1000. The wide scatter in the results indicates that the number of bursts detected per unit time varies significantly depending on which detection algorithm is used. In an attempt to explain some of those differences, Bogard and Tiederman (1986) used simultaneous flow visualization and velocity probe measurements to show that each of the most popular technique were detecting related ejection phenomena. They concluded that the Quadrant technique (introduced by Wallace et al., 1972) applied to a single-point velocity measurement can detect bursts when an appropriate threshold is used and when the ejections are grouped into bursts. They also evaluated the effectiveness of the Variable Interval Time Averaging (VITA) method of Blackwelder and Kaplan (1976) and U_Level burst-detection algorithm introduced by Lu and Willmarth (1973). Luchik and Tiederman (1987) modified the U_Level technique so multiple velocity detections were eliminated and concluded that this method did yield a good estimate of the average time between bursts when an appropriate value of the grouping parameter is used. Tiederman (1989) confirmed their study by extending their low Reynolds-numbers results to high Reynolds-numbers.

The main purpose of this study is to determine the average bursting period over a relatively large Reynolds numbers range and hence to evaluate the correct scaling law on smooth and rough walls flow, which is very important from both an engineer's viewpoint as well as that of researchers in turbulence. Wei and Willmarth (1989) indicate that there are fundamental differences between the turbulent flows in

Contributed by the Fluids Engineering Division for publication in the JOURNAL OF FLUIDS ENGINEERING. Manuscript received by the Fluids Engineering Division October 16, 1998; revised manuscript received July 13, 1999. Associate Technical Editor: P. R. Bandyopadhyay.

a circular pipe, a rectangular channel and a zero-pressure-gradient boundary layer. They have observed that in the channel flow, the inner-region structure from the opposing walls interacted. There was a constant interchange of counter-rotating vorticity between the two inner regions due to bursting. There cannot be a similar phenomenon occurring in a boundary layer because there is only one wall. The circular pipe flow will be more complex. The curvature of the pipe wall means that the inner-region structure from different circumferential locations can interact at the center of the pipe. Clearly, the resulting turbulent structure of the three flow geometries will be different. In their paper, they studied the Reynolds-number effects on the structure of a turbulent channel flow over the Reynolds-number range of 3000–40000. They concluded that inner scaling laws of the fluctuating quantities in the inner region are Reynolds-number independent over the range examined. Near the wall, at $y^+ = 15$, power spectra of the streamwise velocity fluctuations appear to scale with inner variables over most of the energy-containing frequency range. However, at the same $y^+ = 15$ location, spectra of the velocity fluctuations normal to the wall and the fluctuating Reynolds stress do not scale on inner variables in the energy-containing frequency range. They underlined that the lack of inner scaling is primarily due to increased stretching of the inner-region vorticity field in the stream direction. In a paper reviewing the state of the art of Reynolds-number effect in wall-bounded shear flow turbulence, Gad-el-Hak and Bandyopadhyay (1994) noted that the present knowledge of Reynolds-number effect is basically phenomenological and a good theoretical understanding is largely lacking.

The present measurements have been made in a fully developed smooth and k -type rough walls turbulent channel flow for a relatively large Reynolds numbers range. The bursting period was determined by three methods: MODUL calibrated by Luchik and Tiederman (1987), TERA (Turbulent Energy Recognition Algorithm) proposed by Falco and Gendrich (1990) and Quadrant analysis introduced by Wallace et al. (1972).

A great deal of attention has been given to the study of the structure of the turbulent boundary layer over smooth walls. By contrast, the corresponding boundary layer over rough walls has received far less attention because of the complexity of the boundary conditions. Raupach et al. (1991) tackled the general problem raised by the structure of turbulence over rough walls. They underlined the necessity of taking into account some important variables that influence rough wall turbulent flows such as the roughness element aspect ratios and the roughness density. In particular, Bandyopadhyay and Watson (1988) showed the impor-

tance of the spanwise aspect ratio λ_z (span/height) of roughness elements on near-wall turbulence structure. They showed that the near wall structure varied with λ_z .

It has long been considered that the effect of wall roughness on turbulent flows was restricted to the flow region extending out to about five times the roughness height known as the “roughness sublayer.” Outside this region, smooth- and rough-wall boundary layers are assumed to have the same structure at sufficiently large Reynolds numbers. This hypothesis was labelled “wall similarity hypothesis.” With the qualification that measurement errors (especially in the use of X -probes near rough surfaces, e.g., Perry et al., 1987, Antonia, 1994) may be important, the weight of the available experimental evidence indicates fairly strong (though not unanimous) support for the hypothesis. One implication of this hypothesis is that the turbulence structure over a significant part of the layer should be unchanged in spite of significant alterations to the wall. In Raupach’s review (1991) of the turbulence structure in a rough-wall boundary layer, the main differences from a smooth-wall behavior was assumed to be confined to a region near the roughness element or “roughness sublayer.” Outside this region, smooth- and rough-wall boundary layers are assumed to have essentially the same structure. Measurements performed by Krogstad et al. (1992a) at Reynolds numbers sufficiently large to satisfy Reynolds-number similarity, while confirming the expected departure in the vicinity of the roughness, indicate important departures from smooth-wall behavior over a significant portion of the layer. This is a variance with the wall similarity hypothesis and suggests that the degree of interaction between the wall and the outer region may not be negligible. How these differences are reflected in the topology of the large scale motions and how important this interaction in the dynamics of the flow are matters which need to be investigated.

The second aim of the above study is to quantify the differences between the two flows by applying the conditional averaging method to the events detected by MODUL (Modified U_Level). Hence, such information include the shape and amplitude of the pattern of conditional averages, duration and detection rate of the detected events, from which a better understanding of the nature of the structures may be obtained.

2 Experimental Equipment and Data Analysis

2(a) Experimental Details. The experiments were performed in an open circuit wind tunnel with a working section

Nomenclature

a = longitudinal spacing between roughness elements	Re_{2h} = Reynolds-number based on the free-stream or centerline velocity U_0 and channel height $2h$	u, v = components of velocity fluctuations along x and y , respectively
C = constant value required in the TERA method	Re_θ = Reynolds-number based on the free-stream or centerline velocity U_0 and momentum thickness θ	w = roughness element width
$D(t)$ = detection function	Re_τ = Reynolds-number based on the skin friction velocity u_τ and channel height $2h$	δ = boundary layer thickness
Fu = flatness factor of the longitudinal velocity fluctuations	Su = skewness factor of the longitudinal velocity fluctuations	ϵ = shift in origin required in the case of a rough wall dissipation rate (TERA)
F_s = sampling frequency	T_B = mean time between bursts	λ_z = spanwise aspect ratio of the roughness element
F = window size required in the TERA method	Te = time between ejections	ν = kinematic viscosity
h = channel half-height or pipe radius	t, T = time	θ = momentum thickness
H = threshold level required for the Quadrant method	x, y, z = longitudinal, surface normal or spanwise Cartesian coordinates, respectively	τ_e = grouping time
k = roughness height	U_0 = centerline velocity	τ_w = mean wall shear stress
L = threshold level required for MODUL	u_τ = skin friction velocity	
Re = Reynolds-number based on the free-stream or centerline velocity U_0 and channel half-height h or boundary layer thickness δ		Superscripts
		+ = made dimensionless with inner variables
		' or _{rms} = rms value
		- = mean value

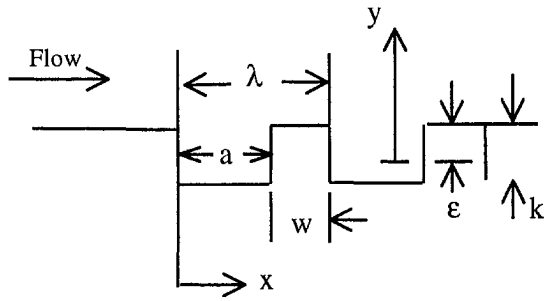


Fig. 1 Two-dimensional roughness geometry

composed of two parallel plates which formed a two-dimensional rectangular channel with a cross-sectional aspect ratio of 16:1.

In the case of the smooth wall, a $0.05 \times 0.9 \text{ m}^2$ wind channel was used for the measurements. The test section is 3 m long. The transition was triggered with 1 mm rods that spanned the test section, on both upper and lower surface, at a distance $x = 30 \text{ mm}$ from the entrance, followed by a 5 cm strip of $N^0 40$ sandpaper.

For the rough channel, the test section was 2 m long and the k -type roughness, defined by $a > w$, consisted of two-dimensional bars of square cross-section uniformly distributed over both plates. The transversally grooved surface is illustrated in Fig. 1. The k -type roughness elements have a height $k = 3 \text{ mm}$ and span the full (800 mm) width of the working section. The roughness element k^+ made dimensionless with the inner variables (the friction velocity u_τ and the kinematic viscosity ν) is reported in Table 2.

The shift in origin ϵ required in the case of a rough wall was determined using the logarithmic form of the velocity distribution. This method described in detail in Perry and Joubert (1963), is largely used in the case of k -type roughness and has shown its efficiency in turbulent flows with or without pressure gradient (Bettermann et al., 1964; Antonia and Luxton, 1971; Sabot et al., 1976). The mean value of the shift obtained from the fitted profile is reported in Table 2. More details of the roughness element are presented in Mazouz et al. (1994).

Measurements of the longitudinal (u) and normal (v) fluctuating velocity components were performed using single and X-wire probes consisting of $2.5 \mu\text{m}$ diameter Platinum-Tungsten wire. For the single probe measurements, the length was 0.5 mm, giving a length to diameter ratio of 200. The hot wires were operated with DANTEC 56 CTA constant temperature anemometers having a frequency response adjusted to be at least 15 KHz. The outputs were linearised and digitised at an appropriate sampling rate. The mean wall shear stress τ_w was determined using pressure-drop measurements and then estimates of the skin friction u_τ , defined by $u_\tau = \sqrt{\tau_w/\rho}$ was calculated. The variation of the Reynolds-number Re_τ , based on u_τ with Re_{2h} is reported on Fig. 2 (where the equations are a fit to the data) and follows typical correlations for channel flow. The overall uncertainties with the wire measurements are: $u_{\text{rms}} = \pm 1\%$ and $v_{\text{rms}} = \pm 2\%$.

2(b) Experimental Conditions. The Reynolds number Re based on the centreline velocity U_0 and channel half-height h , the sampling frequency F_s and the friction velocity u_τ are shown in Table 1 (smooth wall) and Table 2 (rough wall).

3 Mean Flow Description and Reynolds-Number Effects

3(a) The Mean Flow Description. Measurements were carried out according to Tables 1 and 2. Quantities normalized with the inner variables u_τ and ν are denoted by superscript $+$ in the usual fashion.

The question as to whether the flow is fully developed or not, will be first addressed. Comte-Bellot (1965) carried out extensive experiments, studying the downstream development of turbulent

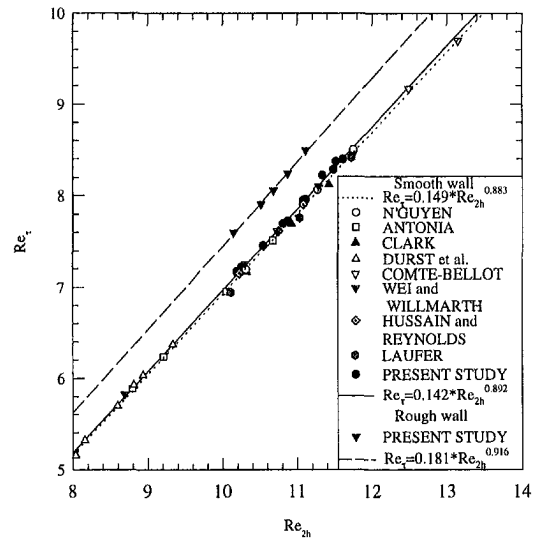


Fig. 2 Variation of the Reynolds-number Re_τ , based on u_τ , with the Reynolds-number Re_{2h} based on the free-stream or centerline velocity U_0 and channel height $2h$

channel flow. Her experiments showed that a good characterisation of the stage of development could be made, based on the values of the skewness and flatness factors on the channel centreline. A channel flow that is not fully developed will show a large negative value of the skewness and a large positive value of the flatness factor. Comte-Bellot found that the fully developed regime, where all statistical moments are independent of the downstream distance, was established about 80 channel heights downstream of the inlet. Measurements of Johansson and Alfredsson (1982) were carried out 63 channel heights from the inlet. In this paper, the downstream development of the smooth wall turbulent channel flow has been studied. In particular, the skewness (Su) and flatness (Fu) factors of the streamwise velocity fluctuations have been measured for different distances from the inlet. Results reported in Figs. 3 and 4 show the variation of the statistical moments at $x/h = 114$ (where h is the channel half-height). Included in these figures are the results of Johansson and Alfredsson (1982) and those obtained by Labraga (1984) at $x/h = 134$ for a natural transition. Those results are consistent with the present data in the outer region. Close to the wall, there are differences on Fu that may be due to Reynolds-number effects ($Re = 17300$ for Johansson and Alfredsson; $Re = 16700$ for Labraga and $Re = 18370$ in the present work). Measurements are therefore carried out at $x/h = 114$ for the smooth wall and $x/h = 68$ for the rough wall.

3(b) Reynolds-Number Effects on Velocity Fluctuations.

For the Reynolds-numbers range investigated, the streamwise turbulence intensities obtained on smooth wall and reported in Figs.

Table 1 Flow characteristics (smooth wall)

U_0 (m/s)	Re_h	u_τ (m/s)	F_s (k Hz)
7	12700	0.39	10
11	18370	0.52	20
15.75	26250	0.68	30
20.5	33400	0.86	50
25	41750	1.12	70
33	55000	1.34	70

Table 2 Flow characteristics (rough wall)

U_0 (m/s)	Re_h	u_τ (m/s)	k^+	ϵ/k	F_s (k Hz)
8	13300	0.60	120	0.31	24
11	18370	0.82	164	0.29	40
13	21700	0.945	189	0.29	60
15.65	26250	1.14	228	0.29	80
20	33400	1.46	292	0.30	90

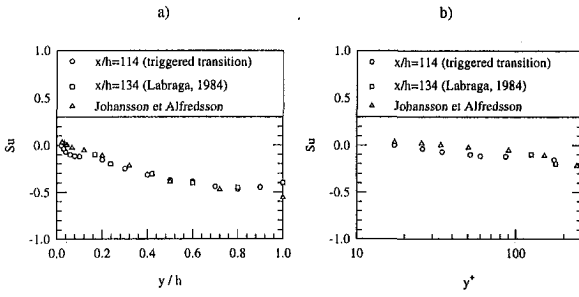


Fig. 3 Skewness factor profiles of the streamwise velocity fluctuations obtained on smooth wall. (a) Outer region, (b) Near-wall region. Uncertainties $S_u = \pm 2\%$.

5(a), 5(b), and 5(c), exhibit a clear Reynolds-number dependence. In the outer region, the turbulence intensities increase with increasing Reynolds-number (Fig. 5(a)) and are consistent with the data of Wei and Willmarth (1989) (Fig. 5(c)) obtained in a turbulent channel flow of water. As underlined by Johansson and Alfredsson (1982) large differences between various studies are at hand for measurements of u^+ in the near-wall region ($y^+ \leq 50$), which cannot be attributed solely to Reynolds-numbers effects. In most studies prior to 1970 nonlinearized anemometer signals were used, and various corrections in the measured quantities were applied. This is, of course, more questionable than to use analog or digital linearization of the anemometer signal. It is also worth mentioning that measurements close to the wall seem to be more influenced by cooling from the wall for hot wires in air than for hot films in liquids. For measurements in air the thermal conductivity of the test-section wall is usually much higher than that of air. The wall will hence act as a heat sink. This effect will also be enhanced by the high overheat temperatures usually employed in air ($\approx 200^\circ\text{C}$). The effects of this additional cooling on measurements of mean and fluctuating quantities are rather uncertain.

For the rough wall (Fig. 6), the Reynolds-number dependence of the turbulence intensity is reduced in magnitude in comparison with the smooth wall.

The skewness factor, obtained on smooth and rough walls, shows a slight Reynolds-number dependence in the near-wall region. The data of Johansson and Alfredsson (1982) and those of Labraga (1984) are consistent with the present data close to the wall (Figs. 7(a) and (b)). For the two flows, the flatness factor seems to be independent of the Reynolds-number close to the wall (Figs. 8(a) and (b)).

4 Coherent Structures Algorithms and Single-Burst Detection

4(a) Modified U_Level (MODUL). The U_Level method was first used by Lu and Willmarth (1973) to study the near-wall bursting. This method associates an event with a large instanta-

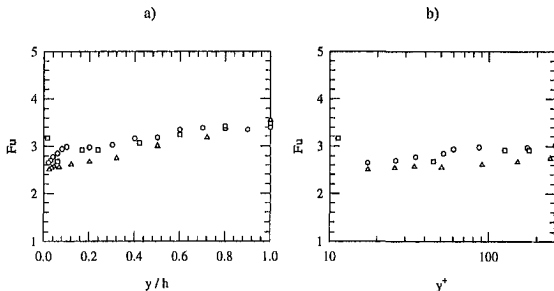


Fig. 4 Flatness factor profiles of the streamwise velocity fluctuation obtained on smooth wall. (a) Outer region, (b) near-wall region. (Symbols are the same as Fig. 3.) Uncertainties $F_u = \pm 2\%$.

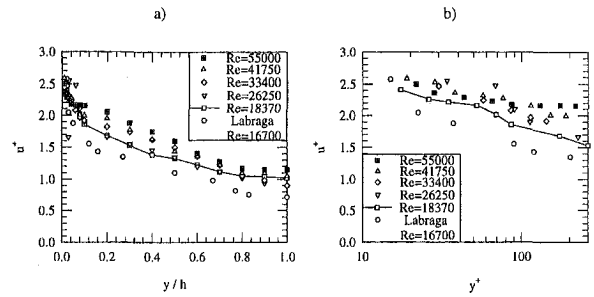


Fig. 5(a and b)

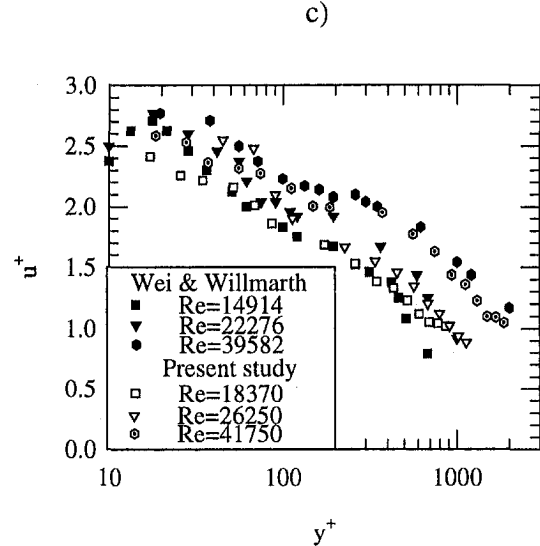


Fig. 5(c)

Fig. 5 Streamwise turbulence intensity profiles obtained on smooth wall. (a) Outer region, (b) near-wall region (symbols are same as (a)), (c) comparison with the data of Wei and Willmarth. Uncertainties $u_{rms} = \pm 1\%$.

neous negative amplitude in the streamwise velocity fluctuations. In the U_Level method, an event is detected when $u < -Lu'$ where L is a threshold and a prime denotes a rms value.

Luchik and Tiederman (1987) added an additional criterion threshold to the original U_Level method in order to eliminate or minimize the chances of multiple detections of a single event. Thus, an event is detected when $u < -Lu'$ and the detection function $D(t)$ is reset to zero when $u \geq -0.25Lu'$.

4(b) Quadrant Analysis. Wallace et al. (1972) and Willmarth and Lu (1972) introduced the uv -quadrant method. According to this method, the detection of the coherent events is

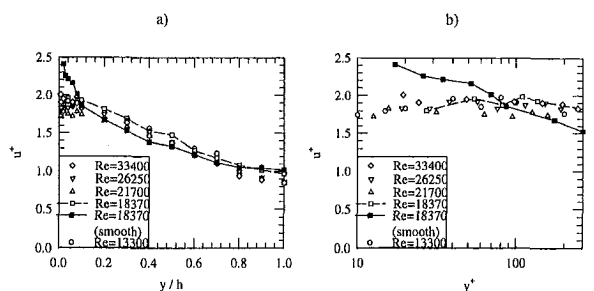


Fig. 6 Streamwise turbulence intensity profiles obtained on rough wall. (a) Outer region, (b) near-wall region. (symbols are the same as (a).) Uncertainties $u_{rms} = \pm 1\%$.

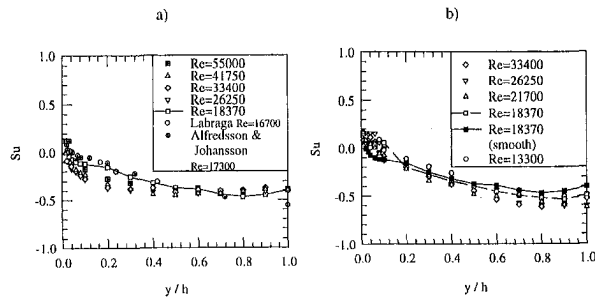


Fig. 7 Distributions of the skewness factor profiles (a) Smooth wall, (b) rough wall. Uncertainties $S_u = \pm 2\%$.

related to large instantaneous values of the Reynolds stress. In particular, the ejection phase of the bursting process, which is a sudden outward motion of the near-wall low-speed fluid, can be associated with instantaneous Reynolds stress of large amplitude in the second quadrant in the uv plane ($u < 0$ and $v > 0$). On the other hand, the sweep process, which is the moving of the outer-layer high-speed fluid toward the wall, can be associated with instantaneous Reynolds stress of large amplitude in the fourth quadrant ($u > 0$ and $v < 0$). Lu and Willmarth (1973) added a threshold condition to the method and defined the above second quadrant event as satisfying: $|uv|_{Q2} > Hu'v'$. The detection of a fourth-quadrant event is similarly defined, that is, when $|uv|_{Q4} > Hu'v'$, where H is a threshold and a prime denotes a rms value. When such an event is detected, the detection function $D(t)$ is set to unity, otherwise it is set to zero.

4(c) **TERA.** This algorithm, proposed by Falco and Gendrich (1990), is based on the idea that a high rate of change of u^2 should be strongly coupled to large values of uv . The argument is based on the transport equation for u^2 :

$$\frac{D}{Dt} \left(\frac{1}{2} u^2 \right) = \frac{p}{\rho} \frac{\partial u}{\partial x} - \overline{uv} \frac{\partial U}{\partial y} - \frac{\partial}{\partial y} \left(\frac{1}{2} u^2 v \right) - \frac{1}{3} \epsilon$$

where ϵ is the dissipation rate.

Since the energy production in the turbulent kinetic energy equation only occurs in the term for $\overline{u^2}$, its rate of change should be strongly coupled to the turbulent shear stress. A detection is identified by inspecting the mean rate of change of $\partial/\partial t (\frac{1}{2} \overline{u^2}) = u(\partial u/\partial t)$ over a predefined window F . The threshold level is determined from the long time standard deviation of the same quantity, $TR = C * [u(\partial u/\partial t)]'$ where C is a constant and a prime denotes a rms value.

4(d) **Method to Group Detections Into Bursts.** Most of the algorithm detections trigger several times during one event. It is therefore necessary to group these detections into one event. The method used in the present study was introduced by Tiederman (1989) which extended the rather low Reynolds results of Luchik and Tiederman (1987) to higher Reynolds numbers. Moreover,

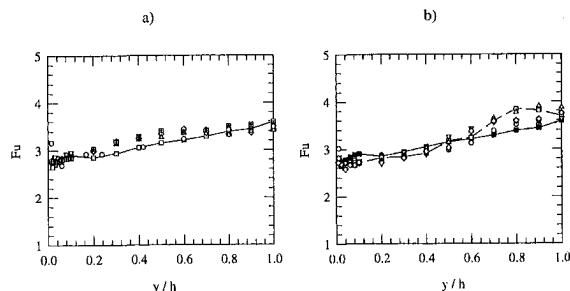


Fig. 8 Distributions of the flatness factor profiles. (a) Smooth wall, (b) rough wall. (Symbols are the same as Fig. 7.) Uncertainties $F_u = \pm 2\%$.

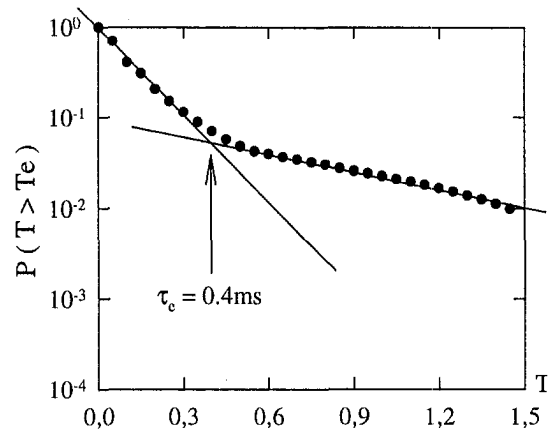


Fig. 9 Typical probability distribution for the time between ejections obtained with MODUL ($L = 1$) on smooth wall at the position $y^+ = 30$ and for a Reynolds-number $Re = 18370$. Uncertainties $T_B = \pm 6\%$.

instead of using the center-to-center time, the time between the trailing edge of one ejection and the leading edge of the next ejection was used. This refinements makes it possible to use the cumulative probability method of Barlow and Johnston (1985) to determine the grouping time. As described by Luchik and Tiederman (1987), the data processing begin by constructing a temporal record of the detections. This record is analyzed to determine the probability that T is greater than Te (the time between ejections) and the results are plotted in semi-log coordinates. For some of the detection methods, an appropriate threshold is required. The threshold is determined so that a fairly threshold independent range is ensured. This means that the average time between bursts must be nearly independent of the threshold for a sufficiently wide range.

It should be kept in mind that the rational foundation of the threshold settings can come only from such theories (Bandyopadhyay, 1998). The cumulative probability method applied to structure-identification techniques that are subjective in nature and the research of a threshold independent range permit to minimize the precarious nature of the threshold level and reduce the risk of subjective error. However, an uncertainty for the average time between bursts on the order of $\pm 6\%$ is reported on the Figs. 10 to 16. This uncertainty was determined using the method reported in Schwarz and Plesniak (1996).

5 Processing of the Experimental Data

5(a) Choice of Parameters

5(a.1) **MODUL and uv -Quadrant Methods.** The grouping technique, suggested by Barlow and Johnston (1985), Luchik and Tiederman (1987), and Tiederman (1989), has been applied here to group MODUL and uv -quadrant detections obtained on smooth and rough walls at different Reynolds numbers. The cumulative probability of the time between the trailing edge of one ejection and the leading edge of the next ejection was found to exhibit two exponential regions. The intersection of these two regions was identified as the maximum time for the interval between consecutive ejections that arise from the same first burst.

As shown in Fig. 9, ejections where the time interval between the trailing edge of one ejection and the leading edge of the next is less than 0.4 ms, are grouped into the same burst detection. If the time interval is larger than 0.4 ms, the ejections are placed in different bursts.

Figure 10 shows that over a range of L from 0.9 to 1.1 a plateau exists where the average time between grouped ejections, detected with MODUL, is independent on the threshold on the smooth wall, for the lowest Reynolds number. For the highest Reynolds number, this range is somewhat narrower. Since the grouping time was

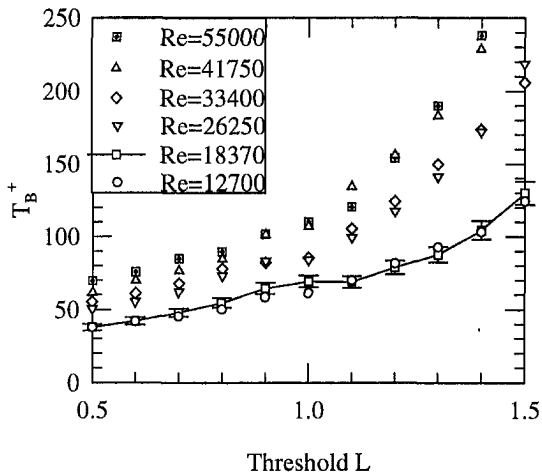


Fig. 10 Average time between bursts (T_B) for MODUL obtained on smooth wall as a function of the threshold L obtained at different Reynolds-numbers. (The vertical bars indicate uncertainty for the Reynolds-number $Re = 18370$; although not shown, the uncertainty for the other numbers is the same.) Uncertainties $T_B = \pm 6\%$.

calculated for $L = 1$ and a fairly independent threshold range is found around $L = 1$, this threshold is used in this study for the smooth wall. Similar curves are found in case of the rough wall and the threshold L has been chosen in the region where the increasing of T_B is the smallest, although this region is very narrow.

For the Quadrant 2 method, threshold independence has been studied. Distributions of the average time between burst, shown in Fig. 11, are similar in shape to those obtained with MODUL. The thresholds found here are consistent with those suggested by Comte-Bellot et al. (1978), Bogard and Tiederman (1986) and Kim and Spalart (1987) and are reported in Tables 3 and 4.

The results obtained with Quadrant 4 method, not reported here, are similar to those obtained with Quadrant 2 method.

5(a2) TERA. Falco and Gendrich (1990) have examined the effect of varying window size and threshold on TERA. They concluded that for windows $F^+ > 7$, window size did not change any of the detection statistics for a given threshold, for $R_\theta = 680$.

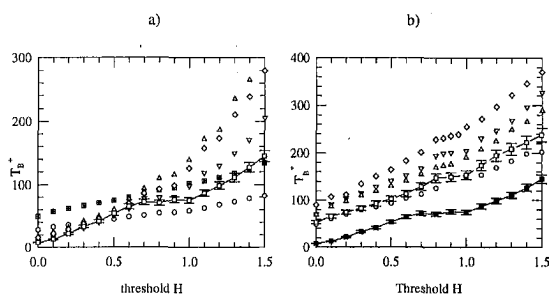


Fig. 11 Average time between bursts (T_B) for Quadrant 2 method as a function of the threshold, obtained at different Reynolds-numbers. (a) Smooth wall (symbols are the same as Fig. 10), (b) rough wall (symbols are the same as Fig. 6). Uncertainties $T_B = \pm 6\%$.

Table 3 Detection parameters used on smooth wall

Re_h	12700		18370		26250		33400		41750		55000	
detection algorithm	Th	τ_c^+	Th	τ_c^+	Th	τ_c^+	Th	τ_c^+	Th	τ_c^+	Th	τ_c^+
MODUL	1	7	1	7	1	7	1	8	1	8	1	8
Quadrant 2	0.90	6	1	6	0.92	6	0.92	8	0.90	10	0.90	7
Quadrant 4	0.84	6	0.84	6	0.63	7	0.65	8	0.66	7	0.65	8
TERA	0.5	35	0.4	35	0.4	35	0.5	35	0.4	35	0.4	35

Table 4 Detection parameters used on rough wall

Re_h	13300		18370		21700		26250		33400	
detection algorithm	Th	τ_c^+	Th	τ_c^+	Th	τ_c^+	Th	τ_c^+	Th	τ_c^+
MODUL	0.80	8	0.80	8	0.80	8	0.80	8	0.80	8
Quadrant 2	1	7	0.90	7	0.84	10	0.85	7	0.84	8
Quadrant 4	0.82	7	0.80	6	0.80	7.5	0.75	6	0.72	6.5
TERA	1.4	35	1	35	1.1	35	1.9	35	1.2	35

For a window size $F^+ = 20$ and a grouping time $\tau_c^+ = 35$, we were able to group TERA detections for which a threshold-independent range could be found on smooth and rough walls. As shown in Fig. 12, this range decreases as Reynolds number increases. This trend supports the results obtained from the above detection methods. Examination of these results suggests the choice of a value for the threshold which is reported in Tables 3 and 4.

5(b) Conditional Averages. The conditional events detected by various techniques are contaminated by the background random turbulence in the flow. In order to remove or minimise this effect, a procedure called 'conditional averaging' or 'phase averaging' is introduced. The procedure is based on the idea that, when a large number of coherent events are aligned at a certain reference point and then ensemble averaged, the contamination by background turbulence will be removed and the general characteristics of the detected coherent events will be brought out.

The conditional average of a time dependent variable $f(\tau)$ can be defined as a special ensemble average expressed as:

$$\langle f(\tau) \rangle = \frac{1}{N} \sum_{i=1}^N f(t_i + \tau)$$

where t_i is the reference (alignment) point of the event, N is the total number of events detected by the coherent structures algorithms, and τ is the time lag relative to t_i .

6 Results and Discussion

6(a) Mean Time Between Events. The time between bursts has been investigated at different y positions on smooth and rough wall. Results reported in Fig. 13 for a Reynolds number of 18370, show that this time is independent of y for the range $15 < y^+ < 100$ in the case of the smooth wall and in the major part of the turbulent channel flow in the case of the rough wall, for all algorithms and for previous determined threshold values. These results are in agreement with those obtained by Krogstad and Kaspersen (1992) and Kaspersen (1996). Results, not reported here, obtained for other Reynolds numbers are similar. Thus, only

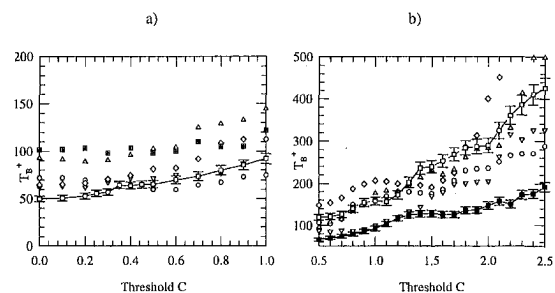


Fig. 12 Average time between bursts (T_B) for TERA method as a function of the threshold obtained at different Reynolds-numbers. (a) Smooth wall (symbols are the same as Fig. 10), (b) rough wall (symbols are the same as Fig. 6). Uncertainties $T_B = \pm 6\%$.

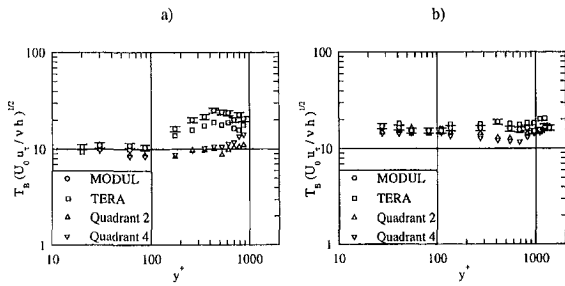


Fig. 13 Average time between bursts as function of y position and detection methods scaled with mixed variables. (The vertical bars indicate uncertainty calculated with MODUL; although not shown, the uncertainty for the other methods is the same.) (a) Smooth wall, (b) rough wall (symbols are the same as (a)). Uncertainties $T_B = \pm 6\%$.

results for $y^+ = 30$ and for different Reynolds numbers are presented here.

The main feature that emerges from Figs. 14 and 15, are, on one hand the agreement between the different algorithms, and on the other hand, the inadequacy of inner and outer scaling for all of the above techniques in the range of Reynolds-numbers investigated.

The average time between bursts is best scaling with mixed variables. A nearly constant value of 11 is found on smooth wall which is consistent with the results found by Kaspersen (1996) (≈ 12). In the case of the rough wall, a constant value of 16 is found.

The relationship between the dimensionless average time between bursts using inner variables and the Reynolds number based on the centreline velocity and the channel half-width is given by:

$$\frac{T_B u_\tau^2}{\nu} = 1.21 * Re^{0.41} \quad \text{for the smooth wall}$$

$$\frac{T_B u_\tau^2}{\nu} = 2.87 * Re^{0.412} \quad \text{for the rough wall}$$

and is shown by the solid curves in Fig. 14.

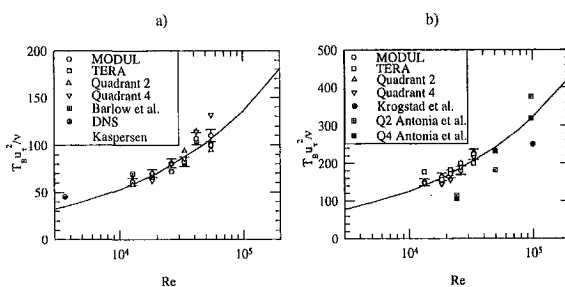


Fig. 14 Average time between bursts using inner scaling at $y^+ = 30$. (The vertical bars indicate uncertainty calculated with MODUL; although not shown, the uncertainty for the other methods is the same.) (a) Smooth wall, (b) rough wall. Uncertainties $T_B = \pm 6\%$.

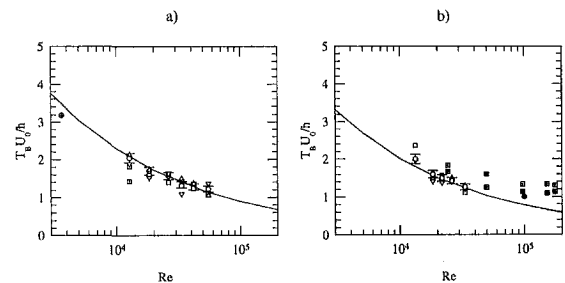


Fig. 15 Average time between bursts using outer scaling at $y^+ = 30$. (a) Smooth wall, (b) rough wall (symbols are the same as Fig. 14). Uncertainties $T_B = \pm 6\%$.

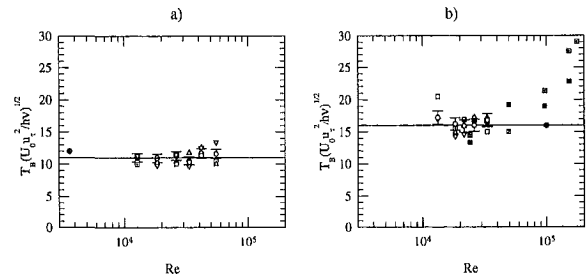


Fig. 16 Average time between bursts using mixed scaling at $y^+ = 30$. (a) Smooth wall, (b) rough wall (symbols are the same as Fig. 14). Uncertainties $T_B = \pm 6\%$.

When the outer variables are used, the relationship is given by:

$$\frac{T_B U_0}{h} = 100 * Re^{-0.41} \quad \text{for the smooth wall}$$

$$\frac{T_B U_0}{h} = 90 * Re^{-0.412} \quad \text{for the rough wall}$$

and is shown by the solid curves in Fig. 15.

Kaspersen (1996) reported results obtained in a DNS channel flow with a numerical code developed by Gavrilakis et al. (1986). The time between bursts, for the DNS channel, are shown in Figs. 14, 15, and 16. Although only one rather low Reynolds number case has been studied ($Re = 3645$), this result is consistent with the present data scaled with inner, outer or mixed variables. The results of Shah and Antonia (1989), not reported here, corroborate the conclusion drawn from the present data: mixed scaling is more relevant than inner and outer scaling for a sufficiently large range of Reynolds number. This trend may be due to the communication between the inner and outer layers which is expected to exist at $y^+ = 30$ in both smooth and rough walls. The differences between the present results and those obtained by Antonia and Krogstad (1993) are unlikely to be a result of different grouping time used.

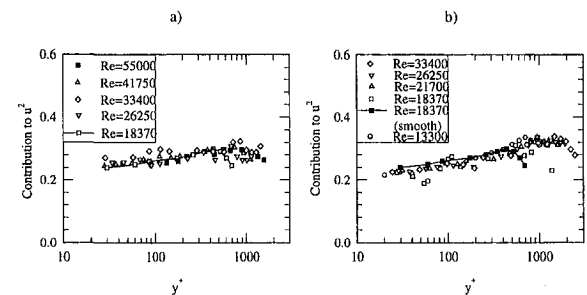


Fig. 17 Contribution to u^2 from the coherent Quadrant 2 structures obtained at different Reynolds-numbers. (a) Smooth wall, (b) rough wall. Uncertainties $u^2 = \pm 2\%$.

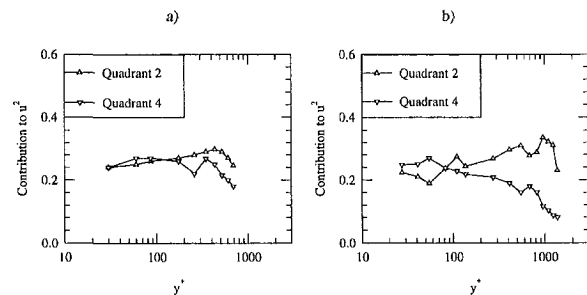


Fig. 18 Coherent contribution to u^2 , based on the Quadrant detections. $Re = 18370$. (a) Smooth wall (b) rough wall (symbols are the same as (a)). Uncertainties $u^2 = \pm 2\%$.

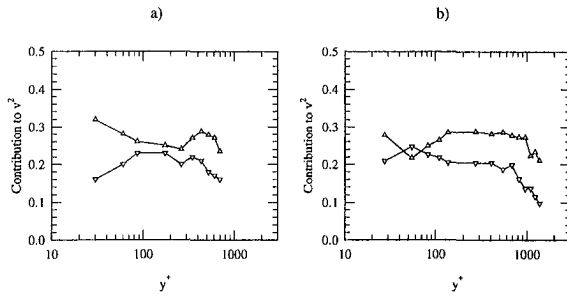


Fig. 19 Coherent contribution to v^2 , based on the Quadrant detections. $Re = 18370$. (a) Smooth wall, (b) rough wall (symbols are the same as Fig. 18). Uncertainties $v^2 = \pm 4\%$.

6(b) Coherent Contribution to the Reynolds Stresses. Since the Quadrant analysis is the only method which gives simultaneously information about the u' , v' and $u'v'$ signals, it is possible to determine the contributions to the Reynolds stresses u^2 , v^2 and uv from the coherent Quadrant 2 structures, which were computed as ($i = 2$):

$$\frac{\overline{(u^2)_i}}{u^2} = \frac{1}{u^2} \lim_{T \rightarrow \infty} \frac{1}{T} \int_0^T u(t)u(t)D(t)dt$$

$$\frac{\overline{(v^2)_i}}{v^2} = \frac{1}{v^2} \lim_{T \rightarrow \infty} \frac{1}{T} \int_0^T v(t)v(t)D(t)dt$$

$$\frac{\overline{(uv)_i}}{uv} = \frac{1}{uv} \lim_{T \rightarrow \infty} \frac{1}{T} \int_0^T u(t)v(t)D(t)dt$$

where $D(t)$ is the detector function, taking the value 1 during an event i ($i = 1 \dots 4$) and 0 elsewhere. The different contributions were computed using detection parameters reported in Tables 3 and 4.

The coherent contributions to u^2 , obtained from Quadrant 2 detections and reported on Fig. 17, are independent of Reynolds number, at least for the range of Reynolds-numbers investigated here.

In the major part of the turbulent duct flow, the ejections account for 80% of uv on smooth wall and for 60–65% in the case of the rough wall (Fig. 20). These results are consistent with the value of 75% found by Lu and Willmarth (1973), Nakagawa and Nezu (1976), Tiederman (1987) on smooth walls, and by Nakagawa and Nezu (1976, $\approx 70\%$) and Krogstad and Kaspersen (1992, $\approx 55\%$) on rough walls.

In the case of the smooth wall (Fig. 20(a)), ejections are more intense than sweeps within the observed range of y^+ . Next, in the equilibrium region as it was defined in Nakagawa and Nezu (1976), the intensity of each event is nearly constant, irrespective

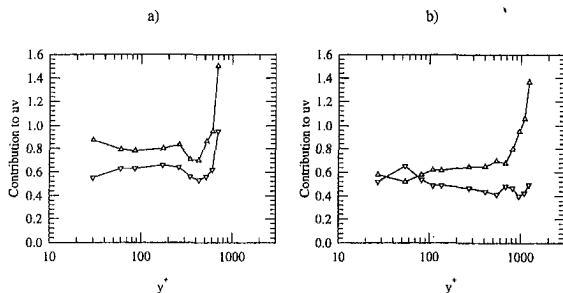


Fig. 20 Coherent contribution to uv , based on the Quadrant detections. $Re = 18370$. (a) Smooth wall (b) rough wall (symbols are the same as Fig. 18). Uncertainties $uv = \pm 3\%$.

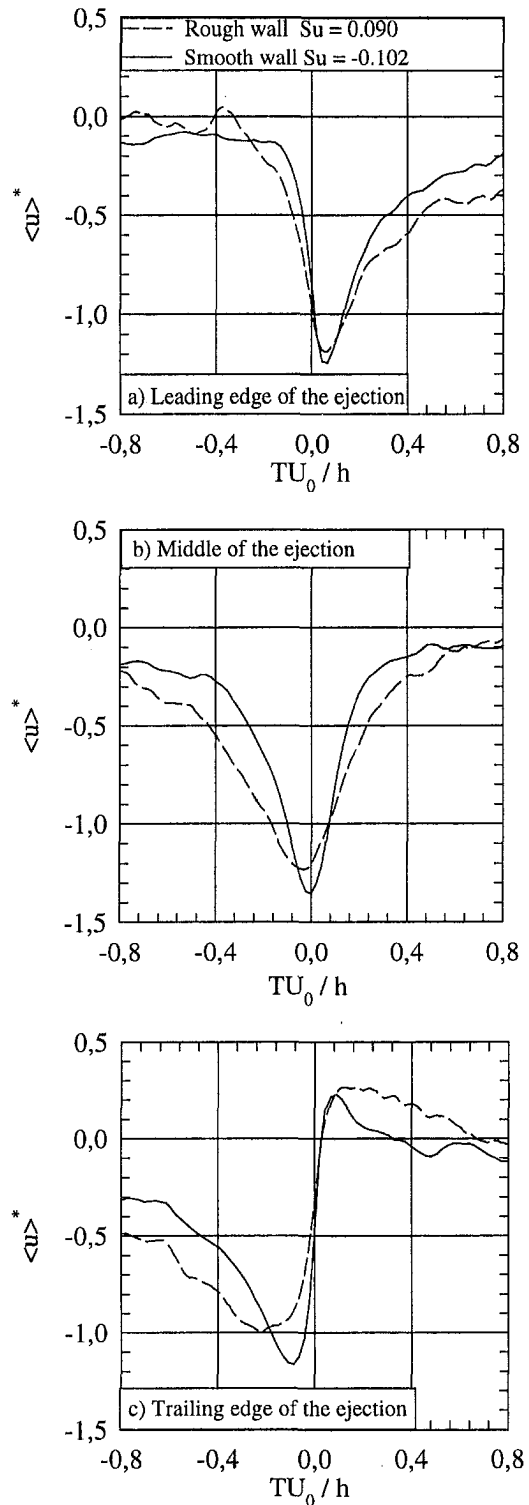


Fig. 21 Conditional averages applied to MODUL. $y^+ = 30$. $Re = 18370$

of the value of y^+ . Since in this region a dynamic equilibrium exists between the turbulence production and dissipation, and a similarity in turbulence structure is expected to exist independently of external boundary condition, it is expected that the bursting process and the accompanying turbulence production may attain a stable equilibrium state in this region, resulting in almost constant intensity for each event (Nakagawa and Nezu, 1976).

In the free-surface region ($y^+ > 500$ or $y/h > 0.6$), the intensity of each event rapidly increases with y^+ . Near the free-surface both ejections and sweeps show a positive stress of over 100%.

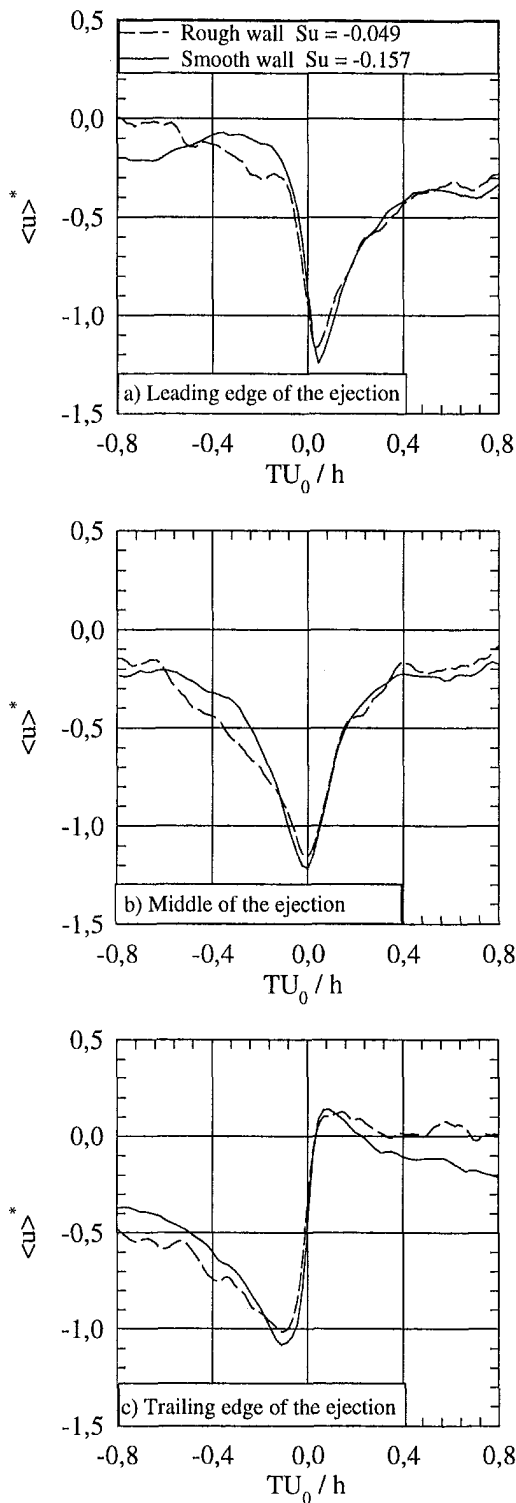


Fig. 22 Conditional averages applied to MODUL. $y^+ = 100$. $Re = 18370$

For the rough wall (Fig. 20(b)), in the range from the wall to the middle of the equilibrium region, where the roughness effect on the turbulence structure may be expected to appear, some differences in the intensity profiles for the rough and smooth walls can be observed. Note that, contrary to the case of the smooth walls, the intensity of ejections decreases toward the wall to become nearly equal or smaller than sweeps, as it was noted by Grass (1971), Nakagawa and Nezu (1976) and Krogstad et al. (1992a). The same result is observed in the representation of the contribution to v^2 and v'^2 (Figs. 18 and 19).

6(c) Conditional Averages. By applying conditional averages to MODUL at different reference times, it is possible to obtain a complete representation of the bursting process. Based on the events detected by the algorithm MODUL obtained with a threshold level $L = 1$ for a Reynolds-number $Re = 18370$ at different positions (y/h or y^+), the conditionally averaged signals for both smooth and rough wall are shown in Figs. 21 to 25. Since the aim of this part is not to study the scale of the conditional average patterns but only the differences between smooth and rough walls turbulent flows, the conditional average patterns are made dimensionless with the outer variables (channel half-height h and centreline velocity U_0) which are the same for the two flows.

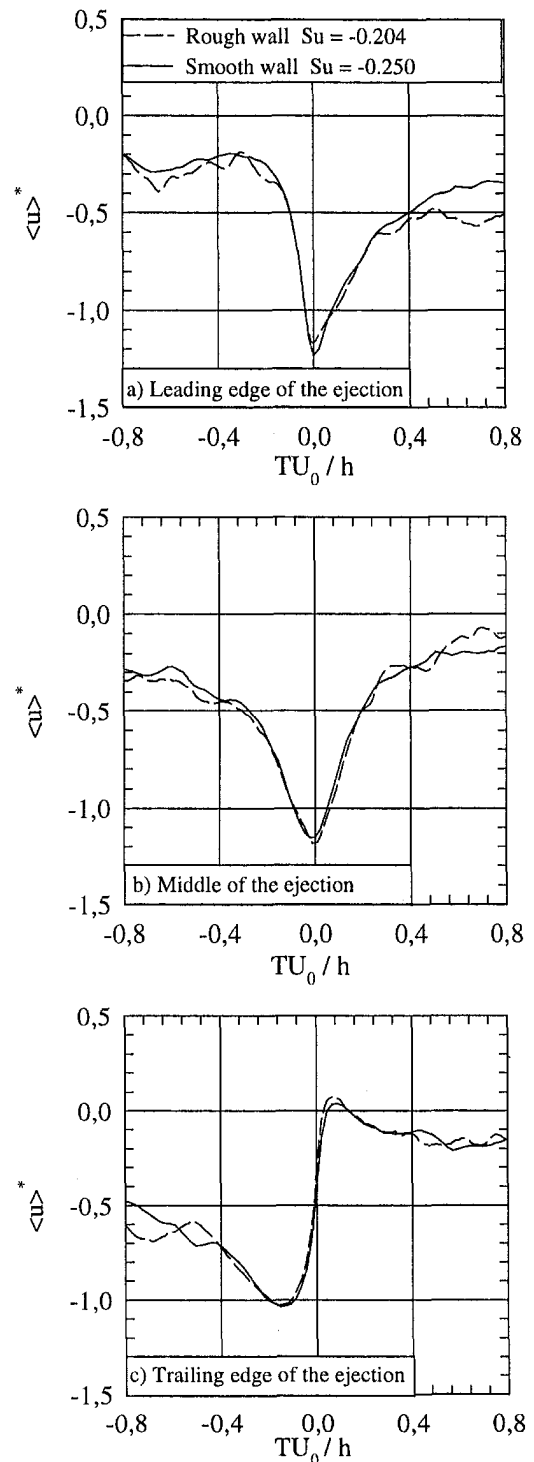


Fig. 23 Conditional averages applied to MODUL. $y^+ = 260$. $Re = 18370$

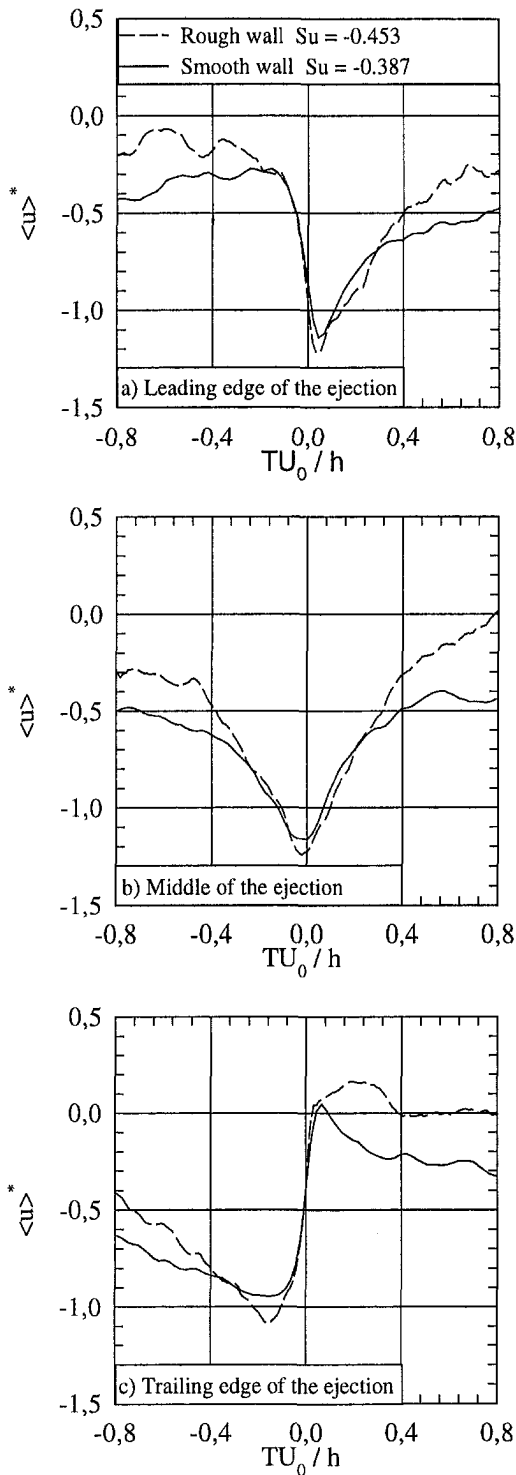


Fig. 24 Conditional averages applied to MODUL. $y/h = 0.6$. $Re = 18370$

The appearance of the detected structures are correlated with the skewness factor (Fig. 6), as it was shown by Johansson and Alfredsson (1982).

The mean event duration obtained from the events detected can be defined using the method introduced by Yuan and Mokhtarzadeh-Dehghan (1994). This duration is defined as the time interval between the points corresponding to the half-level of the peak of the conditional average pattern, if only one peak (positive or negative) is involved. However, if there are two or more peaks present, the mean event duration is taken as the time

interval between the two outward points corresponding to the half-level of the two most outstanding peaks.

At $y^+ = 30$, the mean event duration is larger on rough walls than on smooth walls, which indicates that the roughness effect is very important in this region. This influence is still present at $y^+ = 100$ and in the range ($y/h > 0.6$), where the mean event duration is larger on smooth walls than on rough walls.

In the range from the wall to the middle of the equilibrium region ($y/h \approx 0.1$) and for ($y/h > 0.6$), the roughness effect on the turbulence structures is very marked. This is in good agreement with the results of Nakagawa and Nezu (1976) and those of

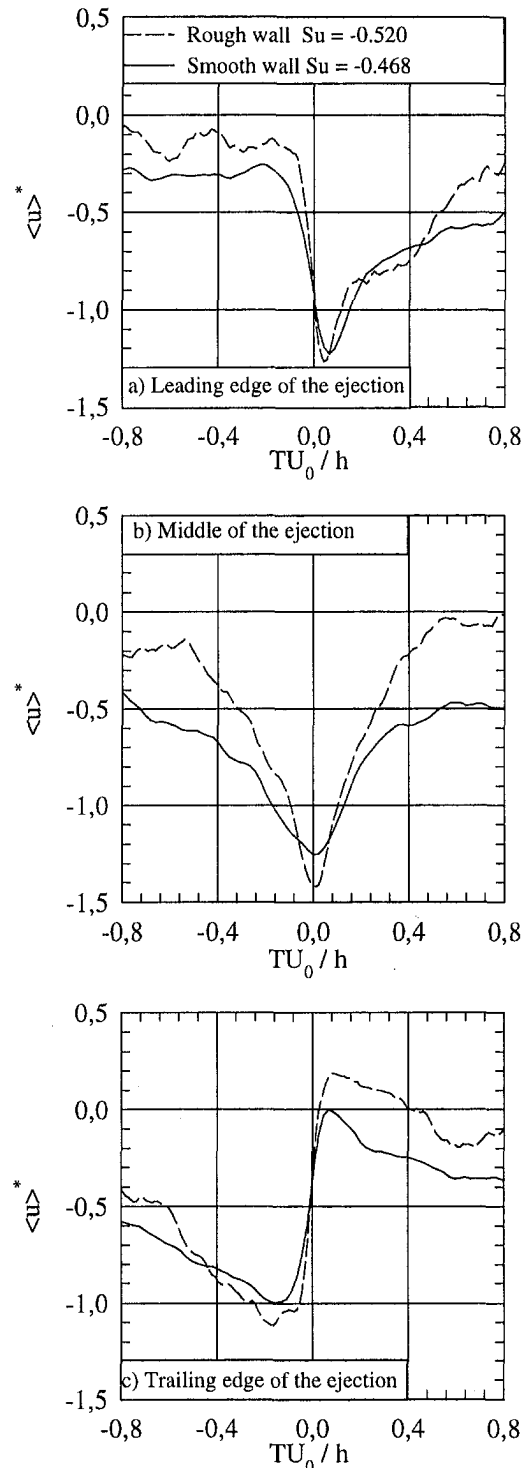


Fig. 25 Conditional averages applied to MODUL. $y/h = 0.8$. $Re = 18370$

Krogstad, Antonia, and Browne (1992a). However in the range ($0.2 < y/h < 0.6$) including the position $y^+ = 260$, no differences appear between the detected events in the two flows, which is in agreement with the representation of the skewness factor on smooth and rough walls in this range (Fig. 7) and the results of Krogstad, Antonia, and Browne (1992a).

7 Conclusion

Hot wire anemometry measurements were made in fully developed turbulent channel flow over a Reynolds-number range of 12,700 to 55,000. The structure of smooth and k -type rough wall turbulent channel flow was examined using a few of the most common detection techniques (Modified U_Level (MODUL), TERA, Quadrant analysis) and conditional averages. The main results that emerge from the present study led to the following conclusions:

(i) When grouping time is used and a threshold-independent range could be found, all algorithms yield approximately the same time between the trailing edge of one burst to the leading edge of the next burst.

(ii) In the range of Reynolds-numbers studied, the mean bursting frequency is best scaled on mixed variables in both smooth and rough walls because of the likely interaction between the inner and outer layers of the flow.

(iii) Study of the coherent contribution to the Reynolds stresses show that both ejections and sweeps are the most important events in the two flows. In particular, in the case of the smooth walls, ejections are more intense than sweeps irrespective of the position over the wall, whereas near the roughness element, sweeps become equal or more dominant than ejections.

(iv) Conditional averages applied to MODUL at different reference times and made dimensionless with outer variables, show that some differences in the intensity profiles and the mean event duration between smooth and rough walls turbulent channel flows appear in both the inner and outer region. Near the roughness element, the detected events have a larger duration and less pronounced peaks than on the smooth wall. However, in the outer region of the flow, this behavior is inverted.

References

Alfredsson, P. H., and Johansson, A. V., 1984, "On the Detection of Turbulence-Generating Events," *Journal of Fluid Mechanics*, Vol. 139, pp. 325–345.

Alfredsson, P. H., and Johansson, A. V., 1984, "Time Scales in Turbulent Channel Flow," *Physics of Fluids*, Vol. 27, pp. 1974–1981.

Antonia, R.-A., 1994, "The Effect of Different Types of Surface Conditions on a Turbulent Boundary Layer," 1st International Conference on Flow Interaction, September 5–9 September 1994, Hong-Kong.

Antonia, R.-A., and Kim, J., 1994, "Low-Reynolds-Number Effects on Near Wall Turbulence," *Journal of Fluid Mechanics*, Vol. 276, pp. 61–80.

Antonia, R.-A., and Krogstad, P. A., 1993, "Scaling of Bursting Period in Turbulent Rough Wall Boundary Layers," *Experiments in Fluids*, Vol. 15, pp. 82–84.

Antonia, R.-A., and Luxton, K. E., 1971, "The Response of a Turbulent Boundary Layer to a Step Change in Surface Roughness, Part 1. Smooth to Rough," *Journal of Fluid Mechanics*, Vol. 48, Part 4, pp. 721–761.

Antonia, R.-A., Teitel, M., Kim, J., and Browne, L., 1992, "Low-Reynolds-Number Effects in a Fully Developed Turbulent Channel Flow," *Journal of Fluid Mechanics*, Vol. 236, pp. 579–605.

Bandyopadhyay, P. R., 1982, "Period Between Bursting in Turbulent Boundary Layers," *Physics of Fluids*, Vol. 24, p. 1751.

Bandyopadhyay, P. R., and Watson, R. D., 1988, "Structure of Rough-Wall Turbulent Boundary Layers," *Physics of Fluids*, Vol. 31, pp. 1877–1883.

Bandyopadhyay, P. R., 1998, "Self-Sustaining Mechanisms of Wall Turbulence, Book Review," *AIAA Journal*, Vol. 36, No. 8, p. 1549.

Barlow, R. S., and Johnston, J. P., 1985, "Structure of Turbulent Boundary Layer on Concave Surfaces," Stanford University, Department of Mechanical Engineering, Report MD-47.

Bettermann, D., Brin, E., and Gougat, P., 1964, "Distribution des vitesses et des températures dans la couche limite de plaques rugueuses," *Compte-rendu de l'académie des sciences*, Tome 258, PAARIS.

Blackwelder, R. F., and Haritonidis, J. H., 1983, "Scaling of the Bursting Frequency in Turbulent Boundary Layers," *Journal of Fluid Mechanics*, Vol. 132, p. 87.

Blackwelder, R. F., and Kaplan, R. E., 1976, "On the Wall Structure of the Turbulent Boundary Layer," *Journal of Fluid Mechanics*, Vol. 76, p. 89.

Bogard, D. G., and Tiederman, W. G., 1986, "Burst Detection with Single-Point Velocity Measurements," *Journal of Fluid Mechanics*, Vol. 162, pp. 389–413.

Cantwell, B. J., 1981, "Organised Motion in the Turbulent Flow," *Annual Review Fluid Mechanics*, Vol. 13, p. 437.

Clark, J. A., 1968, "A Study of Incompressible Turbulent Boundary Layer in Channel Flow," *ASME Journal of Basic Engineering*, Vol. 90, pp. 455–468.

Comte-Bellot, G., 1965, "Ecoulement Turbulent entre Deux Parois Parallèles," Publication Scientifique et Technique du Ministère de l'Air No 419.

Comte-Bellot, G., Sabot, J., and Saleh, I., 1978, "Dynamic Measurements in Unsteady Flows," Marseille, Baltimore, p. 213.

Durst, F., Fischer, M., Kikura, H., and Jovanovic, J., 1996, "Laser-Doppler-Measurements of Near-Wall Turbulent Flows," *Proceedings of 4th International Workshop on Electrochemical Flow Measurement-Fundamentals and Applications*, 17–20 Mar., Lahnstein, Germany.

Falco, R. E., and Gendrich, C. P., 1990, "The Turbulence Burst Detection Algorithm of Z. Zaric," *Near Wall Turbulence*, S. J. Kline and N. H. Afgan, eds., Hemisphere.

Gad-El-Hak, M., and Bandyopadhyay, P. R., 1994, "Reynolds-Number Effects in Wall-Bounded Turbulent Flows," *Applied Mechanics Review*, Vol. 47, No. 8, pp. 307–365.

Gavrilakis, S., Tsai, H. M., Voke, P. R., and Leslie, D. C., 1986, "Large Eddy Simulation of Low Reynolds-Number Channel Flow by Spectral and Finite Difference Method," *Notes on Numerical Fluid Mechanics*, Vieweg, Vol. 15, pp. 105–118.

Grass, A. J., 1971, "Structural Features of Turbulent Flow Over Smooth and Rough Boundaries," *Journal of Fluid Mechanics*, Vol. 50, pp. 233–255.

Hussain, A. K. M. F., 1986, "Coherent Structures and Turbulence," *Journal of Fluid Mechanics*, Vol. 173, pp. 303–356.

Hussain, A. K. M. F., and Reynolds, W. C., 1975, "Measurements in Fully Developed Turbulent Channel Flow," *Journal of Fluid Engineering*, Vol. 97, pp. 568–580.

Johansson, A. V., and Alfredsson, P. H., 1982, "On the Structure of Turbulent Channel Flow," *Journal of Fluid Mechanics*, Vol. 122, pp. 233–236.

Kaspersen, J. H., 1996, "A Study of Coherent Structures Using Wavelet Analysis," Thesis of the University of Science and Technology in Trondheim, Norway.

Kim, J., and Spalart, P. R., 1987, "Scaling of the Bursting Frequency in Turbulent Boundary Layers at Low Reynolds Numbers," *Physics of Fluids*, Vol. 30, pp. 3326–3328.

Krogstad, P.-A., Antonia, R.-A., and Browne, L. W., 1992a, "Comparison Between Rough- and Smooth-Wall Turbulent Boundary Layers," *Journal of Fluid Mechanics*, Vol. 245, pp. 599–617.

Krogstad, P.-A., and Antonia, R.-A., 1994, "Structure of Turbulent Boundary Layer on Smooth and Rough Walls," *Journal of Fluid Mechanics*, Vol. 277, pp. 1–21.

Krogstad, P.-A., and Kaspersen, J. H., 1992, "Methods to Detect Coherent Structures—A Comparison," *Proceedings of the 11th Australian Fluid Mechanics Conference*, Hobart Tasmania.

Labraga, L., 1984, "Etude de l'établissement du régime turbulent entre deux parois parallèles," Thèse de 3^{ème} Cycle, Université de Valenciennes et du Hainaut Cambrésis.

Laufer, J., 1950, "Some Recent Measurements in a Two-Dimensional Turbulent Channel," *Journal of Aeronautical Science*, Vol. 17, pp. 277–287.

Laufer, J., 1951, "Investigation of Turbulent Flow in a Two-Dimensional Channel," NACA-Report, No. 1053.

Lu, S. S., and Willmarth, W. W., 1973, "Measurements of the Structure of the Reynolds Stress in Turbulent Boundary Layers," *Journal of Fluid Mechanics*, Vol. 60, pp. 481–511.

Luchik, T. S., and Tiederman, W. G., 1987, "Timescale and Structure of Ejections and Bursts in Turbulent Channel Flows," *Journal of Fluid Mechanics*, Vol. 174, pp. 529–552.

Mazouz, A., Labraga, L., and Tournier, C., 1994, "Behaviour of Reynolds Stress on Rough Wall," *Experiments in Fluids*, Vol. 1, pp. 39–44.

Nakagaya, H., and Nezu, I., 1976, "Production of the Reynolds Stress from Bursting Events in Open Channel Flows," *Journal of Fluid Mechanics*, Vol. 80, Part 1, pp. 99–128.

N'Guyen, V. T., 1987, "Contribution à l'étude de la structure de la turbulence près d'une paroi lisse," Thèse de Doctorat, Université de PARIS VI.

Perry, A. E., and Joubert, P. N., 1963, "Rough-Wall Turbulent Boundary Layers in Adverse Pressure Gradients," *Journal of Fluid Mechanics*, Vol. 17, pp. 193–211.

Perry, A. E., Lim, K. L., and Henbest, S. M., 1987, "An Experimental Study of the Turbulence Structures in Smooth- and Rough-Wall Boundary Layers," *Journal of Fluid Mechanics*, Vol. 177, pp. 437–466.

Raupach, M. R., 1981, "Conditional Statistics of Reynolds Stress in Rough-Wall and Smooth-Wall Turbulent Boundary Layers," *Journal of Fluid Mechanics*, Vol. 108, pp. 363–382.

Raupach, M. R., Antonia, R.-A., and Rajagopalan, S., 1991, "Rough-Wall Turbulent Boundary Layers," *Applied Mechanics Review*, Vol. 44, pp. 1–25.

Sabot, J., and Comte-Bellot, G., 1976, "Intermittency of Coherent Structures in the Core Region of Fully Developed Turbulent Pipe Flow," *Journal of Fluid Mechanics*, Vol. 74, pp. 767–796.

Schwarz, A. C., and Plesniak, M. W., 1996, "The Influence of Interacting Strain Rates on Turbulence in Convex Boundary Layers," *Physics of Fluids*, Vol. 8, No. 11, pp. 3163–3171.

Shah, D. A., and Antonia, R.-A., 1989, "Scaling of the Bursting Period in Turbulent Boundary Layer and Duct Flows," *Physics of Fluids*, pp. 318–325.

Tiederman, W. G., 1989, "Eulerian Detection of Turbulent Bursts," Kline Afgan edition, *Near Wall Turbulence*, New York, Hemisphere.

Wallace, J. M., Eckelmann, H., and Brodkey, R. S., 1972, "The Wall Region in Turbulent Shear Flow," *Journal of Fluid Mechanics*, Vol. 54, Part 1, pp. 39–48.

Wei, and Willmarth, W. W., 1989, "Reynolds Number Effects on the Structure of a Turbulent Channel Flow," *Journal of Fluid Mechanics*, Vol. 204, Part 1, pp. 57–95.

- Willmarth, W. W., 1975, "Structure of Turbulence in Boundary Layers," *Advances Applied Mechanics*, Vol. 15, pp. 159–254.
- Willmarth, W. W., and Lu, S. S., 1972, "Structure of the Reynolds Stress Near the Wall," *Journal of Fluid Mechanics*, Vol. 55, Part 1, pp. 65–92.
- Wood, D. H., and Antonia, R-A., 1975, "Measurements in a Turbulent Boundary Layer Over a *d*-Type Surface Roughness," *ASME Journal Applied Mechanics*, Vol. 42, pp. 591–597.
- Yuan, Y. M., and Mokhtarzadeh-Dehghan, M. R., 1994, "A Comparison Study of Conditional-Sampling Methods Used to Detect Coherent Structures in Turbulent Boundary Layer," *Physics of Fluids*, Vol. 6, No. 6, pp. 2038–2056.
-

A Modified Model for Diffusion in Second-Moment Turbulence Closures

Anthony G. Straatman

Assistant Professor of Mechanical Engineering,
Department of Mechanical &
Materials Engineering,
The University of Western Ontario,
London, Ontario, Canada N6A 5B9
Mem. ASME

A study has been carried out to determine the relative roles of the three diffusion sub-processes contained in the Lumley (1978) diffusion model. The three sub-processes are described as being the production of turbulent transport, the third-order pressure-velocity process, which regulates the relative magnitudes of the turbulent transport components, and the pressure-diffusion. The present work describes a unique method for calibrating the model based on an analysis of zero-mean-shear turbulence. On the basis of the analysis, and using recent direct numerical simulation and experimental data, the coefficients in the Lumley (1978) model are modified such that the model gives the correct behavior in the diffusive limit. The modified model was then validated by carrying out CFD predictions for three benchmark flows of engineering interest. The modified Lumley (1978) diffusion model has two clear advantages over the more commonly used Daly and Harlow (1970) model. First, unlike the Daly and Harlow (1970) model, the modified Lumley (1978) model is mathematically correct and second, it was shown in the present validation that the modified Lumley (1978) model gives the most consistently reasonable predictions.

1 Introduction

As the speed and capacity of digital computers continues to increase, the use of second-moment turbulence closures in industrial CFD applications is becoming more practical. Most commercial CFD softwares now contain second-moment closure schemes as an optional means for closing the time-averaged mean transport equations. However, in most cases, the available second-moment closure schemes are based on very basic process models, some of which are known to be physically and/or mathematical incorrect. The process considered in this paper is the diffusive transport of the Reynolds stresses, which is almost exclusively modeled using the Daly Harlow (1970) model (or its isotropic variant), despite the fact that this model is known to be mathematically incorrect. The pervasiveness of the Daly and Harlow (1970) model appears to be for at least two reasons. First, the diffusion process is often small in the Reynolds stress budget and therefore, the accurate modeling of diffusion is not considered critical and second, it is the simplest model to implement in a CFD code. In terms of the influence of diffusion, in many cases the diffusive transport is insignificant compared to other processes in the Reynolds stress budget, however, there are many important cases where diffusion plays a significant role. In a generic CFD code, the chosen models should be accurate over as wide a range as possible, including the limits in which they are dominant. The implementation of complex second-moment closure models has been addressed in recent literature (Farhanieh et al., 1993; Lien and Leschziner, 1994). This paper explores the diffusion process further in terms of recent developments and recommends a model that is both physically relevant and mathematically correct.

Recent studies by Demuren and Sarkar (1993), Schwarz and Bradshaw (1994) and Straatman et al. (1998) considered various aspects of modeling the diffusion terms in the Reynolds-stress equation. Demuren and Sarkar (1993) carried out a sys-

tematic study of several existing pressure-strain and diffusion models in the computation of plane channel flow. Their results showed that the diffusion model developed by Mellor and Herring (1973), which is essentially an isotropic-diffusivity version of the better known Hanjalić and Launder (1972) model, gave the best predictions for the relaxation toward isotropy near the center of the channel. Schwarz and Bradshaw (1994) calculated turbulent fluxes in a three-dimensional boundary layer from measured Reynolds-stress data using the Daly and Harlow (1970), Hanjalić and Launder (1972) and Lumley (1978) diffusion models. They concluded that all models gave reasonable predictions of the turbulent fluxes, but the Lumley (1978) model performed best overall. Straatman et al. (1998) examined the diffusion process using zero-mean-shear (ZMS) turbulence. Their study included an analysis to determine the behavior of all of the abovementioned models in the diffusive limit. The main conclusions of their study were that the pressure-velocity processes in both the second- and third-moment equations were important for establishing the correct anisotropy level in diffusive turbulence, and that the Lumley (1978) diffusion model was the only existing model which is capable of modeling the entire diffusion process at the second-moment level. Straatman et al. (1998) also suggested an ad hoc modification to one of the coefficients in the Lumley (1978) model, but suggested that a more comprehensive calibration could be done if more detailed data for ZMS turbulence was available.

In this paper, further analysis is directed at the Lumley (1978) (hereafter denoted as LUM) diffusion model. The main objective of the present work is to develop a calibration method to properly apportion the sub-processes contained in the LUM model. The calibration is done in a systematic manner using a semi-empirical analysis of ZMS turbulence, and by considering recent direct numerical simulation (DNS) and experimental data. Modifications are suggested to the coefficients in the LUM model that control the relative influence of the diffusion sub-processes. The modified model is then tested in a number of flows of engineering interest to demonstrate that it gives consistently reasonable predictions. The predictions are compared to similar predictions obtained using the original LUM model and the commonly used Daly and Harlow (1970) model.

Contributed by the Fluids Engineering Division for publication in the JOURNAL OF FLUIDS ENGINEERING. Manuscript received by the Fluids Engineering Division May 4, 1999; revised manuscript received September 6, 1999. Associate Technical Editor: P. Bradshaw.

2 Mathematical Formulation

The mathematical formulation begins with the incompressible form of the Reynolds- and time-averaged equations for the conservation of mass:

$$\frac{\partial \rho}{\partial t} + \frac{\partial}{\partial x_i} (\rho \bar{U}_i) = 0 \quad (1)$$

and momentum:

$$\begin{aligned} \frac{\partial}{\partial t} (\rho \bar{U}_i) + \frac{\partial}{\partial x_k} (\rho \bar{U}_k \bar{U}_i) \\ = - \frac{\partial \bar{P}}{\partial x_k} \delta_{ki} + \mu \frac{\partial^2}{\partial x_k^2} (\bar{U}_i) - \frac{\partial}{\partial x_k} (\rho \overline{u_i u_k}) \end{aligned} \quad (2)$$

where \bar{U}_i is the fluid velocity, \bar{P} is the pressure, and ρ and μ are the fluid density and dynamic viscosity, respectively. The second-order term on the right-hand side of the Reynolds-averaged momentum equation is the Reynolds-stress term. This term represents the net transfer of fluctuating momentum, ρu_i , by the fluctuating velocity u_k and is perceived in the momentum equation as an apparent stress.

In second-moment turbulence closures, the Reynolds-stress transport equation is solved for each non-zero component of the Reynolds-stress tensor. The Reynolds-stress equation is given as:

$$\underbrace{\frac{\partial \overline{u_i u_j}}{\partial t} + \bar{U}_k \frac{\partial \overline{u_i u_j}}{\partial x_k}}_{\mathcal{C}_{ij}} = - \underbrace{\left(\overline{u_i u_k} \frac{\partial \bar{U}_j}{\partial x_k} + \overline{u_j u_k} \frac{\partial \bar{U}_i}{\partial x_k} \right)}_{\mathcal{P}_{ij}} + \mathcal{D}_{ij} + \pi_{ij} - \epsilon_{ij} \quad (3)$$

The symbolic terms represent the convection, \mathcal{C}_{ij} , the shear production \mathcal{P}_{ij} , the diffusion \mathcal{D}_{ij} , the pressure-strain π_{ij} , and the dissipation ϵ_{ij} of $\overline{u_i u_j}$. The convection and shear production require no approximation, but the remaining processes must be modeled to close the equation set at the second-moment level. The pressure-strain process is modeled in the present work using the Speziale et al. (1991) (denoted hereafter as SSG) relation, which is given as:

$$\begin{aligned} \pi_{ij} = - (C_1 \epsilon + \frac{1}{2} C_1^* \mathcal{P}_{kk}) a_{ij} + C_2 \epsilon (a_{ik} a_{kj} - \frac{1}{3} A_2 \delta_{ij}) \\ + (C_3 - C_3^* A_2^{1/2}) k S_{ij} + C_4 k (a_{ik} S_{jk} + a_{jk} S_{ik} - \frac{2}{3} a_{kl} S_{kl} \delta_{ij}) \\ + C_5 k (a_{ik} W_{jk} + a_{jk} W_{ik}) \end{aligned} \quad (4)$$

where $k (= \frac{1}{2} \overline{u_i u_i})$ is the turbulent kinetic energy and ϵ is the isotropic dissipation rate of k . The additional terms in the SSG model are given as:

$$\begin{aligned} a_{ij} = \frac{\overline{u_i u_j}}{k} - \frac{2}{3} \delta_{ij}, \quad A_2 = a_{ik} a_{ki}, \\ S_{ij} = \frac{1}{2} \left(\frac{\partial \bar{U}_i}{\partial x_j} + \frac{\partial \bar{U}_j}{\partial x_i} \right), \quad W_{ij} = \frac{1}{2} \left(\frac{\partial \bar{U}_i}{\partial x_j} - \frac{\partial \bar{U}_j}{\partial x_i} \right) \end{aligned}$$

and the model coefficients are:

$$\begin{aligned} \{C_1, C_1^*, C_2, C_3, C_3^*, C_4, C_5\} \\ = \{1.7, 0.9, 1.05, 0.8, 0.65, 0.513, 0.2\} \end{aligned}$$

An alternate, and equally popular, approach to modeling the pressure-strain term is to use the return-to-isotropy and isotropization-of-production models as the basis, with additional model relations to account for the interaction with solid boundaries. This model is described in, for example, Demuren and Sarkar (1993), and is denoted hereafter as RTI+IP.

The dissipation of $\overline{u_i u_j}$ is assumed to be isotropic and modeled as:

$$\epsilon_{ij} = \frac{2}{3} \epsilon \delta_{ij} \quad (5)$$

The isotropic dissipation rate, ϵ , is then obtained from the following modeled transport equation:

$$\begin{aligned} \frac{\partial \epsilon}{\partial t} + \bar{U}_k \frac{\partial \epsilon}{\partial x_k} = \frac{\partial}{\partial x_k} \left[C_\epsilon \frac{k}{\epsilon} \left(\overline{u_k u_l} \frac{\partial \epsilon}{\partial x_l} \right) \right] \\ + \frac{1}{2} C_{\epsilon 1} \frac{\epsilon}{k} \mathcal{P}_{kk} - C_{\epsilon 2} \frac{\epsilon^2}{k} \end{aligned} \quad (6)$$

where:

$$\{C_\epsilon, C_{\epsilon 1}, C_{\epsilon 2}\} = \{0.14, 1.44, 1.83\}$$

3 The Diffusion Model

The LUM diffusion model was derived originally by a statistical analysis and is strictly applicable for weakly inhomogeneous flows. The complete model includes components for both the turbulent transport and pressure-diffusion components of \mathcal{D}_{ij} . The diffusion process in Eq. (3) is given in its exact form (neglecting molecular diffusion) as:

$$\mathcal{D}_{ij} = \frac{\partial}{\partial x_k} \left(- \overline{u_i u_j u_k} - \frac{\overline{p' u_j}}{\rho} \delta_{ik} - \frac{\overline{p' u_i}}{\rho} \delta_{jk} \right) \quad (7)$$

where $\overline{u_i u_j u_k}$ is the turbulent transport and the pressure-velocity terms represent pressure-diffusion. LUM derived the following model for the turbulent transport:

$$- \overline{u_i u_j u_k} = C_{s1} \frac{k}{\epsilon} [\mathcal{G}_{ijk} + C_{s2} (\mathcal{G}_i \delta_{jk} + \mathcal{G}_j \delta_{ik} + \mathcal{G}_k \delta_{ij})] \quad (8)$$

where C_{s1} and C_{s2} are coefficients, \mathcal{G}_{ijk} is a third-order tensor given by:

$$\mathcal{G}_{ijk} = \left(\overline{u_i u_l} \frac{\partial \overline{u_j u_k}}{\partial x_l} + \overline{u_j u_l} \frac{\partial \overline{u_i u_k}}{\partial x_l} + \overline{u_k u_l} \frac{\partial \overline{u_i u_j}}{\partial x_l} \right) \quad (9)$$

and $\mathcal{G}_i = \mathcal{G}_{imm}$. The model derived by LUM for the pressure-diffusion component of \mathcal{D}_{ij} is given as:

$$- \frac{1}{\rho} \overline{p' u_k} = P_D \overline{u_k u_m u_m} \quad (10)$$

Unlike the DH model, the LUM model preserves the three-dimensional symmetry of the turbulent transport term and, as such, is rotationally frame invariant.

The coefficients C_{s1} and C_{s2} in the LUM model were originally derived as:

$$C_{s1} = \frac{1}{3 C_L}, \quad C_{s2} = \frac{C_L}{4 C_L + 5}$$

where C_L was specified as a function of the turbulence Reynolds number, Re_t , and the second and third invariants of the anisotropy tensor, a_{ij} . More recently, however, Schwarz and Bradshaw (1994) assigned $C_L = C_1$ where C_1 is the coefficient in the linear return-to-isotropy process in the SSG pressure-strain relation. The coefficient P_D was originally derived as $P_D = \frac{1}{5}$. Straatman et al. (1998) suggested that P_D could be modified to $P_D = \frac{4}{25}$ to give the correct limiting behavior in purely diffusive turbulence. However, this modification was simply to show that the anisotropy level in ZMS turbulence could be properly predicted by slightly adjusting the relative influence of the diffusion sub-processes. It is shown in the next section that a more rigorous calibration is possible.

It is most useful to view the LUM model as a collection of three sub-processes that occur in \mathcal{D}_{ij} . The first sub-process, which is modeled as a coefficient and a time scale multiplying \mathcal{G}_{ijk} , can be viewed as the production of $\overline{u_i u_j u_k}$ at the third-moment level. The full production of $\overline{u_i u_j u_k}$ also contains mean strain terms, but these terms are considered to be small compared to the production by second-moment terms (see, for example, Hanjalić and

Lauder, 1972). The second sub-process in the LUM model, which includes all the terms multiplying C_{s2} , can be viewed to loosely represent the third-moment pressure-velocity process. By loosely, we imply that the terms were not derived to directly represent third-order pressure-velocity correlations, but the terms have essentially the same effect as the third-moment pressure-velocity process, which is to regulate the relative magnitudes of the turbulent flux components. The third sub-process in the LUM model is pressure-diffusion, which is strictly a second-moment process. The coefficients C_{s2} and P_D control the relative influence of these three processes within \mathcal{D}_{ij} and, with the appropriate detailed data, can be set to give the correct behavior of the model. Modifications to these coefficients can be viewed as a calibration to make the model applicable in inhomogeneous flows.

The focus of the forthcoming analysis is to derive expressions for the coefficients in the LUM model by examining ZMS turbulence, and then to establish values for these coefficients based on the best existing DNS and experimental data for ZMS turbulence.

3.1 Analysis of ZMS Turbulence. The analysis presented in this section extends the analysis presented in Straatman et al. (1998). For steady ZMS turbulence, the Reynolds-stress tensor can be simplified to two unique, non-zero components; one for the normal stress in the direction normal to the oscillating grid and one representing the two grid-plane normal stresses, which are equal. In a coordinate system where $x_1 - x_2$ represents the plane of the oscillating grid and x_3 the direction normal to the grid plane, the two unique Reynolds-stresses are $\overline{u_1 u_1}$ and $\overline{u_3 u_3}$. The transport equations for $\overline{u_1 u_1}$ ($=\overline{u_2 u_2}$) and $\overline{u_3 u_3}$, valid for steady ZMS turbulence, are then expressed as:

$$0 = \mathcal{D}_{11}/\epsilon + \pi_{11}/\epsilon - \frac{2}{3} \quad (11)$$

$$0 = \mathcal{D}_{33}/\epsilon + \pi_{33}/\epsilon - \frac{2}{3} \quad (12)$$

The diffusion terms in Eqs. (11) and (12) are given in their exact forms as (see Eq. (7)):

$$\mathcal{D}_{11} = \frac{\partial}{\partial x_3} (-\overline{u_1 u_1 u_3}) \quad (13)$$

$$\mathcal{D}_{33} = \frac{\partial}{\partial x_3} (-\overline{u_3 u_3 u_3} - 2\overline{p' u_3}/\rho) \quad (14)$$

Using the LUM diffusion model, the components of the diffusion terms become:

$$-\overline{u_1 u_1 u_3} = C_{s1} \frac{k}{\epsilon} \left[\frac{\overline{u_3 u_3}}{\overline{u_3 u_3}} \frac{\partial \overline{u_1 u_1}}{\partial x_3} + C_{s2} \left(2\overline{u_3 u_3} \frac{\partial \overline{u_1 u_1}}{\partial x_3} + 3\overline{u_3 u_3} \frac{\partial \overline{u_3 u_3}}{\partial x_3} \right) \right] \quad (15)$$

$$-\overline{u_3 u_3 u_3} = C_{s1} \frac{k}{\epsilon} \left[3\overline{u_3 u_3} \frac{\partial \overline{u_3 u_3}}{\partial x_3} + C_{s2} \left(6\overline{u_3 u_3} \frac{\partial \overline{u_1 u_1}}{\partial x_3} + 9\overline{u_3 u_3} \frac{\partial \overline{u_3 u_3}}{\partial x_3} \right) \right] \quad (16)$$

and:

$$-2 \frac{\overline{p' u_3}}{\rho} = 4P_D \overline{u_1 u_1 u_3} + 2P_D \overline{u_3 u_3 u_3} \quad (17)$$

Using the SSG model, the pressure-strain terms in Eqs. (11) and (12) become:

$$\pi_{11} = -C_1 \epsilon a_{11} + C_2 \epsilon (a_{11}^2 - \frac{1}{3} A_2) \quad (18)$$

$$\pi_{33} = -C_1 \epsilon a_{33} + C_2 \epsilon (a_{33}^2 - \frac{1}{3} A_2) \quad (19)$$

Using the RTI+IP models for pressure-strain, only the leading terms in Eqs. (18) and (19) are retained.

Next, on the basis of experimental evidence, the following solution fields can be introduced (see Straatman et al., 1998):

$$\overline{u_1 u_1} = \frac{B^2}{x_3^2}, \quad \overline{u_3 u_3} = \frac{a^2 B^2}{x_3^2}, \quad \epsilon = \frac{\mathcal{A}_\epsilon B^3}{\beta x_3^4} \quad (20)$$

where $a = \overline{u_{3RMS}}/\overline{u_{1RMS}}$ is the anisotropy of ZMS turbulence in the high Re_i , spatially decaying region, B is a constant related to the source strength, \mathcal{A}_ϵ is an empirical constant in the dissipation rate approximation, and β is the growth rate of integral length scales in the high Re_i , spatially decaying region. Clearly, the expressions in Eq. (20) are not valid over the entire ZMS field, but experiments have shown that there is a considerable region over which these expressions are valid. It is important to note that the expressions derived in this analysis are only useful in the high Re_i region where the expressions in Eq. (20) are valid. Using the expressions from Eq. (20) for the solution field, the diffusion and pressure-strain terms in the above equations are rewritten as:

$$\mathcal{D}_{11}/\epsilon = 3C_{s1} \left(\frac{\beta}{\mathcal{A}_\epsilon} \right)^2 a^2 (2 + a^2) [1 + 2C_{s2} + 3a^2 C_{s2}] \quad (21)$$

$$\mathcal{D}_{33}/\epsilon = 3C_{s1} \left(\frac{\beta}{\mathcal{A}_\epsilon} \right)^2 a^2 (2 + a^2) [(3a^2 + 6C_{s2} + 9a^2 C_{s2}) - P_D (4 + 6a^2 + 20C_{s2} + 30a^2 C_{s2})] \quad (22)$$

and:

$$\pi_{11}/\epsilon = C_1 \left(\frac{2}{3} - \frac{2}{2 + a^2} \right) - \frac{1}{6} C_2 A_2 \quad (23)$$

$$\pi_{33}/\epsilon = C_1 \left(\frac{2}{3} - \frac{2a^2}{2 + a^2} \right) + \frac{1}{3} C_2 A_2 \quad (24)$$

It is evident from these expressions that for constant anisotropy and constant coefficients, the diffusion and pressure-strain components, normalized by ϵ , are constant for high Re_i ZMS turbulence.

To determine the relative influence of the three diffusion sub-processes, the coefficients which control their influence must be isolated and expressed in terms of quantities which are known, or which can be deduced. To isolate the coefficients, we consider two further expressions, which are formed from the above expressions for ZMS turbulence. The first is the ratio of the turbulent flux components:

$$\frac{\overline{u_1 u_1 u_3}}{\overline{u_3 u_3 u_3}} = \frac{1 + 2C_{s2} + 3a^2 C_{s2}}{3a^2 + 6C_{s2} + 9a^2 C_{s2}} \quad (25)$$

Since the x_3 dependence is the same for both turbulent fluxes, the ratio $\overline{u_1 u_1 u_3}/\overline{u_3 u_3 u_3}$ is also constant in the high Re_i , spatially decaying region where a is constant. This was verified by Briggs et al. (1996) and will be discussed subsequently. The expression can be rearranged and solved for C_{s2} as:

$$C_{s2} = \frac{3a^2 \mathcal{R}_1 - 1}{2 + 3a^2 - 6\mathcal{R}_1 - 9a^2 \mathcal{R}_1} \quad (26)$$

where $\mathcal{R}_1 = \overline{u_1 u_1 u_3}/\overline{u_3 u_3 u_3}$. In this manner, C_{s2} has been isolated and expressed in terms of two quantities, a and \mathcal{R}_1 , which must be obtained from ZMS data.

The second expression we consider is the ratio of the diffusion terms:

$$\frac{\mathcal{D}_{11}}{\mathcal{D}_{33}} = \frac{\frac{2}{3} - \pi_{11}/\epsilon}{\frac{2}{3} - \pi_{33}/\epsilon} \quad (27)$$

Substituting expressions for the diffusion terms gives:

$$\frac{(1 + 2C_{s2} + 3a^2C_{s2})}{(3a^2 + 6C_{s2} + 9a^2C_{s2}) - P_D(4 + 6a^2 + 20C_{s2} + 30a^2C_{s2})} = \frac{\frac{2}{3} - \pi_{11}/\epsilon}{\frac{2}{3} - \pi_{33}/\epsilon} \quad (28)$$

which can be rearranged and solved for P_D to give:

$$P_D = \frac{C_{s2}(6 + 9a^2 - 2\mathcal{R}_2 - 3a^2\mathcal{R}_2) + (3a^2 - \mathcal{R}_2)}{C_{s2}(20 + 30a^2) + (4 + 6a^2)} \quad (29)$$

where \mathcal{R}_2 represents the right-hand side of Eq. (28). In this manner, P_D has been isolated and expressed in terms of a , C_{s2} and the ratio of modeled pressure-strain components.

The coefficient C_{s1} from Eq. (8) could also be isolated, but this coefficient does not affect the relative influence of the diffusion sub-processes. The coefficient C_{s1} controls the relative influence of the entire diffusion process, \mathcal{D}_{ij} , in the Reynolds-stress equation. In the present work, the main interest is to determine the relative influences of the components in \mathcal{D}_{ij} ; the value of C_{s1} is assumed to be adequate.

3.2 The Modified Values for C_{s2} and P_D . To establish numerical values for C_{s2} and P_D , data is required for the quantities a and \mathcal{R}_1 . The value of a has been established experimentally to be $a \approx 1.2$ (see Straatman et al., 1998). The value of \mathcal{R}_1 has never been measured and must, therefore, be obtained from another source. The DNS simulations of Briggs et al. (1996) enable the evaluation of \mathcal{R}_1 , however, care must be exercised to ensure that this quantity is evaluated in the high Re, region where the above expressions are valid.

Briggs et al. (1996) presented DNS results for unstratified ZMS turbulence, in which the turbulence Reynolds number was estimated to be $Re_t \approx 60$. In ZMS turbulence experiments (see, for example, Hopfinger and Toly, 1976; Fernando and Long, 1983; E and Hopfinger, 1986), turbulence Reynolds numbers are typically in the range $400 < Re_t < 800$, which is considerably higher than that reported by Briggs et al. (1996). Thus, not surprisingly, the results of Briggs et al. (1996) exhibit low Re, phenomena in much of the spatially decaying turbulence field. To expound, consider the spatial decay law for the horizontal RMS fluctuating velocity, $\bar{u}_{RMS} \propto x_3^{-n}$. In high Re, ZMS turbulence, the exponent n in the decay law has been determined experimentally to be $n = 1$. The physical implication of $n = 1$, combined with a linear growth rate of integral length scales, is that the Re, is approximately constant in the high Re, region. Briggs et al. (1996) reported a value of $n = 1.35$ which means that their Re, was diminishing with distance from the source. This is indicative of low Re, behavior because the eminence of viscous effects causes the turbulence to decay more rapidly. While this observation alone does not render the entire turbulence field to be low Re,, it does suggest that care should be taken in interpreting the results.

A region of high Re, turbulence can be isolated in the results of Briggs et al. (1996) by considering the turbulent kinetic energy budget. In high Re, ZMS turbulence, the kinetic energy budget is essentially a balance of diffusive transport, pressure-velocity interaction (redistribution) and dissipation. In the results of Briggs et al. (1996), most of the spatially decaying region contains a significant contribution from the energy input mechanism. However, a small region exists (approximately $1.8 < y^* < 2.8$) where the balance characteristic of high Re, ZMS turbulence exists (see Briggs, 1996). In this region, the Re, itself is relatively low ($Re_t \approx 30$), but the kinetic energy budget indicates high Re, behavior.

Figure 1 shows the results for \mathcal{R}_1 evaluated from the DNS results of Briggs et al. (1996) for the region $1 < y^* < 4$. The results are plotted as a function of y^* , which represents a non-dimensional distance from the turbulence source. The solid line in

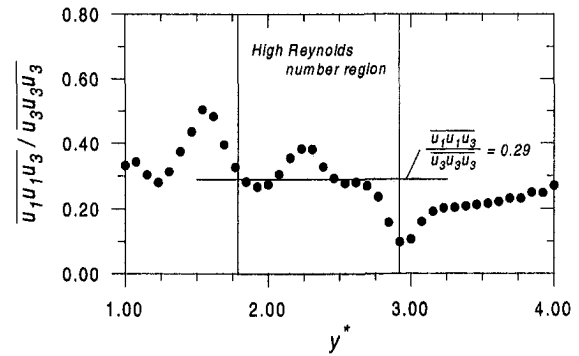


Fig. 1 DNS results from Briggs et al. (1996) for the turbulent flux ratio as a function of distance from the source

Fig. 1 represents the average constant value of $\mathcal{R}_1 = 0.29$ for the region $1.8 < y^* < 2.8$. It is evident from Fig. 1 that \mathcal{R}_1 varies slightly, but there is no apparent trend in this region indicating that \mathcal{R}_1 is increasing or decreasing with y^* . Taking the full (plotted) range into consideration, it appears that \mathcal{R}_1 is decreasing slightly with distance from the source, however, the data from $y^* < 1.8$ can not be utilized because of the large contribution to the k budget from the energy input mechanism. Furthermore, the region $y^* > 2.8$ becomes increasingly dominated by viscous effects.

Using the values $a = 1.2$ and $\mathcal{R}_1 = 0.29$, Eqs. (26) and (29) yield values of:

$$C_{s2} = 0.31, \quad P_D = 0.153 \quad (30)$$

when the SSG pressure-strain relation is used and

$$C_{s2} = 0.31, \quad P_D = 0.142 \quad (31)$$

when the RTI+IP pressure-strain relation is used. These values indicate that the influence of the third-moment pressure-velocity process may be nearly three times higher than that originally derived by LUM, while the influence of pressure-diffusion may be about 25% lower. Physically, this implies that the generation of anisotropy at the third-moment level could be much lower than previously thought, and consequently, the attenuation of anisotropy by pressure-diffusion could also be lower.

Before proceeding to the validation of the modified LUM model, the values of C_{s2} and P_D are discussed in terms of their sensitivity to the ZMS parameters from which they were derived. By examining Eq. (26), it is seen that the value $\mathcal{R}_1 = 0.29$ is relatively close to the value $\mathcal{R}_1 = \frac{1}{3}$, which corresponds to a singularity in the equation for C_{s2} . Hence, small variations of \mathcal{R}_1 on either side of $\mathcal{R}_1 = 0.29$ produce considerably different values of C_{s2} , which correspond to slightly different values of P_D . Furthermore, the value of \mathcal{R}_1 is somewhat dependent on the range of y^* chosen to evaluate the average. Unfortunately, no data exists, besides the computations provided by Briggs et al. (1996), from which \mathcal{R}_1 can be evaluated, and thus the values obtained above are based on the best available information. The forthcoming validation confirms that the present values are reasonable.

To summarize, the analysis of ZMS turbulence presented in this section served to isolate the coefficients C_{s2} and P_D in the LUM diffusion model and express them in terms of a and \mathcal{R}_1 , which were subsequently obtained from experimental and DNS data, respectively. The modified values of the coefficients were determined based on the best existing data, but C_{s2} was shown to be quite sensitive to \mathcal{R}_1 . While the values of the coefficients may change with the availability of more substantial DNS or experimental data, the expressions derived above remain valid for the calibration of the coefficients.

4 Validation of the Modified LUM Model

To validate the model, computations have been carried out for the turbulent plane jet, the plane channel, and the backward-facing

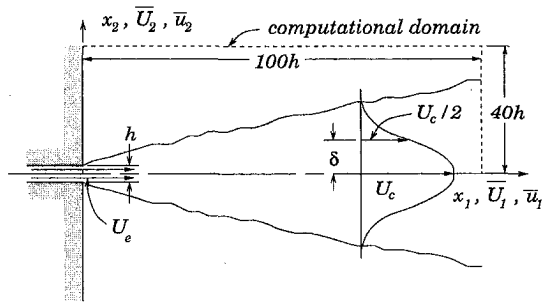


Fig. 2 Schematic representation of the turbulent plane jet geometry

step. In all cases, results were computed using the original and modified LUM models and the commonly employed Daly and Harlow (1970) diffusion model so that comparisons could be made. Computations were carried out using both the SSG and RTI+IP pressure-strain relations to test for consistency. Comparisons of global parameters and computed quantities are presented for all model combinations. Similarities and differences between the results obtained from the two pressure-strain relations are noted in the text.

The transport equations, which included the mass equation, the x_1 and x_2 momentum equations, four Reynolds-stress equations, and the ϵ equation, were discretized and solved elliptically using the finite-volume procedure described by Patankar (1980), except with a collocated variable arrangement. The convective fluxes in the momentum equations were approximated using the QUICK scheme of Leonard (1979), and in the turbulence equations using first-order UDS to promote numerical stability. At solid boundaries, the viscous sub-layer was bridged using standard wall functions valid for hydrodynamically smooth surfaces. The convergence of the computed solutions was based on the sum of the average residuals for each equation normalized by the average level of the particular variable considered. A solution was considered converged when the maximum normalized residuals for all equations was below 10^{-3} . At this level of convergence, the average residual levels were typically of the order 10^{-5} .

4.1 The Turbulent Plane Jet. The plane jet was modeled as a stream of air emerging from a wall slot at a Reynolds number of $Re = U_e h / \nu = 1000$ into an infinite environment of initially quiescent air. Figure 2 gives a schematic of the plane jet showing the coordinate system and the important physical parameters. To ensure that the results were independent of the grid density, computations were carried out on grids of dimensions 60×84 and 80×164 in the streamwise and transverse directions, respectively. The results for spread rate were grid-converged to within 5% on the fine grid, while results of the normalized velocities and turbulence quantities were grid-converged to better than 2%.

The spread rate, s_j , and the decay rate, d_j , for the turbulent plane jet were computed from the results of all model combinations are given in Table 1. The values in the table represent average spread and decay rates calculated over approximately half the length of the computational domain. Table 1 indicates that when

Table 1 Results for the global properties of the turbulent plane jet

Model	s_j	d_j
Experimental data	0.110	0.140–0.220
Modified LUM and SSG	0.081	0.137
Original LUM and SSG	0.099	0.168
DH and SSG	0.086	0.143
Modified LUM and RTI+IP	0.110	0.196
Original LUM and RTI+IP	0.118	0.150
DH and RTI+IP	0.107	0.184

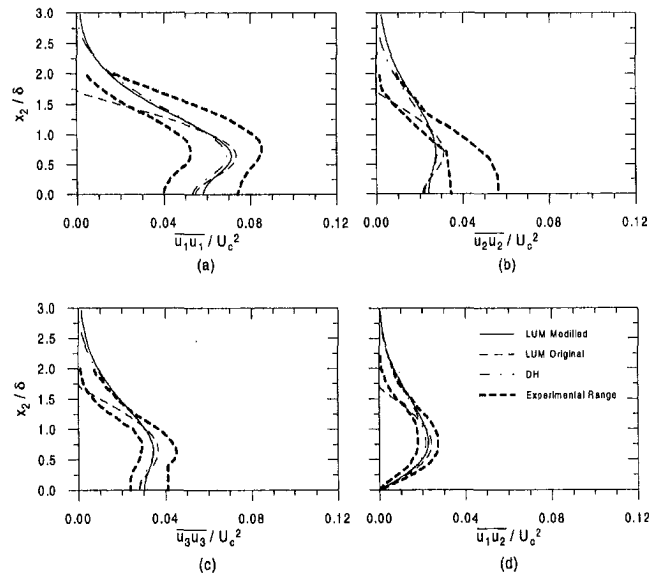


Fig. 3 Distribution of the Reynolds-stress components for the turbulent plane jet. Computations carried out using SSG pressure-strain model.

combined with the SSG model, the original LUM model performs better than both the modified LUM and DH models. However, we will see from the detailed comparisons that this result is misleading. When combined with the RTI+IP pressure-strain model, the modified LUM model gives a marginally better result than the DH model and the original LUM model slightly overpredicts the spread rate.

The predicted Reynolds stress variations from the similarity region of the turbulent plane jet ($>60h$) are given in Figs. 3 and 4. Figure 3 gives predictions obtained using the SSG pressure-strain relation and Fig. 4 gives predictions obtained using the RTI+IP relation for pressure-strain. The experimental range shown in these figures was derived from data obtained from Bradbury (1965), Gutmark and Wagnanski (1976) and Everitt and Robins (1978). Using the SSG pressure-strain model (Fig. 3), the modified LUM and DH models yield predictions that fall within the experimental range for all four of the Reynolds-stress components. The only exception is the under-prediction of u_2u_2 by both

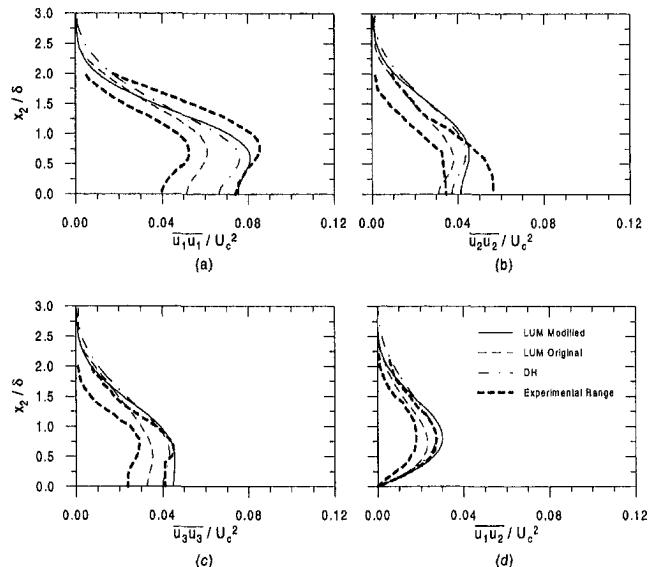


Fig. 4 Distribution of the Reynolds-stress components for the turbulent plane jet. Computations carried out using RTI+IP pressure-strain model.

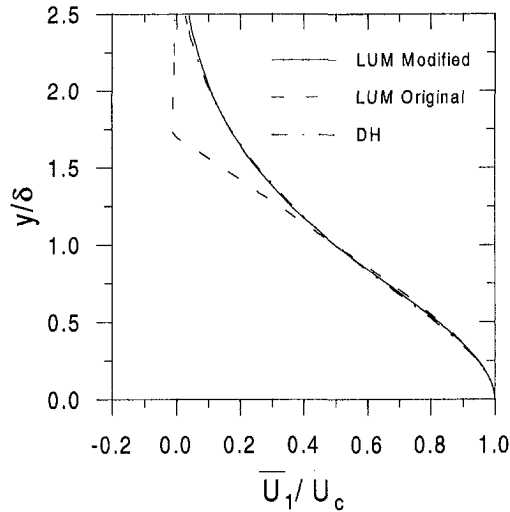


Fig. 5 Streamwise velocity predictions for the turbulent plane jet. Computations carried out using SSG pressure-strain model.

models in the region near the jet centerline. Figure 3 also shows that, in combination with the SSG model, the original LUM model predicts very sharp transitions of the Reynolds-stresses near the edge of the jet. This is further substantiated in Fig. 5, which shows the mean streamwise velocity predictions obtained using the SSG model in combination with all three diffusion models. Again, the predictions obtained using the original LUM model indicate a very sharp transition at the edge of the jet, while the predictions from the modified LUM and DH models are more physically reasonable. It is clear that the sharp transitions of the stresses practically negates the mixing at the edge of the jet, causing the lateral transport of momentum to diminish too rapidly.

Figure 4 shows that predictions made in combination with the RTI+IP pressure-strain model are only slightly different than those described above for the SSG model. The main differences observed for the modified LUM and DH models are the increase in the centerline values of all of the normal stress components and the slight over-prediction of $\overline{u_2 u_2}$ and $\overline{u_3 u_3}$ between $1.0 < x_2/\delta < 2.0$. The most significant differences between Figs. 4 and 3 occur in the original LUM model predictions. Where Fig. 3 indicated sharp transitions of the stresses at the edge of the jet, Fig. 4 indicates smooth, physically reasonable transitions. In fact, from Fig. 4, it appears that the original LUM model gives the best overall predictions of the Reynolds stresses. What is interesting is that the original LUM model gives radically different results depending on which pressure-strain relation is used, whereas the modified LUM model gives consistently reasonable results. The results are clearly influenced by the nonlinear terms in the SSG model, but the presence of the sharp transitions can be explained by examining the apportionment of the diffusion sub-processes in the LUM model. Consider the transverse diffusion term for $\overline{u_2 u_2}$, expanded using the LUM diffusion model:

$$\begin{aligned} \mathcal{D}_{22} \approx & \frac{\partial}{\partial x_2} \left[C_{s1} \frac{k}{\epsilon} \left((3 + 9C_{s2} - 6P_D - 30C_{s2}P_D) \overline{u_2 u_2} \frac{\partial \overline{u_2 u_2}}{\partial x_2} \right. \right. \\ & + (6C_{s2} - 4P_D - 20C_{s2}P_D) \overline{u_1 u_2} \frac{\partial \overline{u_1 u_2}}{\partial x_2} \\ & + (3C_{s2} - 2P_D - 10C_{s2}P_D) \overline{u_2 u_2} \frac{\partial \overline{u_1 u_1}}{\partial x_2} \\ & \left. \left. + (3C_{s2} - 2P_D - 10C_{s2}P_D) \overline{u_2 u_2} \frac{\partial \overline{u_3 u_3}}{\partial x_2} \right) \right] \quad (32) \end{aligned}$$

(Terms containing derivatives with respect to x_1 have been left out for clarity, but all terms were retained in the computations.) In this expression, the terms in parenthesis, that are functions of C_{s2} and P_D , form portions of the effective diffusivities for each of the terms. Using the original coefficients for C_{s2} and P_D , three of the four terms shown in Eq. (32) are negative resulting in a low overall diffusion in the x_2 direction. Using the modified coefficients, all of the terms in Eq. (32) are positive resulting in a higher overall diffusion of $\overline{u_2 u_2}$. In general, only the normal diffusivity term, $C_{s1}(k/\epsilon)(3 + 9C_{s2} - 6P_D - 30C_{s2}P_D)\overline{u_2 u_2}$, from Eq. (32) must be positive. The extra or cross-diffusion terms combine to give a net positive or negative influence, depending on the local flow structure. In terms of the plane jet predictions, where cross-stream diffusion is important, it appears that the modified LUM model gives a more reasonable physical effect and, consequently, performs much better than the original LUM model.

4.2 The Plane Channel. The plane channel was simulated for a Reynolds number $Re_\delta = U_b \delta / \nu = 5 \times 10^4$ based on the channel half-width, δ and the bulk velocity, U_b . Figure 6 illustrates the channel geometry under consideration and shows all important parameters. Fully-developed inlet conditions, obtained from Kim et al. (1987), were imposed at the inlet of the channel to reduce the required length of the computational domain, however, an aspect ratio of 100 was maintained to ensure that the results were a true representation of the models used and not of the inlet conditions. Computations made with an aspect ratio of 200 produced nearly identical results. Computations were carried out on grids of dimensions 15×30 and 30×60 (for the 100 aspect ratio case). Further grid refinements produced no significant changes in the predicted results.

The predicted results for the anisotropy variations in the fully developed region of the plane channel are presented in Figs. 7 and 8. Figure 7 gives the predictions of the three diffusion models in combination with the SSG pressure-strain model and Fig. 8 gives the same predictions computed in combination with the RTI+IP model. Included in the figures are DNS data from Kim et al. (1987) corresponding to a Reynolds number 7600. The influence of the diffusion model in these predictions is most prominent near the center of the channel where the mean shear diminishes and the stresses relax toward the isotropic state. Figure 7 indicates that, in combination with the SSG model, the modified LUM model predicts the most prominent relaxation of the diagonal components of a_{ij} and the correct variation of a_{12} . In contrast, the original LUM model predicts almost no relaxation towards isotropy. The DH model predicts some relaxation, but not to the extent of the modified LUM model. The predicted relaxation using the modified LUM model is essentially the same as that predicted by Demuren and Sarkar (1993) using the Meller and Herring (1973) diffusion model in combination with the SSG model. Note, however, that Straatman et al. (1998) showed that the Mellor and Herring (1973) model performs poorly in the diffusive limit. Figure 8 shows that, in combination with the RTI+IP relation, the predictions from all diffusion models are significantly different. While the relaxation towards isotropy is best predicted using the modified LUM model, the predicted anisotropies from all models are in poor agreement with the data of Kim et al. (1987). These results are essentially in accordance with the results of Demuren and Sarkar (1993) who through a comprehensive study of the plane channel determined that the SSG pressure-strain relation was preferable.

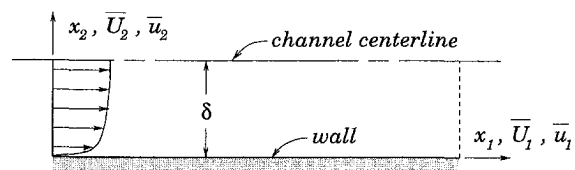


Fig. 6 Schematic representation of the plane channel geometry

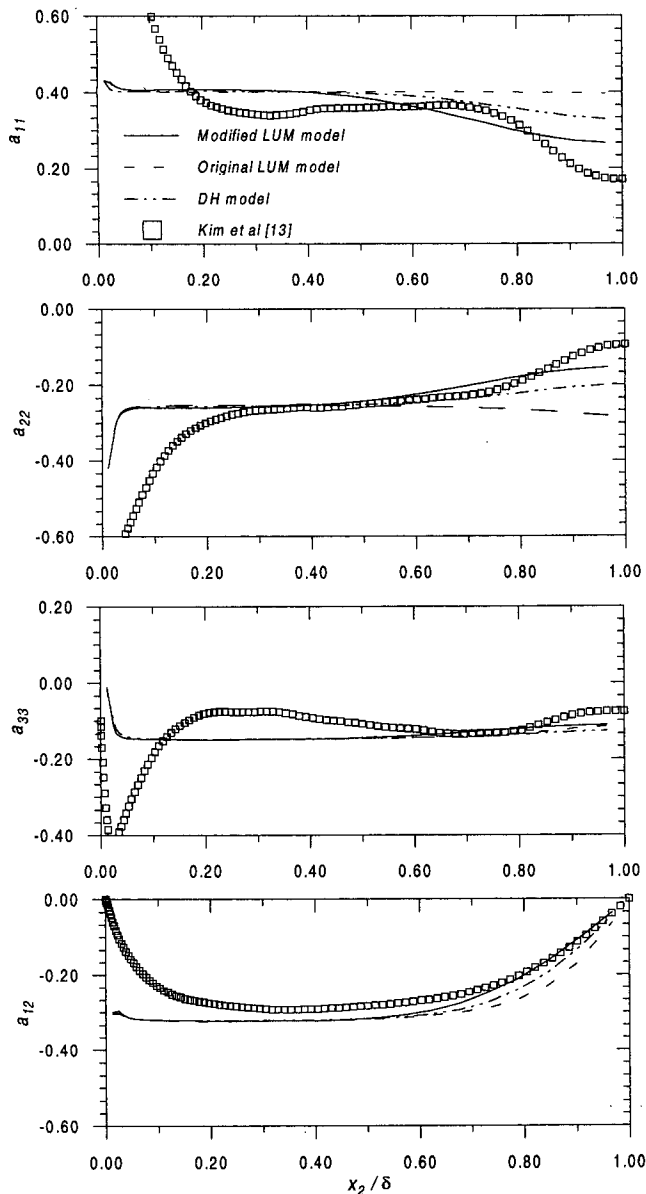


Fig. 7 Components of the anisotropy tensor as a function of x_2/δ in fully-developed plane channel flow. Computations carried out using SSG pressure-strain model.

Further comparisons are presented for the diffusion models in combination with the SSG pressure-strain relation. Figure 9 gives comparisons of the normalized transverse turbulent flux components plotted as a function of x_2/δ in the fully developed region of the channel. The superscript + in Fig. 9 indicates that the components have been normalized by the friction velocity. The modified LUM model yields superior predictions for all components with the exception of $\overline{u_2 u_2 u_2}^+$, while the DH model consistently gives the worst predictions. In particular, the DH model greatly underpredicts the magnitudes of $\overline{u_2 u_2 u_2}^+$ and $\overline{u_1 u_2 u_2}^+$.

4.3 The Backward-Facing Step. The step geometry studied by Kim et al. (1980) was considered for the present computations. A schematic of this geometry is given in Fig. 10. At the inlet, a velocity profile was devised using a mean centerline velocity of $\bar{U}_o = 18.2$ [m/s] and a displacement thickness of $\delta_d = 1.004$ [mm], as reported in Kim et al. (1980). The turbulence intensity at the inlet was assumed to be low based on the shape of the experimental inlet and was assigned a value of $\mathcal{P} = k^{1/2}/\bar{U}_o = 0.01$. An estimate of the dissipation rate at the inlet was then

derived using $\epsilon = 0.61k^{3/2}/0.5h$. Grid independence was established on the basis of computations carried out on grids of 100×40 and 200×80 in the x_1 and x_2 directions, respectively. Between these grids, the difference in the predicted reattachment point was within 2%, and differences in the velocity and turbulence profiles were well within 1%. Thus, for computational economy, all subsequent computations were carried out on the 100×40 grid.

Figure 11 shows the predicted streamlines computed using the SSG pressure-strain relation in combination with the modified LUM (a), original LUM (b), and DH (c), models, respectively. Identical stream function values are shown in all three plots. The flow field for all cases essentially consists of a large, primary recirculation region below the step and a smaller, secondary recirculation region adjacent to the lower corner of the step. The predicted reattachment points of the primary recirculation region are $x_1/h = 7.77, 6.61$ and 6.52 obtained using the modified LUM, original LUM and DH models, respectively, in combination with the SSG pressure-strain model. Predictions made using the RTI+IP pressure-strain relation (not shown) in combination with

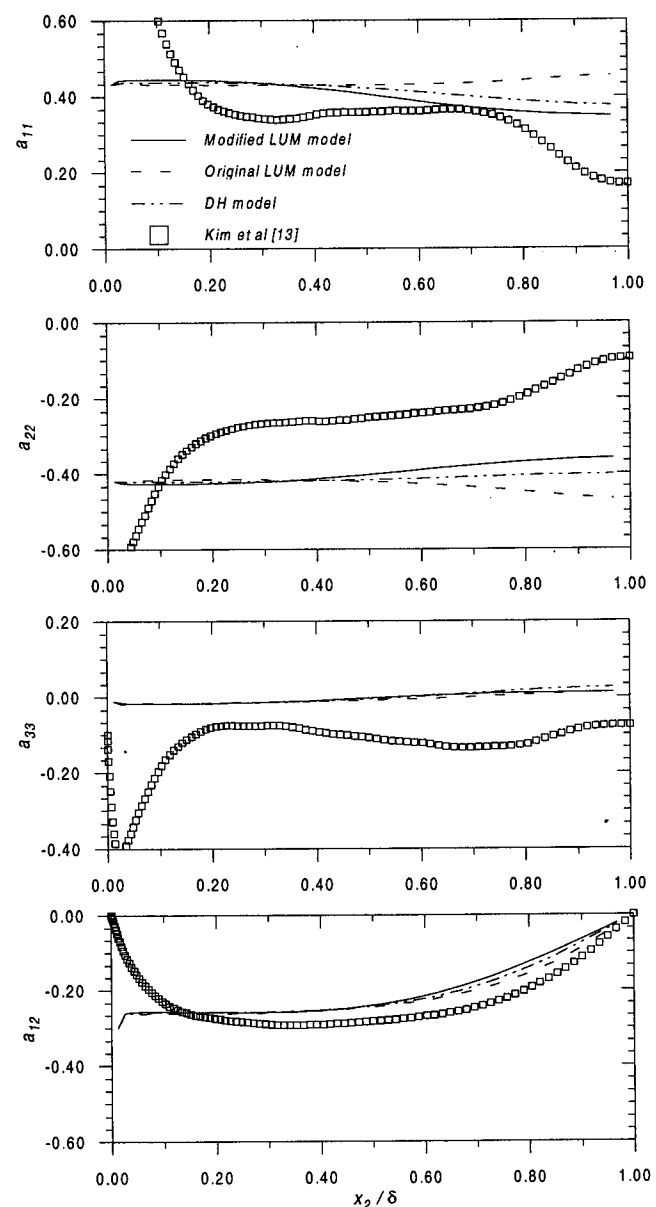


Fig. 8 Components of the anisotropy tensor as a function of x_2/δ in fully-developed plane channel flow. Computations carried out using RTI+IP pressure-strain model.

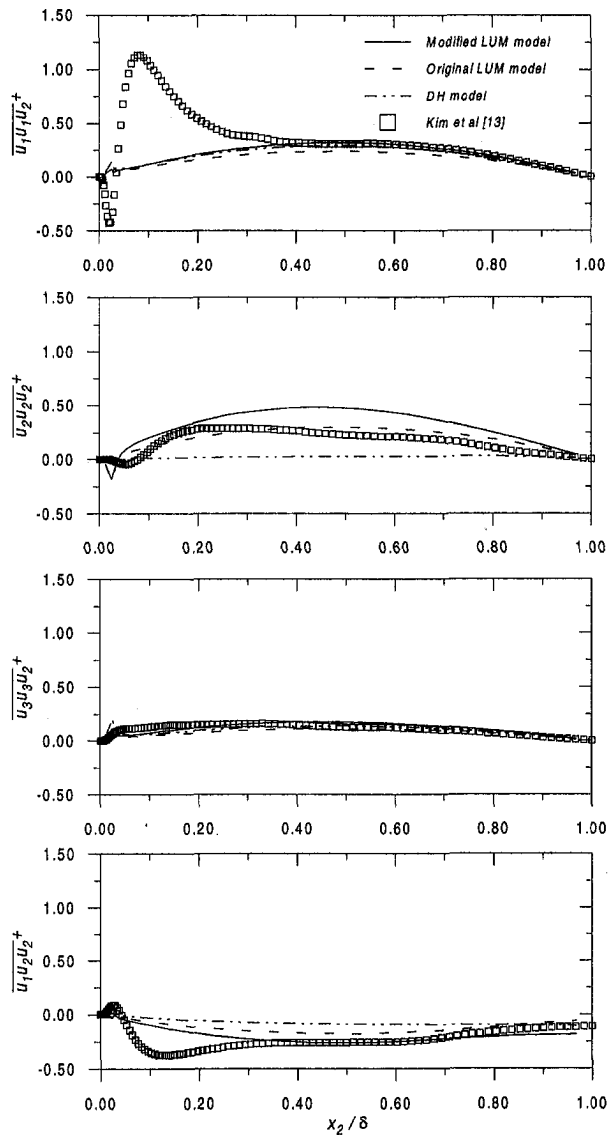


Fig. 9 Normalized turbulent flux components as a function of x_2/δ in fully-developed plane channel flow. Computations carried out using SSG pressure-strain model.

the three diffusion models yielded primary reattachment points of $x_1/h = 7.34, 5.86$ and 6.25 using the modified LUM, original LUM and DH models, respectively. The experimentally determined reattachment point for the primary recirculation region for this step is $x_1/h = 7.60$ (see Obi et al., 1991). Thus, with both pressure-strain models the modified LUM model gives the best predictions of the primary reattachment point. Figure 11 also indicates that the original LUM model predicts a much larger secondary recirculation region than either the modified LUM or

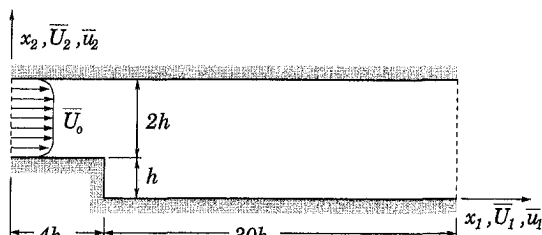


Fig. 10 Schematic of the backward-facing step of Kim et al. (1980)

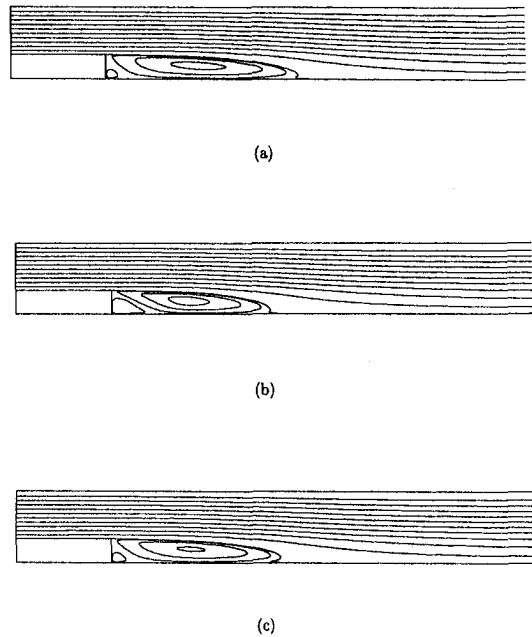


Fig. 11 Streamline plots for the backward-facing step computed using the modified LUM (a), original LUM (b), and DH (c) diffusion models in combination with the SSG pressure-strain model.

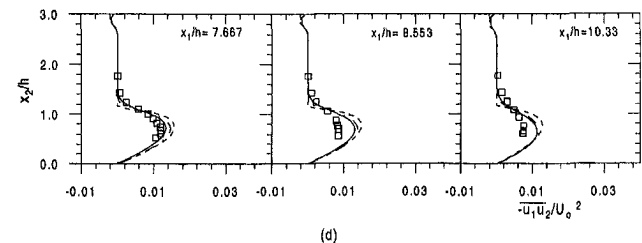
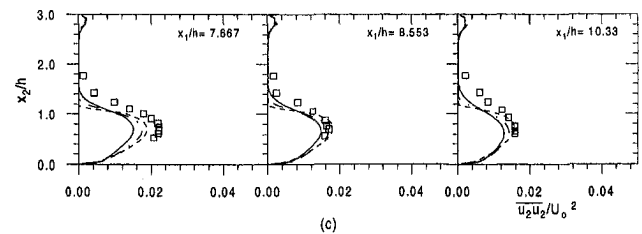
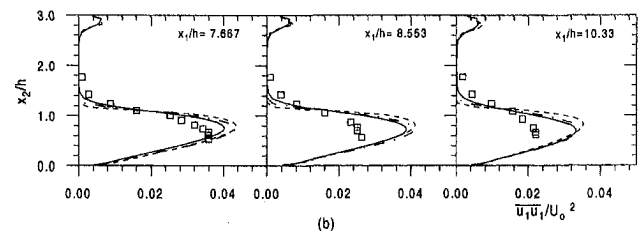
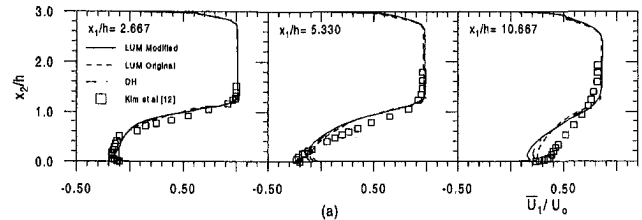


Fig. 12 Variations of streamwise velocity and Reynolds stresses for the backward-facing step for various x_1/h positions. Computations carried out using the SSG pressure-strain model.

the DH model. The same was observed in the computations made with the RTI+IP model. Unfortunately, no data exists for confirmation of the secondary reattachment point.

Figures 12 and 13 show predicted results for the \bar{U}_1 velocity and for the $\overline{u_1 u_1}$, $\overline{u_2 u_2}$ and $\overline{u_1 u_2}$ Reynolds stress components plotted as a function of x_2/h for three different x_1/h positions. Figure 12 gives the results computed in combination with the SSG model and Fig. 13 gives the results computed with the RTI+IP model. Due to the available data, the x_1/h positions used for the velocity profiles are different than those used for the Reynolds stresses. Figures 12(a) and 13(a) indicate that all models give similar predictions of mean velocity within the recirculating region. Outside the recirculation region, at $x_1/h = 10.667$, the model predictions vary slightly, but no model combination gives the correct variation of \bar{U}_1 near the wall. Figure 12(a)–(c) indicates that the modified LUM model gives marginally superior overall predictions of the Reynolds stresses. The most notable differences occur between $1.0 < x_2/h < 2.0$, where in every case the modified LUM model gives the smoothest transition from the high shear to the low shear region. While the predicted transition is still somewhat different than the data, the trend towards a smoother transition is in accordance with the data. In contrast to the modified LUM model, the original LUM model predicts very sharp transitions, as in the plane jet, and the DH model predicts transitions only slightly better than the original LUM model. Figure 13(a)–(c) shows that essentially the same Reynolds-stress variations are predicted using the

RTI+IP pressure-strain model. The only notable differences are the slightly lower peak values and the slightly smoother transitions from the high to low shear regions. Note that in this case, the transitions predicted by the original LUM model are still relatively sharp even when combined with the RTI+IP relation.

5 Concluding Remarks

A study has been carried out to examine the relative influence of the three sub-processes contained in the LUM diffusion model. In the analysis, the coefficients which control the influence of each of the diffusion sub-processes were isolated and expressed in terms of quantities which could be obtained from ZMS data. On the basis of the analysis, and using recent DNS and experimental data, the coefficients in the Lumley (1978) model were modified such that the model gives the correct behavior in the diffusive limit. Because of the sensitivity of the modified coefficients to the ZMS data from which they were deduced, more detailed data for high Re, ZMS turbulence is necessary to substantiate their values. However, the expressions devised in the analysis of ZMS turbulence remain valid.

The modified LUM model was validated by comparing computed predictions for the plane jet, the plane channel and the backward-facing step. By comparing these predictions to similar predictions computed using the original LUM model and the DH model, the modified LUM model was shown to be the only model which yielded consistently reasonable predictions. In contrast, the original LUM model consistently yielded the poorest results.

While the predictions from the modified LUM model were not radically different from those predicted using the DH model, there are two clear benefits associated with using the modified LUM model. First, unlike the DH model, the modified LUM model is mathematically correct; i.e., it preserves the three-dimensional symmetry of the turbulent transport term and it is rotationally invariant. Second, predictions made using the modified LUM model were shown to be more consistently better than similar predictions made using the DH model. While it was not shown in this paper, it is also reasonable to assume that the modified LUM model would be most suitable for three-dimensional computations.

Acknowledgments

The author gratefully acknowledges financial support received from the Natural Sciences and Engineering Research Council of Canada.

References

- Bradbury, L. J. S., 1965, "The Structure of the Self-Preserving Turbulent Plane Jet," *Journal of Fluid Mechanics*, Vol. 23, pp. 31–64.
- Briggs, D. A., 1996, "Turbulent Entrainment in a Shear-Free Stably Stratified Two-Layer Fluid." Ph.D. thesis, Stanford University, Stanford, California, USA.
- Briggs, D. A., Ferziger, J. H., Koseff, J. R., and Monismith, S. G., 1996, "Entrainment in a Shear-Free Turbulent Mixing Layer," *Journal of Fluid Mechanics*, Vol. 310, pp. 215–241.
- Daly, B. J., and Harlow, F. H., 1970, "Transport Equations in Turbulence," *Physics of Fluids*, Vol. 13, No. 11, pp. 2634–2649.
- Demuren, A. O., and Sarkar, S., 1993, "Perspective: Systematic Study of Reynolds Stress Closure Models in the Computations of Plane Channel Flows," *ASME JOURNAL OF FLUIDS ENGINEERING*, Vol. 115, pp. 5–12.
- E, X., and Hopfinger, E. J., 1986, "On Mixing Across an Interface in Stably Stratified Fluid," *Journal of Fluid Mechanics*, Vol. 166, pp. 227–244.
- Everitt, W. K., and Robins, G. A., 1978, "The Development and Structure of Plane Jets," *Journal of Fluid Mechanics*, Vol. 80, pp. 795–797.
- Farhanieh, B., Davidson, L., and Sundén, B., 1993, "Employment of Second-Moment Closure for Calculation of Turbulent Recirculating Flows in Complex Geometries With Colocated Variable Arrangement," *International Journal for Numerical Methods in Fluids*, Vol. 16, pp. 525–544.
- Fernando, H. J. S., and Long, R. R., 1983, "The Growth of a Grid-Generated Turbulent Mixed Layer in a Two-Fluid System," *Journal of Fluid Mechanics*, Vol. 133, pp. 377–395.
- Gutmark, E., and Wagnanski, I., 1976, "The Planar Turbulent Jet," *Journal of Fluid Mechanics*, Vol. 73, pp. 465–496.
- Hanjalić, K., and Launder, B. E., 1972, "A Reynolds Stress Model of Turbulence and its Application to Thin Shear Flows," *Journal of Fluid Mechanics*, Vol. 52, pp. 609–638.
- Hopfinger, E. J., and Toly, J. A., 1976, "Spatially Decaying Turbulence and its

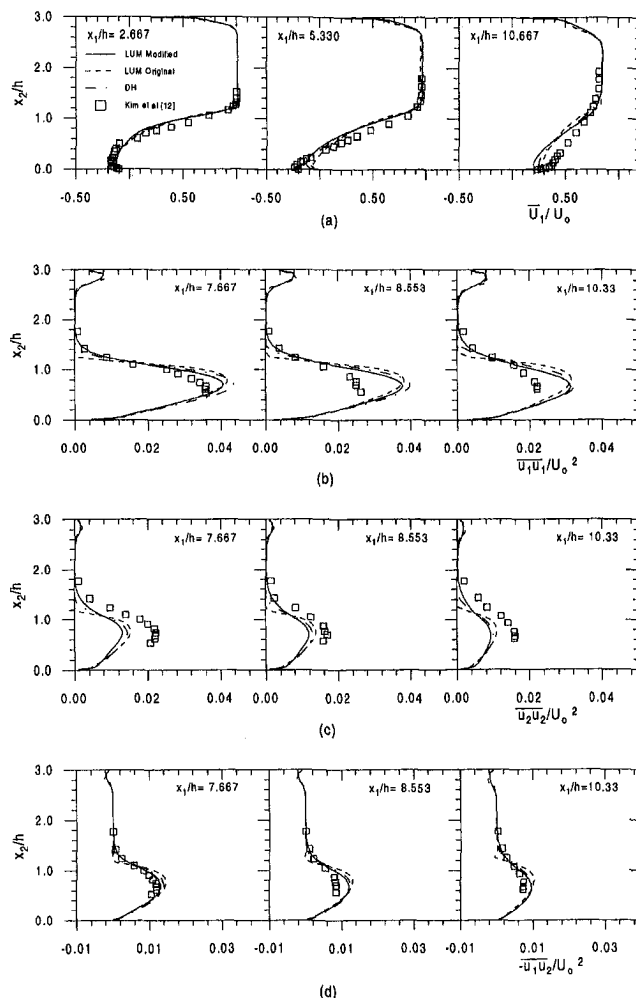


Fig. 13 Variations of streamwise velocity and Reynolds stresses for the backward-facing step for various x_1/h positions. Computations carried out using the RTI+IP pressure-strain model.

Relation to Mixing Across Density Interfaces," *Journal of Fluid Mechanics*, Vol. 78, pp. 155–175.

Kim, J., Kline, S. J., and Johnson, J. P., 1980, "Investigation of a Reattaching Turbulent Shear Layer: Flow over a Backward-Facing Step," *ASME JOURNAL OF FLUIDS ENGINEERING*, Vol. 102, pp. 302–308.

Kim, J., Moin, P., and Moser, R., 1987, "Turbulence Statistics in Fully Developed Channel Flow at Low Reynolds Number," *Journal of Fluid Mechanics*, Vol. 177, pp. 133–166.

Leonard, B. P., 1979, "A Stable and Accurate Convection Modelling Procedure Based on Quadratic Upstream Interpolation," *Computer Methods in Applied Mechanics and Engineering*, Vol. 19, pp. 59–98.

Lien, F. S., and Leschziner, M. A., 1994, "A General Non-Orthogonal Collocated Finite Volume Algorithm for Turbulent Flow at all Speeds Incorporating Second-Moment Turbulence Transport Closure, Part 1: Computational Implementation," *Computer Methods in Applied Mechanics and Engineering*, Vol. 114, pp. 123–148.

Lumley, J. L., 1978, "Computational Modelling of Turbulent Flows," *Advances in Applied Mechanics*, Academic Press, Vol. 18, pp. 123–176.

Mellor, G. L., and Herring, H. J., 1973, "A Survey of the Mean Turbulent Field Closure Models," *AIAA Journal*, Vol. 11, No. 5, pp. 590–599.

Obi, S., Perić, M., and Scheuerer, G., 1991, "Second-Moment Calculation Procedure for Turbulent Flows with Collocated Variable Arrangement," *AIAA Journal*, Vol. 29, No. 4, pp. 585–590.

Patankar, S. V., 1980, *Numerical Heat Transfer and Fluid Flow*, Hemisphere Publishing.

Schwarz, W. R., and Bradshaw, P., 1994, "Term-by-Term Tests of Stress-Transport Turbulence Models in a Three-Dimensional Boundary Layer," *Physics of Fluids*, Vol. 6, pp. 986–998.

Speziale, C. G., Sarkar, S., and Gatski, T. B., 1991, "Modelling the Pressure-Strain Correlation of Turbulence: An Invariant Dynamical Systems Approach," *Journal of Fluid Mechanics*, Vol. 227, pp. 245–272.

Straatman, A. G., Stubble, G. D., and Raithby, G. D., 1998, "Examination of Diffusion Modelling Using Zero-Mean-Shear Turbulence," *AIAA Journal*, Vol. 36, No. 6, pp. 929–935.

Analytical and Experimental Investigation of Laminar Channel Flow With Respect to Flow Metering

Franz Peters

Professor,
Universität Essen,
Schützenbahn 70,
45127 Essen, Germany
e-mail: FRANZ.PETERS@UNI-ESSEN.DE

Laminar flow through converging narrow channels is investigated. An analytical as well as a parameter model formulation is given of the flow rate through this channel. Experiments with water in a straight channel and with air in a circular channel are presented and compared with theory. The achieved agreement is considered a solid basis for flowmetering instruments.

1 Introduction

The basis of most flowmetering devices is a common fluid dynamic effect. Vortex meters make use of the Karman vortex street. Floating element meters and baffleplate rely on the drag force, orifices use Bernoulli's principle and so forth (Fiedler 1992). These fluid dynamic effects are beneficial in providing strong and stable signals, yet they are mostly too complex for analytical description. As a result the developers of flowmeters tend to neglect the fluid dynamic analytical aspects concentrating on the measurement and data evaluation side. The fluid mechanics are eventually taken care of by the calibration curve. The main drawback of this procedure is the problem of scaling: one wants to be able to predict the flow rate as it depends on driving potential and the significant parameters of the instrument which is difficult or even impossible. The lack of predictability can hardly be made up for by numerical analysis which is rather apt to analyze a given situation. Bückle et al. (1992) show that in case of a floating element.

This work pursues the idea to make use of flows for flowmetering that have analytical accessibility from the beginning. A laminar 2-D channel flow is chosen. It is shown how well predicted flow rates are confirmed by experiments and how the channel flow may be the nucleus of a flowmeter instrument. For more practical purposes we add a very effective two-parameter model in which one parameter is obtained from the analysis and the other remains free. A convincing feature of this model is the possibility of expressing a flow rate coefficient as function of Reynolds number.

Previously, we have already provided experimental evidence of the feasibility of channel flow between a piston and a cylinder for flow metering, however without any analysis (Peters and Kuralt, 1995). A similar arrangement with a cylindrical annulus has been tried by Wojtkowiak et al. (1997) accompanied by numerical calculations. An early attempt to utilize an analytical laminar flow is the pad resistor proposed by Morsi (1976) and calibrated by Wieners et al. (1978). If our piston-cylinder arrangement is to be associated with existing methods the v-cone flowmeter by Harvill et al. (1995) ought to be mentioned and of course the widespread floating element meters featuring a flow through a variable gap of complex geometry.

2 Analysis of Channel Flow

Laminar flow is considered in a narrow channel at low Reynolds number. By a channel we mean the space between two straight walls inclined at a small angle with respect to each other. The flow enters at the wide side, accelerates between the walls and exits where the walls end at a remaining narrow gap. The aspect ratio in terms of gap length to width is large. In case of a straight channel between flat plates this makes edge effects negligible. In case of a circular channel between a piston and a cylinder wall this means that the flow may still be treated as plane 2-D flow although the gap is circular (presently the ratio was of the order 10^4). The basic equations of flow in a converging channel are readily found in text books on laminar flow (e.g., Constantinescu, 1995). I will briefly discuss the analysis with respect to the flow situation that is to be investigated and derive expressions for the flow rate.

The basic flow arrangement is depicted in Fig. 1. The pressure difference $p_1 - p_2$ drives the flow from region 1 through the channel to region 2 (the gap). Cylindrical coordinates are employed with the velocity in the negative radial direction. The velocity depends on r and φ

$$u = u(r, \varphi). \quad (1)$$

It is zero at the boundaries $\varphi = 0$ and $\varphi = \alpha$ and has a maximum at $\alpha/2$. (In principle, more complex flow patterns are conceivable including even back flow, however for the small angles involved no back flow is expected.) The Mach number is small enough to allow the conservation equations of mass and momentum in r - and φ -direction to be written with constant density ρ . Assuming small angles α gravity g is included in r -direction as a constant and left out in φ -direction.

$$\frac{\partial(ur)}{\partial r} = 0 \quad (2)$$

$$u \frac{\partial u}{\partial r} = -\frac{1}{\rho} \frac{\partial p}{\partial r} + \frac{\nu}{r^2} \frac{\partial^2 u}{\partial \varphi^2} - g \quad (3)$$

$$0 = -\frac{1}{\rho} \frac{\partial p}{\partial \varphi} + \frac{2\nu}{r} \frac{\partial u}{\partial \varphi}. \quad (4)$$

Elimination of the pressure p by crosswise differentiation and subsequent partial integration with respect to φ yields

$$\frac{1}{2} \frac{\partial u^2}{\partial r} - \frac{\nu}{r^2} \frac{\partial^2 u}{\partial \varphi^2} - \frac{4\nu}{r^2} u = C(r) \quad (5)$$

with the yet unknown function of $C(r)$. With Eq. (2) the product (ur) is no function of r , so that with the function $f(\varphi)$

Contributed by the Fluids Engineering Division for publication in the JOURNAL OF FLUIDS ENGINEERING. Manuscript received by the Fluids Engineering Division April 29, 1999; revised manuscript received September 5, 1999. Associate Technical Editor: D. R. Williams.

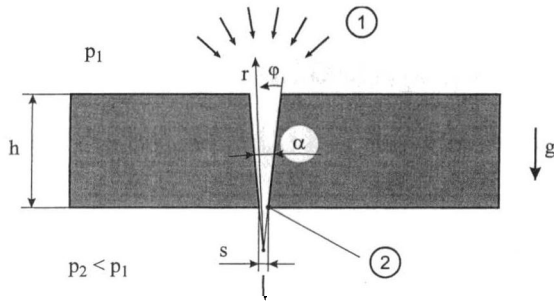


Fig. 1 Channel geometry

$$f(\varphi) = \frac{ur}{\nu} \quad (6)$$

the independent variables are separated in Eq. (5) where f primed denotes differentiation with respect to φ

$$f^2 + f'' + 4f = -C(r) \frac{r^3}{\nu^2}. \quad (7)$$

With the left side being a function of φ and the right side being a function of r both sides need to be equal to a constant A . Since $f = 0$ at the wall denoted by subscript w it follows

$$A = f_w'''. \quad (8)$$

On the other hand, f_w''' is determined from Eq. (3) for $u = 0$ so that

$$A = \frac{r^3}{\nu^2} \left[\frac{1}{\rho} \left(\frac{\partial p}{\partial r} \right)_w + g \right]. \quad (9)$$

A is determined by integration of this equation using the inlet and outlet wall pressures provided from the experiment

$$A = \frac{2}{\rho \nu^2} \frac{p_w(r_1) - p_w(r_2) + \rho g(r_1 - r_2)}{\frac{1}{r_2^2} - \frac{1}{r_1^2}}. \quad (10)$$

With A known Eq. (7) is multiplied by f' and integrated resulting in

$$\frac{2}{3} f^3 + f'^2 + 4f^2 = 2Af + 2B. \quad (11)$$

The integration constant B is inferred from the condition that the velocity profile is symmetric and has its maximum at $\alpha/2$, i.e., $f'(\alpha/2) = 0$ and $f(\alpha/2) = f_{\max}$

$$2B = \frac{2}{3} f_{\max}^3 + 4f_{\max}^2 - 2Af_{\max}. \quad (12)$$

Then, with Eq. (11) the derivative of f is

$$f' = \pm \sqrt{\frac{2}{3}(f_{\max}^3 - f^3) + 4(f_{\max}^2 - f^2) - 2A(f_{\max} - f)} \quad (13)$$

where the negative sign applies when $0 \leq \varphi \leq \alpha/2$ and the positive sign when $\alpha/2 \leq \varphi \leq \alpha$. The integrated form between zero and $\alpha/2$ reads

$$\varphi = - \int_0^f \frac{df}{\sqrt{\frac{2}{3}(f_{\max}^3 - f^3) + 4(f_{\max}^2 - f^2) - 2A(f_{\max} - f)}}. \quad (14)$$

While a solution to this integral is mathematically not straightforward (elliptic integrals) it is relatively simple to extract $f_{\max}(\alpha/2)$ numerically. To this end the left side is put equal to $\alpha/2$ and the upper integration limit to f_{\max} . Now, f_{\max} is varied while the integral is evaluated numerically until its value meets $\alpha/2$. The infinitesimal mass flux through a partial channel of angle $d\varphi$ amounts to

$$d\dot{m} = \rho L \nu f d\varphi \quad (15)$$

and the total mass flux with known f_{\max} to

$$\dot{m} = -2\rho \nu L \times \int_0^{f_{\max}} \frac{f}{\sqrt{\frac{2}{3}(f_{\max}^3 - f^3) + 4(f_{\max}^2 - f^2) - 2A(f_{\max} - f)}} df \quad (16)$$

in which the integration runs from zero to $\alpha/2$ and the factor 2 doubles the result. \dot{m} turns out with a negative sign in accordance with the velocity. A is determined from Eq. (10) on basis of the experimental data.

The numerical evaluation of Eqs. (14), (16) encounters improper integrals at the upper boundary f_{\max} . It is suggested to linearize the integrand in the vicinity of the boundary delineated by f^* which is very close to f_{\max} . This way an analytical expression is obtained for the vicinity and only the proper part needs numerical evaluation. Using $g(f)$ for the expression under the root in Eq. (16) this procedure yields

$$\dot{m} = -2\rho \nu L \left[\int_0^{f^*} \frac{f}{\sqrt{g(f)}} df - 2f^* \left(\frac{f^* - f_{\max}}{g'(f_{\max})} \right)^{1/2} + \frac{4}{3} g'(f_{\max}) \times \left(\frac{f^* - f_{\max}}{g'(f_{\max})} \right)^{3/2} \right] \quad (17)$$

In the limit of small flow rates an analytical linear solution results. For $\dot{m} \rightarrow 0$ the function $g(f)$ reduces to $-2A(f_{\max} - f)$. The remaining term allows integration and we get from Eqs. (14) and (16)

$$\dot{m} = -\frac{1}{12} \rho \nu L \alpha^3 A. \quad (18)$$

With A from Eq. (10) and with the approximation $s = \alpha r_2$, justified for small angles, Eq. (18) takes the form

$$\dot{m} = -\frac{L \alpha s^2}{6\nu} \frac{p_w(r_1) - p_w(r_2) + \rho g(r_1 - r_2)}{1 - (r_2/r_1)^2}. \quad (19)$$

Pressure Distribution. The pressure distribution along the channel walls follows from Eq. (9), (10) in the normalized form (neglecting gravity)

$$\frac{p_w(r) - p_w(r_1)}{p_w(r_2) - p_w(r_1)} = \frac{1 - (r_1/r)^2}{1 - (r_1/r_2)^2} \quad (20)$$

Evidently, this result is independent of viscosity and flow rate. The same result is, in fact, obtained from Bernoulli's equation. Therefore, we are dealing with the peculiarity that only the pressure away from the wall is affected by fluid properties and flow rate. This can be seen e.g., for the centerline ($\alpha/2$) pressure $p_c(r)$ where with Eq. (4)

$$p_c(r) - p_w(r) = \frac{2\rho \nu^2 f_{\max}}{r^2} \quad (21)$$

which also tells us, since $f_{\max} < 0$, that the pressure drops from the wall toward the centerline. In downstream direction the pressure decreases with $1/r^2$ meaning that the essential pressure drop occurs close to the exit. Therefore, if anything goes wrong with the analytical solution in comparison with experimental data the reason has to be looked for at the exit rather than at the inlet.

Parameter Model. It is useful to have a simple parameter model of the flow rate for quick scaling calculations and a best fit representation of data for calibration purposes. The model is simply based on the energy equation saying that the drop of pressure from inlet to outlet is composed of a frictional term $\zeta(\epsilon u_s)$ and an

inertia term $(\epsilon u_s)^2$ where u_s is the mean outlet velocity and the inlet kinetic energy is neglected

$$p_1 - p_2 + \rho g(r_1 - r_2) = \frac{\rho}{2} (\epsilon u_s)^2 + \rho \zeta (\epsilon u_s). \quad (22)$$

The friction coefficient ζ can be obtained from the analytical solution for the limiting case of small mass flux where the velocity squared term vanishes and Eqs. (22) and (19) can be combined. In this combination mean pressure and wall pressure cannot be distinguished since the energy equation is one-dimensional. Also the sign of \dot{m} is ignored. The result is

$$\zeta = \frac{6\nu}{\epsilon \alpha s} (1 - (r_2/r_1)^2). \quad (23)$$

The coefficient ϵ may be interpreted as a correction of u_s meaning that the given ambient pressure p_2 does not exactly correspond to u_s but rather to a corrected (ϵu_s) in the discharging jet downstream of the exit. Due to the vena contracta principle it may be expected that the jet contracts ($\epsilon > 1$). Equation (23) transforms Eq. (22) into an equation for u_s or the mass flux, respectively, when multiplied by area and density

$$u_s = -\frac{\zeta}{\epsilon} + \sqrt{\frac{\zeta^2}{\epsilon^2} + \frac{p_1 - p_2 + \rho g(r_1 - r_2)}{\epsilon^2 \rho/2}}. \quad (24)$$

It is illustrative and useful to express the flow rate in terms of a discharge coefficient depending on Reynolds number. The coefficient relates the actual flow rate to the ideal one, the latter resulting from Bernoulli's equation (Eq. (24) for $\zeta = 0$) with the velocity

$$u_{sB} = \sqrt{\frac{1}{\epsilon^2} \frac{p_1 - p_2 + \rho g(r_1 - r_2)}{\rho/2}} \quad (25)$$

The Reynolds number is conveniently based on (ϵu_{sB}) and extended by a geometry parameter, so that

$$Re = \frac{\epsilon u_{sB} s}{\nu} \frac{\alpha}{1 - (r_2/r_1)^2} \quad (26)$$

and finally for the coefficient

$$\frac{u_s}{u_{sB}} = -\frac{6}{\epsilon Re} + \sqrt{\frac{36}{\epsilon^2 Re^2} + 1}. \quad (27)$$

Figure 2 demonstrates how the coefficient depends on Reynolds number and ϵ . With increasing Reynolds number the actual rate approaches the ideal one ($u_s/u_{sB} \rightarrow 1$). This finding is consistent with Eq. (22) that assumes that the pressure drop is shared between two terms, the quadratic production of kinetic energy in the gap and the linear friction. At small Re the second dominates and the quadratic term vanishes. Then, when Re increases the situation reverses with the first term growing so much that the second becomes relatively small.

3 Experiments With Water in a Straight Channel

Experiments with water were carried out with the apparatus sketched in Fig. 3. A vertically mounted glass cylinder of 300 mm inner diameter is filled with water. The bottom plate of the cylinder incorporates a straight horizontal channel of 189 mm length shown in sectional view. The angle between the channel walls is 1 deg leaving a gap width at the exit of 0.31 mm. It is rather difficult to determine the gap width exactly, especially because it varies slightly along the length of the gap. Feeler gauges down to 1/100 of a mm were used and it was made sure that the gap was greater than 0.30 mm and smaller than 0.32 mm. In flow direction ($r_1 \rightarrow r_2$) the channel measures $h = 38$ mm. At the exit the water either enters ambient air as a free jet or it mixes with water. In both cases the exit pressure is atmospheric as it is up on the water surface. In the water case this is secured by the shown overflow pipe dis-

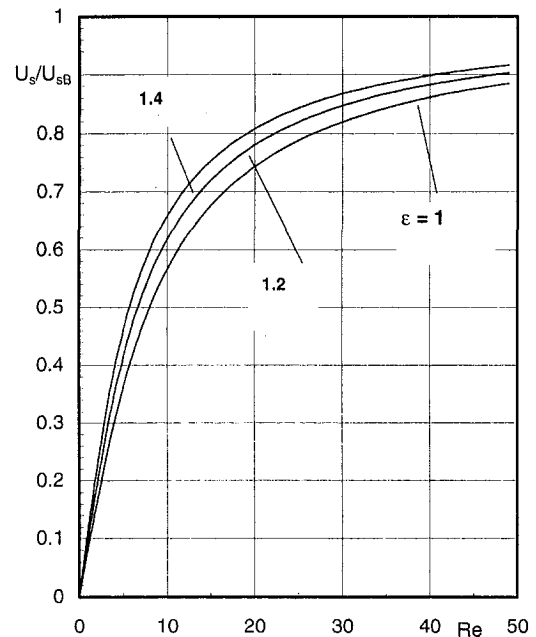


Fig. 2 Discharge coefficient defined as real over ideal gap velocity plotted versus Reynolds number and a correction parameter ϵ

charging the water level with the channel exit. The pressure loss in the overflow pipe is negligible due to its relatively large cross section.

Two downstream conditions were studied for the following reason. The above theory deals with the flow inside the channel. Its downstream boundary condition is the wall pressure at a certain location in the channel. Nothing is included about the abrupt transition from a narrow gap to an infinite space and possible upstream effects on e.g., the velocity distribution. Since it may be argued that an upstream effect could be different under different downstream conditions both cases, i.e., water in air and water in water, were tested and compared.

As the arrangement is set up the flow is simply driven by the water head $\rho g H$. When the water flows out through the channel the head decreases and thus the flow rate also decreases. By measuring the head versus time we have, in one measurement, the pressure difference and the flow rate. This is achieved by a heavy float driving an incremental angle transmitter by means of a thin rope. After calibration the pulse frequency of the transmitter is an accurate measure of the flow rate with a water head resolution of

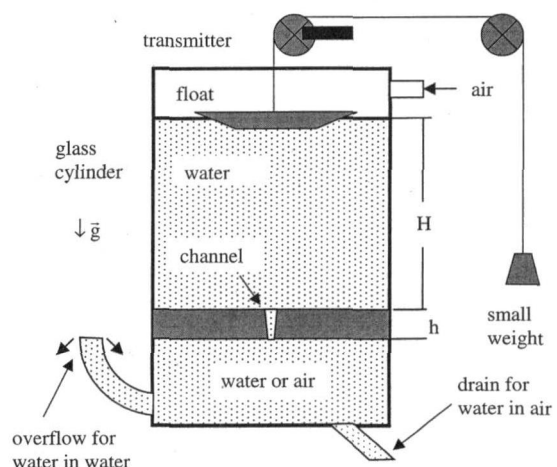


Fig. 3 Glass cylinder apparatus with channel for water tests

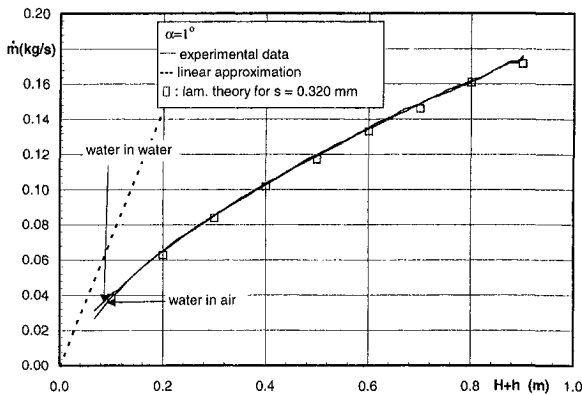


Fig. 4 Comparison of experimental results for water with laminar theory

less than a mm. A personal computer was employed to record the frequency as it drops over a whole run. The uncertainty of the flow rate is mainly due to the slightly varying cross section of the glass cylinder. Yet, this is a local inaccuracy contributing to a random error scatter rather than a systematic uncertainty.

The results are presented in Fig. 4 where the mass flux is plotted versus $H + h$. Due to the proximity of float and channel entrance data recording became difficult close to 0.1m and unreliable below. In the first place it is evident that the runs with water in water and water in air are not discernible from each other except at the unreliable lower end. The two curves simply coincide. The slight waviness in the curves is due to the glass cylinder inaccuracies as mentioned.

In evaluating the theory the pressures in Eq. (10), (19) have to be inserted correctly. With Fig. 3 that is

$$p_w(r_1) - p_w(r_2) + \rho g(r_1 - r_2) = \rho g(H + h). \quad (28)$$

To include the theory in Fig. 4 a few points were evaluated and plotted (\square). Very good agreement is found for the gap width of 0.320 mm which is the upper limit of the determined possible gap width range. Therefore, it may be said that the analytical model works well in predicting the flow rate for a gap width that is known to the specified accuracy. A more accurate analysis would require a more accurate gap which is difficult to make. The initial slope of the theoretical curve is indicated by the broken straight line representing the linear approximation Eq. (19). Note that this is not quite possible in the current setup since the water level should not drop below the channel inlet.

It is now of interest to check the predicted Reynolds number dependency. To that end excerpted experimental data points of the curve of Fig. 4 are transferred to Fig. 5 and plotted versus the corresponding Reynolds number. We see that the Reynolds num-

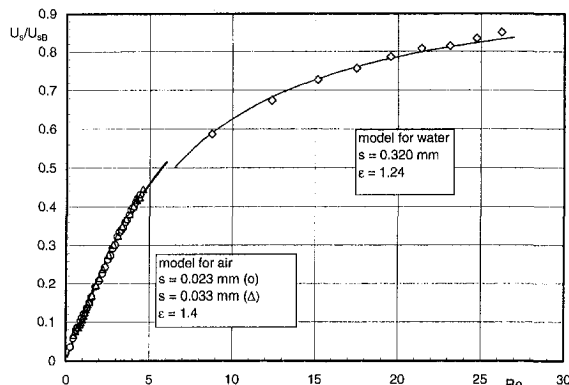


Fig. 5 Discharge coefficient versus Reynolds number. Experimental results compared with parameter model.

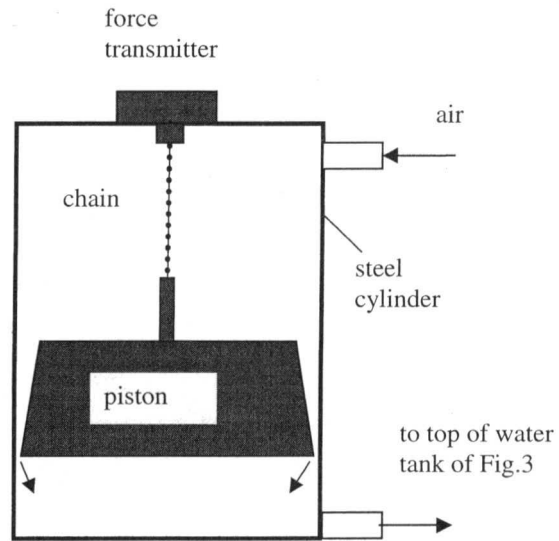


Fig. 6 Piston-cylinder arrangement for tests with air

ber trend is in fact confirmed with a best fit for $\epsilon = 1.24$ in Eq. (27).

4 Experiments With Air in a Circular Convergent Channel

In principle, air flow could also be investigated in the straight channel as used for water. Yet, since the available reference flow rate was limited the gap width had to be smaller. Then, a circular gap is advantageous, since it is easier to make and measure. Furthermore, we already had experimented with a circular piston and cylinder set-up before (Peters and Kuralt, 1995), which proved to work nicely. Figure 6 shows the present design. A precision steel cylinder of 100 mm inner dia. and an ovality of less than 1/100 mm was mounted upright with top and bottom lids. A high quality aluminum piston of 40 mm height was machined on a lathe to have a flank angle of 2.3 deg and a diameter slightly above 100 mm. In a final step, the bottom surface was machined off carefully until the desired gap width was reached. In doing so, the lathe chisel was exclusively moved radially inwards in order to get a sharp and clean edge. As with the straight channel the gap width was determined by feeler gauges. When e.g., a 4/100 mm gauge slides in the gap easily and a 5/100 won't at all the gap is greater than 2/100 and smaller than 2.5/100 mm. It is important to carry out gap and flow measurement at the same temperature because of the different thermal expansion of piston and cylinder. The completed piston was attached to the force balance placed on the top lid ranging from zero to 30 Newton at a resolution of a mN. In selecting the attachment two requirements have to be met. It has to be inelastic lengthwise to avoid oscillations and it has to be highly flexible sideways in order not to act on the piston radially. A perfect choice is the type of ball chain used for sink plugs. Air enters from above, flows through the channel formed by piston and cylinder and leaves at the bottom. The channel flow stabilizes the piston in the center of the cylinder due to an equilibrium of radial wall pressure forces. We have shown earlier (Peters and Kuralt, 1995) that the parameter $s/h \tan \alpha$ should be small for maximum stability where $h = 40$ mm is the piston height. The air is pumped away from under the piston through a hose running to the top of the water tank of Fig. 3. Now the falling water column serves as pump and reference at the same time. As the flow rate of the draining water is measured precisely, as explained above, the flow rate of the air sucked into the glass cylinder is equally known. The best mode of operation was to remove the bottom plate including the straight channel and drain the water through a fine control valve. This way sufficient periods of time with constant flow rates could be attained.

Results are presented in Fig. 7. For a first piston the gap was

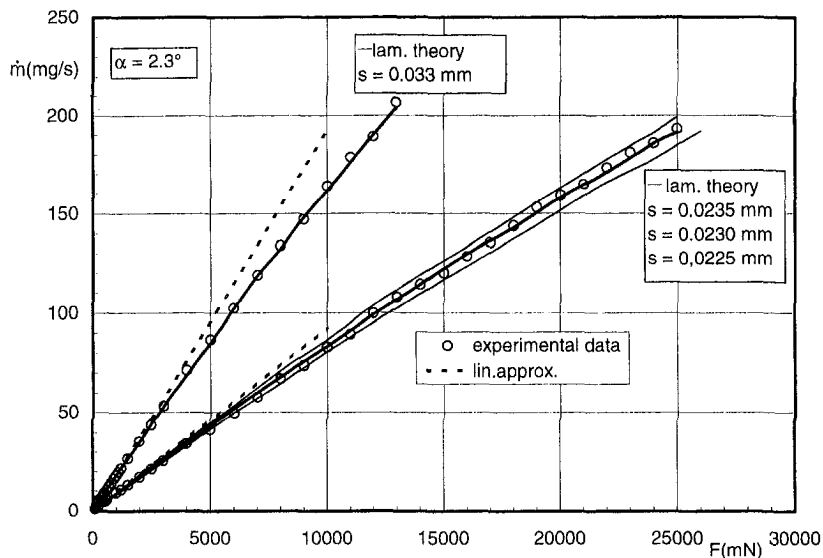


Fig. 7 Comparison of experimental results for air with laminar theory

determined greater than 0.02 and smaller than 0.025 mm. Plotted is the mass flux \dot{m} in mg/s based on the density 1.19 kg/m^3 at 20°C versus the force in mN acting on the force transducer by the flow (circles). The pressure difference in the analysis is replaced by force over cylinder cross section. Four theory curves are added for comparison. There are three curves evaluated for gap width 0.0225, 0.0230 and 0.0235 mm. The middle one fits the data nicely. The gap width 0.0230 mm is right in the middle of the limits set by the gap measurement. Therefore, a very reasonable agreement is achieved. Again, it is not possible to determine the real gap width with higher accuracy unless an extremely precise cylinder—piston set is machined on the μm scale. The straight broken line starting from zero gives the linear approximation from Eq. (19) corresponding to 0.0230 mm.

Additional support for the theory is provided by a second gap width resulting in the upper curve. The same piston was used. Its bottom was machined down by $2/100 \text{ mm}$ in diameter with great care. The theory curve corresponds to the new measure $s = 0.033 \text{ mm}$ and the broken line to the linear approximation. The upper limit of the measuring range was set by the reference measurement. The lower curve was limited by the force measurement. Without these limits a much wider measuring range would be possible up to the limit where compressibility effects become significant.

The experimental data points were recomputed and transferred to Fig. 5 (circles). We see that these air data correspond to smaller Reynolds number than the water data. For both gap widths the model curve fits very well for $\epsilon = 1.4$.

5 Conclusions

The present investigation has shown that the laminar theory of channel flow predicts accurately the flow rate in a water as well as in an air channel although these channels were of finite length suggesting a deviation from ideality at least at the channel outlet. In case of water it was found that it doesn't matter whether the water discharges into water or air. A combination of laminar theory and integral energy equation brings forward that a discharge coefficient can simply be expressed as function of Reynolds number and a fitting parameter. The latter turns out to be greater than unity which means that the jet emanating from the channel outlet contracts while it progressively assumes the ambient pressure.

These findings are considered an excellent basis for flow metering purposes. A channel may be scaled and designed according to the desired flow rate. Certainly, since small gaps are difficult to make a calibration will always be necessary. The proposed simple

Reynolds number model is helpful in modelling the calibration curves. When the flow rate becomes very small this model and the laminar analysis collapse onto a simple linear formula.

The question of accuracy is twofold concerning the theory and a possible instrument. We have seen that the laminar theory predicts the flow rate very well however a quantification of its accuracy would require precision gaps accurate at least to a μm . When these are not available the accuracy of an actual instrument would still be determined in comparison with a normal of higher precision. From the experience with stability and reproducibility of the current measurements an accuracy in the sub-1% range seems realistic.

The results could be utilized in designing throttle units like valves with the intention to get the flow rate from the geometry and the pressure drop along with the valve itself. When it comes to separate measuring instruments the proposed piston-cylinder arrangement seems to be appropriate. Its most remarkable property is the freely floating, selfcentering piston allowing wide measuring ranges. Evidently, a measuring principle like this based on low Reynolds number flow involves inevitable pressure drop and is out of the question for many applications. On the other hand the drop is not unusual and found in comparable methods like the floating element meter. It seems that accurate measurements for preferably small flow rates would be the primary field of application.

Acknowledgment

Part of this work was funded by grant Me 484/29 of Deutsche Forschungsgemeinschaft (DFG).

References

- Fiedler, O., 1992, "Strömungs- und Durchflußmeßtechnik," R. Oldenbourg, Verlag, München.
- Bückle, U., Durst, F., Howe, B., and Melling, A., 1992, "Investigation of a floating element flowmeter," *Flow Measurement and Instrumentation*, Vol. 3(4), pp. 215–225.
- Peters, F., and Kuralt, T., 1995, "A Gas Flowmeter of High Linearity," *Flow Measurement and Instrumentation*, Vol. 6(1), pp. 29–32.
- Wojtkowiak, J., Kim, W. N., and Hyun, J. M., 1997, "Computations of the Flow Characteristics of a Rotating-Piston-Type Flowmeter," *Flow Measurement and Instrumentation*, Vol. 8(1), pp. 17–25.
- Morsi, S. A., 1976, "The Pad and Quad Resistor—Two Methods of Fluid Flow Measurements," *Proc. Instn. Mech. Engrs.*, Vol. 190, p. 205.
- Wieners, N., Peters, F., and Merzkirch, W., 1978, "Calibration of a Linear Pad Resistor," *Flow Measurements of Fluids*, By H. H. Dijkstra and E. A. Spencer, eds., pp. 275–278, North-Holland Amsterdam.
- Harvill, L. R., Ifft, S. A., and Thompson, P. A., 1995, "Hydrodynamic Drag on a V-Cone Flowmeter," Morrison, G. L., ed., *Fluid Measurement and Instrumentation*, Vol. 211 FED, ASME, pp. 57–61.
- Constantinescu, V. N., 1995, *Laminar Viscous Flow*. Springer-Verlag.

Zhigang Feng

Institute of Paper Science and Technology,
Atlanta, GA 30318.

Xiaodong Wang

Department of Mechanical Engineering,
Brooklyn, NY 11201.

Larry J. Forney

School of Chemical Engineering,
Georgia Tech, Atlanta, GA 30332

Single Jet Mixing at Arbitrary Angle in Turbulent Tube Flow

An asymptotic procedure is presented to evaluate the tracer trajectory in a two-stream turbulent pipe mixing unit with an oblique branch. The proposed mixing jet trajectory estimate near the injection point is compared with the existing experimental data and used to calculate the critical mixing configurations. In addition, it is shown that the well-known tracer jet profile can be recovered for the case of a normally issued tracer turbulent jet.

1 Introduction

The problem of mixing two fluid streams by turbulent jet injection into a pipeline has various applications in areas such as chemical reactions, heat transfer operations, and mixing and combustion processes in industry. As a simple but effective method to mix two fluids, pipeline mixers have been studied extensively. The first systematic study was conducted by Chilton and Genereaux (1930) in which smoke visualization techniques were used to determine the optimum mixing conditions at a glass tee. Forney and Kwon (1979) proposed a similarity law, which was derived from approximate solutions to the equations of motion for the case of a single, fully developed turbulent jet issuing normally to the flow. Forney and Lee (1982) further established the importance of the diameter and velocity ratio for geometrically similar flows. Maruyama et al. (1981, 1982) studied the jet injection of fluid into the pipeline over several pipe diameters from the injection point, and they proposed the standard deviation as a mixing quality indicator. Ger and Holley (1976) and Fitzgerald and Holley (1981) conducted some experiments and compared standard deviations of measured tracer concentrations far downstream from the side tee. Sroka and Forney (1989) derived a scaling law for the second moment of the tracer concentration within the pipeline when the turbulent jet injection is normal to the pipeline.

However, most of the research has been conducted for a configuration in which the jet is normal to the pipeline. In the present study, we consider a more general case in which the turbulence jet injects fluid at an angle θ_o ($0^\circ < \theta_o < 180^\circ$), and we derive asymptotic solutions for both jet trajectory and tracer concentration profiles in the near region of the jet injection point. The proposed analytical solutions are compared with the existing experimental results for turbulent mixing of two fluid streams at an oblique branch (Maruyama et al., 1981, 1982) and the analytical solutions for T-junctions (Forney et al., 1979).

In chemical engineering it is desirable to have the side-issued jet contact the opposite wall in order to enhance rapid mixing. However, in the paper industry, the tracer jet is often issued at an angle θ_o ($45^\circ \leq \theta_o \leq 60^\circ$) to avoid contact with the opposite wall and, in this way, to minimize flow disturbance and pressure pulsation. The presented analytical solution of the tracer jet trajectory will provide valuable information on the conditions under which the tracer jet will contact the opposite wall. In addition, such straightforward estimates of jet trajectories can be used to confirm both experimental and computational data.

2 Jet Injection at an Arbitrary Angle

2.1 Theory. The configuration of a general pipeline mixer with an angle θ_o is shown in Fig. 1, in which a jet with diameter d (or radius $b_o = d/2$) issues fluid containing tracer into a tube of diameter D . The ambient fluid velocity of the tube is v , and the initial tracer jet velocity is u_o . The phenomenon of jet mixing of a tracer in turbulent tube flow involves two phases. In the initial stage, the mixing process is dominated by self-induced jet turbulence. After a distance, the jet evolves into a geometrically centered jet, and the mixing of the tracer is dominated by turbulence in the main stream. Forney and Kwon (1979) proposed a characteristic length l_m , which represents the distance over which the jet travels before it bends over in the cross flow. This momentum length is defined as follows:

$$l_m = \frac{du_o \sin \theta_o}{v} \quad (1)$$

For convenience, we also introduce the following dimensionless length:

$$R = \frac{l_m / \sin \theta_o}{d} = \frac{u_o}{v} \quad (2)$$

2.2 Field Equations. Our goal is to derive an asymptotic expression for the jet trajectory at the first stage, i.e., close to the jet orifice. The governing equations for the present problem include the conservation of mass and momentum. The well-known entrainment model first developed by Houtl, Fay, and Forney (1969) is employed in this paper. The model assumes that there are two additive entrainment mechanisms, one is due to the tangential difference between the local jet velocity u and ambient fluid velocity component parallel to the jet, and the other to the ambient fluid velocity normal to the jet. For the configuration in Fig. 1, we can write the conservation of mass as follows:

$$\frac{1}{2b} \frac{d}{ds} (b^2 u) = \alpha(u - v \cos \theta) + \beta v \sin \theta, \quad (3)$$

where s , θ , u , b , α , and β stand for the mixing jet's arc length, tangential angle, jet velocity, equivalent cross-sectional radius, and the tangential and normal entrainment parameters, respectively.

The conservation of tangential momentum can be written as:

$$\frac{d}{ds} (b^2 u^2) = v \cos \theta \frac{d}{ds} (b^2 u), \quad (4)$$

and similarly for the normal momentum, we have

$$b^2 u^2 \frac{d\theta}{ds} = -v \sin \theta \frac{d}{ds} (b^2 u). \quad (5)$$

The conservation of tracer concentration c gives

Contributed by the Fluids Engineering Division for publication in the JOURNAL OF FLUIDS ENGINEERING. Manuscript received by the Fluids Engineering Division April 4, 1998; revised manuscript received August 9, 1999. Associate Technical Editor: M. S. Cramer.

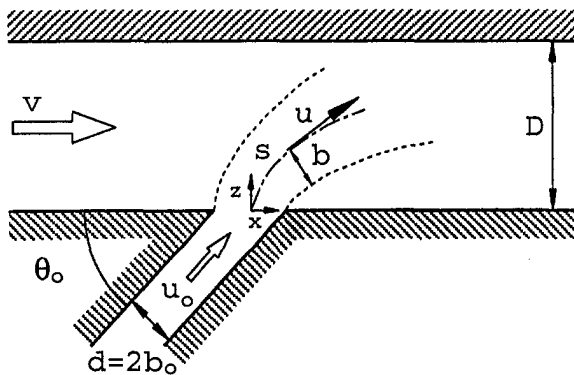


Fig. 1 Two fluid streams mixing at an oblique branch

$$\frac{d}{ds}(cb^2u) = 0. \quad (6)$$

The boundary conditions at the jet orifice are specified as:

$$s = 0, \quad \theta = \theta_o, \quad u = u_o, \quad b = b_o, \quad c = c_o.$$

2.3 Asymptotic Solutions. Because we are interested in an asymptotic expression for the jet trajectory close to the orifice, we assume that the departure of θ from θ_o is small; furthermore, the Reynolds number of the orifice is restricted to large values to ensure jet turbulence, and the effect of buoyancy is neglected. Under these assumptions, from Eq. (3), we have

$$\frac{b^2u}{b_o^2u_o} \approx 1 + 4\Omega \frac{s}{d}, \quad (7)$$

in which Ω is a constant given by

$$\Omega = \alpha \left(1 - \frac{\cos \theta_o}{R} \right) + \beta \frac{\sin \theta_o}{R}, \quad (8)$$

and from Eqs. (4) and (5), we obtain

$$\frac{b^2u^2}{b_o^2u_o^2} = \frac{\sin \theta_o}{\sin \theta}. \quad (9)$$

Furthermore, Eqs. (5) and (9) give us

$$R \frac{d\theta}{ds} = - \frac{\sin^2 \theta}{\sin \theta_o} \frac{d}{ds} \left(\frac{ub^2}{u_o b_o^2} \right). \quad (10)$$

By integrating Eq. (10), we have, within the first-order approximation,

$$\theta \approx \theta_o - 4\Omega \sin^2 \theta_o \frac{s}{l_m}, \quad (11)$$

and consequently, by the nature of Eq. (6), we obtain

$$\frac{c}{c_o} = \frac{1}{1 + 4\Omega s/d}. \quad (12)$$

To convert the above expression into cartesian coordinates (x , z), we introduce the following relations:

$$\begin{aligned} dz &= ds \sin \theta = ds \sin(\theta_o + \delta\theta) \\ &\approx ds(\sin \theta_o + \cos \theta_o \delta\theta), \end{aligned} \quad (13)$$

$$\begin{aligned} dx &= ds \cos \theta = ds \cos(\theta_o + \delta\theta) \\ &\approx ds(\cos \theta_o - \sin \theta_o \delta\theta). \end{aligned} \quad (14)$$

For the region near the orifice, we have

$$\delta\theta = \theta - \theta_o \approx -4\Omega \sin^2 \theta_o \frac{s}{l_m}. \quad (15)$$

Integrating Eqs. (13) and (14), we obtain the following two key parametric equations for the asymptotic jet trajectory:

$$z = s \sin \theta_o - \Omega \sin \theta_o \sin 2\theta_o s^2/l_m, \quad (16)$$

$$x = s \cos \theta_o + 2\Omega \sin^3 \theta_o s^2/l_m. \quad (17)$$

Furthermore, the tracer trajectory is given implicitly by the following relation:

$$\begin{aligned} x^2 \cos^2 \theta_o + xz \sin 2\theta_o + z^2 \sin^2 \theta_o \\ - \frac{l_m}{2\Omega \sin^2 \theta_o} (x \sin \theta_o - z \cos \theta_o) = 0, \end{aligned} \quad (18)$$

while the tracer concentration profile, in cartesian coordinates, becomes

$$\frac{c}{c_o} = \frac{1}{1 + R(\sqrt{\cos^2 \theta_o + 8\Omega \sin^3 \theta_o x/l_m} - \cos \theta_o)/\sin^2 \theta_o}. \quad (19)$$

In particular, for the case of normal jet injection, in which $\theta_o = 90^\circ$, Eq. (18) reduces to

$$\frac{z^2}{l_m^2} - \frac{x}{2\Omega l_m} = 0, \quad (20)$$

or

$$\frac{z}{l_m} = \sqrt{\frac{x}{2l_m\alpha + 2l_m\beta/R}} \quad (21)$$

which is exactly the same result as given by Forney and Kwon (1979). As pointed out by Forney and Kwon (1979), although Eq. (21) is restricted to the condition $x/l_m \ll 1$, i.e., valid for the region close to the orifice, a numerical solution obtained by Hoult and Weil (1972), indicates that the range of validity of Eq. (21) can be extended away from the orifice, and there are no significant deviations between the approximate result and the numerical result until $x \gg l_m$. For the general case of the present problem, further numerical computation will be needed to confirm the claim that Eq. (18) can be extended away from the near field region where $x/l_m \ll 1$.

2.4 Impact on the Opposite Wall. In chemical engineering, it is assumed that optimal mixing and reaction take place when the issued jet impacts the opposite wall, while in the paper industry, in order to minimize the pressure pulsation and flow disturbance in the approach flow system, it is desirable to avoid having the jet impact on the wall. Therefore, the following estimate of those conditions under which the jet trajectory will intercept the wall, i.e., the conditions under which there exists a solution of Eq. (16) yielding an x for $z = D$, plays an important role in the design of pipeline mixers.

From Eq. (16), by substituting $z = D$, we obtain the arc length s from the start point to the first intercept point with the opposite wall,

$$s = \frac{\sin \theta_o - \sqrt{\sin^2 \theta_o - 4D\Omega \sin \theta_o \sin 2\theta_o/l_m}}{2\Omega \sin \theta_o \sin 2\theta_o/l_m}. \quad (22)$$

The corresponding intercept coordinate x_i is then calculated using Eq. (17). Of course, the existence of such a solution requires that

$$R \frac{d}{D} \sin^2 \theta_o \geq 8 \cos \theta_o \Omega, \quad (23)$$

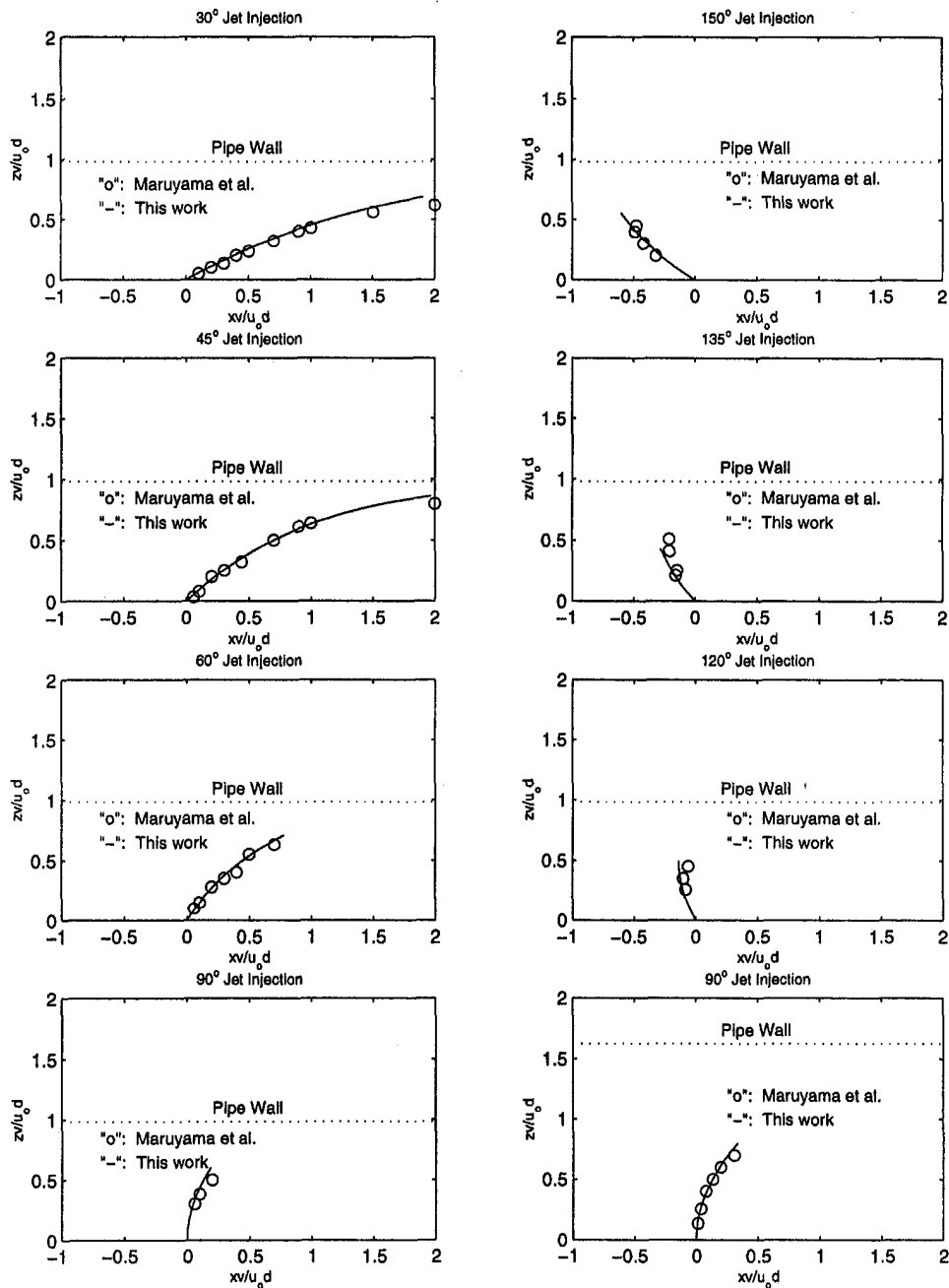


Fig. 2 Mixing stream trajectories near the injection points at different angles. For the bottom-right case, $d = 0.8$ cm, $D = 5.1$ cm, $R = 3.9$; for the other cases, $d = 1.3$ cm, $D = 5.1$ cm, $R = 4.0$.

where the equal sign yields the critical jet injection angle at which the impact on the opposite wall will happen.

From Eqs. (16) and (17), we also obtain

$$x \sin \theta_o - z \cos \theta_o = 2\Omega \sin^2 \theta_o s^2 / l_m \quad (24)$$

Therefore, we may conclude that $x_i > D \tan \theta_o$, which is consistent with the fact that the nearest possible position at which the jet can impact the opposite tube wall is $D \tan \theta_o$, when the tube ambient fluid velocity $v = 0$.

2.5 Correlation of Data. The solutions of the two parametric equations for the asymptotic jet trajectory Eqs. (16) and (17) are plotted and compared with the experimental data of Maruyama et al. (1981, 1982). The comparison with seven branch angles covering the range from $30^\circ \sim 150^\circ$ is shown in Fig. 2. The tangential

and normal entrainment coefficients are chosen as $\alpha = 0.11$ and $\beta = 0.6$, which are the so-called universal constants discussed in (Hoult et al., 1969) (Hoult and Weil, 1972). Moreover, Hoult and Weil (1972) also concluded that the entrainment constants have constant values which for α is known to within 20 per cent accuracy and for β is to 25 per cent accuracy.

The experimental data represent hot-wire anemometer measurements of maximum jet velocities and, in this case, may not represent the geometric center of the jet, and they are the actually measured data reported in detail in Maruyama et al. (1981, 1982). We find that the correlation is good for branch angles $\theta_o \leq 90^\circ$ while the asymptotic solutions deviate significantly from the measured data for $\theta_o > 90^\circ$. Our understanding is that in the latter case, the jet is projected upstream and turns abruptly near the origin, and the assumption of small

deviation of θ from θ_0 is violated. Nevertheless, the fact that in all branch angle cases the predicted trajectories match with the experimental measurements near the injection point confirms the assumption we use in deriving the parametric equations (16) and (17), which in fact explains the reason why we only present the asymptotic solutions near the injection point. Finally, we note that the real jet trajectory will bend down when it experiences the effects or existence of the opposite wall and the asymptotic estimate of the impact point is on the conservative side.

3 Conclusion

The problem of a turbulent jet in a crossflow at an arbitrary injection angle is studied analytically. By employing the entrainment model and exploring the conservation equations of mass, momentum, and tracer, we derived asymptotic solutions for jet trajectory and tracer concentration of a region close to the jet injection point under the assumptions of a near region where ambient turbulence on the mixing process can be neglected relative to jet-induced turbulence. The proposed asymptotic solutions are straightforward and match well with the existing experimental data. In addition, a critical jet injection angle estimate is also presented.

Acknowledgment

We would like to thank the Institute of Paper Science and Technology and the School of Chemical Engineering at the Georgia Institute of Technology for their support.

References

- Chilton, T. H., and Genereaux, R. P., 1930, "The Mixing of Gases for Reaction," *AIChE Transaction*, Vol. 25, pp. 102–122.
- Fitzgerald, S. D., and Holley, E. R., 1981, "Jet Injections for Optimum Mixing in Pipe Flow," *Journal of Hydraulic Division of ASCE*, Vol. 107(HY 10), pp. 1179–1195.
- Forney, L. J., and Kwon, T. C., 1979, "Efficient Single-Jet Mixing in Turbulent Tube Flow," *AIChE Journal*, Vol. 25, No. 4, pp. 623–630.
- Forney, L. J., and Lee, H. C., 1982, "Optimum Dimensions for Pipeline Mixing at a T-Junction," *AIChE Journal*, Vol. 28, No. 6, pp. 980–987.
- Ger, A. M., and Holley, E. R., 1976, "Comparison of Single-Point Injections in Pipe Flow," *Journal of the Hydraulics Division of ASCE*, Vol. 102, No. HY6, pp. 731–746.
- Hoult, D. P., Fay, J. A., and Forney, L. J., 1969, "A Theory of Plume Rise Compared with Field Observations," *Journal of the Air Pollution Control Association*, Vol. 19, No. 8, pp. 585–590.
- Hoult, D. P., and Weil, J. C., 1972, "Turbulent Plume in a Laminar Cross Flow," *Atmospheric Environment*, Vol. 6, pp. 513–531.
- Maruyama, T., Mizushima, T., and Watanabe, F., 1982, "Turbulent Mixing of Two Fluid Streams at an Oblique Branch," *International Chemical Engineering*, Vol. 22, No. 2, pp. 287–294.
- Maruyama, T., Suzuki, S., and Mizushima, T., 1981, "Pipeline Mixing Between Two Fluid Streams Meeting at a T-Junction," *International Chemical Engineering*, Vol. 21, No. 2, pp. 205–212.
- Sroka, L. M., and Forney, L. J., 1989, "Fluid Mixing with a Pipeline Tee: Theory and Experiment," *AIChE Journal*, Vol. 35, No. 3, pp. 406–414.

Effect of Injected Longitudinal Vorticity on Particle Dispersion in a Swirling, Coaxial Jet

Ryan B. Wicker

Assistant Professor,
Department of Mechanical and Industrial
Engineering,
The University of Texas at El Paso,
El Paso, TX 79968-0521

John K. Eaton

Professor,
Department of Mechanical Engineering
Stanford University,
Stanford, CA 94305-3030

A passive particle dispersion control technique was investigated in which longitudinal vortices were injected into a developing coaxial swirling jet with sufficient annular swirl for flow recirculation to occur. Four vortex generators, separated by 90 degrees and placed along the outside of the annular nozzle, injected vorticity opposite in sign to the mean swirl, significantly altering the structure of the swirling jet. The injected vorticity competed with the mean swirl to reduce azimuthal particle flinging and to disrupt the development of the vortex rings in the outer shear layer. Axial flow visualization showed the formation of axial structures at the forcing frequency but considerable azimuthal asymmetry. Horizontal cross sections showed a four-lobed structure which persisted in the natural jet for at least eight inner jet diameters. The particle concentration field was measured using digital processing of pulsed laser sheet images. Outward radial particle dispersion reduced while inward dispersion toward the jet centerline increased indicating that the injected vorticity sufficiently reduced particle flinging by large-scale vortices.

Introduction

Coaxial jets, in which an annular jet with or without swirl surrounds a central round jet, arise in many applications. In pulverized coal utility boilers, a typical flow configuration consists of a central, coal-laden jet surrounded by one or several swirling annular streams. The present authors (Wicker and Eaton, 1994) previously showed that nearly axisymmetric vortex rings exist, at least intermittently, in a natural coaxial swirling free jet, and that these vortex rings produce instantaneous regions of high particle concentration. The vortex rings could be organized and strengthened using plane wave excitation allowing detailed examination of particle interaction with the vortex rings. It was found that particles were preferentially concentrated between vortex rings and were flung outward on the downstream side of each vortex ring in results similar to the single jet studies of Longmire and Eaton (1992). Coal combustion research has shown that the conversion of nitrogen containing species to NO_x strongly depends on the local stoichiometry. It thus seems desirable to control both the preferential concentration of particles into clumps and the flinging of particles away from the flame zone.

Our previous work showed that active control of the vortex structures using acoustic forcing is possible. However, passive control techniques involving only changes to the geometry of the jet nozzle are preferred in applications. Thus, the current investigation examines a passive control strategy that might provide an effective means for particle dispersion control.

Numerous passive control techniques for single jets have been reported in the literature. Most of these techniques involve the injection or formation of longitudinal vortices in the jet shear layer. For example, longitudinal vortices are formed in an elliptic jet due to asymmetric self-induction of the vortex ring structures (e.g., Ho and Gutmark, 1987; Hussain and Husain, 1989). In triangular and square jets, the large-scale vortices form along the sides, with small-scale mixing occurring at the vertices. Quinn (1992) found counter-rotating pairs of longitudinal vortices emanating from the corners of a square jet which helped explain the increased mixing rates when compared to round jets.

Jet characteristics can be similarly altered by maintaining a round jet cross-section but varying the axial location of the jet exit around the jet circumference. Wlezien and Kibens (1986) and Kibens and Wlezien (1985) studied jets issuing from inclined and stepped nozzles, referred to as "indeterminate origin" nozzles, for forced and natural flow. They found the nonplanar nozzles to effectively distort the flow from axisymmetry, producing large changes in near-field entrainment. Longmire et al. (1992) used crown-shaped nozzles (non-planar exits with no inclination relative to the flow) to introduce strong longitudinal vorticity into the jet shear layer in an attempt to control particle dispersion in a single round jet. This caused rapid spreading of the fluid and a highly asymmetric structure. The particle concentration field was only weakly affected because the time-scale of the longitudinal vortices was too short to produce significant motions of the heavy particles.

More "control" over the longitudinal vorticity might be provided by directly injecting the longitudinal vorticity into the flow field through the use of small tabs or vortex generators. Tabs have been recognized for a number of years for their ability to eliminate screech from supersonic nozzles (e.g., Powell, 1953 and Tanna, 1977), and have received considerable recent attention. It has been fairly well established that the flow obstructions inject streamwise vorticity in the flow which interacts with the naturally occurring structures, altering near field vortex dynamics. Rectangular and triangular tabs inject a pair of counter-rotating vortices into the flow while half delta wing generators inject single vortices. The effects of various configurations have been studied by Zaman et al. (1994), Rogers and Parekh (1994), Carletti and Rogers (1994), Carletti et al. (1993), and Surks et al. (1992, 1994). The experiments of most interest in the present case are the ones by Surks et al. (1992, 1994) who found the greatest increase in mixing using four equally spaced generators all producing vortices of the same sign.

In many situations, the presence of the longitudinal vortices accounts for increased near field mixing between the jet and ambient fluid. However, our goal is to reduce the flinging of particles by the large-scale structures present in the outer shear layer. The large-scale structures can fling individual particles completely free of the outer shear layer. In combustion applications, the flung particles would react in an uncontrolled, locally fuel-lean environment. Therefore, we have attempted to maintain effective

Contributed by the Fluids Engineering Division for publication in the JOURNAL OF FLUIDS ENGINEERING. Manuscript received by the Fluids Engineering Division May 10, 1995; revised manuscript received September 2, 1999. Associate Technical Editor: D. P. Telionis.

gas-phase mixing while changing the scale and orientation of the dominant shear layer eddies.

The specific objectives of this work were to explore the use of delta-wing vortex generators to control particle dispersion in swirling, co-flowing jets. We were particularly interested in the effect of the longitudinal vortices on the large-scale vortex rings which cause non-uniform dispersion by particle flinging and preferential particle concentration. Our previous research has shown that large-scale vortex rings are present in the natural jet. However, since the natural rings appear at random times with random spacings, the effects are difficult to quantify. In the work described herein, acoustic forcing is used to organize the vortex ring structure of the jet. The forcing both enhances and phase-locks the vortex rings, which has two consequences. First, the enhancement of the vortex ring strength provides a more severe test case for the use of longitudinal vortices for passive control. The forcing also facilitates the experiments by allowing the effects of the longitudinal vortices to be measured at specific phases of the vortex ring evolution.

The forced, coaxial swirling jet with longitudinal vortex injection has many free parameters including the jet Reynolds number, core/annular velocity ratio, core/annular diameter ratio, and swirl number, the forcing frequency and amplitude, and the vortex generator size, number, and angle of attack. A comprehensive study of the parameter space would be a huge undertaking. We studied instead a single case in detail where the jet parameters were chosen to produce a stable central recirculation zone with all of the jet parameters in the range characteristic of industrial burners. The forcing was chosen to produce vortex rings similar to naturally occurring ones, but phase-locked to allow detailed study. The vortex generators were chosen based on previous experience with simpler jets. The goal then of this study was to determine if longitudinal vortex injection could be used to reduce particle flinging, leaving optimization of the configuration, and a full understanding of the vortex structure for later studies.

Experimental Facility and Techniques

The coaxial jet facility is shown in Fig. 1. Compressed air entered the flow facility through three separately metered lines: the inner flow line, the annular flow line and/or the smoke flow line. The inner flow was directed to the ceiling of the flow facility where an Accurate Model 302 screw feeder was used for particle injection. The coaxial jet issued into the ambient fluid through concentric round nozzles with coplanar exits. The inner flow was supplied from a 5-cm diameter plenum chamber exiting through a 6.45:1 area contraction aluminum nozzle with a 2-cm exit diameter. Tangential plus axial injectors, connected to the 158-cm² annular plenum chamber, were used to supply the swirling annular flow. The annular flow exited a 6.30:1 area contraction nozzle with a 6-cm exit diameter. All nozzle profiles were specified by fifth-order polynomial curve fits with zero slope and curvature specified at their respective inlet and exit. The inner nozzle had a knife edge exit boundary condition resulting from a 15° chamfer on the outer surface. Thus, the annular exit width was 2-cm, yielding an outer-

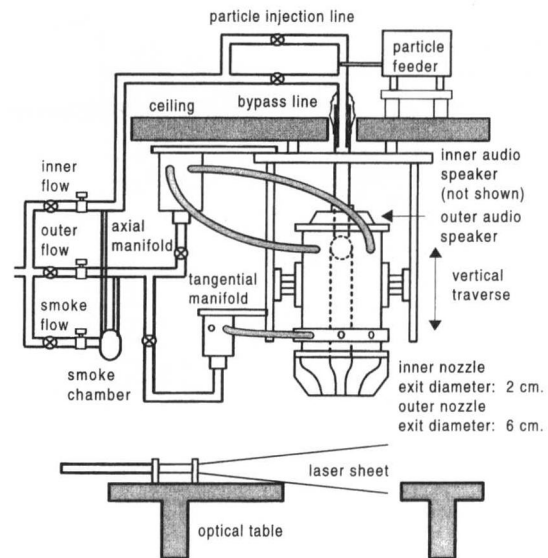


Fig. 1 Coaxial Jet facility

to-inner exit diameter ratio and area ratio of three and eight, respectively. A single baseline flow condition was used for all the work reported here. This consisted of an inner jet bulk velocity of 10 m/s ($Re_i = 13,000$), velocity ratio, U_o/U_i , of 1.15, and swirl number of 0.92, measured without the vortex generators installed. Additional details of the jet apparatus can be found in Wicker and Eaton (1994).

A Draco 8-in audio speaker attached to the top of the annular plenum chamber provided annular plenum chamber excitation. An IBM XT computer with a Data Translation DT 2801 series board was used to supply the acoustic driver with a periodic waveform using one of its two D/A channels. The computer-generated waveform was low-pass filtered with a Frequency Devices Model 901F filter and amplified with a Sony STR-AV210 amplifier prior to being sent to the driver. The other D/A channel was used to trigger the laser at a specific phase in the forcing cycle for flow visualization. Sinusoidal forcing at a frequency of 50 Hz was used for all the experiments reported here. The excitation was adjusted to produce a set velocity fluctuation, u'_i/U_o , of 20% measured at the exit plane of the jet (the natural annular jet exit turbulence intensity, u'_o/U_o , was 10%).

The particles used were Ferro Cataphote class III MS-XL glass shot of 90 μm nominal diameter. The particle size distribution was measured with a Coulter counter yielding a particle number mean diameter of 86.1 μm with a 12.5 μm standard deviation. The particle time constant based on the nominal diameter of 90 μm and Stokes flow is 62 ms. Corrected for nonlinear drag, the time constant is 48 ms, corresponding to a Stokes number of 2.4 based on the forcing frequency. The particle feeder was set to inject 22.7 grams/min of the 90 μm particles, which corresponded to a 10%

Nomenclature

D = jet exit diameter	U = fluid velocity	τ_f = fluid time scale
G_ϕ = axial flux of angular momentum	U_i = bulk inner jet exit velocity (= 10 m/s)	τ_p = particle time constant
G_x = axial flux of axial momentum	U_o = bulk annular jet exit velocity (= 11.5 m/s)	Subscripts
N_T = total number of particles	f = forcing frequency	i = inner jet
R = jet exit radius	r = radial coordinate	o = annular jet
Re = Reynolds number	x = axial coordinate	r = radial coordinate
S = swirl number; $S = G_\phi/R_o G_x$	θ = azimuthal coordinate	x = axial coordinate
St_p = Strouhal number; $St = fD/U$	ϕ = forcing frequency phase angle	θ = azimuthal coordinate
St_k = Stokes number; $St_k = \tau_p/\tau_f$		

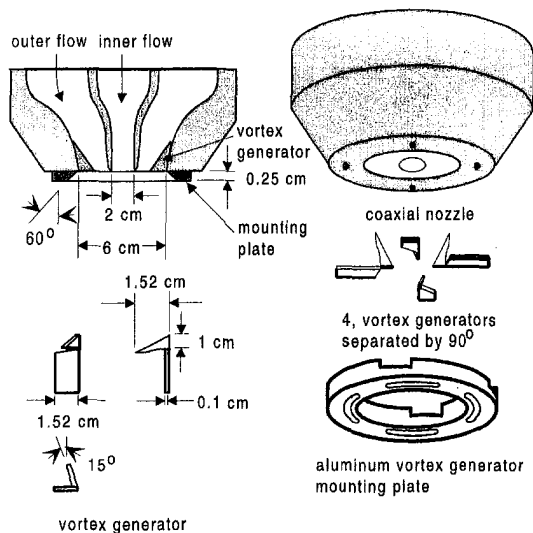


Fig. 2 Vortex generator assembly

mass loading ratio (mass flux particles/mass flux inner air). Although the particle feeder was extremely accurate over long time-averages, comparisons of instantaneous photographs showed variations in the total number of particles from picture-to-picture. Uncertainty in instantaneous number flux based on comparison of the number of identified particles in 32 instantaneous photographs yielded an estimate of 10% for a 95% confidence interval. Since the particle loadings were low enough not to affect the turbulence structure and at least fifty independent images were averaged to obtain particle concentrations, the $\pm 10\%$ variation in instantaneous particle concentration was not expected to alter the results.

The vortex generator assembly and specifications are shown in Fig. 2. Nominal dimensions were as follows: 1.52-cm height, 1-cm width and 15 deg angle from vertical. The surface that contacts the contoured nozzle was ground to fit the nozzle wall. The vortex generators were held firmly against the face of the annular nozzle with a 0.25-cm thick aluminum mounting plate that could be rotated about the jet centerline to facilitate flow field asymmetry measurements. Measured flow angles at the outer edge of the annular nozzle were approximately 45 deg, which yielded a 30 deg vortex generator angle of attack. Surks et al. (1992) used a similar configuration for a single round jet and found that 30 deg angle of attack provided greater entrainment and mixing when compared to 20 deg angle of attack. The above configuration resulted in longitudinal vorticity from the vortex generators which was opposite in sign to the mean annular swirl.

The laser sheet used for flow visualization was produced by one of two lasers: a Plasma Kinetics 151, 10 Watt copper vapor laser or a Continuum Minilite Nd:YAG laser. Both lasers could be triggered externally so that a single laser pulse could be captured on film. The laser pulse width for both lasers was sufficiently short to freeze the flow (30 ns for the copper vapor laser and 3–5 ns for the Nd:YAG laser). All of the images were captured on TMAX 3200 black and white film push processed to 6400 using a Nikon FE2 35 mm camera with a Micro-Nikkor 2.8, 55 mm lens.

The particle concentration field was investigated by taking instantaneous or phase-locked particle-laden images, printing the photographs on photographic paper, then scanning the photographs using a 8-bit Hewlett Packard ScanJet Plus scanner with a maximum resolution of 118 dots per cm. This resolution roughly corresponded to 45 dots per cm in the actual flow field. This value was a function of the distance from the camera to the illuminated plane and the magnification used in the printing process. Typical scanned particle sizes ranged from two to 100 pixels depending on the actual particle size, the particle location in the laser sheet and the actual size of the image field. If a particle was located toward

an edge of the laser sheet, it appeared smaller than a comparable particle located in the center of the sheet.

For the 90 μm particles used in this study, individual projected particle images printed on 4-in by 6-in Kodak Royal paper were large enough to be scanned and processed. After scanning the photographs, software was used to identify the position, size and moment of inertia for each particle in the photograph. During the search routine, once an on pixel was identified, the on pixel's four nearest neighbors were also searched; the corners were neglected. If an adjacent on pixel was identified, its nearest neighbors were also searched. The search continued until all adjacent on pixels were identified and the particle's centroid, pixel area and moment of inertia were calculated. These pixels were then turned off and the search for other particles continued until all on pixels had been turned off. A maximum particle size of 1000 contiguous on pixels was allowed. Even in the highest concentration regions in the flow, this criteria was not met. However, in high particle concentration regions, there was significant overlapping of particles. Due to the wide variation of particle concentration in the flow, it was decided to avoid developing a complicated discrimination scheme to determine the number of particles corresponding to the identified number of pixels and moment of inertia. Therefore, in high concentration regions where overlapping particles would be expected, results are biased toward smaller and more uniform concentrations.

Particle locations were put in proper jet coordinates using reference marks in the images. Two pins at a known separation and distance from the jet intersected the light sheet. The approximate size and location of the pins on the images were sufficient to identify the reference marks. Every particle location identified was rotated, translated and scaled based on the orientation of the reference mark centroids to put it in a consistent coordinate system. With each particle image in proper jet coordinates, additional images corresponding to the same flow condition could be superimposed for analysis. To determine particle concentration, the superimposed images were divided into a uniform spatial grid and the number of particles per grid was counted. Particles with particle positions that did not coincide with a grid point were fractionally assigned to the four nearest grid points. The resulting particle concentration per image was also normalized by the total number of particles identified in the image as well as the laser sheet thickness. The grid spacing was selected to be 10 mm which corresponded to one inner jet radius ($\frac{1}{2}D_i$). Approximately, 750 particles were identified in each full field photograph. For the interested reader, further details of the particle concentration measurement technique can be found in Wicker and Eaton (1994).

Two methods will be used in the following to present the normalized particle concentration results. First, differences in normalized particle concentrations between the forced jet and the natural jet were calculated simply by subtracting the normalized particle concentrations at each location in the grid. Contours of these "forced minus natural" normalized particle concentrations provide information about the particle dispersion effectiveness of the forced jet. All images used in the comparisons were taken consecutively to remove possible errors due to sheet location, flow condition, etc. Second, normalized particle concentrations for two phases in a forcing cycle 180 deg apart were subtracted. Contours of these single frequency, two phase ("forced minus forced") subtractions provide information about preferential concentration (since the physical location of the large-scale vortex ring is a function of the phase of the forcing cycle).

Typically, 15,000 total particles were identified in a set of images, so the minimum and maximum contour levels correspond to differences of approximately 4 and 75 particles, respectively. For particles assumed to be uniformly distributed within the grid, there would be approximately 6 particles at each grid location. However, in the actual flow field, the particle distribution was extremely non-uniform, due to preferential particle concentrations. Individual grid point particle concentrations resulting from a sum of all the images varied from zero to as high as 280 particles on the jet centerline in the stagnation region.

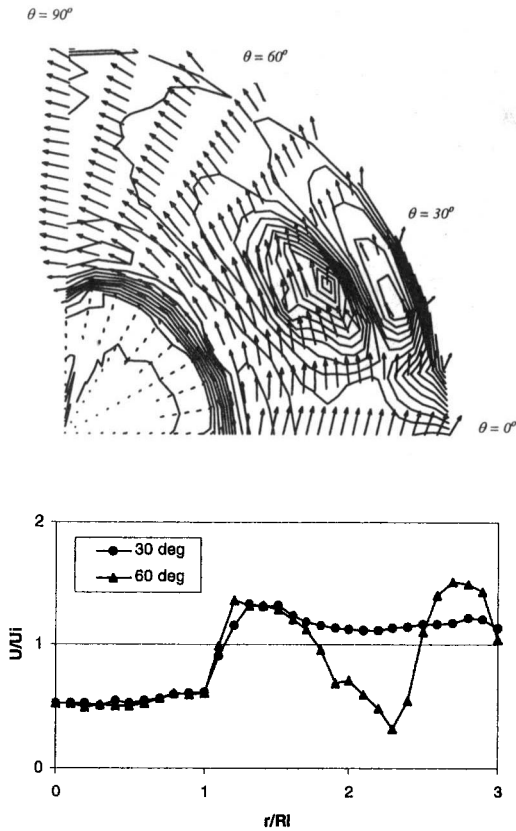


Fig. 3 Jet axial velocity distribution at $x/D_t = 1$. Vortex generators located at $\theta = 0, 90, 180, 270$ deg. (Top) Vector and contour plot of velocity distribution. (Bottom) Axial velocity profiles along two radial lines (30 deg, 60 deg). The probe calibration was accurate to ± 0.3 degree for yaw and pitch angles. Total uncertainties in reported mean velocity magnitudes are expected to be less than 3% with a 95% confidence interval in the majority of the flow (uncertainties can be higher in large velocity gradient regions, see Wicker and Eaton, 1994).

Results

Initial Condition. The jet exit conditions were measured using a five hole probe placed at $x/D_t = 1$, and the velocity field was measured at $\theta = 0$ to 90 deg in 10 deg increments, where vortex generators were located at $\theta = 0, 90, 180$, and 270 deg. Details of the five hole probe and the measurement procedure can be found in Wicker and Eaton (1994). Figure 3 shows the measured velocity distribution, normalized by the bulk inner jet exit velocity of 10 m/s. Contours of axial velocity are given along with the vectors representing the vector sum of the radial and azimuthal velocities. The longitudinal vortex produced by the vortex generator is located in the velocity deficit region in the annular flow. The minimum measured axial velocity in this region was 3 m/s, which is below the inner flow axial velocity of 5 m/s at this location and well below the annular axial velocity of approximately 13 m/s. The low inner flow axial velocity at this axial location is a result of the adverse pressure gradient and rapid radial growth of the inner jet (see Wicker and Eaton, 1994).

The velocity data in Fig. 3 were used to calculate the axial vorticity distribution and the results are given in Fig. 4. Axial vorticity into the page has been shaded to show that the vortex generators were injecting a single sign of vorticity opposite in sign to the mean swirl. The highest axial vorticity is contained in the shear layer between the outer swirling and inner non-swirling jets. The location of the highest vorticity into the page coincides with the maximum axial velocity deficit in Fig. 3.

Flow Visualization. To determine the effect of the injected longitudinal vorticity on the structure of the swirling jet, smoke

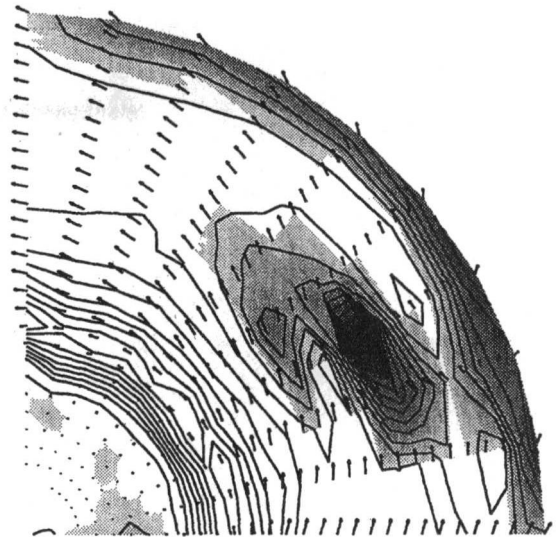


Fig. 4 Jet axial vorticity distribution at $x/D_t = 1$. Vortex generators located at $\theta = 0, 90, 180, 270$ deg. Axial vorticity into the page shaded to illustrate the sign of the injected vorticity.

seeded flow visualization was performed using axial as well as horizontal cuts of the flow. It was anticipated that the longitudinal vorticity would disrupt the natural development of the axial vortex rings. The flow without vortex generators had been previously found by Wicker and Eaton (1994) to respond to 50 Hz forcing, forming axisymmetric structures similar to those found in single axisymmetric shear layers. Axial cuts of the flow for $f = 50$ Hz and $\phi = 0$ deg and 180 deg are contained in Fig. 5. The figure contains phase-averaged images with annular smoke seeding for

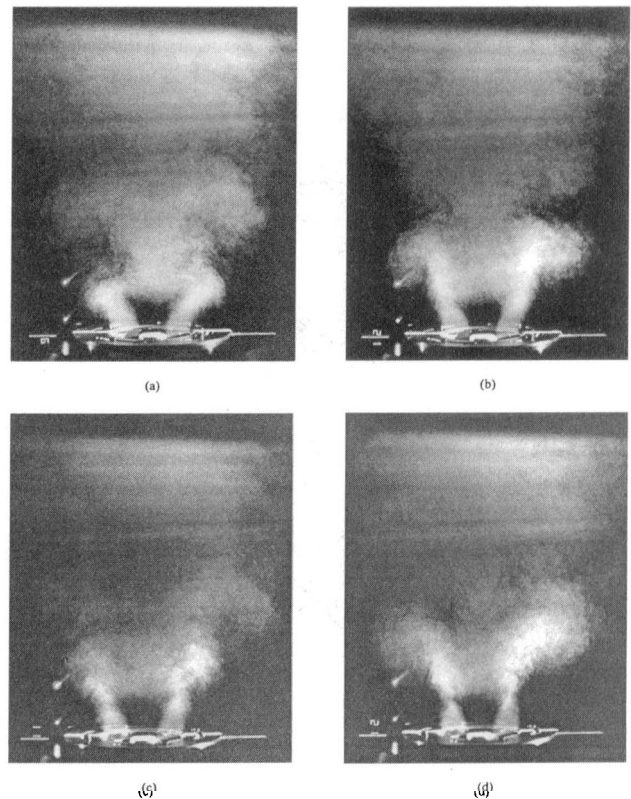


Fig. 5 Phase-averaged axially excited smoke flow visualization with annular seeding: (a) VG-0 deg, $\phi = 0$ deg, (b) VG-0 deg, $\phi = 180$ deg, (c) VG-45 deg, $\phi = 0$ deg, (d) VG-45 deg, $\phi = 180$ deg.

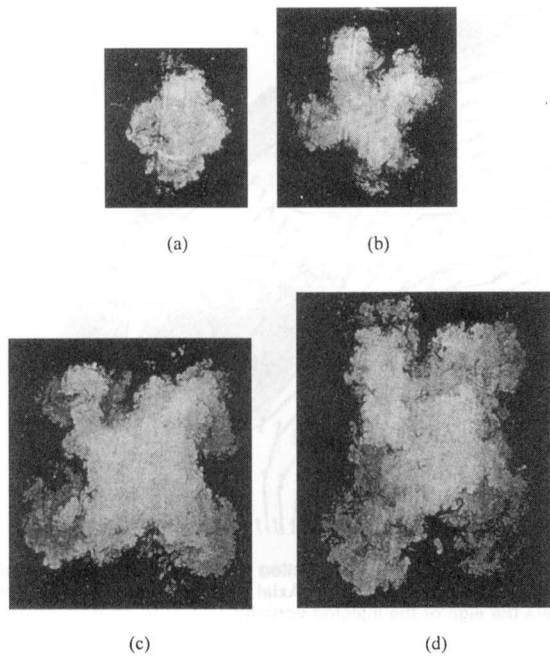


Fig. 6 Instantaneous smoke flow visualization of the natural jet with vortex generators, annular smoke seeding, and horizontal cross sections: (a) $x/D_i = 2$, (b) $x/D_i = 4$, (c) $x/D_i = 6$, (d) $x/D_i = 8$.

the two forcing phases and two vortex generator positions. VG-0 deg refers to the vortex generators positioned at $\theta = 0, 90, 180$, and 270 deg and VG-45 deg refers to the vortex generators positioned at $\theta = 45, 135, 225$ and 315 deg.

The axial cuts show the appearance of an apparent axisymmetric structure similar to the ones found in the jet without vortex generators, although a comparison of the images suggests flow asymmetry. For VG-0 deg (Fig. 5(a)), the first vortex is located at approximately $x/D_i = 1.6$ and the second vortex appears to be located at $x/D_i = 5.3$. These locations are close to the ones identified in the images without vortex generators. However, for

VG-45 deg contained in Figs. 5(c) and 5(d), the first vortex appears to be located at $x/D_i = 2.5$, indicating that the vortex ring is tilted by the vortex generators. The appearance of the second vortex in Fig. 5(c) ($x/D_i = 5.5$) is not significantly different from the second vortex in Fig. 5(a) (VG-0 deg), suggesting that the effect of the vortex generators is not sufficiently strong to break up the vortex rings. The similarity of the $\phi = 180$ deg forcing conditions (Figs. 5(b) and 5(d)) further suggests that the effects of the vortex generators are confined to regions close to the nozzle exit, say, $x/D_i < 3$.

To more completely determine the effects of the vortex generators on the swirling jet structure, horizontal flow visualization was performed at axial stations of $x/D_i = 2, 4, 6$ and 8 for the natural and forced flow with and without the vortex generators. The horizontal flow visualization represents instantaneous cross sections of the flow, and clearly shows the widely varying turbulent scales and extremely complex characteristics of the swirling jet. In the natural jet, the onset of recirculation is slightly before $x/D_i = 2$ and the recirculation zone closes between $x/D_i = 5$ and 6 (see Wicker and Eaton, 1994).

Figure 6 contains natural jet images with vortex generators installed for the four axial locations. The effect of the four vortex generators can be seen quite clearly. At $x/D_i = 2$, the annular jet and the inner jet have four distinct lobes that appear symmetrical. It is believed that the dark regions in the image correspond to entrained ambient fluid due to flow in the longitudinal vortex toward the jet centerline. The four lobed jet structure remains evident at the downstream axial locations, but has become highly asymmetrical. This effect is most likely a result of the rotation of the four lobed structure due to the mean swirl. By $x/D_i = 8$, there is still evidence of the vortex generators effects, but the structure has become highly turbulent.

Particle Concentration Field. Particle concentration measurements were made on two axial slices of the flow separated by 45 degrees in azimuth. Figure 7 presents concentration data for three cases, the forced jet with no vortex generators, the forced jet with vortex generators measured at zero azimuthal angle, and the forced jet with vortex generators measured at a 45 degree azimuthal angle. In each case, the normalized concentration distribution for the natural (unforced) jet with no vortex generators has

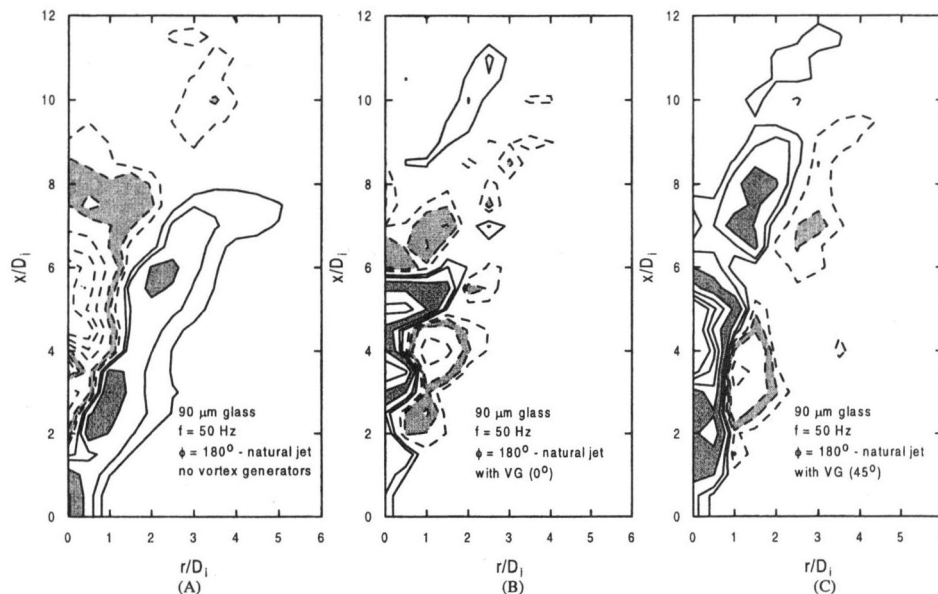


Fig. 7 Normalized particle number density subtractions for the phase-averaged forced jet minus the time-averaged natural jet: (a) without vortex generators, (b) VG-0 deg, (c) VG-45 deg. Contour levels: $\pm 0.00025, 0.0005, 0.001, 0.002, 0.003, 0.004$, and 0.005 . Area enclosed by third lowest contour level (± 0.001) is shaded for convenience. Calculated statistical uncertainties in contour levels are 10% near the jet centerline and as high as 25% near the edge of the jet (e.g., near $r/D_i = 2.0, x/D_i = 4.0$).

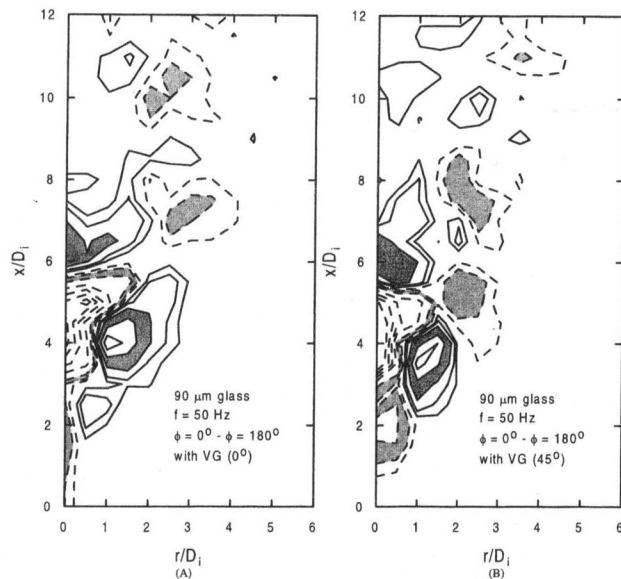


Fig. 8 Phase-averaged normalized particle number density subtractions for the forced ($\phi = 0$ deg) minus forced ($\phi = 180$ deg) jet: (a) VG-0 deg, (b) VG-45 deg. Contour levels: $\pm 0.00025, 0.0005, 0.001, 0.002, 0.003, 0.004, \text{ and } 0.005$. Area enclosed by third lowest contour level (± 0.001) is shaded for convenience. Calculated statistical uncertainties in contour levels are 10% near the jet centerline and as high as 25% near the edge of the jet (e.g., near $r/D_i = 2.0, x/D_i = 4.0$).

been subtracted to emphasize the differences from this base state. All three sets of data were acquired at forcing phase, $\phi = 180$ deg. The solid contour lines represent regions in the flow where the normalized particle number density in the forced jet exceeds that in the natural jet, and dashed contours represent the opposite case. Without the vortex generators (Fig. 7(a)), the forced jet appears to more effectively disperse particles radially when compared to the natural jet. Also, the highest concentration regions in the forced jet shown by the solid contour lines illustrate preferential particle concentrations at $x/D_i = 3$ and 6, associated with the vortex rings. This corresponds to the finding of Longmire and Eaton (1992) in a simple forced jet indicating that even in this complex jet, the particle transport is dominated by vortex rings.

The corresponding particle concentration subtractions for VG-0 deg and VG-45 deg are shown in Figs. 7(b) and 7(c), respectively. Comparison of Figs. 7(b) and 7(c) to Fig. 7(a) shows a marked difference. Without vortex generators, preferential particle concentrations and increased radial particle dispersion were clearly indicated. With vortex generators, the forcing does not increase the radial dispersion, leaving more particles concentrated near the centerline. The three dimensional perturbations induced by the vortex generators apparently weaken the vortex rings since they no longer have a large effect on the particle motion. The large axial velocity variations seen in Fig. 3 produce azimuthal variations in the vortex core position as seen in Fig. 5. A distorted vortex ring is subject to self-induced stretching which reduces the length scale of the vortices. Also, the longitudinal vortices induce an azimuthally non-uniform radial velocity which further distorts the vortex rings (Fig. 6). The net effect is to substantially reduce the radial flinging of particles by the vortex rings.

To better illustrate preferential particle concentrations, particle concentration subtractions were performed on the forced jet at two different phases in the forcing cycle separated by 180 deg. Figure 8 illustrates these forced minus forced normalized particle subtractions. The solid contour lines represent regions in the flow where the normalized particle number density for the $\phi = 0$ deg phase exceeds the $\phi = 180$ deg phase, and the dashed contours represent the opposite case. A comparison of Figs. 8(a) and 8(b) indicates flow asymmetry. The first region where the particle concentration for $\phi = 0$ deg is greater than $\phi = 180$ deg in Fig. 8(a) is at $x/D_i =$

4, while it is located at $x/D_i = 3.5$ in Fig. 8(b). The second appearance of $\phi = 0$ deg greater than $\phi = 180$ deg is approximately at the same location ($x/D_i = 6$), indicating decreasing asymmetry with axial distance. This reinforces the conclusion that three dimensional perturbations induced by the VGs cause three dimensionality of the vortex rings thus modifying their effects on the particle motion.

Conclusions

Four vortex generators, separated by 90 degrees and placed in the outer nozzle, significantly altered the structure of the swirling jet. The vortex generators injected longitudinal vorticity and disrupted the development of the axial vortex rings, thereby reducing radial particle dispersion and particle flinging. The injected longitudinal vorticity was opposite in sign to the mean swirl so as not to increase the likelihood of particle flinging by the longitudinal vortices themselves. Axial flow visualization showed the formation of the axial structures at the forcing frequency but considerable azimuthal asymmetry. Horizontal cross sections showed a four lobed structure which persisted in the natural jet for at least eight inner jet diameters.

To examine the effectiveness of the vortex generators on reducing particle dispersion, the flow was perturbed and axial particle images were obtained and analyzed at two azimuthal jet cross sections. The vortex generators significantly altered the signature of the particle concentration field. The forced jet did not disperse particles radially more effectively than the natural jet, although it appeared to increase the dispersion toward the jet centerline. The particle concentrations at the two cross-sections suggested azimuthal asymmetry in the particle concentration field. In general, preferential particle concentrations remain but the large-scale structures do not appear to significantly increase the radial particle dispersion. It is concluded that the initial asymmetry in the axial structures due to the injected longitudinal vorticity was sufficient to disrupt the effectiveness of the vortex rings to disperse particles radially. We further believe that the observations of preferential concentration by vortex structures in the forced jet are relevant to particle interactions with naturally formed structures in the unforced jet. Thus, the ability of the vortex generators to reduce particle flinging by vortex rings may be important in practical applications.

Acknowledgments

This work was funded by the Electric Power Research Institute under Contract No. RP 8005-02 monitored by Dr. George Offen.

References

- Carletti, M. J., and Rogers, C. B., 1994, "The Effect of Streamwise Vorticity on Jet Behavior," ASME FED-Vol. 193, *Turbulence Control*, pp. 19–25.
- Carletti, M. J., and Rogers, C. B., and Parekh, D. E., 1993, "The Use of Streamwise Vorticity to Enhance Ejector Performance," AIAA Shear Flow Conference, AIAA 93-3247.
- Ho, C. M., and Gutmark, E., 1987, "Vortex Induction and Mass Entrainment in a Small-Aspect-Ratio Elliptical Jet," *Journal of Fluid Mechanics*, Vol. 179, pp. 383–405.
- Hussain, F., and Husain, H. S., 1989, "Elliptical Jets. Part 1. Characteristics of Unexcited and Excited Jets," *Journal of Fluid Mechanics*, Vol. 208, pp. 257–320.
- Kibens, V., and Wlezien, R. W., 1985, "Active Control of Jets from Indeterminate-Origin Nozzles," AIAA Shear Flow Conference, Boulder, Colorado, AIAA-85-0542.
- Longmire, E. K., and Eaton, J. K., 1992, "Structure of a Particle-Laden Round Jet," *Journal of Fluid Mechanics*, Vol. 236, pp. 217–257.
- Longmire, E. K., Eaton, J. K., and Elkins, C. J., 1992, "Control of Jet Structure by Crown-Shaped Nozzles," *AIAA Journal*, Vol. 30, No. 2, pp. 505–512.
- Powell, A., 1953, "On the Mechanism of Choked Jet Noise," *Proceedings of the Physical Society*, London, Sec. B, Vol. 66, pp. 1039–1056.
- Quinn, W. R., 1992, "Streamwise Evolution of a Square Jet Cross Section," *AIAA Journal*, Vol. 30, No. 12, pp. 2852–2857.
- Rogers, C. B., and Parekh, D. E., 1994, "Mixing Enhancement by and Noise Characteristics of Streamwise Vortices in an Air Jet," *AIAA Journal*, Vol. 32, No. 3, pp. 464–471.

Surks, P., Rogers, C. B., and Parekh, D., 1992, "The Effect of Streamwise Vorticity on the Mixing and Acoustic Characteristics of an Air Jet," Report TR-TF-892, Department of Mechanical Engineering, Tufts University, Medford, MA.

Surks, P., Rogers, C. B., and Parekh, D. E., 1994, "Entrainment and Acoustic Variations in a Round Jet From Introduced Streamwise Vorticity," *AIAA Journal*, Vol. 32, No. 10, pp. 2108–2110.

Tanna, H. K., 1977, "An Experimental Study of Jet Noise, Part II Shock Associated Noise," *Journal of Sound and Vibration*, Vol. 50, No. 3, pp. 429–444.

Wicker, R. B., and Eaton, J. K., 1994, "Structure and Control of a Particle-Laden Coaxial Jet With and Without Annular Swirl," Report MD-68, Thermosciences Division, Department of Mechanical Engineering, Stanford University.

Wlezien, R. W., and Kibens, V., 1986, "Passive Control of Jets with Indeterminate Origins," *AIAA Journal*, Vol. 24, No. 8, pp. 1263–1270.

Zaman, K. B. M. Q., Reeder, M. F., and Samimy, M., 1994, "Control of an Axisymmetric Jet Using Vortex Generators," *Physics of Fluids*, Vol. 6, No. 2, pp. 778–793.

J. Dang
Research Scientist,
Maritime Research Institute Netherlands,
P.O. Box 28,
6700 AA Wageningen,
The Netherlands

G. Kuiper
Professor,
Delft University of Technology,
and,
Maritime Research Institute Netherlands,
P.O. Box 28,
6700 AA Wageningen,
The Netherlands

Re-Entrant Jet Modeling of Partial Cavity Flow on Two-Dimensional Hydrofoils

A potential based panel method is developed to predict the partial cavity flow on two-dimensional hydrofoil sections. The Dirichlet type dynamic boundary condition on the cavity surface and the Neumann type kinematic boundary condition on the wetted section surface are enforced. A re-entrant jet cavity termination model is introduced. A validation is accomplished by comparing the present calculations with cavitation experiments of a modified Joukowski foil and a NACA 66(MOD) $a = 0.8$ section.

1 Introduction

Cavitation on ship propeller blades is a major source of noise and vibrations. In order to prevent excessive noise and vibrations, either cavitation has to be eliminated entirely or its behavior has to be controlled. Since for reasons of efficiency the propeller always operates in the wake of the hull, which is highly nonuniform, cavitation can generally not be avoided. The increasing speed and power installed in ships nowadays make the problems worse. It is therefore important to control the dynamic behavior of cavitation.

Cavitation on a ship propeller is three-dimensional and unsteady. The inflow variations into the propeller have a low frequency, however. Although the blade loading is highly unsteady and has to be calculated as such, it seems acceptable as a first approximation to consider the cavity as quasi-steady. Only few authors have investigated the three-dimensional characteristics of cavity flow (e.g., de Lange (1996), Kinnas and Fine (1993)). Most attention has been given to two-dimensional cavity flows. Excellent reviews of the research on cavity flows have been given by Wu (1972) and Uhlman (1987). The classic linear solution of cavity flow around a hydrofoil by Tulin (1980), Wu (1956), and Geurst (1959) was modified by Kinnas (1991) to predict the leading edge partial cavity flow. Different from traditional linear method, this method predicts the cavity length to decrease with an increase of foil thickness. A systematic investigation from 2-D foil to 3-D propeller cavitation has been performed recently at MIT by Kinnas and Fine (1990, 1992 and 1993). A so-called split-panel technique is used to avoid re-paneling of the cavity-foil surface. At the end of the cavity, a simple algebraic expression of the pressure recovery is empirically enforced over a given range of the cavity length with this method. But this approach of artificial recovery may influence the final results. Also, the detailed flow structure at the trailing edge of the cavity is ignored and no insight is obtained in its behavior.

In real flow a re-entrant jet will occur, especially in two-dimensional flow. The formation of such a jet determines the shedding of cloud cavitation and the subsequent generation of noise by the cloud's implosion. The re-entrant jet also influences the volume of the cavity. In this paper a method is developed to numerically predict the re-entrant jet at the end of a two-dimensional cavity and to assess its effect on the cavity shape and volume.

In our investigation, a potential based lower order panel method is used. A re-entrant jet cross section is introduced as a boundary of the problem, on which surface a normal velocity into the cavity

is prescribed which equals the free-stream velocity on the cavity surface. A Dirichlet dynamic boundary condition is enforced on the cavity surface, and Neumann boundary conditions are enforced both on the jet boundary and on the wetted surface of the foil section. An initial cavity surface is assumed and then iterated. The kinematic boundary condition on the cavity surface is satisfied by iterating the cavity length and shape. Upon convergence, both the dynamic and kinematic boundary conditions on the cavity surface are satisfied and a re-entrant jet with a certain thickness is automatically formed.

2 Mathematical Formulation

2.1 Expression of the Problem. Consider a cavity flow around a two-dimensional foil section in an unbounded fluid as shown in Fig. 1. The inflow V_0 has an angle of incidence α to the nose-tail line of the foil section. A steady partial cavity is formed on the surface of the foil when the ambient pressure is lower than the cavitation inception pressure, which can be taken as the vapor pressure. A re-entrant jet is formed at the end of the cavity and flows inward to the cavity with the same speed as the speed on the cavity surface. Let us suppose that the re-entrant jet flows through an intersection surface of the jet (S_j in Fig. 1) and disappears. Then the flow around the cavity and the foil can be treated as an inviscid fluid flow field with a total potential Φ that satisfies the Laplace equation. The universal solution of the Laplacian for the disturbance potential φ can be obtained by Green's identity on a closed boundary. Since the two-dimensional flow field around the foil section is not a simple connected zone, a cut has to be introduced to connect the foil trailing edge to infinity. A boundary condition should also be enforced on this cut. Then we have,

$$2\pi\varphi_p = \int_S \varphi \frac{\partial}{\partial n} \ln r_{p,q} ds - \int_S \frac{\partial \varphi}{\partial n} \ln r_{p,q} ds \quad (1)$$

where, $S = S_b + S_c + S_w + S_j$, q is a point on the boundary S and p is a point in the field.

Instead of developing a singularity distribution code based on the induced velocity, we developed a potential based panel code subjected to a mixed boundary condition of Dirichlet and Neumann.

2.2 Boundary Conditions. The kinematic boundary condition on the surface of the cavity and the foil are as follows,

$$\mathbf{n} \cdot \nabla \Phi = 0 \quad \text{on } S_b \text{ and } S_c \quad (2)$$

So the boundary condition for the perturbation potential is,

Contributed by the Fluids Engineering Division for publication in the JOURNAL OF FLUIDS ENGINEERING. Manuscript received by the Fluids Engineering Division January 26, 1999; revised manuscript received September 8, 1999. Associate Technical Editor: C. L. Merkle.

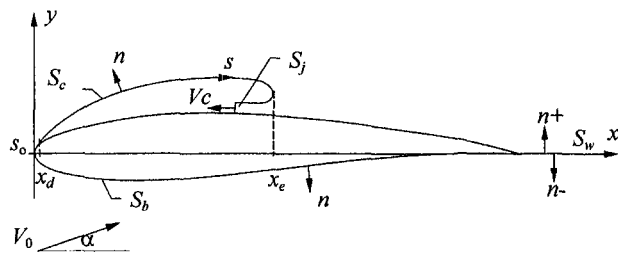


Fig. 1 Partially cavitating hydrofoil with re-entrant jet

$$\frac{\partial \varphi}{\partial n} = -\mathbf{n} \cdot \mathbf{V}_0 \quad \text{on } S_b \text{ and } S_c \quad (3)$$

where, \mathbf{n} denotes the outward normal unit vector both on the foil surface and on the cavity surface.

A dynamic boundary condition is also needed on the cavity surface that states the pressure on the cavity surface to be constant for the steady cavity flow and equal to the vapor pressure p_c .

$$p = p_c \quad (4)$$

To prescribe easily the pressure in terms of velocity on the cavity surface, an alternative expression is used. Consider a curved coordinate s along the cavity surface starting from the detachment point s_0 of the cavity near the leading edge toward the end of the cavity. Then,

$$V_c = \nabla \Phi \cdot \mathbf{t} = V_0 \sqrt{1 + \sigma} \quad (5)$$

where, \mathbf{t} denotes the tangential unit vector on the cavity surface along s . Then,

$$\frac{\partial \varphi}{\partial s} = -\tilde{V}_0 \cdot \tilde{\mathbf{i}}(s) + V_0 \sqrt{1 + \sigma} \quad \text{on } S_c \quad (6)$$

Integrating from the detachment point to any points on the cavity, we get the prescribed potential on the cavity surface based on the potential at s_0 ,

$$\varphi(s) = \int_{s_0}^s [V_0 \sqrt{1 + \sigma} - \mathbf{V}_0 \cdot \mathbf{t}(s)] ds + \varphi_0(s_0) \quad \text{on } S_c \quad (7)$$

On the jet cross section S_j , only the kinematic boundary condition is needed, which is,

$$\nabla \Phi \cdot \mathbf{n} = -V_c \quad (8)$$

where \mathbf{n} is the normal unit vector on the jet boundary toward the fluid field. For the perturbation potential, we have,

$$\frac{\partial \varphi}{\partial n} = -V_0 \sqrt{1 + \sigma} - \mathbf{V}_0 \cdot \mathbf{n} \quad \text{on } S_j \quad (9)$$

On the wake surface S_w , the velocity in magnitude is considered to be continuous while the potential has a jump across the wake, but is kept constant along the wake from the trailing edge to infinity. It is expressed in the perturbation potential as,

$$\frac{\partial \varphi}{\partial n^+} = \frac{\partial \varphi}{\partial n^-} \quad \text{on } S_w \quad (10)$$

$$\Delta \varphi = \varphi_w^+ - \varphi_w^- \quad \text{on } S_w \quad (11)$$

where $\Delta \varphi$ is the potential jump across the wake surface and superscripts + and - denote the variables on the upper and lower surface of the wake, respectively.

A Kutta condition is enforced at the trailing edge to keep the velocity at the trailing edge finite.

At the detachment point of the cavity, a so-called Brillouin-

Villat condition is always demanded in potential flow, which states that the curvature of the cavity surface at the detachment point must be continuous with the curvature of the foil surface at the same position. In real flow, it has been found e.g., by Shen and Peterson (1978) that the detachment point is always a little bit downstream of the negative pressure peak of the wetted flow or starts from the separation point of the laminar boundary layer near the leading edge. It is still difficult, up to present day, to treat the detachment point precisely in numerical simulation. For simplicity, the detachment position of the cavity is treated as an input parameter for this method.

Substitute Eqs. (10) and (11) into Eq. (1) when point p is on the boundaries S , we get,

$$\pi \varphi_p = \int_{S_b + S_c + S_j} \varphi \frac{\partial}{\partial n} \ln r_{p,q} ds - \int_{S_b + S_c + S_j} \frac{\partial \varphi}{\partial n} \ln r_{p,q} ds + \int_{S_w} \Delta \varphi \frac{\partial}{\partial n} \ln r_{p,q} ds \quad (12)$$

Then Eq. (12) can be solved under the mixed boundary conditions of (3), (7), and (9) with a Kutta condition at the trailing edge. The unknown potential or the normal derivative of the potential on the boundary is obtained.

Instead of solving the equations by giving a fixed cavity length and calculating the corresponding cavitation number, a more direct way is used in the present method, which prescribes a cavitation number and solves the equation by iterating the cavity surface until it has converged.

2.3 Iteration Scheme for the Cavity Surface. An estimated cavity length and shape, and a re-entrant jet cross section boundary are first assumed at the beginning of the calculation. The dynamic Dirichlet boundary condition (7) is imposed on the cavity surface, and the kinematic Neumann boundary conditions (3) and (9) are imposed on the wetted part of the foil and on the cross section surface of the jet. Only the kinematic boundary condition on the cavity surface is not satisfied at this moment. The potential on the wetted part of the foil and on the cross section of the jet, and the normal derivative of the potential on the cavity surface are calculated by solving Eq. (12). These calculated normal derivatives of the potential on the cavity surface are usually not equal to the value prescribed in Eq. (3). The difference ΔV_n defined as,

$$\Delta V_n = \left. \frac{\partial \varphi}{\partial n} \right|_{\text{req.}} - \left. \frac{\partial \varphi}{\partial n} \right|_{\text{cal.}} \quad (13)$$

where, subscript req. and cal. denotes the value prescribed by equation (3) and the calculated value, respectively.

Our aim is to realign the cavity surface to make the flow on the cavity surface tangential to its surface.

$$\frac{d\Delta \eta}{ds} = \frac{\Delta V_n}{V_c} = \frac{\Delta V_n}{V_0 \sqrt{1 + \sigma}} \quad (14)$$

where, η is orthogonal to the cavity surface coordinate s . Then,

$$\Delta \eta = \int_{s_0}^s \frac{\Delta V_n}{V_0 \sqrt{1 + \sigma}} ds \quad (15)$$

2.4 Cavity Volume and Hydrodynamic Forces. The most important parameter of the cavity is its volume. If the cavity thickness is described by $\tau(x)$, then the cavity volume is simply obtained by the following integration,

$$\bar{V} = \int_{x_d}^{x_e} \tau(x) dx \quad (16)$$

where, x_d denotes the position of the cavity detachment point and x_e denotes the position of the maximum cavity length (see Fig. 1). The lift L and drag D on the foil section is calculated by integrating the pressure all over the surface.

3 Numerical Implementation

3.1 Discrete Expression of the Problem. Instead of using the higher order panel method, we used the lower order panel method with constant source and dipole distributions on every panel, so that the solution always approaches the analytic one when the number of panels approaches infinity. For a two-dimensional problem, CPU time consuming is not a considerable problem.

The foil, cavity and jet surfaces are represented by N straight-line panels. The control points are located at the center of each panel. The constant source and dipole strength distributed on the i th panel are $(\partial\varphi/\partial n)_i$ and φ_i respectively. Thus Eq. (12) can be expressed by the following discrete form for every control point i ,

$$\pi\varphi_i = \sum_{j=1}^N A_{i,j}\varphi_j - \sum_{j=1}^N B_{i,j}\left(\frac{\partial\varphi}{\partial n}\right)_j + C_i\Delta\varphi \quad i = 1, 2, \dots, N \quad (17)$$

where N is the total number of panels on the boundary and $A_{i,j}$, $B_{i,j}$ and C_i are induction coefficients of the dipoles and the sources on the surface and the induction coefficient of the wake dipoles, respectively,

$$A_{i,j} = \int_{(S_b+S_c+S_j)_j} \frac{\partial}{\partial n} \ln r_{i,j} ds \quad (18)$$

$$B_{i,j} = \int_{(S_b+S_c+S_j)_j} \ln r_{i,j} ds \quad (19)$$

$$C_i = \int_{S_w} \frac{\partial}{\partial n} \ln r_i ds \quad (20)$$

where $(S_b + S_c + S_j)_j$ is the boundary of the j th panel on S_b , S_c , and S_j .

The kinematic boundary conditions of Eqs. (3) and (9) prescribe the source strength on the wetted part of the foil and on the jet boundary respectively, while on the cavity surface the dynamic boundary condition of Eq. (7) prescribes the dipole strength on its surface. The unknowns are the source strength on the cavity surface and the dipole strength on the foil surface.

There are different approaches to the implementation of the Kutta condition (Shen and Peterson, 1978; Crighton, 1985) for steady and unsteady flows. In the present work only the simplest numerical Kutta condition given by Morino (1974) is chosen. For two-dimensional cases, this condition states that the wake dipole strength should be equal to the difference of the dipoles on the upper surface and on the lower surface at the trailing edge. It is written as,

$$\Delta\varphi = \varphi_{T.E.}^u - \varphi_{T.E.}^l \quad (21)$$

where, subscript T.E. means the trailing edge and superscript u and l represents upper surface and the lower surface of the foil respectively.

It should be noted that all of the prescribed dipole strength on the cavity surface are related to the dipole strength on the panel just ahead of the detachment point of the cavity as described in Eq. (7) by φ_0 . Suppose the cavity starts at panel N_d , and ends at panel N_e , the integration of Eq. (7) is written numerically as a sum giving by the following expression,

$$\varphi_i = \sum_{k=N_d}^i [V_0\sqrt{1+\sigma} - (\vec{V}_0 \cdot \vec{t})_k] \Delta S_k + \varphi_{N_d-1} \quad k = N_d, \dots, N_e \quad (22)$$

where, $\Delta S_k = \frac{1}{2}(l_k + l_{k-1})$ and l_k is the length of the k th panel.

Because of the mixed type boundary conditions, the linear Eqs. (17) are composed of both Fredholm equations of the second kind and the Fredholm equations of the first kind. The matrix is no longer a diagonal dominated. Furthermore, Eqs. (21) and (22) makes the condition of the matrix even worse. A more accurate direct solver is needed.

At the beginning of each calculation, after the length of the cavity is assumed, a re-entrant jet surface with very small height is first erected vertically to the surface at this point and the cavity thickness distribution is assumed to increase from the detachment point to the jet linearly. If the cavity length is under estimated, the cavity will grow up very quickly over the jet boundary. If the end of the cavity surface goes into the foil surface, the program simply truncates that part. But if the end of the cavity is above the foil surface, the jet boundary is set there to connect this end point vertically to the foil surface. No more restrictions are enforced and the re-entrant jet can evolve automatically.

3.2 Surface Paneling. The surface of the cavity and foil system is divided into small panels. Around the leading and trailing edge, and around the re-entrant jet of the cavity, the curvature of the surface is quite large. Especially at the end of the cavity and at the thin re-entrant jet, very fine grids are needed to obtain a converged result.

On the lower surface of the foil, a cosine distribution of the panel from the leading edge to trailing edge is used. On the cavity surface, two sets of panels are used. Half of the panels on the cavity surface are used for the last 5% of the arc length on the cavity surface.

$$s_i = 0.95 \left(0.5 - 0.5 \cos \frac{(i-1)}{N_{cav}/2} \pi \right) \quad i = 1, 2, \dots, N_{cav}/2 \quad (23)$$

$$s_i = 0.95 + 0.05 \frac{i - N_{cav}/2}{N_{cav} - N_{cav}/2} \quad i = N_{cav}/2, \dots, N_{cav} + 1 \quad (24)$$

where, N_{cav} is the total panel numbers on the cavity surface. For the paneling on the foil surface after the cavity end a similar distribution is used with fine paneling close to the re-entrant jet. Figure 2 shows an example of the panel arrangement around the re-entrant jet under the above scheme of paneling.

4 Results and Discussion

4.1 Convergence Test. We took NACA16-006 at an angle of attack 4 deg and a cavitation number of 0.87513 as a test case. Figure 3 and Fig. 4 show the test results.

It is obvious that the solution has quickly converged with the increase of the panels. When both of the number of panels on the cavity surface and on the foil surface downstream of the cavity is increased to 80, the cavity length and the re-entrant jet thickness have converged. So, 100 panels on the cavity surface and 100 panels on the foil surface downstream of the cavity are enough.

Figure 5 and Fig. 6 show the cavity convergence procedure on a NACA16-006 section at an angle of attack of 4 deg for two different cavitation numbers respectively. It is found that the convergence is slow toward the final result. From our experience, although the steps needed for the iteration depend on the initial assumption of the cavity, 100 steps are always needed to achieve a result with a maximum error, between the calculated velocity on the cavity surface and the prescribed freestream cavity velocity, less than 1%. The maximum errors always occur at the intersection

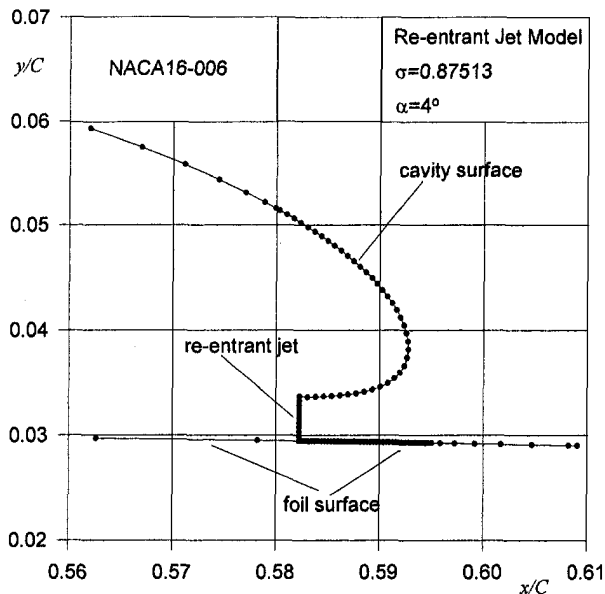


Fig. 2 Surface paneling around the re-entrant jet surface and the cavity end. (NACA 16-006 section at an angle of attack 4 deg, and cavitation number 0.87513.)

of the cavity and the re-entrant jet. But on most part of the cavity surface, the tangential velocity is already exactly equal to the prescribed velocity.

The influence of the detachment point on the final cavity volume and cavity length has been well investigated by Uhlman (1987). Since we have not found a good way to treat the position of the detachment point, a detachment is always set at the leading edge in all of the calculations in the following paragraphs.

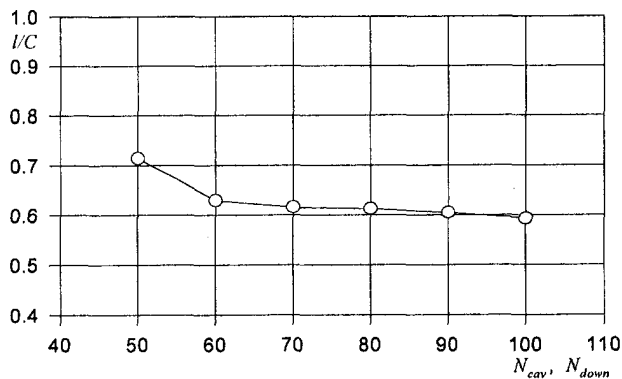


Fig. 3 The cavity length varies with the panel numbers

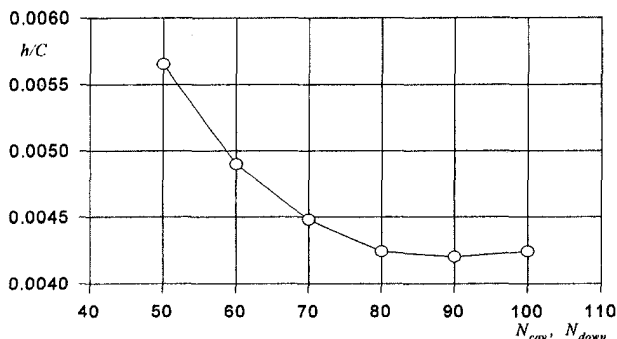


Fig. 4 The jet thickness varies with the panel numbers



Fig. 5 Changes of the cavity shape with the iteration steps. (NACA 16-006, $\alpha = 4$ deg, $\sigma = 0.87513$, $l_{initial}/C = 0.37550$, converged $l/C = 0.59279$.)

4.2 Predictions for NACA16 Series Sections. A calculation for the cavity flow with a re-entrant jet on the NACA 16-006 section at an angle of attack of 4 deg is carried out at a cavitation number of 0.87513. This cavitation number is chosen because the authors wanted to make a comparison with the result of Uhlman's (1987) cavity termination wall model. The converged shape of the cavity and its re-entrant jet and the final pressure distribution on the cavity and on the wetted part of the foil are drawn in Fig. 7. Details about the re-entrant jet are shown in Fig. 2 with the panel arrangement.

Figure 7 shows that the velocity on the cavity surface equals to the prescribed freestream velocity. It means that both the dynamic boundary condition and the kinematic boundary condition on the cavity surface are very well satisfied. Only at the control point of the last panel on the cavity, the velocity is a little bit higher than the free-stream velocity, but the relative error is still less than 1%. A stagnation point is clearly visible downstream the end of the cavity.

The flexibility of the present program makes it very easy to change the kinematic boundary condition on the jet section from Eq. (9) to a nonpenetrative condition similar to Eq. (3) and find the solution with a cavity termination wall model. The result is shown in Figs. 8.

The special feature of the present method is the re-entrant jet calculation. Figure 9 shows the re-entrant jet thickness versus cavitation number for three sections. It can be found in this figure that the re-entrant jet thickness decreases with increasing cavitation number.

When we plotted the ratio of the re-entrant jet to the maximum cavity thickness against the cavity length, we obtained Fig. 10. It

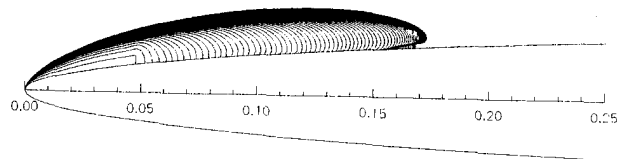


Fig. 6 Changes of the cavity shape with the iteration steps. (NACA 16-006, $\alpha = 4$ deg, $\sigma = 1.4$.)

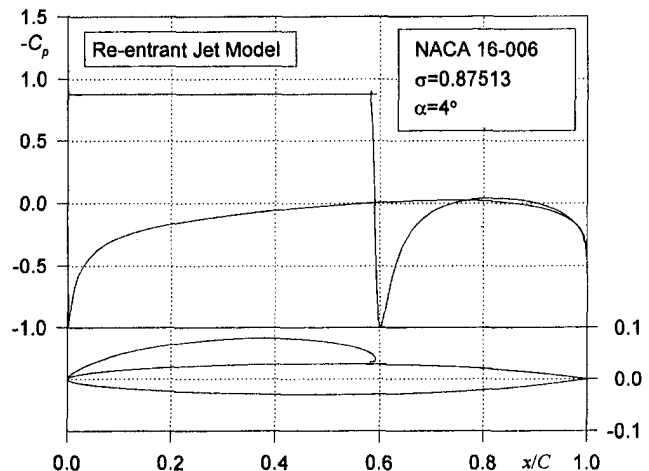


Fig. 7 Pressure distribution on the cavity and foil surface

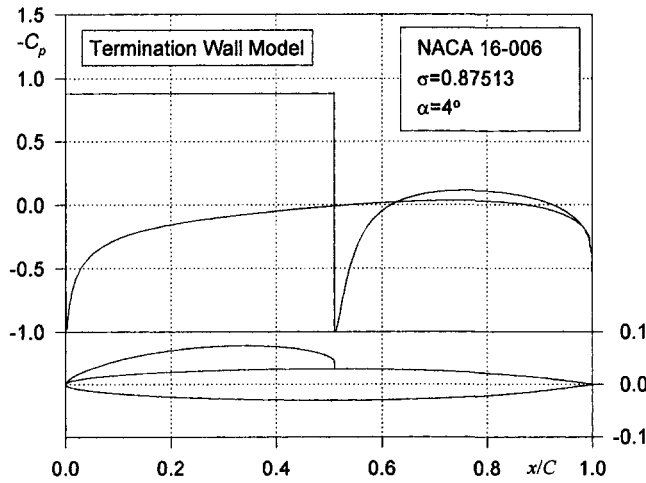


Fig. 8 Pressure distribution on the cavity and foil surface

shows that the re-entrant jet thickness is always a certain percentage of the maximum cavity thickness t_{max} , irrespective of the cavitation number and the profile thickness. This percentage is around 8% to 10%. It is also found that the maximum cavity thickness is also always located at 60% of the total cavity length (Fig. 11), irrespective of the cavitation number and the profile thickness as well. These characteristics of the re-entrant jet could also be found in Gilbarg's (1946) calculation of the re-entrant jet after an obstacle.

4.3 Comparison With Other Linear and Nonlinear Results. In order to find out the difference of the prediction results between the present method and those of other linear methods with

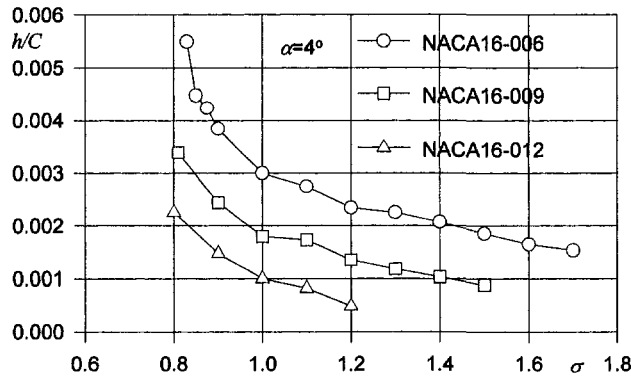


Fig. 9 Cavity re-entrant jet thickness h/C versus cavitation number σ

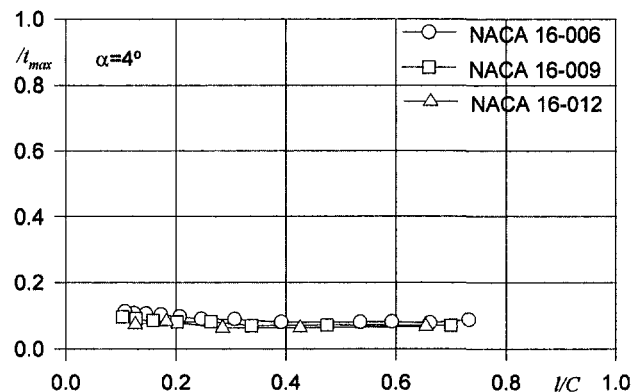


Fig. 10 The re-entrant jet thickness as a percentage of the cavity maximum thickness versus the cavity length

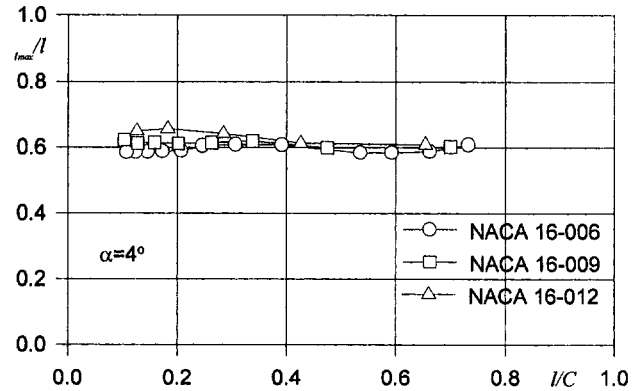


Fig. 11 The maximum cavity thickness position

thickness correction and the nonlinear methods with termination wall model, comparisons are made for NACA 16 series sections at an angle of attack 4 deg for different cavitation numbers.

Uhlman (1987)'s method is based on velocity. A cavity termination wall model is employed in his method. The cavity length is prescribed, while a cavitation number is calculated. When the shape of the cavity was converged, the cavitation number is obtained. By assuming the velocity on the jet boundary to be zero in the present method, we can also obtain the solution with a termination wall model. A comparison is shown in Table 1. It can be said that the results are very close to each other. The cavity length predicted by present method is 2% longer than the length predicted by Uhlman.

The calculated cavity lengths are now compared with the nonlinear results of Uhlman (1987) and shown in Fig. 12. It is found that the results for NACA16-009 are very close to each other. While the cavity predicted by present method is longer for NACA16-006 section but shorter for NACA16-012 section comparing to the nonlinear results by Uhlman (1987). Another comparison has been made between the present results and the linear results with thickness correction from Uhlman (1987). This is

Table 1 Comparison of different approaches for the same cavity termination wall model

	Uhlman's results	Present Results	Relative Differences
Cav. Number σ	0.87513	0.87513	0.00%
Cavity Length l/C	0.5000	0.5100	+2.00%
Cavity Volume C_v	0.01670	0.01794	+7.4%
Lift Coeff. C_L	0.53562	0.51705	-3.5%

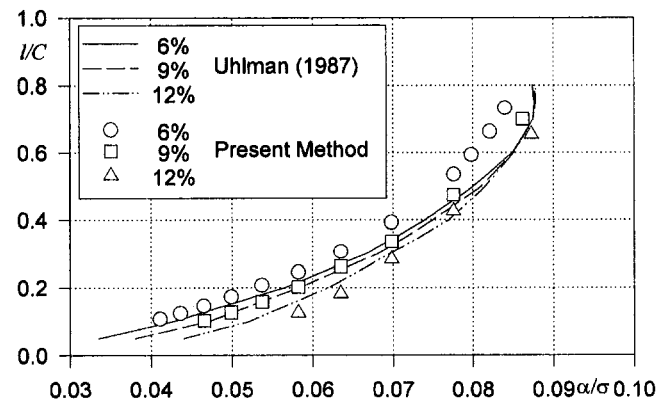


Fig. 12 Comparison between present method and the nonlinear method of Uhlman (1987)

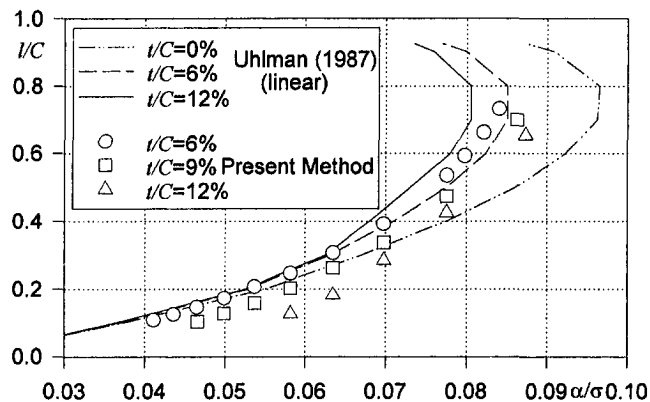


Fig. 13 Comparison between present method and the linear method from Uhlman (1987)

shown in Fig. 13. The linear method with thickness correction gives very good results comparing to the present nonlinear method for NACA16-006 but over-predicts the cavity length for NACA16-012. The present method predicts a cavity length decrease with increasing of thickness while the linear method predicts an increase. Since the tendency is different, we cannot say the linear method is accurate enough for a cavity flow on a very thin section, especially when the cavity is long.

As for the cavity volume, a comparison is shown in Fig. 14 of the present method and the linear method. The tendency that the cavity volume decreases with increasing foil thickness is the same but the results are very different. The linear method seems to over-predict the cavity volume. For NACA16-012 section, the volume predicted by linear method is twice as large as that predicted by the present method.

4.4 Free Development of the Re-Entrant Jet. Furness and Hutton (1975) have filmed the process of the re-entrant jet formation by a high-speed cinaphotography method. From the framing speed of the film, the velocity of the re-entrant jet was measured. The measurement shows that the maximum speed of the re-entrant jet is a little smaller than the free-stream velocity of the cavity. To investigate the influence of the re-entrant jet velocity on the cavity volume and length, the predictions for NACA 16-006 at an angle of attack 4 deg are calculated both for a prescribed re-entrant jet velocity and for a free jet. The result is shown in Fig. 15.

The free jet here means that we did not use the jet boundary and the jet is no longer cut off. So, with the iteration continuing, the jet evolves automatically. Figure 15 shows that when the free jet is developed long enough, these two methods give exactly the same result. It seems that the jet boundary is not really needed. Since it is not easy to erect a jet boundary on the surface of a three-

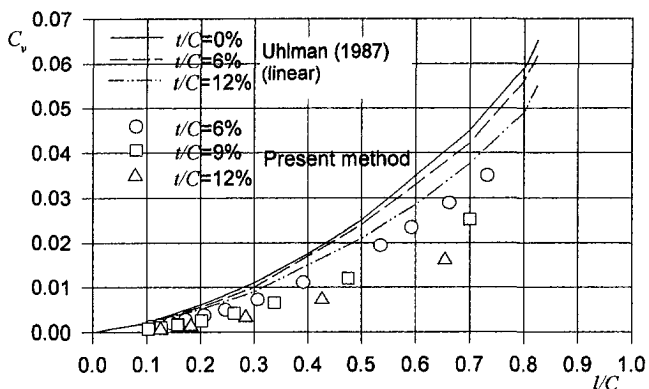


Fig. 14 Comparison of cavity volume ($C_v = \text{volume}/C^2$)

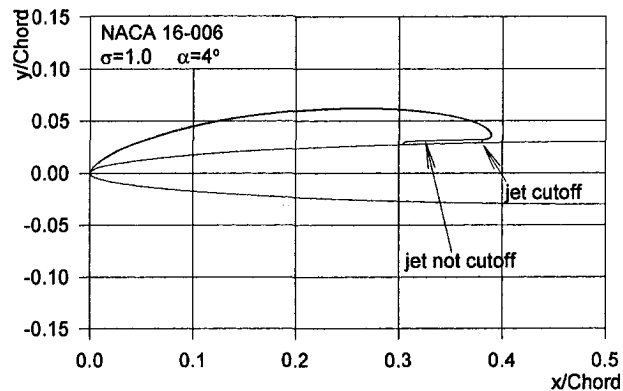


Fig. 15 Comparison of the cavity shapes with and without jet section

dimensional body, like a propeller blade, a free jet method is applicable.

4.5 Comparison With Experimental Measurements. In order to validate the present method, we compared the calculations with Shen (1978, 1989) experimental measurements both for a modified Joukowski profile and for a NACA 66 (MOD) $a = 0.8$ section. Since the leading edge sheet cavity is very sensitive to the pressure distribution on the suction side of the profile, a careful investigation of the influence of the viscosity, the boundary layer separation and the wall effect in experiment should be done before the comparison could be made.

The viscosity has not only strong effects on the cavity flow, but also on wetted flow (Shen, 1989). The experimental results show that the lifting coefficient of NACA 66(MOD) $a = 0.8$ section from experiment is 0.531 at an angle of attack of 3 deg when the Reynolds number is 3×10^6 , while the potential theory predicts 0.626, which is 15% larger than experiment. Correspondingly, the calculated pressure distribution is also lower than the measured ones. For the cavity flow, Avellan (1989)'s recent experiment shows that the leading edge cavity on a NACA 009 symmetric profile at 2.5 deg incidence is 30% chord length when the water speed is 20 m/s, but 45% chord length when the water speed is 35 m/s.

This may be resulted by the differences of the boundary development on the suction side and on the pressure side at different Reynolds numbers. For the NACA 66 (MOD) $a = 0.8$ section, the transition points of the boundary layer on both sides are reported to be at 13% of the chord length on the suction side and at 89% of the chord length on the pressure side. At Reynolds number of 5×10^5 , the flow is almost laminar all over the section surface. In the real flow the section is actually decambered by the boundary layer. This de-cambering could be treated accurately by a careful calculation of the boundary layer development on the section surface. A viscous/inviscid interaction calculation (Kinnas, 1994) for a 2-D section has shown this strong effect already. Any simple comparison based on equal angle of attack or equal lifting coefficient does not work. In the equal angle of attack comparison, the potential method always over-estimates the cavity length and volume because the negative pressure on the suction side is always over-predicted. But in the equal lifting coefficient comparison, the potential theory always under-predicts the negative pressure peak at the leading edge.

The authors of this paper are not going to carry out the boundary layer calculation for this comparison because the deference of the pressure distribution may result not only from the boundary layer flow but also from the blockage of the test section (Deshpande, 1994). We think that if the cavity is small, the boundary layer on the suction side of the section is not influenced too much by the cavity, and a comparison could be done on an equivalent section that has the same pressure distribution as measured at wetted condition.

A simple empirical method like Pinkerton's (1936) is used. An arbitrary function is used to de-camber the section,

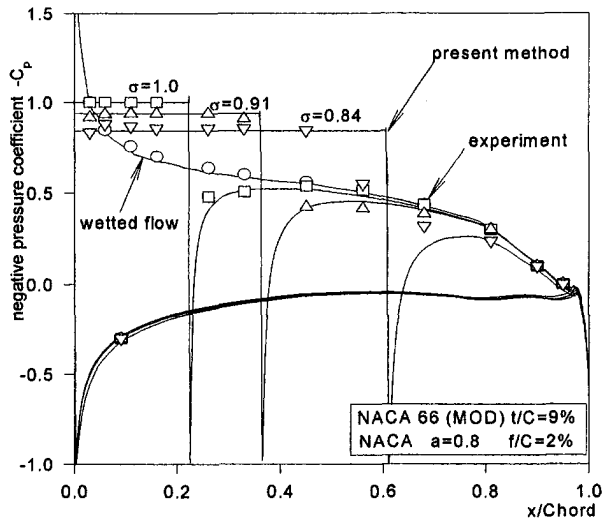


Fig. 16 Comparison of the pressure distributions at an angle of attack of 4 deg

$$\Delta(f/C) = (f/C)_{T.E.} \cdot (1 - (x/C)^2)$$

where, $(f/C)_{T.E.}$ is the total de-camber amount at the trailing edge. For this NACA 66(MOD) $a = 0.8$ section, $(f/C)_{T.E.} = -0.009$ gives a good correlation between the experiments and the calculations both for pressure distribution and for the lift, as shown in Fig. 16.

Based on this de-cambered profile, the calculations are done for three cavitation numbers (0.84, 0.91, and 1.00) at an angle of attack of 4 deg. The agreements are quite good as shown in Table 2.

In order to estimate, roughly, how strong the viscous effect is, a test for the same section at a condition of $\alpha = 4$ deg and $\sigma = 1.0$ is calculated both for the original geometry and for the de-cambered geometry. The results are plotted in Fig. 17. As expected, the predicted cavity length on the original geometry is 2.5 times as long as that predicted on the de-cambered section.

But this result could not be generalized because it strongly depends on the pressure distribution on the section surface. For a NACA 66 section, which has a relative flat pressure (Fig. 16) on a large part of the suction surface at wetted flow condition, the cavity length and volume are very sensitive to the pressure. On the other

Table 2 Comparison of the cavity length and lifting coefficients

Cavitation Number σ	Experiments		Calculations	
	l/C	C_L	l/C	C_L
1.00	0.20	0.645	0.223	0.619
0.91	0.36	0.670	0.363	0.652
0.84	0.60	0.699	0.610	0.678

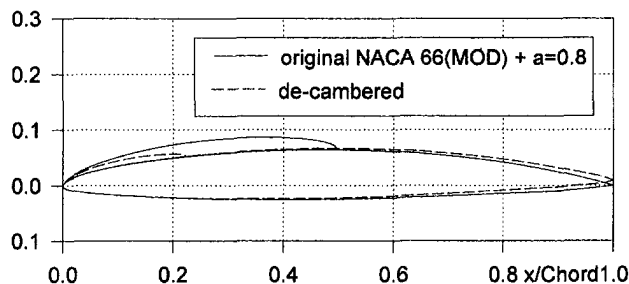


Fig. 17 Comparison of the cavity shape for the de-cambered and the original section

Table 3 Comparison of cavity length calculations with experiments

α	Experiments	Calculations
3.8°	0.25	0.249
4.3°	0.39	0.395

hand, for a section like the modified Joukowski section (Shen, 1980), a de-cambering seems not needed because the pressure is not so flat on the suction side. The calculated cavity lengths for two different angle of attacks are listed in Table 3. The agreement is very satisfactory.

Since there is no available good experimental results for the cavity volume, no comparison is done at present.

5 Conclusions

A potential based surface panel method is developed to predict the cavity flow around an arbitrary two-dimensional foil section. Lots of numerical calculations show that this method is quite stable for different geometry.

The result obtained by using a cavity termination wall model in present method shows a good agreement with Uhlman's nonlinear termination wall result. Lots of calculations for NACA 16 series sections with three different thickness to chord ratio (6%, 9% and 12%) have been performed. The present calculations show the same trend, like other nonlinear methods, that the cavity length decreases with increasing foil thickness.

It is very important to have found that the re-entrant jet thickness is always a certain percentage of the cavity maximum thickness, irrespective of the cavitation number, the cavity length and the foil thickness. The locations of the maximum cavity thickness for different conditions are also fixed at 60% of the cavity length from the detachment point.

The present method is validated by comparing with experimental data. The comparisons were done by de-cambering the original NACA section into a modified section in order to take the displacement of the boundary layer on the section surface into consideration. Three cases ($\sigma = 1.00, 0.91, 0.84$) have been investigated for this de-cambered section and a good correlation has been found.

In summary, the re-entrant jet modeling with the potential theory for two-dimensional cavity flows is a quite stable and convergent method. If the viscous effect could be included in the method, it could provide a rather precise prediction. A benchmark test of the cavity volume for steady condition should be carried out to verify the present theory. A further extension of the method to three-dimensional predictions and unsteady cavity flow around hydrofoils and propeller blades seems feasible.

Acknowledgments

This work was supported by the Maritime Research Institute Netherlands (MARIN). The authors would like to express their appreciation to the comments of Eric H. C. J. van Wijngaarden and to the discussions with Prof. S. L. Ceccio when he was visiting MARIN.

References

- Avellan, F., Dupont, P., and Ryhming, I., 1989, "Generation Mech. and Dynamics of Cav. Vortices Downstream of A Fixed L. E. Cavitation," 17th ONR, The Hague.
- Bose, N., 1994, "Explicit Kutta Condition for an Unsteady Two-Dimensional Constant Potential Panel Method," Technical Notes, AIAA Journal, Vol. 32, No. 5.
- Crighton, D. G., 1985, "The Kutta Condition in Unsteady Flow," *Annual Review of Fluid Mechanics*, Vol. 17, pp. 411-45.
- Deshpande, M., Feng, J., and Merkle, C. L., 1994, "Cavity Flow Predictions Based on the Euler Equations," *ASME JOURNAL OF FLUIDS ENGINEERING*, Vol. 116, pp. 36-44.
- Furness, R. A., and Hutton, S. P., 1975, "Experimental and Theoretical Studies of Two-Dimensional Fixed-Type Cavities," *ASME JOURNAL OF FLUIDS ENGINEERING*, pp. 515-522.

- Geurst, J. A., 1959, "Linearized Theory for Partially Cavitated Hydrofoils," *International Shipbuilding Progress*, Vol. 6, No. 60, Aug., pp. 369–384.
- Gilbarg, D., and Rock, H. H., 1946, "On Two Theories of Plane Potential Flows with Finite Cavities," NOLM report No. 8718, Washington D.C.
- Kinnas, S. A., and Fine, N. E., 1990, "Nonlinear Analysis of the Flow Around Partially or Super-cavitating Hydrofoils by a Potential Based Panel Method," *Proc. of Boundary Integral Methods*, IABEM-90, Rome Italy.
- Kinnas, S. A., 1991, "Leading Edge Corrections to the Linear Theory of Partially Cavitating Hydrofoils," *JSR*, Vol. 35, No. 1, March, pp. 15–27.
- Kinnas, S. A., and Fine, N. E., 1992, "A Nonlinear Boundary Element Method for the Analysis of Unsteady Propeller Sheet Cavitation," 19th ONR, Seoul, Korea.
- Kinnas, S. A., and Fine, N. E., 1993, "A Numerical Nonlinear Analysis of the Flow Around 2- and 3-Dimensional Partially Cavitating Hydrofoils," *Journal of Fluid Mechanics*, Vol. 254.
- Kinnas, S. A., Mishima, S., and Brewer, W. H., 1994, "Nonlinear Analysis of Viscous Flow Around Cavitating Hydrofoils," 20th ONR, Santa Barbara, CA.
- de Lange, D. F., 1996, "Observation and Modeling of Cloud Formation behind a Sheet Cavity," Ph.D. thesis of Twente University, April.
- Morino, L., and Kuo, C. C., 1974, "Subsonic Potential Aerodynamics for Complex Configurations: A General Theory," *AIAA Journal*, Vol. 12, No. 2, pp. 191–197.
- Pinkerton, R. M., 1936, "Calculated and Measured Pressure Distributions over the Midspan Section of the NACA 4412 Airfoil," NACA report No. 563.
- Shen, Y. T., and Peterson, F. B., 1978, "Unsteady Cavitation on an Oscillating Hydrofoil," *Proceedings of 12th ONR*, Washington D.C.
- Shen, Y. T., and Peterson, F. B., 1980, "The Influence of Hydrofoil Oscillation on Boundary Layer Transition and Cavitation Noise," 13th ONR, Tokyo.
- Shen, Y. T., and Dimotakis, P. E., 1989, "The Influence of Surface Cavitation on Hydrodynamic Forces," *Proceedings of 22nd ATTC*, St. Johns.
- Shen, Y. T., and Dimotakis, P. E., 1989, "Viscous and Nuclei Effects on Hydrodynamic Loadings and Cavitation of a NACA 66 (MOD) Foil Section," *ASME JOURNAL OF FLUIDS ENGINEERING*, Vol. 111, pp. 306–316.
- Tulin, M. P., and Hsu, C. C., 1980, "New Application of Cavity Flow Theory," *Proceedings of 13th Symposium on Naval Hydrodynamics*, Tokyo, Japan.
- Uhlman Jr., J. S., 1987, "The Surface Singularity Method Applied to Partially Cavitating Hydrofoils," *JSR*, Vol. 31, No. 2, June, pp. 107–124.
- Wu, T. Y., 1956, "A Note on the Linear and Nonlinear Theories for Fully Cavitated Hydrofoils," Technical Report on No. 21–22, CIT, California, August.
- Wu, T. Y., 1972, "Cavity and Wake Flow," *Annual Review of Fluid Mechanics*, Vol. 4.

Re-Entrant Jet Modeling of Partial Cavity Flow on Three-Dimensional Hydrofoils

J. Dang

Research Scientist,
Maritime Research Institute Netherlands,
P.O. Box 28,
6700 AA Wageningen,
The Netherlands

G. Kuiper

Professor,
Delft University of Technology, and
Maritime Research Institute Netherlands,
P.O. Box 28,
6700 AA Wageningen,
The Netherlands

A potential-based lower-order surface panel method is developed to calculate the flow around a three-dimensional hydrofoil with an attached sheet cavity at the leading edge. A Dirichlet type dynamic boundary condition on the cavity surface and a Neumann boundary condition on the wetted surface are enforced. The cavity shape is initially assumed and the kinematic boundary condition on the cavity surface is satisfied by iterating the cavity length and shape. Upon convergence, both the dynamic boundary condition and the kinematic boundary condition on the cavity surface are satisfied, and a re-entrant jet develops at the cavity closure. The flow at the closure of the cavity and the mechanism of the re-entrant jet formation is investigated. Good agreement is found between the calculated results and MIT's experiments on a 3-D hydrofoil.

1 Introduction

It is important to control the dynamic behavior of cavitation on a propeller blade in order to reduce the cavitation induced ship vibrations. As has been shown in the previous research (de Lange, 1996) that the re-entrant jet at the end of the sheet cavity plays an important role in the instability of the cavity and the formation of the cloud cavitation. The surface of a sheet cavity is initially smooth, transparent and stable. In many situations, the sheet cavity surface will distort and break partially into small bubbles at the end of the cavity (20th ITTC Report, 1993). When the angle of attack is increased, a strong re-entrant jet forms at the end of the cavity. If the re-entrant jet touches the cavity surface, the cavity will break up and part of the cavity will be shed and form cloud cavitation in the wake.

A re-entrant jet is always needed to close a two-dimensional cavity. A steady three-dimensional cavity flow, however, can have a smooth closure over much of its extent, even when a re-entrant jet is formed. A lot of observations, both at model and full scale, show that a sheet cavity can be very stable if the re-entrant jet is able to find a good exit (Kuiper, 1994). A typical exit for highly skewed propeller blades is in the cavitating tip vortex. This makes the sheet cavity on the propeller blades quite stable.

Most of the prediction methods for 3-D cavity flow are aiming at the influence of the cavitation on the hydrodynamic forces. Only few methods tried to predict the cavity volume accurately in recent years. At first, methods were developed only for the high aspect ratio hydrofoils (Leehey, 1971; Furuya, 1975; Uhlman, 1978; and Van Houten, 1983) by matching the asymptotic expansion of the inner and outer solutions. Later on, Jiang and Leehey (1977) accomplished a complete 3-D calculation. Because of the difficulty to determine the cavity planform, a closure condition for each individual spanwise strip was used. Recently, nonlinear methods were developed for arbitrary hydrofoils. Pellone and Rowe (1981) calculated the supercavitating flow on a 3-D hydrofoil with free surface by a velocity-based panel method. Peallat and Pellone (1996) developed a nonlinear method for the prediction of the partial cavity flow. Systematic research on partial cavity flow using potential-based panel methods for 3-D hydrofoils and propeller blades has been performed at MIT in the last ten years (Kinnas, 1992, 1993; Fine, 1993). A so-called split-panel technique is used

to avoid re-paneling of the cavity-foil surface and a fast convergence in iterations is achieved in their method.

In order to predict accurately the cavity volume and to analyse the possible influence of the jet on the stability of the cavity, a re-entrant jet simulation at the cavity end is needed. Calculations of the re-entrant jet formation at the end of a 2-D cavity were first carried out by Furness and Hutton (1975) and recently by de Lange (1996) for arbitrary hydrofoil sections. But no 3-D simulation of the re-entrant jet is found in the public literature. The authors of this paper were encouraged by the successful simulation of the re-entrant jet in the 2-D cavity flow (Dang and Kuiper, 1998) and extended this method to the steady 3-D partial cavity flow on arbitrary hydrofoils in this paper.

2 Formulation

Consider a 3-D partially cavitating hydrofoil in a uniform inflow V_0 , as shown in Fig. 1. A sheet cavity exists on the suction side of the hydrofoil at the leading edge and a re-entrant jet is formed at the end of the cavity. The wake S_w extends to infinity. If the perturbation potential of the cavity-foil system to the uniform inflow is φ , the total potential Φ can be written as,

$$\Phi = \vec{V}_0 \cdot \vec{r} + \varphi, \quad (1)$$

where, \vec{r} is the position vector. The perturbation potential must satisfy Green's identity,

$$4\pi\varphi_p = \int_S \varphi \frac{\partial}{\partial n} \frac{1}{r_{p,q}} dS - \int_S \frac{\partial \varphi}{\partial n} \frac{1}{r_{p,q}} dS + \int_{S_w} \varphi_w \frac{\partial}{\partial n} \frac{1}{r_{p,q}} dS, \quad (2)$$

where, p denotes a point in the field and q a point on the boundary $S = S_b + S_c$ (Fig. 1). φ_w is the potential strength on the wake surface.

On the wetted surface of the hydrofoil and on the cavity surface, the kinematic boundary conditions are the same,

$$\frac{\partial \varphi}{\partial n} = -\vec{n} \cdot \vec{V}_0 \quad \text{on } S_b \text{ and } S_c \quad (3)$$

where, \vec{n} denotes the outward unit normal vector.

The dynamic boundary condition on the cavity surface requires

Contributed by the Fluids Engineering Division for publication in the JOURNAL OF FLUIDS ENGINEERING. Manuscript received by the Fluids Engineering Division January 26, 1999; revised manuscript received September 8, 1999. Associate Technical Editor: C. L. Merkle.

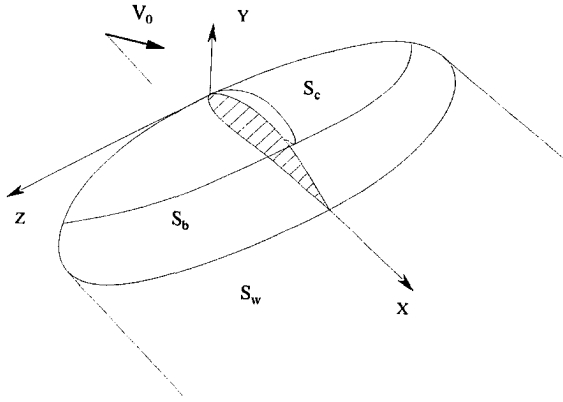


Fig. 1 Partial cavity flow with a re-entrant jet on a 3-D hydrofoil

the pressure on the surface to be the cavitation pressure, or simply to be the vapor pressure p_v . If we define the cavitation number as,

$$\sigma = \frac{p_0 - p_v}{\frac{1}{2} \rho V_0^2}, \quad (4)$$

Using Bernoulli's equation, the free-stream velocity V_c on the cavity surface can be written as,

$$V_c = \nabla \Phi \cdot \vec{t} = V_0 \sqrt{1 + \sigma} \quad (5)$$

where \vec{t} denotes the unit vector along the streamline on the cavity surface. The free-stream velocity on the cavity surface can also be written as the derivative of the total potential Φ with respect to the curvilinear coordinates on the cavity surface as shown in Fig. 2. When the chordwise curvilinear coordinate is s_1 and the spanwise coordinate is s_2 , the corresponding tangential unit vectors are \vec{t}_1 and \vec{t}_2 respectively. If we establish local coordinates (a_1, a_2) with a_1 in the direction of s_1 and a_2 perpendicular to a_1 on the surface of the body (Fig. 2), the two components u_1, u_2 of the perturbation velocity \vec{u} can be expressed as the derivatives of the perturbation potential by,

$$u_1 = \frac{\partial \varphi}{\partial a_1} = \frac{\partial \varphi}{\partial s_1} \quad (6)$$

$$u_2 = \frac{\partial \varphi}{\partial a_2} = \frac{\partial \varphi / \partial s_2 - (\vec{t}_2 \cdot \vec{e}_1) \partial \varphi / \partial s_1}{(\vec{t}_2 \cdot \vec{e}_2)}, \quad (7)$$

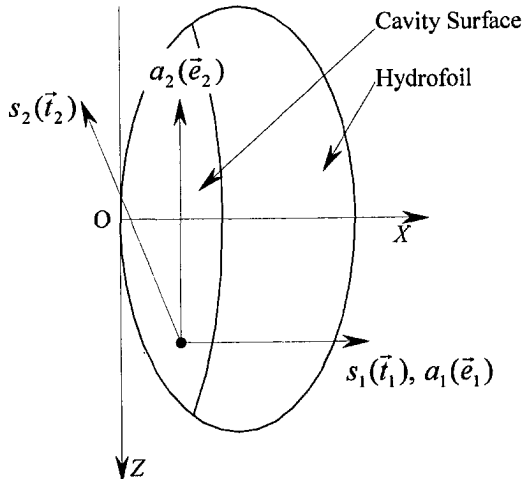


Fig. 2 The curvilinear coordinates on the cavity-foil surface

where \vec{e}_1 and \vec{e}_2 denote the unit vectors along a_1 and a_2 , respectively. Integrating the perturbation potential along s_1 , we obtain the Dirichlet type dynamic boundary condition on the cavity surface, which prescribes chordwisely the potential on the cavity surface as,

$$\varphi = \int_0^{s_1} (\sqrt{(1 + \sigma)V_0^2 - (U_2 + u_2)^2} - U_1) ds_1 + \varphi_0 \quad (8)$$

where, U_1 and U_2 are the components of the inflow V_0 in a_1 and a_2 directions, respectively.

A Kutta condition and Brillouin-Villat condition is needed in this case. The Morino (1974) formulation is sufficient for the present calculations, which means that

$$\varphi_w = \varphi_{T.E.}^u - \varphi_{T.E.}^l \quad (9)$$

where subscript $T.E.$ means the trailing edge and superscript u and l respectively denote the upper and lower surface of the foil. It has been found, e.g., by Shen and Peterson (1978), that the detachment point is always slightly downstream of the negative pressure peak of the wetted flow and starts from the separation point of the laminar boundary layer near the leading edge. It is still difficult to compute the detachment point precisely in numerical simulations. For simplicity, it is treated as input in present method.

Subject to boundary conditions of (3) and (8), Eq. (2) becomes an integral equation for the dipole strength φ on the foil surface and the source strength $\partial \varphi / \partial n$ on the cavity surface, respectively,

$$2\pi\varphi_p = \int_S \varphi \frac{\partial}{\partial n} \frac{1}{r_{p,q}} dS - \int_S \frac{\partial \varphi}{\partial n} \frac{1}{r_{p,q}} dS + \int_{S_w} (\varphi_{T.E.}^u - \varphi_{T.E.}^l) \frac{\partial}{\partial n} \frac{1}{r_{p,q}} dS \quad (10)$$

where, p denotes the point on the cavity-foil surface.

3 Numerical Implementation

In order to find the solution of this formulation with a numerical method, the cavity surface and the wetted part of the hydrofoil are divided into small panels. To avoid possible gaps between planar panels, both the boundary surface S and the wake surface S_w are approximated by a number of quadrilateral hyperboloidal panels (Hoshino, 1989). Along the span, the panels are distributed simply by a cosine distribution. At the end of the cavity, a finer chordwise panel distribution is required to simulate the cavity re-entrant jet, as discussed in detail by Dang and Kuiper (1998).

Because the numerical solution approaches the analytical solution when the number of panels is increased, we use constant dipole and source distributions in present calculations. The control point is set to the centroid of each panel. Then Eq. (10) is satisfied at each control point and can be written into the following linear algebraic equations,

$$2\pi\varphi_i - \sum_{j=1}^{N_b} D_{i,j} \varphi_j + \sum_{j=1}^{N_c} S_{i,j} \frac{\partial \varphi_j}{\partial n} = \sum_{j=1}^{N_c} D_{i,j} \varphi_j - \sum_{j=1}^{N_b} S_{i,j} \frac{\partial \varphi_j}{\partial n} + \sum_{j=1}^{N_w} D_{i,j} (\varphi_w)_j \quad i = 1, 2, 3, \dots, N_b + N_c \quad (11)$$

where, $N_b, N_c,$ and N_w denote the total panel numbers on the foil surface, the cavity surface and the wake surface, respectively, $D_{i,j}$ and $S_{i,j}$ denote the influence coefficients of the j th dipole and the j th source to the i th control point. The calculation of the two influence coefficients has been discussed extensively by Morino (1974), Kerwin (1987), and Hoshino (1989).

Since the potential on the cavity surface and the potential

derivatives on the foil surface are known, the right-hand terms in Eqs. (11) are known. The unknowns are the potential on the foil surface and derivatives of the potential on the cavity surface, which are on the left-hand side of this equation. By solving Eq. (11), we obtain the unknowns and thereby the whole flow field.

It should be noted that, because of Eq. (8), the potentials prescribed on the cavity surface are all related to the potential at the detachment point, which is given by the following numerical expression,

$$\varphi_k^l = \sum_{j=1}^k (\sqrt{(1+\sigma)V_0^2 - (U_{2j}^l + u_{2j}^{l-1})^2} - U_{1j}^l) \Delta s_j^l + \varphi_0^l \quad (12)$$

where, j means the panel number from the detachment point on each chordwise strip, l denotes the iteration step for the cavity surface, Δs is the arc length between the centroid points of two adjacent panels in s_1 direction and φ_0 is the potential of the panel on the foil surface just in front of the cavity panel at the location of detachment. Because the cross flow u_2 is not known a priori, the result from the previous iteration step is adopted here.

4 Cavity Shape and Re-Entrant Jet Evolution

To solve the cavity flow problem in a more direct way and make the scheme more flexible for calculating the cavity flow on propeller blades in the future, the cavitation number is prescribed and the cavity shape is calculated iteratively. We start our calculation by a guessed cavity planform and enforce the boundary conditions of Eqs. (3) and (12) on this planform. After we solve the problem by the method described in the previous chapter, the solution is not the final result because the kinematic boundary condition on the cavity surface is not satisfied. Suppose the cavity surface is given by the local coordinates (a_1, a_2, η) as,

$$F = \eta - f(a_1, a_2) = 0 \quad (13)$$

where η is the third coordinate perpendicular to the a_1, a_2 plane. Then we have the following expression for any material surface like the cavity surface in steady flow,

$$U_{a_1} \frac{\partial F}{\partial a_1} + U_{a_2} \frac{\partial F}{\partial a_2} + U_\eta \frac{\partial F}{\partial \eta} = 0 \quad (14)$$

where U_{a_1}, U_{a_2}, U_η is the total velocity in each of the three directions, respectively. To express this equation in the curvilinear surface coordinates, we obtain the partial differential equation for the cavity surface η as,

$$A \frac{\partial \eta}{\partial s_1} + B \frac{\partial \eta}{\partial s_2} = U_\eta = U_0 \cdot \vec{n} + \frac{\partial \varphi}{\partial n} \quad (15)$$

where,

$$A = U_{a_1} - \frac{\vec{i}_2 \cdot \vec{e}_1}{\vec{i}_2 \cdot \vec{e}_2} U_{a_2}; \quad B = \frac{1}{\vec{i}_2 \cdot \vec{e}_2} U_{a_2}$$

Equation (15) is a first-order hyperbolic differential equation for η . Since the flow is chord-wise dominant for hydrofoils, B is relatively smaller than A . If we use fine grid along the chord direction (this is always needed to simulate the re-entrant jet) but relatively coarse grid in span direction, then an explicit difference scheme for Eq. (15) is always stable. The calculation starts from the detachment points of the cavity where $\eta = 0$ and goes downstream to other grid points.

The strategy for iteration we use in our method is as follows. If the cavity surface goes into the hydrofoil surface, the cavity surface is truncated at the intersection between the cavity and the foil surface. If the whole cavity surface does not touch the foil surface at the end of the cavity, the end of the cavity is connected to the foil surface. No more restrictions are enforced.

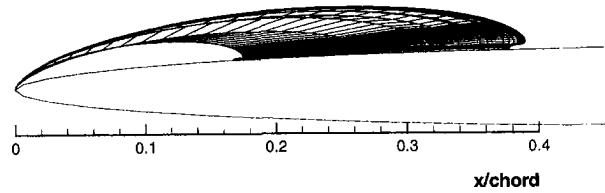


Fig. 3 The side view of the cavity shape on a NACA 16-006 rectangular hydrofoil

5 Convergence Test and Numerical Validation

A convergence test has been carried out successfully for the 2-D simulation of the cavity flow with a re-entrant jet (Dang and Kuiper, 1998). Quite a large number of panels were needed in the 2-D case to achieve an accurate result.

In this paper we take a high aspect ratio ($AR = 500$) rectangular hydrofoil as an example. The cross section is NACA 16-006. The angle of attack is chosen to be 4 degrees, which is representative for the situation on a propeller blade. In our test the spanwise number of panels is maintained at 20 for the half-span while the chordwise number of panels on the cavity surface is varied from 20 to 50. A side view of this converged cavity shape is given in Fig. 3. The re-entrant jet is clearly shown for every spanwise position in this figure.

Because the hydrofoil has a very high aspect ratio, the cavity length is uniform over the whole span, except for the region very close to the tip. The flow at mid-span can be regarded as a purely 2-D flow in this case. The cavity end and the re-entrant jet are quite similar to the 2-D result, as will be illustrated below.

Since the prediction of the volume of the cavity is important for the prediction of the pressure fluctuations from a cavity, the cavity volume is used as a criterion to check convergence. Not all the boundary conditions on every cavity panel are satisfied in that case, especially on the last few panels at the cavity end. But the calculations show that the shape of the cavity and its volume converges much earlier than the kinematic boundary condition on the cavity surface. Figure 4 shows the cavity volume with varying chordwise panel numbers on the cavity surface. When the number of panels is increased to 50, convergence is approached. A reasonable result can be expected when the chordwise number of panels is around 50 to 60. The cavity length for the same calculation is also drawn in Fig. 5. This is also compared with the previous 2-D result. A satisfactory result is found again when the number of panels is 50.

Because we intend to simulate the cavity re-entrant jet, a very fine panel grid is applied at the end of the cavity. The correction of the cavity surface in the iteration steps can not be too large because otherwise a small waviness of the surface will result in a twisted

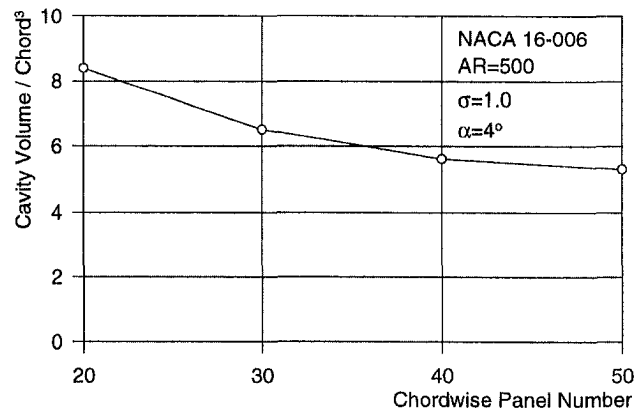


Fig. 4 Cavity volume as a function of the number of chordwise panels on the cavity surface

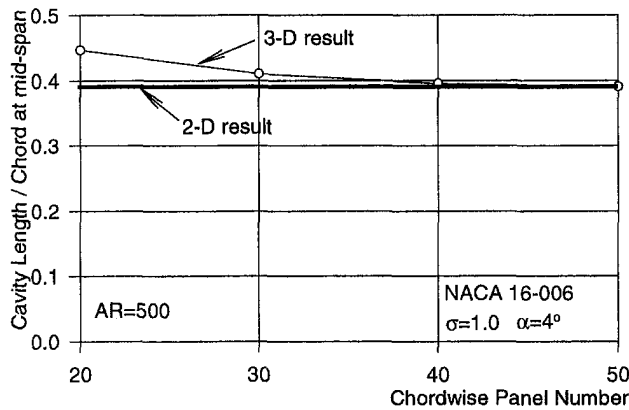


Fig. 5 Cavity length as a function of the number of chordwise panels on the cavity surface

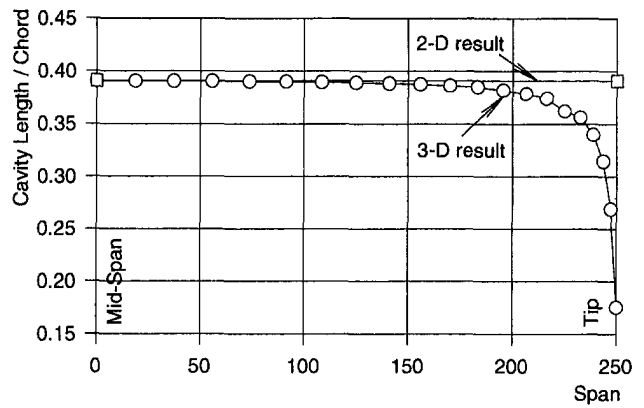


Fig. 7 Comparison of the cavity length at midspan between 2-D calculation and 3-D calculation

cavity end. So, a relaxation factor of around 0.2 to 0.4 is used. The disadvantage of this relaxation factor is that it makes the convergence slower and more iteration steps are needed. Figure 6 shows the change of the cavity volume with the number of iteration steps. When the number of iteration steps is more than 40, the cavity volume does not change any more. The change of the cavity shape after 40 iteration steps is mainly in the re-entrant jet, while the whole upper part of the cavity has already converged.

A validation of the present 3-D method is obtained by comparing this prediction for the high aspect ratio hydrofoil with the 2-D calculations (Dang and Kuiper 1998). The cavity shape at midspan calculated by the 3D method should be the same as the 2D result. These comparisons are shown for the cavity length, the cavity cross section areas and the re-entrant jet thickness in Figs. 7, 8, and 9, respectively. The agreement is quite satisfactory. This is true even for the re-entrant jet. Although the kinematic boundary condition on the jet is not fully satisfied, the calculated jet thickness in 3D is still the same as the result from the 2-D calculation: about 9% of the maximum cavity thickness.

6 Three-Dimensional Calculation Results

To show the behavior of 3-D cavity flow and its re-entrant jet on hydrofoils, both a flat rectangular hydrofoil and a twisted rectangular hydrofoil at an angle of 4 degrees have been chosen in the following calculations. The aspect ratios of these two hydrofoils are set to 2 in order to provide the geometry and the working condition similar to that of a propeller blade.

For the flat rectangular hydrofoil, the cavitation number is set to 0.5 and the initial cavity length is chosen to be a uniform length ($l_{initial}/Chord = 0.5$) all over the span.

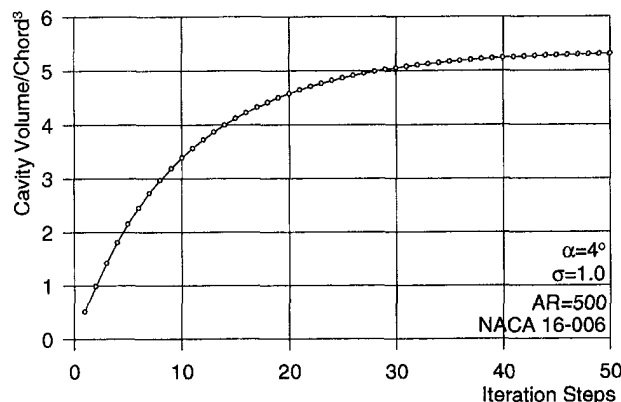


Fig. 6 Cavity volume as a function of the number of iteration steps

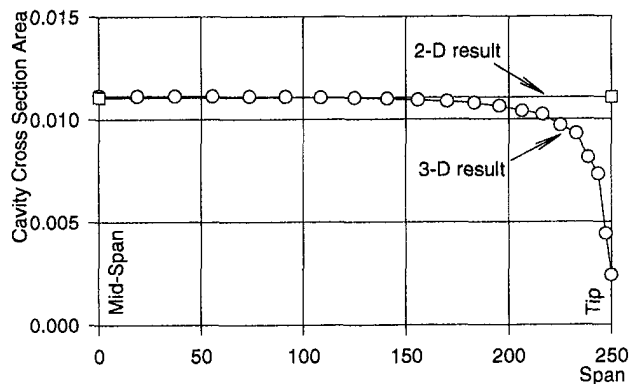


Fig. 8 Comparison of cavity volume at midspan between 2-D and 3-D calculation

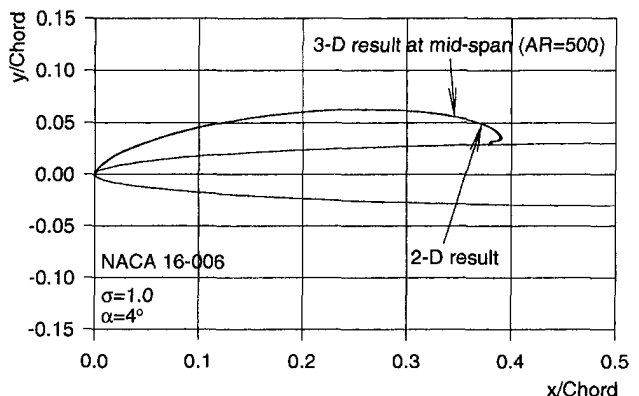


Fig. 9 Comparison of the cavity shape at midspan

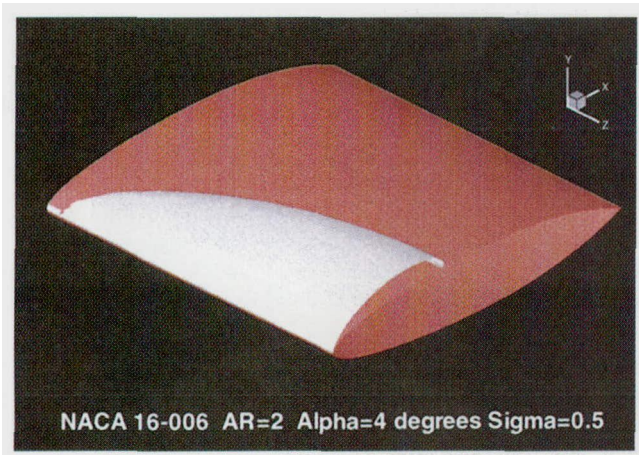


Fig. 10 The calculated 3-D cavity-hydrofoil system ($\alpha = 4$ deg, $\alpha = 0.5$)

attack of the sections at different spanwise positions varies according to the following formula,

$$\alpha = \alpha_0 \left(1 - \frac{12}{AR^2} |Z|^2 + \frac{16}{AR^3} |Z|^3 \right)$$

where, $\alpha_0 = 4$ deg and $AR = 2$. The twisting is realized by the rotating of the nose-trail line of each section around its trailing edge. The twist is chosen in order to concentrate the cavity to a limited region around the mid-span and to avoid cavitation at the tip. This will lead to a 3D-cavity shape that is suitable for experimental verification.

Figure 13 shows the calculated cavity planform when the cavitation number in the inflow is 0.3. The arrangement of the panels as adapted during the calculation, both on the cavity surface and on

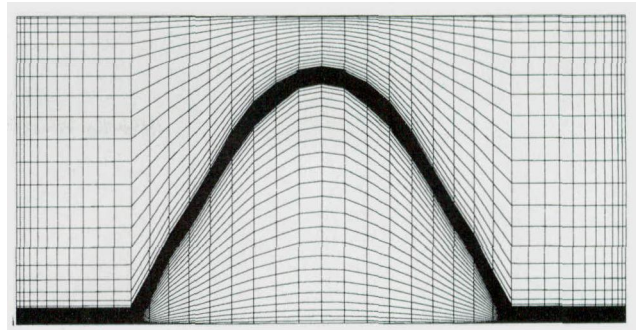


Fig. 13 The calculated cavity planform of the twisted 3-D hydrofoil ($\alpha = 0.3$)

the foil surface downstream of the cavity, are given in the same figure.

7 Streamline and Re-Entrant Jet Direction

Theoretically the re-entrant jet is always needed for a 2-D cavity flow because the cavity must be closed with the same pressure as the pressure on the cavity surface. But in the 3-D case, a re-entrant jet is not needed when a strong cross flow exists at the end of the cavity. The flow characteristics around the trailing edge of the cavity end are therefore of interest. Both the experiment of a swept hydrofoil (Fig. 2.6 in de Lange 1996) and the experiment of a conventional propeller (Fig. 15 in Kuiper, 1994) show that the re-entrant jet turns away from the flow direction on the cavity surface. It is supposed that the flow is 'reflected' at the end of the cavity by de Lange (1996), but no visualization or theoretical calculations have been carried out.

In order to understand the characteristics of the flow at the end of the cavity, the streamlines on the cavity surface and in the re-entrant jet are calculated for the hydrofoil in Fig. 10 in the same conditions. The result is given in Fig. 14. Also drawn in this figure is the distribution of negative pressure coefficient on the cavity and foil surface. From the pressure coefficients it is found that a stagnation point is present on the foil surface after the end of the cavity, especially at mid-span. But in the tip region, where the gradient of the cavity length is large, no stagnation pressure is calculated. From the streamlines in this figure, we can find that in that region the flow is almost tangential to the cavity. Consequently, no re-entrant jet is found. But in the region close to the mid-span, the flow remains perpendicular to the inflow direction and a re-entrant jet is found. A detail of the flow in the region without stagnation pressure is shown in Fig. 15. It is quite clear that the flow is indeed "reflected" at the cavity extent. That means the angle between the jet and the cavity extent is equal to the angle

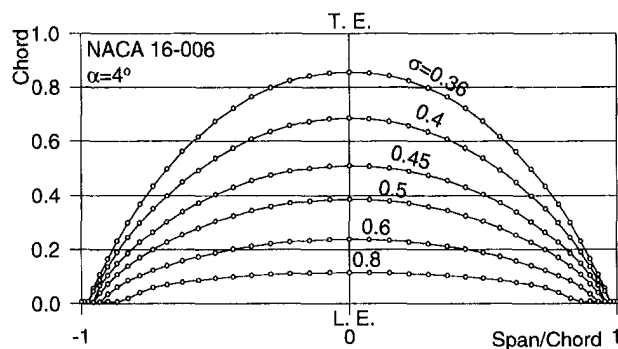


Fig. 11 The calculated cavity planform for different cavitation numbers

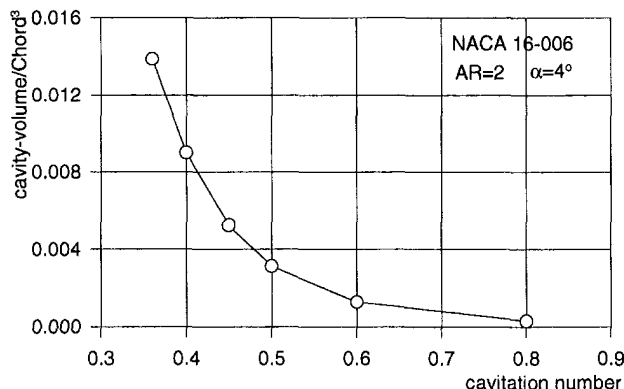


Fig. 12 The cavity volume at different cavitation numbers

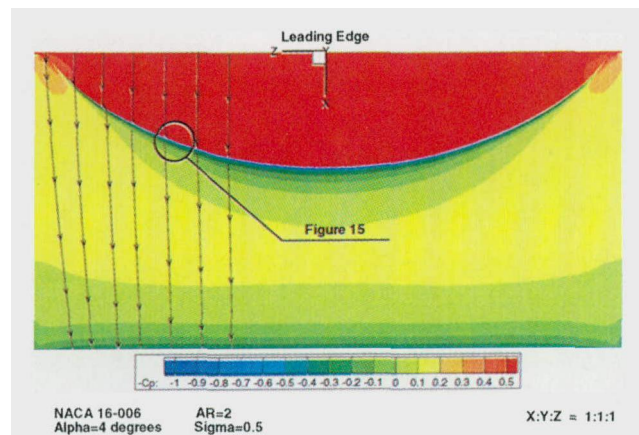


Fig. 14 Pressure distribution and streamline on the cavity-foil surface

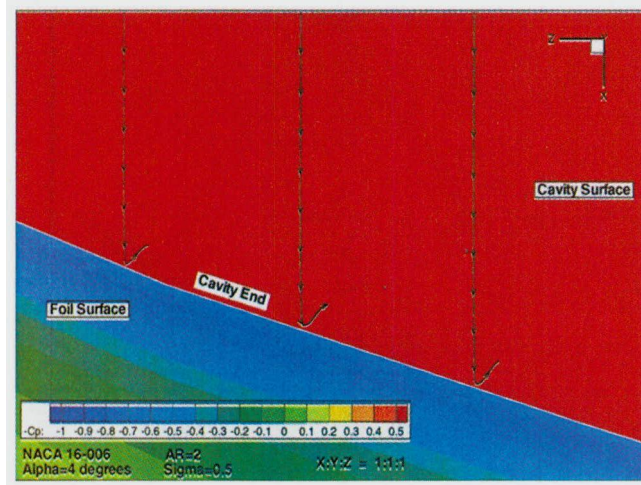


Fig. 15 The flow "reflects" at the end of the cavity

between the cavity end line and the flow on the cavity. So the cavity can be stable when the spanwise gradient of the cavity extent is large enough. Since the re-entrant jet is cut off in our calculations, no prediction of the behavior of the jet internally in the cavity and thus of the shedding of cloud cavitation can be derived yet.

8 Comparison With Experimental Data

Until now good and accurate 3-D experimental data on cavity flow are not available in public literature. An example of available data is the experiment conducted at MIT by Kinnas and Fine (1993). Unfortunately, there is uncertainty about the angle of attack and the section geometry. To make a rough and qualitative comparison can still be used to validate our calculations qualitatively. A NACA65a section in the present calculation approaches the cross section of the foil. Its main parameters can be found in Kinnas (1993). The angle of attack is 6.5 deg. Only the cavity length has been measured at two different cavitation numbers. No information about the cavity volume is available.

The calculated cavity length along the span is compared with

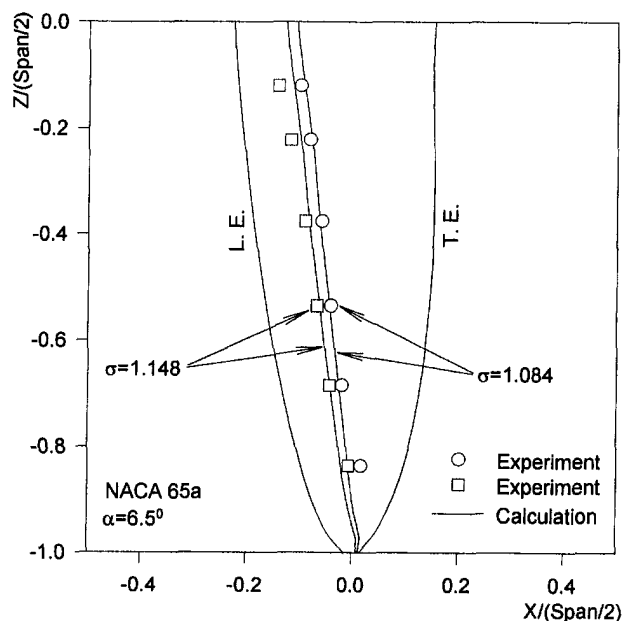


Fig. 16 Comparison of calculated cavity length with experiment data

Table 1 Calculated cavity volume

Cavitation number	1.084	1.148
Cavity volume/(Span/2) ³	1.40×10 ⁻³	1.04×10 ⁻³

experimental data in Fig. 16. The calculation shows a very good correlation with the data over most part of the hydrofoil surface. Slight deviations occur at the tip and at the midspan. The calculated cavity volume is listed in Table 1 and the calculated cavity shapes for several span positions are shown in Fig. 17 for cavitation number of 1.084.

9 Conclusions

A potential based panel method is successfully developed by the authors to calculate the steady 3-D cavity flow on a hydrofoil surface. A three-dimensional cavity re-entrant jet is simulated in this method. Systematic convergence testing of the present method shows that the method is quite stable and convergent. Calculation of the cavity on a high aspect ratio hydrofoil shows good agreement with previous non-linear 2-D calculations for both cavity length and cavity volume. Some 3-D calculations for a flat and a twisted rectangular hydrofoil with NACA 16-006 wing section have been made at different cavitation numbers. The calculated results show that the re-entrant jet is not always needed. At the tip region, the fluid at the end of the cavity flows in a direction tangential to the cavity end. The calculations confirm that the flow on the cavity surface is "reflected" at the cavity end line when the re-entrant jet exists. A preliminary experimental validation of the present method has been made for a MIT hydrofoil. The present method gives a quite good prediction of the cavity length over the whole span.

In order to validate the present method systematically, more experimental data are needed, especially on the cavity shape and volume in 3-D flows. The authors intend to carry out some benchmark test for 3-D cavitating hydrofoils in the near future.

Acknowledgments

This work has been carried out in the R&D program of the Maritime Research Institute Netherlands (MARIN). The authors greatly appreciate the advice of Dr. H. C. Raven. Support for the use of the Cray Y-MP of SARA was given by the "Foundation National Computer Facilities (NCF)".

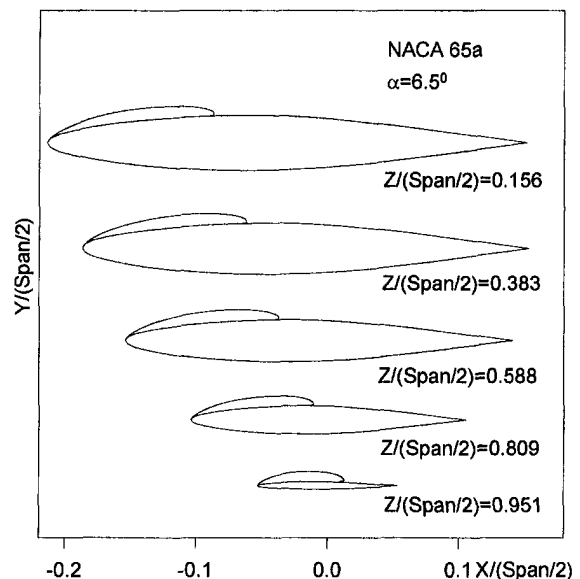


Fig. 17 Cavity shapes at different spanwise positions

References

- Dang, J., and Kuiper, G., 1998, "Re-entrant Jet Modeling of Partial Cavity Flow on Two Dimensional Hydrofoils," *3rd Inter. Symp. on Cavitation*, Grenoble.
- De Lange, D. F., 1996, "Observation and Modeling of Cloud Formation behind a Sheet Cavity," Ph.D. Thesis of Twente University.
- Fine, N. E., and Kinnas, S. A., 1993, "A Boundary Element Method for the Analysis of the Flow Around 3-D Cavitating Hydrofoils," *JSR*, Vol. 37, No. 3.
- Furness, R. A., and Hutton, S. P., 1975, "Experimental and Theoretical Studies of Two-Dimensional Fixed-Type Cavities," *ASME JOURNAL OF FLUIDS ENGINEERING*, pp. 515-522.
- Furuya, O., 1975, "Three-Dimensional Theory on Supercavitating Hydrofoils near a Free Surface," *JFM*, Vol. 71, Part 2, pp. 339-359.
- Hoshino, T., 1989, "Hydrodynamic Analysis of Propellers in Steady Flow Using a Surface Panel Method," *JSNAJ*, Vol. 165, pp. 55-70.
- Jiang, C. W., and Leehey, P., 1977, "A Numerical Method for Determining Forces and Moments on Supercavitating Hydrofoils of Finite Span," *Proceeding of the 2nd International Conference on Numerical Ship Hydrodynamics*, Berkeley.
- Kerwin, J. E., Kinnas, S. A., Lee, J. T., and Shih, W. Z., 1987, "A Surface Panel Method for the Hydrodynamic Analysis of Ducted Propellers," *Trans. SNAME* 95.
- Kinnas, S. A., and Fine, N. E., 1992, "A nonlinear Boundary Element Method for the Analysis of Unsteady Propeller Sheet Cavitation," 19th ONR, Seoul, Korea.
- Kinnas, S. A., and Fine, N. E., 1993, "A Numerical nonlinear Analysis of the Flow around 2- and 3-Dimensional Partially Cavitating Hydrofoils," *JFM*, Vol. 254.
- Kuiper, G., 1994, "Cavitation and New Blade Sections," FED-Vol. 190, *Cavitation and Gas-Liquid Flow in Fluid Machinery and Devices*, ASME.
- Leehey, P., 1971, "Supercavitating Hydrofoil of Finite Span," *IUTAM Symposium on Non-Steady Flow of Water at High Speeds*, Leningrad.
- Morino, L., and Kuo, C. C., 1974, "Subsonic Potential Aerodynamics for Complex Configurations: A General Theory," *AIAA Journal*, Vol. 12, No. 2, pp. 191-197.
- Peallat, J. M., and Pellone, C., 1996, "Experimental Validation of Two- and Three-Dimensional Numerical Analysis of Partially Cavitating Hydrofoils," *JSR*, 40-3.
- Pellone, C., and Rowe, A., 1981, "Supercavitating Hydrofoils in Nonlinear Theory," 3rd International Conference on Numerical Ship Hydrodynamics, Paris.
- Report of the Cavitation Committee of 20th ITTC. Proceedings, San Francisco, California, Sept. 19-25, 1993.
- Shen, Y. T., and Peterson, F. B., 1978, "Unsteady Cavitation on an Oscillating Hydrofoil," *12th Symposium on Naval Hydrodynamics*, Washington.
- Uhlman, J. S., 1978, "A Partially Cavitating Hydrofoil of Finite Span," *Transaction of ASME*, Vol. 100, No. 3, pp. 353-354.
- Van Houten, R. J., 1983, "The Numerical Prediction of Unsteady Sheet Cavitation on High Aspect Ratio Hydrofoils," 14th ONR, Washington D.C.

Y. Dong
Graduate Assistant.

B. Lakshminarayana
Evan Pugh Professor of
Aerospace Engineering,
Director, Center for Gas Turbines and Power.

Center of Gas Turbine and Power,
The Pennsylvania State University,
153 Hammond Bldg.,
University Park, PA 16802

Experimental Investigation of the Flow Field in an Automotive Torque Converter Stator

The flow field at the exit of a torque converter stator exit was measured using a miniature conventional five-hole probe. The data at speed ratio 0.8, 0.6, and 0.065 are presented. At the speed ratio 0.6, the stator exit flow is dominated by a large free-stream, accompanied by the blade wake and corner flow separation. A strong secondary flow is observed at the stator exit, the flow is overturned near the core and underturned near the shell. The secondary flow at inlet produces large radial transport of mass flow inside the stator passage. The shell-suction corner flow separation has a large blockage effect, resulting in losses. To determine the nature of the transitional flow in the stator passage, the surface hot-film sensors were mounted on the stator blade surface. The data confirm that the stator flow field is turbulent.

Introduction

Working as a torque reactor, the main function of the stator is to change the flow direction and provide angular momentum to the fluid. The stator receives the fluid from the turbine and redirects it back to the pump inlet at an ideal incidence. When the speed ratio is low, the flow undergoes large turning through the stator blade passage, thus producing a torque multiplication in the torque converter. The mass-averaged flow turning angle of the stator is directly related to the torque ratio of the converter. The flow losses in the stator blade passage decrease the torque converter's overall efficiency. Moreover, the stator exit flow field passes through the pump; affecting the entire flow structure in the pump passages.

The flow field in the stator of the automotive torque converter is highly three dimensional and dominated by corner separation, secondary flow and wakes. Very little is known about the nature of flows in the modern torque converter stator. It is not known whether the flow is laminar, transitional, or turbulent in their passage. There have been many conflicting and contradicting assumptions made regarding the nature of transitional flow due to the relatively low Reynolds number encountered in these devices. In addition, the torque converter operates in a wide range of speed ratio and through flow, resulting in appreciable range of inlet incidence. The flow path at the exit of the turbine (inlet of the stator) and inlet of the pump (exit of the stator) is complex with considerable curvature. These physical features result in complex, unsteady, three-dimensional flow with appreciable flow separation and radial variation in flow properties. Further improvements in the torque converter and the fuel economy of the vehicle have to come from a better understanding of the flow field in the torque converter. This is the objective of this paper. An additional objective of this paper is to resolve the controversy regarding the nature of transitional flows, which would be of considerable significance in the computation and design of these stators.

Previous work in this area has been carried out in older torque converter stators, which have been replaced by a new generation design. Marathe et al. (1994) measured the torque converter stator exit flow field using a miniature conventional five-hole probe. The flow was also predicted by a two-dimensional N-S code at the mid-span. Good agreements between the measured and the predicted velocity profile and loss were achieved at the speed ratio

0.6. Bahr et al. (1990) carried out LDV measurement and observed that the flow separation occurs at the speed ratio 0.8 and disappears at 0.065. Watanabe et al. (1997) conducted flow visualization in the torque converter stator passage using a laser sheet lighting method. It was observed that the flow around the leading edge has differing separation regions along the blade span. A two-dimensional laser Doppler velocimeter was also used to measure the steady and unsteady flow field in the stator passage.

The flow field in the stator of a new 245 mm diameter torque converter, simulating a more recent production design, was investigated. The objective is to provide detailed and accurate knowledge of the inlet and the exit flow fields. The inlet flow field is drawn from the turbine exit measurements reported in Dong et al. (1998). A miniature conventional five-hole probe was used in the flow field measurement of the stator exit. The nature of transitional flow was investigated using surface hot-film sensors embedded on the stator surface. All these data are presented and interpreted in this paper.

Experimental Facility and Measurement Technique

This experimental investigation was accomplished using the Torque Converter Research Facility at the Penn State University. The facility consists of six main components; drive motor, absorb dynamometer, control system, hydraulic system, test unit, and data acquisition system. Marathe (1994) gives a detailed description of this facility. The torque converter test unit investigated in this research is a new 245 mm diameter torque converter. The stator, pump, and turbine have 17, 32, and 36 blades, respectively. The detail geometric parameters and cross section of this torque converter are given in Dong et al. (1998). The stator passage and blade configurations are shown in Figs. 1 and 2. The stator design incidence angles (with reference to the camber line) are -14.2 , 30.5 , 60.5 , 74.0 , and 79.7 deg, respectively, at speed ratios of 0.8, 0.6, 0.4, 0.2, and 0.065.

The flow field at the stator exit was measured using a miniature conventional five-hole probe. The probe is traversed at 6 radial locations ranging from 11.4% to 88.6% of the blade height and 25 tangential positions to cover 120% of the blade spacing. The exit measurement grid and the stator blade profiles are shown in Figs. 1 and 2, respectively. A total of 120 measuring grid points in one stator blade passage and 30 points in another blade passage are used for the repeatability test. The axial distance from the blade trailing edge to the measurement plane is 4 mm, which is about 14.2% of the stator blade mid-span chord length. The stator exit flow field was measured at five different speed ratios, 0.8, 0.6, 0.4,

Contributed by the Fluids Engineering Division for publication in the JOURNAL OF FLUIDS ENGINEERING. Manuscript received by the Fluids Engineering Division July 6, 1998; revised manuscript received August 9, 1999. Associate Technical Editor: D. P. Telionis.

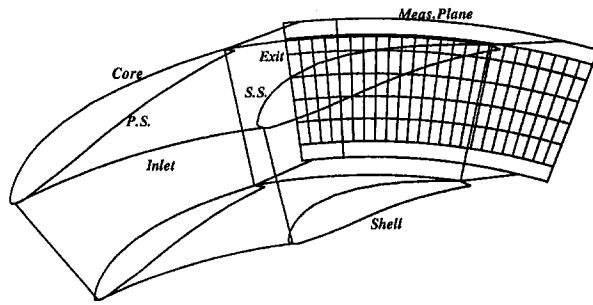


Fig. 1 Measurement grid at the stator exit

0.2, and 0.065. The flow field at the speed ratios 0.6, 0.8 (the peak efficiency condition), and 0.065 (the near stall condition) are presented and discussed in this paper. The coupling point of this torque converter is at the speed ratio 0.91. The accuracy of this probe measurement is: ± 0.15 m/s in total velocity, ± 1.5 deg in flow angles, and ± 700 Pa in pressure.

The velocities and pressures presented in this paper are normalized using the following equations:

$$V_{\text{norm.}} = \frac{V}{V_{\text{ref}}}, \quad V_{\text{ref}} = \pi D \frac{n_p}{60} \sqrt{1 - \frac{n_t}{n_p}} \quad (1)$$

$$P_{\text{norm.}} = \frac{P - P_{\text{hub}}}{P_{\text{ref}}}, \quad P_{\text{ref}} = \frac{1}{2} \rho V_{\text{ref}}^2 \quad (2)$$

where D is the diameter of the torque converter, which is 245 mm, P_{hub} is the static pressure measured at the stator hub.

The secondary flow is defined as:

$$\mathbf{V}_{\text{sec}} = (V_{\theta\text{measured}} - V_{\theta\text{ideal}})\mathbf{i}_\theta + (V_{r\text{measured}} - V_{r\text{ideal}})\mathbf{i}_r \quad (3)$$

$$V_{\theta\text{ideal}} = V_{z\text{measured}} \tan \beta_{\text{avg}} \quad (4)$$

$$V_{r\text{ideal}} = V_{z\text{measured}} \tan \alpha_{\text{avg}} \quad (5)$$

where β_{avg} and α_{avg} are the passage-mass-averaged flow yaw and pitch angles.

In order to determine the nature of the transitional flow in the stator passage, the wall shear stress (surface hot-film sensor) measurements on the stator blade surface were acquired at speed ratios 0.8 and 0.6. As shown in Fig. 2, six surface hot-film sensors were mounted on the stator blade surface at the mid-span; three on the pressure surface and three on the suction surface. The thickness of the sensor is 0.05 mm. The thickness of the viscous sub-layer on the stator blade surface is estimated larger than 0.09 mm. An

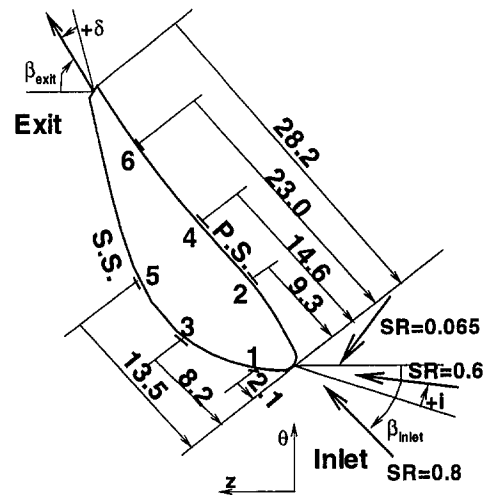


Fig. 2 Surface hot-film sensors on the stator blade surface (unit:mm)

overheat ratio 1.2 was used for all the sensors during the measurement.

The surface hot-film sensors were operated at an elevated temperature using constant-temperature anemometry. With this method, the relationship between wall shear stress at the sensor τ_w , and the rate of heat transfer from the sensor is given by:

$$\tau_w = k \left(\frac{E^2 - A^2}{\Delta T} \right)^3 \quad (6)$$

where E is the instantaneous output voltage from the anemometer, ΔT is the temperature difference between the liquid and the heated sensor, and variables k and A are calibration constants. For the present measurement, direct calibration of each sensor was not possible. The quasi wall shear stress $q\tau_s$ was employed, which is given in the form of:

$$q\tau_w = \left(\frac{E^2 - E_o^2}{E_o^2} \right)^3 \quad (7)$$

where E_o is the output voltage under zero-flow condition.

The measurement was carried out under two operating conditions; speed ratio 0.8 and 0.6. At the speed ratio 0.8, the measured inlet flow angle is about 55 deg at the mid-span of stator and 15 deg at the speed ratio 0.6. To change the flow Reynolds Number (Re) inside the torque converter, the pump was operated at five different rotating speeds, 300, 500, 700, 900, and 1100 rpm ($SR =$

Nomenclature

C_f = skin friction coefficient
 f_p = pump blade passing frequency
 $(32 \times n_p)$
 f_t = turbine blade passing frequency
 $(36 \times n_t)$
 h = spanwise distance from shell, mm
 H = blade height, mm
 h/H = relative radial position, (core
 $h/H = 0$, shell $h/H = 1$)
 i = incidence angle, difference between inlet blade angle and inlet flow angle, positive on the pressure side, (Fig. 2)

n_p, n_t = pump and turbine rotating speeds, respectively, (rp)
 P = static pressure
 P_o, P_{tot} = stagnation pressure
 P_{ref} = reference pressure (Eq. (4))
 $P.S., S.S.$ = blade pressure and blade suction surface, respectively
 Re = Reynolds number
 SR = speed ratio, n_t/n_p
 T = oil temperature
 U = pump blade tip rotating speed
 V_o, V_{tot} = total velocity
 V_z, V_{axi} = axial velocity
 V_t, V_θ = tangential velocity

V_r = radial velocity
 V_{ref} = reference velocity (Eq. (1))
 V_{sec} = secondary velocity (Eq. (3))
 α = flow pitch angle, core-to-shell direction
 β = flow yaw angle, blade-to-blade direction
 δ = deviation angle, difference between exit blade angle and exit flow angle, positive on the suction side, (Fig. 2)
 μ = oil viscosity
 ρ = oil density
 τ_w = wall shear stress (Eqs. (6) and (8))
 ν = oil kinematic viscosity

0.8) or 1160 rpm ($SR = 0.6$), and two different oil temperatures, 28°C and 60°C. The kinematic viscosity of the oil is $15.6 \times 10^{-6} \text{ m}^2/\text{s}$ at the temperature 28°C, and $5.3 \times 10^{-6} \text{ m}^2/\text{s}$ at 60°C. The Re varies by a factor of 3.67 ($SR = 0.8$) or 3.87 ($SR = 0.6$) due to the change in the pump speed and 2.94 due to the change in the operating temperature.

Result and Discussions

Stator Inlet Flow Properties. Details of stator inlet flow (turbine exit), which was measured using a high-frequency response five-hole probe, is covered in Dong (1998) and Dong et al. (1998). Only the passage average properties are presented in Fig. 3 to facilitate interpretation of the exit flow data. At the speed ratio 0.6, the total velocity is nearly uniform along the span, but the axial velocity decreases from the shell to the core, vice versa for tangential velocity. One of the major features to note here is the large variation in the flow angle (β) from the shell to the core. This leads to substantial variation in the incidence angle at the off-design conditions, and three dimensionality at the inlet. This is also evident from the pitch angle. The inlet flow is highly three-dimensional. Similar trend is observed at speed ratio 0.8. But, one of the major difference between the two speed ratios is the static pressure distribution and the stagnation pressure distribution. The data at the speed ratio 0.8 indicates increased turbine core flow separation resulting in lower pressure drop or higher pressures. This trend is opposite to those observed at the speed ratio 0.6. The data at speed ratio 0.065 indicates that the flow field is nearly uniform (due to almost idle turbine) and the stagnation pressure decreases toward the core, this decrease in pressure from shell-to-core is mainly the result of meridional curvature effect and the convex (core) and concave (shell) curvature effects.

Blade Surface Hot-Film Sensor Measurement. For the sake of brevity, only typical data at speed ratio 0.6 are presented and interpreted. The complete data set can be found in Dong (1998). The spectrums of the quasi wall shear stress are shown in Fig. 4. It is clear that the flow has a strong periodic signal at the lowest pump speed (300 rpm) and at low oil temperature (28°C) condition, where the Re is about 1/11 of the Re at the normal operating condition (60°C and 1160 rpm). The periodic fluctuation at turbine blade passing frequency is dominant at #1 sensor location (Fig. 2), because it is very close to the stator blade leading edge. A combination of the pump blade frequency and the turbine blade frequency ($f_p - f_t$) is also observed. At sensor #6, the signal of $f_p - f_t$ is the strongest one because this sensor is close to the stator blade trailing edge where the potential effect due to the pump blade becomes stronger. The broad-band signal is very weak at the low Re condition. At the normal operating condition (60°C and 1160 rpm), no periodic signal is observed by any of sensors. This is consistent with the fast-frequency response five-hole probe turbine exit flow measurement (Dong et al., 1998) in which no periodic flow is observed. The broad-band signal at high Re is much stronger than that at the low Re condition.

The time averaged quasi wall shear stress of sensor #1 and #6 at speed ratio 0.6 are shown in Fig. 5. The data processing technique is described in Dong (1998). The quasi skin friction coefficient qC_f and the Reynolds Number Re are defined as follows:

$$\tau_w = C_f \frac{1}{2} \rho V^2 \quad \text{and} \quad V \propto n_p, \quad C_f \propto \frac{\tau_w}{n_p^2} \quad (8)$$

$$qC_f = \frac{q\tau_w}{(n_p/100)^2}, \quad Re = \pi \frac{n_p D^2}{60 \nu} \quad (9)$$

At the lowest Re condition (28°C and 300 rpm), the quasi wall shear stress varies considerably with the turbine blade angular position, about 30% for sensor #1 and 8% for sensor #6. The RMS values of the unresolved unsteadiness in quasi wall shear stress (shown as vertical bar) are about 4% of the steady quasi shear

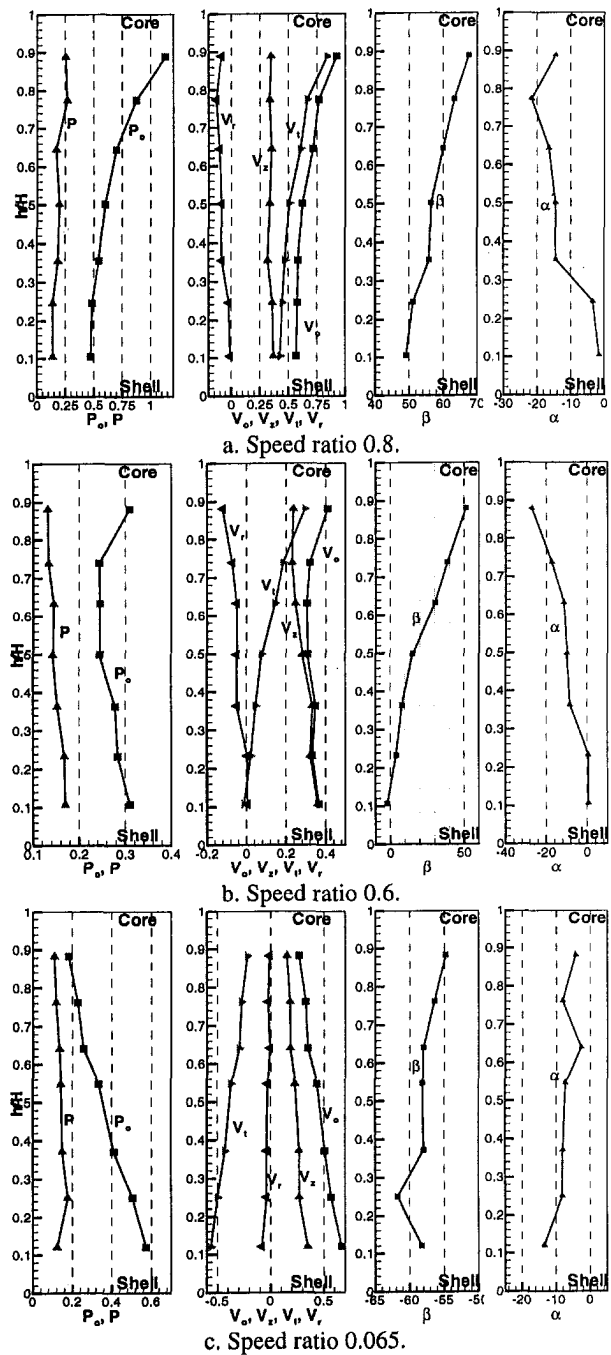


Fig. 3 Radial distribution of the mass averaged flow parameters at the stator inlet

stress. At the normal operating condition (60°C and 1160 rpm), the steady quasi wall shear stress is about 10 times larger than that at the lowest Re condition because of the increased velocity. The quasi shear stress does not change with the turbine blade angular position at the normal operating condition. The RMS values of the unresolved unsteadiness in quasi wall shear stress are about 8% of the steady quasi wall shear stress. The absolute level of the unresolved unsteadiness is about 25 times higher than that in the lowest Re condition.

The variation of quasi shear stress (from sensors #1 and #6) with Reynolds number are shown in Fig. 6. The unresolved unsteadiness RMS values in qC_f are also shown in figures as the vertical bar. For all sensors, the qC_f follow the trend for laminar flow relationship $qC_f \propto Re^{-1/2}$, which is shown as the dashed lines at the low temperature condition. The data in the turbulent range follow

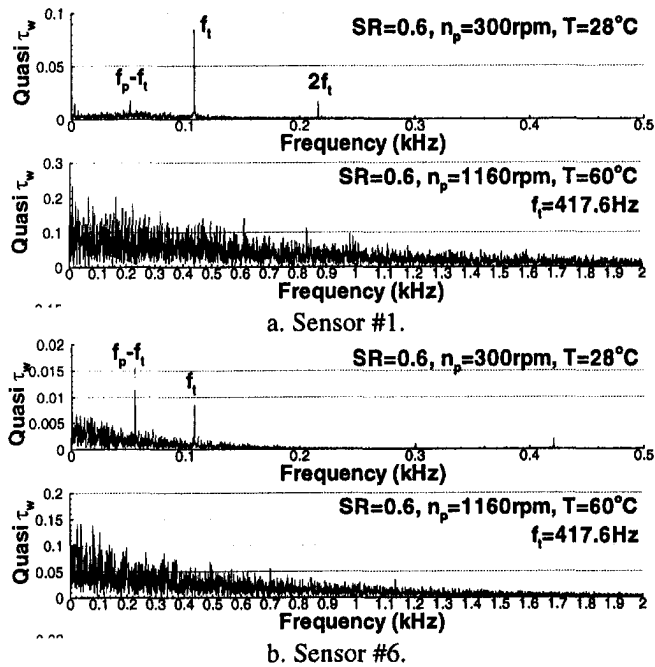


Fig. 4 Spectrums of quasi wall shear stress on stator blade surface at speed ratio 0.6

the trend for the turbulent pipe flow $qC_f \propto Re^{-1/4}$, which is shown as the solid lines at the normal operating temperature. The higher levels of the unsteadiness RMS values at the normal temperature also confirm that the flow has a larger fluctuation and is turbulent.

It is concluded that the flow in the torque stator blade passage is laminar at the low temperature (28°C) and is turbulent at the normal temperature (60°C) condition. The normal operating conditions of the Penn State facility are in the turbulent range. At the normal operating condition, the turbine blade wake decays rapidly due to turbulent mixing before it reaches the stator passages. Thus, no periodic signal is observed.

Stator Exit Flow Field at Speed Ratio 0.6. The contours of stagnation pressure, total velocity, axial velocity, yaw angle, and secondary flow velocity vectors at the design condition are shown in Figs. 7(b), 8(b), 9(b), 10(b), and 11(b), respectively. The radial variation of the passage average properties is shown in Figs. 12(b), 13, and 14.

Some of the major features observed at this speed ratio can be explained on the basis of the entry flow. The inlet flow near the shell is nearly axial (with an incidence angle 29 deg, Fig. 13) and the core flow has a high swirl (with a negative incidence of -24 deg). Such large variation in inlet angle, axial velocity, tangential velocity, and static pressure (Fig. 3(b)) result in severe off design conditions, three dimensionality, flow separation, and secondary flow. All these features are observed at the stator exit. Very high positive incidence near the shell is likely to separate the flow in the shell-suction corner. This will result in blockage effect, accelerating the flow near the pressure side of the shell. This induces secondary flow, inward radial flow along the suction surface, outward flow along the pressure surface, as shown in Fig. 11(b). The flow turning and the separation, in combination with the entry shear flow, are major causes of the secondary flow observed. This has many consequences. The shell separation region will have low axial and total velocities, stagnation pressure, and very high losses. The core flow is fairly clean with only wake as the undesirable effect. But severe migration of the flow results in very low axial velocity, in the core region. The axial velocity profile deteriorates considerably from inlet (Fig. 3(b)) to exit (Fig. 12(b)). Some of the details will be discussed in the following.

The total pressure contours indicate that most of the stator exit

area is covered by the free-stream, and there are two regions of high losses (Fig. 7(b)). The free-stream covers more than 80% of the measurement area. One of the high loss regions is the blade wake, which covers about 15% width of the blade spacing and spans from shell to core. Another high loss region is at the corner of the shell and the blade suction side, which covers about 30% width of the blade spacing and spans only from shell to 20% blade height. The total pressure contours show a very high loss in this small region, which is much higher than that in the blade wake. This flow structure can also be seen in the total velocity contours (Fig. 8(b)). The presence of high loss is due to high incidence and large turning in this region.

In the free-stream, the total pressure is relatively uniform (Fig. 7(b)) from core to shell and pressure side to suction side. On the shell-pressure corner, the total pressure reaches its highest value. This is because the stator inlet total pressure is higher near the shell (Fig. 3(b)). The total velocity is low near the core (Fig. 8(b)), which is consistent with the low incidence at this region. This is partly caused by the mass flow distribution at the stator inlet (Fig. 3(b)). The axial velocity contours at the stator exit (Fig. 9(b)) show the same trend; low near the core and high near the shell. The flow is overturned near the core and underturned near the shell (Fig. 10(b)), and the secondary flow vectors confirm this flow feature (Fig. 11(b)). The total velocity reaches the highest value near the shell-pressure corner (Fig. 8(b)). The high kinetic energy fluid is kept near the shell-pressure corner because of the radial static

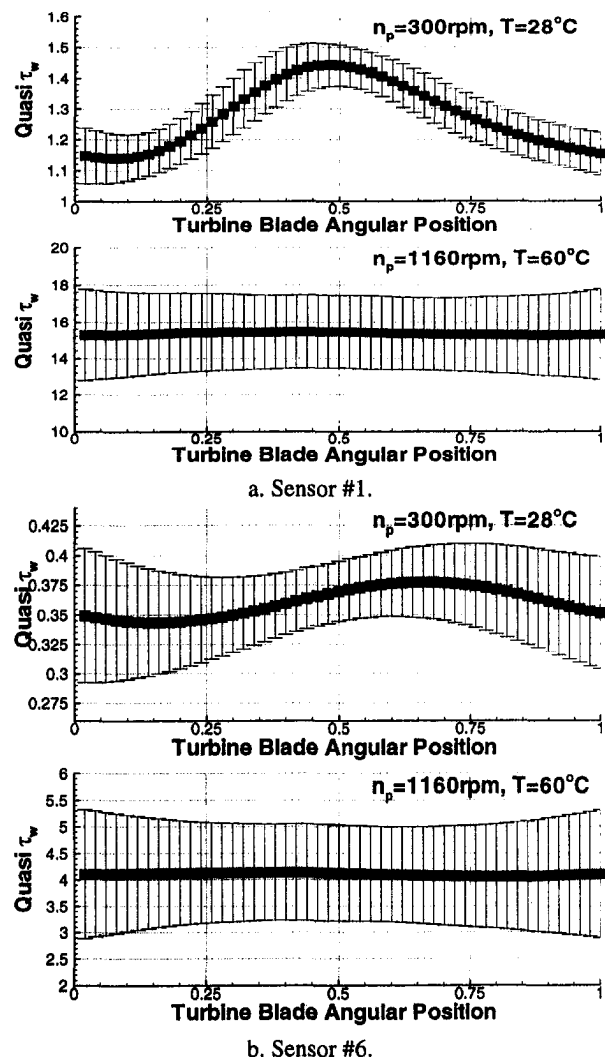


Fig. 5 Time averaged quasi wall shear stress and unsteady rms values (vertical bar) at the speed ratio of 0.6

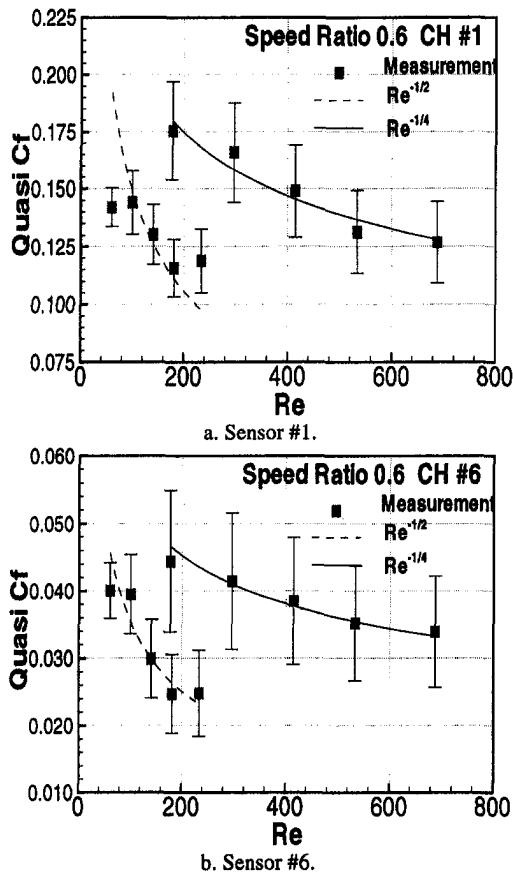


Fig. 6 Time averaged quasi skin friction coefficient and its unsteady RMS (vertical-bar) at speed ratio of 0.6

pressure gradient, which is from core to shell at the stator exit (Fig. 12(b)). This is mainly caused by incidence and flow turning distribution shown in Figs. 3(b) and 12(b).

At the stator inlet, the averaged axial velocity increases from core to shell by 50% (Fig. 3(b)). It is observed that this non-uniform axial velocity distribution deteriorates as the flow progresses through the stator. At the stator exit, the averaged axial velocity near the shell is about three times larger than that near the core (Fig. 12(b)). This indicates large radial mass transport towards the shell in the stator passage flow field. At the stator inlet, most of the passage area has an inward radial flow (Fig. 3(b)); because from the core to 23% of the blade span, the turbine exit flow has not been turned completely to the axial direction at the measurement plane. The radial inward flow is confirmed by the radial distribution of the mass average pitch angle at the stator inlet (Fig. 3(b)). This is the major cause for the radial transport of mass towards the shell.

Figure 11(b) shows a strong counter-clockwise (looking from downstream to upstream) secondary flow at the stator exit. The flow is overturned in the upper half of the passage, underturned in the lower half, highly radial inward along the suction side, and radial outward along the pressure side. The magnitude of these secondary velocity vectors are nearly the same order of magnitude as the average axial velocity. A general discussion on secondary flow is given in Lakshminarayana (1996). For this torque converter stator flow, several reasons could be attributed to the strong secondary flow. (1) A counter-clockwise vorticity (swirl flow) is found at the stator inlet due to the non-uniform radial distribution of the tangential velocity. The angular momentum is high near the core and low near the shell (Fig. 3(b)). (2) At speed ratio 0.6, the stator inlet has a 7.6 deg incidence and the flow turning angle across the stator is 45.3 deg. Such large flow turning develops strong secondary flow. (3) The core flow at the turbine exit (stator

inlet) has high shear gradients and this causes strong secondary flow to develop. The through flow velocity is low near the core. (4) The boundary layer near the blade suction surface is very thick, with possible flow separation as the stator inlet has a positive incidence on most of the blade span. The low kinetic energy fluid near the suction side is forced radially inward by the radial pressure gradient, which is from the core to the shell. It is believed that this radial inward flow has a major effect on the radial mass transport, which enhances the nonuniformity of the radial distribution at the stator exit (Fig. 12(b)).

At the stator exit measurement plane, the stator wake has decayed to some extent, because it mixes with the free-stream and becomes increasingly wider and weaker. The streamwise distance between the blade trailing edge and the probe tip is about 9.5 mm, about 30% chord length of the stator blade. The wake can be seen clearly from the total pressure and total velocity contours (Figs. 7(b) and 8(b)). The total pressure and total velocity are low in the wake and the static pressure maintains the same trend as the free-stream region. The wake is slanted (Figs. 7(b) and 8(b)) due to the secondary flow. The flow overturning near the core, underturning near the shell, and their effect on the wake results in a highly distorted and skewed wake flow. Thus, when the wake reaches the measurement plane, it seems to be slanted in the counter-clockwise direction.

The shell-suction corner is a complex flow region because of the flow separation. The total velocity and axial velocity are very low due to the flow separation (Figs. 8(b) and 9(b)). The high flow losses due to the separation cause very low total pressure and static pressure in this region. It is believed that high incidence and

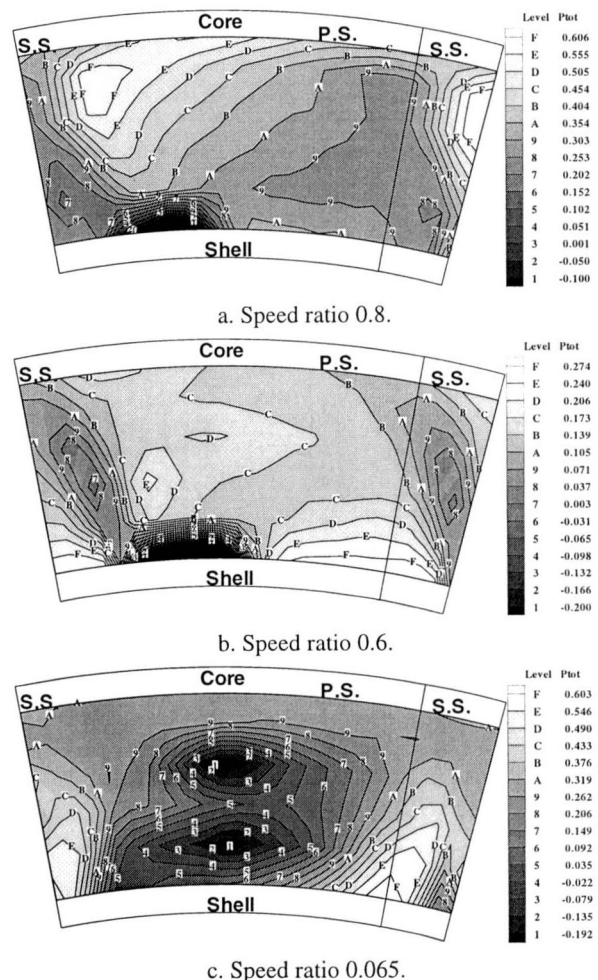
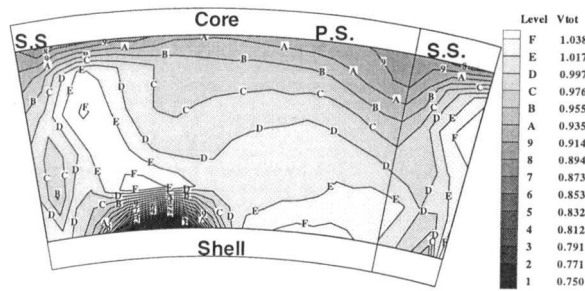
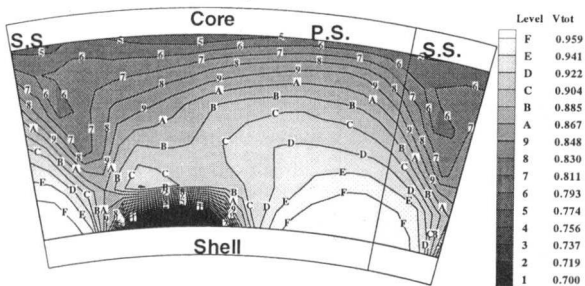


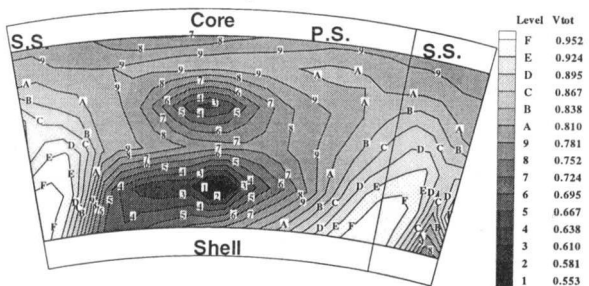
Fig. 7 Normalized total pressure contours at the stator exit



a. Speed ratio 0.8.



b. Speed ratio 0.6.



c. Speed ratio 0.065.

Fig. 8 Normalized total velocity contours at the stator exit

secondary flow are major causes of this corner separation. The low kinetic energy fluid near the blade suction surface is transported radially inward to the shell-suction corner by the secondary flow and is kept there by the tangential pressure gradient. The accumulation of the low kinetic energy fluid enhances the flow separation in this corner.

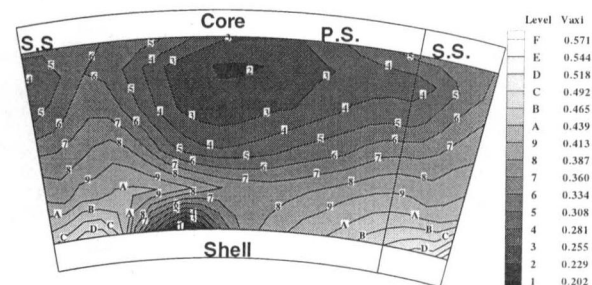
The blockage effect caused by the corner separation can be seen in the total velocity and axial velocity contours (Figs. 8(b) and 9(b)). The flow is concentrated near the pressure side, and the total velocity and axial velocity reach the highest values near the shell-pressure corner. It is clear that the total flow loss in the stator is enhanced by this corner separation. The flow loss in the pump also increases due to non-uniform flow at the stator exit, caused by the corner separation and its blockage effect.

Comparing the radial distribution of mass-averaged flow properties at the stator inlet with the stator exit (Figs. 3(b) and 12(b)), it is found that the radial static pressure gradient changes direction from shell-to-core at inlet to core-to-shell at the exit. This is mainly caused by large variation of flow turning in the spanwise direction. The exit flow angle from core-to-shell changes by about 25 deg (Fig. 12(b)). The deviation angle (Fig. 13) clearly shows overturning in the core region and underturning near the shell, even though the flow turning is highest in the shell region due to high incidence. The total pressure loss is high near the end-wall regions and higher near the shell due to the shell-suction corner separation as shown in Fig. 14.

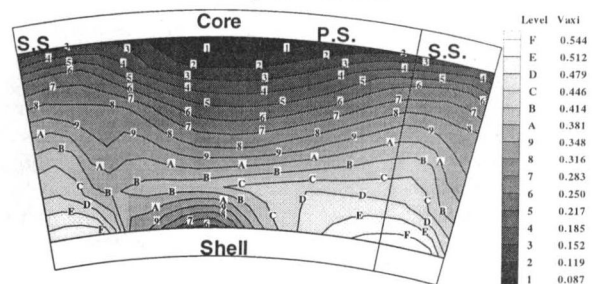
In general, the stator exit flow is dominated by the free-stream accompanied by the blade wake and a corner separation. A strong counter-clockwise secondary flow is found at the exit flow field,

which is caused by the stator inlet vorticity, flow turning, the axial velocity deficit near the core, and the shear gradient. The radial inward flow at the inlet and the secondary flow results in a large radial transport inside the stator passage. The shell-suction corner flow separation, which is caused by the radial inward flow along the suction surface, has a large blockage effect and enhances the loss in the stator.

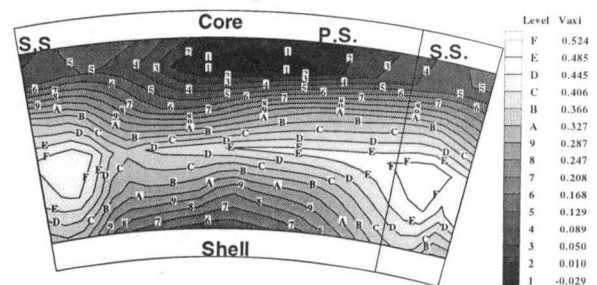
Stator Exit Flow Field at Speed Ratio 0.8. The data at the speed ratio 0.8 are also shown in Figs. 3, and 7 to 13. Some of the major feature observed at this speed ratio can be interpreted on the basis of the entry flow. Here again, the inlet angle varies from the core (68 deg) to the shell (49 deg), with a corresponding incidence angle of -41 and -22 deg. The incidence is such that the turning, as well as loading, is lower than the speed ratio 0.6. The turning angle are 3 and 14 deg at the core and shell. With such low turning angle, the losses, secondary flow, and the loading should be much less severe. But the turbine exit conditions (stator inlet conditions) reveal that the turbine core flow separation is much larger giving rise to higher pressure near the core (lower pressure drop). The axial velocity is nearly uniform radially, and the swirl near the core is still higher than the shell, but the radial gradients are not severe. The exit flow reveals that the loss near the core is higher than that near the shell (Fig. 14). This is probably due to the thicker boundary layer on the core (which could not be measured), caused by flow separation on the core inside the turbine passage. The overall difference between the speed ratio 0.6 and 0.8 is that turning angles and incidence angles are much smaller at the higher speed ratio. The shell-suction corner flow separation region has



a. Speed ratio 0.8.



b. Speed ratio 0.6.



c. Speed ratio 0.065.

Fig. 9 Normalized axial velocity contours at the stator exit

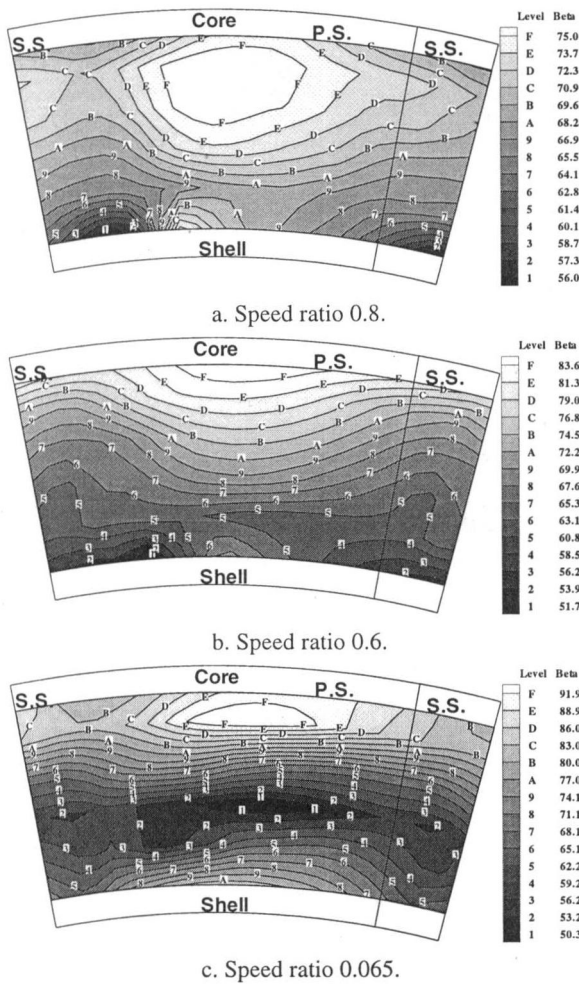


Fig. 10 Flow yaw angle contours at the stator exit (unit $^{\circ}$)

been reduced. The non-uniformity in the total pressure distribution is reduced as the flow passes through the passage, resulting in a smoother distribution. The secondary flows are generally lower (Fig. 11(a)) than those observed at the speed ratio 0.6. Detailed interpretation of the data is given below.

At the speed ratio 0.8, the total pressure is high near the suction side and low near the pressure side (Fig. 7(a)) in the free-stream. The total pressure reaches the highest value near the core-suction corner instead of in the shell-pressure corner. Unlike those observed at the speed ratio 0.6, the total velocity is high near both the suction side and the shell-pressure corner (Fig. 8(a)). This is believed to be caused by the change in the blade inlet incidence (Fig. 13). At the speed ratio 0.8, the stator has a -31.9 deg average incidence, which is almost 40 deg lower than that at the speed ratio 0.6 (Fig. 15(a)). It also should be noted that the incidence is in the positive direction, the inlet flow is impinging on the suction side (Fig. 2). There is probably a small separation bubble on the blade pressure side close to the leading edge. The flow is forced to the passage suction side by the blockage effect. This is the reason for the high total pressure and the total velocity found near the suction side. The high total velocity in the shell-pressure corner is still due to the blockage effect caused by the shell-suction flow separation.

The blade wake at the speed ratio 0.8 is thinner and weaker than that at the speed ratio 0.6 as evidenced by the total pressure and total velocity contour plots (Figs. 7(a) and 8(a)). This means the size of the wake is smaller and decays more rapidly. As mentioned earlier, the negative incidence angle greatly reduces the thickness of the boundary layer on the blade suction surface. The width of the wake is much smaller than that at speed ratio 0.6. The high

total velocity on the suction side also increases the mixing between the wake and the free-stream.

At the speed ratio 0.8, the secondary flow is much weaker than that at speed ratio 0.6 (Figs. 11(a) and (b)). Possible reasons for the reduced secondary flow are as follows. (1) The stator inlet counter-clockwise vorticity (swirl flow) is weaker. (2) The stator flow turning angle is small (10°) compared to the large turning angle (45.3 deg) at the speed ratio 0.6. (3) The negative incidence at stator inlet largely reduces the thickness of the boundary layer on the blade suction surface. The radial transport of the low kinetic energy fluid along the suction surface is reduced. The size of the shell-suction corner separation is also smaller. (4) The stator inlet has a nearly uniform radial distribution of the axial velocity (Fig. 3(a)). The secondary flow caused by the non-uniform inlet condition is greatly reduced. (5) The radial pressure gradient at the stator exit is smaller than that at the speed ratio 0.6 (Fig. 12).

At the speed ratio 0.8, the stator inlet has a 20 deg incidence change from core-to-shell (Fig. 13). There is almost no flow turning across the stator blade near the core, and very small turning (about 10 deg) in the rest of the passage. At this speed ratio, the stator plays a limited role as a reactor and the torque converter has a very small torque multiple. The radial pressure gradient is from core-to-shell at both the stator inlet and the exit (Figs. 3(a) and 12(a)). A higher total pressure loss is found near the core (Fig. 14). This is partly due to the flow mixing as evidenced by the high unsteadiness at the turbine exit near the core, as mentioned earlier. The stator inlet has a -41° incidence near the core (Fig. 13). The flow is separated on the pressure surface near the leading edge, which causes high total pressure loss. The radial mass flow trans-

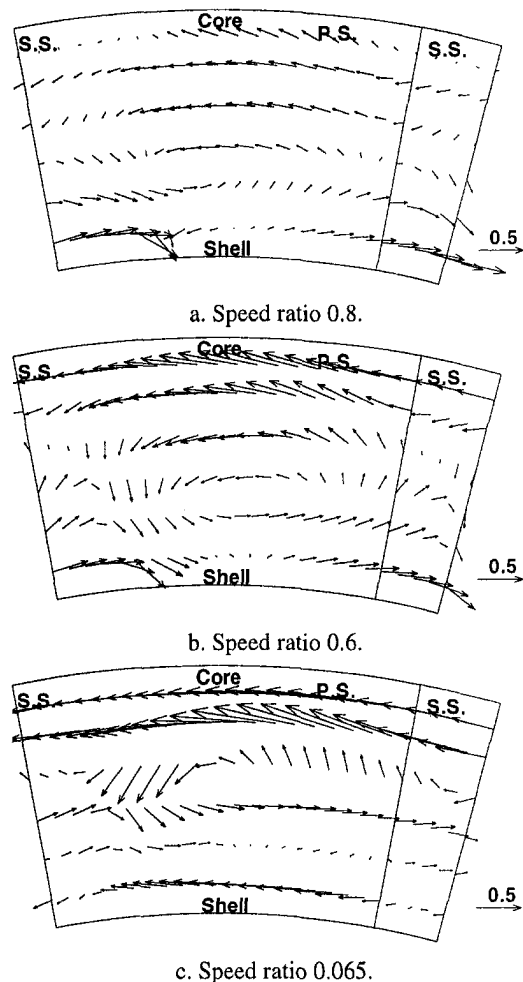


Fig. 11 Normalized secondary flow vectors at the stator exit

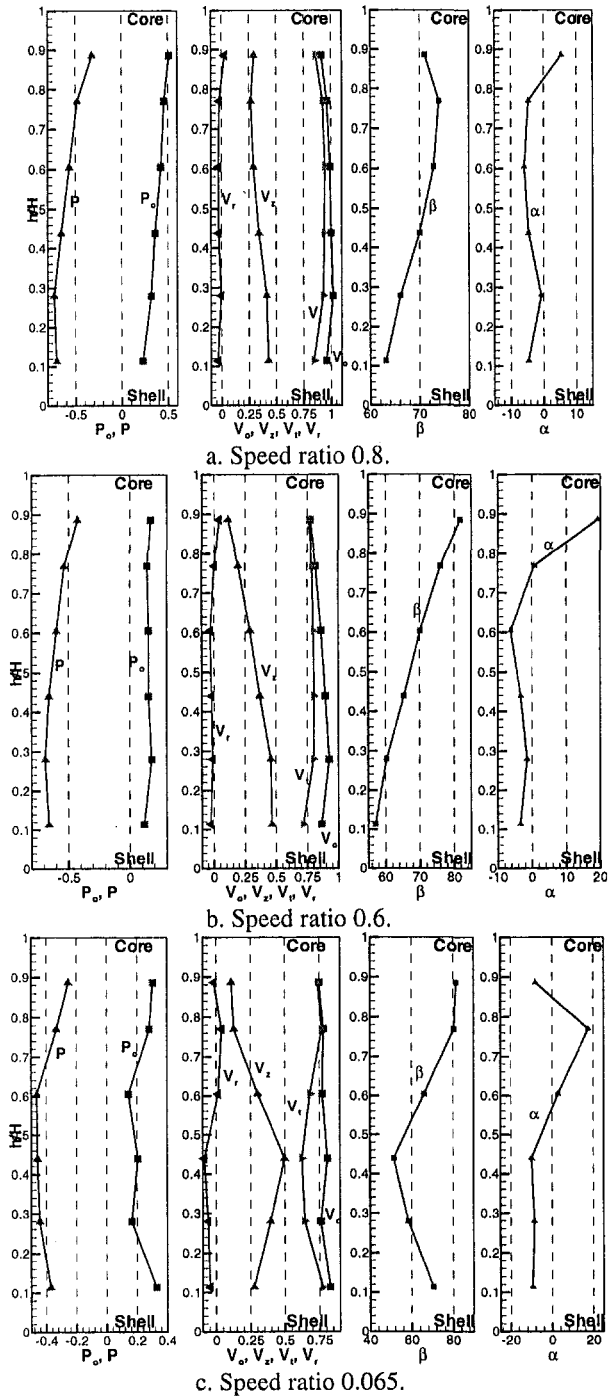


Fig. 12 Radial distribution of the mass averaged flow parameters at the stator exit

port is also smaller. The radial distribution of the axial velocity at the stator exit is more uniform than that at the speed ratio 0.6 (Figs. 12(a) and (b)). The deviation angle near the shell is reduced (Fig. 13) due to the smaller flow turning and the weaker secondary flow.

Stator Exit Flow Field at Speed Ratio 0.065. The data at speed ratio 0.065 are shown in the bottom of Figs. 3, and 7 to 12. The flow at this speed ratio experiences most severe off design conditions, and the incidence is very large as shown in Figs. 2 and 3(c). The inlet angle is nearly uniform (about -58 deg) and the outlet angle shows large deviation near the mid-span region (Fig. 13). The incidence and the flow turning angles are nearly 85 and 120 deg, respectively. Such severe conditions results in very heavy

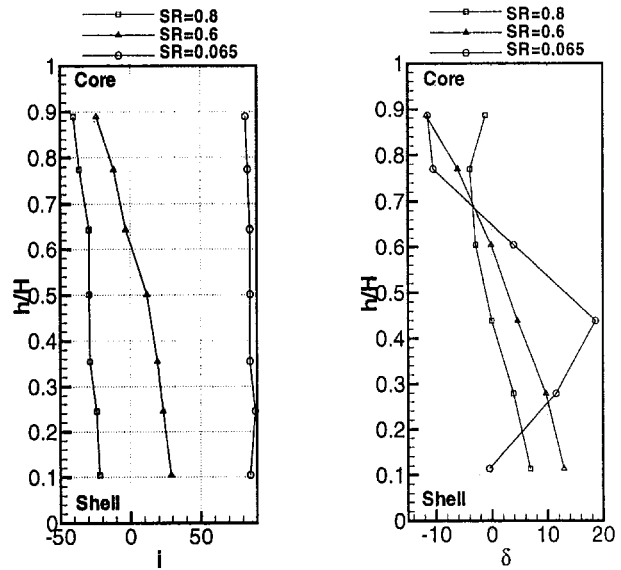


Fig. 13 Radial distribution of mass averaged incidence and deviation angles of the stator

blade load with substantial flow separation all the way from core-to-shell, secondary flow and losses. Most importantly, the incoming flow is three-dimensional with appreciable radial flows. The three-dimensional flow should result in considerable flow mixing inside the passage and is evident from Fig. 14, where the core flow experiences an increase in the stagnation pressure and the shell experiences very large losses. The flow with high total pressure near the shell has been swept towards the core by the secondary flow resulting in the observed phenomena. Increased secondary flow is evident from Fig. 11(c), and increased flow separation is evident from Figs. 7 to 10.

At the speed ratio 0.065, there is no free-stream in stator exit flow field. The blade wake has decayed due to large mixing, and no flow separation is observed near the shell-suction corner. However, high loss regions are observed in the middle of the passage (Fig. 7(c)), and the reverse flow is detected near the core region (Figs. 9(c) and 10(c)).

A large positive incidence angle at the blade inlet is the main cause of the complex flow at the speed ratio 0.065. The incidence angle increases about 80° from the speed ratio 0.6, and the average

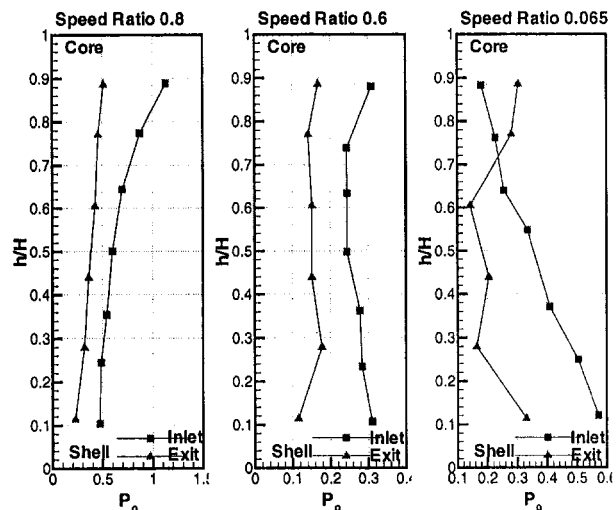


Fig. 14 Radial distribution of normalized total pressure at the stator inlet and exit

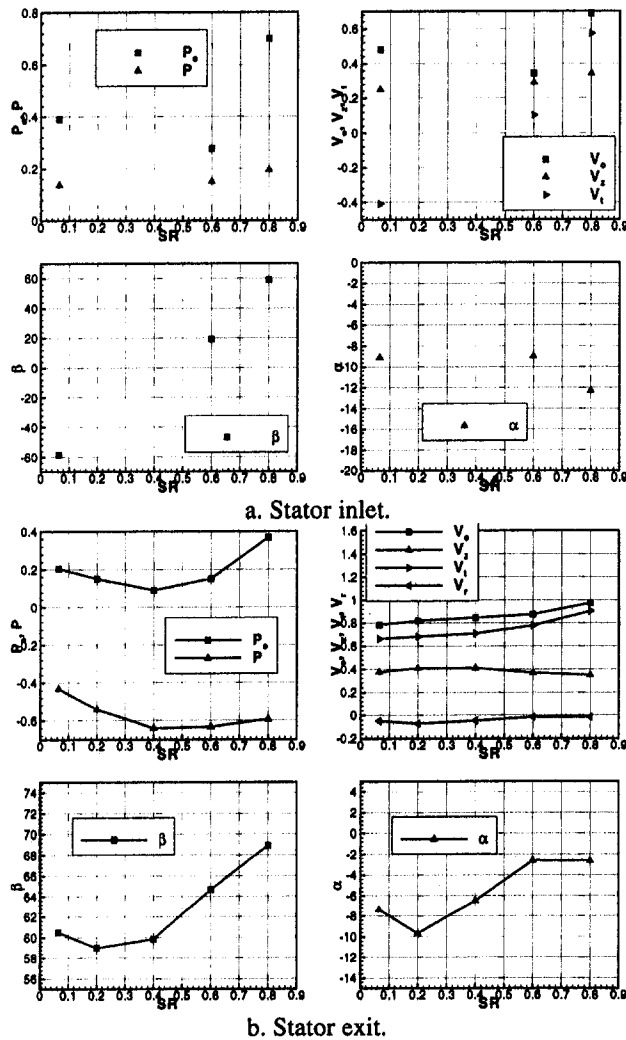


Fig. 15 Passage mass-averaged flow parameters versus speed ratio

incidence angle is 85.4 deg (Fig. 15(a)). The average flow turning angle is 119.1°. This large positive inlet incidence causes flow separation on the blade suction surface. Total pressure contours show that high loss flow structures cover most of the passage area (Fig. 7(c)), and the total velocity contours show a similar feature.

One of the important features of the stator exit flow field at speed ratio 0.065 is that a vortex is observed near the mid-span. The total pressure and static pressure are very low in the center of the vortex, and the total velocity is also very low in this region (Figs. 7(c) and 8(c)). The secondary velocity vectors support the existence of this vortex (Fig. 11(c)), which is a counter-clockwise secondary flow vortex. The secondary flow is enhanced by the interaction with the flow separation on the blade suction surface.

It is clear that the secondary flow is strong and complex (Fig. 11(c)). The flow is highly overturned near the core, radially inward near the suction side, underturned near the mid-span, radially outward near the pressure side in the upper half of the passage, and overturned near the shell. This indicates the presence of a counter-clockwise secondary vortex in the upper half of the passage and a clockwise secondary vortex in the lower half of the passage. Compared with the speed ratio 0.6, in which only one counter-clockwise secondary vortex is observed at the measurement area, the counter-clockwise secondary vorticity in the upper half passage is enhanced by the existence of the clockwise secondary vorticity in the lower half passage. At the stator inlet, the axial vorticity is in the counter-clockwise direction at the speed ratio 0.065 (Fig. 3(c)).

The radial distribution of the mass-averaged axial velocity is linear and nearly uniform at the stator inlet, with some deficit near the core (Fig. 3(c)). The radial velocity is in the inward direction, but the magnitude is very small. However, a large axial velocity deficit is found near both the core and the shell at the stator exit measurement plane (Fig. 12(c)). This means that the flow field inside the stator passage is highly three-dimensional at this speed ratio, and the secondary flow has a large effect on the radial transport. The mass flow rate is concentrated near the blade mid-span at the exit (Fig. 9(c)). A reverse flow is observed near the mid-passage near the core (Fig. 9(c)). The axial velocity deficit near the core clearly is the result of this reverse flow.

Another feature of the stator exit flow at speed ratio 0.065 is that the shell-suction corner flow separation does not stay in that corner, but moves to the mid-passage and 30% of the blade span. The total pressure and the total velocity are very low at the center of the separation (Figs. 7(c) and 8(c)), and the static pressure is low. The blockage effect can also be clearly seen from the total velocity contours (Fig. 8(c)), the total velocity is very high beside the separation region. The change in the location of the separation zone may be caused by several causes. First, as the blade inlet incidence angle increases, the flow condition on the suction surface becomes worse. The shell-suction corner flow separation could start earlier, where the separation starting point moves upstream on the blade surface. Stronger secondary flow in the blade passage will also cause the flow separation to occur further upstream. As the flow separation propagates downstream, it detaches from the blade surface and the shell wall. Both the blade suction surface and the shell wall have some curvature, and the flow separation can not follow these curvatures. Second, the flow overturning near the shell may result in separation near the blade mid-span. It is also clear that this flow separation interacts with the strong secondary flow vortex, which is located just above it. The interactions between these two flow structures clearly affect their respective positions in the blade passage.

In general, the stator exit flow field at the speed ratio 0.065 differs substantially from those at the speed ratio 0.6. The flow is highly three-dimensional and much more complicated. The free-stream and the blade wake can no longer be found at the measurement plane. A strong secondary flow vortex is observed near the center of the passage. The shell-suction corner flow separation detaches from that corner, and moves toward the middle of the passage.

Effect of Speed Ratio on the Stator Exit Flow. It is clear that the largest flow turning occurs at the lowest speed ratio in the stator blade passage and the stator provides the largest angular momentum change. From speed ratio 0.8 to 0.065, the flow turning angle increases by about 110 deg, while the torque ratio increases from 0.976 to 1.922 (as measured at the Penn State facility). The flow structure inside the blade passage is dominated by such large changes in the turning angle.

From the data presented in this section, the speed ratio has a major influence on the stator exit flow field. The inlet incidence angle (Fig. 13) to the stator blade depends on the speed ratio, which changes more than 110 deg from the peak efficiency condition to the stall condition. The extent of the free-stream, the flow separation on the blade surface and the end-wall, the strength and structure of the secondary flow, the exit flow deviation angle (Fig. 15), total pressure loss (Fig. 14), etc. are strongly influenced by the blade inlet incidence. The stator inlet axial velocity distribution, radial velocity distribution, and magnitude of axial vorticity (swirling flow) are also very much dependent on the speed ratio.

The variation of mass-averaged flow parameters at the inlet of stator (exit of the turbine), with the speed ratio, is shown in Fig. 15(a). Flow measurements at the exit of turbine were conducted at speed ratios; 0.8, 0.6, and 0.065. The variation of the stator exit mass-averaged flow parameters with the speed ratio are shown in Fig. 15(b). As the stator has a 27 deg inlet blade angle, the measured inlet incidence angle changes from 85.4 to -31.9 deg as

the speed ratio is increased from 0.065 to 0.8. The stator blade has a 70 deg exit angle, and the measured exit deviation angle changes from 1 to 10 deg as the speed ratio is decreased from 0.8 to 0.065, and the deviation angle increases sharply from speed ratio 0.8 to 0.4.

Conclusion

The following conclusions are drawn from this investigation:

(1) At normal test conditions, the flow in the stator passage is found to be turbulent based on the surface hot-film sensor data. The turbine exit periodic flow is decayed completely by the turbulent mixing before it reaches the stator passage.

(2) At the speed ratio 0.6, the stator exit flow field is dominated by the free-stream, accompanied by the blade wake and shell-suction corner flow separation. The total pressure is relatively uniform in the free-stream, and the total velocity is low near the core and high near the shell-pressure corner. The total pressure and total velocity are very low in the shell-suction corner flow separation region.

(3) A strong secondary flow is found at the stator exit flow, and the flow is overturned near the core and underturned near the shell. The main reasons for the secondary flow are the swirling flow at the stator inlet, the axial velocity deficit near the core, and the flow turning. The wake is slanted at the measurement plane due to the overturning and underturning of the flow.

(4) The radially inward velocity at the stator inlet and the secondary flow produce a large radial transport of mass flow inside the stator passage, especially at low speed ratios. The shell-suction corner flow separation, which is caused by the radially inward flow along the blade suction surface, has a large blockage effect and introduces flow losses to the stator and pump flow.

(5) From the core to the shell, the stator inlet has more than a 50 deg incidence change along the blade height at the speed ratio 0.6, and the exit flow angle has about a 25 deg variation. The mass-averaged incidence angle is 7.6 deg, and the deviation angle is 5.3 deg at the speed ratio 0.6.

(6) At the speed ratio 0.8, the stator blade has a -31.9 deg incidence. High total pressure and total velocity are found on the suction side at the exit due to the blockage caused by the inlet flow separation. The blade wake is decayed more rapidly due to the mixing with the high velocity free-stream. The secondary flow is weaker, and the mass flow radial transport is smaller.

(7) At the speed ratio 0.065, the mass-averaged incidence angle is 85.4 deg, and the flow turning is 119.1 deg. The stator exit flow field is significantly different from the speed ratio 0.6 because of the large change of inlet flow angle. High loss flow structures are found in the middle of the passage. A strong secondary flow vortex is observed in the center of the passage, with both low total and static pressures. The secondary flow is enhanced by an interaction with the large flow separation on the blade suction surface. The shell-suction corner flow separation moves to the mid-passage and 30% blade span.

Acknowledgment

This project was sponsored by the Powertrain Division of the General Motors Corporation. The authors wish to express their gratitude to Mr. Donald G. Maddock of GM for his assistance, comments, and encouragement. Assistance by J. Burningham and B. Marathe is gratefully acknowledged.

References

- Bahr, H., Flack, R., By, R., and Zhang, J., 1990, "Laser Velocimeter Measurements in the Stator of a Torque Converter," SAE Paper 901769.
- Dong, Y., 1998, "An Experimental Investigation on Fluid Dynamics of An Automotive Torque Converter," Ph.D thesis, The Pennsylvania State University.
- Dong, Y., Lakshminarayana, B., and Maddock, D., 1998, "Steady and Unsteady Flow Field at Pump and Turbine Exit of a Torque Converter," *ASME JOURNAL OF FLUIDS ENGINEERING*, Vol. 120, No. 3, pp. 538–548.
- Lakshminarayana, B., 1996, *Fluid Dynamics and Heat Transfer of Turbomachinery*, Wiley-Interscience, Publication, Wiley & Sons.
- Marathe, B., Lakshminarayana, B., and Dong, Y., 1994, "Experimental and Numerical Investigation of Stator Exit Flow Field of an Automotive Torque Converter," *ASME Journal of Turbomachinery*, Vol. 118, No. 3, pp. 835–843.
- Wantanabe, H., Tetsuo, K., and Kojima, M., 1997, "Flow Visualization and Measurement in the Stator of a Torque Converter," SAE 970680.

Toshiyuki Osada

Assistant Manager,
Mitsubishi Heavy Industries, Ltd.,
Chiyoda, Tokyo, Japan

Takashi Kawakami

Manager,
Mitsubishi Heavy Industries, Ltd.,
Takasago Machinery Works,
Takasago, Hyogo, Japan

Tadashi Yokoi

Senior Principal Engineer,
Toyo Engineering Corporation,
Narashino, Chiba, Japan

Yoshinobu Tsujimoto

Professor,
Osaka University,
Engineering Science,
Toyonaka, Osaka, Japan

Field Study on Pump Vibration and ISO's New Criteria

ISO 10816-3 (a new standard of International Organization for Standardization) was established as vibration criteria for industrial rotating machinery based on the bearing housing vibration in situ. The appropriateness of the application of the proposed vibration criteria to pumps was discussed and studied by a work group in Japan. For the assessment, the data of vibration level in field were measured, and the effects of driver output, rotational speed, and pump type were studied. This paper describes the applicability of the new ISO criteria to the evaluation of vibration level of pumps, based on the results of the field measurements. It was found that the new boundaries of evaluation zones, which are acceptable for unrestricted long-term operation of pumps, are quite appropriate and satisfactory.

Introduction

For the evaluation of the integrity of rotating machinery the vibration level is one of the most important indexes. It can also be used for evaluating the appropriateness of design and manufacturing. Currently, it is often requested by the users to reduce the vibration below a certain level. In such cases, the vibration criteria of ISO (International Organization for Standardization), API (American Petroleum Institute), and HI (Hydraulic Institute) are often referred to.

ISO 10816-3 "Mechanical vibration evaluation of machine vibration by measurements on non-rotating parts" was newly established as vibration criteria for industrial rotating machinery based on the bearing housing vibration in situ. For the purpose of discussing the appropriateness of the application of the proposed vibration criteria to pumps, a work group (W. G.) was established in the Turbomachinery Society of Japan in December 1992. The W. G. is composed of eighteen engineers and researchers from universities, pump users, pump plant engineering companies, and pump manufacturers. There have been some discussions on vibration criteria (Maten, 1972; Hancock et al., 1974; Lifson et al., 1987). However, since it was found that no results of a systematic survey on the rms value of pump vibration velocity were available for the assessment, it was decided to carry out field measurements of vibration level. The vibration level was measured in rms and zero-to-peak values, since the former value is specified in the new criteria while the latter is used in conventional standards. Based on 161 sets of measured vibration data, the effects of driver output, rotational speed and pump type are studied.

The present paper discusses the applicability of the new ISO criteria to the evaluation of the vibration level of pumps, based on the results of the field measurements.

History of ISO Vibration Criteria

The magnitude of the vibration level of a machine is influenced by many factors such as structure, design, operating condition,

mounting condition, and so on. This makes it very difficult to predict the allowable vibration level for an individual machine.

It is obvious that a lower vibration level is favorable for more reliable operation. However, the requirements of an excessively low vibration level may lead to excessive cost, weight, and space. A good design should be based on a good balance between performance, reliability, and cost. Under these circumstances it is convenient to have appropriate vibration criteria to avoid the cost of excessive quality.

It is common practice for designers to set their own vibration criteria for their own machines based on some official standard taking into account their experience and the results gained from similar machines. From the viewpoint of the maintenance of rotating machinery, it is convenient to have a unified vibration standard applicable to all types of rotating machinery.

In 1939, Rathbone (U.S.A.) proposed a chart showing the relation between rotational speed and displacement, which became the origin of today's vibration criteria (Sagisawa, 1981). After that, the evaluation criteria were separated into those for bearing housing vibration and for shaft vibration as shown in Fig. 1. As for the bearing housing vibration, the German standard VDI 2056 (1964) was established and eventually became the basis of the international standard. This standard introduced the scale of vibration severity, in which vibrations with the same rms velocity anywhere in the frequency band 10 to 1000 Hz are considered to be of equal severity. In this standard, the machines are categorized into six groups according to their power, type (e.g., rotating or reciprocating) and the rigidity of foundation. The vibration level was classified into four evaluation zones. The standard of ISO 2372 (1974) has nearly the same contents as VDI 2056. The standard ISO 3945 (1977) for larger rotating machinery provides definite definitions of evaluation zones A to D. See Table 1.

The newly prepared ISO 10816 gives the vibration evaluation criteria for monitoring and maintenance in situ to facilitate the practical applications of the above two ISO criteria (ISO 2372 and ISO 3945). The outline of ISO 10816-3 (1998) can be summarized as follows.

- (1) Machine type: see Fig. 1
- (2) Rated power above 15 kW, rotational speed 120 to 15,000 rpm

Contributed by the Fluids Engineering Division for publication in the JOURNAL OF FLUIDS ENGINEERING. Manuscript received by the Fluids Engineering Division June 10, 1998; revised manuscript received July 13, 1999. Associate Technical Editor: B. Schiavello.

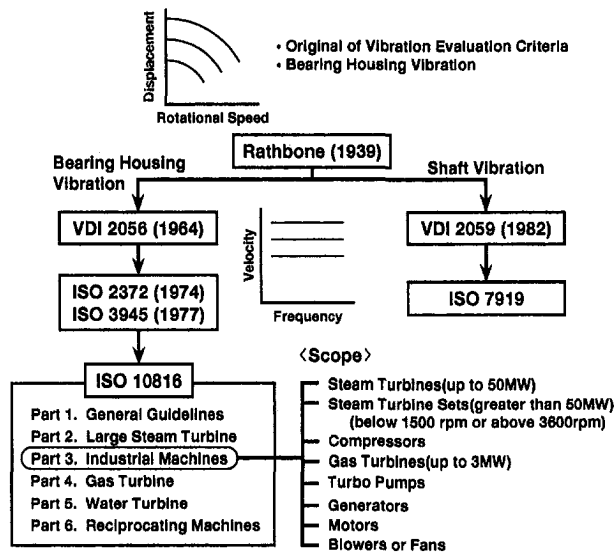


Fig. 1 Change of ISO vibration evaluation criteria

- (3) Evaluation scale: rms values of vibration velocity and displacement
- (4) Measuring frequency: 10 to 1000 Hz (for machines below 600 rpm: 2 to 1000 Hz)
- (5) Classification of rotating machines
 - Group 1: large machines with rated power above 300 kW
 - Group 2: medium-size machines with rated power 15 kW to 300 kW
 - Group 3: pumps with separate driver—with rated power above 15 kW
 - Group 4: pumps with integrated driver—with rated power above 15 kW
- (6) Support flexibility
 - flexible: lowest natural frequency $< 1.25 \times$ main excitation frequency
 - rigid: lowest natural frequency $> 1.25 \times$ main excitation frequency
- (7) Evaluation zone A to D.

The definitions of evaluation zone A to D are given in detail as shown in Table 1. The values of rms displacement and velocity for the A/B, B/C and C/D zone boundaries are specified for each machine group as shown in Table 2.

Group 3 and Group 4 are added to take the following pump vibrations considerations into account. The pump vibration is mainly caused by the hydraulic forces which cannot be balanced by a simple mechanical balancing. In addition, there are many cases in which pumps are operated satisfactorily even above the levels of the vibration criteria which limit the operation of Group 1 and Group 2 machines.

It is stated in the main text of the ISO 10816-3 that the values of Group 3 and Group 4 in Table 2 are applicable only for the operations at the rated flow but higher vibration values may occur at non-rated conditions. In the following sections, vibration data

Table 1 Definitions of vibration evaluation zones

ISO Zone	VDI 2056 ('64)	ISO 3945 ('77)	ISO 10816-3
A	Gut (good)	Good	Newly commissioned machines would normally fall within this zone
B	Brauchbar (useful)	Satisfactory	Normally considered acceptable for unrestricted long-term operation
C	Noch Zulässig (still allowable)	Unsatisfactory	Normally considered unsatisfactory for long-term continuous operation
D	Unzulässig (not allowable)	Unacceptable	Normally considered to be of sufficient severity to cause damage

obtained by the W. G. are presented to discuss the adequacy of the proposed vibration criteria. The criteria for vibration velocity are mainly discussed since the criteria for displacement can be easily satisfied by appropriately designing the support system.

Characteristics of Pump Vibration

Vibration characteristics of pumps are very different from those of electric or gas handling machines. It is well known (Someya et al., 1989) that the contributions of the hydraulic forces are very large in the static and dynamic loads on the shaft. Even at the rated flow, the hydraulic excitation force may become several times as large as the residual mechanical unbalance. In addition, the hydraulic excitations are largely dependent on the operating conditions (Kanki et al., 1981). Generally they are composed of rotational frequency f_N , blade passing frequency $f_N Z_i$, their harmonics and the broad band components at low frequencies caused by the turbulence in the flow. At reduced flowrate the blade passing and broad band components increase significantly. The vibration level of a pump caused by these hydraulic forces is generally higher than other rotating machines. However, the hydraulic forces on the impeller shrouds and wear rings generally act to reduce vibration at subcritical speeds, as shown by the spring and damping effect of the wear rings. This might be the reason why the pumps can be operated without problems with higher levels of vibration measured at the bearing housing.

Figure 2 shows the relation between the vibrations at rated and non-rated flow including all types of pumps (overhung or between bearing pumps with horizontal shaft, and vertical shaft pumps) of the present survey. The rated flow is basically defined as the best efficiency point, and the non-rated flow is defined below 40% of it, in this figure. Although we observe large scatter the vibration level at non-rated flow is, on the average, about 2.7 times as large as that at rated flow. This fact is reflected in the ISO 10816-3 by restricting the application of the vibration criteria only to the rated operating conditions.

Measurements of Vibration Severity

The vibration severity is defined as the rms values. Vibration severity rms values are more widely used than zero-to-peak values. For sinusoidal waves, the rms values can be estimated by dividing

Nomenclature

f = frequency (Hz)
 f_c = lowest natural frequency (Hz)
 f_N = rotational frequency of pump (Hz)
 L = driver output (kW)
 N = rotational speed of pump (rpm)
 n = number of pumps

V = rms value of vibration velocity (mm/s rms)
 V_{nr} = rms value of vibration velocity at non-rated flow (mm/s rms)
 V_p = zero-to-peak value of vibration velocity (mm/s^{0.5})

V_r = rms value of vibration velocity at rated flow (mm/s rms)
 Z = mechanical impedance
 Z_i = number of impeller blades

Table 2 Zone boundaries of ISO 10816-3

Support Class	Zone Boundary	Velocity (mm/s rms)				Displacement ($\mu\text{m rms}$)			
		Group 1	Group 2	Group 3	Group 4	Group 1	Group 2	Group 3	Group 4
Rigid	A/B	2.3	1.4	2.3	1.4	29	22	18	11
	B/C	4.5	2.8	4.5	2.8	57	45	36	22
	C/D	7.1	4.5	7.1	4.5	90	71	56	36
Flexible	A/B	3.5	2.3	3.5	2.3	45	37	28	18
	B/C	7.1	4.5	7.1	4.5	90	71	56	36
	C/D	11.0	7.1	11.0	7.1	140	113	90	56

the zero-to-peak values by the square root of 2. However, pump vibrations are composed of various frequency components and the above relation may not be applicable for estimating the rms values. This relationship was checked at an early stage of the present survey. Figure 3 shows the ratio of rms values to the zero-to-peak values measured on horizontal shaft pumps around rated flow. It shows that the ratio is significantly smaller than the ratio of unity to square root of 2 and large scatters are included. Based on this data, estimation of the rms values from zero-to-peak values was abandoned and vibration severity meters based on ISO 2954 (1975) using "rms" were used throughout this study. It should be mentioned that some severity meters detect the "average" or "rms" value, but are scaled to display this as the "peak" reading of a sinusoidal signal; this does not give a true "zero-to-peak" measurement for other kinds of signal.

Results of Measurements

It is most appropriate for the discussion of the vibration criteria to be based on the in situ vibration data of a long-term operated pump without vibration problems. So, the vibration measurements were carried out for low power pumps with power up to 300 kW and for high-speed and high-power pumps such as boiler feed pumps as well as pumps with integrated driver. The measurements were made following an unified procedure and the data were

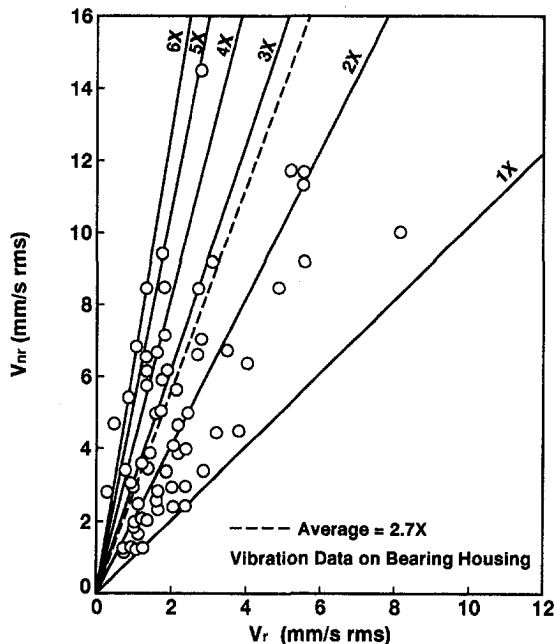


Fig. 2 Relationship between rated flow and non-rated flow vibrations (measurement uncertainty in $V_r \pm 2$ percent, in $V_{nr} \pm 2$ percent)

Horizontal Shaft Pump
Measurement Direction
Vertical, Horizontal & Axial (Total 294 Data)

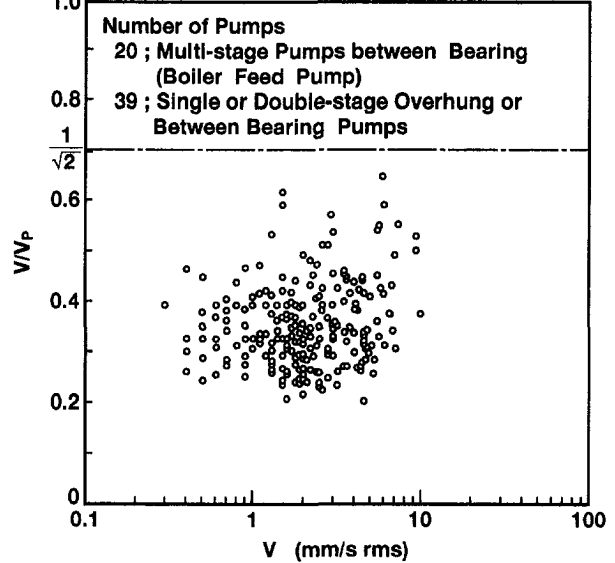


Fig. 3 The ratio of rms value of zero-to-peak value (measurement uncertainty in $V \pm 2$ percent, $V/V_p \pm 4$ percent)

recorded on a form prepared by the W. G.. Vibration meters based on ISO 2954 were used after calibration.

Low Power Pumps With Separate Driver. To unify the design conditions, pumps based on ISO or API were selected for the survey, which have been operated satisfactorily over ten years in situ. The outline of the measurements is summarized as follows:

- (1) Driver output: 15 to 300 kW
- (2) Pump type: 100 sets in total
 - Mainly single or double-stage pumps
 - 53 sets of overhung pumps with horizontal shaft
 - 31 sets of between bearing pumps with horizontal shaft
 - 16 sets of vertical shaft pumps
- (3) Locations and directions of vibration measurement point:
 - Horizontal shaft pumps: at the center of bearing housings (vertical, horizontal and axial)
 - Vertical shaft pumps: at the top of the motor frame (discharge direction, normal to the discharge direction and vertical direction)
- (4) Measuring items:
 - Vibration velocity, vibration displacement (rms and 0-P)
 - Predominant frequency and operating flowrate
 - Natural frequency of pump structures
- (5) Measuring conditions:
 - At rated speed and temperature (15 to 315°C)
 - Around rated flow: flow range from 50 to 120% of best efficiency point

In Fig. 4, the maximum vibration velocity taken from the data for three vibration directions is plotted against the driver output or rotational speed. We observe no systematic dependences on the power or speed. This shows that the classification depending on power is not required for pumps, unlike other types of rotating machines. The measurements were made around rated flow. Figure 5 shows the histograms of the pump number distributions against the vibration velocity for horizontal shaft pumps. Figure 5(a) is for the pumps with power 15 to 300 kW. In Fig. 5(a) the velocity criteria for Groups 2 and 3 for rigid supports are shown since most of the pumps in this category have rigid supports. If we apply the criteria for Group 2 machines, only 73% of the healthy pumps fall

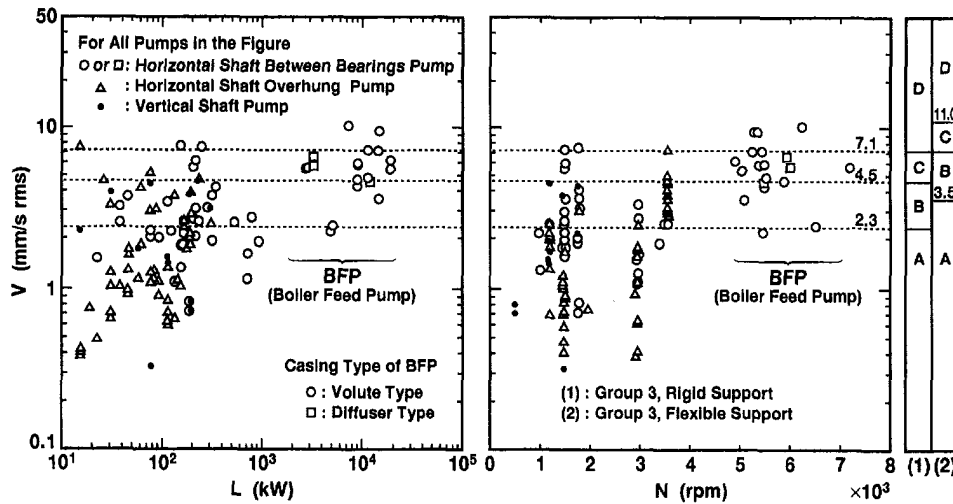


Fig. 4 Vibration velocity level of pumps with separate driver (Group 3) (measurement uncertainty in $V \pm 2$ percent)

into zone A or B categories but this number increases to 90% if we apply the criteria for Group 3. This shows the appropriateness of specifying the criteria for pumps as Group 3. On the other hand, vertical shaft pumps usually have flexible supports and all of the present data fall into zone A or B even if we apply the criteria for Group 3 machines.

High Speed, High Power Pumps With Separate Driver.

The vibration levels of the pump sets with power above 300 kW, which have been operated satisfactorily over ten years in situ, were also measured according to the same procedures as explained for low power pumps. Figure 4 includes 26 data of pumps with power above 300 kW. To unify pump design, high-speed, high-power, horizontal shaft, multi-stage pumps exceeding 3600 rpm and 1 MW such as used for BFPs (boiler feed pumps) in thermal power plants were selected, including 17 sets with volute type casing and 3 sets with diffuser type casing. Vibration data on pumps were obtained with their speed range 4900 to 7200 rpm and power range 2.7 to 18.5 MW. The flowrate was kept between 70% and 110% of the best efficiency point, and the rotational speed range was above 90% of rated speed. The temperature of the fluid was kept between 150 and 190°C, which was rated temperature for the pump. As an example, the data sheet of a boiler feed pump is shown in Fig. 6.

As shown in Fig. 4, the vibration levels of BFPs are significantly higher than these of low power pumps. This is considered to be caused by higher rotational velocity and flexible supports of these types of pumps. Figure 5(b) is for the pumps above 1 MW and exceeding 3600 rpm, and shows that only 20% of the present data fall into zone A or B if we apply the criteria for Group 3 rigid support but 80% based on the flexible support criteria. Figure 7 shows the vibration spectrum of the BFP shown in Fig. 6. The

blade passing frequency ($f_N Z_i = 420$ Hz) component is predominant. This is typical for high speed pumps. Figure 8 shows the result of excitation test on the BFP shown in Fig. 6. The lowest natural frequency of the pump structure (51.5 Hz) is smaller than the pump rotational frequency and the predominant blade passing

Measured Vibration Data for Pumps

Pump Name	Boiler Feed Pump		Pump Type	Horizontal Multi Stage			
Use	Boiler Feed for Thermal Power Station		Driver	Double Volute			
Rated Flow (m ³ /h)	1750		Driver Output (kW)	18500			
Rated Head (m)	3350		Rotational Speed (rpm)	5250			
B.F.P. Flow (m ³ /h)	1750		Bearing Type	Sleeve			
Liquid	Boiler Feed Water		Standard	JIS			
Liquid Temp. (°C)	149		VIBROPORT (SCHENK)				
Operating Years	17 Years		Vibration Meter Type (Maker)	VIBROPORT (SCHENK)			
Measured Value	Measured Data Aug., 25, 1995						
Measured Condition							
Flow (m ³ /h) Q	Speed (rpm) N		f_N ; Rotational Frequency of Pump (Hz)				
1650	5040		Z_i ; Number of Impeller Blades (-5)				
Bearing Housing Vibration							
Coupling Side							
End Side							
Vertical Horizontal Axial Vertical Horizontal Axial							
Velocity	mm/s rms	4.9	5.3	3.2	5.2	4.0	4.2
Velocity	mm/s O-P	16.1	18.2	13.4	19.8	11.6	15.3
Displacement	mm rms	8.9	8.0	2.6	7.9	7.1	3.5
	mm P-P	21.5	30.0	16.2	34.2	30.3	21.6
Dominant Freq. (Hz)	840 (2f _N Z _i)	420 (f _N Z _i)	84 (f _N)	420 (f _N Z _i)	84 (f _N)	84 (f _N)	840 (2f _N Z _i)

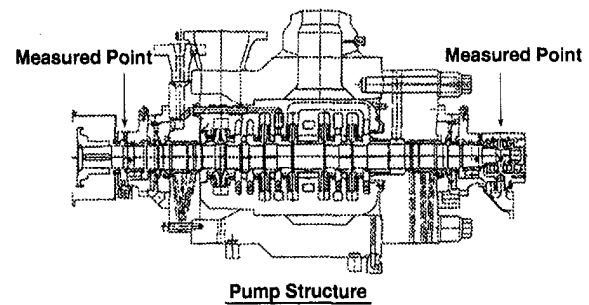


Fig. 6 An example of BFP vibration investigation

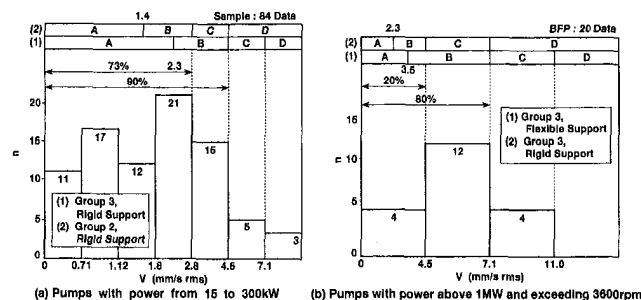


Fig. 5 Pump number distribution against vibration level, horizontal shaft pumps (measurement uncertainty in $V \pm 2$ percent)

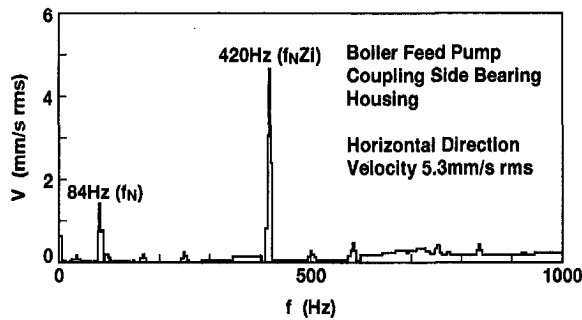


Fig. 7 An example of BFP vibration spectrum (measurement uncertainty in $f \pm 2.5$ Hz, in $V \pm 2$ percent)

frequency ($f_n Z_i = 420$ Hz). It means that the pump is classified to have flexible support. Generally structures of BFP have the lowest natural frequency below 100 Hz which is much smaller than the blade passing frequency. Hence, the application of the flexible support criteria to the boiler feed pumps is quite reasonable.

Pumps With Integrated Driver. Smaller values of vibration criteria are proposed for Group 4 pumps with integrated driver such as sealless type pumps. This might be because the vibration caused by the misalignment can be avoided for these pumps. For this type of pump, 35 sets of data on overhung, single-stage, and sealless type pumps were obtained with their power range 0.85 to 400 kW. Figure 9 shows the plots of these data similar to those in Fig. 4, and includes 21 sets of the data for pumps below 15 kW. These data are outside the range covered by the ISO 10816-3, but helpful to examine the vibration characteristics of integrated driver pumps including those above 15 kW. The natural frequency could be measured for 13 pumps, and the results are shown in Fig. 10. Owing to the higher rotational speed (2 poles: 50 Hz or 60 Hz) and larger mass/support flexibility ratio (caused by the integrated driver), the lowest natural frequency is around or smaller than the rotational frequency. So the pumps with integrated driver have flexible supports. All of the present pumps show a smaller vibration level than the B/C boundary for flexible support pumps. However the criteria should be reexamined when pumps with higher speed and higher power are developed in the future.

Comparison of Fig. 9 with Fig. 4 shows that the vibration level of integrated driver pumps is not significantly smaller than for other types of pumps. This may be caused by the flexible supports of integrated driver pumps.

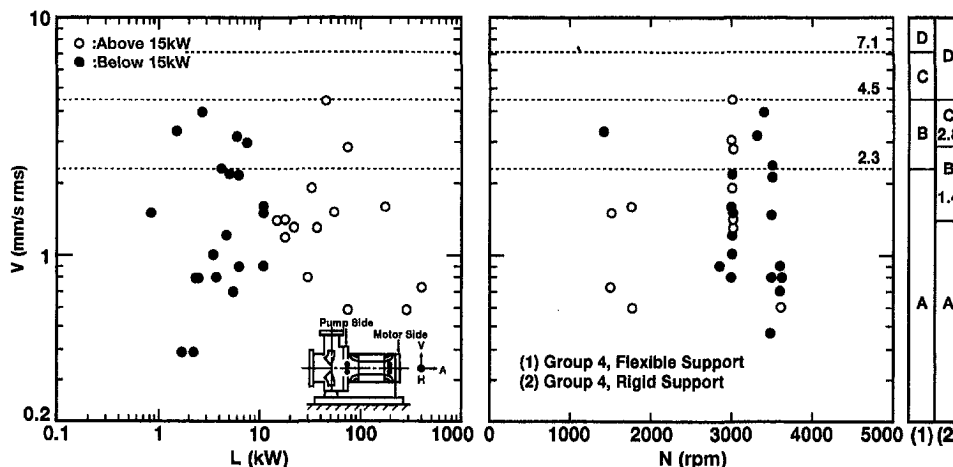


Fig. 9 Vibration velocity level of pumps with integrated driver (Group 4) (measurement uncertainty in $V \pm 2$ percent)

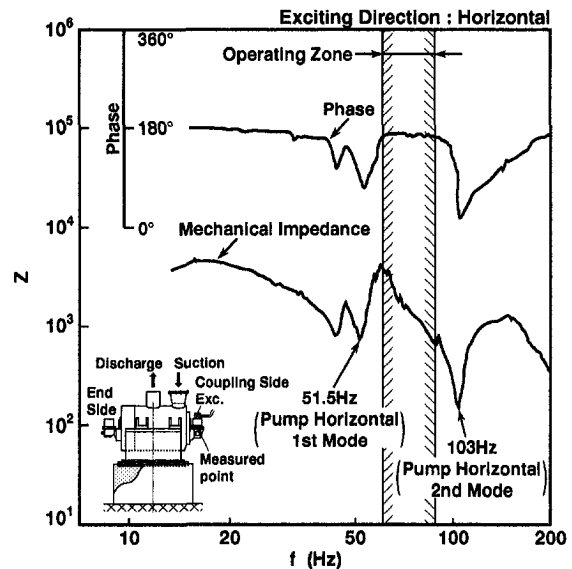


Fig. 8 BFP excitation test result (measurement uncertainty in $f \pm 0.25$ Hz, in $Z \pm 4$ percent)

From the above discussions the ISO 10816-3 proposes more reasonable criteria at least for B/C boundaries.

The Definition of Zone A. So far the discussions have mainly concentrated on the B/C boundaries. In the ISO 10816-3 a new definition for zone A is introduced: "newly commissioned machines would normally fall within this zone." This definition might be adequate for other types of machines but not for pumps as shown by the data in Figs. 5 and 9. There should be further discussion on it. One possible definition for pumps might be "the machines which fall within this zone are considered to be fine."

Comparison With Other Vibration Criteria

If we assume that the vibration is a sinusoidal one with a known frequency, the vibration criteria in displacement and velocity can be related with each other and shown in one chart. Also the conversion from rms values to zero-to-peak values is possible. For the comparison of the ISO 10816-3 with other criteria, the B/C boundary for Group 3 with rigid support is converted to zero-to-peak values and shown in Fig. 11 along with other criteria for pumps (API 610-7th, 1989; API 610-8th, 1995; HI, 1982; JIS B

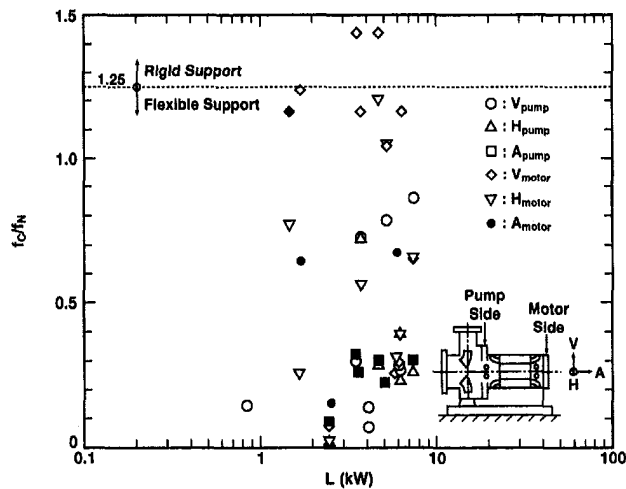


Fig. 10 Support condition for pumps with integrated driver (measurement uncertainty in $f_0/f_N \pm 4$ percent)

8301, 1990). The portion with positive slope comes from the limits on the displacement and the flat part from the velocity. We observe that the B/C boundary with rigid support is very close to other criteria for pump vibration apart from API 610 8th edition defined as lower vibration levels.

Conclusion

Results of field measurements of pump vibrations are presented. No explicit systematic dependence on driver output or rotational speed was observed. However, it was found that BFPs with larger driver output and higher rotational speed have larger vibration levels than those pumps of less than 300 kW driver output. This might be caused by the higher hydrodynamic forces due to higher rotational speed and by the flexible support for the BFPs. Although it is expected that pumps with integrated driver have lower vibration level, the measured level was not significantly lower than for other types of pumps. This is supposed to be caused by flexible supports of those pumps.

These data were used to examine the vibration criteria of the ISO 10816-3. It was found that the criteria for B/C boundary is

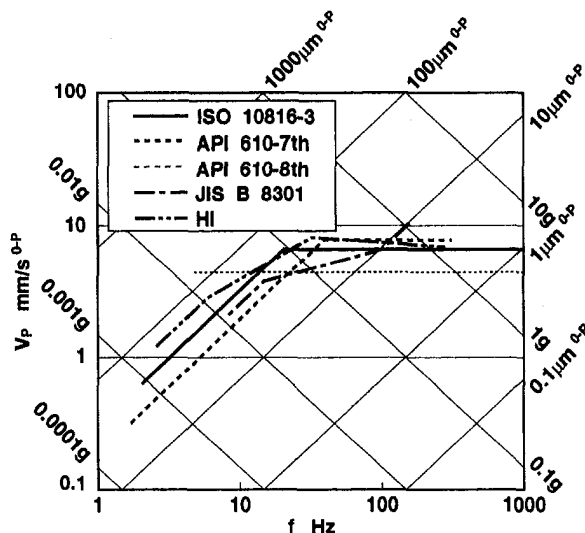


Fig. 11 Comparison of ISO with other vibration criteria

quite satisfactory, although the definition of zone A may require further discussion.

Acknowledgments

The present field study was made possible by the understanding and support of pump users. The authors would like to express sincere thanks to them. Professors H. Kanki of Kobe University, J. Kurokawa of Yokohama National University, K. Kikuyama of Nagoya University should be acknowledged for their valuable discussion and support. The present study was carried out under the cooperation of the following committee members of the W. G. of the Turbomachinery Society of Japan. Their contributions should be greatly acknowledged.

List of the W. G. Members

Chairman:

Professor Yoshinobu Tsujimoto of Osaka University

Manager:

Takashi Kawakami of Mitsubishi Heavy Industries, Ltd.

Committee:

Akira Manabe of Hitachi, Ltd.

Hideki Kanno of Ebara Corporation

Kotaro Karita of Teikoku Electric Mfg. Co., Ltd.

Masateru Toride of Nikkiso Co., Ltd.

Masato Eguchi of Ebara Research Co., Ltd.

Masayuki Kon of Osaka Gas Co., Ltd.

Shoichi Yonemura of Kubota Corporation

Tadashi Yokoi of Toyo Engineering Corporation

Taizou Aoyama of Chiyoda Corporation

Tatsumi Kimura of DMW Corporation

Tetsuro Ozono of Ishikawajima-Harima Heavy Industries Co., Ltd.

Toshikazu Irie of Osaka Gas Co., Ltd.

Toshiyuki Osada of Mitsubishi Heavy Industries, Ltd.

Yasuo Handa of Torishima Pump Mfg. Co., Ltd.

Yoshitomi Katsube of Awamura Manufacturing Co., Ltd.

Yuji Kanemori of Torishima Pump Mfg. Co., Ltd.

References

- API Standard 610, 1989, "Centrifugal Pumps for General Refinery Services," American Petroleum Institute, 7th edition, pp. 19-Fig. 6A.
- API Standard 610, 1995, "Centrifugal Pumps for Petroleum, Heavy Duty Chemical, and Gas Industry Services," American Petroleum Institute, 8th edition, pp. 2-18-Table 2-5.
- Hancock, W. P., et al., 1974, "How to Control Pump Vibration," *Hydrocarbon Processing*, Mar., pp. 107-113.
- Hydraulic Institute Standards for Centrifugal, 1982, "Rotary & Reciprocating Pumps," Hydraulic Institute, 14th edition, pp. 118.
- ISO 2372, 1974, "Mechanical Vibration of Machines with Operating Speeds from 10 to 200 rev/s-Basis for Specifying Evaluation Standards," International Organization for Standardization.
- ISO 2954, 1975, "Mechanical Vibration of Rotating and Reciprocating Machinery-Requirements for Instruments for Measuring Vibration Severity," International Organization for Standardization.
- ISO 3945, 1977, "Mechanical Vibration of Large Rotating Machines with Speed Range from 10 to 200 rev/s-Measurement and Evaluation of Vibration Severity in Situ," International Organization for Standardization.
- ISO 10816-3, 1998, "Mechanical Vibration-Evaluation of Machine Vibration by Measurements on Non-rotating Parts-," International Organization for Standardization.
- Japanese Industrial Standard JIS B8301, 1990, "Testing Methods for Centrifugal Pumps, Mixed Flow Pumps and Axial Flow Pumps," Japanese Standards Association.
- Kanki, H., et al., 1981, "Experimental Research on the Hydraulic Excitation Force on the Pump Shaft," ASME 81-DET-71, pp. 5.
- Lifson, A., et al., 1987, "Vibration Limits for Rotating Machinery," *Mechanical Engineering*, June, pp. 60-63.
- Maten, S., 1972, "Velocity Criteria for Machine Vibration," *Vibration and Acoustic Measurement Handbook*, Spartan Books, New York, Washington, pp. 267-277.
- Rathbone, T. C., 1939, "Vibration Tolerance," *Power Plant Engineering*, Vol. 43, pp. 721.
- Sagisawa, S., et al., 1981, (in Japanese), *Vibration Engineering Handbook*, Yokendo, Ltd., Tokyo, pp. 775.
- Someya, T., et al., 1989, *Journal-Bearing Databook*, Springer-Verlag, Berlin, Germany, pp. 313-323.
- VDI 2056, 1964, "Beurteilungsmaßstäbe für Mechanische Schwingungen von Maschinen."

Chen Zuoyi

Professor.

Wang Jihong

Doctor.

Liu Hong

Ph. D. Student.

Department of Thermal Engineering,
Tsinghua University,
Beijing, China, 100084

Three-Dimensional Numerical Analysis of Flow-Induced Vibration in Turbomachinery

1 Introduction

Flow induced vibration is an important subject in fluid engineering, for it concerns the safety of the fluid-body system. It exists in the power and energy, oceanic, civil, chemical, mechanical, and biological engineering. It involves interacting of the fluid oscillation and body deformation, and solution of this kind of problem involves solution of unsteady fluid dynamic problem and that of the aeroelastic problem. Because it often occurs under complex flow conditions, an experimental method is not always applicable or effective or economical. Many 2-D and 3-D numerical methods have been developed in the past decade (Wolff and Fleeter, 1990; Osama et al., 1990; Kandil and Chang, 1989; He and Deton, 1994). An evaluation of the 3-D inviscid method is given by Gerolymos and Vallet (1996). The purpose of this paper is to develop a 3-D viscous numerical method for analyzing the safety of the fluid-body system in turbomachinery.

The basic idea of analyzing the problem with the oscillating fluid mechanics method (OFMM) is as follows. When a body is vibrating in the flow field, the motion of the body interacts with the fluid around it. The vibration will be excited or attenuated by the oscillating hydrodynamic force. The stability of the vibrating system is subjected to the energy criterion. If energy is transferred from the oscillating flow to the vibrating body, the vibration system will be unstable. There are two kinds of flow induced vibration. One is the self-excited vibration, in which the vibration of the body is produced originally by a mechanical or some other outer disturbance (this type of disturbance is unavoidable), and the vibration starts at the intrinsic frequency of the body. For example, the flutter of wings or blades belongs to this kind, with respect to which, it is of interest whether the flow field will excite the vibration when it starts. At the beginning, the oscillating of the flow field caused by the vibrating body is relatively small to the steady flow. Therefore, an oscillating parameter can be decomposed into the steady quantity and a small perturbation. The other kind is the flow forced vibration, in which the vibration of the body is caused originally by the unsteady flow field around it and may contain various frequency elements. For example, nonuniform coming flow from upstream will cause vibration of the rotating blades. To this type of vibration, the perturbation is not relatively small to the flow field. Then, local linearization is used to model the unsteady $N-S$ equations. On the basis of Fourier transformation, an oscillating parameter consists of a series of small harmonic components, each of which is solved, respectively, by using the amplitude equations.

A semi-analytical numerical method—Parametric Polynomial

Method (PPM) (Chen and Shu, 1990) is used to solve the 3-D steady and oscillating flow. According to the PPM, flow parameters are expanded with the polynomials of coordinate variables. The coefficients of the polynomials are only functions of the coordinate variable along the main flow direction. Thereby, the partial differential equations are transformed into the ordinary differential equations. This approach can save a lot of computing time and storage.

Upon applying this 3-D numerical method, three types of flow induced vibrations have been analyzed, which are stall flow induced stall flutter in steam turbine, labyrinth seal flow induced shaft vibration, non-uniform coming flow induced rotor blades vibration. The numerical results are compared with the experimental data.

2 Physical and Mathematical Model of 3-D Viscous Flow

According to the basic relations of oscillating fluid mechanics (Chen and Jiang, 1988), if the vibration of the body causes a small perturbation in the flow field, the flow parameters and their time derivatives can be represented as,

$$q(\xi, \eta, \zeta, t) = \bar{q}(\xi, \eta, \zeta) + \tilde{q}(\xi, \eta, \zeta)e^{i\omega t} \quad (1)$$

$$q_i(\xi, \eta, \zeta, t) = i\omega\tilde{q}_i(\xi, \eta, \zeta)e^{i\omega t} \quad (2)$$

In which, ω is the angular velocity of the vibrating body ($\omega = 2\pi f$). The superscript ' \sim ' designates steady components, which are solved through the steady equations. ' $\tilde{}$ ' designates the amplitude of the oscillating components. Substituting them into the basic equations leads to the amplitude $N-S$ equations as follows,

Amplitude continuity equation:

$$i\omega\bar{\rho} + \nabla \cdot (\bar{\rho}\bar{\mathbf{W}}) + \nabla \cdot (\bar{\rho}\tilde{\mathbf{W}}) = 0 \quad (3)$$

Amplitude momentum equations:

$$i\omega\bar{\rho}\bar{\mathbf{W}} + \bar{\rho}\tilde{\mathbf{W}} \cdot \nabla\bar{\mathbf{W}} + \bar{\rho}(\bar{\mathbf{W}} \cdot \nabla\tilde{\mathbf{W}} + \tilde{\mathbf{W}} \cdot \nabla\bar{\mathbf{W}}) + \bar{\mathbf{G}} = -\nabla\bar{p} + \nabla \cdot \bar{\mathbf{\Pi}} \quad (4)$$

Amplitude energy equation

$$i\omega(\bar{\rho}\bar{p} - \gamma\bar{\rho}\bar{p}) + \bar{\rho}\tilde{\mathbf{W}} \cdot \nabla\bar{p} + \bar{\rho}(\bar{\mathbf{W}} \cdot \nabla\tilde{p} + \tilde{\mathbf{W}} \cdot \nabla\bar{p}) - \gamma\bar{\rho}\tilde{\mathbf{W}} \cdot \nabla\bar{p} - \gamma\bar{\rho}(\bar{\mathbf{W}} \cdot \nabla\tilde{p} + \tilde{\mathbf{W}} \cdot \nabla\bar{p}) = (\gamma - 1)(\bar{\rho}\tilde{\Phi} + \bar{\rho}\tilde{\Phi}) \quad (5)$$

In which, such terms as $\bar{\rho}\nabla \cdot \bar{\mathbf{W}}$, $\bar{\rho}\tilde{\mathbf{W}} \cdot \nabla\bar{p}$ etc. couple the steady flow with the oscillating flow, denoting the dependence of the amplitude parameters on the steady parameters. Velocities are nondimensionalized by the inlet axial velocity w_{z0} , density is

Contributed by the Fluids Engineering Division for publication in the JOURNAL OF FLUIDS ENGINEERING. Manuscript received by the Fluids Engineering Division February 8, 1999; revised manuscript received June 8, 1999. Associate Technical Editor: D. P. Telionis.

nondimensionalized by the inlet density ρ_0 , and static pressure is nondimensionalized by $\rho_0 W_{20}^2$. First, the steady equations are solved to determine the steady parameters. Then, amplitude equations (3)–(5) are solved on the basis of the steady flow field.

Both steady parameters and amplitude parameters are represented by parametric polynomials of coordinates ξ and η , the polynomial coefficients are only the function of coordinate ζ , that is

$$q(\xi, \eta, \zeta) = \sum_{j=0}^J \sum_{k=0}^K C_{jk}(\zeta) \xi^j \eta^k \quad (6)$$

The amplitude parameters \bar{w}_r , \bar{w}_θ , \bar{w}_z , $\bar{\rho}$, \bar{p} are represented as,

$$\begin{aligned} \bar{w}_r &= \sum_{j=0}^{J_1} \sum_{k=0}^{K_1} C_{jk}^1(\zeta) \xi^j \eta^k, & \bar{w}_\theta &= \sum_{j=0}^{J_2} \sum_{k=0}^{K_2} C_{jk}^2(\zeta) \xi^j \eta^k, \\ \bar{w}_z &= \sum_{j=0}^{J_3} \sum_{k=0}^{K_3} C_{jk}^3(\zeta) \xi^j \eta^k \\ \bar{\rho} &= \sum_{j=0}^{J_4} \sum_{k=0}^{K_4} C_{jk}^4(\zeta) \xi^j \eta^k, & \bar{p} &= \sum_{j=0}^{J_5} \sum_{k=0}^{K_5} C_{jk}^5(\zeta) \xi^j \eta^k \end{aligned} \quad (7)$$

Upon substituting them into Eqs. (3)–(5), the basic equations are then transformed to ordinary differential equations about the polynomial coefficients $C_{jk}^1, \dots, C_{jk}^5$. Equations (3)–(5) are rewritten as,

$$\begin{aligned} \sum_{j=0}^{J_1} \sum_{k=0}^{K_1} Q^1 \frac{dC_{jk}^1}{d\zeta} + \sum_{j=0}^{J_2} \sum_{k=0}^{K_2} Q^2 \frac{dC_{jk}^2}{d\zeta} + \sum_{j=0}^{J_3} \sum_{k=0}^{K_3} Q^3 \frac{dC_{jk}^3}{d\zeta} \\ + \sum_{j=0}^{J_4} \sum_{k=0}^{K_4} Q^4 \frac{dC_{jk}^4}{d\zeta} + \sum_{j=0}^{J_5} \sum_{k=0}^{K_5} Q^5 \frac{dC_{jk}^5}{d\zeta} = S \end{aligned} \quad (8)$$

where

$$Q^1 = \begin{bmatrix} \bar{\rho} \zeta_r r^j \theta^k \\ \bar{\rho} \chi r^j \theta^k \\ 0 \\ 0 \\ 0 \end{bmatrix}, \quad Q^2 = \begin{bmatrix} \bar{\rho} \zeta_\theta r^j \theta^k \\ 0 \\ \bar{\rho} \chi r^j \theta^k \\ 0 \\ 0 \end{bmatrix}, \quad Q^3 = \begin{bmatrix} \bar{\rho} \zeta_z r^j \theta^k \\ 0 \\ 0 \\ \bar{\rho} \chi r^j \theta^k \\ 0 \end{bmatrix},$$

$$Q^4 = \begin{bmatrix} \chi r^j \theta^k \\ 0 \\ 0 \\ 0 \\ -\gamma \bar{p} \chi r^j \theta^k \end{bmatrix}, \quad Q^5 = \begin{bmatrix} 0 \\ \zeta_r r^j \theta^k \\ \zeta_\theta r^j \theta^k \\ \zeta_z r^j \theta^k \\ \chi r^j \theta^k \end{bmatrix}$$

and

$$\chi = (\bar{w}_r \zeta_r + \bar{w}_\theta \zeta_\theta + \bar{w}_z \zeta_z)$$

The parametric polynomial coefficients $C_{jk}^1, \dots, C_{jk}^5$ are to be solved. All other terms in Eqs. (3)–(5) are placed in the right-hand side of Eq. (8), and they are computed explicitly. The polynomial order i.e., J and K is related with the flow character. In this paper, J and K are all equal to three.

3 Solving Procedure

The model equation of (8) is,

$$B(\mathbf{Y}) \frac{d\mathbf{Y}(\zeta)}{d\zeta} = f(\zeta, \mathbf{Y}),$$

$$\mathbf{Y} = (C_{11}^1, \Lambda, C_{1K_1}^1, \Lambda, C_{11}^5, \Lambda, C_{J_4 K_4}^5)^T \quad (9)$$

Rotor diameter	d=150.0mm
Seal pitch	B=5.08mm
Seal height	h=3.18mm
Seal width	b=1.5mm
Clearance gap	l=1.25mm

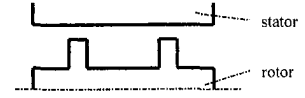


Fig. 1 The seal calculated

where B is a matrix whose elements are only related to the steady parameters, so the function is linear. While solving the steady flow field, B is a matrix function of the polynomial coefficients of the steady parameters; the corresponding model equation is a nonlinear one. The space-marching procedure from the number n station to the $n+1$ of above equation consists of two steps,

Step 1. Predicting step

$$B(\mathbf{Y}_n)(\mathbf{Y}_{n+1}^0 - \mathbf{Y}_n) = \Delta \zeta \cdot f(\zeta_n, \mathbf{Y}_n) \quad (10)$$

Step 2. Modifying step

$$B(\mathbf{Y}_{n+1}^k)(\mathbf{Y}_{n+1}^k - \mathbf{Y}_n) = 0.5 \Delta \zeta \cdot [f(\zeta_n, \mathbf{Y}_n) + f(\zeta_{n+1}, \mathbf{Y}_{n+1}^k)] \quad (11)$$

Which is iterated till

$$\|\mathbf{Y}_{n+1}^k - \mathbf{Y}_{n+1}^{k-1}\| < \text{Expected precision}$$

Generally, less than 5 iterations are necessary to attain a reasonable accuracy. A single sweep is suitable for the amplitude equations; multiple sweeps is needed for the steady equations.

While analyzing the forced vibration induced by oscillating coming flow, in which small perturbation theory is inapplicable, the Fourier transformation is used. An unsteady parameter can be represented as,

$$q(\xi, \eta, \zeta, t) = \bar{q}(\xi, \eta, \zeta) + \sum_{j=1}^N \bar{q}_j(\xi, \eta, \zeta) e^{i\omega_j t} \quad (12)$$

By substituting it into Eqs. (3)–(5), the same kind of amplitude equations as Eqs. (3)–(5) will be derived out for each harmonic. What should be emphasized here is that correlative terms of low frequency harmonics will appear in the amplitude equations of the higher frequency harmonic.

4 Calculation Examples

(a) **Labyrinth Seal Flow Induced Shaft Vibration.** The labyrinth seal is important. It reduces the leakage in turbomachinery and improves efficiency. But the seal flow induced vibration can produce serious damage. There are two procedures in order to analyze seal flow induced vibration, one is to analyze stability of the seal itself, the other is to obtain the stiffness coefficient and damping coefficient of the seal, which is used as the basic data in analyzing stability of the whole axis system. By applying the 3-D numerical analysis system in this paper, the stiffness and damping coefficient of seal as shown in Fig. 1 are calculated. The calculated results are compared with the experiment and two control model method. As shown in Figs. 2 and 3, the 3-D numerical method in this paper is more advantageous than the two control volume model method.

(b) **Stall Flow Induced Vibration of Blades in a Steam Turbine.** Peak load, heat providing and air-cooling steam turbines often run at small flow conditions. It is known that when the flow rate reduces to a certain value, stall flow will occur in the last stage. This may induce the stall flutter of the last stage rotating blade. In order to ensure the safe running of the machine, it is necessary to analyze this type of flow-induced vibration. The stall flow field and stall flow-induced vibration in the last stage of a 200 MW steam turbine are calculated using the 3-D analysis method.

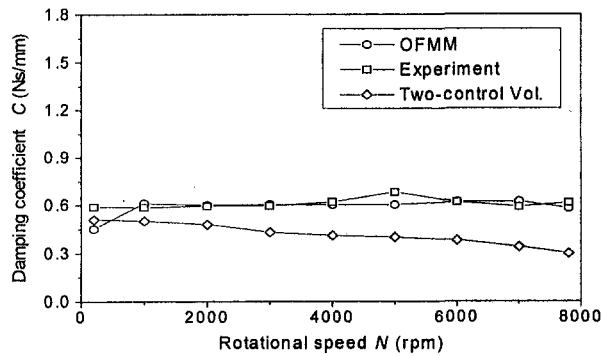


Fig. 2 Variation of damping coefficient versus rotational speed

The height of the stall region at the rotor outlet and the dynamic stress in the rotating blade are measured in an in-situ test. Comparison of the experimental and calculated stall height at the last rotor outlet is shown in Fig. 4. The work done by unsteady aerodynamic force under various operating conditions is shown in Fig. 5. At the point $G/G_0 = 0.32$ (G is the off design flow rate, G_0 is the design flow rate), the unsteady aerodynamic work changes from negative to positive. According to the energy criterion, the stall flow field will excite vibration of the blade. At the same time, the dynamic stress increases rapidly. The measured dynamic stress of the blade under various operating conditions is also shown in Fig. 5. It can be seen that the dynamic stress increases to a maximum at $G/G_0 = 0.34$, demonstrating agreement of the numerical result with the experimental data.

(c) **The Nonuniform Coming Flow Induced Vibration of Rotor Blades.** Nonuniform incoming flow induced vibration of blades in a testing turbine cascades is also calculated using the 3-D

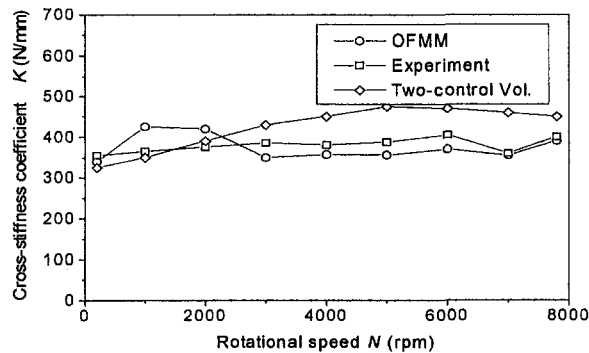


Fig. 3 Variation of cross-stiffness coefficient versus rotational speed

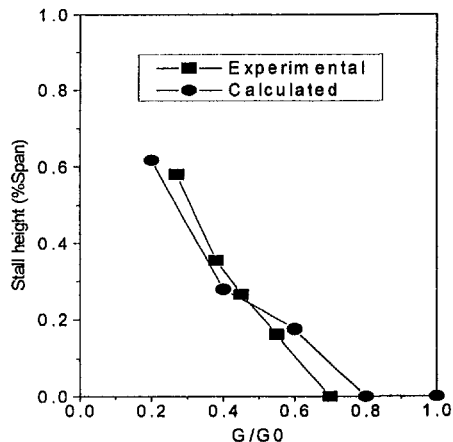


Fig. 4 Comparison of calculated stall height with the measured data

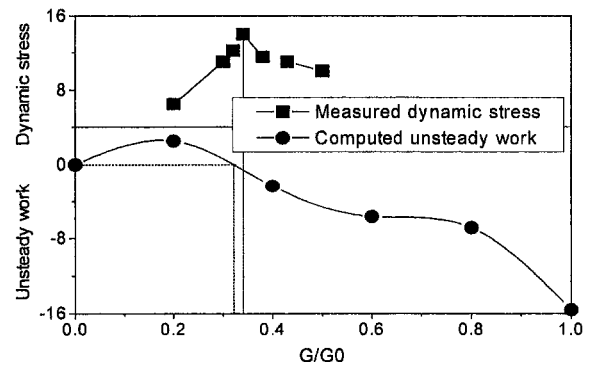


Fig. 5 Variation of calculated unsteady work and measured dynamic stress on the relative flow rate

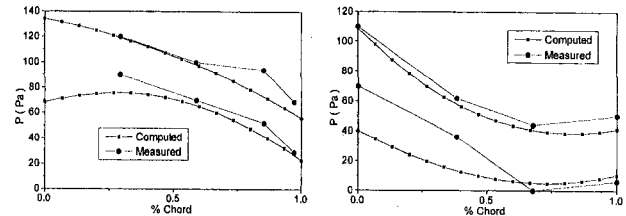


Fig. 6 Comparison of calculated maximum and minimal unsteady pressure distribution with the measured data (a) on the pressure surface, (b) on the suction surface

numerical method. The experiment is performed in the Gas Turbine Laboratory in Tsinghua University. The profile of the coming flow is,

$$w_z = w_{z0} \{1.0 - 0.3 \exp[-50.0(\theta/\Delta\theta)^2]\} \quad (13)$$

And other parameters are,

- Diameter of hub $d=45$ cm
- Height of blade $h=9$ cm
- Rotational speed $N=37$ rpm
- Number of blade $n=66$
- Incidence $i=0$
- Inlet Total Pressure $P_0=120$ Pa (gauge pressure)
- Outlet Pressure $P_2=25$ Pa (gauge pressure)
- Inlet mean velocity $w_{z0}=13.6$ m/s

Equation (12) is used to model the unsteady flow. The oscillations of the unsteady parameters are decomposed to seven harmonics, the frequencies of which are respectively the one to seven times of the blade's intrinsic frequency. The calculated maximum and minimum unsteady pressure distribution at mid span of the blade are shown in Fig. 6. The calculated results predict the same varying tendency of the amplitude of the oscillating pressure along the axial direction as in the experiment, demonstrating the effectiveness of the 3-D numerical analysis method.

Conclusion

A 3-D numerical method for analyzing flow-induced vibrations is developed, which combines the Oscillating Fluid Mechanic Theory with the Parametric Polynomial Method. It is an effective safety analysis approach for the design and operation of turbines. Labyrinth seal flow induced vibration, stall flow induced flutter of rotating blades and non-uniform coming flow induced vibration of rotor blades are analyzed using the method. Comparison with the experimental results demonstrates the reliability of the method in engineering application.

Acknowledgments

This work was supported by the National Natural Science Foundation of China.

References

- Blevins, R. D., 1977, *Flow Induced Vibration*, Van Nostrand Reinhold, pp. 10–30.
- Chen Zuoyi, Jiang Zikang, and Sun Xijiu, 1988, *Oscillating Fluid Mechanics*, China Hydroelectric Press, Beijing, pp. 22–44.
- Chen Zuoyi, and Shu Hong, 1990, "The Parametric Polynomial Method for Determining Complex Flow," *Journal of Engineering Thermophysics*, Vol. 11, No. 1, pp. 44–46.
- Gerolymos, G. A., and Vallet, I., 1996, "Validation of Three-Dimensional Euler Method for Vibrating Cascade Aerodynamics," *ASME Journal of Turbomachinery*, Vol. 118, No. 10, pp. 771–782.
- He, L., and Deton, J. D., 1994, "Three-Dimensional Time-Marching Inviscid and Viscous Solution for Unsteady Flow Around Vibrating Blades," *ASME Journal of Turbomachinery*, Vol. 116, pp. 469–478.
- Kandil, O. A., and Chuang, H. A., 1989, "Unsteady Navier-Stokes computation Past Oscillating Delta Wing at High Incidence," AIAA-89-0081, pp. 1–10.
- Kirtley, K. R., and Lakshminarayana, B., 1985, "Computation of Internal Incompressible Separated Flows Using a Spacing-Marching Technique," 18th Fluid Dynamics and Plasmas Dynamics and Lasers Conference, Cincinnati, AIAA-85-1624, pp. 1–12.
- Kandil, Osama A., Chuang, H. Andrew, and Salman, Ahmed, A., 1990, "Unsteady Flow Computation of Oscillating Flexible Wings," 31st AIAA/ASME/ASCE/AHS/ASC Structures, Structural Dynamics and Materials Conference, New York, Part 3 (of 4): Structural Dynamics, AIAA-90-0937, pp. 1370–1381.
- Ramamurti, R., Ghia, U., and Ghia, K. N., 1991, "A Semi-Elliptic Analysis for 2-D Viscous Flows Through Cascade Configurations," *Computers and Fluids*, Vol. 20, No. 3, pp. 223–242.
- Rubin, S. G., and Reddy, D. R., 1983, "Analysis of Global Pressure Relaxation for Flow With Strong Interaction and Separation," *Computers and Fluids*, Vol. 11, No. 4, pp. 281–306.
- Wolff, J., and Fleeter, S., 1992, "Viscous Oscillating Cascade Aerodynamics and Flutter by a Locally Analytical Method," *Computational Mechanics*, Vol. 10, No. 3-4, pp. 203–215.
- Scharror, J. K., 1987, "Theory Versus Experiment for the Rotot Dynamic coefficients of Labyrinth Gas Seals Part 1—A Two Control volume Model," *Proceedings of 11 Biennial Conference on Mechanical Vibration and Noise*, Boston, MA, pp. 27–30.

A. Bernard

Postdoctoral Research Associate
Laboratoire de Mécanique de Lille,
Cité Scientifique, avenue Paul Langevin,
59655 Villeneuve D'Ascq Cédex
France

L.-E. Brizzi
Lecturer.

J.-L. Bousgarbiès
CNRS Researcher.

Laboratoire d'Etudes Aérodynamiques,
Boulevard 3, Teleport 2, BP 179,
86690 Futuroscope Cédex
France

Study of Several Jets Impinging on a Plane Wall: Visualizations and Laser Velocimetry Investigations

Different experimental techniques have been used in order to describe the flow pattern generated by fifteen jets impinging on a plane wall. The spreading over method revealed the jet influence on the impinging surface, particularly reattachment and detachment lines. The laser sheet visualizations show complex vortical structures such as the ground vortex and secondary rolling-ups near the target plate have been deduced. Velocity measurements have been realised to confirm these observations and to specify the flow pattern. A schema of the flow near the impinging wall is thus drawn.

Introduction

Various configurations are employed in the process of hot wall cooling. The "film cooling" technique used in the aeronautic industry to protect surfaces (combustion chamber walls or turbines blades) from thermal aggression gives good results. However, it is currently associated with a more recent method consisting of jets impinging on a wall. The cooling process obtained by this association is greatly improved and strengthens the protection of surfaces subject to strong thermal gradients. The improvement of these cooling techniques necessitates a better understanding of the involved fluid dynamic process.

Many investigations have been concerned with single jet impingement on a flat surface (Barata et al., 1993; and Knowles and Bray, 1993). The presence of a cross flow, induced or not, gives rise to a dominant structure upstream of the jet near the impinged wall named "ground vortex" that has already been observed experimentally (Barata et al., 1993; and Knowles and Bray, 1993) and found numerically (Barata et al., 1992; and Barata, 1991). Several jet configurations have been studied essentially from the thermal viewpoint (Van Treuren et al., 1993; and Liguó Li et al., 1990).

The dynamic aspect of the flow produced by a device consisting of fifteen jets impinging on a flat wall in a confined environment has been observed. To describe the flow near the impinged plate, various experimental techniques have been used (spreading over method, LASER sheet visualizations and velocity measurements).

Experimental Device

The test chamber is a right-angled parallelepiped in Altuglas ($240 \times 120 \times 20 \text{ mm}^3$) closed on three of its lateral sides (Fig. 1, Bernard, 1997). The fourth side is open and connected to a blower (operating in suction) by means of a metallic convergent device. A flowmeter is inserted between the convergent exit and the blower to regulate and measure the total flow rate Q_v . All channel walls (10 mm thick) are transparent to make visualisations and measurements by laser velocimetry easier. The upper wall is drilled with fifteen holes ($D = 10 \text{ mm}$) distributed in five rows of three orifices. Each hole is separated from the neighboring hole by a distance of $4D$. The lower wall which is the impinging surface is $2D$ under the injection one. On starting the blower, the ambient air

penetrates through the holes and impinges on the lower wall before flowing to the open exit. The injection Reynolds number characterizing the flow is based on the total flow rate Q_v and on the hole diameter D . This geometry was chosen with an industrial partner who has made computations to design a model that presents characteristics of a real blade, so in this study the main case of reference is for $Re_j = 12,600$.

Visualizations on the impinged wall have been realized by spreading a mixture of calcium carbonate particle suspended in oil (350 g/l) over the impinged wall before starting the blower. After a complete drying, the removable impinged plate is dismantled and then photographed.

Laser sheet visualizations have been performed with an Argon-Ion laser (7W maximal power) fitted with an optic fibre (10 m long) and an optical device giving a thin light sheet ($\approx 1 \text{ mm}$ thick). This device is used to illuminate sections of the flow seeded with a glycerine and water spray delivered by a generator.

Pictures have been recorded with a classical S-VHS camera (50 images per second). Some images have been chosen to be digitised and analyzed with a PC.

The velocity field has been measured by an LDA system with a DSA (Doppler Signal Analyser from Aerometrics). The light source was the same as that used for laser sheet visualizations. For LDA measurements the ambient air is seeded with an aerosol provided by a vegetable oil particle generator. Measurements have been taken in backward scatter mode coming into the test channel in a $2D$ high lateral side. The emission/reception probe emits four laser beams in two components measurements. These four beams form a pyramid with a 11.4° top angle and which is 300 mm high (focal length of the optical system). With this configuration, the volume probe size was 0.08 mm in diameter and 0.8 mm in length.

This particular arrangement, with beams entering the model through the lateral side, makes it difficult to obtain velocity measurements near the walls and the channel median plane. Each profile has been measured in three steps, by changing the incidence angle of the optical system. This angle is positive (inclination upwards $i = 6^\circ$) to obtain measurements in the vicinity of the upper wall ($1.4 \leq z \leq 2$) and negative (inclination downwards $i = -6^\circ$) for the measurements near the lower wall ($0 \leq z \leq 0.6$). For measurements in the central part of the channel ($0.6 \leq z \leq 1.4$) the optical system axis is not inclined. The angle change does not influence the mean value of the W component in the plane $y = 0$. Indeed, the two measured components are U (in the x direction) and $W^* = W \cos(i) \pm V \sin(i)$. As the mean value of V is zero in the symmetry plane ($y = 0$), then $W^* = W \cos(i) \approx W$ ($\cos(i) \approx 1$). Of course, this result cannot be applied

Contributed by the Fluids Engineering Division for publication in the JOURNAL OF FLUIDS ENGINEERING. Manuscript received by the Fluids Engineering Division August 4, 1997; revised manuscript received June 9, 1999. Associate Technical Editor: J. K. Eaton.

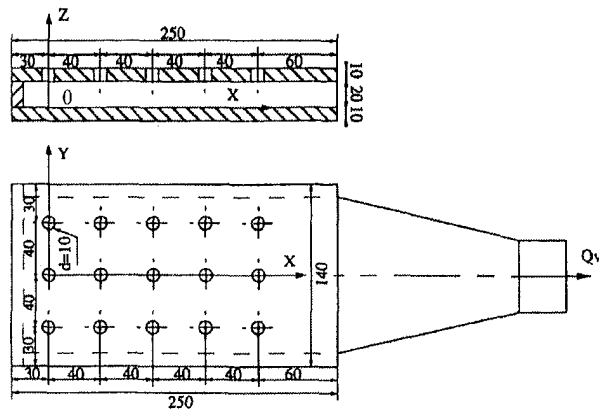


Fig. 1 Experimental test chamber

to the fluctuation values because generally the instantaneous V component is not zero, even in the symmetry plane. Results of measurements given elsewhere show that V and W are generally of the same order of magnitude, so that the term $V \sin(i)$ is about 10% of W^* .

No particular treatment has been used on the LDA results. The precision of the measurement has been estimated to be less than 1%, and the maximum bias at 3% for the mean values and at 6% for the RMS values. These include the statistical bias and the probe position uncertainty.

Results

Wall Streamlines Pattern. The spreading over method gives good results for the appearance of the flow in the immediate vicinity of the impinged wall. However, care must be taken when interpreting these results. The main disadvantage of this method is the integration of effects it produces because the coating drying time is variable. The wall streamlines have been obtained for five Reynolds numbers between 5,700 and 22,600. In each case, the results have shown a flow pattern similar to the one presented in Fig. 2.

This general view reveals the cellular aspect of the flow near the impinged wall and the symmetry property versus the median plane $y = 0$. In addition all impingement zones of the same row have a similar aspect. They indicate that the flow shows a quasi-periodic aspect along the lateral direction y , and that the planes $y = \pm 2$ and $y = \pm 6$ can be considered as partial symmetry planes. The symmetry property with respect to the planes $y = \pm 6$ shows that the lateral walls have approximately the same influence on the flow as two fictive rows of jets located in the virtual planes $y = \pm 8$.

Impingement zones characterized by divergent streamlines are clearly separated from each other. The central point from which all wall streamlines diverge can be located approximately. This one increasingly moves apart from the corresponding injection orifice axis as when moving to downstream positions. The impingement shape which is quasi quadrangular for the first row (on the left), rounds increasingly in its upstream part while approaching the

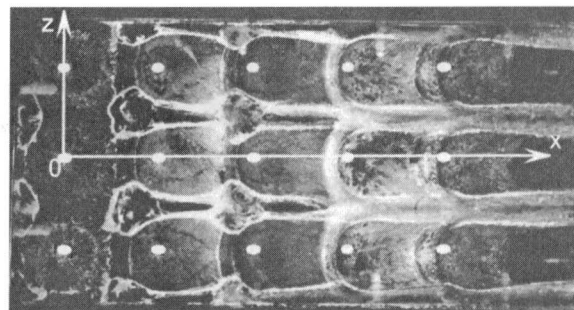


Fig. 2 General view of the wall streamlines ($Re_j = 12,600$)

exhaust (on the right). This evolution is due to the progressive increase of the flow rate along the test section. Indeed the flow rate per section increases with the x abscissa shown in Fig. 3. The impingement area shape also depends on the Reynolds number. A main characteristic of Fig. 2 is the presence of accumulated coating lines, with a horseshoe form, surrounding the upstream and sides of each impingement zone. This accumulation originates from a detachment phenomenon induced by the collision of two radial divergent flows generated by two neighboring impingements.

Visualizations such as Fig. 2 show that between two neighboring detachment lines there is a band in which streamlines present an "ear shape" structure characteristic of a reattachment phenomenon. This configuration type can be clearly observed on the picture presented in Fig. 4 which concerns the impingement zone of the central jet of the fourth row. Ear shape streamlines can be observed in front of the rounded part of the accumulation line which indicates that a detachment phenomenon exists also in this boundary region between impingements of the central jets of the third and fourth rows. There are no ear shape configurations downstream of the impingement zone (right side of Fig. 4) because the coating has not been added over this part of the surface in this case. Therefore the streamlines observed in this region have been created by the coating coming from upstream which does not penetrate into the impingement cell of the central jet of the next row. This observation confirms the existence of the detachment line downstream of each impingement zone. Visualizations by spreading over method show a network of individual streamlines near the impinged wall surface.

Laser Sheet Visualizations. To confirm some of the interpretations deduced from the examination of the wall streamlines, laser sheet visualizations have been carried out. A longitudinal section of the central jet of the fourth row ($y = 0$), is presented in Fig. 5. Only this jet is seeded. As it nears the impingement wall it can be observed that the jet deviates in the downstream direction. The distance between the impingement point and the corresponding injection orifice axis increases from row to row while progressing from upstream to downstream. The increase of the flow rate with the abscissa along the test section is responsible for this phenomenon.

Upstream of the impingement region, a negative vorticity rolling-up (clockwise rotation) is observed. This structure inten-

Nomenclature

D = hole diameter, mm	W^* = dimensionless velocity component along an inclined direction	RMS_u = dimensionless velocity fluctuation in x directions, normalized with $V_j = 4Q_v/15\pi D^2$
Q_v = global flow rate, m^3/h	i = incidence angle of the optical probe of the LDA system, degree	x, y, z = reduced coordinates normalized with D
Re_j = injection Reynolds number, $Re_j = 4Q_v/15\pi D\nu$		ν = air kinematic viscosity, m^2/s
U, V, W = dimensionless velocity components in x, y, z directions, normalized with $V_j = 4Q_v/15\pi D^2$		

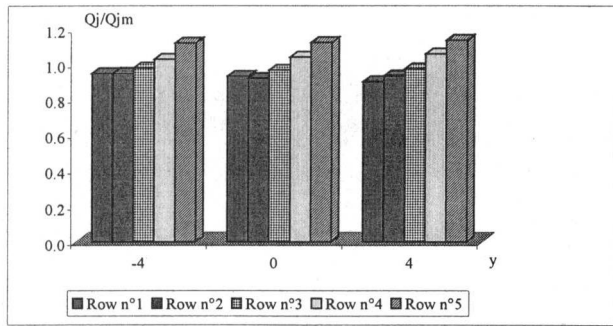


Fig. 3 Flow rate distribution ($Re_j = 12,600$)

sively studied in the case of the single impinging jet with a cross flow, is commonly named “ground vortex” (Barata et al., 1993; Kwoles and Bray, 1993; and Blake and Stewart, 1993). It is the result of the wall jet, due to the observed impingement interacting with the oncoming wall jet of the previous impinging jet. This interaction gives rise to a detachment phenomenon which explains the accumulating line formation seen before (Fig. 4).

The same flow pattern is encountered on the cross view in Fig. 6 ($x = 12$). The collision between radial wall jets of the central impingement and of the jet on its right creates a fountain upwash flow. This result shows that each impingement zone is surrounded by a horseshoe vortex as in the case of the single impinging jet with cross flow (Barata et al., 1993). A small region without seeding can also be observed near the impinged wall, between the two rolling-ups. Its location is the same as that previously visualised (Fig. 4), where the ear shape wall streamlines indicated the presence of a reattachment. The existence of such a phenomenon in the plane $y = 2$ indicates the presence of two small counter-rotating vortices between the wall and the main rolling-up pair.

Velocity Measurements. The three velocity component profiles have been successively measured in the symmetry plane $y = 0$ for different longitudinal positions. Only the U longitudinal component is analyzed, the two other components do not give

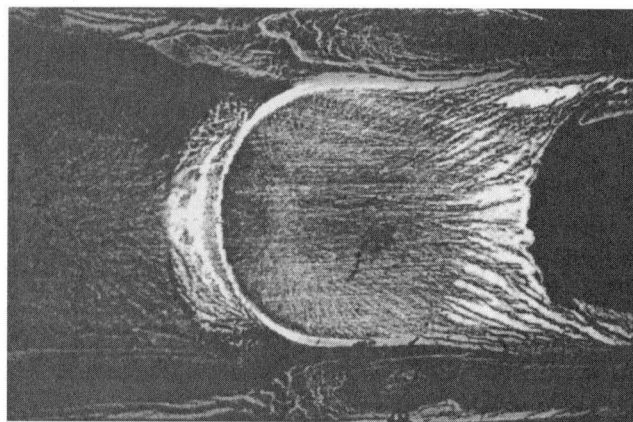


Fig. 4 Streamlines of one impingement zone ($Re_j = 12,600$)

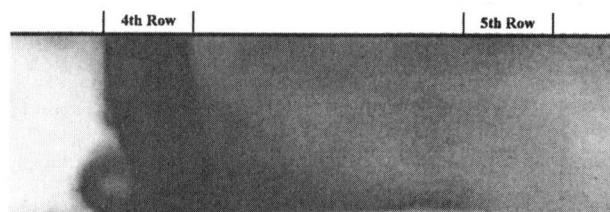


Fig. 5 Side view of the central jet of the fourth row by laser sheet visualization ($Re_j = 12,600$)

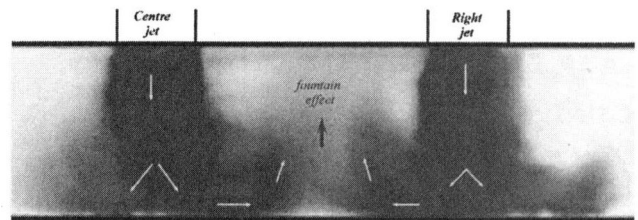


Fig. 6 Cross view of the fourth row by laser sheet visualization ($Re_j = 12,600$)

crucial supplementary information: The V component has a practically zero value in the symmetry plane while the W component very strong at the injection exit, decreases rapidly to zero on the impingement surface (Bernard et al., 1996).

The profile realised at $x = 11$ characterizes the flow issuing from the jet of the third row (Fig. 7(a)). The velocity decreases gradually until $z = 0.5$ before increasing rapidly to a maximum for $z = 0.1$, and finally decreasing near the impingement wall. The maximum characterizes the jet spreading along the impinging surface. The same profile shape is found behind the jet ($x = 14$ and $x = 15$, Figs. 7(e) and 7(f)). The time average velocity fluctuations remain constant until $z = 0.5$ (about 10%) then grow and become appreciably constant in the zone where the velocity peak has been previously observed. This increase of the RMS_u values seems to be linked to the presence of the wall jet and more particularly to the unsteady behavior of the flow in this region.

The next profile (Fig. 7(b)) has been realized along the injection orifice axis. The U component grows until $z = 1$ then decreases until $z = 0.4$ characterizing the jet inclination under the cross flow influence. It decreases rapidly to become negative in the boundary layer near the impingement wall. This change of sign corresponds to the ground vortex and it is accompanied by an increase in RMS_u value. From the velocity profile we can deduce the center of this structure which is found at a height between $z = 0.25$ and $z = 3$.

The profile measured just downstream of the jet exit ($x = 12.6$, Fig. 7(c)) shows that the longitudinal velocity component is negative in the upper half of the test section. This indicates that the

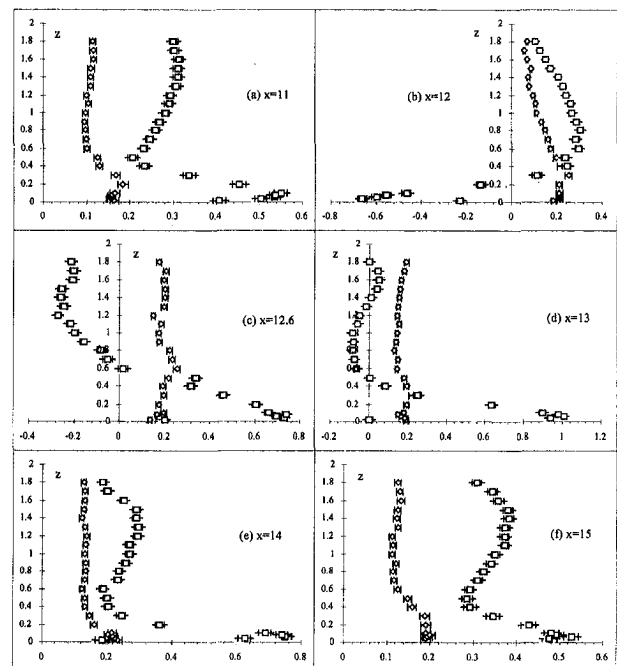


Fig. 7 Velocity and RMS profiles of the longitudinal component in the plane $y = 0$ for the fourth row (\square U , \diamond RMS_u , $Re_j = 12,600$)

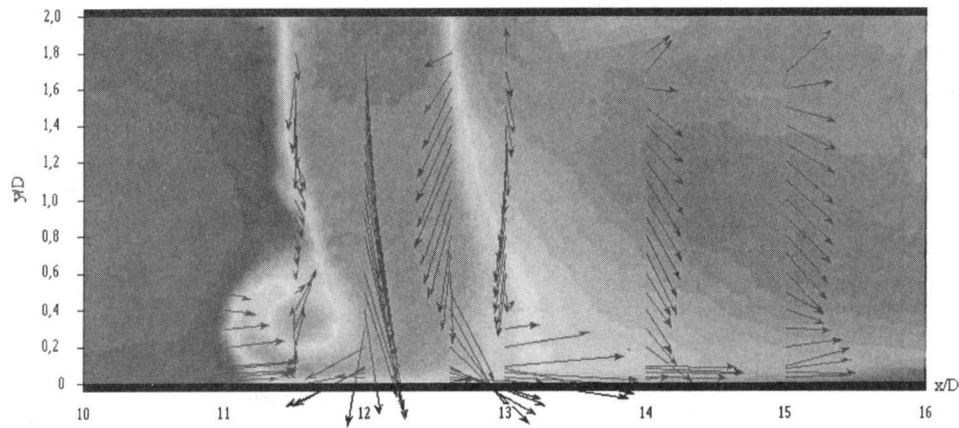


Fig. 8 Velocities field projection on a laser sheet visualization ($Re_j = 12,600$)

suction effect of the surrounding fluid by the jet issuing from the injection hole results in the formation of a reverse flow region downstream of the jet. This region spreads out to $z = 0.7$ where U becomes zero. The velocity then increases gradually to reach a maximum near the target wall. In this region the jet, strongly deflected in the downstream direction, begins to spread radially outward from the impingement point. The RMS_u profile indicates that the fluctuating rate is high and remains approximately constant in the upper part of the flow ($0.8 \leq z \leq 2$). This high level of turbulence intensity is due to the structures produced in the wake of the jet similar to those observed in the case of a jet in a cross flow (Werle, 1977; Fric and Roshko, 1989; and Brizzi et al., 1995). The fluctuating level increases in the region where the higher mean velocity gradient has been measured ($z = 0.5$) while showing a minimum when the U velocity is maximum ($z = 0.2$). This indicates that these fluctuations are induced by the large scale unsteadiness of the structures generated at the boundary of the jet already observed on the laser sheet visualizations.

The U profile measured along the line crossing the test section at $x = 13$ (Fig. 7(d)), shows that the longitudinal velocity is near zero in the jet wake between the injection wall ($z = 2$) and $z = 0.5$. The deflected jet which becomes almost parallel to the impingement plate behaves similarly to a radial wall jet in the fluid layer near the impinged wall ($0 \leq z \leq 0.5$). The RMS profile is similar to that obtained at the previous station ($x = 12.6$).

The mean velocity profiles measured at the two last positions have the same shape (Figs. 7(e) and 7(f)). Between the upper wall and the region about $z = 0.4$, the U component remains constant with positive value. It increases sharply in the wall jet zone ($0 \leq z \leq 0.4$).

As can be seen from the examination of Figs. 7(d) to 7(f) for $13 \leq x \leq 15$, the velocity peak intensity decreases demonstrating the strong interaction between the two opposite motions shown by longitudinal flow visualizations.

In Fig. 8, the velocity vector field (U, W) in the symmetry plane ($y = 0$) is presented. It gives complementary information on the flow organisation in the region corresponding to the central jet of the fourth row (Fig. 1). The fluid area included between injection and impingement walls can be divided into two regions.

In the upper part of the test section ($z > 0.6$) we observe a flow configuration of "jet in cross flow" type. Indeed the jet issuing from the injection orifice located at the upper part of the figure is gradually deviated downstream as it penetrates into the test section. At the same time the cross flow generated by fluid from the impinging jets located upstream is oriented to the impingement surface. Near the injection wall and upstream of the jet the fluid is directed towards the injection orifice. This result confirms the presence of the well known vortical structure, with a horseshoe form (Werle, 1977; Fric and Roshko, 1989; and Brizzi et al., 1995). This rolling-up surrounds the upstream of the jet, passes

round the injection hole and feeds a part of the wake. This one shows a reverse flow zone where the fluid is drawn by the jet, and a downstream region where the fluid is flowing toward the following jet. The boundary between the two wake zones is the $x = 13$ line where the horizontal velocity value is near zero for $0.3 \leq z \leq 2$. An analogous result has already been observed by Barata et al. (1992) in the case of a single impingement. In all the wake region located in the vicinity of the symmetry plane and for $0.3 \leq z \leq 1.7$, the flow is clearly oriented towards the impingement surface ($W < 0$), while near the injection wall, the fluid is flowing towards the wall.

The flow velocity is almost everywhere parallel to the surface near the impingement wall. This is particularly the case in the region located downstream of the impingement centre where the jet fluid spreads out along the surface. The fluid located in the upstream part of the impingement undergoes a change of direction near the wall. It should be noted that this deflection in the upstream direction is very steep and occurs very close to the impingement surface. For example, along the injection hole axis ($x = 12$), the velocity vector becomes parallel to the wall only at the position $z = 0.04$. Thus, there is a collision between the thin fluid layer flowing upstream and the flow coming from the preceding impingement. The interaction between these two opposite motions gives rise to the rolling-up which makes the fluid move apart from the impinged surface, as vectors located at the $x = 11.5$ abscissa show. The superposition of a velocity field on a digitized picture of a flow visualization in Fig. 8 shows a good agreement between these results, especially for the large scale rolling-up location. The influence of this rolling-up is already noticeable at the $x = 11$ abscissa as the orientation of measured velocity vectors near the wall ($0 \leq z \leq 0.4$) indicates. The fluid zone thickness which causes the separation/detachment from the wall to be drawn in the rolling-up is close to 0.35 (location of the sign change of the W component). This thickness is slightly less upstream of the fifth jet impingement as vectors measured at the $x = 15$ abscissa show (Fig. 8). Indeed, at this position, the interaction phenomenon between the fourth and fifth jets is the same as that for the third and fourth jets. This phenomenon will give rise to a new rolling-up and to the detachment corresponding to the accumulation line shown on the visualization picture presented in Fig. 4.

Lateral sections of the flow (planes $x = \text{constant}$) presented elsewhere (Bernard and Bousgarbiès, 1996; and Bernard, 1997) show that the same type of interaction exists between two neighboring impingement zones of the same row and that it generates a "fountain effect" as noted by Barata et al. (1992). These results with the characteristic pattern of accumulation lines of coating (Fig. 4) show that rolling-ups, such as those observed in Fig. 8, are traces of a horseshoe vortex network that surrounds the impingement zones. Vortices of a same jet line coalesce while those in a same row create "fountain effects."

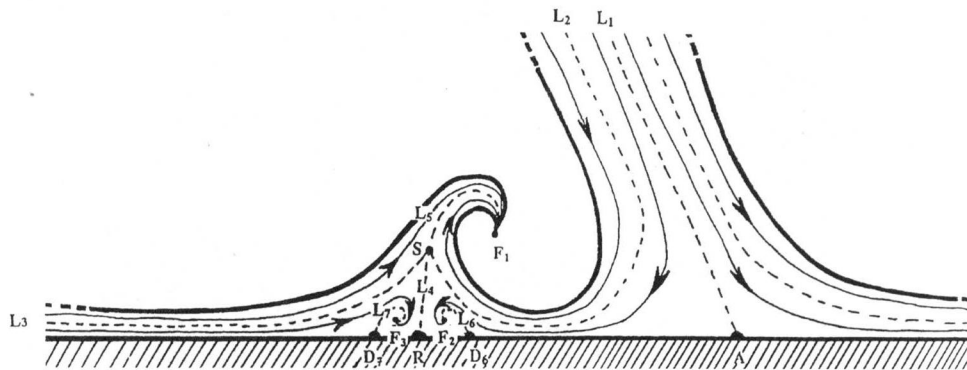


Fig. 9 Schema of the flow near an impingement zone

Topology. The analysis of many video recordings of several transverse and longitudinal planes associated with the results of velocity measurements has enabled us to propose a topology of the flow near the impinging wall in the symmetry plane $y = 0$ (Fig. 9).

The first particular line L_1 , that ends at the impingement point A represents the frontier between the jet fluid that rolls in the ground vortex and the one that flows to the exit section alongside the wall. The stagnation point A corresponds to the impingement centre seen by spreading over method. The line L_4 connecting point S to point R, which is the reattachment line trace, and the line L_5 joining S to the focus point F_1 show the limit between fluid zones fed respectively by the present jet and by the upstream one. Lines L_2 and L_3 separate present fluid that is drawn by the rolling-up from the one that remains near the wall to be at the origin of a secondary vortices pair (focus points F_2 and F_3).

These two structures, of smaller size than the primary vortex pair, are located on either side of the reattachment point R, between this point and detachment points D_6 and D_7 (traces in this plane of two detachment lines). L_6 and L_7 are two singular streamlines connecting D_6 and D_7 respectively to focus points F_6 and F_7 .

Conclusion

The combination of flow visualizations and velocity measurements has provided much information concerning the general aspect of the flow caused by several distributed jets impinging on a plane wall. The spreading over method allows to study the fluid behavior in the immediate vicinity of the impinged wall by revealing its detachment and reattachment lines. In addition, the laser sheet visualizations make the observation of large scale structure organisation possible for such a configuration. In particular, the ground vortex and the fountain effect due to the result of the interaction between two jet impingements are clearly shown. The qualitative aspect revealed by flow visualisations is quantitatively strengthened by velocity measurements.

All the results obtained in this study have allowed a more elaborate schema of the flow at the impingement wall vicinity to be proposed. In this region the interaction between the various vor-

tical structures leads to a complex and strongly three-dimensional velocity field. Impingement regions and the fountains have revealed zones of intense velocity fluctuations.

Acknowledgments

This work was supported financially by the DRET and was made with the assistance of SNECMA.

References

- Barata, J. M. M., 1991, "Fountain Flows Produced by Multiple Impingement on a Ground Plane," *Journal of Aircraft*, Vol. 30, No. 1, pp. 50–56.
- Barata, J. M. M., Durao, D. F. G., Heitor, M. V., and McGuirk, J. J., 1992, "The Turbulence Characteristics of the Single Impinging Jet Through a Crossflow," *Experimental Thermal and Fluid Science*, Vol. 5, pp. 487–498.
- Barata, J. M. M., Durao, D. F. G., Heitor, M. V., and McGuirk, J. J., 1993, "On the Analysis for Impinging Jet on Ground Effects," *Experiments in Fluids*, Vol. 15, pp. 117–129.
- Bernard, A., 1997, "Aérodynamique de configurations de jets impactants appliquées au refroidissement de parois," Ph.D. thesis, Poitiers.
- Bernard, A., and Bousgarbiès, J. L., 1996, "Velocity Field Characteristics of Multiple Jets Impinging on a Flat Plate," *Proceedings, 8th International Symposium on Applications of Laser Techniques to Fluid Mechanics*, Lisbon.
- Blake, W. B., and Stewart, V. R., 1993, "Experiments on the Ground Vortex Formed by an Impinging Jet in Crossflow," *Proceedings, AGARD Meeting Computational and Experimental Assessment of Jets in Crossflow*, paper 15.
- Brizzi, L.-E., Foucault, E., and Bousgarbiès, J. L., 1995, "On the Vortical Structures Generated at the Boundary of a Circular Jet Emerging Normally Into a Boundary Layer," *Compte Rendu à l'Académie des Sciences Paris*, t. 321, Série IIb, pp. 217–223.
- Fric, T. F., and Roshko, A., 1989, "Measurements of the Flow and Turbulence Characteristics of Round Jets in Crossflow," *ASME JOURNAL OF FLUIDS ENGINEERING*, Vol. 111, pp. 165–170.
- Knowles, K., and Bray, D., 1993, "Ground Vortex Formed by Impinging Jets in Crossflow," *Journal of Aircraft*, Vol. 30, No. 6, pp. 50–56.
- Liguo Li, Zingzhou Zhang, and Yun Zhu, 1990, "Thermal Visualisation of Heat Transfer Characteristics for Jet Array Impingement with Initial Crossflow," *Proceedings, 9th International Heat Transfer Conference*, Jerusalem.
- Van Treuren, K. W., Wang, Z., Ireland, P. T., Jones, T. V., and Kohler, S. T., 1993, "Application of the Transient Liquid Crystal Technique to Measure Heat Transfer and Adiabatic Wall Temperature Beneath an Array of Impinging Jets," *Proceedings, Eurotherm Heat Transfer in Single-Phase Flow*, Oxford.
- Werlé, H., 1977, "Écoulement le long d'une paroi plane comportant des jets normaux ou inclinés de section circulaire," Rapport technique ONERA n°65/7106 ENA.

Experimental Investigation of Blade Loading Effects at Design Flow in Rotating Passages of Centrifugal Impellers

Nicholas H. Hesse

Research Engineer,
Trojan Technologies Inc.,
3020 Gore Road,
London, Ontario, Canada, N5V 4T7
e-mail: nhesse@trojanuv.com

J. H. G. Howard

Professor Emeritus,
Department of Mechanical Engineering,
University of Waterloo,
Waterloo, Ontario, Canada, N2L 3G1

Data Bank Contribution*

Laser-Doppler Anemometry (LDA) was used to study the effect of blade loading on the relative velocity field in a rotating passage of a centrifugal-pump impeller. Two variations of the impeller, 8-bladed and 16-bladed, were investigated. The measured primary and secondary velocities and turbulence show that the effect of blade loading is not that previously predicted. The 16-blade impeller with high blade loading has a rapidly thickening suction side boundary layer, suggesting the onset of transient separation near the exit. However, for the 8-blade impeller with even higher blade loading, the onset of separation is not indicated at any measured location in the impeller. At the design flow, it is concluded that the stronger potential eddy and lower solidity associated with the very high blade loading caused a change in the secondary flow pattern, retarding the growth and the likelihood of transitory separation of the suction side boundary layer.

Introduction

A low-specific-speed centrifugal pump impeller creates a velocity field which has predominantly radial and tangential components. The flow field in the rotating passage is controlled by both inviscid effects (including the potential eddy which gives rise to higher relative velocities on the suction side of the passage than on the pressure side) and viscous effects associated with boundary layers on all passage walls. The wall layers on the hub and shroud surfaces are three-dimensional in nature and associated with cross-passage (or "secondary") velocity components. Blade pressure-side and suction-side boundary layers may be subject to Coriolis and curvature effects in addition to the influence of streamwise pressure gradients, and are strongly affected by the passage secondary flow field. It is convenient to define the primary flow field as the flow in the direction of the passage centerline and the secondary flow as the flow in the plane perpendicular to the primary flow. The secondary flow is generated by both viscous effects and by Coriolis and curvature accelerations interacting with velocity gradients (e.g., Hirsch, Kang and Pointel, 1996).

Experimental observation of a centrifugal-pump impeller, originally by Fischer and Thoma (1932), revealed suction-side separation and wake formation under many flow conditions. Many studies sought to define when this separation might occur and what design criteria should be used to delay it. The impeller investigated by Howard and Lennemann (1971) and McDonald, Lennemann and Howard (1971) exhibited separation, while that reported on by Howard and Kittmer (1975), although having a similar specific speed, had no separation. The difference in flow field was ascribed to a combination of secondary flow, passage diffusion and blade loading differences. Internal velocity measurements in a radial-pump impeller by Hamkins and Flack (1986) showed suction side separation at low flow rates. Moore (1973a, b) observed and explained how the impeller rotation created a relative eddy. This

relative eddy tends to create pressure side reverse flow and drives the secondary flow to bring the low momentum fluid from the hub and shroud surfaces to the suction side, leading to separation and wake formation.

Kline (1959) investigated flow separation in stationary straight-walled diffusers, using flow visualization. He found four different stages of separation, depending on diffuser angle and aspect ratios, the second of which is large transitory stall (time dependent 3D flow). He also quoted a report by Stratford (1959) where, in studies of a boundary layer which was almost but not quite entirely separated, Stratford observes "a special region of flow with very high turbulence level close to the wall." Johnston, Halleen and Lezius (1972) described the observed effect of Coriolis and curvature on the turbulence structure in a boundary layer. The suction side layer is observed to have enhanced stability in its turbulent flow field which reduces the wall shear stress, and would make it more likely to separate if subject to an adverse pressure gradient. Rothe and Johnston (1976) extended the study to high aspect ratio rotating diffusers where suction side separation was observed at area ratios (exit passage area/inlet passage area) which varied as the Coriolis effect, expressed by a rotation number, was varied. Their data suggested that, at area ratios below 1.4, no separation would occur, no matter how high the rotation number was, while at zero rotation number, corner exit stall was observed at area ratios above 1.8. At all tested rotation numbers, higher area ratios were required before full exit plane stalling was observed. They specifically noted the absence of large transitory stall in their tests, but were not able to explain its absence. Howard, Patankar and Bordynuk (1980) used a Coriolis-modified turbulence model in a finite difference analysis to reproduce the low shear stress on the suction surface of the Johnston rotating passage, and demonstrated that for a low aspect ratio nondiffusing passage, secondary flows contribute strongly to a predicted lowering of suction-surface shear stress. Dengel and Frenholz (1990) used a stationary axisymmetric wind tunnel to measure flow separation with different pressure gradients. They reported that transient flow separation occurred at a turbulence intensity roughly equivalent to 16% (as defined in this paper), or $(\bar{u}'^2/\bar{u}_s^2)_{\max} = 0.023 - 0.026$ (using their definitions).

For the usual geometry of the centrifugal-impeller passage, a useful measure of the level of Coriolis and curvature effects is a

* Data have been deposited to the JFE Data Bank. To access the file for this paper, see instructions on p. 924 of this issue.

Contributed by the Fluids Engineering Division for publication in the JOURNAL OF FLUIDS ENGINEERING. Manuscript received by the Fluids Engineering Division April 1, 1998; revised manuscript received July 6, 1999. Associate Technical Editor: B. Schiavello.

blade loading parameter. This can be presented as the blade-to-blade velocity difference divided by the passage mean velocity or as a parameter based directly on the Coriolis and passage curvature accelerations normal to the blade. These two approaches are equivalent if the velocity difference is in the passage normal direction. Using data from Hill and Moon (1962), Morris and Kenny (1970) suggested a limiting value of the loading parameter (0.7), above which separation would be expected. The use of this or similar limits are now common in the design of centrifugal compressors and many centrifugal pumps. This simple loading criterion avoids consideration of the influence of the secondary flow pattern, as well as passage diffusion. Howard (1978) suggested a correlation between loading and area ratio in predicting separation by reploting the Rothe and Johnston (1976) data.

Abramian and Howard (1994a, b) measured the flow velocities in the blade passage of a highly-loaded, very-low-specific-speed, backward swept centrifugal impeller with an upstream swirl inducer. They did not detect any suction side separation. Based on the blade-loading parameter, suction side separation should have occurred along most of the blade. The lack of separation in the blade passage was thought to be a result of the extremely high blade loading, associated with a very strong potential eddy, which forced high energy primary flow from the pressure side to the suction side, except near the passage exit. This transfer of high-energy fluid reduced the growth of the suction-side boundary layer and prevented early separation. Visser (1996) also measured separation-free internal flows in a pump impeller with low specific speed and demonstrated a very close comparison with potential flow.

The present series of experiments studied the character of the flow in a low-specific-speed, backward-swept, radial impeller, and the effect of blade loading on the pattern of primary and secondary velocities and turbulence inside the radial blade passage, using direct LDA measurements in the rotating frame of reference. The blade loading was changed by removing half the blades from the impeller. The radial and tangential velocities at various locations in the blade passage were measured, separately, using a single component LDA system rotating with the impeller. Unfortunately, the LDA filter settings eliminated any negative velocities, so only positive radial and tangential velocities were collected. All measurements were carried out at the design flow rate. There was no volute, and the collected velocity data was not analyzed for angular-dependent influences. In this paper, the blade loading parameter is calculated using Howard, Osborne and Japikse (1994):

$$BL = (W_{\text{suction}} - W_{\text{pressure}})/W \quad (1)$$

Experimental Apparatus

The experimental apparatus measured fluid velocities in a rotating centrifugal-impeller blade-passage, in the rotating frame of reference. A single component LDA system was used to measure separately the radial and tangential velocity components of the flow in a radial-flow blade-passage. The details of the apparatus

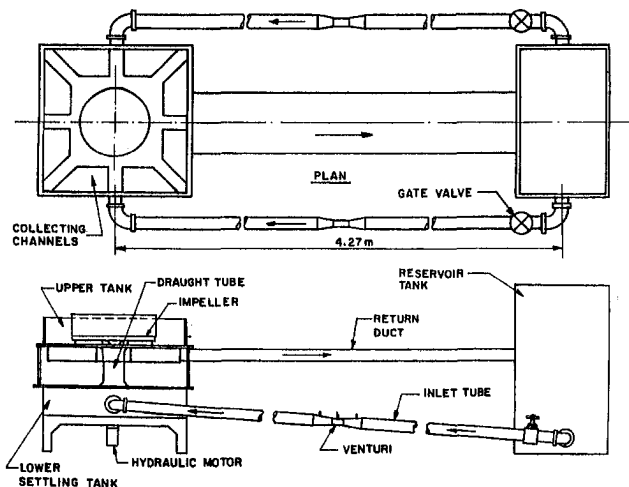


Fig. 1 Experimental test rig

are discussed in Abramian and Howard (1994a) and Hesse (1997). Part of the LDA system rotated with the impeller, and employed an optical derotator, allowing measurements in the rotating frame of reference.

Experimental Test Rig. The test rig is the same as used by Abramian and Howard (1994a, b) (see Fig. 1). The rig was a closed circuit consisting of a supply tank and a test section, connected by two inlet pipes and a return duct. A closed circuit system was used to conserve water, and to conserve the seed particles required for the LDA measurements. The test section consisted of a lower settling tank, an upper settling tank and a vertical draft tube connecting the two. The upper tank was open to the atmosphere. A vertical shaft extended from below the lower tank, through the draft tube into the upper tank. The shaft, which was used to drive an impeller being tested, was driven using a hydraulic motor mounted below the lower tank. The impeller being tested was mounted on the upper end of the shaft, in the upper tank. The impeller torque and shaft rpm were measured by a torque meter with an integral speed sensor mounted between the hydraulic motor and the shaft, under the lower tank.

The water flowed from the reservoir tank, through both inlet pipes into the lower tank, up through the draft tube, through the impeller, into the upper tank, and back to the reservoir tank via the return duct. Each inlet pipe was fitted with a gate valve and a venturi, to control and measure the flow rate to the impeller. This large diameter, low speed rig was specifically designed to allow the upper surface of an impeller or a volute to be directly exposed to air. This design was required for the LDA measurements and previous flow visualization studies. Experimental limitations restricted the flow rate obtained during these experiments to a minimum of $.004 \text{ m}^3/\text{s}$ and a maximum of $.017 \text{ m}^3/\text{s}$.

Nomenclature

β = relative flow angle
 ω = angular rate of rotation
 A = cross-sectional area
 b = hub to shroud blade height
 BL = blade loading parameter
 g = 9.8 m/s^2
 H = head rise
 Q = volumetric flow rate
 r = radial cylindrical polar coordinate

Rossby No. = $(Q/A_1)/\omega W_1$

TI = turbulence intensity
 U_2 = circumferential velocity at exit
 w' = relative RMS velocity
 W = mean relative velocity
 $\phi = Q/A_2 U_2$
 $\psi = gH/U_2^2$

Subscripts

1 = inlet value
 2 = outlet value

b = blade
 bep = best efficiency point
 flow = flow direction
 pressure = pressure side
 r = radial component
 s = shroud lip value
 suction = suction side
 t = tangential component

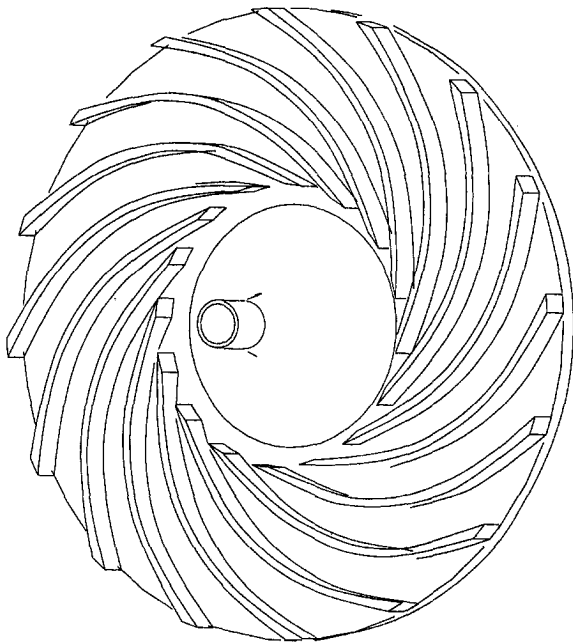


Fig. 2 Line drawing of 16-blade test impeller (shroud removed)

Test Impeller. The impeller for this investigation was designed for ease of manufacture and measurement. The impeller is shown in Fig. 2, and details of its design parameters and geometry are given in Table 1.

The inlet blade height (b_1) was constrained by the test apparatus, such that the impeller blade inlet area was approximately the same as the annular cross-sectional area of the draft tube, to limit the diffusion required at the axial to radial bend, downstream of the impeller inlet. The impeller is partially unshrouded at the first part of the vane. A hyperbolic blade profile in the unshrouded portion was used to follow the draft tube surface as closely as possible. A linear blade height profile in the shrouded portion of the impeller was chosen to simplify construction of the impeller. The exit blade angle was chosen as 30 deg from tangential (−60 deg from meridional). The exit blade height (b_2) of 19.1 mm was a compromise between the heights calculated using Stepanoff (1957) and Sabersky, Acosta and Hauptmann (1989).

The impeller was made of aluminum and polycarbonate. Both the hub and shroud plates were aluminum disks, with 16 logarithmic spiral grooves. Each blade was a piece of polycarbonate sheet, 6 mm thick, bent to fit into the grooves. The leading and trailing blade edges were machined to a constant radius, and filed to remove any burrs. A hole was cut in the hub plate, and a glass window inserted. The window was shaped to expose 2 of the 16 inter-blade passages. The window extended from $r/r_2 = 0.512$ to 0.968.

After the 16-blade measurements were completed, the impeller was disassembled, cleaned and half the blades were removed. The open grooves were filled, sanded flush with the plate surface, and the impeller re-assembled with 8 blades.

Performance. The overall performance of the impeller with both 8 and 16 blades is shown in Fig. 3. For the 16-blade case, the efficiency curve is fairly flat, until the design flow rate is reached, after which efficiency decreases with decreasing flow rate. For the 8-blade case, the efficiency curve decreases with decreasing flow rate, with a plateau near the test flow rate. Both sets of LDA measurements were performed at the design flow rate ($0.014 \text{ m}^3/\text{s}$, $\phi = 0.121$). The flat portions of the curve probably represent a broad peak in the efficiency curve. The test rig was not able to support higher flow rates, where the performance curves would be expected to show a decrease in both efficiency and head coefficient.

Table 1 Impeller geometry

Q (Design Flow Rate)	0.0142 m ³ /s
$\phi_{beP} = Q/(A_2 U_2)$	0.121
H (Design Head Rise)	0.762 m(H ₂ O)
$\psi_{beP} = gH/U_2^2$	0.492
ω (Design Speed)	15.71 rad/s
r_1 (Inlet Radius)	0.111 m
r_s (Shrouded Inner Radius)	0.124 m
r_2 (Exit Radius)	0.248 m
r_1/r_2	0.448
r_s/r_2	0.500
b_1 (Inlet Blade Height)	0.0251 m
b_s (Shrouded Blade Height)	0.0219 m
b_2 (Exit Blade Height)	0.0191 m
b_1/r_2	0.101
b_s/r_2	0.088
b_2/r_2	0.077
b_1/b_2	1.314
b_s/b_2	1.147
t (Blade Thickness)	0.0060 m
β_b (Blade Angle)	30° from Tangential
Z (Number of Blades)	8 or 16
Blade Rake	0
Volute	None

cient, or lower flow rates, where the head coefficient would be expected to rise. At the design flow rate, the measured head coefficients were $\psi = 0.478$ and 0.510 for the 8-blade impeller and 16-blade impeller, respectively. The measured efficiencies, at the design flow rate, were 91% and 78% for the 8-blade impeller and 16-blade impeller, respectively. The error range for the efficiency

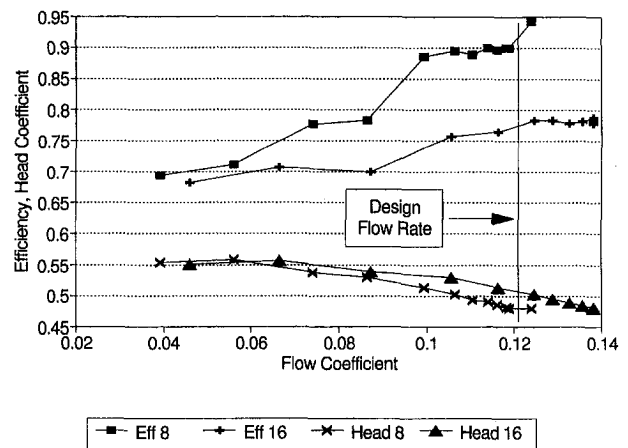


Fig. 3 Impeller performance (uncertainty in efficiency ± 10 percent, in head coefficient ± 2 percent)

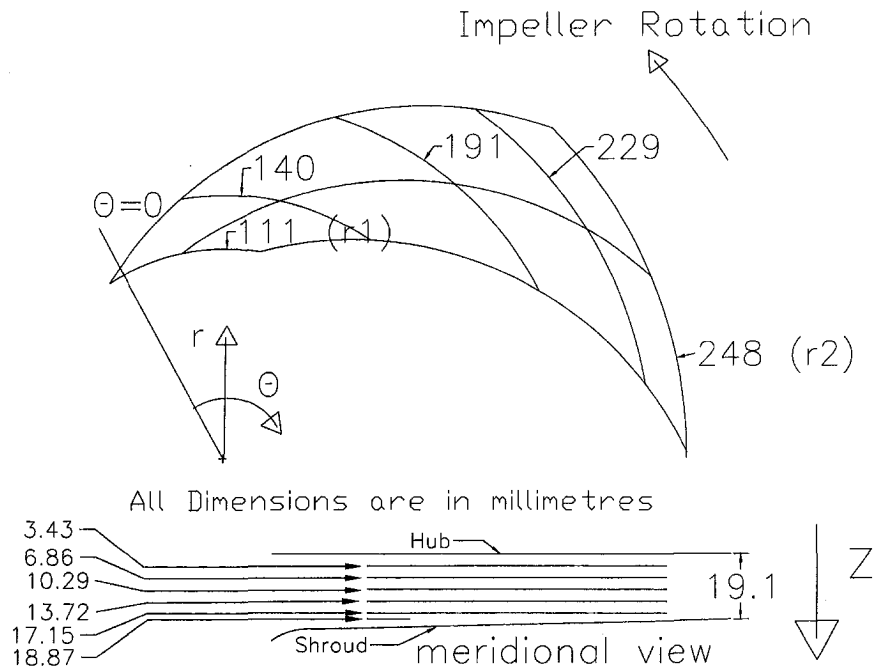


Fig. 4 Schematic of the measurement locations

values is roughly 10%. At the measured design points, the nondimensional impeller specific speeds were 0.420 (1140 US) and 0.400 (1080 US) for the 8 and 16 blade impellers, respectively.

Experimental Instrumentation

This investigation builds on the previous research of Abramian and Howard (1994a, b), using similar equipment and methods.

The LDA equipment consisted of a stationary and a rotating section. The stationary optical system consisted of the laser source, the fibre optic link and a conventional one component LDA system. The fibre optic link was used to connect the floor mounted laser to the optics mounted on the impeller. The LDA optics were a one component, dual beam Doppler system operating in backscatter mode. The LDA control volume was ellipsoidal, with a length of 0.143 mm, and a diameter of 0.040 mm. To allow detection of any reverse flow, one of the input laser beams was frequency shifted using a Bragg cell. However, any reverse flow data was rejected by the LDA filter settings. The rotating optical system consisted of 6 slip rings, a Dove prism, a two mirror periscope, a focusing lens and two stepper motors. All this equipment was mounted on an aluminum disk, which was mounted on the impeller. The Dove prism, rotating at half the impeller speed, was used to transfer the two laser beams and the backscattered light between the stationary and the rotating optical systems. The rotating periscope consisted of two 45 deg mirrors and a focusing lens, which were used to position the beam control volume at the desired (r - θ - z) location.

Experimental Procedures

Arrival time sampling was used because of the wide range of data rates obtained. Typically, 15,000 samples were collected for each data point. The filter settings used to validate the LDA data only accepted positive velocities. This means that the collected data cannot confirm the presence or absence of transient separation. The measured velocity distributions never had a velocity of zero within three standard deviations of the measured mean, which suggests an absence of fully developed stall.

Measurements were taken only at design flow, at two-degree increments, at 8 different radii ($r/r_2 = 0.564, 0.613, 0.665, 0.718, 0.770, 0.819, 0.871, 0.923$) and 5 different depths

($b/b_2 = 0.180, 0.359, 0.539, 0.718, 0.898$) at all radii and an additional depth ($b/b_2 = 0.988$) at the two inner radii ($r/r_2 = 0.564, 0.613$). Measurements were only taken at $b/b_2 = 0.988$ at the two inner radial locations, because of excessive reflection from the shroud surface. Measurements were not taken beyond $r/r_2 = 0.923$, because of equipment limitations. Both radial and tangential velocities were measured at these locations for both the 8 and 16 blade configurations. Only the measurements taken at $r/r_2 = 0.564, 0.770, 0.923$ are discussed in this paper. The complete measurements are included in Hesse (1997).

The combined error in the measured velocity due to the experimental errors was 1.2% in the mean velocity, and 2.2% in the RMS velocity. The major error contribution was due to the combined effect of the Individual Realization Bias (IRB) and Bragg Bias errors.

Results and Discussions

The results for the impeller passage flows are presented as blade-to-blade distributions of the mean primary velocity, the mean secondary velocity (both nondimensionalized with the circumferential velocity at the outer radius (U_2)), and the total turbulence intensity. A region spanning 45 deg was measured in order to collect data from 2 blade passages of the 16-blade impeller and 1 blade passage of the 8-blade impeller. The primary velocity was calculated as the component of the relative velocity along the passage mean line (i.e., at 30 deg from tangential), rather than the true mean streamline. The secondary velocity was calculated as the component of the relative velocity perpendicular to the passage meanline. This secondary velocity includes only the blade-to-blade velocity and not the hub-to-shroud velocity, due to constraints of the measurement method, giving 2D flow. The velocities are calculated normal to the blade passage, but were measured on the surfaces of constant radius (see Fig. 4). The secondary velocity arises from a combination of the bulk motion induced by the potential eddy and any local motion induced by vortices in the passage flow. The secondary velocities may contain a component of the exact streamwise velocity in addition to the cross-stream velocity, because the passage mean line (β_b) may not coincide with the mean streamline (β_{flow}), especially at larger radii, where slip becomes significant. The secondary velocity is taken as pos-

itive from the pressure side to the suction side. The turbulence intensity is calculated from the radial and tangential velocity data using:

$$TI = \frac{(w_r'^2 + w_t'^2)/2}{(W_r^2 + W_t^2)^{.5}} \quad (2)$$

The turbulence intensity presented includes the contribution of the actual turbulence in the flow field, as well as the contribution of a fluctuating velocity component. This fluctuating component will arise because of any relative motion between the control volume and velocity gradients present in the flow field. It is known that the control volume has some "wobble" (see Abramian and Howard, 1994a). The flow field is also likely to have moving velocity gradients, especially in the regions of transient flow separation and in the boundary layers. This combination of moving control volume and moving velocity gradients will result in a broadening of the probability density function of the velocity, which would be interpreted as "turbulence."

The data are presented as constant radius, hub-to-shroud, blade-to-blade plots at the various measurement radii. The plots extend 45 deg in the x -direction, to include the measured data, as well as the regions that could not be measured due to blade blockage or blade shadowing effects. The angular location of the blade surfaces are shown on the first 16- and 8-blade primary velocity plots.

Both the 8 and 16 blade impellers are subject to inlet flow distortions. Just upstream of the actual impeller inlet, the flow makes a 90 deg bend from the axial to the radial direction. Also, at the shroud inner radius ($r_s = r/r_2 = 0.50$), the flow path is disrupted by both a step in the shroud surface, and a change from a stationary to a rotating surface. The step is less than 5 mm, and varies circumferentially. This step was a result of the manufacturing and assembly process of the test equipment. On the hub, the surface is rotating well upstream of the bend, allowing the fluid sufficient time to adjust to the rotating surface. At the shroud, the transition from the stationary to rotating surface takes place just inside the impeller passage, distorting the flow. Also, a short length of the impeller blades is unshrouded, allowing the formation of tip vortices and other secondary flow features common in unshrouded impellers, which will propagate downstream. The tip clearance was caused by a step on the shroud surface.

16-Blade Impeller. All the 16-blade plots show the data from the two adjacent blade passages investigated. The gap in the middle of the plots is occupied by the blade separating the two passages.

The progress of primary flow downstream through the blade passages is shown in Fig. 5. The primary flow starts off as potential flow, with significant inlet distortions, but becomes non-potential before $r/r_2 = 0.770$. Near the exit, the flow is strongly modified by the rapidly growing suction side boundary layer.

The progress of secondary flow downstream through the blade passages is shown in Fig. 6, while Fig. 7 illustrates the major secondary flow vortices deduced from the data. At the upstream plane, the secondary velocity is higher at the hub than at the shroud, suggesting a single major vortex (see Fig. 7(a)). This single vortex is consistent with the secondary flow pattern near the inlet of a shrouded impeller measured by Howard and Kittner (1975). The high secondary velocity in the inviscid core flow of the impeller is consistent with the difference in flow direction between the mean streamline and the passage mean line, which is associated with the potential eddy. The double vortex pattern sweeps low energy fluid from the hub and shroud boundary layers into the suction side boundary layer. The reason for the change in the primary flow at $r/r_2 = 0.770$ is seen in the secondary velocity plot (see Fig. 6(b)). The single vortex has become a double vortex (see Fig. 7(b)).

The overall secondary velocity is now negative, because the potential eddy has also started to induce cross-passage flow from the suction side to the pressure side. This reversal of the influence

of the potential eddy may also contribute to the evolution of the vortex from a single to a double vortex. The potential eddy moves the core flow from the pressure side towards the suction side at low radii, and from the suction side towards the pressure side at the higher radii. The downstream secondary velocity plot (see Fig. 6(c)) continues to show a double vortex. The overall secondary velocity is now quite strongly negative, due to the strengthening crossflow induced by the potential eddy.

The progress of turbulence intensity downstream through the

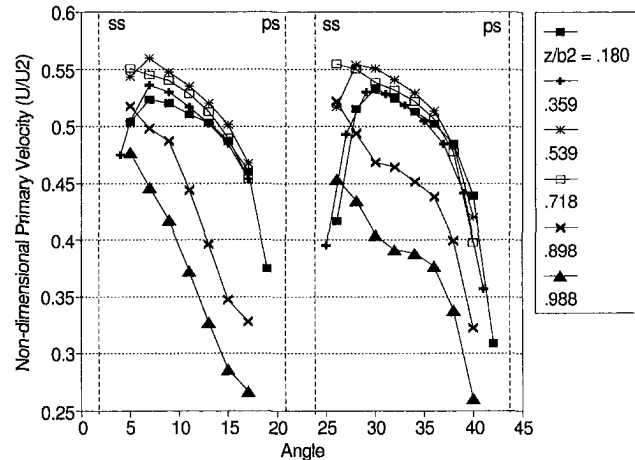


Fig. 5(a)

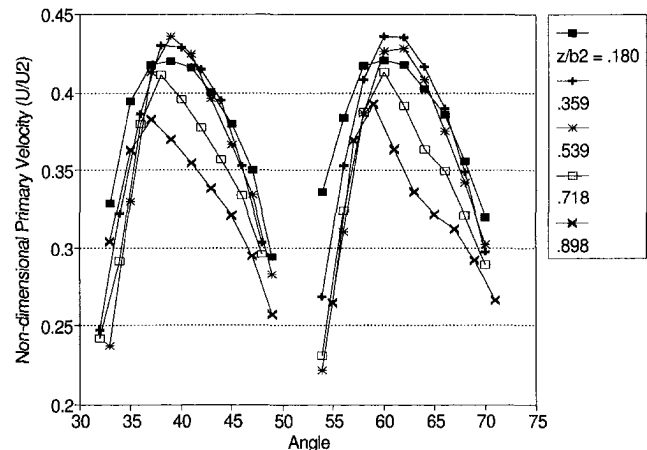


Fig. 5(b)

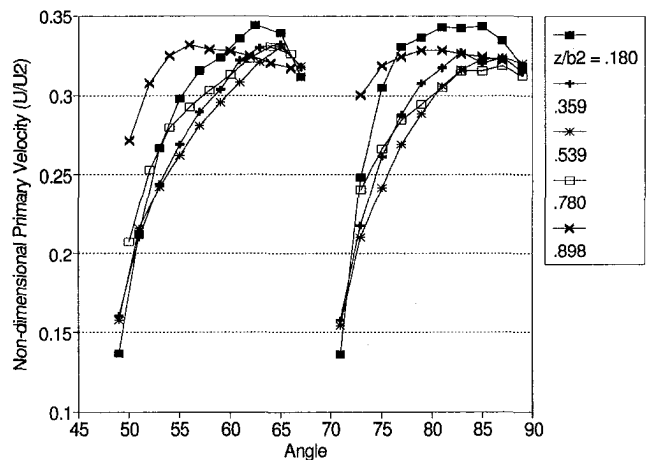


Fig. 5(c)

Fig. 5 Nondimensional primary velocity [UU_2] for 16 blades (uncertainty in $UU_2 \pm 1.2$ percent)

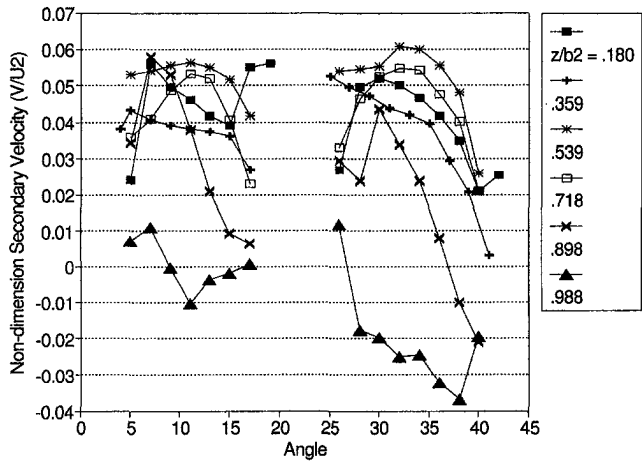


Fig. 6(a)

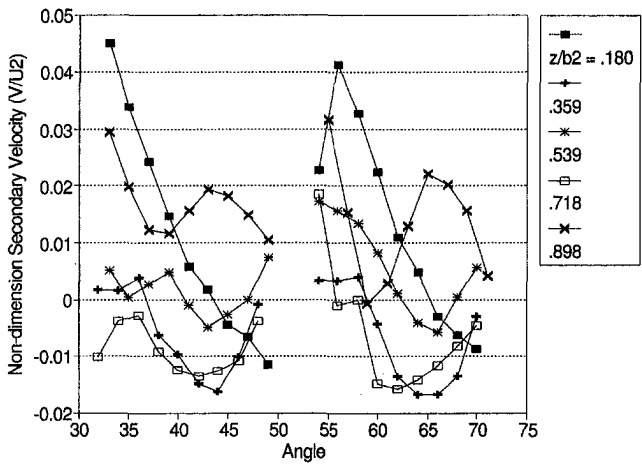


Fig. 6(b)

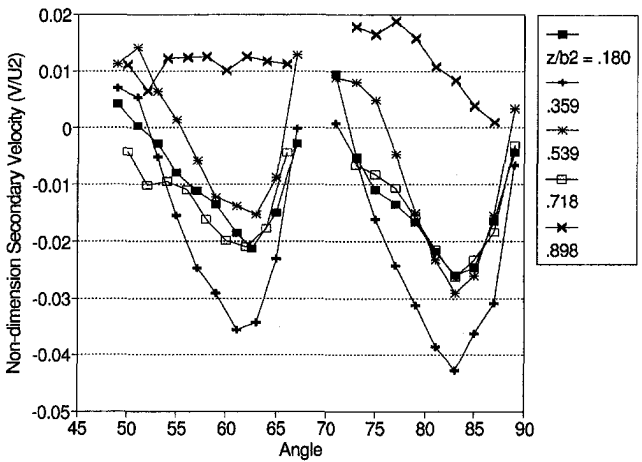


Fig. 6(c)

Fig. 6 Nondimensional secondary velocity [V/U_2] for 16 blades (uncertainty in $V/U_2 \pm 2.2$ percent)

blade passages is shown in Fig. 8. The turbulence intensity decreases with increasing distance from the passage walls. Near the inlet, the turbulence intensity is considerably higher in the highly distorted shroud flow than anywhere else in the passage. The high turbulence intensity is indicative of transient separation (Kline, 1959). LDA would measure transient separation as a reduction in average velocity, and an increase in turbulence intensity, because

of the wider range of velocities measured. Any negative velocities were ignored, because of the filter settings used in this experiment.

The downstream turbulence intensity plot (see Fig. 8(c)) shows an elevated turbulence intensity in the corners of the suction side boundary layer. Kline (1959) and Rothe and Johnston (1976) both observed stall initially in the corners of their flow passages. This high level of turbulence intensity suggests transient flow separation. The suction-side boundary-layer hub-corner turbulence intensity also increases dramatically at the two highest measurement radii (from 14 to 20 to 22%), suggesting transient flow separation. This flow separation is not indicated by either the primary or the secondary velocity plots, but rapid growth of the suction side boundary layer is observed. There also seems to be pressure side transient flow separation at the first measurement location. This would be due to the potential eddy and shroud side separation.

The blade loading, using the BL parameter (see Eq. (1)), is plotted in Fig. 9. For this impeller, the BL parameter was calculated in each of the two blade passages, based on the highest and lowest velocity values at each measurement radius and height, and then averaged. In this impeller, the blade loading does exceed the recommended value of 0.7 (Morris and Kenny, 1970), which is consistent with the signs of transient flow separation observed in the turbulence intensity plot (see Fig. 8(c)) at the outer radii.

The area ratio of the 16-blade impeller, when the area is measured normal to the blades, and including only those portions of the passage fully defined by the blades, is approx. 1.9. Using the Rothe and Johnston (1976) data, replotted by Howard (1978), such an area ratio would be expected to lead to separation for blade loading (BL) exceeding 0.5. No steady separation is observed. The equivalent diffuser angle is about 2 degrees, and the Rossby number is about 5.1.

8-Blade Impeller. The same plotting conventions are used for the 8-blade impeller plots as for the 16-blade impeller plots.

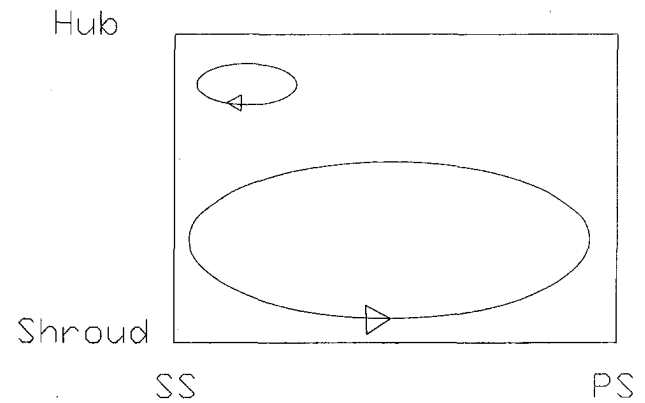


Fig. 7(a)

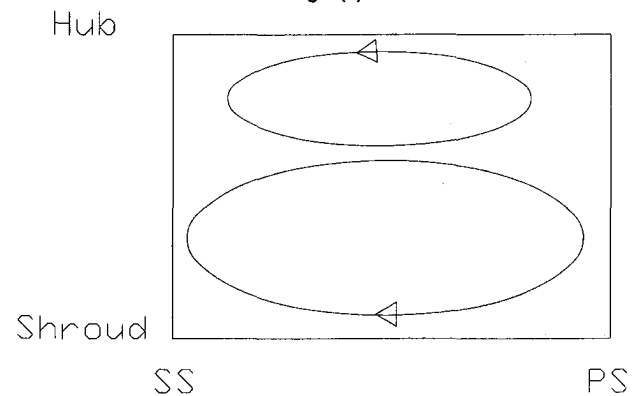


Fig. 7(b)

Fig. 7 Schematic of the 16-blade impeller secondary vortices

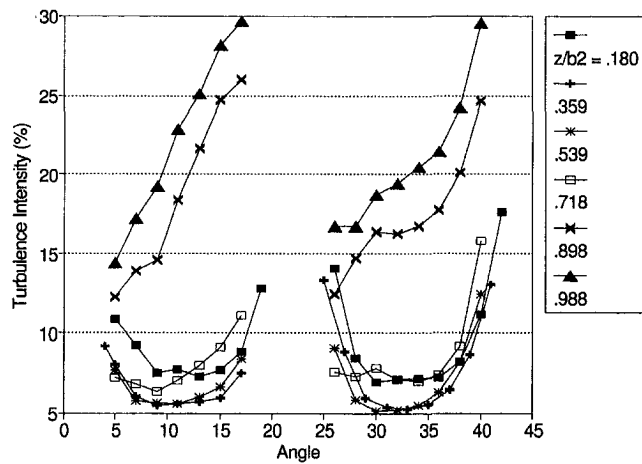


Fig. 8(a)

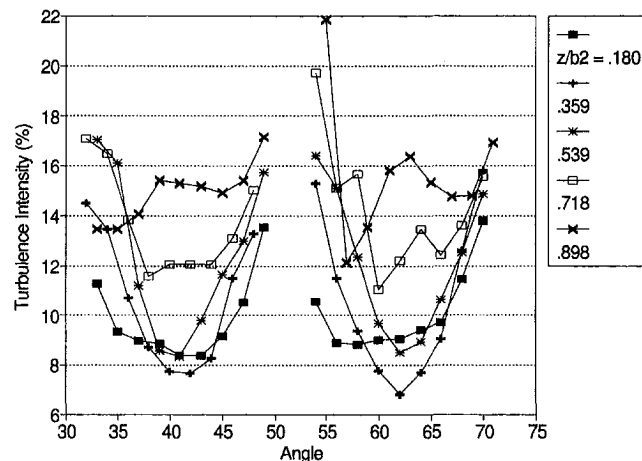


Fig. 8(b)

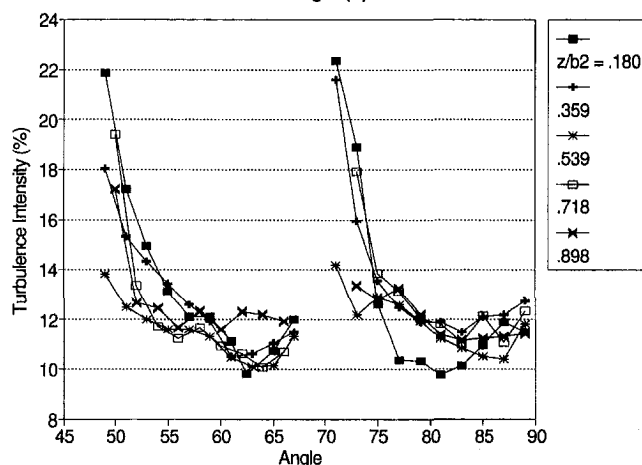


Fig. 8(c)

Fig. 8 Turbulence Intensity [%] for 16 blades (uncertainty in $Tl \pm 2.5$ percent)

The progress of primary flow downstream through the blade passage is shown in Fig. 10. The flow resembles potential flow for the majority of the blade passage length, becoming non-potential at the outer radii.

The progress of secondary flow downstream through the blade passage is shown in Fig. 11, while the deduced principal secondary flow vortices are shown in Fig. 12. The upstream secondary velocity plot (see Fig. 11(a)) shows a bulk motion from the pressure to the suction side, consistent with the existence of a

potential eddy. The superimposed vortex pattern is one with two dominant side-by-side vortices (see Fig. 12(a)). This is not the pattern normally found. This side-by-side vortex pattern would prevent the movement of low energy fluid from the shroud boundary layer toward the suction side boundary layer. This reduces the amount of low energy fluid being added to the suction side boundary layer. Instead, fluid from the pressure side and shroud boundary layers is drawn into the middle of the passage where it is re-energized.

The middle secondary velocity (see Fig. 11(b)) shows a simpler flow pattern than at the previous location (see Fig. 12(b)). The overall motion is now strongly from the suction to the pressure side, but the two counter-rotating vortices are now located in mid-channel. The shroud vortex rotates clockwise and the much weaker hub vortex rotates counter-clockwise.

The downstream secondary velocity (see Fig. 11(c)) shows the overall motion is now strongly from the suction to the pressure side, but there seems to be only one vortex observable, the hub vortex having negligible strength.

The progress of turbulence intensity downstream through the blade passages is shown in Fig. 13. The turbulence intensity at the inlet is considerably higher in the highly distorted shroud flow than anywhere else in the passage. There is likely transient flow separation along the shroud surface. Also, there seems to be pressure side transient separation at the first measurement location, probably due to the potential eddy. The downstream turbulence intensity plots show no evidence of transient boundary layer separation.

The blade loading (see Eq. (1)), is plotted in Fig. 14. The BL parameter was calculated as with the 16-blade case. The blade-loading figure shows that the calculated blade loading varies considerably with radius, but is more consistent with axial location (depth). Again, the blade loading at the design flow does exceed the recommended value of 0.7, which is inconsistent with the lack of transient flow separation inferred for this impeller, perhaps due to the location of the peak loading relative to the location of the potential eddy. The peak loading takes place near a radius of 175 mm, which is near the location of the minimum measured secondary flow velocities. At radii less than 175 mm, the secondary flow acts to increase the fluid velocity along the suction side boundary layer, preventing flow separation. Once the flow is downstream of the center of the potential eddy, the blade loading decreases with increasing radius, where the boundary layer is normally thicker because of friction losses. This reduces the tendency toward boundary layer separation.

The measured area ratio of this impeller is approximately 1.5. Based on the Rothe and Johnston (1976) criteria, some separation should be expected at any loading, and from Howard (1978), full exit stall for BL exceeding 0.8. Thus, simple blade loading and

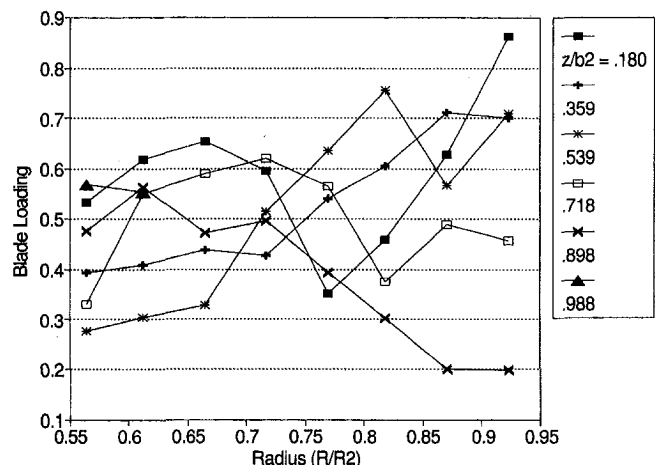


Fig. 9 Blade loading for 16-blade impeller (uncertainty in $BL \pm 1.7$ percent)

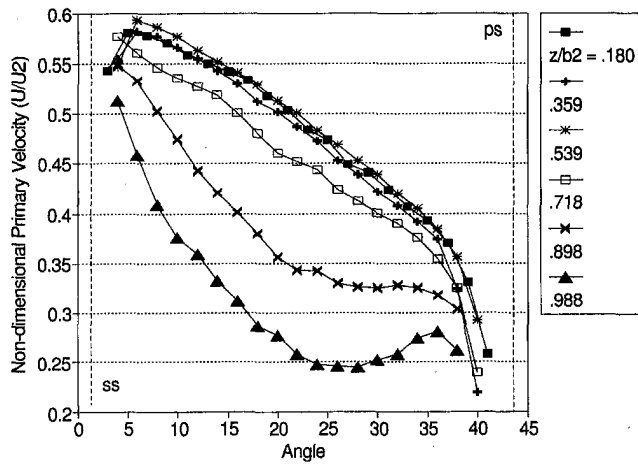


Fig. 10(a)

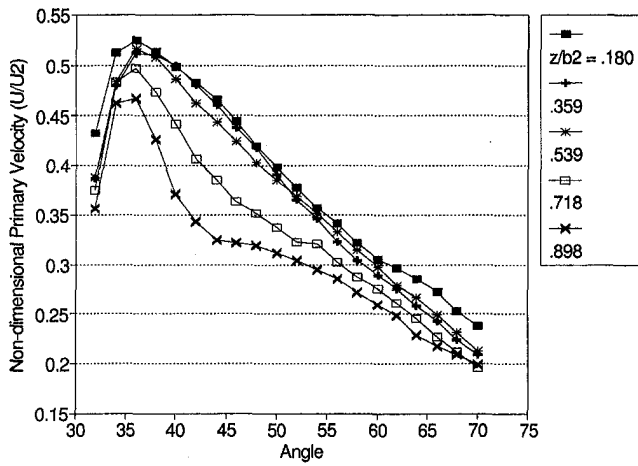


Fig. 10(b)

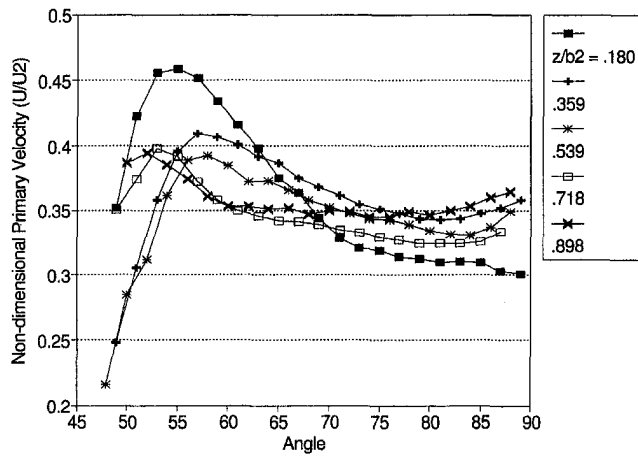


Fig. 10(c)

Fig. 10 Nondimensional primary velocity $[U/U_2]$ for 8 blades (uncertainty in $U/U_2 \pm 1.2$ percent)

area ratio criteria do not provide accurate guidance for this case. The equivalent diffuser angle is about 3 degrees, and the Rossby number is about 2.2.

Comparison Between 16 and 8 Blade Impellers. According to inviscid theory, the blade loading for the 8-blade impeller should be higher than the 16-blade impeller, because only half the blades are available to induce the change in flow direction. As

shown in Figs. 9 and 14, the peak blade loading for the 8-blade impeller is not significantly higher than the peak blade loading for the 16-blade impeller. Despite the greater theoretical blade loading, the 8-blade case retains the characteristics of potential flow for most of the length of the blade passage, while the 16-blade case exhibits significant suction side boundary layer growth, and signs of transient flow separation at higher radii. Suction side boundary layer growth does occur in the 8-blade case, but it never dominates the passage flow.

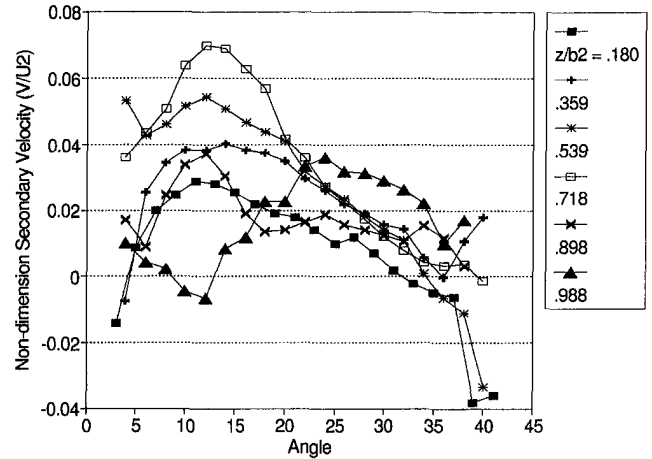


Fig. 11(a)

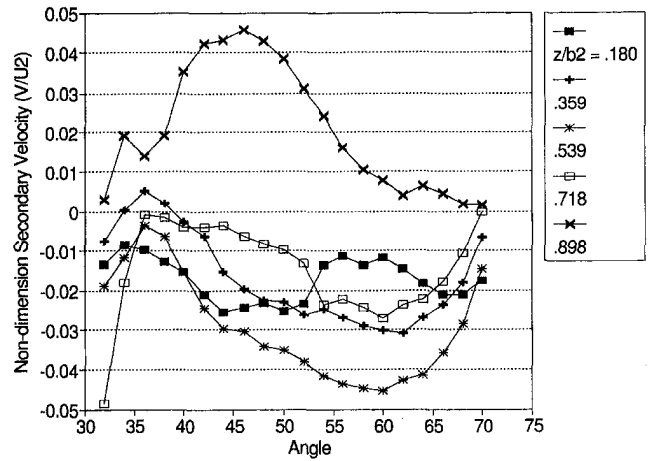


Fig. 11(b)

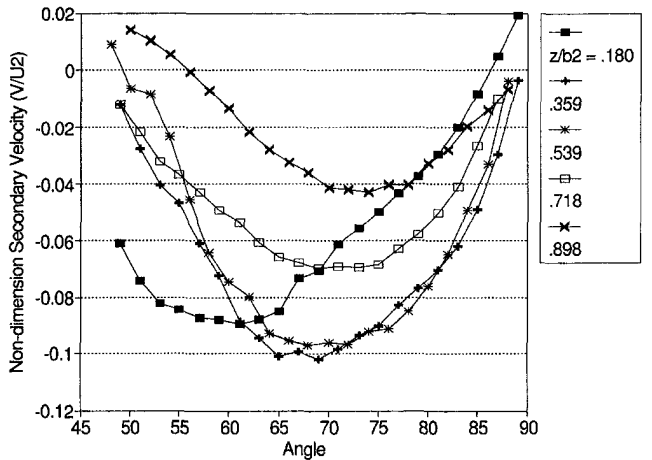


Fig. 11(c)

Fig. 11 Nondimensional secondary velocity $[W/U_2]$ for 8 blades (uncertainty in $W/U_2 \pm 2.2$ percent)

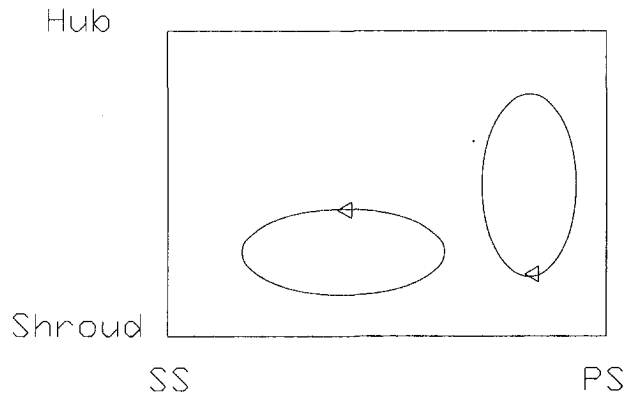


Fig. 12(a)

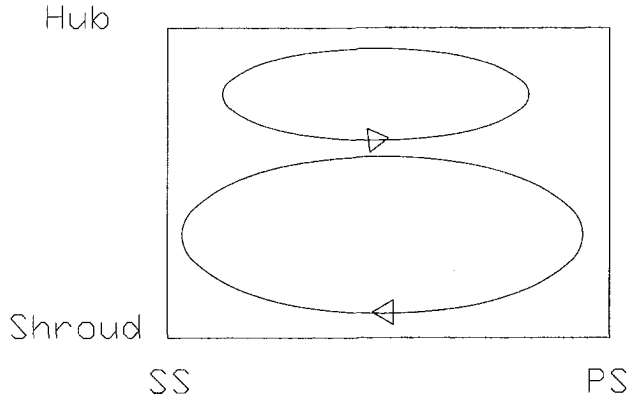


Fig. 12(b)

Fig. 12 Schematic of the 8-blade impeller secondary vortices

The bulk secondary flows in the 8-blade impeller are much stronger than for the 16-blade impeller, because of the stronger potential eddy. The eddy in the 8-blade impeller can be much stronger than for the 16-blade impeller, because the solidity is much lower. The superimposed vortex patterns are also different in the 8 and 16 blade impellers. The 16-blade impeller starts with one main vortex, and ends with hub and shroud vortices, while the 8-blade impeller starts with suction- and pressure-side vortices and also ends with hub and shroud vortices. This unusual vortex pattern may be caused by the stronger secondary flow generated in the passage by the stronger potential eddy. At higher radii the strong potential eddy stops driving the passage flow toward the suction surface and, near the exit, drives it toward the pressure surface. Thus, in that region, the normal vortex pattern develops in the 8-blade case.

The core flow turbulence intensities for both impellers drop as the flow progresses downstream. However, the 16-blade case shows a dramatic increase in the turbulence intensity of the suction-side hub-corner at high radii, while the 8-blade case shows no similar increase. This increase could signal the onset of transient flow separation, which would then be present in the 16-blade case but not the 8-blade case. This is consistent with Dengel and Frenholz (1990), who measured transient flow separation at turbulence intensities greater than 16%.

Comparison With Other High Blade Loading Impellers. It is useful to compare the present results with the previous investigation by Abramian and Howard (1994b) of a very low specific speed centrifugal impeller with 8 blades. The specific speed was 0.19 (515 US). The measurement techniques and apparatus were essentially the same as described in this investigation. Abramian reported no evident signs of separation in his impeller at design flow, even though the blade loading parameter (C_3) reached 2.5

(Fig. 11 of Abramian and Howard, 1994b). This maximum value, which occurred at the exit of the impeller, is more than twice the maximum blade loading calculated for the current 8-blade impeller. In neither case was any separation fully evident. The area ratio for the Abramian impeller was approximately 1.6. An area ratio of 1.6 is likely to lead to strong separation (full exit stall) at any loading exceeding $C_3 = 0.7$, according to Rothe and Johnston

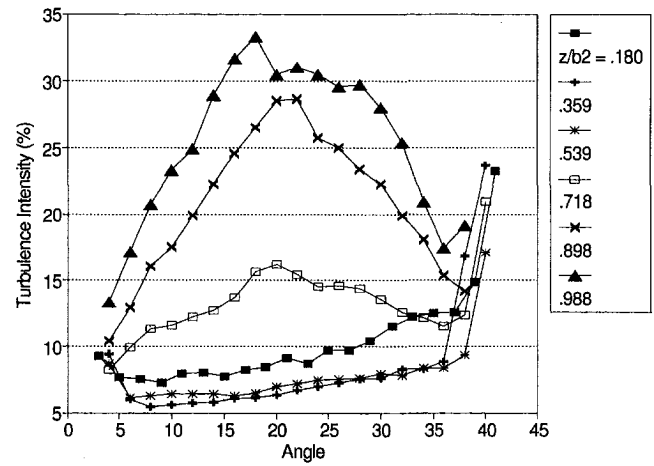


Fig. 13(a)

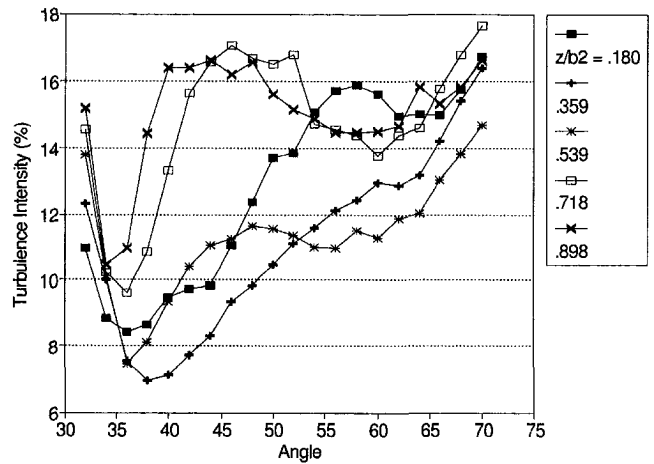


Fig. 13(b)

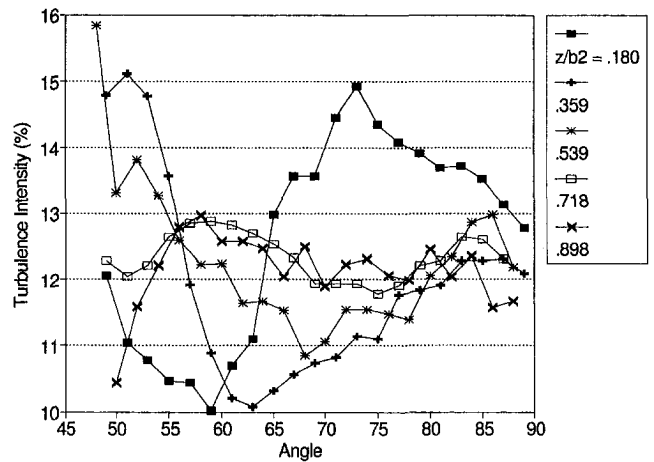


Fig. 13(c)

Fig. 13 Turbulence intensity [%] for 8 blades (uncertainty in 71 ± 2.5 percent)

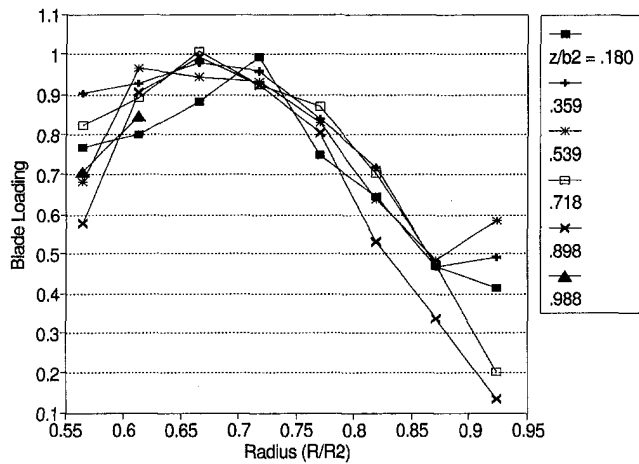


Fig. 14 Blade loading for 8-blade impeller (uncertainty in $BL \pm 1.7$ percent)

(1976) and Howard (1978). The Abramian impeller had a swirl inducer in the inlet region, which may help reduce the tendency for separation to occur, by changing the angle of incidence at the impeller inlet, and the equivalent diffuser angle. It may be observed that the tendency for separation to occur in centrifugal impellers with extremely high blade loading is not well predicted by assuming that separation occurs if BL exceeds 0.7. In this respect, the 8-blade impeller shares the same characteristic, while the 16-blade impeller with lower loading shows signs of suction surface flow approaching separation.

Conclusions

The principal observation arising from the study of the two impellers is that the 8-blade impeller, with the higher blade loading, displayed a near-potential flow through the entire blade passage, together with a thinner suction side boundary layer. In both the 8 and 16-blade impellers, the primary flow is predominantly potential flow at low radii. In the 16-blade impeller, which had a lower blade loading (although still high according to usual criteria), the suction side boundary layer grows significantly after the midpoint of the blade passage, until the primary flow can no longer be represented as potential flow. This is opposite to what would be expected if blade loading were a universal criterion for suction side boundary layer growth and definitive flow separation.

For the 16-blade case, the secondary vortex pattern starts with a dominant vortex, which develops into hub and shroud vortices moving fluid from their respective boundary layers toward the suction side boundary layer. The 8-blade case starts with an unusual pattern of two side-by-side vortices, which develops into the same hub and shroud vortices like the 16-blade case, as the flow progresses downstream. The initial side-by-side vortex pattern likely reduces the motion of low energy fluid from the shroud boundary layer towards the suction side boundary layer at low radii, reducing the suction side boundary layer growth and the tendency towards suction side separation. A potential eddy is measured in both impellers, but no pressure side flow stagnation was measured.

The turbulence intensity plots for the 16-blade case suggest that transient flow separation may exist in the suction-side hub-corner at high radii (Dengel and Frenholz, 1990). There is no direct evidence of flow separation at design flow from the velocity data from either impeller.

Simple conventional blade loading criteria based on peak vane loading are apparently not suitable for predicting suction side separation in this form of pump impeller. The addition of area ratio limits, based on tests with high aspect ratio rotating diffusers, is

also not useful here, although the lower area ratio of the more highly loaded impeller passage also contributes to the modest growth of the suction side boundary layer. The measurements of the velocity fields suggest that a changed pattern of secondary flow, as found in the 8-blade impeller, has restrained the growth of the suction side boundary layer and its tendency to separate. This changed pattern seems to be associated with the interaction of the potential vortex and the through flow in the rotating passages of the radial pump impeller with low-medium specific speed. High blade loading can be tolerated without premature flow separation, by having a strong eddy vortex at appropriate location along the blade passage.

Acknowledgment

This research was supported by a grant from the Natural Sciences and Engineering Research Council of Canada.

Data Bank Contribution

These files contain the fluid velocity data for all the experimental measurement points from my thesis, not just the points reported in this paper. Each data file contains a number of individual tables. Each table is one measurement line, with constant axial and radial location. Each line in a single table is at a different angular location, and specifies the angle and the four velocity values at that location. The four velocity values are: mean radial velocity, RMS radial velocity, mean tangential velocity and RMS tangential velocity. The data for the 16 bladed impeller is in one file and the data for the 8 bladed impeller is in the other files.

References

- Abramian, M., and Howard, J. H. G., 1994, "A Rotating Laser Doppler Anemometry System for Unsteady Relative Flow Measurements in Model Centrifugal Impellers," *ASME Journal of Turbomachinery*, Vol. 116(2), pp. 260–268.
- Abramian, M., and Howard, J. H. G., 1994, "Experimental Investigation of the Steady and Unsteady Relative Flow in a Model Centrifugal Impeller Passage," *ASME Journal of Turbomachinery*, Vol. 116(2), pp. 269–279.
- Dengel, P., and Frenholz, H. H., 1990, "An experimental investigation of an incompressible turbulent boundary layer in the vicinity of separation," *Journal of Fluid Mechanics*, Vol. 212, pp. 615–636.
- Fischer, E. H., and Thoma, D., 1932, *Investigation of the Flow Conditions in a Centrifugal Pump*, *Trans. ASME*, Vol. 54, paper HYD-54-8.
- Hamkins, C. P., and Flack, R. D., 1986, "Laser Velocimeter Measurements in Shrouded and Unshrouded Radial Flow Pump Impellers," *ASME Journal of Turbomachinery*, Vol. 109(1), pp. 70–76.
- Hesse, N., 1997, "Experimental Investigation of Blade Loading Effects in Rotating Passages of Centrifugal Impellers," University of Waterloo, Waterloo, Ontario, Canada.
- Hill, P. G., and Moon, I. M., 1962, "Effects of Coriolis on the Turbulent Boundary Layer in Rotating Fluid Machines," *Technical Report No. 69*, Gas Turbine Laboratory, M.I.T., June.
- Hirsch, Ch., Kang, S., and Pintel, G., 1996, "A Numerically Supported Investigation of the 3D Flow in Centrifugal Impellers, Part II: Secondary Flow Structures," *ASME Paper No. 96-GT-152*, New York, NY.
- Howard, J. H. G., 1978, "The Use of Parameters based on Accelerations Normal to a Relative Streamline in Centrifugal Impeller Design," *Proc. of First International Conference of Centrifugal Compressor Technology*, A1-1–A1-13, Madras, India.
- Howard, J. H. G., and Kittmer, C. W., 1975, "Measured Passage Velocities in a Radial Impeller with Shrouded and Unshrouded Configurations," *ASME Journal of Engineering for Power*, Vol. 97, pp. 207–213.
- Howard, J. H. G., and Lennemann, E., 1971, "Measured and Predicted Secondary Flows in a Centrifugal Impeller," *ASME Journal of Engineering for Power*, Vol. 93(1), pp. 126–132.
- Howard, J. H. G., Osborne, C., and Japikse, D., 1994, "A Rapid Aerodynamic Loading Procedure for Centrifugal Impeller Design," 94-GT-148, ASME, New York.
- Howard, J. H. G., Patankar, S. V., and Bordinuik, R. M., 1980, "Flow Prediction in Rotating Ducts Using Coriolis-Modified Turbulence Models," *ASME JOURNAL OF FLUIDS ENGINEERING*, Vol. 102(4), pp. 456–461.
- Johnston, J. P., Halleen, R. M., and Lezius, D. K., 1972, "Effects of Spanwise Rotation on the Structure of Two-Dimensional Fully Developed Turbulent Channel Flow," *Journal of Fluid Mechanics*, Vol. 56(3), pp. 533–557.
- Kline, Stephen J., 1959, "On the Nature of Stall," *ASME Journal of Basic Engineering*, Vol. 81(3), pp. 305–320, Sept.
- McDonald, G. B., Lennemann, E., and Howard, J. H. G., 1971, "Measured and Predicted Flow Near the Exit of a Radial Flow Impeller," *ASME Journal of Engineering for Power*, Vol. 93, pp. 441–446.
- Moore, J., 1973, "A Wake and an Eddy in a Rotating, Radial-Flow Passage, Part 1: Experimental Observations," *ASME Journal of Engineering for Power*, Vol. 95, pp. 205–212.

Moore, J., 1973, "A Wake and an Eddy in a Rotating, Radial-Flow Passage. Part 2: Flow Model," *ASME Journal of Engineering for Power*, Vol. 95, pp. 213-219.

Morris, R. E., and Kenny, D. P., 1971, "High Pressure Ratio Centrifugal Compressors for Small Gas Turbine Engines," *Advanced Centrifugal Compressors*, Turbomachinery Committee of the ASME Gas Turbine Division, ASME, New York, pp. 118-146.

Rothe, P. H., and Johnston, J. P., 1976, "Effect of System Rotation on the Performance of Two-Dimensional Diffusers," *ASME JOURNAL OF FLUIDS ENGINEERING*, Vol. 98, pp. 422-430.

Sabersky, R. H., Acosta, A. J., and Hauptmann, E. G., 1989, *Fluid Flow, 2nd Ed.*, Chapter 11, MacMillan, New York.

Stepanoff, A. J., 1957, *Centrifugal and Axial Flow Pumps, 2nd ed.*, Wiley, New York.

Stratford, B. S., 1959, "The Prediction of Separation of the Turbulent Boundary Layer," *Journal of Fluid Mechanics*, Vol. 5(1), pp. 1-16.

Visser, F. C., 1996, "On the Flow in Centrifugal Impellers," University of Twente, The Netherlands.

Turbulence Modeling and Computation of Viscous Transitional Flows for Low Pressure Turbines

A. Chernobrovkin
Graduate Assistant.

B. Lakshminarayana
Evan Pugh Professor.

Center for Gas Turbines and Power,
The Pennsylvania State University,
153 Hammond Building,
University Park, PA 16802
e-mail: b1laer@engr.psu.edu

Variation of the flow Reynolds number between the take off and cruise conditions significantly affects the boundary layer development on low-pressure turbine blading. A decreased Reynolds number leads to the flow separation on the suction surface of the blading and increased losses. A numerical simulation has been carried out to assess the ability of a Navier-Stokes solver to predict transitional flows in a wide range of Reynolds numbers and inlet turbulence intensities. A number of turbulence models (including the Algebraic Reynolds Stress Model) and transition models have been employed to analyze the reliability and accuracy of the numerical simulation. A comparison between the prediction and the experimental data reveals good correlation. However, the analysis shows that the artificial dissipation in the numerical solver may have a profound effect on the prediction of the transition in a separated flow.

Introduction

One challenging problem in turbomachinery is to understand the flow physics of the transitional flows associated with the laminar separation and the rotor-stator interaction in Low-Pressure (LP) turbines. The rotor-stator interaction flow is inherently unsteady and transitional. Additional complexities arise due to the extended lengths of transitional boundary layers along the blade surfaces. Such complex unsteady and transitional boundary layer flow is known to affect the aerodynamic and thermal performance of a turbomachine. The transition from laminar-to-turbulent flow on the blade surface is a common, yet complex, phenomenon in turbomachinery. The boundary layer development, losses, efficiency, and heat transfer are greatly affected by the transition. The ability to accurately predict the onset and length of the transition is very important in the design of efficient and reliable machines. Transition in a low-pressure turbine may occur in either bypass form, an attached boundary layer, or through the development of a separation bubble, depending on the Reynolds number at the take-off and the cruise condition. At cruise condition, the flow Reynolds number may be less than half of the value at the take-off condition. This may result in separated flow and efficiency degradation. Development of a reliable prediction technique may lead to an improved efficiency and thrust/weight characteristics.

Considerable effort has been spent in investigating the ability of different turbulence models to predict various types of transitional flows. A systematic approach undertaken by the ERCOFTAC group is summarized by Savill (1997). Nevertheless, very few investigations focused on turbomachinery flows with transition over a laminar separation bubble, especially at a high level of freestream turbulence (Michelassi et al., 1997; Huang et al., 1998).

The objective of the investigation reported in this paper is to gain a detailed understanding of the unsteady transitional flows in low-pressure turbines, with emphasis on separation-induced, steady transition. The test case chosen for this study is the simulation of separation and transition of the flow over the suction surface of a low-pressure turbine cascade blade investigated experimentally by Qiu and Simon (1997) and Simon and Qiu (1999).

The influences of freestream turbulence and pressure gradient are investigated. An existing Navier-Stokes unsteady flow solver is used. Three low-Reynolds-number forms of two-equation turbulence models and an ARSM have been incorporated and tested for accuracy. In order to overcome the over-prediction of turbulence kinetic energy and the dissipation rate near the leading edge, several modifications of the production terms have been incorporated in the two-equation models.

Description of the Test Case

The experimental data in a simulated LP turbine cascade have been used to assess the ability of the numerical solver. A schematic of the facility is shown in Fig. 1 (Qiu and Simon, 1997). The cascade flow was simulated using a channel with a convex and a concave wall profiled as suction and pressure surfaces of a turbine blade. A flow suction device was utilized to simulate periodic flow near the leading edge. Experiments were carried out with the inlet flow velocity ranging from 3 to 12.5 m/s, which corresponds to Re number based on chord length from 50,000 to 200,000. A number of turbulence generators were utilized to generate flows with 0.5, 2.5, and 10% inlet turbulence intensities. Boundary layer characteristics were measured using a hot-wire probe. Coordinates of measurement locations are given in Table 1. According to Qiu and Simon (1997), the uncertainty in the mean velocity is 3.6%, and the fluctuating velocity is 4%.

Numerical Procedures and Models

The flow solver is based upon full, Favre-averaged, Navier-Stokes equations. An explicit, four-stage Runge-Kutta scheme is used for the time integration of both mean-flow and turbulence equations. A compact second-order accurate, central difference, flux evaluation scheme is employed for the convection terms. Diffusion terms are discretized using second-order-accurate central differences. A detailed description of the numerical procedure for the steady solver can be found in Kunz and Lakshminarayana (1992). The solver was extensively verified and validated for different flows. A modified solver was successfully utilized for the numerical simulation of unsteady transitional flows in compressor and turbine cascades (Chernobrovkin and Lakshminarayana, 1998). A set of low Re; k - ϵ turbulence models (Chien, 1982, denoted as CH; Lam-Bremhorst, 1981, denoted as LB; and Fan-

Contributed by the Fluids Engineering Division for publication in the JOURNAL OF FLUIDS ENGINEERING. Manuscript received by the Fluids Engineering Division December 14, 1998; revised manuscript received September 16, 1999. Associate Technical Editor: P. Bradshaw.

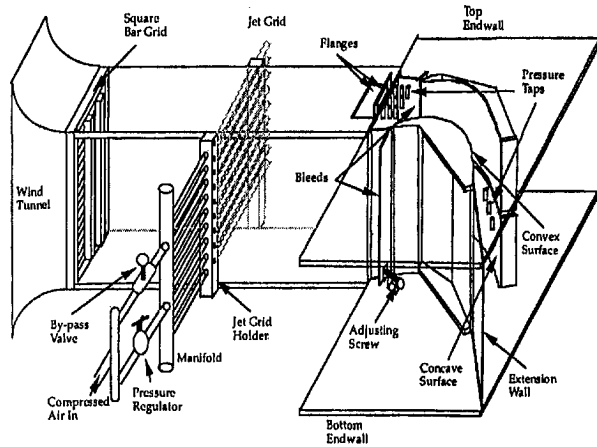


Fig. 1 Schematic of the experiment

Lakshminarayana-Barnett, 1993, denoted as FLB), and hybrid ARS/ $k-\epsilon$ models are employed for the numerical simulation. The ARS component of the model represents an implicit ARSM (Rodi, 1976). To avoid the problem with the low-Re, ARS model, the near wall region is calculated using a low-Re, $k-\epsilon$ model. Turbulence quantities (R) based on the ARS model are interfaced with those based on the low-Re, $k-\epsilon$ model using the matching function:

$$f_m = \frac{1}{2} \left(\frac{\tanh \left(\beta \frac{Re_y}{1.83} / y_{match}^+ - 1 \right)}{\tanh(\beta)} + 1 \right)$$

$$R_{vis} = f_m R_{ARSM} + (1 - f_m) R_{k-\epsilon}$$

where: y_{match}^+ is the inner variable at matching point, and β is the slope constant.

Numerical simulation shows that for the LP turbine flow, utilization of the explicit ARSM does not modify the solution outside the boundary layer, but may cause a stability problem. To avoid this instability and minimize the CPU time, the ARSM is used only up to twice the boundary layer thickness from the blade surface.

Experimental data were acquired assuming two-dimensionality of the flow. However, turbulent and, especially, transitional fields are essentially three-dimensional. To address this feature, the numerical simulation based on the ARSM/ $k-\epsilon$ approach is carried out using a three-dimensional solver. The symmetry boundary condition in the spanwise direction forces the mean flow to be two-dimensional. Nevertheless, the turbulence field includes the spanwise component of Reynolds stress tensor.

Table 1 Locations of the experimental data points on the suction blade surface

N	x/C_x	N	x/C_x	N	x/C_x
P1	0.	P6	0.5506	P11	0.8593
P2	0.0398	P7	0.6247	P12	0.9111
P3	0.2111	P8	0.6889	P13	0.9728
P4	0.3778	P9	0.7457		
P5	0.4667	P10	0.8173		

Experimental data were acquired in a "channel" type configuration, while "cascade" configuration was chosen for the numerical simulation. Utilization of a bleeding device to model the cascade flow may lead to a discrepancy in the flow angle in the vicinity of the leading edge. To verify the potential effect of this discrepancy, a numerical simulation of the cascade flow with different inlet flow angles was carried out. A comparison of the predicted and the measured blade pressure distribution indicate that the best prediction has been achieved at the design flow angle (Fig. 2).

Another potential source of the discrepancy between the channel and cascade configurations is the flow near the trailing edge. An extension wall employed in the experiment provides a smooth development of the boundary layer beyond the point of the virtual trailing edge. In contrast, the flow over a real trailing edge is characterized by a sudden change in the flow angle, local variation of the pressure, etc. The numerical experiment shows that, in the case of the attached flow, utilization of either approach leads to a practically identical solution except in the region 5% upstream of the trailing edge. However, the flow prediction based on cascade configuration results in significant instability as soon as the reattachment point moves downstream of the trailing edge. In order to reduce the effect of this phenomenon, but keep the cascade approach, the blade has been extended using an extension wall with zero thickness for cases with a separation bubble.

The numerical investigation requires a verification to ensure grid independence. A number of grids (121×71 , 141×91 , and 241×181) were utilized to study the grid dependency of the solution. The maximum distance between the surface and the first grid point varies between $y^+ = 0.8$ for the coarse grid to $y^+ = 0.12$ for the finest grid. At $x/c_x = 0.65$, the coarse grid has 20 grid points within the boundary layer and 18 grid points within the laminar sublayer. The fine grid has 35 and 15 points correspondingly. Numerical predictions based on coarse and fine grids are very close to each other. In some cases, the fine grid solution was not stable in the transition region over a separation bubble. The difference between the solutions based on fine and coarse grids is minimal for the converged solution. All the reported simulation

Nomenclature

C_p = Pressure coefficient, $C_p = (p_{01} - p)/(p_{01} - p_2)$
 C_x = axial chord length
 k = turbulent kinetic energy
 k_{2ke} = Coefficient of the second-order artificial dissipation, turbulence equations
 k_4 = coefficient of the fourth-order artificial dissipation
 P_k = production of turbulent kinetic energy
 \bar{S} = strain rate tensor
 \bar{R} = rotation rate tensor
 Re_θ , Re_x = Reynolds number, based on θ , x
 Re_y = turbulent Re number, \sqrt{ky}/ν

T_u = turbulence intensity
 x = axial length measured from leading edge
 y = distance normal to surface
 u', v', w' = $x, y,$ and z components of fluctuating velocity
 u' = total fluctuating velocity in Figs 5–9, 12, 13 (RMS value)
 U = total velocity
 V = y -component of velocity
 y^+ = inner variable, $u, y/\nu$
 ϵ = turbulence dissipation rate
 θ = momentum thickness
 γ = intermittency

Subscripts

0, inl = total, inlet, free stream
 1 = inlet
 2 = outlet
 ARSM = based on algebraic Reynolds stress model
 e = values at the edge of the boundary layer
 $k-\epsilon$ = based on $k-\epsilon$ model
 Ref = reference value
 s = separation inception
 t = turbulent
 tr = transition inception
 Vis = viscous
 W = quantity at the wall

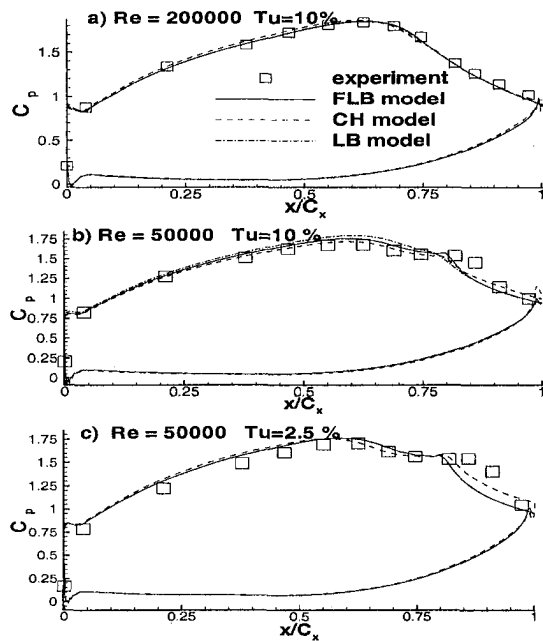


Fig. 2 Surface pressure distribution

data in this paper are based on the 141×91 grid. Additional discussion on the code verification is presented later.

The numerical simulation of transitional flow in turbomachinery cascades reveals a deficiency of the standard $k-\epsilon$ model in predicting flow with a high free stream turbulence level. Non-physical increase in the turbulence intensity near the stagnation point may "contaminate" the boundary layer turbulence and trigger an earlier transition. An elevated level of the turbulence at the mid-passage, in the zone of maximum flow acceleration, leads to 2–3% higher level of freestream turbulence at the boundary layer edge. The replacement of the turbulence production term based on $\vec{S} \cdot \vec{S}$ with one based on $\sqrt{S^2 R^2}$ is used to improve the prediction of the turbulence field near the stagnation point. The standard form of the production term is utilized for the flow calculation in the free stream. After incorporating the modification to the production term, the inlet distribution of the dissipation rate is set so that the predicted kinetic energy distribution along the boundary layer edge correlates with measured one.

Prediction Using $k-\epsilon$ Model

Case $Re = 200,000$, $Tu = 10\%$. The distribution of the surface pressure predicted by different turbulence models is compared with the experimental data in Fig. 2. Since the flow is fully attached at this Reynolds number, the pressure increases monotonically along the rear part of the suction surface. There is no difference between the blade pressure distribution predicted by various turbulence models. Flow with $Re = 200,000$ and $Tu = 10\%$ is fully attached on the suction surface according to the prediction based on FLB model (Fig. 3). This flow pattern is different from those observed at $Re = 50,000$ and $Tu = 10\%$ where transition takes place over a laminar separation bubble, as shown in Fig. 4.

In the laminar part of the boundary layer (experimental locations P2–P7, Table 1), the predicted velocity field exactly matches the measured values. For brevity, this comparison is not shown. Velocity and turbulence intensity profiles at locations P8–P13 are shown in Fig. 5. The beginning and the end of the transition, as well as the separation location predicted by various turbulence models, are compared with the data in Table 2.

In the laminar boundary layer, the prediction based on the LB model is identical to that based on the FLB model. The turbulence

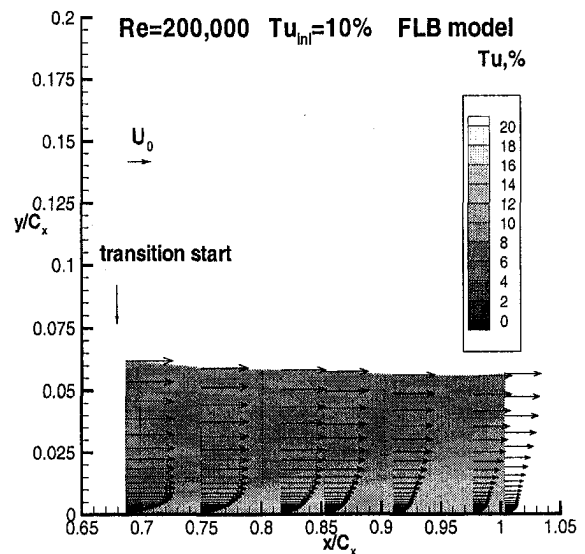


Fig. 3 Transition in attached boundary layer

intensity profile shows that the CH model predicts an amplification of the turbulent kinetic energy in the laminar boundary layer. While the eddy viscosity predicted by the CH model is four to five times higher than the eddy viscosity predicted by the FLB or LB models, it is still small. Although the ratio of eddy viscosity to laminar viscosity is about 4, this part of the boundary layer has laminar features. The primary source of the elevated level of turbulence in the boundary layer predicted by the CH model is the lack of the dissipation to disperse the increase in the turbulent kinetic energy near the leading edge, convected downstream. This increased level of turbulence intensity predicted by the CH model contributes to an earlier transition.

The simulation based on the CH model predicts the transition at about 58% of the chord. The best agreement between the measured and the predicted velocity profile is achieved in simulations based on FLB and LB models. At locations P8 and P11, the predicted velocity profiles are identical to the experimental data. At locations, P9 and P10, the measured profiles are less full in comparison with the numerical solution. The turbulence profile at P10 is very close to a 'fully developed' profile shape. As a consequence of this, the predicted velocity profiles at P9–P10 are closer to a turbulent profile when compared to those of the data.

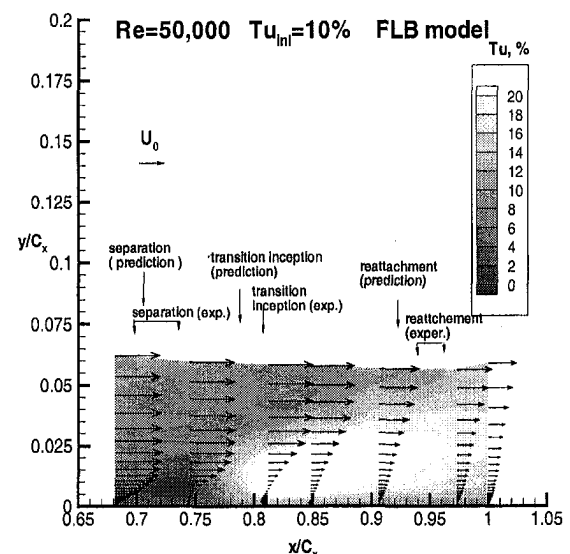


Fig. 4 Transition over a laminar separation bubble

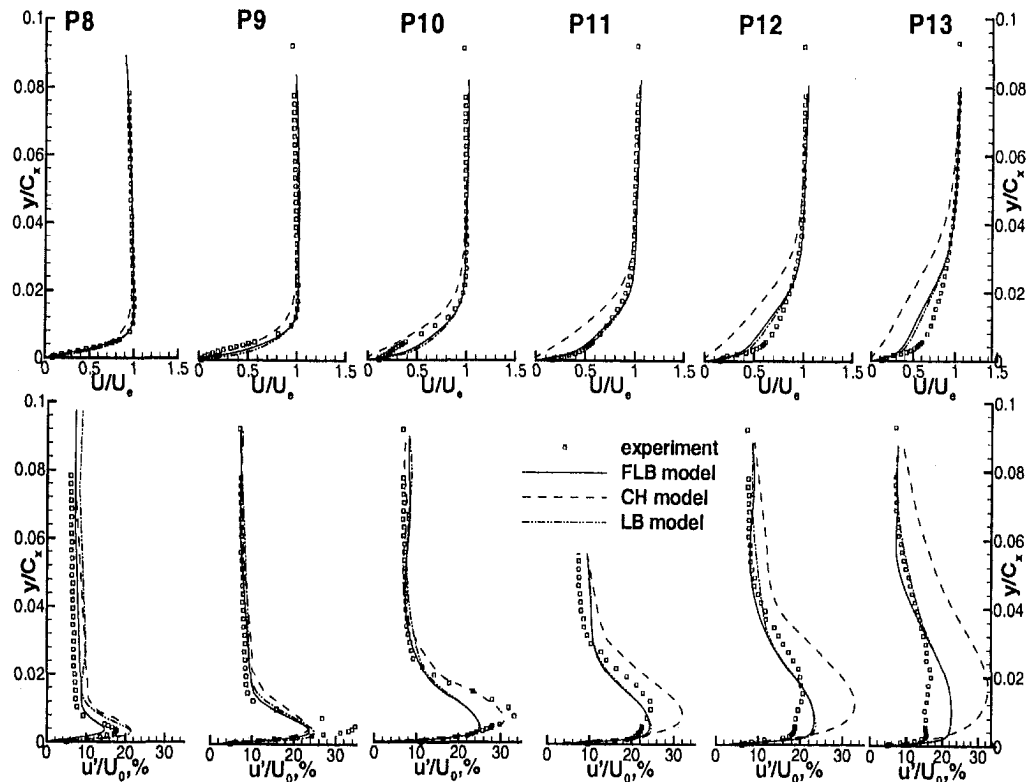


Fig. 5 Velocity and turbulence intensity, $Tu = 10\%$, $Re = 200000$

The main drawback of the CH model is the existence of a very thin separation zone near 75% of the chord. The CH model, based on y^+ , is known for its poor performance in separated flows. The CH model thus over-predicts the turbulence intensity in the turbulent boundary layer by 50–70%.

Case $Re = 50000$, $Tu = 10\%$. The reduced Re number results in the development of a medium-size separation bubble (Fig. 4). The separation zone is characterized by the presence of a flat zone in the pressure distribution at $x/C_x \sim 0.75$ on the suction surface of the blade (Fig. 2(b)). A solution based on the FLB model correctly predicts this trend, but shows an earlier return to an adverse pressure gradient in comparison with the experimental data. As confirmed by the velocity profiles, this is due to a smaller separation bubble and earlier reattachment of the flow. In spite of the presence of the separation bubble in the simulation based on LB and CH models, the region of constant pressure is not so clearly predicted by these two models.

Velocity profiles are plotted in Fig. 6. Experimental data indicate that the flow separates at about 74% of the chord and transition to turbulence occurs over a laminar separation bubble at about 75–82% of the chord length. All three models predict the inception of laminar separation at the same location; $x/C_x = 71\%$ of the chord. The length of the laminar region inside the separation bubble varies for different models. The CH model predicts the transition inception to occur immediately after the inception of the

separation at 71% of the chord. A simulation based on the FLB model predicts the transition inception at 78% of the chord, with the distance between the separation point and inception of transition equal to 7%, which is close to the measured value.

Transition to turbulence over the separation bubble is characterized by the inception of the transition in the shear layer with further penetration through the separation zone. The maximum turbulence intensity is located farther from the wall, in comparison with high- Re cases (Fig. 6, Fig. 5). Contrary to the measured data, the numerical simulation predicts strong backward flow inside the separation flow (point P10). Additional turbulence production due to higher shear stresses in the zone of separated flow increases the turbulence intensities in the separation bubble. The predicted turbulence profile has a smoother distribution, and its maximum is located closer to the wall, in comparison with the experimental data. In the case of FLB and LB models, an increased level of turbulence in the separation zone leads to a smaller thickness of the separation bubble and an earlier reattachment. A comparison between the numerical simulation and the data is given in Table 3.

Case $Re = 50000$, $Tu = 2.5\%$. This case is the most difficult to compute. A low level of turbulence at a low Re number leads to an inherently unsteady flow with an unsteady separation bubble and a time-varying transitional zone. Even though the results presented in this paper are based on the steady solution, the analysis of the convergence and unsteady flow simulation indicates

Table 2 Inception and length of the transition, separation and reattachment points, $Re = 200000$, $Tu = 10\%$

	Experiment	Prediction FLB model	Prediction CH model	Prediction LB model
Transition inception, x/C_x	62–69%	~65%	57–59%	61%
End of transition, x/C_x	74–81%	82%	94%	80–82%
Separation, x/C_x	71% ¹	attached	75%	attached
Reattachment, X/C_x	82% ¹	—	no reattachment	—

¹ Flow visualization indicates the presence of a very small separation bubble at $x/C_x = 0.7$.

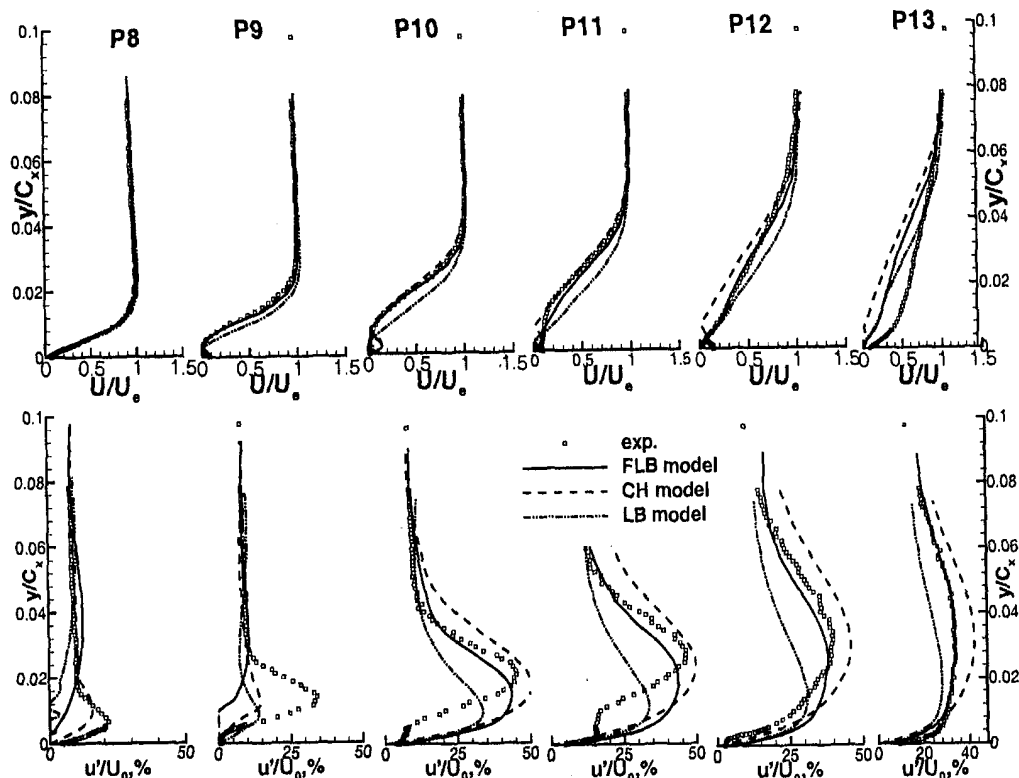


Fig. 6 Velocity and turbulence intensity, $Tu = 10\%$, $Re = 50000$

the need for implementation of a time accurate simulation to achieve better resolution of the flow physics. No results for the LB model are presented because attempts to stabilize the solution using increased artificial dissipation resulted in total damping of the separated flow. For the CH and FLB models, the flow has moderate fluctuation in the size and extent of the separation bubble. The data presented are calculated as averages of these fluctuations. This variation affects the rear part of the separation region and does not influence the location of the separation or of the transition inception points.

A comparison between the predicted and the measured surface pressure distribution is shown in Fig. 2(c). Both models underpredict the extent of the separation bubble, which results in a shorter zone of constant pressure. A comparison of the measured and the predicted velocity and turbulence intensity profiles (Fig. 7) shows similar trends to the cases described earlier. The numerical solver overpredicts the turbulence intensity in the transition zone; while for the flow with high freestream turbulence level, the maximum turbulence intensity is underpredicted (similar to $Re = 200,000$ and $Tu = 10\%$ case). There is no peak in the predicted turbulence fluctuations above the separation bubble in the transition region, observed in the experimental data. The prediction based on the FLB model has a smaller separation bubble thickness and a slightly earlier reattachment. The thickness of the separation bubble is equal to the experimental thickness at point P9, about $\frac{1}{2}$ of the experimental thickness at point P10 and $\frac{1}{3}$ at point P11. For the

FLB model, the variation in the thickness of the separation bubble was 50%. A low level of the freestream turbulence delays predicted reattachment from the 93% to 99% of the chord. A comparison between the numerical simulation and the data is given in Table 4.

Prediction Using Hybrid ARSM/ $k-\epsilon$ Model

Experimental data for transition over a laminar separation bubble shows a strong redistribution of the turbulent kinetic energy among components in the transition zone. The $k-\epsilon$ model is unable to capture this redistribution zone, as well as the overall anisotropy of the turbulence field associated with the transition process. A numerical simulation based on the hybrid $k-\epsilon$ /ARSM has been carried out to investigate the ability of this model to improve the prediction of the transition over the LP turbine blading. Results of the current research as well as previously reported simulations (e.g., Abid et al., 1995) indicate that a numerical solution strongly depends on the $k-\epsilon$ model used. A comparison of the prediction based on hybrid models (ARSM/ $k\epsilon$) with different low-Re, $k-\epsilon$ (CH, FLB, LB) models indicates that the transition inception is controlled by the $k-\epsilon$ model and is close to those predicted by a corresponding $k-\epsilon$ model. Therefore, the FLB model has been chosen as the model with the best results, based on previous computations. It is used in the $k-\epsilon$ /ARSM model to follow.

For high Re and high turbulence cases, results of the numerical

Table 3 Inception and length of the transition, separation and reattachment points, $Re = 50000$, $Tu = 10\%$

	Experiment	FLB model	CH model	LB model
Transition inception, x/C_x	75–82%	78%	72%	75%
End of transition, x/C_x	>p13 97.28%	84%	85%	86%
Separation, x/C_x	70%	71%	72%	72%
Reattachment, X/C_x	92%	93%	no reattachment	no reattachment

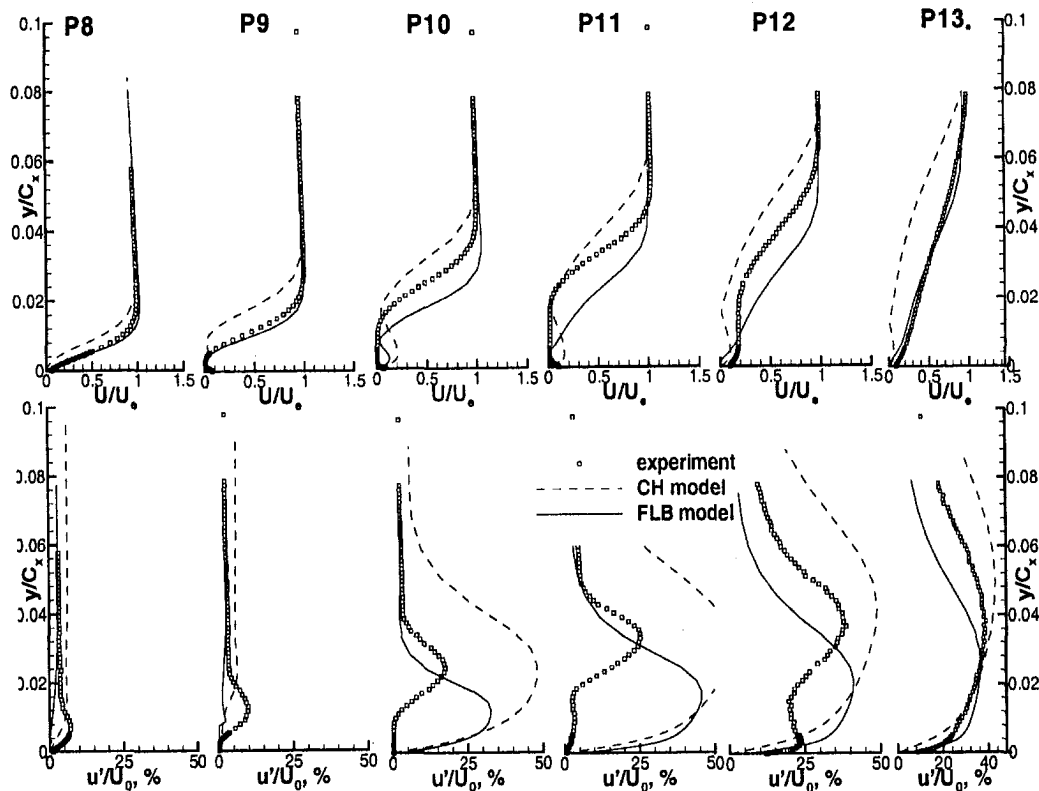


Fig. 7 Velocity and turbulence intensity, Tu = 2.5%, Re = 50000

simulation based on hybrid $k-\epsilon$ /ARSM are identical to the prediction based on the $k-\epsilon$ approach. The high-Re case is characterized by transition in an attached boundary layer or very small separation bubble. Maximum shear stresses are located close to the blade surface in the region where turbulence terms are calculated using $k-\epsilon$ model. The ARSM part is used only for the outer layer. Therefore, the influence of the hybrid approach is minimal. In contrast, the shear layer above the separation zone is located in the zone where turbulence terms are calculated using the ARSM. Thus, the hybrid approach has a more profound effect in this region. For the high Tu case (Re = 50 000, Tu = 10%), this effect is minimal and can be seen only in the turbulence field. The utilization of a hybrid model moves the peak value of the fluctuating velocity farther from the wall, and closer to the measured location. There is only a minor change in the predicted velocity field. A comparison between the predicted and the experimental data for the case with Re = 50,000 and Tu = 2.5% (Fig. 8) reveals an improvement in both the predicted velocity and the turbulence.

Current numerical simulations have been carried out without the pressure strain terms. As a result, the w' component is equal to the v' component. An analysis of the turbulent case indicates that the streamwise component has about 50% of the total turbulent kinetic energy, while v' and w' have 25% each. No significant change in the balance between the different components is found in the transition region (no more than 5% variation). The hybrid turbulence model over-predicts the maximum amplitude of the fluctu-

ation velocity similar to those observed with the $k-\epsilon$ model. However, redistribution of the turbulence energy between turbulence components plays a major role in improving the velocity prediction.

Prediction Using a $k-\epsilon$ Model in Conjunction With the Transition Model

The numerical simulation of the transitional flows based on the turbulence model generally does not provide an adequate level of accuracy and robustness. Incorporation of transition models is a potential way to improve the transition prediction. Transition models use an empirical or a semi-empirical correlation to calculate the inception and end of transition, as well as the intermittency distribution in the transition region zone. A number of models are available to calculate the inception and end of transition in an attached flow. The most common approach is the calculation of the transition inception using an empirical correlation and the calculation of the intermittency distribution using the approach suggested by Dhawan and Narasimha (1958), in conjunction with the correlation for the non-dimensional spots breakdown parameter (e.g., Gostelow and Walker, 1991; Mayle, 1991). In the current research, a model by Abu-Ghannam and Show (1980) is utilized for the transition prediction in an attached flow:

$$Re_{thr} = 163 + \exp \left[F(\lambda) - \frac{F(\lambda) \cdot Tu}{6.91} \right]$$

Table 4 Inception and length of the transition, separation and reattachment points, Re = 50000, Tu = 2.5%

	Experiment	Prediction FLB model	Prediction CH model	Prediction LB model
Transition inception, x/C_x	84–85%	~80%	~78%	69%
End of transition, x/C_x	>p13, >97%	86%	88%	97%
Separation, x/C_x	69%	71%	69%	72%
Reattachment, X/C_x	96%	99%	no reattachment	90%

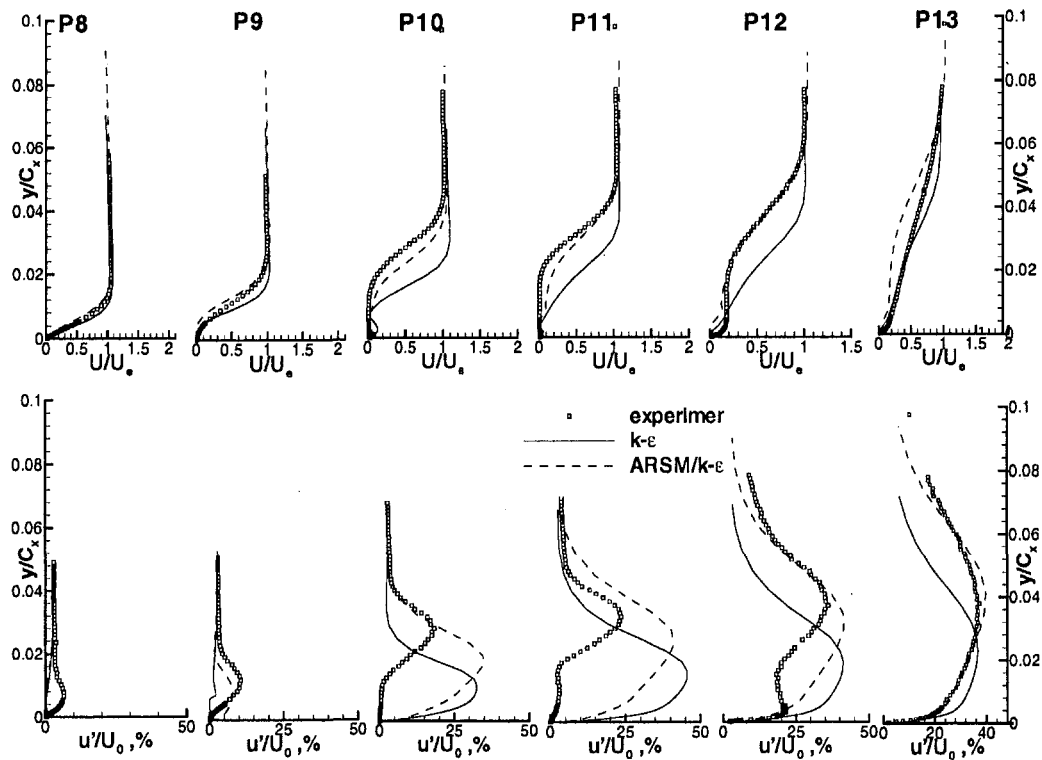


Fig. 8 Velocity and turbulence intensity, $Tu = 2.5\%$, $Re = 50000$, prediction based on hybrid ARSM/ $k-\epsilon$ approach

$$F(\lambda) = \begin{cases} 6.91 + 12.75 \cdot \lambda + 63.64 \cdot \lambda^2 & \text{if } \lambda \leq 0 \\ 6.91 + 2.48 \cdot \lambda - 12.27 \cdot \lambda^2 & \text{if } \lambda > 0 \end{cases}$$

$$\text{where } \lambda = \frac{\theta^2 \left(\frac{\partial p}{\partial x} \right)}{\mu U_e}$$

transition is completed when:

$$Re_{\theta} = 2 Re_{\theta_{tr}}$$

The intermittency distribution is based on Dhawan and Narasimha (1958).

Transition models for separated flows correlate the distance between the separation and transition inceptions. In the current paper, the model due to Davis et al. (1985) is used:

$$Re_{x_{tr}} - Re_{x_s} = 25 \cdot 10^3 \log_{10} [\coth(17.32 Tu_e)]$$

As in the case of attached flow, an intermittency distribution is based on the Dhawan and Narasimha (1958) formula. Even though this relation was suggested for attached flow, a comparison presented in Qiu and Simon (1997) indicates that it can be applied to the separated flow.

Utilization of the transition model provides a more reliable prediction, in comparison with the "pure" turbulence model. Nevertheless, the transition model has a number of weak points. Empirical correlations are based on data that has a significant spread. The accuracy of the transition model deteriorates as flow parameters deviate from those used for the derivation of the model. A comparison between the intermittency distribution based on the transition model and the measured data shows that the transition model tends to predict an earlier transition. In addition to the transition models described earlier, calculations with the transition model based on the measured intermittency factor have been carried out to investigate an effect of the "ideal" transition model. For the attached flow case ($Re = 200,000$, $Tu = 10\%$), there is no significant difference in the predicted velocity and turbulence

fields simulated with and without transition model. This is due to the fact that the predicted transition inception based on Abu-Ghannam and Shaw correlation is located upstream of the transition inception predicted by a "pure" turbulence model. Therefore, the transition model has a minimal impact on the solution. For the separated flow, the transition model used is practically identical with the experimental data for the case with $Re = 50,000$ and $Tu = 10\%$. However, as described in Qiu and Simon (1997), for other cases with a high freestream turbulence, the correlation was not perfect.

Different approaches can be used to incorporate an intermittency distribution. Methods based on a separate solution for the laminar and turbulent parts show potential for improved flow prediction (e.g., Steelant and Dick, 1996). Nevertheless, for engineering application, it is more advantageous to have a single solver throughout the flow field. This is especially preferred from the point of view of the model extension to three-dimensional flows in turbomachines. Two methods are tried for the incorporation of an intermittency factor into the existing code. In the first method, an additional damping function $F(\gamma)$ is utilized for the calculation of the eddy viscosity (this transition model is denoted as Var. 1):

$$\mu_t = \frac{k^2}{\epsilon} c_{\mu} f_{\mu} F(\gamma), \quad \text{where } F(\gamma) = \gamma$$

where $c_{\mu} = 0.09$ and f_{μ} is the wall damping function.

This approach implicitly assumes that the eddy viscosity based on local scales is 'turbulent' in nature. If the distribution of the turbulent kinetic energy and the turbulent dissipation rate are transitional in nature, this approach may lead to an underprediction of the local eddy viscosity due to the 'double' damping by the transition model and the low- Re $k-\epsilon$ model itself. Assuming that the eddy viscosity in the transition region can be calculated correctly using the same expression for μ_t as for the turbulent part, the intermittency distribution can be utilized only through the modification of the turbulent equations. An additional damping function based on γ is applied only to the calculation of the production term (this case is denoted as Var. 2):

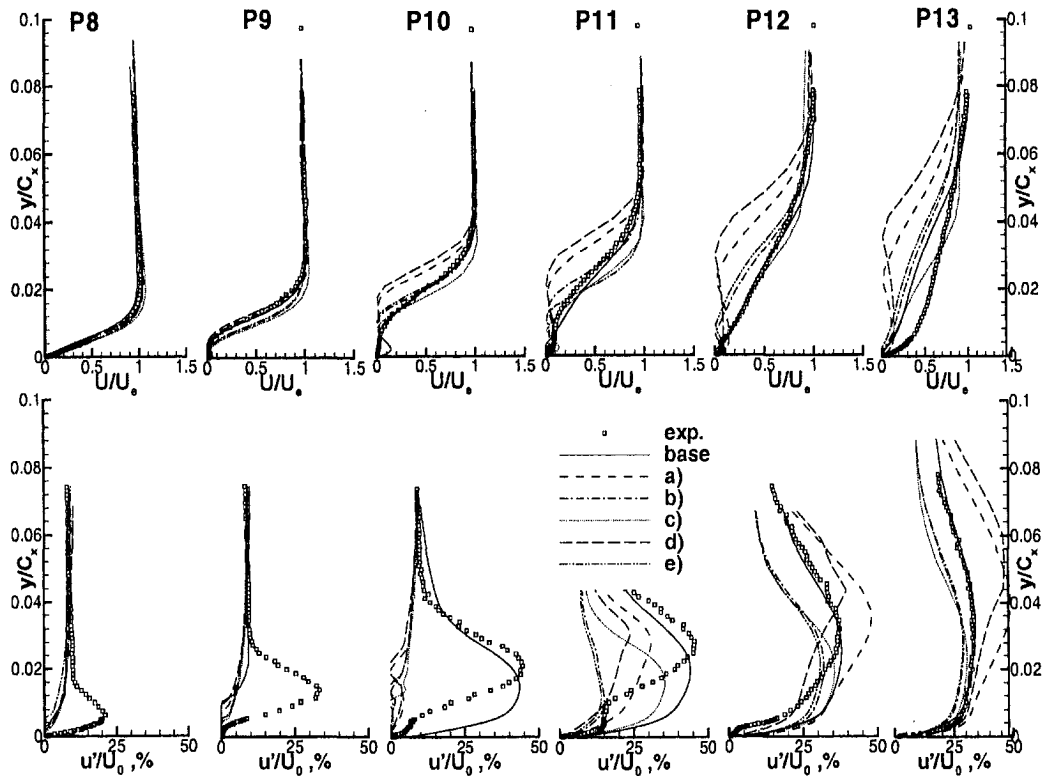


Fig. 9 Velocity and turbulence intensity, $Tu = 10\%$, $Re = 50000$, effect of the transition model utilization (a) 1d model Var1, (b) 1d model Var2, (c) "step" model, (d) 2d model Var1, (e) 2d model Var2

$$P = P^*F(\gamma), \quad \text{where } P \text{ is the turbulence production}$$

The mean flow is affected implicitly through the eddy viscosity.

In the transition zone, the intermittency distribution has a complex, two-dimensional distribution. Most transition models vary intermittency only in the streamwise direction. Based on the experimental distributions, the calculations have been carried out with the variation of γ in both streamwise and crossflow directions. To avoid an interaction between the transition model and the turbulence model itself, simulations have been performed with the intermittency factor set to zero upstream of the transition inception location and to unity downstream of it. Overall, six combinations of transition model implementations have been analyzed. Two approaches have been used to incorporate intermittency distribution into the solver; through an additional damping function in the eddy viscosity calculation, denoted as Var. 1, and through a damping function in an expression for the turbulence production, denoted as Var. 2. Each case was combined with three different distributions of the intermittency factor:

- 1) Step distribution: $\gamma = 0$, for $x < x_{tr}$ and $\gamma = 1$, for $x > x_{tr}$
- 2) One dimensional: $\gamma(x) = \text{Max}_y(\gamma(x, y))$ (i.e., maximum intermittency across boundary layer at current location) or $\gamma(x)$ based on transition model
- 3) Two-dimensional: $\gamma = \gamma(x, y)$

All cases are calculated using the FLB turbulence model, which gave the best prediction among the CH, LB, and FLB models.

The implementation of the transition model in attached flow does not have any significant effect on the velocity and turbulence distribution. No significant influence of the method of the implementation of the transition model (Var. 1, Var. 2, or type of γ) is found. As stated above, the utilization of the Abu-Ghannam and Shaw correlation predicts an earlier transition in comparison with both the experiment and the prediction based on a "pure" turbulence model. The current approach may only postpone the transition inception. Therefore, the prediction based on the pure turbu-

lence model and the transition model produce practically identical flow fields. Simulation with the experimental distribution of the intermittency factor improves the prediction of the turbulence kinetic energy distributions in the vicinity of the transition inception and predicts an earlier end of transition. Nevertheless, there is no improvement in the velocity distribution at location P10.

In contrast to the high- Re cases, the way the transition model is incorporated and the type of intermittency distribution used has a profound effect on the prediction of low- Re flow (Fig. 9). The incorporation of the transition model, with the direct effect on the eddy viscosity (Var. 1), resulted in the development of the larger separation bubble in comparison with the experimental data (Fig. 9). The separation zone extends beyond the location of the trailing edge. Utilization of the two-dimensional distribution of the intermittency factor led to a further increase in the separation bubble size. The flow prediction based on the application of the intermittency distribution to the calculation of the production term (Var. 2) leads to the prediction of a much smaller separation bubble and reattachment near the trailing edge. The predicted height and extent of the separation zone are closer to the measured values, which is a consequence of the delayed inception of transition. However, overall deviations of the predicted velocity profile from the experimental data are greater in comparison with the "pure" turbulence model for all cases, except for the "step" transition model. This is due to the double damping of the eddy viscosity in a transition zone, as mentioned earlier. Even though the γ distribution indicates that the transition zone should extend beyond the trailing edge, all but one model (one-dimensional model, Var. 1) has the end of the transition upstream of the trailing edge. A numerical prediction based on the one dimensional distribution and the "step" distribution in conjunction with Var. 2, gave the most accurate prediction of the separation bubble size and location, even though it does not improve the turbulence intensity distribution in comparison with the simulation without the transition model.

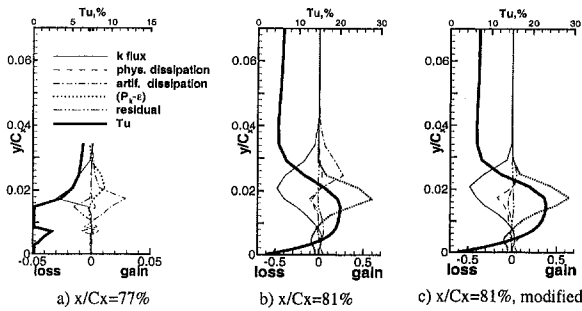


Fig. 10 Turbulent kinetic energy balance, $Tu = 10\%$, $Re = 50000$

Effect of Artificial Dissipation on the Transition Prediction

The stability consideration requires an analysis of the differential approximation of the original partial differential equations, which is not possible. Numerical experiments have been carried out to assess the influence of the artificial dissipation on the prediction of transition. The major objective of the current validation is to establish the limits of its influence.

A number of realizations of the artificial dissipation terms have been analyzed. The original version of the code employed a hybrid second/fourth-order artificial term with a switch based on the local turbulence field. Velocity scaling and eigenvector scaling are incorporated to keep the artificial dissipation at a minimum level in the boundary layer. Nevertheless, an analysis of the turbulent kinetic energy in the transition zone (Fig. 10(b)) indicates that the level of the artificial dissipation reaches 50% of the source term ($P_k - \epsilon$) for the base case. In Fig. 10, the distribution of the convective flux, physical dissipation, artificial dissipation, residue, and $P_k - \epsilon$ in the turbulent kinetic energy equation are shown to reveal the relative influence of the artificial dissipation. The base case has artificial dissipation coefficient $k_{2ke} = 0.01$, which is about twice the minimum level required to avoid odd-even numerical instability. To minimize the level of artificial dissipation, the artificial dissipation term was modified to include only the streamwise variation of k . The k -balance based on this modification is shown in Fig. 10(c). All calculations presented in this paper are based on this modified approach, even though it does not affect the prediction beyond a small zone of high gradients in the transition region.

The effect of utilizing only the fourth-order artificial dissipation term has been also investigated. This approach does not alter the result of the analysis presented below (beyond absolute values of the artificial dissipation coefficient). However, the employment of only fourth-order artificial dissipation leads to a significantly increased sensitivity of the code to the turbulence field development near the leading edge. A moderate flow disturbance generates a significant increase in the turbulence kinetic energy, which decreases rapidly downstream. Numerical modeling shows that this increase can not be explained as a transition with relaminarization farther downstream. This phenomenon can be reproduced at any location within the first 30% of the chord by placing the disturbance source (e.g., locally skewed grid).

The predicted location of the inception of separation, beginning and end of the transition, and reattachment point, as a function of the artificial dissipation, is shown in Fig. 11. Both the insignificant as well as excessive levels of artificial dissipation result in an earlier transition. The values of k_4 and k_{2ke} vary from the level below the stability limit to a level at which the artificial dissipation causes a significant non-physical diffusion.

It should be noted, based on previous experience with the solver, that the recommended variation of the k_{2ke} was 0.01 – 0.02. Within this range, the variation of the predicted and measured location of the transition inception is within 2.5% of the chord. An earlier-transition inception results in a smaller separation bubble

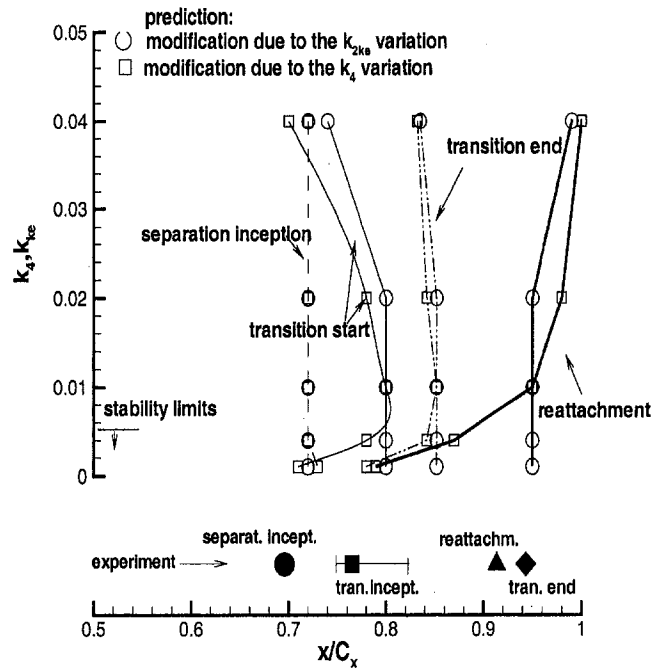


Fig. 11 Effect of artificial dissipation on predicted location of transition and separation inception, $Tu = 10\%$, $Re = 50000$

(Fig. 12). However, the variation of the artificial dissipation in the mean flow equation does not significantly influence the predicted mean flow profile (Fig. 13).

The primary source of the early transition in the case of a small k_{2ke} is a slight numerical instability of the scheme. For $k_{2ke} \leq 0.075$, a moderate odd-even numerical instability generates a premature transition from laminar to turbulent boundary layer flow. An increase in the artificial dissipation also results in an earlier transition inception. It is possible to identify zones with different behavior of the scheme. For simulations with $k_{2ke} < 0.02$, the variation of the artificial dissipation term affects only the transition inception, but the transition length is essentially constant. This fact indicates that, within this range, the artificial dissipation acts as a destabilizing factor. A comparison of the streamwise distribution of the turbulent kinetic energy based on differing values of k_{2ke} shows that $(\partial k / \partial x)$ is constant; i.e., the

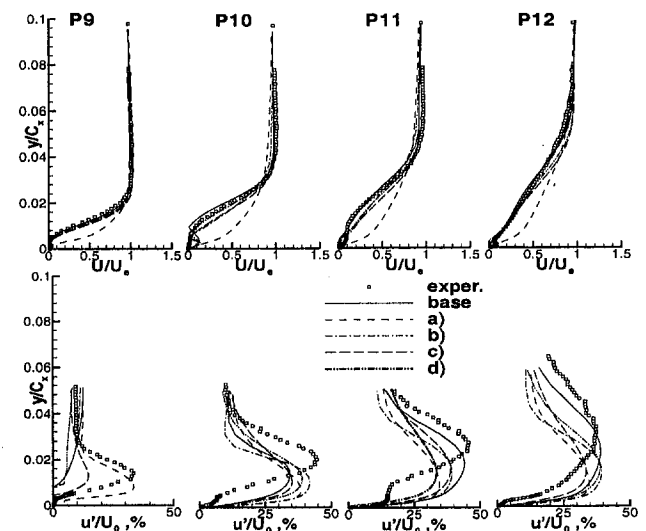


Fig. 12 Influence of the artificial dissipation; $Tu = 10\%$, $Re = 50000$, $k_4 = 0.01$ a) $k_{2ke} = 0.001$ b) $k_{2ke} = 0.004$ c) $k_{2ke} = 0.02$ d) $k_{2ke} = 0.04$

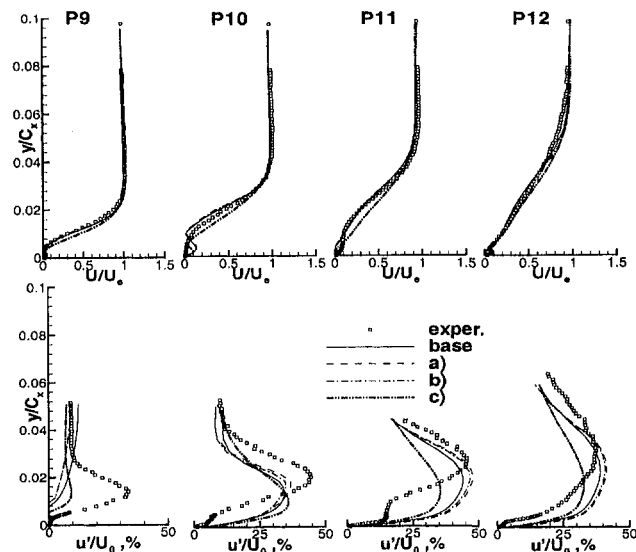


Fig. 13 Influence of the artificial dissipation, $Tu = 10\%$, $Re = 50000$, $k_{2ke} = 0.01$ a) $k_4 = 0.001$ b) $k_4 = 0.02$ c) $k_4 = 0.04$

transition zone is shifted upstream without diffusion of the k field. Therefore, in this zone, the artificial dissipation is similar to the physical disturbances (freestream turbulence, noise etc.). For $k_{2ke} > 0.02$, the artificial dissipation leads to both an earlier transition and an increased transition length. This is the consequence of the streamwise diffusion of the turbulent kinetic energy.

The influence of the artificial dissipation in the mean flow equation on the predicted velocity and turbulent fields is presented in Fig. 13. In contrast to the k_{2ke} variation, the variation of k_4 does not affect the accuracy of the mean flow, except at very high levels of artificial dissipation.

Concluding Remarks

A numerical simulation of the flow in a low-pressure turbine shows that best results were obtained with the FLB model (without a transition model). Implementation of the hybrid $k-\epsilon$ /ARSM improves the prediction for $Re = 50,000$, $Tu = 2.5\%$. While having minimum impact in all other cases, this modification contributed to the redistribution of the turbulent kinetic energy between various components in the transition region.

Utilization of a transition model does not result in an improved flow simulation. Analysis of the turbulence characteristics in the transition zone shows that the lack of improvement is due to interference between the transition model and the low-Re turbulence model. In the current prediction, transition inception from the pure $k-\epsilon$ model is located only about 4% of the chord upstream of the measured location. An enforcement of the transition through the intermittency function leads to a double damping of turbulence in the transition zone.

A number of factors have been found to be essential for an accurate prediction of the transition. The first factor is the need to limit turbulence production near the leading edge to ensure an accurate development of the laminar boundary layer. Implementation of the fourth-order artificial dissipation in $k-\epsilon$ equations, without modification for the leading edge flow, may lead to the development of the pseudo-turbulent boundary layer. A second factor is the need to modify the freestream turbulence equation. This problem, as well as the first one, is due to the poor performance of a standard $k-\epsilon$ model in the case of strong normal stresses. Without the adjustment of the freestream turbulence, the turbulence intensity may be overpredicted by 2–3% affecting the transition inception prediction.

The establishment of the reliability range for the solver is

needed for its application to the design problem. Even though grid independency has been verified through the numerical modeling, further analysis shows that the predicted location is affected by the level of artificial dissipation. For small values of k_{2ke} , the variation of the artificial dissipation acts as a disturbance (i.e., affecting the transition inception without diffusing k in the transition zone). This makes assessment of the reliability of the prediction more complex; because in addition to grid and turbulence model characteristics, the numerical scheme (i.e., form of differential approximation) and numerical details (e.g., the way the reliability of k is ensured) contribute to the variation in the transition prediction. For the current solver, the potential error associated with this phenomenon can be estimated to be 2% of the chord for the prediction of the location of inception of transition. To ensure a reliable prediction of the separated flow cases, this level should be improved because even a moderate variation in the predicted transition inception results in a significant variation of the separation bubble thickness and length.

Acknowledgment

This work was supported by the NASA Grant NAG 3-2025, with Dr. David Ashpis as the technical monitor. The authors wish to acknowledge the availability of the Supercomputer time at NASA Ames and the San Diego NSF Supercomputing Center.

References

- Abid, R., Rumsey, C., and Gatski, T., 1995, "Prediction of Non-Equilibrium Turbulent Flows with Explicit ARSM," *AIAA Journal*, Vol. 33, No. 11, Nov.
- Abu-Gannam, B. J., and Shaw, R., 1980, "Natural Transition of Boundary Layers—The Effect of Turbulence, Pressure Gradient, and Flow History," *Journal of Mechanical Engineering Science*, Vol. 22, No. 5, pp. 213–228.
- Chernobrovkin, A., and Lakshminarayana, B., 1998, "Experimental and Numerical Study of Unsteady Viscous Flow due to Rotor-Stator Interaction in Turbines; Part II: Simulation, Integrated Flow Field and Interpretation," AIAA 98-3596, (To be published in *AIAA J. Propulsion and Power*, Dec. 1999).
- Chien, K.-Y., 1982, "Predictions of Channel and Boundary-Layer Flows With a Low-Reynolds-Number Turbulence Model," *AIAA Journal*, Vol. 20, No. 1, pp. 33–38.
- Davis, R. L., Carter, J. E., and Reshotko, E., 1987, "Analysis of Transitional Separation Bubbles on Infinite Swept Wings," *AIAA Journal*, Vol. 25, No. 3, March, pp. 421–428.
- Dhawan, S., and Narasimha, R., 1958, "Some Properties of Boundary Layer During the Transition from Laminar to Turbulent Flow Motion," *Journal of Fluid Mechanics*, Vol. 3, pp. 418–436.
- Fan, S., Lakshminarayana, B., and Barnett, M., 1993, "Low-Reynolds-Number $k-\epsilon$ Model for Unsteady Turbulent Boundary-Layer Flows," *AIAA Journal*, Vol. 31, No. 10, pp. 1777–1784, October 1993.
- Gostelow, J. P., and Walker, G. J., 1991, "Similarity Behavior in Transitional Boundary Layer Over a Range of Pressure Gradient and Turbulence Levels," *ASME Journal of Turbomachinery*, Vol. 112, pp. 198–205.
- Huang, P. G., and Xiong, G., 1998, "Transition and Turbulence Modeling of Low Pressure Turbine Flows," AIAA Paper-98-0339.
- Kunz, R., and Lakshminarayana, B., 1992, "Three-dimensional Navier-Stokes Computations of Turbomachinery Flows Using an Explicit Numerical Procedure and a Coupled $k-\epsilon$ Turbulence Model," *ASME Journal of Turbomachinery*, Vol. 114, pp. 627–642, July.
- Lam, C. K. G., and Bremhost, K., 1981, "A Modified Form of the $k-\epsilon$ Model for Predicting Wall Turbulence," *ASME JOURNAL OF FLUIDS ENGINEERING*, Vol. 103, Sept., pp. 456–460.
- Mayle, R. E., 1991, "The Role of Laminar-Turbulent Transition in Gas Turbine Engines," *ASME Journal of Turbomachinery*, Vol. 113, pp. 509–537.
- Michelassi, V., Rodi, W., and Gieb, P.-A., 1997, "Experimental and Numerical Investigation of Boundary-Layer and Wake Development in a Transonic Turbine Cascade," ASME paper 97-GT-483.
- Qiu, S., and Simon, T. W., 1997, "An Experimental Investigation of Transition as Applied to Low Pressure Turbine Suction Surface Flows," ASME 97-GT-455, ASME Turbo Expo 97, Orlando, FL, June 1997.
- Rodi, W., 1976, "New Algebraic Relation for Calculation of the Reynolds Stresses," *ZAMM*, Vol. 56, p. 219.
- Savill, A. M., 1997, "COST-ERCOTAC Transition SIG. Evaluation of Turbulence Models for Predicting Transition in Turbomachinery Flows," Minnowbrook II, "Workshop on Boundary Layer Transition in Turbomachines," NASA CP-206958, J. E. LeGraft and D. E. Ashpis, eds., Sept. 7–10.
- Simon, T. W., and Qiu, S., 1999, "Measurements in a Transitional Boundary Layer under Low-Pressure Turbine Airfoil Conditions," NASA-CR (to be published).
- Steelant, J., and Dick, E., 1996, "Modeling of the Heat Transfer in Bypass Transitional Boundary Layer Flows," *International Journal for Numerical Methods in Fluids*, Vol. 32, pp. 193–220.

Satoshi Watanabe¹
JSPS Research Fellow.

Kotaro Sato²
Research Associate.

Yoshinobu Tsujimoto
Professor.

Osaka University,
Graduate School of Engineering Science,
1-3 Machikaneyama, Toyonaka,
Osaka 560-8531, Japan

Kenjiro Kamijo
Professor,
Tohoku University,
Institute of Fluid Science,
2-1-1 Katahira, Aoba, Sendai,
Miyagi 980-8577, Japan

Analysis of Rotating Cavitation in a Finite Pitch Cascade Using a Closed Cavity Model and a Singularity Method

A new method is proposed for the stability analysis of cavitating flow. In combination with the singularity method, a closed cavity model is employed allowing the cavity length freely to oscillate. An eigen-value problem is constituted from the boundary and supplementary conditions. This method is applied for the analysis of rotating cavitation in a cascade with a finite pitch and a finite chordlength. Unlike previous semi-actuator disk analyses (Tsujimoto et al., 1993 and Watanabe et al., 1997a), it is not required to input any information about the unsteady cavitation characteristics such as mass flow gain factor and cavitation compliance. Various kinds of instability are predicted. One of them corresponds to the forward rotating cavitation, which is often observed in experiments. The propagation velocity ratio of this mode agrees with that of experiments, while the onset range in terms of cavitation number is larger than that of experiments. The second solution corresponds to the backward mode, which is also found in semi-actuator disk analyses and identified in an experiment. Other solutions are found to be associated with higher order cavity shape fluctuations, which have not yet been identified in experiments.

Introduction

During the development of the liquid oxygen turbopump of the H-II rocket main engine, LE-7, a supersynchronous shaft vibration due to rotating cavitation was observed (Kamijo et al., 1993). Although this vibration was suppressed by a modification of the inducer casing, rotating cavitation is still one of the most important problems in the development of modern high performance rocket pump inducers (de Bernardi et al., 1993 and Ryan et al., 1994).

The first theoretical explanation of rotating cavitation was given by using 2-D semi-actuator disk analysis (Tsujimoto et al., 1993). It was shown that rotating cavitation is caused by the positive mass flow gain factor (which means that the cavity volume increases/decreases due to the decrease/increase of flow rate) and is definitely different from rotating stall which is caused by the positive slope of the pressure performance of the impeller. It was also found that there can be two modes of rotating cavitation: One of them rotates faster than the impeller and the other rotates in the direction opposite that of the impeller rotation, with nearly identical onset range. Forward rotating cavitation is generally found in experiments, while there has been only one experimental observation of backward rotating cavitation (Hashimoto et al., 1997). As the next steps in theoretical analysis, three-dimensional analysis (Watanabe et al., 1997a) and compressible flow analysis (Watanabe et al., 1997b) were carried out, their results basically supporting the results of the 2-D linear analysis. All of the above-mentioned analyses are based on a semi-actuator disk method where the cavitation is modelled by using the unsteady cavitation characteristics such as cavitation compliance K and mass flow gain

factor M . However, it is difficult to determine the exact value of K and M for specific machines.

In the present study, the rotating cavitation in a cascade with a finite pitch and a finite chordlength cascade is analyzed without using K and M . In combination with the singularity method, the closed cavity model is employed allowing the cavity length to oscillate freely (Furuya, 1982). This method has been used for the analysis of cavity response to external disturbances and the value of K and M are determined for cascades with a wide range of geometrical parameters (Watanabe et al., 1998). The present study extends the methods for stability analysis of rotating cavitation which can also be used for more general cavitation instabilities.

Fundamental Flow Field

We consider a cascade of flat plates with chordlength C , spacing h and stagger angle β as shown in Fig. 1. We assume a main flow of magnitude U and an incidence angle α at upstream infinity. We define the index of blades n by taking into account the periodicity for an inducer with blade number Z_N : The blade on the x -axis is given the index zero, and the index increases in the positive direction of the y -axis and returns to zero at the Z_N th blade. We consider the case of partial cavitation which fluctuates with a complex angular frequency ω . By allowing the interblade phase difference of fluctuations, $\Delta\varphi = 2\pi m/Z_N$ (m : number of cells), we can simulate the circumferential propagation of fluctuations in rotating cavitation.

The flow disturbance due to the existence of blades and cavities is represented by a source distribution q_n on the cavitating region, vortex distributions γ_{1n} and γ_{2n} along the blades, and a trailing free vortex distribution γ_m along the wake surface of the blades. The singularities are distributed on the blades and their extensions downstream assuming that both steady and unsteady flow disturbances are small. Thus, the complex potential $W(z, t)$ can be represented as follows:

¹ Currently, Lecturer at Kyushu University, Graduate School of Engineering, Fukuoka 812-8581, Japan.

² Currently, Associate Professor at Kougakuin University, Faculty of Engineering, Shinjuku, Tokyo 163-8677, Japan.

Contributed by the Fluids Engineering Division for publication in the JOURNAL OF FLUIDS ENGINEERING. Manuscript received by the Fluids Engineering Division March 12, 1998; revised manuscript received September 14, 1999. Associate Technical Editor: C. L. Merkle.

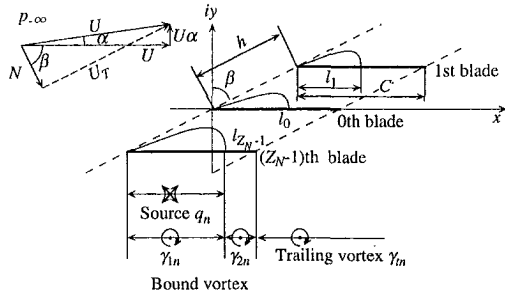


Fig. 1 Model for present analysis

$$W(z, t) = Ue^{-i\alpha z} + \frac{1}{2\pi} \sum_{n=0}^{Z_N-1} \left\{ \int_0^1 [q_n(s_1) + i\gamma_{1n}(s_1)] \right. \\ \times \left[F_n(z, l_n s_1) + \frac{\pi}{h} e^{i\beta z} \right] l_n ds_1 + i \int_1^2 \gamma_{2n}(s_2) \left[F_n(z, (C - l_n)s_2 + 2l_n - C) + \frac{\pi}{h} e^{i\beta z} \right] (C - l_n) ds_2 \\ \left. + i \int_C^\infty \gamma_m(\xi) \left[f_n(z, \xi) + \frac{\pi}{h} e^{i\beta z} \right] d\xi \right\}, \quad (1)$$

$$F_n(z, \xi) = \sum_{k=-\infty}^{+\infty} \log [z - (\xi + (kZ_N + n)h)e^{i(\pi/2 - \beta)}] \\ = \log \left\{ \sin \left[\frac{\pi}{Z_N h} (z - \xi) e^{-i(\pi/2 - \beta)} - \frac{n\pi}{Z_N} \right] \right\} \quad (2)$$

where i denotes the imaginary unit in space. Coordinates s_1 and s_2 are introduced to take into account the fluctuating cavity lengths l_n and are defined by

$$\xi = l_n s_1 \quad (\text{for } 0 < \xi < l_n, 0 < s_1 < 1), \quad \text{and} \quad (3)$$

$$\xi = (C - l_n)s_2 + 2l_n - C \quad (\text{for } l_n < \xi < C, 1 < s_2 < 2), \quad (4)$$

where ξ is a coordinate fixed to the blades showing the locations where the strengths of singularities are defined. All singularities are specified on these coordinates, s_1 and s_2 , which stretch and shrink with the fluctuating cavity lengths l_n .

The complex conjugate velocity can be represented as follows:

$$w(z, t) = u - iv = \partial W / \partial z = Ue^{-i\alpha} + \frac{1}{2\pi} \sum_{n=1}^{Z_N-1} \left\{ \int_0^1 [q_n(s_1) + i\gamma_{1n}(s_1)] \left[f_n(z, l_n s_1) + \frac{\pi}{h} e^{i\beta} \right] l_n ds_1 + i \int_1^2 \gamma_{2n}(s_2) \right. \\ \times \left[f_n(z, (C - l_n)s_2 + 2l_n - C) + \frac{\pi}{h} e^{i\beta} \right] (C - l_n) ds_2 \\ \left. + i \int_C^\infty \gamma_m(\xi) \left[f_n(z, \xi) + \frac{\pi}{h} e^{i\beta} \right] d\xi \right\} \quad (5)$$

$$f_n(z, \xi) = \frac{\partial F_n(z, \xi)}{\partial z} = \frac{\pi}{Z_N h} e^{-i(\pi/2 - \beta)} \\ \times \cot \left[\frac{\pi}{Z_N h} (z - \xi) e^{-i(\pi/2 - \beta)} - \frac{n\pi}{Z_N} \right]. \quad (6)$$

The strengths of all singularities and the cavity length are divided into steady and unsteady components as follows:

$$q_n(s_1) = U\alpha C_q(s_1) + \bar{q}(s_1) \exp(j\omega t - n\Delta\varphi), \\ \gamma_{1n}(s_1) = U\alpha C_{\gamma_1}(s_1) + \bar{\gamma}_1(s_1) \exp(j\omega t - n\Delta\varphi), \\ \gamma_{2n}(s_2) = U\alpha C_{\gamma_2}(s_2) + \bar{\gamma}_2(s_2) \exp(j\omega t - n\Delta\varphi), \\ \gamma_m(\xi) = \bar{\gamma}_t(\xi) \exp(j\omega t - n\Delta\varphi), \quad \text{and} \\ l_n = l_s + \bar{l} \exp(j\omega t - n\Delta\varphi), \quad (7)$$

Nomenclature

A, B = coefficient matrices and a constant vector in Eqs. (27) and (28)
 C = chordlength
 $C_q, C_{\gamma_1}, C_{\gamma_2}$ = normalized strengths of steady singularity distributions
 $F_n(z, \xi)$ = function defined in Eq. (2)
 $f_n(z, \xi)$ = function defined in Eq. (6)
 h = spacing of cascade
 i = imaginary unit in space ($i^2 = -1$)
 j = imaginary unit in time ($j^2 = -1$)
 k = complex propagation velocity ratio in a frame moving with a cascade, defined in Eq. (29)
 k^* = complex propagation velocity ratio in a stationary frame, defined in Eq. (30)

k_x^* = propagation velocity ratio in a stationary frame
 k_t^* = decay rate
 l = cavity length
 m = number of cells
 N = axial velocity
 n = blade index
 p = pressure
 p_v = vapor pressure
 q = source distribution
 S = location of discrete points on the blades
 s = coordinate fixed to oscillating cavity
 t = time
 U = main flow velocity
 U_T = tangential velocity of cascade
 u, v = velocity in the x - and y -directions
 W = complex potential
 w = complex conjugate velocity, $= u - iv$
 Z_N = number of blades

α = incidence angle
 β = stagger angle
 γ = vortex distributions
 $\Delta\varphi$ = interblade phase difference
 η = cavity thickness (= location of cavity surface)
 ρ = density
 σ = cavitation number
 ω = complex angular frequency of fluctuations
 ξ = coordinate fixed to the blades

Superscript

\sim = unsteady disturbance components

Subscripts

1, 2 = cavitating and non-cavitating region
 c = cavity surface
 n = blade index
 s = steady disturbance components
 t = wake

where $C_q(s_1)$, $C_{v_1}(s_1)$, and $C_{v_2}(s_2)$ are normalized strengths of steady components of singularities, and j denotes the imaginary unit in time. We have introduced two kinds of imaginary units, i and j . Here, we should note that $i \cdot i = j \cdot j = -1$ but $i \cdot j \neq -1$.

After introducing the expressions of Eq. (7) into Eq. (5), we can divide the velocity into uniform steady velocity $Ue^{-i\alpha}$, steady disturbance (u_s, v_s) and unsteady disturbance (\tilde{u}, \tilde{v}) as follows:

$$\begin{aligned} u &= U + u_s + \tilde{u}e^{j\omega t}, \quad \text{and} \\ v &= U\alpha + v_s + \tilde{v}e^{j\omega t}, \end{aligned} \quad (8)$$

where it has been assumed that $\alpha \ll 1$. We further assume that $|\tilde{u}|, |\tilde{v}| \ll |u_s|, |v_s| \ll U$; linearizations are made throughout the present study based on these assumptions.

Boundary and Supplementary Conditions

All boundary and supplementary conditions are applied to the 0th blade and all values are evaluated on the coordinates s_1 and s_2 which stretch and shrink with the fluctuating cavity length. The locations where the boundary and supplementary conditions are applied are represented as follows in terms of the coordinate x fixed to the blades:

$$x \pm 0i = l_0 s_1 \pm 0i \quad (0 < x < l_0, 0 < s_1 < 1), \quad \text{and} \quad (9)$$

$$\begin{aligned} x \pm 0i &= (C - l_0)s_2 + 2l_0 - C \pm 0i \\ &(l_0 < x < C, 1 < s_2 < 2). \end{aligned} \quad (10)$$

Boundary Condition on the Cavity Surface. We assume that the pressure on the cavity surface ($0 < x < l_0, y = +0$) is constant and equals the vapor pressure. From the linearized momentum equation on the cavity surface, we obtain the following equation:

$$\frac{\partial u}{\partial t} + \frac{U}{l_s} \frac{\partial u}{\partial s_1} = -\frac{1}{\rho} \frac{1}{l_s} \frac{\partial p}{\partial s_1} = 0. \quad (11)$$

From this equation, we can express the velocity on the cavity surface ($U + u_c$) as follows:

$$u_c(s_1, t) = u_{cs} + \tilde{u}_c e^{-j\omega l_s s_1 / U} e^{j\omega t}. \quad (12)$$

Using the expression of velocity, Eq. (5), we obtain the following boundary condition on the cavity surface,

$$\text{Re}\{w(l_0 s_1 + 0i, t)\} = U + u_c(s_1, t) \quad (0 < s_1 < 1). \quad (13)$$

Boundary Condition on the Wetted Surfaces. The flow tangency condition on the wetted surfaces can be represented as follows:

$$\text{Im}\{w(l_0 s_1 - 0i, t)\} = 0 \quad (0 < s_1 < 1), \quad \text{and} \quad (14)$$

$$\text{Im}\{w((C - l_0)s_2 + 2l_0 - C, t)\} = 0 \quad (1 < s_2 < 2). \quad (15)$$

Cavity Closure Condition. Although various cavity models have been proposed mainly to simulate the loss or drag by potential flow calculation, we choose the unsteady closed cavity model (Furuya, 1982) because of its simplicity. By using this model, we can simulate the unsteady cavitation phenomena without any empirical factors.

The kinematics of cavity thickness $\eta_n(s_1, t)$ can be expressed as follows:

$$\frac{\partial \eta_n}{\partial t} + \frac{1}{l_n} \left(U - s_1 \frac{dl_n}{dt} \right) \frac{\partial \eta_n}{\partial s_1} = v(l_n s_1, +0) = q_n(s_1). \quad (16)$$

The cavity thickness is divided into the steady and unsteady components,

$$\eta_n(s_1, t) = \eta_s(s_1) + \tilde{\eta}(s_1) \exp(j\omega t - n\Delta\varphi). \quad (17)$$

Equation (16) is separated into steady and unsteady parts after linearization. By integrating these equations, we obtain

$$\eta_s(s_1) = U\alpha l_s \int_0^{s_1} C_q(s'_1) ds'_1, \quad \text{and} \quad (18)$$

$$\begin{aligned} \tilde{\eta}(s_1) &= \frac{l_s}{U} \int_0^{s_1} \tilde{q}(s'_1) e^{-j\omega l_s (s_1 - s'_1) / U} ds'_1 \\ &+ U\alpha l \int_0^{s_1} (1 + j\omega l_s s'_1 / U) C_q(s'_1) e^{-j\omega l_s (s_1 - s'_1) / U} ds'_1. \end{aligned} \quad (19)$$

Then the cavity closure conditions can be expressed as follows:

$$\eta_s(1) = \tilde{\eta}(1) = 0. \quad (20)$$

Kutta's Condition. We assume that the pressure difference across the blade vanishes at the trailing edge of each blade. By applying the linearized momentum equation to both surfaces of the blades, we can express this condition as follows:

$$\begin{aligned} \frac{d}{dt} \left[\int_0^1 \gamma_{10}(s_1) l_0 ds_1 + \int_1^2 \gamma_{20}(s_2) (C - l_0) ds_2 \right] \\ + U\gamma_{20}(2) = 0. \end{aligned} \quad (21)$$

This is known as the unsteady Kutta's condition.

Equation (21) is equivalent to the Kelvin's circulation conservation law and signifies that the vortex wake with strength $\tilde{\gamma}_1(C)$ is shed from the trailing edge of the blade on the mean velocity U , corresponding to the change in the blade circulation.

Since the trailing free vorticity $\tilde{\gamma}_1(\xi)$ is transported on the free stream with velocity U , it can be represented by using $\tilde{\gamma}_2(2)$ as follows:

$$\tilde{\gamma}_1(\xi) = \tilde{\gamma}_2(2) \exp[-j\omega(\xi - C)/U]. \quad (22)$$

Upstream Flow Condition. We assume that there should be no disturbances at upstream infinity. The expression of Eq. (5) has been determined such that the velocity disturbance vanishes at upstream infinity. Applying the unsteady version of Bernoulli's equation between the upstream infinity and the leading edge of cavity, and equating the pressure disturbance at upstream infinity to zero, we obtain the following equation:

$$\frac{\partial \text{Re}[W(-\infty, t)]}{\partial t} = \frac{\partial \text{Re}[W(0, t)]}{\partial t} + \frac{1}{2} |w(0, t)|^2 + \frac{p_v}{\rho} \quad (23)$$

where p_v is the vapor pressure. Linearizing the above equation and separating it into steady and unsteady components, we obtain

$$u_{cs} = \frac{p_{-\infty} - p_v}{\rho U} = \frac{\sigma U}{2}, \quad \text{and} \quad (24)$$

$$j\omega \text{Re}[\tilde{W}(0, t) - \tilde{W}(-\infty, t)] + Uu_c = 0, \quad (25)$$

where $\sigma = 2(p_{-\infty} - p_v)/\rho U^2$ is the cavitation number. The unsteady component of complex potential \tilde{W} can be derived by separating the expression of Eq. (1) into steady and unsteady components.

Analytical Method and Conditions for Numerical Examples

The unknown quantities in this problem are the steady and unsteady components of singularity distributions, $q_n(s_1)$, $\gamma_{1n}(s_1)$ and $\gamma_{2n}(s_2)$, the cavity length l_n , and the tangential velocity on the cavity surface, u_{cn} . They are determined from the steady and unsteady parts of Eqs. (13)–(15), (20) and (21) with Eqs. (24) or

(25) where the expressions of the complex potential and the velocity, Eqs. (1) and (5), should be used wherever needed.

We specify the strengths of singularity distributions at the following nodes as unknowns:

$$S_{1k} = \frac{1}{2} \left[1 - \cos \left(\frac{k-1}{N_c-1} \pi \right) \right] \quad (0 < s_1 < 1, k = 1, 2, \dots, N_c), \quad \text{and}$$

$$S_{2k} = 1 + \frac{1}{2} \left[1 - \cos \left(\frac{k-1}{N_B-1} \pi \right) \right] \quad (1 < s_2 < 2, k = 1, 2, \dots, N_B), \quad (26)$$

where N_c and N_B are the number of nodes in the cavitating and noncavitating regions, respectively. We used $N_c = N_B = 37$ for the present calculations. The nodes are densely distributed near the leading and trailing edges of the cavity and the blade. Between nodes, the strengths of singularity distributions are basically assumed to be linear. Near the leading and trailing edge of the cavity, however, the singular behavior of linearized cavitating flow obtained by Geurst (1959) should be taken into account. Near the leading edge of the cavity, the singularity distributions are assumed to be $q_n(s_1) \sim s_1^{-1/4}$ and $\gamma_{1n}(s_1) \sim s_1^{-1/4}$. Near the trailing edge, it is assumed that $q_n(s_1) \sim (1-s_1)^{-1/2}$, $\gamma_{2n}(s_2) \sim (s_2-1)^{-1/2}$.

The control points, where boundary conditions are applied, are placed at the middle of each node given by Eq. (26). By evaluating the integral in Eqs. (1) and (5), we can express the boundary and supplementary conditions as follows:

For the steady components,

$$[A_s(l_s)] \begin{Bmatrix} C_q(S_{11}) \\ \vdots \\ C_{\gamma 1}(S_{11}) \\ \vdots \\ C_{\gamma 2}(S_{21}) \\ \vdots \\ \sigma/2\alpha \end{Bmatrix} = \{B_s\}, \quad (27)$$

and for the unsteady components,

$$[\tilde{A}(l_s, \omega)] \begin{Bmatrix} \tilde{q}(S_{11}) \\ \vdots \\ \tilde{\gamma}_1(S_{11}) \\ \vdots \\ \tilde{\gamma}_2(S_{21}) \\ \vdots \\ \tilde{u}_c \\ \alpha \tilde{l} \end{Bmatrix} = \{0\}, \quad (28)$$

where $A_s(l_s)$ and $\tilde{A}(l_s, \omega)$ are coefficient matrices on the unknown vectors shown by $\{ \}$ on the left hand sides, and B_s is a constant vector.

The steady flow can be determined from Eq. (27), which shows that $\sigma/2\alpha$ is a function of the steady cavity length l_s , or equivalently, that l_s is a function of $\sigma/2\alpha$. Equation (28) is a set of homogeneous linear equations. In Eq. (28) the effects of σ and α are included only in $\alpha \tilde{l}$ and in $\tilde{A}(l_s, \omega)$ through l_s , which depends only on $\sigma/2\alpha$. Therefore, the unknown vector depends only on l_s or $\sigma/2\alpha$. Because $\alpha \tilde{l}$ is constant for the same value of the steady cavity length l_s as we can see from Eq. (28), the amplitude of cavity length fluctuation \tilde{l} is inversely proportional to α for the cases with the same value of l_s , or equivalently $\sigma/2\alpha$. For the

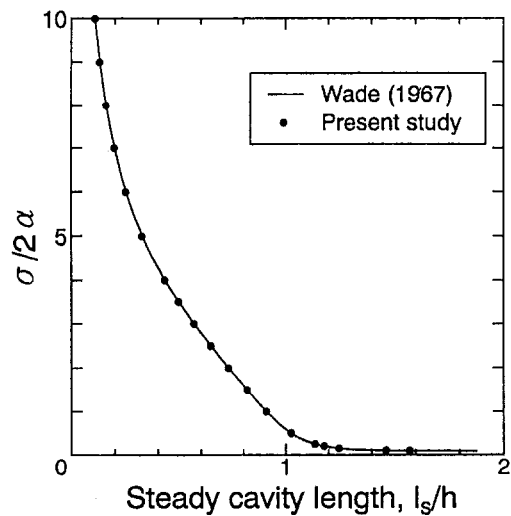


Fig. 2 Steady cavity length, compared with Wade (1967)

existence of non-trivial solutions, the determinant of the coefficient matrix $\tilde{A}(l_s, \omega)$ should be equal to zero. This condition gives a characteristic equation which determines the complex angular frequency ω , which is also a function of $\sigma/2\alpha$.

The complex propagation velocity ratio (propagation velocity/ U_T) in a frame moving with the cascade, k , is defined as

$$k = k_R + jk_I = \frac{\omega/m}{2\pi} \frac{Z_N h}{U_T}, \quad (29)$$

by using the complex frequency ω and the tangential velocity U_T of the cascade. The propagation velocity ratio is not a function of only $\sigma/2\alpha$ any more because U_T is expressed as $U_T = U \sin(\beta + \alpha)$. The direct effect of the incidence angle α , however, is quite small for the cases with small α and large stagger angle β , which is the case for typical inducers. The complex propagation velocity ratio in a stationary frame, k^* , is given by

$$k^* = k_R^* + jk_I^* = (1 - k_R) + jk_I, \quad (30)$$

where k_R^* is the propagation velocity ratio in a stationary frame and k_I^* is the decay rate. For $k_R^* > 1$, the corresponding disturbance rotates faster than the impeller. If $k_I^* < 0$, the disturbance is amplifying.

Numerical results are shown for a cascade with solidity of $C/h = 1.88$ and stagger of $\beta = 79.73$ [deg]. As previously mentioned, the unsteady flow components can be determined as functions of $\sigma/2\alpha$, whereas the cavity length fluctuation \tilde{l} and the complex propagation velocity ratio k^* include the direct effect of α . The value of incidence angle, $\alpha = 4.66$ [deg], is used for the calculation of propagation velocity ratio and unsteady cavity shapes described below. However, the stability limit ($k_I^* = \omega_r = 0$) of all disturbances remains as a function of only $\sigma/2\alpha$.

Figure 2 shows the steady cavity lengths l_s/h obtained from Eq. (28) and those obtained by the conformal mapping method (Wade, 1967) for various values of $\sigma/2\alpha$. They are in good agreement.

Results and Discussions

Solutions of Characteristic Equation and Corresponding Modes. Figure 3 shows an example of complex solutions for the case of the number of blades $Z_N = 3$, the number of cells $m = 1$, and $\sigma/2\alpha = 0.25$. Although only five solutions are shown in the figure, many other solutions were found in the region with larger absolute propagation velocity. In the present study, we focus on the solutions with a lower propagation velocity, Mode I–III. Mode

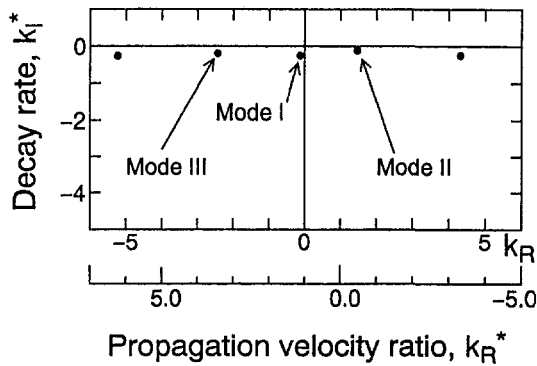


Fig. 3 Example of solutions obtained with characteristic equation

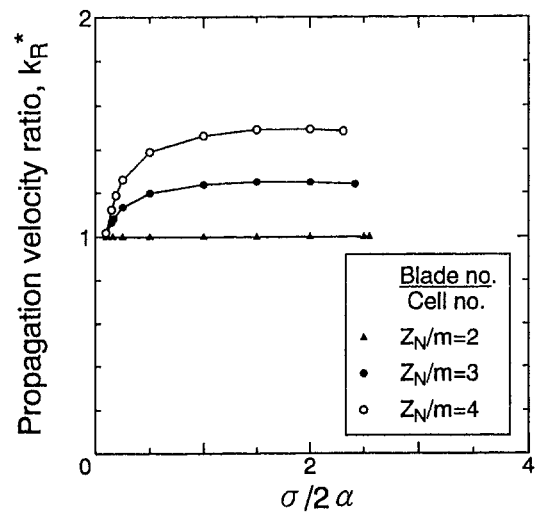
I and III are forward rotating modes whereas Mode II is a backward rotating mode.

Figure 4(a)–(c) show the cavity shape fluctuations for Mode I–III shown in Fig. 3. The cavity shape of Mode I fluctuates so that the cavity thickness changes with the same phase throughout the cavity. On the other hand, propagating waves on the cavity surfaces are found for Mode II and III.

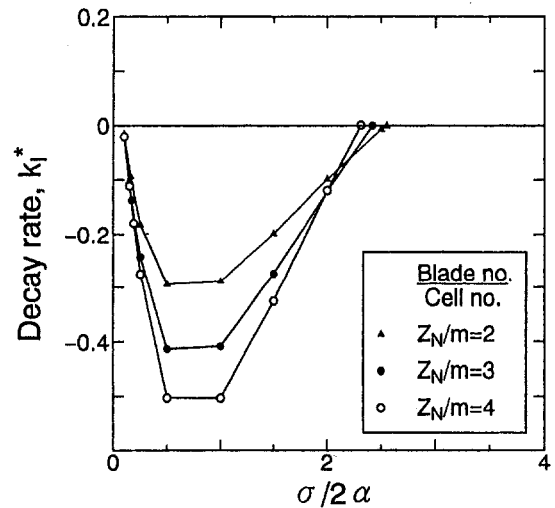
Effects of Blade and Number of Cells. Figure 5(a)–(c) shows the results of Mode I–III for various values of $\sigma/2\alpha$ and Z_N/m . The case of $Z_N/m = 2$ corresponds to the rotating cavitation with 1 cell in a 2-bladed inducer or 2 cells in a 4-bladed inducer. On the other hand, $Z_N/m = 3$ and 4 correspond to the 1 cell rotating cavitations in 3- and 4-bladed inducers, respectively.

Figure 5(a) shows the results for Mode I. It is shown that the propagation velocity ratio k_R^* increases as $\sigma/2\alpha$ increases for $Z_N/m = 3$ and 4. The propagation velocity ratio k_R^* for $Z_N/m = 4$ is larger than that for $Z_N/m = 3$. On the other hand, the propagation velocity ratio k_R^* is unity for $Z_N/m = 2$. This corresponds to the alternate blade cavitation which is often observed in experiments with a 2- or 4-bladed inducer (Huang et al., 1998, and de Bernardi et al., 1993). Since the flow under the alternate blade cavitation is steady in a frame moving with the cascade, it can be treated by steady flow analysis (Horiguchi et al., 1998). The present results predict that both the forward rotating cavitation with 1 cell and alternate blade cavitation with 2 cells can occur in a 4-bladed inducer. Figure 5(a) also shows that the destabilizing region with $k_I^* < 0$ is the largest for $Z_N/m = 2$. Thus, in the case of a 4-bladed inducer, it is predicted that, as the cavitation number decreases, the alternate blade cavitation with 2 cells occurs first, and then the forward rotating cavitation with 1 cell will follow. This tendency agrees with the experimental observations by de Bernardi et al. (1993).

Figure 5(b) and (c) shows the results for Mode II and III, respectively. It is shown that the absolute value of propagation velocity ratio, $|k_R^*|$, is much larger than that of Mode I and is the largest for the case of $Z_N/m = 4$. The figures of decay rate k_I^* show that the destabilizing regions of Mode II and III are larger than that of Mode I, indicating



Propagation velocity ratio



Decay rate

Fig. 5(a) Mode I

that the phenomena with larger propagation velocity may occur prior to Mode I. However, the existence of the higher order mode, Mode III, has not been confirmed experimentally.

Comparison With Experimental Results. Figure 6 shows comparisons of theoretical and experimental results for Mode I.

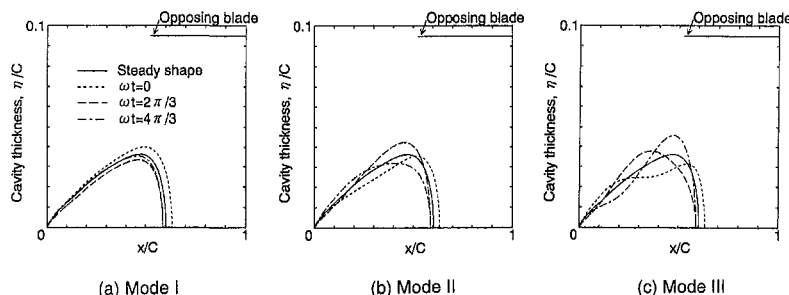
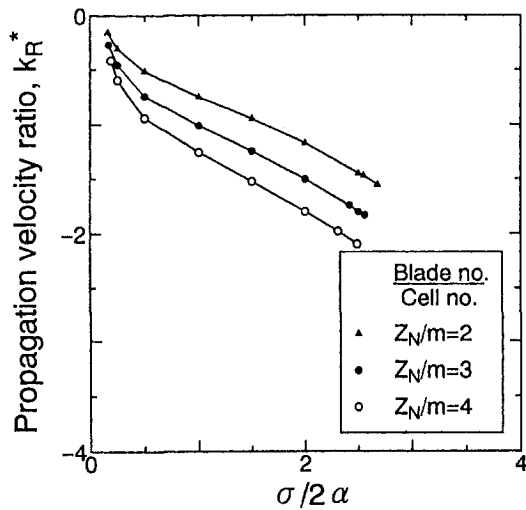
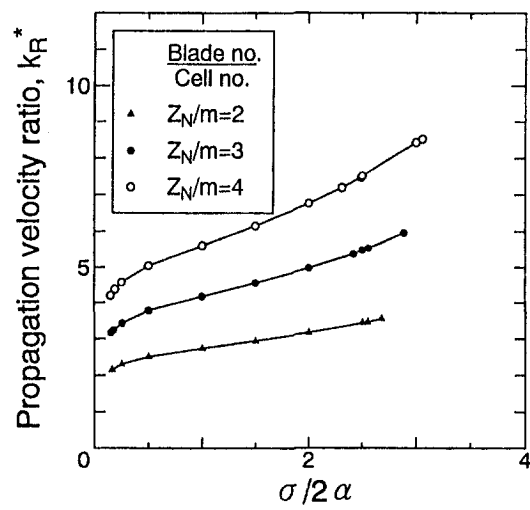


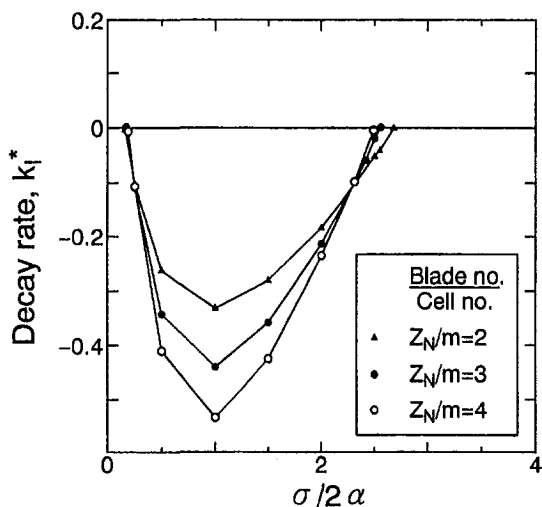
Fig. 4 Cavity shape fluctuations of Mode I–III shown in Fig. 3



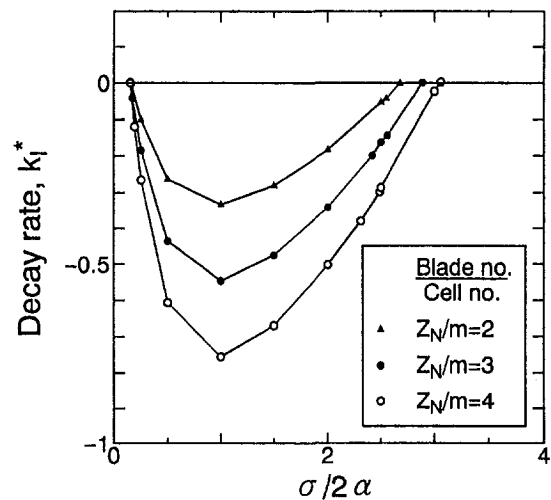
Propagation velocity ratio



Propagation velocity ratio



Decay rate



Decay rate

Fig. 5(b) Mode II

Fig. 5(c) Mode III

Fig. 5 Solutions corresponding to Mode I–III for various values of $\sigma/2\alpha$ [Blade number/cell number, $Z_N/m = 2, 3, 4$]

The experimental data are drawn from Kamijo et al. (1993) and Tsujimoto et al. (1997) for 3-bladed inducers, and from de Bernardi et al. (1993) and the recent results at Osaka University for 4-bladed inducers. The present model can simulate the following characteristics: (i) The propagation velocity ratio k_R^* increases as $\sigma/2\alpha$ increases. (ii) The propagation velocity ratio k_R^* is larger for a 4-bladed inducer than for a 3-bladed inducer. However, the predicted destabilizing regions in terms of $\sigma/2\alpha$ are much larger than those of experiments.

Figure 7 shows the onset regions of various cavitation instabilities in experiments (Tsujimoto et al., 1997). The onset region of rotating cavitation is denoted by iv. Lines for $\sigma/2\alpha = 0.5$ and 1.0 are drawn in the figure. It can be seen that the boundaries of various cavitation instabilities are nearly parallel to the lines with constant $\sigma/2\alpha$. This supports the finding of the present study that rotating cavitation depends on the value of $\sigma/2\alpha$ or the steady cavity length l_s .

Here, we further compare the present results with experimental results from the standpoint of cavity length. As already shown in Fig. 2, the steady cavity length l_s/h is a function of $\sigma/2\alpha$. At the point A shown in Fig. 7, the mean cavity length (of tip cavitation)

is approximately 85 percent of spacing h . The steady cavity length of Mode I at the neutrally stable point is $l_s/h = 0.65$. The difference in the cavity length is not very large if we consider that the experimental result is not for a neutrally stable condition and that cavities on the blades are shorter than tip cavities. Thus, we can obtain closer agreement if we compare the onset region in terms of steady cavity length l_s , rather than $\sigma/2\alpha$.

Figure 8 shows a comparison of theoretical and experimental results for Mode II. Mode II corresponds to the backward rotating cavitation which has been rarely found, there being only one report, that of Hashimoto et al. (1997). The value of propagation velocity ratio k_R^* in the present study is not very different from the experimental value. However, further study is needed to explain why the backward mode is rarely found in experiments.

Conclusions

A new method was proposed for the stability analysis of cavitating flow. This method was applied for the analysis of rotating

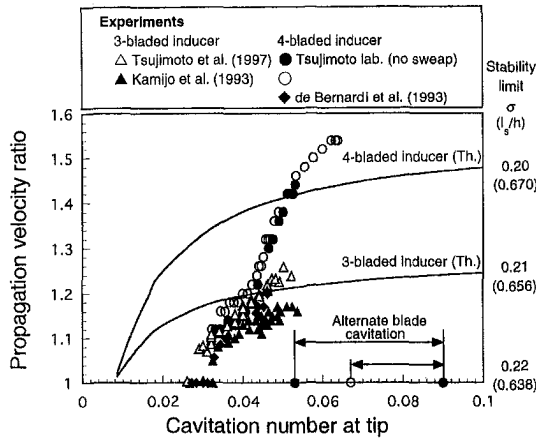


Fig. 6 Comparisons of Mode I with forward rotating cavitation in experiments

cavitation in a cascade with finite pitch and finite chordlength. The following results were obtained.

- (1) Rotating cavitation basically depends on the ratio of cavitation number to twice the incidence angle, $\sigma/2\alpha$, or equivalently on the steady cavity length l_s , not on the individual values of σ and α .
- (2) Various kinds of instabilities were predicted, including forward and backward rotating cavitations and their higher order modes.
- (3) The propagation velocity ratio of the forward mode agrees qualitatively with experimental results. The ranges of onset in $\sigma/2\alpha$ predicted by the present study were found to be much larger than those in experiments. However, better agreement with experiments was obtained when we compared the onset range in terms of steady cavity length.
- (4) The propagation velocity ratio of the backward mode agrees reasonably with an experimental result. The range of onset is nearly identical to that of the forward mode. The present model fails to explain why the backward mode is rarely found in experiments.

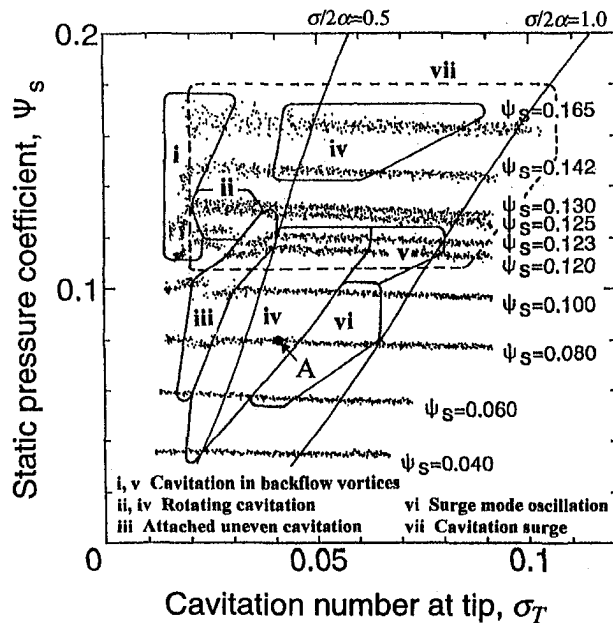


Fig. 7 Onset regions of various cavitation instabilities, from Tsujimoto et al. (1997)

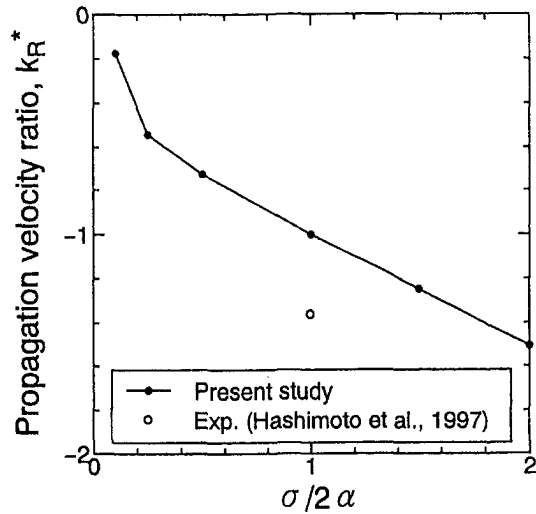


Fig. 8 Comparison of Mode II with backward rotating cavitation in 3-bladed inducer

- (5) Higher order modes with a wavy cavity surface shape propagate much faster than the fundamental mode of forward and backward rotating cavitations. These modes have not as yet been identified experimentally.
- (6) The proposed method will be useful for the analyses of other cavitation instabilities.

Acknowledgments

This study was partly supported by the Grant-in-Aid for Scientific Research from the Ministry of Education, Science, Sports and Culture.

References

de Bernardi, J., Joussellin, F., and Von Kaenel, A., 1993, "Experimental Analysis of Instabilities Related to Cavitation in a Turbopump Inducer," *Proceedings of 1st International Symposium on Pump Noise and Vibrations*.

Furuya, O., 1982, "Dynamic Characteristics of Cavitating Pumps and Inducers," ASME Paper, pp. 147-155.

Geurst, J. A., 1959, "Linearized Theory for Partially Cavitated Hydrofoils," *International Shipbuilding Progress*, Vol. 6, No. 60, pp. 369-384.

Hashimoto, T., Yoshida, M., Watanabe, M., Kamijo, K., and Tsujimoto, Y., 1997, "Experimental Study on Rotating Cavitation of Rocket Propellant Pump Inducers," *AIAA Journal of Propulsion and Power*, Vol. 13, No. 4, pp. 488-494.

Horiguchi, H., Watanabe, S., Tsujimoto, Y., and Aoki, M., 1998, "A Theoretical Analysis of Alternate Blade Cavitation in Inducers," *Proceedings of ASME Fluids Engineering Division Summer Meeting, Cavitation and Multiphase Flow Forum*, FEDSM98-5083.

Huang, J. D., Aoki, M., and Zhang, J. T., 1996, "Alternate Blade Cavitation on Inducer," *JSME International Journal, Series B*, Vol. 41, No. 1, pp. 1-6.

Kamijo, K., Yoshida, M., and Tsujimoto, Y., 1993, "Hydraulic and Mechanical Performance of LE-7 LOX Pump Inducer," *AIAA Journal of Propulsion and Power*, Vol. 9, No. 6, pp. 819-826.

Ryan, R. S., Gross, L. A., Mills, D., and Mitchell, P., 1994, "The Space Shuttle Main Engine Liquid Oxygen Pump High-Synchronous Vibration Issue, the Problem, the Resolution Approach, the Solution," AIAA Paper, 94-3153.

Tsujimoto, Y., Kamijo, K., and Yoshida, Y., 1993, "A Theoretical Analysis of Rotating Cavitation in Inducers," *ASME JOURNAL OF FLUIDS ENGINEERING*, Vol. 115, No. 1, pp. 135-141.

Tsujimoto, Y., Yoshida, Y., Maekawa, M., Watanabe, S., and Hashimoto, T., 1997, "Observations of Oscillating Cavitations of an Inducer," *ASME JOURNAL OF FLUIDS ENGINEERING*, Vol. 119, No. 4, pp. 775-781.

Wade, R. B., 1967, "Linearized Theory of a Partially Cavitating Cascade of Flat Plate Hydrofoils," *Applied Scientific Research*, Vol. 17, pp. 169-188.

Watanabe, S., Tsujimoto, Y., Kamijo, K., and Furuya, O., 1998, "An Analysis of Unsteady Cavitation Characteristics by a Singularity Method," (in Japanese) *Transactions of JSME, Series B*, Vol. 64, No. 621, pp. 1285-1292.

Watanabe, S., Yokota, K., Tsujimoto, Y., and Kamijo, K., 1997a, "Three-Dimensional Analysis of Rotating Cavitation in Inducers—Linear Cascade Model Spanning between Two Parallel Plates—," *Proceedings of JSME Centennial Grand Congress, International Conference on Fluid Engineering*, Tokyo, Vol. III, pp. 1377-1382.

Watanabe, S., Yokota, K., Tsujimoto, Y., and Kamijo, K., 1997b, "Theoretical Analyses of Rotating Cavitation in Inducers," *Proceedings of the 8th International Symposium on Aerodynamics and Aeroelasticity of Turbomachines*, T. H. Fransson, ed., Kluwer Academic Press, pp. 3-17.

Transient Behavior of a Cavitating Centrifugal Pump at Rapid Change in Operating Conditions—Part 1: Transient Phenomena at Opening/Closure of Discharge Valve

T. Tanaka

Assistant Professor,
Department of Mechanical and Electrical
Engineering,
Yatsushiro National College of Technology,
Yatsushiro, 866-8501, Japan

H. Tsukamoto

Professor,
Department of Mechanical Engineering,
Kyushu Institute of Technology,
Tobata, Kitakyushu, 804-8550, Japan

A series of studies on the dynamic characteristics of noncavitating centrifugal pumps were extended to the cavitating case. An experimental study was carried out on the transient behavior of a cavitating centrifugal pump at the sudden opening/closure of the discharge valve. Cavitation behavior in the centrifugal pump was visualized during the transient period by using high speed video camera, and instantaneous pressure and flowrate were measured at the pump suction and discharge section with rotational speed during the transient period. Unsteady pressure, as well as flowrate, was related to the time-dependent cavitation behavior. As a result of the present study, pressure and flowrate fluctuations were found to occur due to oscillating cavitation or water column separation at rapid transient operations.

Introduction

The transient phenomena under transient operation of pumps usually have been calculated under the assumption that the characteristics of a pump during unsteady operation closely follow its steady-state characteristic curves (Knapp, 1937). However this assumption, called hereafter quasi-steady change, would be inadequate in the case of rapid transient operation, since the pump cannot respond quickly enough to traverse its steady-state characteristic curves when the change in operating condition exceeds a certain limit. Therefore there has been a need for understanding the dynamics of the pump characteristics in unsteady operations.

Pressure response during pump rapid starting or stopping was studied by Tsukamoto and Ohashi (1982), Saito (1983), Tsukamoto et al. (1986), Barrand et al. (1993, 1996), Nguyen Duc et al. (1993), and Lefebvre and Barker (1995); while the pump transient characteristics during rapid opening/closure of the discharge valve were studied by Kaneko and Ohashi (1982) and Tsukamoto and Tanaka (1994). However, most of the work done in the past is limited to the case of cavitation-free flow. Therefore we don't know whether the data on the noncavitation case can be extended to the transient characteristics of cavitating pump or not.

A series of studies on the dynamic characteristics of cavitating centrifugal pump under a variety of unsteady operations has been performed as extension of similar investigation by the present authors (1982, 1986, 1995) for the cavitating case. In order to make clear the transient phenomena, the tests are conducted for a very rapid change rate of flowrate as well as for a rotational speed, which rarely occurs in practice. Such extreme test conditions result in marked phenomena and help in understanding the mechanism of the transient phenomena. In the present paper, transient behavior will be shown for the rapid change in flowrate under constant rotational speed. In the successive papers, the transient behavior at

rapid starting/stopping of a pump will be presented, and then the transient phenomena at transient operations will be summarized.

Test Equipment and Method

A single-stage, volute type centrifugal pump is used for the experiments with principal specifications as summarized in Table 1. The pump is equipped with transparent impeller front shroud, front casing and suction pipe for flow visualization. The arrangement of the test setup and instrumentation system is schematically illustrated in Fig. 1(a).

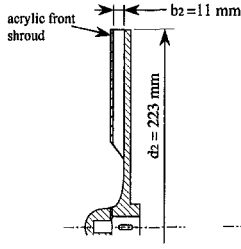
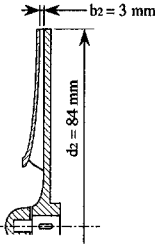
The test pump is driven by a 4-pole 7.5 kW induction motor which has enough power to keep a constant rotational speed of the pump during rapid change in flowrate. The variable speed operation of the motor is achieved by an inverter. To achieve the desired change rate of flowrate for the tests in the sudden closure or opening of the discharge valve, a pneumatic ball valve is adopted (Tsukamoto and Tanaka, 1994). The change rate of flowrate can be adjusted to some extent by controlling the pressure of compressed air. The output of the limit switch which makes the actuation or deactuation of the ball valve shaft is recorded to find out the exact moment when the ball valve begins to rotate or stop the operation.

The suction line is connected to a large reservoir with a water level of 1 m above the pump center through a short inlet pipe. The suction pressure can be adjusted by a vacuum pump connected to the reservoir. The discharge line is connected to a large accumulator and thus the fluctuations in flowrate and pressure are limited to the region between the two reservoirs. Before starting each test, the pump and piping loop are completely filled with water. The discharge valve is adjusted so that the initial/final flowrate coincides with the desired one. Both the discharge valve setting and suction head are kept unchanged during each test.

The rotational speed of the pump is detected by the pulse signals (60 pulses per revolution), which are fed to a frequency-analog converter for the recording. The suction and discharge pressure are measured by semi-conductor type pressure transducers, which are installed directly on the pressure taps in order to prevent the decrease of natural frequency due to pressure transducers fluid connecting lines. The flowrate is measured both at suction and

Contributed by the Fluids Engineering Division for publication in the JOURNAL OF FLUIDS ENGINEERING. Manuscript received by the Fluids Engineering Division March 12, 1998; revised manuscript received June 22, 1999. Associate Technical Editor: B. Schiavello.

Table 1 Specifications of test pump

	Pump A	Pump B
Suction diameter	65 mm	25 mm
Discharge diameter	50 mm	25 mm
Impeller :		
		
Outer diameter	223 mm	84 mm
Outer passage width	11 mm	3 mm
Number of vanes	6	6
Number of volute	1	1
Design conditions:		
Rotational speed	1780 rpm	3600 rpm
Flow rate	0.56 m ³ /min	0.04 m ³ /min
Total head rise	17.0 m	7.5 m
Specific speed	156 (rpm, m ³ /min, m)	130 (rpm, m ³ /min, m)
ϕ_r / ϕ_{bep}	1.02	1.05

discharge stations by electromagnetic flowmeters installed in the suction and discharge line. A variable frequency AC excitation has been adopted to avoid severe drift problems encountered in the DC excited flowmeter and to get better accuracy in instantaneous flowrate. The turbine flowmeter installed on another discharge line is used for the static and dynamic calibration of electromagnetic flowmeters. Dissolved oxygen is measured before each test by using the dissolved oxygen meter inserted in the pump suction. And each test is carried out for the dissolved oxygen below 1 ppm.

The instantaneous rotational speed N , suction and discharge flowrate, Q_s and Q_d , suction and delivery pressure, p_s and p_d , are transmitted to an A/D converter, and then recorded at the sample rate of 5 kHz on the data file in the computer. From the data file, instantaneous rotational speed $N(t)$, suction and discharge flowrate, $Q_s(t)$ and $Q_d(t)$, suction and delivery pressure, $p_s(t)$ and $p_d(t)$ are read out as a function of time t .

The dynamic behavior of the cavitation inside the test impeller

is visualized through transparent wall casing and suction pipe by using high speed video camera. Figure 2 shows the schematics of the flow visualization system. The high speed video camera is synchronized with stroboscope (flashing time: 5 μ s) by using signal generated by the photo-coupler.

In order to derive the nondimensional parameters which regulate the transient characteristics, we consider the unsteady phenomena in pumping system with geometrically similar pump and piping. Once we fix the following eight parameters, i.e., the representative length of the pump d_2 , equivalent total length of the piping l_{eq} , fluid density and viscosity: ρ and μ , rotational speed N , valve opening/closure time T_v , pipe resistance coefficient ζ , total pressure at pump suction P_s , a unique experimental condition can be established, under which a specific transient phenomenon takes place. According to the theory of dimensional analysis, the above eight physical quantities can be reduced to five independent nondimensional parameters, i.e., Reynolds number $Nd_2^2/(\mu/\rho)$, normalized piping length l_{eq}/d_2 , pipe resistance coefficient $\zeta \propto \phi_{Nf,0}/\phi_r$, cavitation number $\sigma = 2gH_{sv}/u_2^2$ and a newly introduced parameter, i.e., the reduced time for transient operation NT_v . Here ϕ_{Nf} or ϕ_{N0} is the final/initial flow coefficient under noncavitation conditions, and ϕ_r is the rated flow coefficient (=0.058) i.e., at design point.

The latter four parameters can be controlled in the experiment by adjusting the pipe length, the discharge valve opening, the suction pressure, and the time for transient operation, i.e., opening or closure of discharge ball valve. The influence of Reynolds number on transient characteristics is omitted from the present study.

In order to study the effect of the pipe length of the pump system on the transient phenomena, the other experiment is carried out by using the test rig shown in Fig. 1(b). In the piping system B with the test pump B, specifications of which are shown in Table 1, the suction and discharge pipe diameter is smaller than that in the piping system A. The pipe length in the piping system B has been changed as shown in Table 2. With this piping system, however, flowrate was not measured, and only the suction and delivery pressure, and valve opening/closure time are recorded.

Test Results and Discussion

Many experiments were made for a variety of combinations of the above experimental parameters. Due to the limited space, only the data for the test conditions listed in Table 3 and 4 are shown in Part 1 of the present paper. Further discussion will be presented in Part 3 of this study.

Nomenclature

b_2 = impeller outer passage width [m]
 d_2 = impeller outer diameter [m]
 H = total head [m]
 H_{sv} = available NPSH = $(P_s - p_v)/(\rho g)$ [m]
 N = rotational speed [revolution/sec]
 $NPSH_R$ = required NPSH at 3% head drop [m]
 P_s = total pressure at pump suction [Pa]
 p = static pressure [Pa]
 p_v = vapor pressure of liquid [Pa]
 Re = Reynolds number = $Nd_2^2/(\mu/\rho)$
 Q = flowrate [m³/s]
 T = average time period of discharge pressure fluctuations [s]

T_v = time of valve opening or closure [s]
 t = time [s]
 u_2 = impeller outer peripheral velocity = $\pi d_2 N$ [m/s]
 \dot{v} = rate of change in cavitation volume = $Q_d - Q_s$ [m³/s]
 ϕ = flow coefficient = $Q_d/(\pi d_2 b_2 u_2)$
 ϕ_{Nf}, ϕ_{N0} = parameter for discharge valve opening (ϕ at noncavitating steady conditions) = $Q_{Nf,0}/(\pi d_2 b_2 u_2)$
 μ = liquid viscosity [Pa · s]
 ρ = liquid density [kg/m³]
 σ = cavitation number = $2gH_{sv}/u_2^2$
 σ_R = cavitation number at $NPSH_R = 2gNPSH_R/u_2^2$

ψ = total head coefficient = $2gH/u_2^2$

Subscripts

0 = initial value
 bep = best efficiency point
 cr = critical
 d = pump discharge
 f = final value
 N0 = initial value at noncavitation conditions
 Nf = final value at noncavitation conditions
 r = rated
 s = pump suction

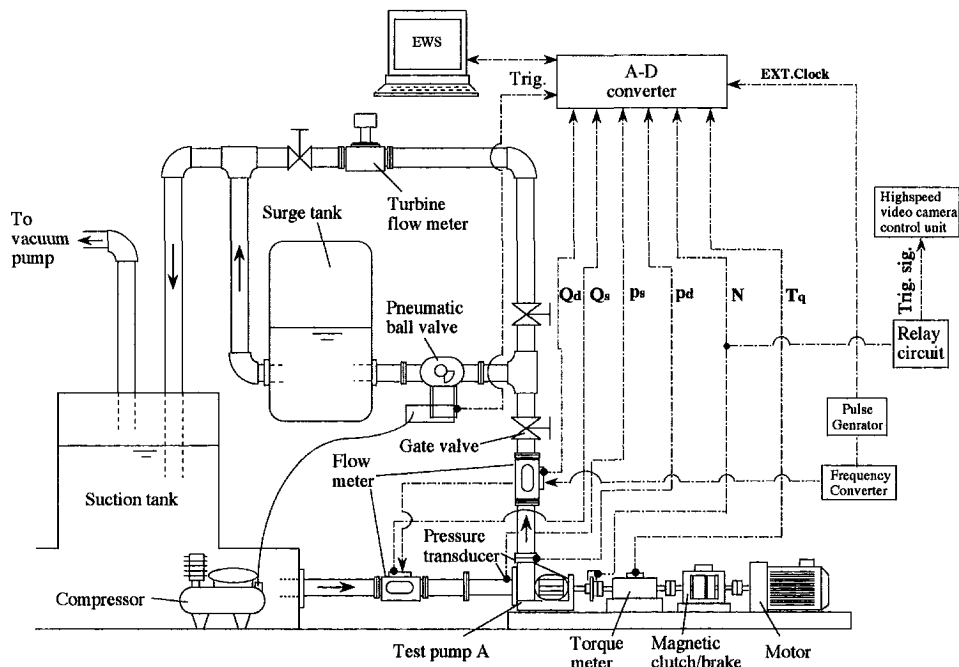


Fig. 1(a) Pump system A

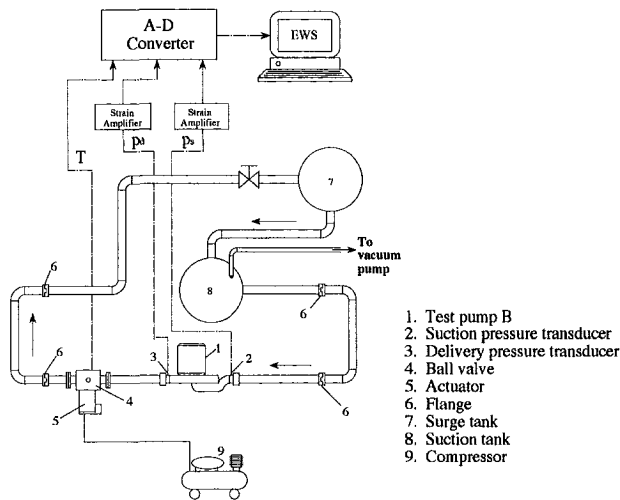


Fig. 1(b) Pump system B

Fig. 1 Schematic view of the test setup and instrumentation system

pump at the instant corresponding to the stage from (a) to (h) in Fig. 3. At the initial stages from (a) to (b), p_s and p_d tend to decrease rapidly with increasing Q_d , but there is no cavitation in the pump. After passing through the stage (b) cavitation appears near the leading edge of impeller vanes and it continues to grow in volume through (c) to (d) when p_d continues to decrease with

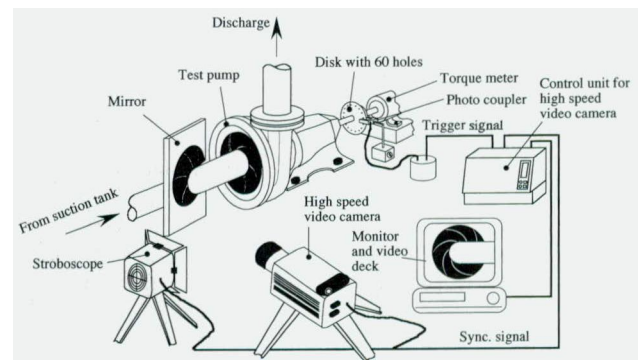


Fig. 2(a) Flow visualization system

Transient Phenomena at Opening of Discharge Valve

Relationship Between Cavitation Behavior and Transient Phenomena. Figure 3 presents the time histories of the measured suction and discharge flowrate, Q_s and Q_d , suction and delivery pressure, p_s and p_d for the highest attainable change rate of the valve opening at low suction pressure with $\sigma_f = 0.05$ (Case VO-6). In the dynamic operation of the pump, the flowrate difference between suction and discharge is caused by the growth or shrinkage of the total volume of the vapor within the pump, while the flowrate difference is zero in steady-state operation. The mass conservation equation for the volume reduces to the following equation for the changing rate of the cavitation volume (Sack and Nottage, 1965; Greitzer, 1981):

$$\dot{v} = Q_d - Q_s \quad (1)$$

The time histories of \dot{v} are also shown in Fig. 3.

Figure 4 shows the photographs of the cavitation behavior in the

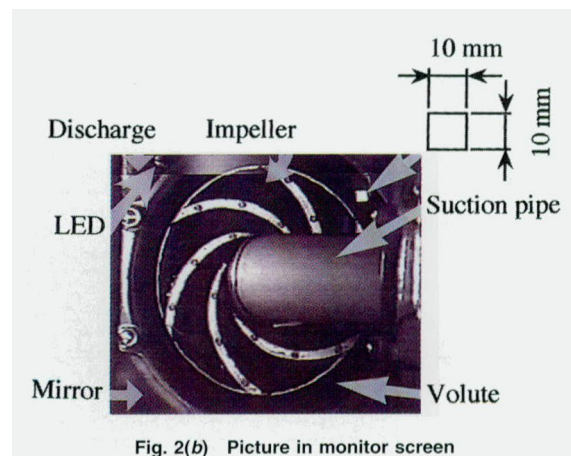


Fig. 2(b) Picture in monitor screen

Fig. 2 Schematic view of the flow visualization system

Table 2 Pipe length of piping system B

	Suction pipe length	Discharge pipe length
Case 1 (Original)	50.8D _d	145.6D _d
Case 2 (Longer suction pipe)	90.8D _d	145.6D _d
Case 3 (Longer discharge pipe)	50.8D _d	177.6D _d

D_d : Discharge pipe inner diameter

Table 3 Test condition for opening of discharge valve (pump system A: $l_{eq}/d_2 = 15.7$, $\zeta = 235.3$, Reynolds number $Nd_2^2/(\mu/\rho) = 1.46 \times 10^6$)

Case No.	σ_f	σ_R	N [rpm]	T _v [s]	NT _v	ϕ_{Nf}/ϕ_r
VO - 1	0.05	0.135	29.7	0.054	1.6	1.0
VO - 2	0.05	0.135	29.7	0.256	7.6	1.0
VO - 3	0.05	0.135	29.7	0.976	29.0	1.0
VO - 4	0.12	0.135	29.7	0.054	1.6	1.0
VO - 5	0.25	0.135	29.7	0.054	1.6	1.0
VO - 6	0.05	0.158	29.7	0.054	1.6	1.25
VO - 7	0.05	0.113	29.7	0.054	1.6	0.75

Table 4 Test condition for closure of discharge valve (pump system A: $l_{eq}/d_2 = 15.7$, $\zeta = 235.3$, Reynolds number $Nd_2^2/(\mu/\rho) = 1.46 \times 10^6$)

Case No.	σ_o	σ_R	N [rpm]	T _v [s]	NT _v	ϕ_{No}/ϕ_r
VC - 1	0.05	0.135	29.7	0.054	1.6	1.0
VC - 2	0.05	0.135	29.7	0.263	7.8	1.0
VC - 3	0.05	0.135	29.7	1.114	33.1	1.0
VC - 4	0.12	0.135	29.7	0.054	1.6	1.0
VC - 5	0.42	0.135	29.7	0.054	1.6	1.0
VC - 6	0.05	0.158	29.7	0.054	1.6	1.25
VC - 7	0.05	0.113	29.7	0.054	1.6	0.75

increasing Q_d . At stage (d), where the cavitation spreads in the volute passage, Q_d begins to decrease. At stage (e), when the pump is cavitating and the p_s and p_d approach the vapor pressure p_v ($=2.33$ kPa), Q_d decreases whereas Q_s continues to increase. Then p_d tends to increase from (e) to (f) when the cavitation decreases in volume. At the next stage from (f) to (g) where the cavitation tends to grow in volume, Q_d and p_d show fluctuation first increasing and then decreasing. The fluctuations of Q_d and p_d are repeated at the stage from (g) to (h) similar to the stage from (e) to (f), but the amplitudes decay.

These fluctuations of both the delivery pressure and the dis-

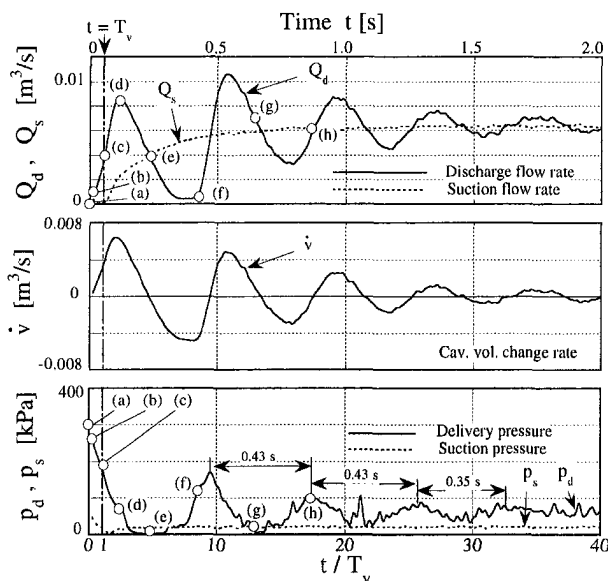


Fig. 3 Time histories of Q_d , Q_s , \dot{v} , p_d , and p_s at sudden opening of the discharge valve (VO-6); experimental uncertainty in Q_d and $Q_s = \pm 5.5\%$, and in p_d and $p_s = \pm 3.5\%$

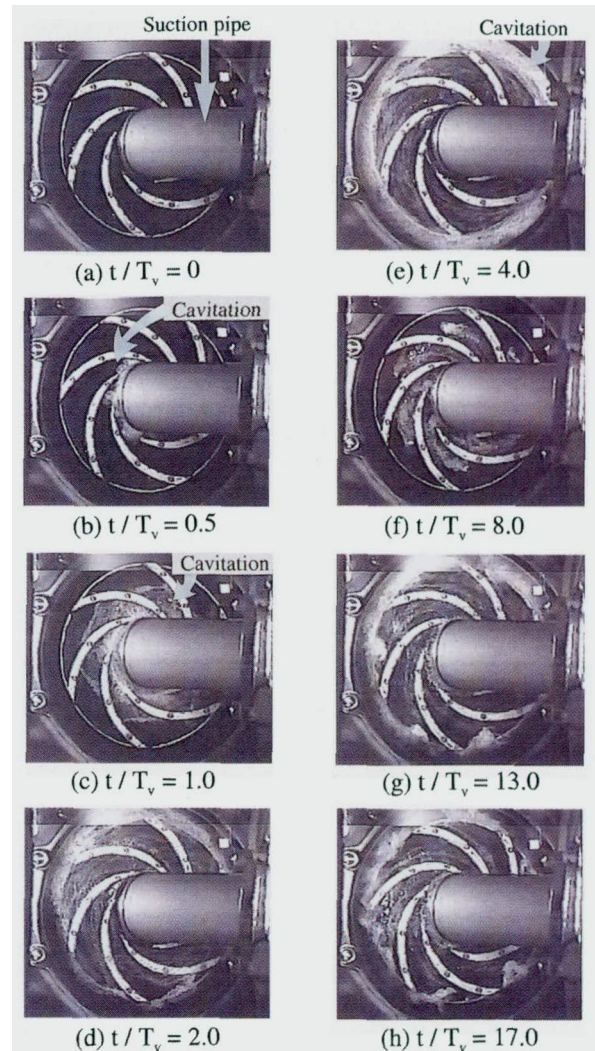


Fig. 4 Dynamic behavior of cavitation at sudden opening of the discharge valve

charge flowrate are the peculiar aspects of the pump cavitation behavior with fast opening of the discharge valve.

Effect of Valve Opening Time. Figure 5 presents the effect of nondimensional valve opening time NT_v on the transient phenomena. The time histories of Q_d , Q_s , \dot{v} , p_d and p_s for Cases VO-1 ($NT_v = 1.6$), VO-2 ($NT_v = 7.6$) and VO-3 ($NT_v = 29.0$) are shown in Fig. 5, for constant $\sigma_f = 0.05$ (lowest value) and $\phi_{Nf}/\phi_r = 1.0$.

The discharge flowrate Q_d in VO-3 increases with time and approaches the final flowrate, whereas Q_d in VO-1 and VO-2 shows oscillations before reaching its final value. As shown by the flow visualization tests, these oscillations of Q_d are related with the time evolution of cavitation volume inside the impeller. It is worthy noticing that p_d , Q_d and \dot{v} in Case VO-1 show the most remarkable unsteady variations among these three cases, while Case VO-3 shows a more smooth transient because of a small cavitation volume change rate \dot{v} at slow opening of the discharge valve. The fluctuations of Q_d and p_d increase with decreasing NT_v , as can be seen in Fig. 5.

Effect of Cavitation Number. The effect of cavitation number σ_f on the transient behavior is shown in Fig. 6. This figure presents the time histories of Q_d , Q_s , \dot{v} , p_d and p_s for Cases VO-1 ($\sigma_f = 0.05$), VO-4 ($\sigma_f = 0.12$) and VO-5 ($\sigma_f = 0.25$) for constant $NT_v = 1.6$ (smallest value) and $\phi_{Nf}/\phi_r = 1.0$.

As can be seen in this figure, the delivery pressure and the

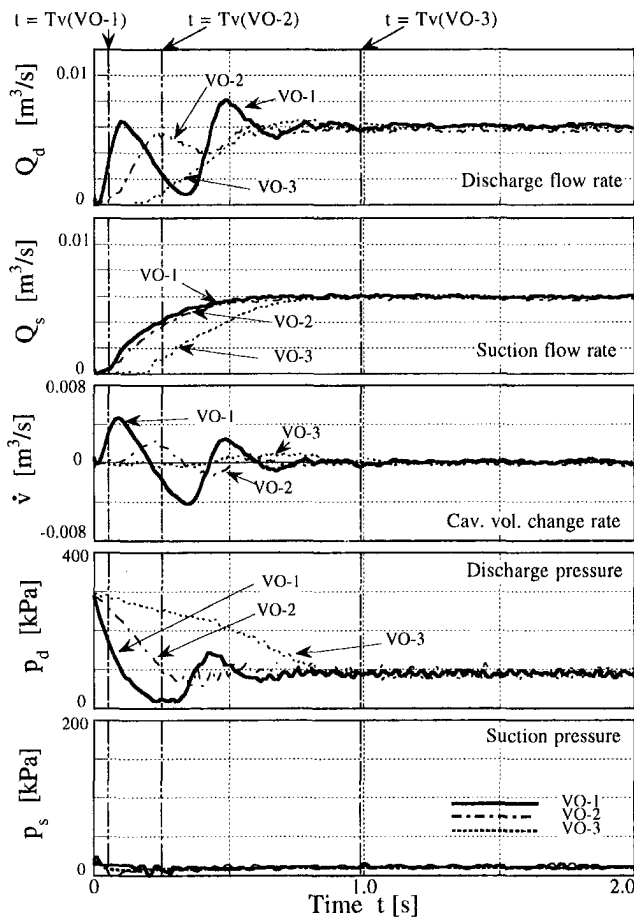


Fig. 5 Effect of NT_v on time histories of Q_d , Q_s , \dot{v} , p_d and p_s at sudden opening of the discharge valve; experimental uncertainty in Q_d and $Q_s = \pm 5.5\%$, and in p_d and $p_s = \pm 3.5\%$

discharge flowrate present the most violent fluctuations in Case VO-1, which correspond to the biggest variation in cavitation volume among these three cases, as shown by the flow visualizations. Thus, a lower σ_f results in bigger pressure and flowrate fluctuations at pump discharge. The pressure fluctuations of p_d and p_s in Case VO-5 seem to be caused by water hammer, because the time interval of p_d fluctuations agrees with that of p_s fluctuations, and p_s does not decrease below the vapor pressure.

Effect of Discharge Valve Opening. Figure 7 shows the effect of discharge valve opening ϕ_{NI}/ϕ_r on the transient behavior. The time histories of Q_d , Q_s , \dot{v} , p_d and p_s for Cases VO-6 ($\phi_{NI}/\phi_r = 1.25$), VO-1 ($\phi_{NI}/\phi_r = 1.0$) and VO-7 ($\phi_{NI}/\phi_r = 0.75$) for constant $NT_v = 1.6$ (smallest value) and $\sigma_f = 0.05$ (lowest value) are shown in Fig. 7. The parameters p_d , Q_d and \dot{v} clearly show oscillations for all three cases. Moreover, the fluctuations of p_d , Q_d , and \dot{v} increase with increasing ϕ_{NI}/ϕ_r .

All of the above results indicate that large fluctuations of p_d , Q_d and \dot{v} occur with smaller NT_v , lower σ_f and larger ϕ_{NI}/ϕ_r for discharge valve opening operation.

Criteria for Fluctuations of Discharge Pressure and Flow Rate. The fluctuations of delivery pressure and discharge flowrate are caused by oscillating cavitation volume in the pump, as described above. The time interval of transient fluctuations can be examined by introducing the unsteady parameter $K = NT_v/\phi_{NI}$ for many σ_f values including ones in Table 3, as shown in Fig. 8.

Figure 8 presents the relationship between the time interval of pressure oscillations \bar{T} and cavitation number σ_f with the effect of K at the opening of the discharge valve. Here the time interval \bar{T} is the average value of the first three periods of pressure fluctuations. As is

evident in Fig. 8, the average period \bar{T} increases with decreasing cavitation number σ_f and there is little effect of K . It can be observed that \bar{T} changes abruptly near $\sigma_f = 0.2$, below which oscillating cavitation occurs. Also, water hammer appears at a higher cavitation numbers than a σ_f corresponding to a transition region. These results of the pressure fluctuation average period indicate that the transient phenomena change suddenly from a water hammer situation to an oscillating cavitation regime with decreasing cavitation number σ_f with the opening of the discharge valve.

Further, the occurrence of transient fluctuation can be examined by using the unsteady parameter K for many σ_f values including ones in Table 3, as shown in Fig. 9: smaller K and lower σ_f result in the fluctuations of delivery pressure and discharge flowrate due to oscillating cavitation at sudden increase in flowrate with the opening of the discharge valve.

Transient Phenomena at Closure of Discharge Valve

Relationship Between Cavitation Behavior and Transient Phenomena. Figure 10 presents the time histories of the measured suction and delivery pressure, p_s and p_d , and suction and discharge flowrate, Q_s and Q_d , for the highest attainable change rate of valve closure at low suction pressure with $\sigma_0 = 0.05$ (Case VC-6). The cavitation volume changing rate, $\dot{v} = Q_d - Q_s$, is also shown in the same figure. From the comparison of Fig. 10 with Fig. 3, the wave form of both the suction and delivery pressure fluctuations at the valve closure is found to be qualitatively different from that at the valve opening. Impulsive pressures appear at the pump suction and discharge for sudden valve closure, whereas the pressure shows sinusoidal oscillations at the pump discharge for sudden valve opening.

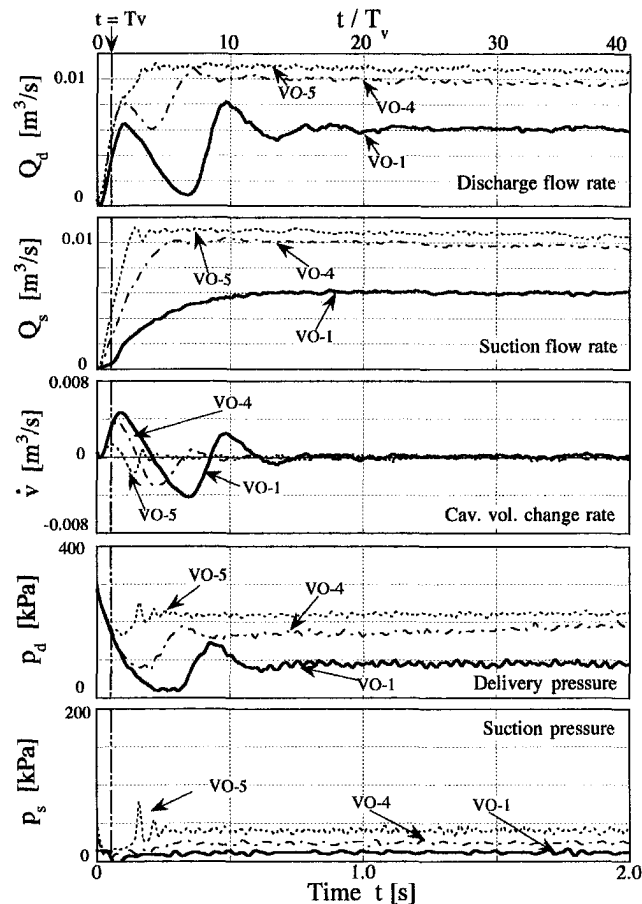


Fig. 6 Effect of σ_f on time histories of Q_d , Q_s , \dot{v} , p_d and p_s at sudden opening of the discharge valve; experimental uncertainty in Q_d and $Q_s = \pm 5.5\%$, and in p_d and $p_s = \pm 3.5\%$

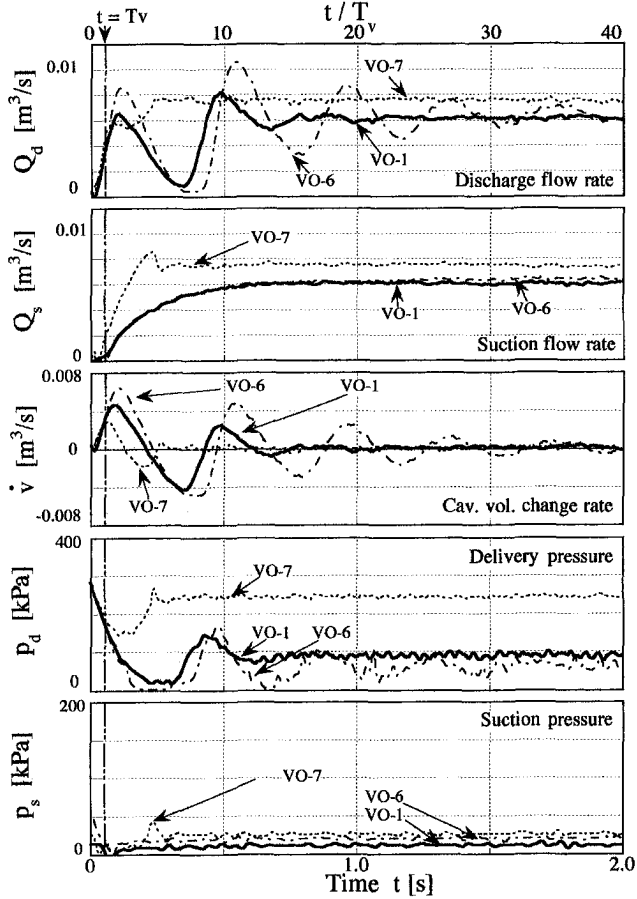


Fig. 7 Effect of ϕ_{Nf}/ϕ_r on time histories of Q_d , Q_s , \dot{v} , p_d and p_s at sudden opening of the discharge valve; experimental uncertainty in Q_d and $Q_s = \pm 5.5\%$, and in p_d and $p_s = \pm 3.5\%$

Figure 11 shows the photographs of cavitation pattern in the pump at the instant corresponding to the stages from (a) to (f) in Fig. 10. The cavitation in the pump decreases with time at the beginning of the transient from stage (a) to (c). The pump was still cavitating and the water was flowing into the pump through the suction pipe after the instant (b), when the discharge valve was closed. At stage (c), when the suction flowrate Q_s reaches zero and thus \dot{v} equals zero, the suction and delivery pressure, p_s and p_d ,

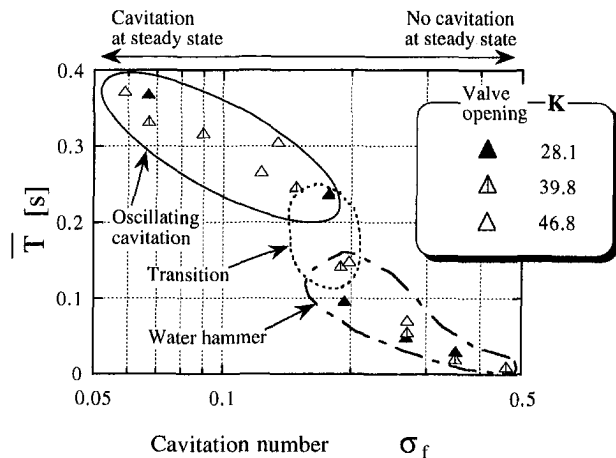


Fig. 8 Time interval of oscillation at rapid opening of the discharge valve; experimental uncertainty in $\sigma_f = \pm 5.5\%$, in $\bar{T} = \pm 7.5\%$, and in $K = \pm 5.5\%$

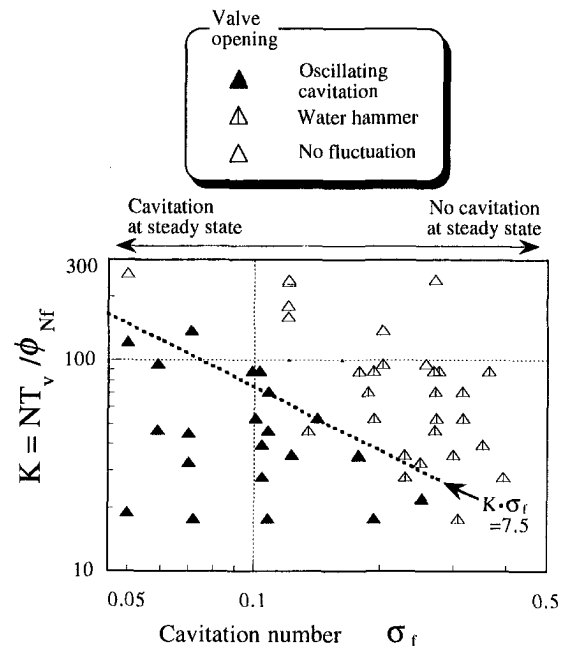


Fig. 9 Transient phenomena at rapid opening of the discharge valve; experimental uncertainty in $\sigma_f = \pm 5.5\%$, and in $K = \pm 5.5\%$

show impulses due to the collapse of the cavitation bubbles. At stage (d), after the collapse of the cavitation bubbles, a water column separation occurred in the suction pipe as indicated by negative Q_s value. The column separation continues to grow in volume to the instant (e) when the negative suction flow again reaches zero. The p_s and p_d show impulses at stage (f) when the water column separation in the suction line restarts.

Effect of Valve Closure Time. Figure 12 presents the effect of nondimensional valve closure time NT_v on the transient phenomena. The time histories of Q_d , Q_s , \dot{v} , p_d , and p_s are shown for Cases VC-1 ($NT_v = 1.6$), VC-2 ($NT_v = 7.8$) and VC-3 ($NT_v = 33.1$) in Fig. 12 for constant $\sigma_0 = 0.05$ (lowest value) and $\phi_{Nf}/\phi_r = 1.0$.

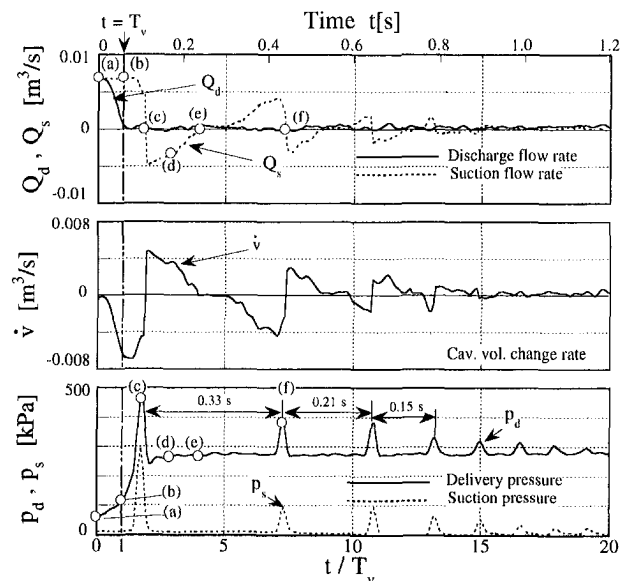


Fig. 10 Time histories of Q_d , Q_s , \dot{v} , p_d and p_s at sudden closure of the discharge valve (VC-6); experimental uncertainty in Q_d and $Q_s = \pm 5.5\%$, and in p_d and $p_s = \pm 3.5\%$



Fig. 11 Dynamic behavior of the cavitation at sudden closure of the discharge valve

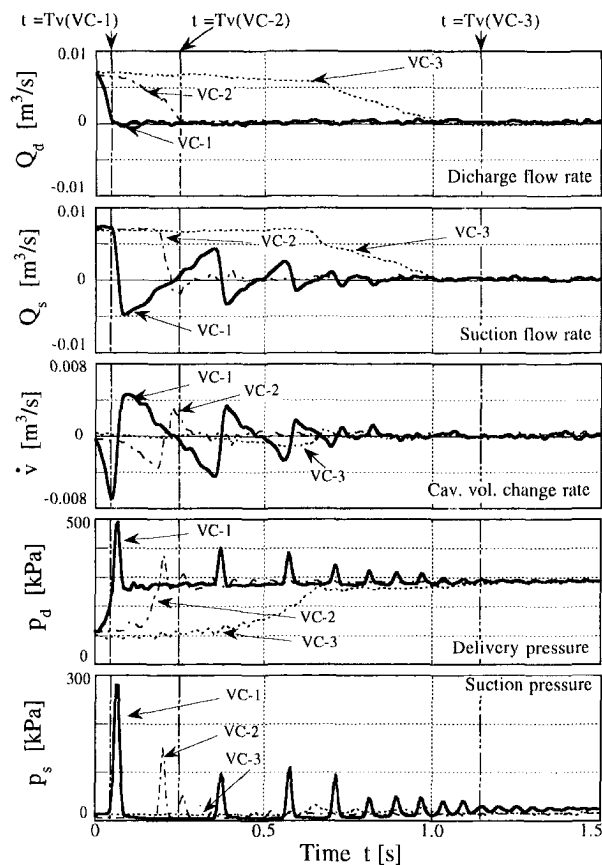


Fig. 12 Effect of NT_v on time histories of Q_d , Q_s , \dot{v} , p_d and p_s at sudden closure of the discharge valve; experimental uncertainty in Q_d and $Q_s = \pm 5.5\%$, and in p_d and $p_s = \pm 3.5\%$

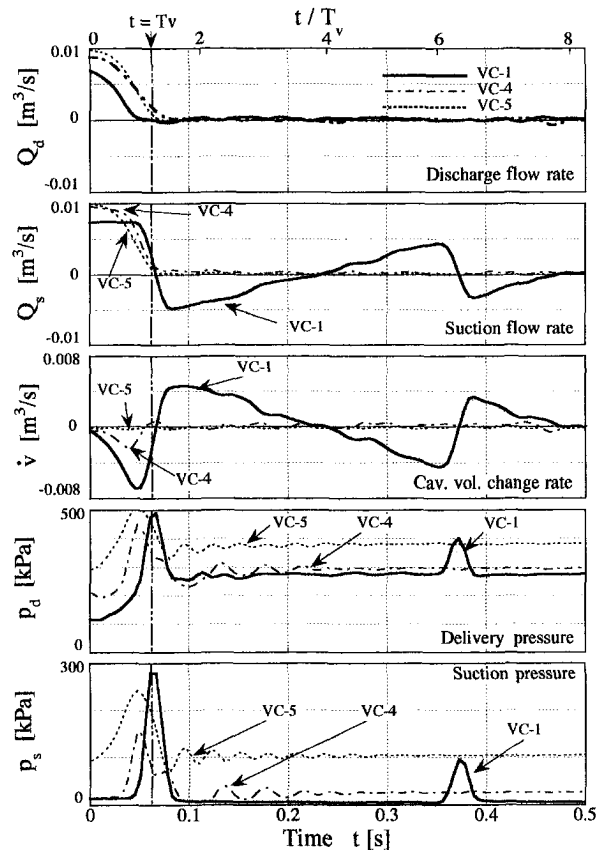


Fig. 13 Effect of σ_0 on time histories of Q_d , Q_s , \dot{v} , p_d and p_s at sudden closure of the discharge valve; experimental uncertainty in Q_d and $Q_s = \pm 5.5\%$, and in p_d and $p_s = \pm 3.5\%$

The negative suction flowrate Q_s and the fluctuations of Q_s , p_d , p_s , and \dot{v} become larger with decreasing NT_v , whereas Q_d reaches zero when the discharge ball valve is shut at $t/T_v = 1.0$. In Cases VC-1 and VC-2, the impulsive pressures due to the rejoining of the separated water column in the suction line appear in p_d and p_s , while p_d in VC-3 increases uniformly with decreasing Q_d . High impulsive pressures are attributed to large scale water column separation in the suction piping with decreasing NT_v .

Effect of Cavitation Number. The effect of cavitation number σ_0 on the transient behavior is shown in Fig. 13. This figure presents the time histories of Q_d , Q_s , \dot{v} , p_d and p_s for Cases VC-1 ($\sigma_0 = 0.05$), VC-4 ($\sigma_0 = 0.12$) and VC-5 ($\sigma_0 = 0.42$), for constant $NT_v = 1.6$ (smallest value) and $\phi_{N0}/\phi_r = 1.0$.

Impulsive pressures are observed in p_d and p_s for Case VC-1 due to water column separation. In Cases VC-4 and VC-5, the fluctuations of both p_d and p_s have similar wave form and the same time interval. Compared with the ones in Case VC-1, however, the pressure fluctuations have shorter time intervals of oscillation and smaller amplitude, and there is no negative suction flowrate in Cases VC-4 and VC-5. The pressure oscillations in Case VC-5 are caused by water hammer without water column separation, because the suction pressure p_s is greater than the vapor pressure p_v ($=2.33$ kPa) during the transient period. Case VC-4 is the criterion for the occurrence of water column separation, in which p_s reaches vapor pressure. Decreasing σ_0 leads to larger impulsive pressure and negative suction flowrate due to water column separation as can be seen in Fig. 13.

Effect of Discharge Valve Opening. The effect of discharge valve opening ϕ_{N0}/ϕ_r on the transient behavior is shown in Fig. 14, which presents the time histories of Q_d , Q_s , \dot{v} , p_d , and p_s for Cases VC-6 ($\phi_{N0}/\phi_r = 1.25$), VC-1 ($\phi_{N0}/\phi_r = 1.0$) and VC-7 ($\phi_{N0}/\phi_r =$

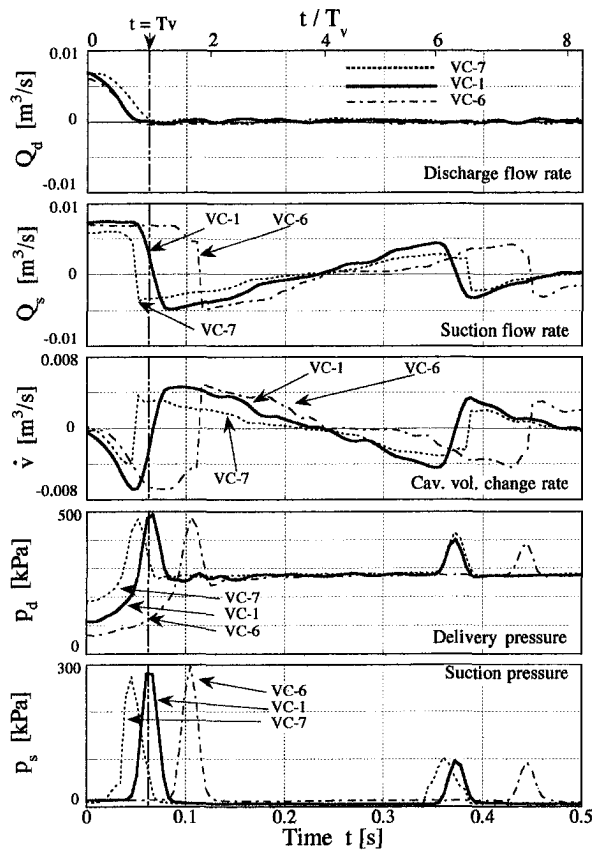


Fig. 14 Effect of ϕ_{N0}/ϕ_r on time histories of Q_d , Q_s , \dot{v} , p_d and p_s at sudden closure of the discharge valve; experimental uncertainty in Q_d and $Q_s = \pm 5.5\%$, and in p_d and $p_s = \pm 3.5\%$

0.75) at constant $NT_v = 1.6$ (smallest value) and $\sigma_0 = 0.05$ (lowest value). The negative suction flowrate ($Q_s < 0$) appears with the occurrence of water column separation in all cases. The amplitude of the impulsive pressures, both p_d and p_s , which are caused by the rejoining of the separated water column increases with increasing ϕ_{N0}/ϕ_r . This might be due to a larger velocity difference between pump suction ($Q_s > 0$) and pump discharge ($Q_d = 0$) at larger ϕ_{N0}/ϕ_r , because a larger velocity difference results in larger impulsive pressure at the rejoining of the separated water column.

As mentioned above, larger scale water column separation and higher impulsive pressure occur with decreasing NT_v and σ_0 and increasing ϕ_{N0}/ϕ_r at valve closure operation.

Criteria for Fluctuations of Suction and Discharge Pressure.

The suction and discharge pressure fluctuations are caused by the rejoining of separated water column in the suction line as described above. The time interval of transient fluctuations can be examined by introducing the unsteady parameter $K = NT_v/\phi_{N0}$ for many data including ones in Table 4, as shown in Fig. 15.

Figure 15 presents the relationship between the time interval of the delivery pressure oscillations \bar{T} and the cavitation number σ_0 with the effect of K at closure of the discharge valve. The time interval \bar{T} increases abruptly below a certain cavitation number σ_{cr} with decreasing σ_0 whereas \bar{T} is constant at higher cavitation numbers, as clearly evident in Fig. 15. The critical cavitation number σ_{cr} increases with the decreasing K . Moreover, \bar{T} becomes larger at $\sigma_0 < \sigma_{cr}$, while K gets smaller for the same σ_0 . One might consider that this is due to decreasing wave propagation velocity caused by the occurrence of large scale water column separation when σ_0 is low and K is small.

Also, the occurrence of fluctuations can be observed by using the unsteady parameter K for many σ_0 values including ones in Table 4, as shown in Fig. 16. As can be seen, smaller K and lower σ_0 result in

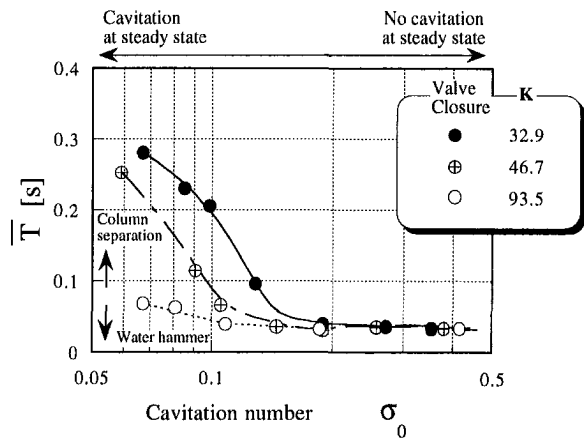


Fig. 15 Time interval of oscillation at rapid closure of the discharge valve; experimental uncertainty in $\sigma_0 = \pm 5.5\%$, and in $\bar{T} = \pm 7.5\%$, and in $K = \pm 5.5\%$

the pressure pulsations due to water column separation at sudden decrease in flowrate with the closure of the discharge valve.

Effect of Pipe Length

Figure 17 shows the effect of suction and discharge pipe length on the time interval of the delivery pressure oscillations for the piping system B, schematics of which are presented in Fig. 1(b). Figures 17(a) and (b) correspond to the valve opening and closure case, respectively. The time interval of pressure oscillations \bar{T} increases with decreasing cavitation number σ_{f0} in both cases as in Figs. 8 and 15. In the rapid valve opening case shown in Fig. 17(a), the \bar{T} is independent of pipe length in the range from $\sigma_r = 0.09$ to 0.2. This is because the pressure oscillations are attributed to the cavitation behavior within the pump during the transient period. On the other hand, in the rapid valve closure case shown in Fig. 17(b), the suction pipe length (Case 2) has a dominant effect on \bar{T} in the range from $\sigma_0 = 0.09$ to 0.3 while the discharge pipe length (Case 3) has not such a

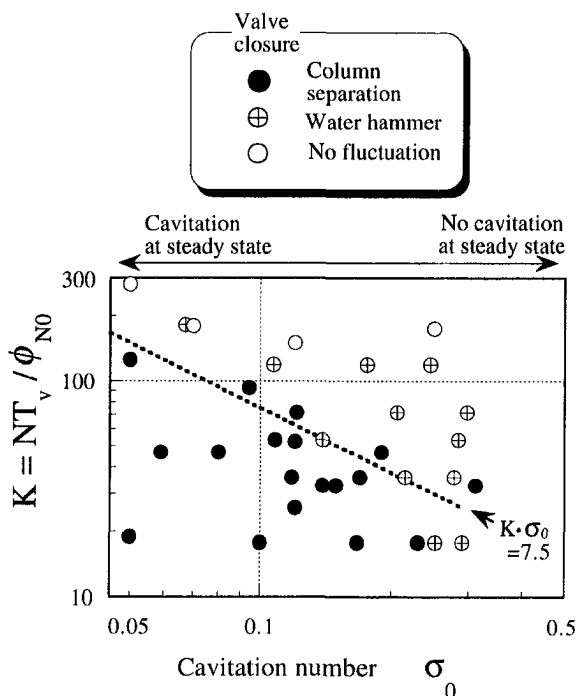


Fig. 16 Transient phenomena at rapid closure of the discharge valve; experimental uncertainty in $\sigma_0 = \pm 5.5\%$, and in $K = \pm 5.5\%$

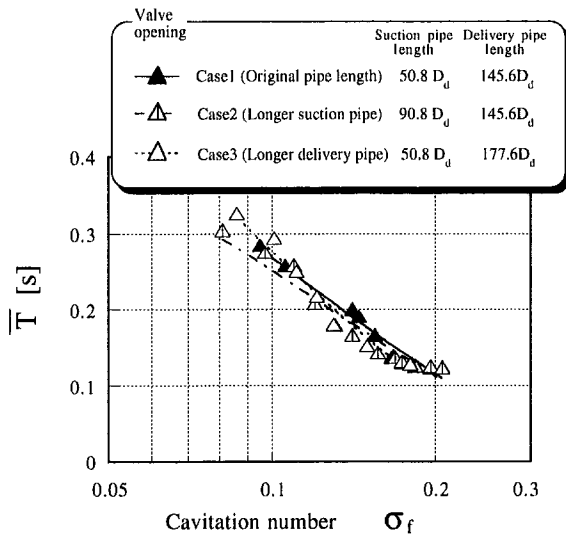


Fig. 17(a) Opening of discharge valve

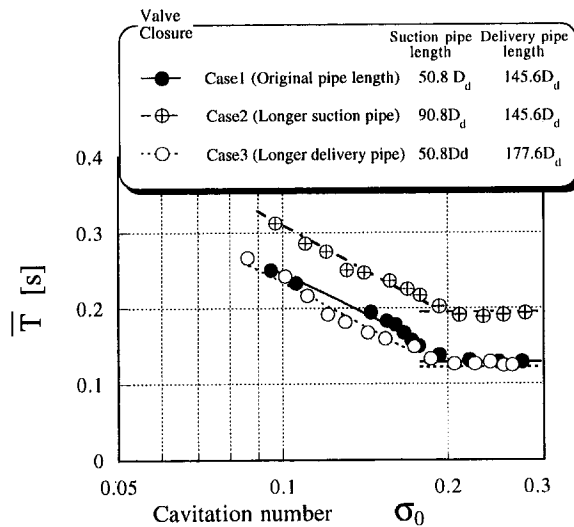


Fig. 17(b) Closure of discharge valve

Fig. 17 Effect of pipe length; experimental uncertainty in $\sigma_{f,0} = \pm 5.5\%$, and in $\bar{T} = \pm 7.5\%$

remarkable influence on \bar{T} . This is likely due to water hammer, because \bar{T} depends on the pipe length from the suction tank to the ball valve. The time period \bar{T} is independent from σ_0 at higher cavitation number over $\sigma_0 = 0.2$ whichever is the pipe length. This is because the wave propagation velocity does not depend on σ_0 at the higher cavitation number. Wave propagation velocity decreases with decreasing σ_0 because of the occurrence of water column separation, and thus \bar{T} increases with decreasing σ_0 .

As indicated above, the transient phenomena with sudden valve opening are quite different from those with sudden valve closure.

Conclusions

An experimental study was carried out on the transient behavior of a cavitating centrifugal pump during the sudden opening/closure of the discharge valve. The dynamic phenomena were related to the cavitation in the pump or column separation in the suction piping, leading to the following conclusions:

- (1) A rapid opening/closure of the discharge valve results in pressure and flowrate fluctuations, and the occurrence of the oscillations depends on NT_v , $\sigma_{f,0}$ and $\phi_{Nf,0}/\phi_r$.
- (2) Transient pressure fluctuations at valve closure are caused by water column separation, whereas the pressure fluctuations at sudden valve opening are attributed to oscillating cavitation.
- (3) Smaller NT_v , lower $\sigma_{f,0}$ and larger $\phi_{Nf,0}/\phi_r$ lead to greater transient oscillations of pressure and flowrate at rapid transient operation.
- (4) Time interval of oscillations at rapid valve closure is dependent on cavitation number and suction pipe length as well. On the other hand, the time interval of pressure oscillations at rapid valve opening depends on cavitation number but is independent from pipe length.

References

- Barrand, J. P., 1996, "Qualitative Flow Visualizations During Fast Start-up of Centrifugal Pumps," *Hydraulic Machinery and Cavitation*, E. Cabrera et al., ed., Kluwer Academic Publishers, pp. 671–680.
- Barrand, J. P., Ghelici, N., and Caignaert, G., 1993, "Unsteady Flow During The Fast Start-Up of a Centrifugal Pump," ASME FED-Vol. 154, *Pumping Machinery*, pp. 143–150.
- Greitzer, E. M., 1981, "The Stability of Pumping Systems," ASME JOURNAL OF FLUIDS ENGINEERING, Vol. 103, pp. 193–242.
- Kaneko, M., and Ohashi, H., 1982, "Transient Characteristics of a Centrifugal Pump During Quick Change of Flow Rate," *Trans. JSME*, Series B, Vol. 48, No. 426, pp. 229–237 (in Japanese).
- Knapp, R. T., 1937, "Complete Characteristics of Centrifugal Pumps and Their Use in the Prediction of Transient Behavior," *Trans. ASME*, Vol. 59, pp. 683–689.
- Lefebvre, P. J., and Barker, W. P., 1995, "Centrifugal Pump Performance During Transient Operation," ASME JOURNAL OF FLUIDS ENGINEERING, Vol. 117, No. 1, pp. 123–128.
- Nguyen Duc, J. M., Von Kaenel, A., and Danguy, F., 1993, "Transient Behaviour of Liquid Hydrogen Pumps During Start-Up And Shutdown of Rocket Engines," ASME FED-Vol. 154, *Pumping Machinery*, pp. 159–170.
- Sack, L. E., and Nottage, H. B., 1965, "System Oscillations Associated With Cavitating Inducers," ASME *Journal of Basic Engineering*, Vol. 87, pp. 917–924.
- Saito, S., 1983, "The Transient Characteristics of a Pump During Start Up," *Bulletin of JSME*, Vol. 25, No. 201, pp. 372–379.
- Tsukamoto, H., Matsunaga, S., Yoneda, H., and Hata, S., 1986, "Transient Characteristics of a Centrifugal Pump During Stopping Period," ASME JOURNAL OF FLUIDS ENGINEERING, Vol. 108, No. 4, pp. 392–399.
- Tsukamoto, H., and Ohashi, H., 1982, "Transient Characteristics of a Centrifugal Pump During Starting Period," ASME JOURNAL OF FLUIDS ENGINEERING, Vol. 104, No. 1, pp. 6–14.
- Tsukamoto, H., and Tanaka, T., 1994, "Transient Characteristics of a Cavitating Centrifugal Pump System at Rapid Change in Flow Rate," ASME FED-Vol. 190, *Cavitation and Gas-Liquid Flow in Fluid Machinery and Devices*, pp. 175–183.
- Tsukamoto, H., Yoneda, H., and Sagara, K., 1995, "The Response of a Centrifugal Pump to Fluctuating Rotational Speed," ASME JOURNAL OF FLUIDS ENGINEERING, Vol. 117, No. 3, pp. 479–484.

Transient Behavior of a Cavitating Centrifugal Pump at Rapid Change in Operating Conditions—Part 2: Transient Phenomena at Pump Startup/Shutdown

T. Tanaka

Assistant Professor,
Department of Mechanical and Electrical
Engineering,
Yatsushiro National College of Technology,
Yatsushiro, 866-8501, Japan

H. Tsukamoto

Professor,
Department of Mechanical Engineering,
Kyushu Institute of Technology,
Tobata, Kitakyushu, 804-8550, Japan

In the 1st report, the dynamic behavior of a cavitating centrifugal pump was related to the transient phenomena at the sudden opening/closure of the discharge valve. In this paper, the experimental study was extended to the transient behavior of the cavitating centrifugal pump at rapid starting/stopping of the pump. Unsteady pressures and flowrate were related to time-dependent cavitation behavior in a similar manner as for the rapid operation of the discharge valve. As a result of the present study, pressure fluctuations were found to occur due to water column separation at the sudden stop of the pump similarly to pressure oscillations associated with the sudden closure of the discharge valve. Moreover, the experimental results on the transient behavior at pump startup indicated that the transient fluctuations of delivery pressure and discharge flowrate are caused by oscillating cavitation similarly to the ones occurring at the opening of the discharge valve.

Introduction

Following Part 1 (Tanaka, and Tsukamoto, 1999), in which the transient phenomena at the sudden opening/closure of the discharge valve were related to the cavitation behavior in a centrifugal pump, the transient behavior of a cavitating pump system is shown for the case when the pump starts or stops rapidly. In order to make clear the transient phenomena, the tests are conducted for a very rapid change rate of rotational speed which rarely occurs in practice. Such extreme test conditions produce more pronounced phenomena and help for understanding the mechanism of the transient behavior of a cavitating pump under rapid start/stop. In the present study, a rapid operation of the pump is intended as an operation during which pressure and flowrate fluctuations occur during the transient period. Quantitative criteria for the occurrence of pressure and flowrate fluctuations were presented in Part 1 (see Fig. 9 and Fig. 16) and will be further discussed in Part 2. However, a clear criterion for the limit between quasi-steady operation and rapid operation (pump fluid transient) has not yet been established. It will require a further work.

Nomenclature

Refer to Part 1

New Parameters:

T_{na} = nominal acceleration time of pump [s]

T_{nd} = nominal deceleration time of pump [s]

Test Equipment and Method

Tests were made by using the same instrumentation and visualization system described in Part 1.

The rapid startup and shutdown of the test pump were realized by the activation of an electromagnetic clutch and brake, which connects or disconnects the pump and motor shafts depending on the exciting current in the magnetic coil (Tsukamoto and Ohashi, 1982; Tsukamoto et al., 1986). The rotational speed, N , was calculated based on pulses (60 pulses per a revolution) as indicated in Part 1. And the sampling frequency is 5 kHz which is high enough to capture the pulse signals. The motor has enough power for a rapid acceleration and pump shaft is rigid enough. The acceleration (or deceleration) rate of rotational speed dN/dt is not constant for the entire starting (or stopping) period. It is, therefore, difficult to express this complicated acceleration (or deceleration) history by a simple parameter. In this paper, the rate of acceleration or deceleration of the rotational speed is defined as the time (nominal acceleration or deceleration time, T_{na} or T_{nd}) required for reaching 63.2% of the final rotational speed N_f (Tsukamoto and Ohashi, 1982), and 36.8% of the initial rotational speed N_0 (Tsukamoto et al., 1986), respectively.

Using the same considerations about the nondimensional parameters which regulate the transient characteristics described in Part 1, the following five independent nondimensional parameters are introduced; i.e., Reynolds number $N_{f,0}d_2^2/(\mu/\rho)$, equivalent normalized piping length l_{eq}/d_2 , pipe resistance coefficient $\zeta \propto \phi_{Nf,0}/\phi_r$, cavitation number $\sigma = 2gH_{sv}/u_2^2$ and a newly introduced parameter, i.e., the reduced time for transient operation $N_{f,0}T_{na,nd}$. Here ϕ_{Nf} or ϕ_{N0} is the final/initial flow coefficient under noncavitation condition, and ϕ_r is the rated flow coefficient (=0.058).

The latter three parameters can be controlled in the experiment by adjusting the discharge valve opening, the suction pressure, and the time for transient operation, i.e., acceleration or deceleration of the pump rotational speed. The influence of Reynolds number on the transient characteristics is omitted from the present study.

Contributed by the Fluids Engineering Division for publication in the JOURNAL OF FLUIDS ENGINEERING. Manuscript received by the Fluids Engineering Division March 12, 1998; revised manuscript received June 22, 1999. Associate Technical Editor: B. Schiavello.

Table 1 Test condition for pump startup (pump system A: $l_{eq}/d_2 = 15.7$, $\zeta = 235.3$, Reynolds number $Nd_2^2/(\mu\rho) = 1.46 \times 10^6$)

Case No.	σ_f	σ_R	N_f [rps]	T_{na} [s]	$N_f T_{na}$	ϕ_{Nf}/ϕ_r
PA - 1	0.07	0.158	29.7	0.094	2.8	1.25
PA - 2	0.07	0.158	29.7	0.158	4.7	1.25
PA - 3	0.07	0.158	29.7	0.387	11.5	1.25
PA - 4	0.12	0.158	29.7	0.094	2.8	1.25
PA - 5	0.25	0.158	29.7	0.094	2.8	1.25
PA - 6	0.07	0.135	29.7	0.094	2.8	1.0
PA - 7	0.07	0.113	29.7	0.094	2.8	0.75

Table 2 Test condition for pump shutdown (pump system A: $l_{eq}/d_2 = 15.7$, $\zeta = 235.3$, Reynolds number $Nd_2^2/(\mu\rho) = 1.46 \times 10^6$)

Case No.	σ_o	σ_R	N_o [rps]	T_{nd} [s]	$N_o T_{nd}$	ϕ_{No}/ϕ_r
PD - 1	0.05	0.158	29.7	0.141	4.2	1.25
PD - 2	0.05	0.158	29.7	0.282	8.4	1.25
PD - 3	0.05	0.158	29.7	0.599	17.8	1.25
PD - 4	0.12	0.158	29.7	0.141	4.2	1.25
PD - 5	0.42	0.158	29.7	0.141	4.2	1.25
PD - 6	0.05	0.135	29.7	0.141	4.2	1.0
PD - 7	0.05	0.113	29.7	0.141	4.2	0.75

Test Results and Discussion

Among many experiments made for a variety of combinations of the above experimental parameters, only the data for the test conditions listed in Tables 1 and 2 are shown in Part 2 of this study. Further discussion will be presented in Part 3 of this study.

Transient Phenomena at Pump Start-Up

Relationship Between Cavitation Behavior and Transient Phenomena. Figure 1 presents the time histories of the measured

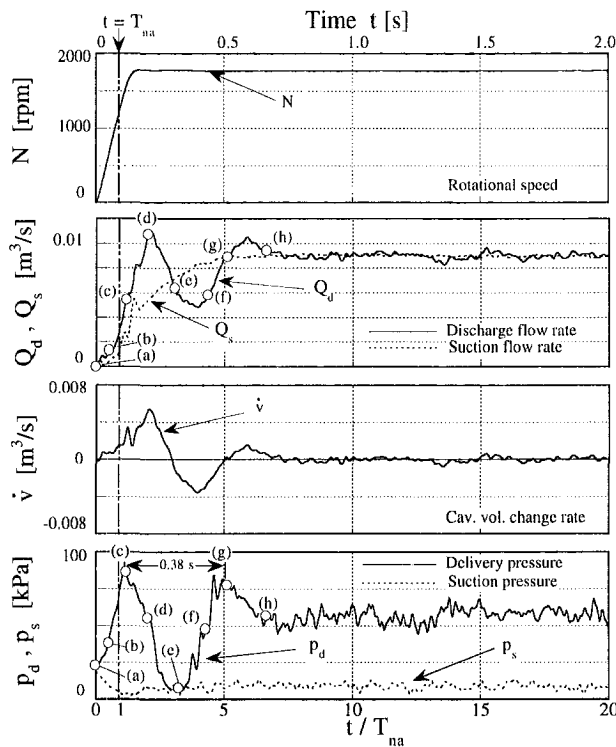


Fig. 1 Time histories of N , Q_d , Q_s , \dot{v} , p_d and p_s at rapid startup of the pump (PA-1); experimental uncertainty in $N = \pm 3.5\%$, in Q_d and $Q_s = \pm 5.5\%$, and in p_d and $p_s = \pm 3.5\%$

rotational speed N , suction and delivery pressure, p_s and p_d , suction and discharge flowrate, Q_s and Q_d for the highest attainable acceleration of the pump rotational speed at low suction pressure with $\sigma_f = 0.07$ (Case PA-1). The cavitation volume change rate, $\dot{v} = Q_d - Q_s$, is also shown in Fig. 1. Figure 2 shows the photographs of the cavitating behavior in the pump at the instant corresponding to the stage from (a) to (h) in Fig. 1.

At the initial stages from (a) to (b), Q_s , Q_d and p_d tend to increase with increasing N , but there is no cavitation in the pump. After passing through stage (c), cavitation bubbles appear near the leading edge of the impeller vanes and continue to grow in volume from (c) to (d) when N is still increasing, while Q_s and Q_d continue to increase and p_d begins to decrease. At stage (d), when N has already reached the full steady value and \dot{v} shows the maximum value, the cavitation expands to the volute passage. The cavitation within the pump increases, and the volute passage is filled with the cavitation bubbles at the instant (e). At that time, both p_s and p_d approach the vapor pressure $p_v (=2.33 \text{ kPa})$. These phenomena are similar to the ones observed in the case of the discharge valve opening shown in Part 1. Then Q_d and also p_d tend to increase from (e) to (g) when the cavitation decreases in volume. During the next interval from stage (g) to (h), the cavitation tends to grow again in volume and reaches the final pattern, while Q_d shows a final fluctuation first increasing and then decreasing to the steady state value. In the same time interval p_d decreases and reaches final value with reduced fluctuations. No cavitation was observed in the suction pipe during the entire transient period (Fig. 2).

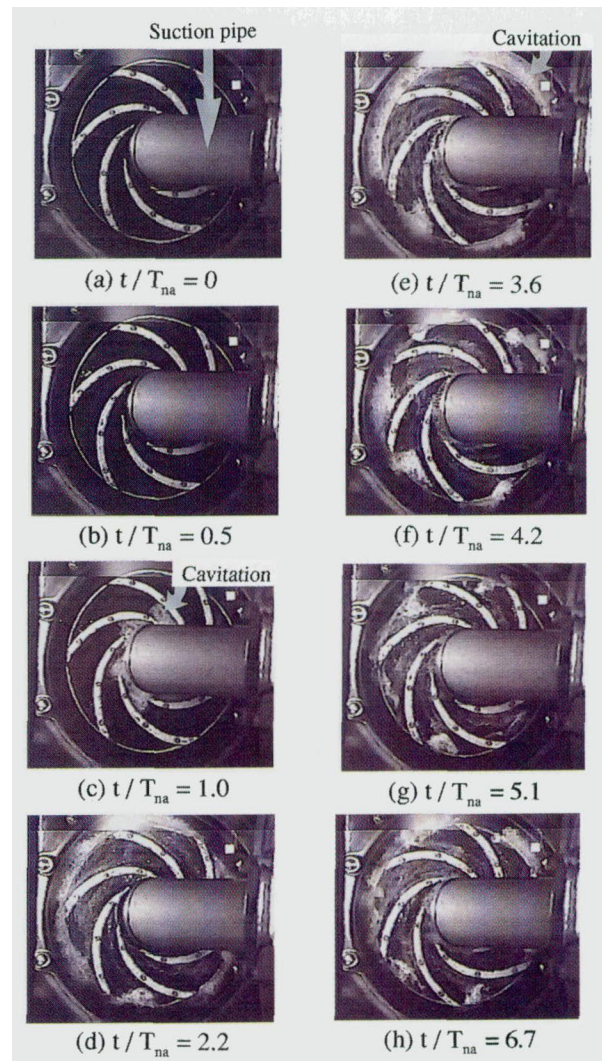


Fig. 2 Dynamic behavior of cavitation at rapid startup of pump

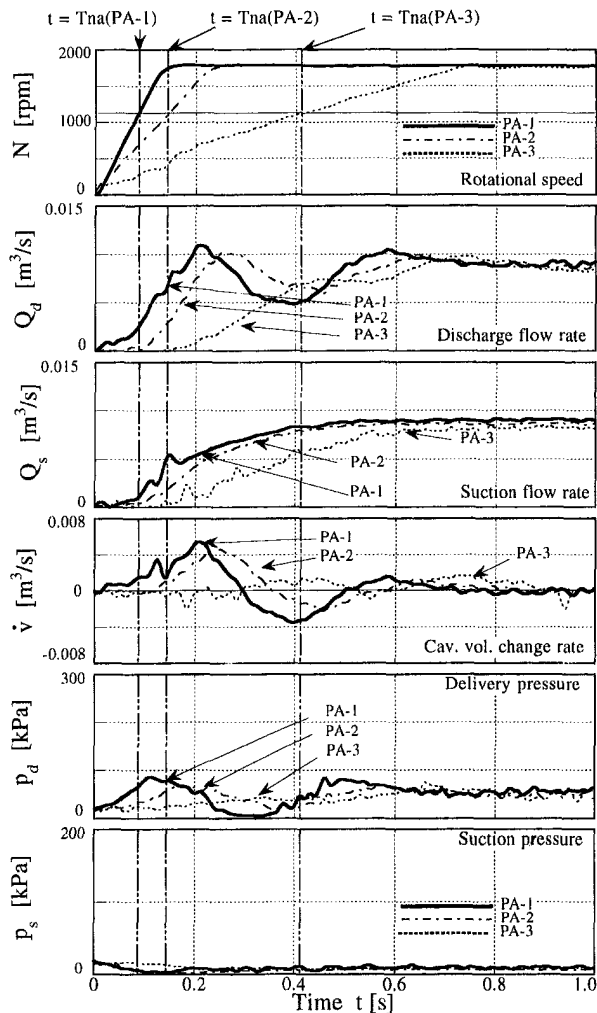


Fig. 3 Effect of $N_f T_{na}$ on time histories of N , Q_d , Q_s , \dot{v} , p_d and p_s at rapid startup of the pump; experimental uncertainty in $N = \pm 3.5\%$, in Q_d and $Q_s = \pm 5.5\%$, and in p_d and $p_s = \pm 3.5\%$

The transient phenomena, i.e., the fluctuations of the delivery pressure and the discharge flowrate, are strictly related with the cavitation behavior inside the pump, as it can be seen in these figures. Moreover, the transient behavior is quite similar to the one observed in the case of the rapid valve opening described in Part 1.

Effect of Acceleration Time. Figure 3 presents the effect of nondimensional acceleration time $N_f T_{na}$ on the transient phenomena. The time histories of N , Q_d , Q_s , \dot{v} , p_d and p_s for Cases PA-1 ($N_f T_{na} = 2.8$), PA-2 ($N_f T_{na} = 4.7$) and PA-3 ($N_f T_{na} = 11.5$) are shown in Fig. 3, for constant $\sigma_f = 0.07$ (lowest value) and $\phi_{Nf}/\phi_r = 1.25$ (largest value).

The magnitudes of fluctuations in Q_d and p_d are found to increase with decreasing $N_f T_{na}$. This is because the cavitation in the pump shows a bigger variation in the volume for smaller $N_f T_{na}$, i.e., fastest acceleration rate of the rotational speed. This tendency with $N_f T_{na}$ is similar to that with NT_v at the rapid opening of the discharge valve presented in Part 1.

Effect of Cavitation Number. The effect of cavitation number σ_f on the transient behavior is shown in Fig. 4, which presents the time histories of N , Q_d , Q_s , \dot{v} , p_d and p_s for three different σ_f cases: Cases PA-1 ($\sigma_f = 0.07$), PA-4 ($\sigma_f = 0.12$) and PA-5 ($\sigma_f = 0.25$), with constant $N_f T_{na} = 2.8$ (smallest value) and $\phi_{Nf}/\phi_r = 1.25$ (largest value).

As can be seen in the Fig. 4, the lower σ_f results in greater fluctuations of Q_d and p_d due to bigger change of cavitation

volume with time as indicated by the change in \dot{v} . The peaks of p_d and p_s near $t/T_{na} = 3.5$ ($t = 0.33$ [s]) in Case PA-5 seem to be caused by water hammer, because the p_d changes synchronously with p_s . This tendency with σ_f is analogous to the same one occurring at the valve opening discussed in Part 1.

The ratio ϕ_{Nf}/ϕ_r , which is the same for PA-1, PA-4 and PA-5, gives the quasi-steady operating point at noncavitating condition (pump flow coefficient relative to design flow coefficient). At given ϕ_{Nf}/ϕ_r corresponds a discharge valve opening, which is maintained while the total suction pressure and so σ_f is varied. Even with the same ϕ_{Nf} , the actual final flowrate differs depending on σ_f . The occurrence of large scale cavitation leads to the decrease in flowrate and so the final flowrate reaches a value dependent from the total suction pressure.

Effect of Discharge Valve Opening. Figure 5 presents the effect of discharge valve opening ϕ_{Nf}/ϕ_r on the transient behavior, showing the time histories of N , Q_d , Q_s , \dot{v} , p_d and p_s for three different valve openings: Cases PA-1 ($\phi_{Nf}/\phi_r = 1.25$), PA-6 ($\phi_{Nf}/\phi_r = 1.0$) and PA-7 ($\phi_{Nf}/\phi_r = 0.75$), for constant $N_f T_{na} = 2.8$ (lowest value) and $\sigma_f = 0.07$ (smallest value).

Larger ϕ_{Nf}/ϕ_r leads to bigger variation of the cavitation volume in the pump, and thus results in larger fluctuations of p_d and Q_d . This tendency is similar to the one at the sudden opening of the discharge valve shown in Part 1.

As described above, smaller $N_f T_{na}$, lower σ_f , and larger ϕ_{Nf}/ϕ_r result in larger fluctuations of p_d and Q_d . This transient behavior shows quite similar tendencies observed for the case of the rapid

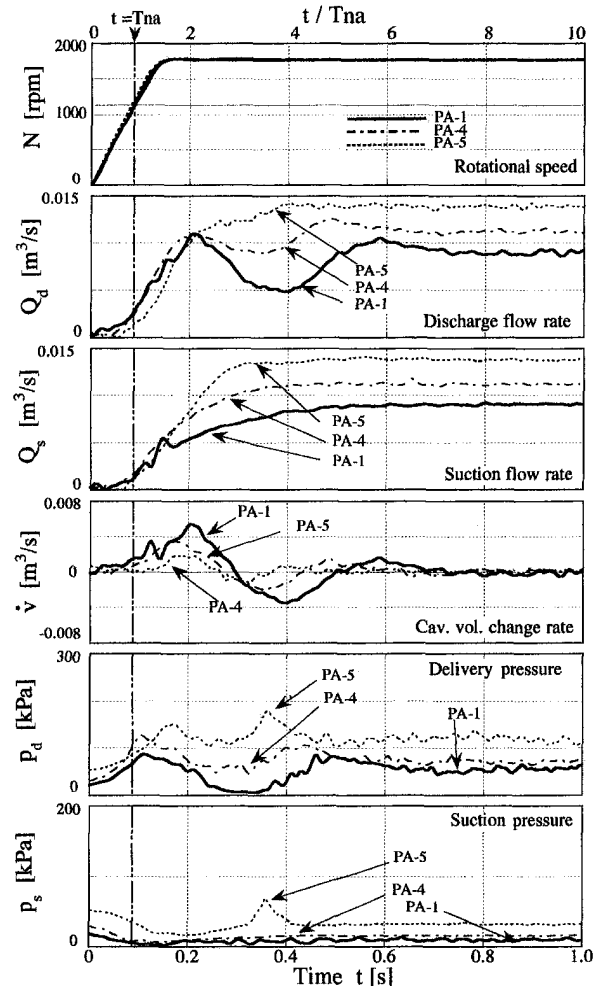


Fig. 4 Effect of σ_f on time histories of N , Q_d , Q_s , \dot{v} , p_d and p_s at rapid startup of the pump; experimental uncertainty in $N = \pm 3.5\%$, in Q_d and $Q_s = \pm 5.5\%$, and in p_d and $p_s = \pm 3.5\%$

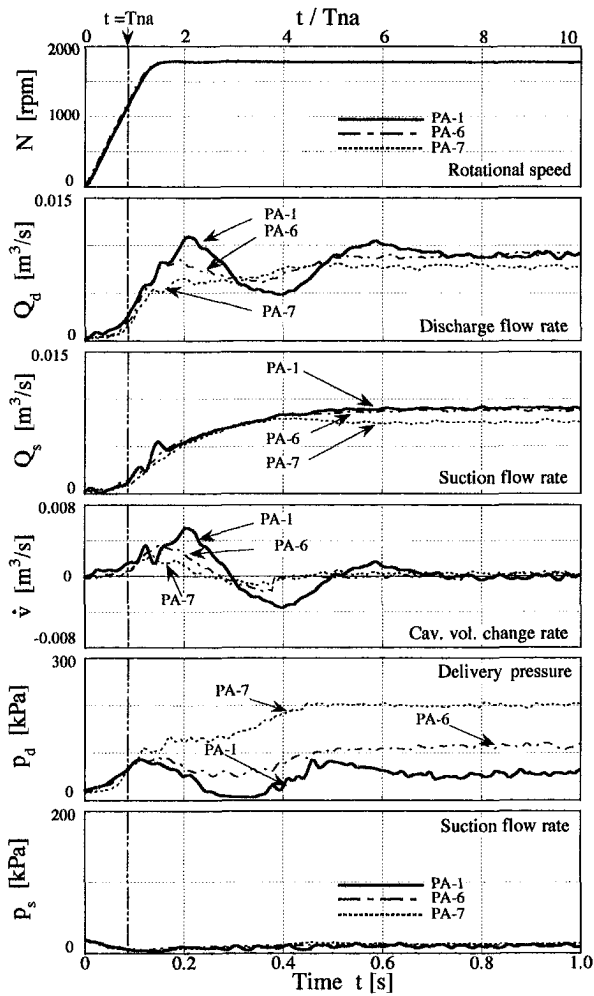


Fig. 5 Effect of ϕ_{NF}/ϕ_f on time histories of N , Q_d , Q_s , \dot{v} , p_d and p_s at rapid startup of the pump; experimental uncertainty in $N = \pm 3.5\%$, in Q_d and $Q_s = \pm 5.5\%$, and in p_d and $p_s = \pm 3.5\%$

valve opening, in the sense that the fluctuations of delivery pressure and discharge flowrate are strictly related with the change of the cavitation volume in the pump in both cases, i.e., fast pump startup and rapid discharge valve opening under high degree of cavitation due to low σ_f .

Criteria for Fluctuations of Discharge Pressure and Flow Rate. The fluctuations of the delivery pressure and the discharge flowrate are caused by oscillating cavitation volume in the pump, as described above. The transient fluctuations are further analyzed by introducing the unsteady parameter $K = N_f T_{na} / \phi_{NF}$ for many σ_f values including ones in Table 1.

Figure 6 presents the relationship between the time interval of the delivery pressure oscillations \bar{T} and the cavitation number σ_f with the effect of K at pump startup. Here the time interval \bar{T} is the average value of the first three periods of pressure fluctuations. It is evident from Fig. 6 that there is little effect of K on \bar{T} . However, \bar{T} changes abruptly near $\sigma_f = 0.2$ in the same way seen with the valve opening case. The cavitation volume in the pump oscillates in the range of cavitation numbers lower than 0.2 ($\sigma_f < 0.2$). These results indicate that the transient phenomena change suddenly from water hammer (σ_f above 0.2) to oscillating cavitation with decreasing cavitation number σ_f , as presented in Fig. 4. Further the occurrence of the transient phenomena can be examined by using the unsteady parameter K , as shown in Fig. 7: smaller K and lower σ_f lead to the fluctuations of delivery pressure and discharge flowrate due to oscillating cavitation at pump startup.

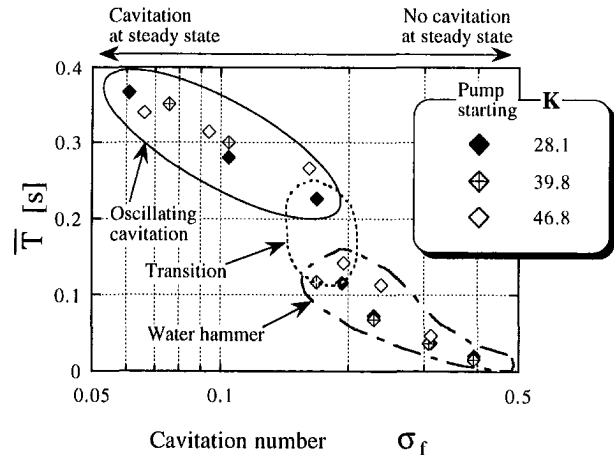


Fig. 6 Time intervals of oscillation at rapid startup of the pump; experimental uncertainty in $\sigma_f = \pm 5.5\%$, in $\bar{T} = \pm 7.5\%$, and in $K = \pm 5.5\%$

These tendencies are similar to those characteristics of the rapid opening of the discharge valve, as shown in Part 1.

Transient Phenomena at Pump Stop

Relationship Between Cavitation Behavior and Transient Phenomena. Figure 8 presents the time histories of the measured rotational speed N , suction and delivery pressure, p_s and p_d , suction and discharge flowrate, Q_s and Q_d for the highest attainable deceleration rate of the pump rotational speed at low suction pressure, $\sigma_0 = 0.05$ (Case PD-1). The cavitation volume change rate, $\dot{v} = Q_d - Q_s$, is also shown in Fig. 8. Figure 9 shows the photographs of the cavitation behavior in the test pump at the instant corresponding to the stage from (a) to (f) in Fig. 8. The discharge flowrate Q_d tends to decrease with decreasing rotational speed, whereas the suction flowrate Q_s does not decrease before the rotational speed N reaches zero. Q_s begins to decrease suddenly from stage (d), and then the suction and delivery pressure, p_s and p_d , show impulses at stage (e) when the cavitation bubbles collapse. At stage (f), when p_s reaches again the vapor pressure p_v ,

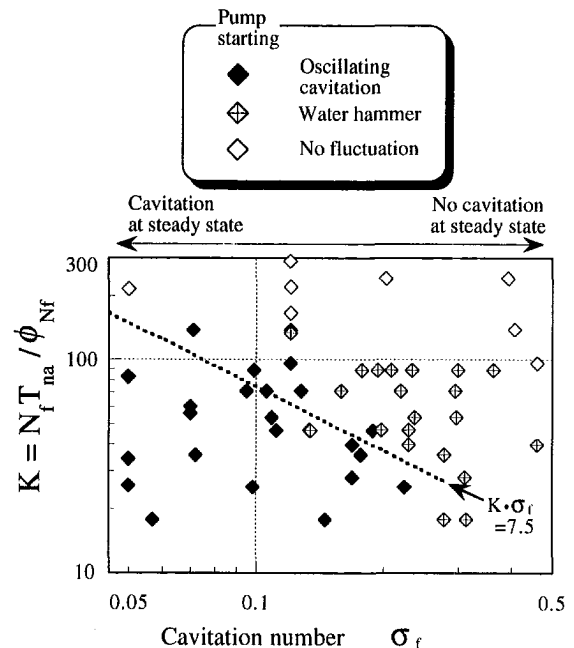


Fig. 7 Transient phenomena at rapid startup of the pump; experimental uncertainty in $\sigma_f = \pm 5.5\%$, and in $K = \pm 5.5\%$

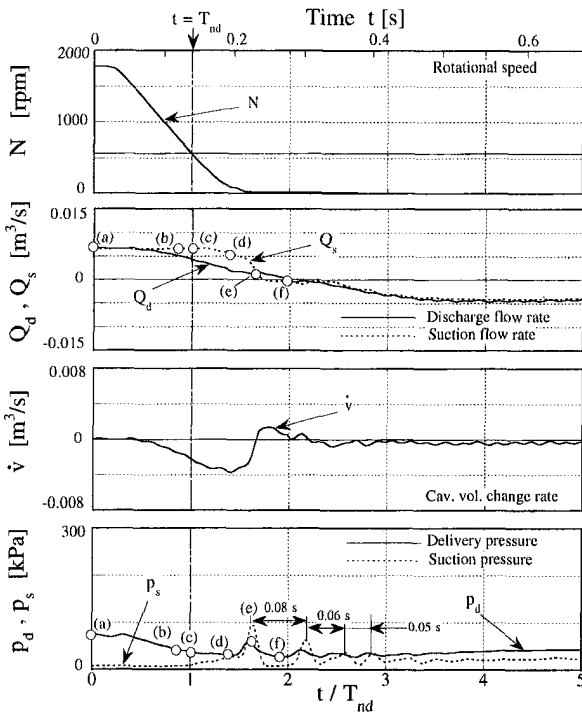


Fig. 8 Time histories of N , Q_d , Q_s , \dot{v} , p_d and p_s at rapid shutdown of the pump (PD-1); experimental uncertainty in $N = \pm 3.5\%$, in Q_d and $Q_s = \pm 5.5\%$, and in p_d and $p_s = \pm 3.5\%$

(=2.33 kPa), the cavitation bubbles appear again in the pump impeller and casing. After passing through the stage (f), impulsive pressure peaks appear in p_d and p_s due to rejoining of the water column with the collapse of the cavitation bubbles. When the

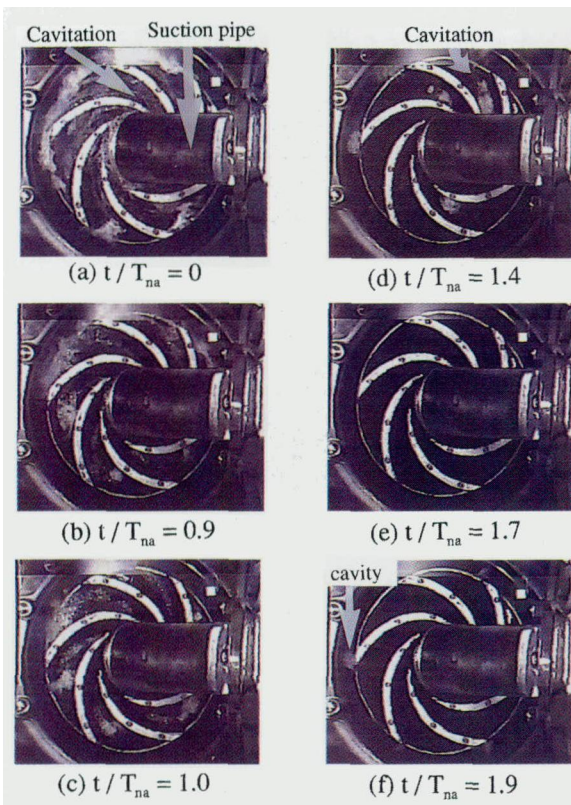


Fig. 9 Dynamic behavior of cavitation at rapid shutdown of the pump

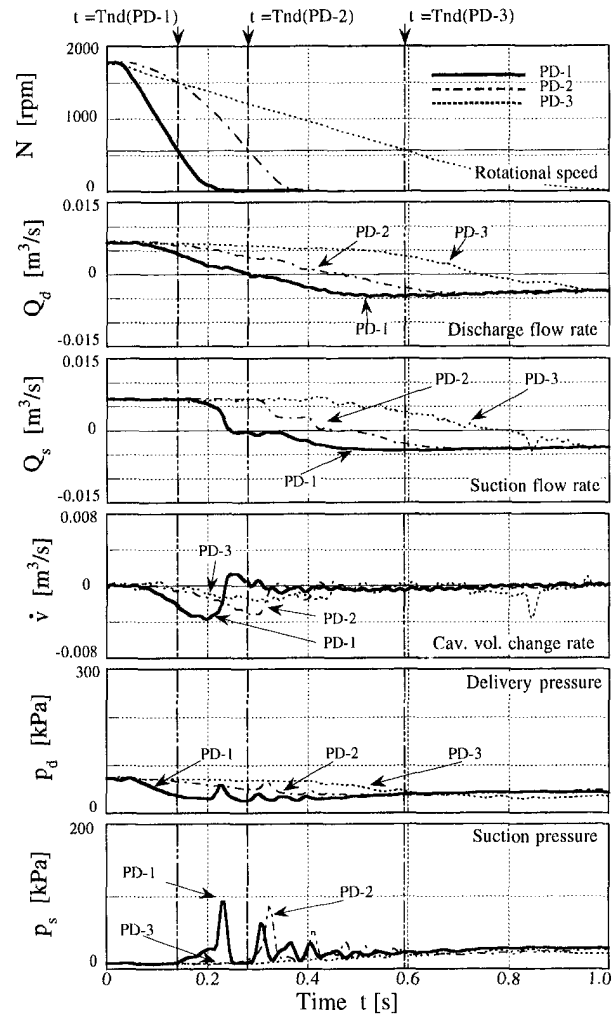


Fig. 10 Effect of $N_0 T_{nd}$ on time histories of N , Q_d , Q_s , \dot{v} , p_d and p_s at rapid shutdown of the pump; experimental uncertainty in $N = \pm 3.5\%$, in Q_d and $Q_s = \pm 5.5\%$, and in p_d and $p_s = \pm 3.5\%$

rotational speed is suddenly zero from initial condition N_0 , there is still pressure difference between the surge tank, P_{surge} , and the suction tank, $P_{suction}$. At that time, Q_s and Q_d have reverse flow, because P_{surge} is larger than $P_{suction}$.

The impulsive pressures appeared in the case of pump stop are quite different from the sinusoidal fluctuations of p_d observed in the case of pump startup shown in Fig. 1. This is because the impulsive pressures of p_d and p_s are caused by the rejoining of the water column due to the rapid collapse of the cavitation bubbles, similarly to rejoining of the separated water column in the case of rapid closure of the discharge valve, while the pressure fluctuations at pump startup are attributed to oscillating cavitation.

The above difference between startup and shutdown of the pump is analogous to the difference between the sudden opening and closure of the discharge valve presented in Part 1.

Effect of Deceleration Time. Figure 10 presents the effect of nondimensional deceleration time $N_0 T_{nd}$ on the transient phenomena. The time histories of N , Q_d , Q_s , \dot{v} , p_d and p_s are shown for Cases PD-1 ($N_0 T_{nd} = 4.2$), PD-2 ($N_0 T_{nd} = 8.4$) and PD-3 ($N_0 T_{nd} = 17.8$) for constant $\sigma_0 = 0.05$ (lowest level) and $\phi_{v0}/\phi_r = 1.25$ (largest value).

There are no pressure fluctuations in Case PD-3, whereas the impulsive pressures appear in p_d and p_s in Cases PD-1 and PD-2. Also, a smaller $N_0 T_{nd}$ leads to higher impulsive pressures in p_d and p_s .

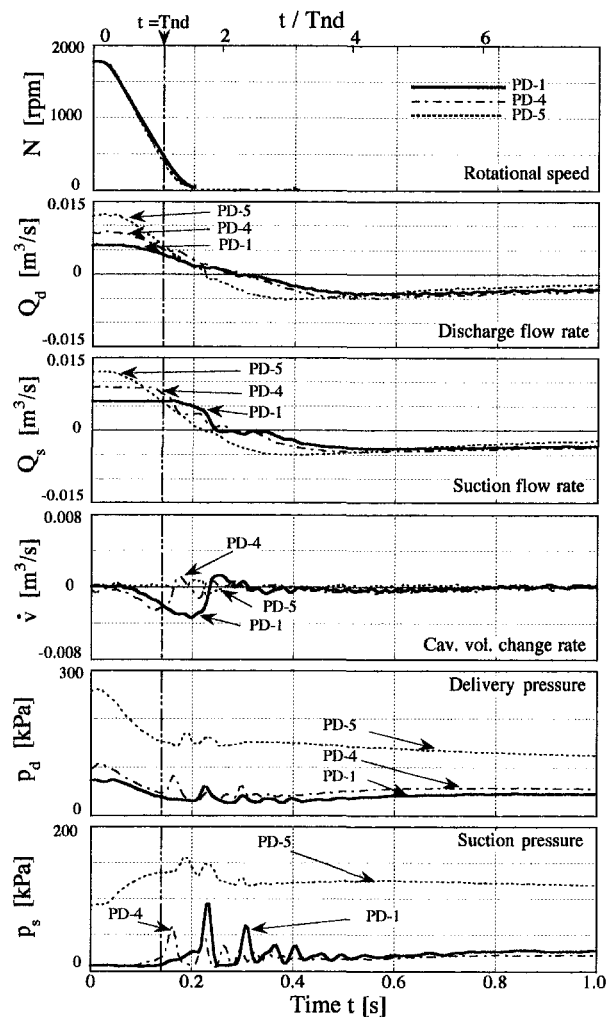


Fig. 11 Effect of σ_0 on time histories of N , Q_d , Q_s , \dot{v} , p_d and p_s at rapid shutdown of the pump; experimental uncertainty in $N = \pm 3.5\%$, in Q_d and $Q_s = \pm 5.5\%$, and in p_d and $p_s = \pm 3.5\%$

Effect of Cavitation Number. The effect of cavitation number σ_0 on the transient behavior is shown in Fig. 11, which presents the time histories of N , Q_d , Q_s , \dot{v} , p_d and p_s for Cases PD-1 ($\sigma_0 = 0.05$), PD-4 ($\sigma_0 = 0.12$) and PD-5 ($\sigma_0 = 0.42$) with constant $N_0 T_{nd} = 4.2$ (smallest value) and $\phi_{N0}/\phi_r = 1.25$ (largest value).

The impulsive pressures are observed in both p_d and p_s at the same instant. The pressure peaks in Cases PD-1 and PD-4 are due to the collapse of cavitation bubbles. On the other hand, the impulsive pressures in Case PD-5 could likely be attributed to water hammer without bubble collapse, as suggested by flow visualization observations. The magnitudes of pressure fluctuations increase with decreasing σ_0 , as in the case of the sudden closure of the discharge valve shown in Part 1.

Effect of Discharge Valve Opening. Figure 12 presents the effect of the discharge valve opening ϕ_{N0}/ϕ_r on the transient behavior. The time dependent N , Q_d , Q_s , \dot{v} , p_d and p_s are shown for Cases PD-1 ($\phi_{N0}/\phi_r = 1.25$), PD-6 ($\phi_{N0}/\phi_r = 1.0$) and PD-7 ($\phi_{N0}/\phi_r = 0.75$) for constant $N_0 T_{nd} = 4.2$ (smallest value) and $\sigma_0 = 0.05$ (lowest level). The impulsive pressures due to the collapse of cavitation bubbles are observed for both p_d and p_s in Cases PD-1 and PD-6, with peak levels larger in Case PD-1 than in Case PD-6.

Higher impulsive pressures due to the collapse of cavitation bubbles occur with smaller $N_0 T_{nd}$, lower σ_0 , and larger ϕ_{N0}/ϕ_r in the case of pump stopping, similarly to the case of the valve closure shown in Part 1.

As described above, the transient phenomena at the rapid pump startup are different from those at the rapid pump shutdown, in the same way they are different in the cases of the sudden opening and sudden closure of the discharge valve.

Criteria for Fluctuations of Suction and Discharge Pressure.

As indicated by the above observations, the suction and discharge pressure fluctuations are caused by the collapse of cavitation bubbles in the pump. The transient phenomena are examined by introducing the unsteady parameter $K = N_0 T_{nd} / \phi_{N0}$ for many σ_0 values including σ_0 in Table 2.

Figure 13 shows the relationship between the time interval of the delivery pressure oscillations \bar{T} and cavitation number σ_0 with the effect of K at pump shutdown. As is evident from Fig. 13, the time interval \bar{T} increases abruptly below a certain cavitation number σ_{cr} with decreasing σ_0 whereas \bar{T} is constant at higher cavitation numbers. The critical cavitation number σ_{cr} increases with decreasing K . Moreover, smaller K for the same σ_0 leads to a larger \bar{T} at $\sigma_0 < \sigma_{cr}$.

Figure 14 demonstrates that the occurrence of transient pressure fluctuations can be examined by using the unsteady parameter K : smaller K and lower σ_0 result in pressure pulsations due to the rejoining of the water column with the rapid collapse of the cavitation bubbles when the pump stops.

These tendencies are similar to those characteristics of the rapid closure of the discharge valve, as shown in Part 1.

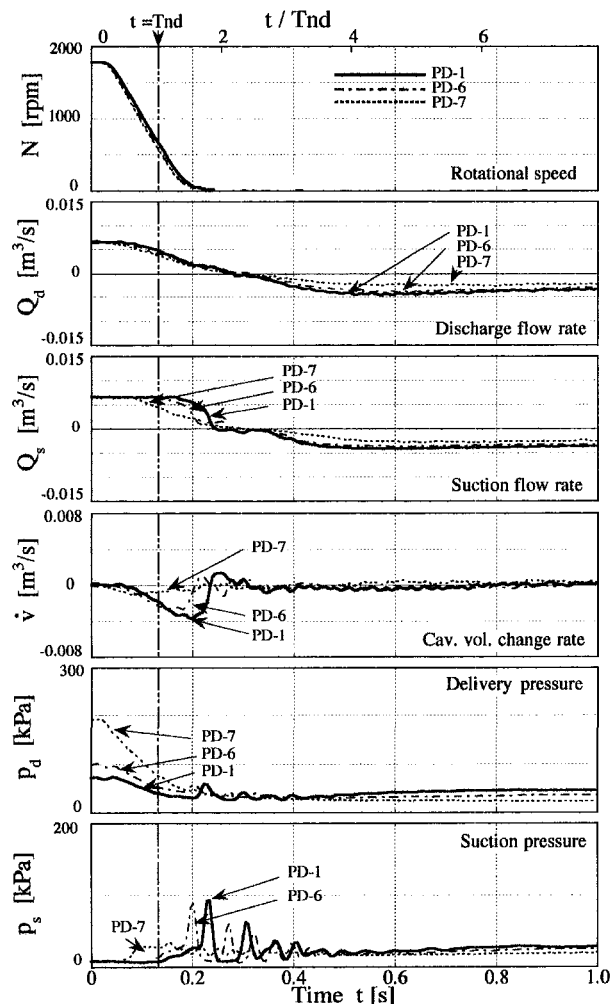


Fig. 12 Effect of ϕ_{N0}/ϕ_r on time histories of N , Q_d , Q_s , \dot{v} , p_d and p_s at rapid shutdown of the pump; experimental uncertainty in $N = \pm 3.5\%$, in Q_d and $Q_s = \pm 5.5\%$, and in p_d and $p_s = \pm 3.5\%$

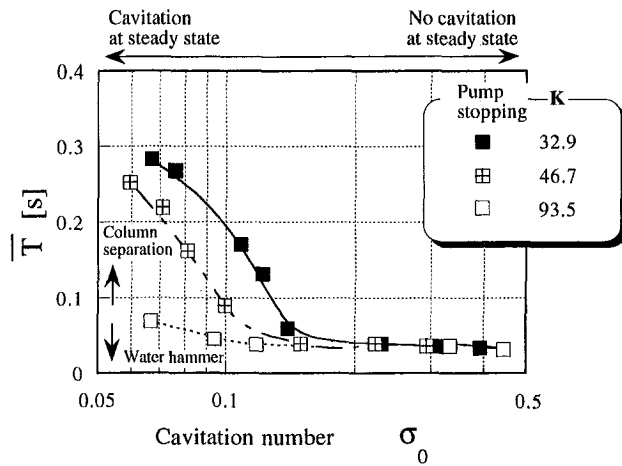


Fig. 13 Time interval of oscillation at rapid shutdown of the pump; experimental uncertainty in $\sigma_0 = \pm 5.5\%$, in $\bar{T} = \pm 7.5\%$, and in $K = \pm 5.5\%$

Conclusions

An experimental study was carried out on the transient behavior of a centrifugal pump at low NPSH during the pump start or stop periods. The dynamic phenomena were related to the cavitation in the pump or column separation, leading to the following conclusions:

(1) A rapid starting/stopping of the pump results in pressure and flowrate oscillations, and the occurrence of the oscillations depends on $N_{f,0}T_{na,nd}$, $\sigma_{f,0}$ and $\phi_{Nf,0}/\phi_r$.

(2) Transient pressure fluctuations at the sudden stop of the pump are caused by the collapse of cavitation bubbles, whereas the ones at sudden startup are due to oscillating cavitation bubbles in the pump.

(3) Smaller $N_{f,0}T_{na,nd}$, $\sigma_{f,0}$ and larger $\phi_{Nf,0}/\phi_r$ lead to greater transient fluctuations of the suction and delivery pressure, and also the suction and discharge flowrate at rapid transient operation.

(4) Transient phenomena at pump startup are analogous to the ones observed at the sudden opening of the discharge valve. The fluctuations of the delivery pressure and discharge flowrate are caused by oscillating cavitation bubbles in both cases.

(5) Transient phenomena at pump shutdown are similar to the

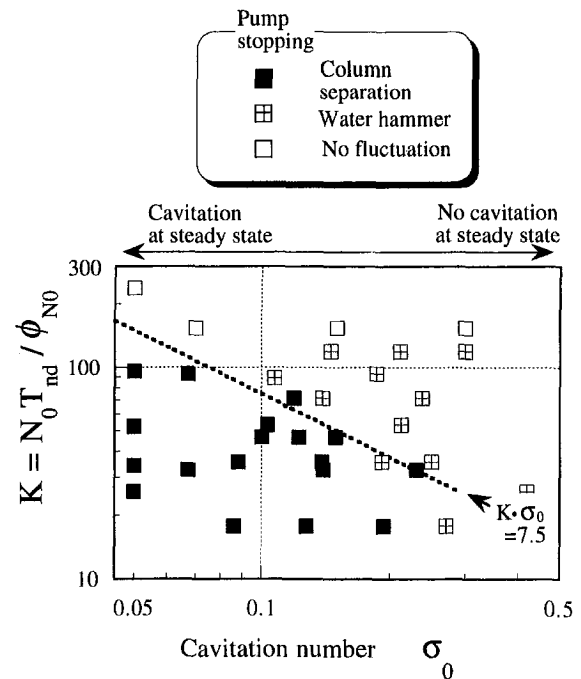


Fig. 14 Transient phenomena at rapid shutdown of the pump; experimental uncertainty in $\sigma_0 = \pm 5.5\%$, and in $K = \pm 5.5\%$

ones observed at the sudden closure of discharge valves. The pressure fluctuations are attributed to the collapse of cavitation bubbles and rejoining of separated water columns in both cases.

References

- Tanaka, T., and Tsukamoto, H., 1999, "Transient Behavior of a Cavitating Centrifugal Pump at Rapid Change in Operating Conditions—Part 1: Transient Phenomena at Opening/Closure of Discharge Valve," *ASME JOURNAL OF FLUIDS ENGINEERING*, published in this issue, pp. 841–849.
- Tsukamoto, H., Matsunaga, S., Yoneda, H., and Hata, S., 1986, "Transient Characteristics of a Centrifugal Pump During Stopping Period," *ASME JOURNAL OF FLUIDS ENGINEERING*, Vol. 108, No. 4, pp. 392–399.
- Tsukamoto, H., and Ohashi, H., 1982, "Transient Characteristics of a Centrifugal Pump During Starting Period," *ASME JOURNAL OF FLUIDS ENGINEERING*, Vol. 104, No. 1, pp. 6–14.

Transient Behavior of a Cavitating Centrifugal Pump at Rapid Change in Operating Conditions—Part 3: Classifications of Transient Phenomena

T. Tanaka

Assistant Professor,
Department of Mechanical and Electrical
Engineering,
Yatsushiro National College of Technology,
Yatsushiro, 866-8501, Japan

H. Tsukamoto

Professor,
Department of Mechanical Engineering,
Kyushu Institute of Technology,
Tobata, Kitakyushu, 804-8550, Japan

Analytical studies were developed on the transient behavior of a cavitating centrifugal pump during the transient operations, including the sudden opening/closure of the discharge valve and the pump startup/shutdown. In order to investigate the mechanism of the low cycle oscillations of both the pressure and the flowrate at a rapid change of the pump system conditions, an unsteady flow analysis was made for the cavitating pump-system by assuming the transient pump performance to be quasi-steady. The calculated unsteady pressure and flowrate during the transient period agree with the corresponding measured time histories. It is shown that the fluctuations of delivery pressure and discharge flowrate at pump rapid startup or sudden valve opening are caused by peculiar oscillating cavitation dynamics inside the pump at rapid increase in flowrate, while the fluctuations at pump rapid shutdown or sudden valve closure are related to the collapse of cavitation bubbles or water column separation in the suction pipe at rapid decrease in flowrate. Moreover, the occurrence of transient fluctuations in pressure and flowrate was predicted by examining the critical condition which creates the occurrence of two different flow mechanisms i.e., (A) oscillating cavitation and (B) water column separation including also the collapse of the cavitation bubbles. These flow mechanisms were represented with two flow models i.e., (A) unsteady cavitating flow incorporating effects of cavitation compliance and mass flow gain factor and expressed by a set of ordinary differential equations solved with the Cardano Method and (B) water-hammer type model including Discrete Free Gas Model and solved with method of characteristics. The calculated critical conditions for the occurrence of the oscillating cavitation and water column separation agree qualitatively with measured ones.

Introduction

A similarity was found between the transient phenomena at the sudden opening of the discharge valve and the ones at pump rapid starting, as shown in Part 1 (Tanaka and Tsukamoto, 1999a) and Part 2 (Tanaka and Tsukamoto, 1999b). Also, the transient phenomena at the sudden closure of the discharge valve have appeared to be similar to the ones at pump rapid shutdown. When the discharge valve is opened rapidly or the pump starts suddenly, fluctuations of both the delivery pressure and also the discharge flowrate are occurring due to oscillating cavitation. On the other hand, when the discharge valve is closed suddenly or the pump is stopped rapidly, suction and delivery pressure pulsations are measured due to water hammer as effect of the collapse of cavitation bubbles inside the pump or rejoining of the separated water column in the suction piping.

Based on the experimental results presented in Part 1 and Part 2, the transient characteristics of a cavitating pump system are calculated theoretically for the sudden opening/closure of the discharge valve, and the pump rapid startup/shutdown in the present paper. In order to calculate the transient behavior of the cavitating

pumping system, the unsteady flow analysis of the cavitating pump-system is developed by assuming that the transient pump performance is quasi-steady. This assumption is acceptable in relation to the occurrence of low cycle pressure and flowrate fluctuation, which is the main scope of the theoretical analysis. This is because the pump system characteristics such as resistance and capacitance have bigger effects on fluctuations than the pump characteristics itself. Also, the fluctuations have low cycle, and thus unsteady characteristics can be assumed to be quasi-steady. Moreover the fluctuation frequencies are low enough to assume the transient characteristics of the pipes and valve to be quasi-steady. Also, independent models of analysis are adopted for the dominant cases of oscillating cavitation and bubble collapse, because the mechanism of the fluctuations is considered to be different for these two cases.

Analysis

The experimental results presented in Part 1 and Part 2 indicate that the transient phenomena of the cavitating centrifugal pump at transient operations can be classified into: (A) oscillating cavitation, and (B) water hammer with column separation and cavitation bubbles collapse. Therefore the analysis of the transient phenomena is conducted by using a different model for each case.

Contributed by the Fluids Engineering Division for publication in the JOURNAL OF FLUIDS ENGINEERING. Manuscript received by the Fluids Engineering Division March 12, 1998; revised manuscript received June 22, 1999. Associate Technical Editor: B. Schiavello.

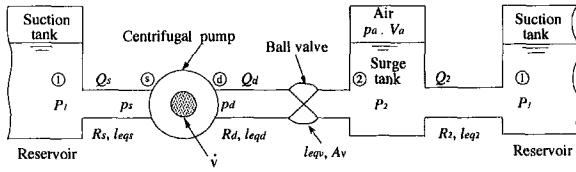


Fig. 1 Model of the pumping system at opening of the discharge valve or pump startup

Rapid Discharge Valve Opening and Pump Startup Case

Model of Flow. Figure 1 shows the schematic diagram of the pumping system for the analysis in the case of discharge valve opening or pump startup. The system consists of the suction tank, cavitating pump, ball valve, and the surge tank. A set of nine equations serves to describe the system, which is summarized as follows:

The difference of total pressure between the suction tank and the pump inlet is

$$P_1 - P_s = \frac{\rho}{2A_0^2} R_s Q_s^2 + \rho \frac{l_{eqs}}{A_0} \frac{dQ_s}{dt} \quad (1)$$

In a similar manner, the total pressure difference between the pump inlet and outlet is expressed by:

$$P_d - P_s = \rho g H(\text{NPSH}, \phi_N, N) - \rho \left(\frac{L_{eqs}}{A_0} \frac{dQ_s}{dt} + \frac{L_{eqd}}{A_0} \frac{dQ_d}{dt} \right) \quad (2)$$

where $H(\text{NPSH}, \phi_N, N)$ is the total head rise across the pump.

Moreover, the total pressure difference between the pump discharge and the surge tank is given by:

$$P_d - P_2 = \frac{\rho}{2A_0^2} R_d(t) Q_d^2 + \rho \left\{ \frac{l_{eqd}}{A_0} + \frac{l_{eqv}(t)}{A_v(t)} \right\} \frac{dQ_d}{dt} \quad (3)$$

in which $R_d(t)$ is the flow resistance of the delivery pipe and the ball valve, and $l_{eqv}(t)$ and $A_v(t)$ are the equivalent pipe length and the cross sectional area of the ball valve, respectively.

Also, the difference of total pressure between the surge tank and the suction tank is

$$P_2 - P_1 = \frac{\rho}{2A_0^2} R_2 Q_2^2 + \rho \frac{l_{eq2}}{A_0} \frac{dQ_2}{dt} \quad (4)$$

The mass conservation between the cavitating pump inlet and outlet gives (Sack and Nottage, 1965; Greitzer, 1981):

$$\dot{v} = Q_d - Q_s \quad (5)$$

The volume of the vapor v , which is contained within the pump due to the cavitation, is a function of the suction flowrate and the suction pressure. Thus the cavitation volume change rate \dot{v} can be expressed with the cavitation compliance and mass flow gain factor, C_b and M_b , as follows (Watanabe and Kawata, 1978):

$$\dot{v} = \frac{dv}{dt} = \frac{\partial v}{\partial p_s} \frac{\partial p_s}{\partial t} + \frac{\partial v}{\partial Q_s} \frac{\partial Q_s}{\partial t} = -C_b \frac{\partial p_s}{\partial t} - M_b \frac{\partial Q_s}{\partial t} \quad (6)$$

By assuming that the fluid acceleration is negligible and the pressure is spatially uniform in the volume of the surge tank, then the continuity equation for the volume between the inlet and outlet of the surge tank is

$$Q_d - Q_2 = -(dV_a/dt) \quad (7)$$

where V_a is the volume of air in the surge tank.

The air volume in the surge tank changes following is assumed to follow an isothermal gas law:

$$p_a V_a = \text{const} (= p_{a0} V_{a0}) \quad (8)$$

The total pressure at the surge tank becomes

$$P_2 = p_a + \rho g h_0 + \rho g \int_0^i \{(Q_d - Q_2)/A_2\} dt \quad (9)$$

Nomenclature

Refer to Part 1 and Part 2

New parameters:

A = cross sectional area [m²]
 A_0 = reference cross-sectional area [m²]
 A_2 = cross-sectional area of surge tank [m²]
 a = wave propagation velocity [m/s]
 C_b = cavitation compliance = $-\partial v/\partial p_s$ [m³/Pa]
 C_r = Courant number = $a\Delta t/\Delta x$
 d = diameter [m]
 g = gravity acceleration [m/s²]
 K = unsteady parameter = $N_{f,0} T_{v,na,nd}/\phi_{Nf,0}$
 L = total length of representative stream line [m]
 L_{eqd} = equivalent pipe length from the trailing edge of impeller to the measurement point of delivery pressure = $\int_{s=LE}^{L_d} \{A_0/A(s)\} ds$ [m]
 L_{eqs} = equivalent pipe length from the measurement point of suction pressure to the leading edge of impeller = $\int_{s=LE}^{L_s} \{A_0/A(s)\} ds$ [m]

l_{eq2} = equivalent pipe length from surge tank to suction tank = $\int_{s=L_2}^{L_1} \{A_0/A(s)\} ds$ [m]
 l_{eqd} = equivalent pipe length of discharge pipe system = $\int_{s=L_d}^{L_2} \{A_0/A(s)\} ds$ [m]
 l_{eqs} = equivalent pipe length of suction pipe system = $\int_{s=0}^{L_s} \{A_0/A(s)\} ds$ [m]
 l_{eqv} = equivalent pipe length at ball valve [m]
 M_b = mass flow gain factor = $-\partial v/\partial Q_s$ [s]
 P = total pressure [Pa]
 p = piezometric pressure [Pa]
 p_a = air pressure in the surge tank [Pa]
 R = pipe resistance
 s = distance [m]
 T_c = time constant of the pumping system [s]
 V_a = air volume in the surge tank [m³]
 v = cavitation volume [m³]
 α = void fraction = $4\Delta V/(\pi d^2 \Delta x)$

τ = nondimensional cross sectional area of the ball valve

Subscripts

1 = suction tank
 2 = surge tank
 a = air
 d = delivery, downstream
 i = instantaneous value
 LE = leading edge of the impeller vane
 TE = trailing edge of the impeller vane
 u = upstream
 v = ball valve
 ΔV = volume of air and vapor
 Δx = distance along pipe

where h_0 is the initial water level in the surge tank.

The above nine equations are solved numerically to get nine unknown variables $p_s, p_d, P_2, p_a, Q_s, Q_d, Q_2, \dot{v}$ and V_a .

Before going to numerical calculation, the basic equations are simplified. First, the resistance terms in Eqs. (1), (3), and (4) are simplified as follows:

$$\frac{\rho}{2A_0^2} R_s = \frac{P_1 - P_{sf}}{Q_{sf}^2} \quad (10a)$$

$$\left. \begin{aligned} \frac{\rho}{2A_0^2} R_d &= \frac{P_{d0} - P_{20}}{Q_{df}^2} - \frac{(P_{d0} - P_{20}) - (P_{df} - P_{2f}) \frac{t}{T}}{Q_{df}^2}; & 0 \leq t \leq T \\ \frac{\rho}{2A_0^2} R_d &= \frac{P_{df} - P_{2f}}{Q_{df}^2}; & t > T \end{aligned} \right\}; \quad \text{Valve opening} \quad (10b)$$

$$\frac{\rho}{2A_0^2} R_d = \frac{P_{df} - P_{2f}}{Q_{df}^2}; \quad \text{Pump starting} \quad (10c)$$

$$\frac{\rho}{2A_0^2} R_2 = \frac{P_{2f} - P_1}{Q_{2f}^2} \quad (10d)$$

where the subscript f and 0 indicates the final and initial value, respectively. The inertia of fluid in the ball valve L_v , which is a function of time, is expressed by the following equation:

$$L_v = l_{eqv}(t)/A_v(t) = \int_0^{l_v} \frac{A_0}{A_v(t)} ds/A_v(t) \quad (11)$$

The cavitation compliance C_b in Eq. (6) may change during the transient period. In the present analysis, however, the C_b is assumed to be constant because the time interval of the fluctuations has been found to be long and nearly constant in the previous experimental results. Therefore, the cavitation compliance C_b is approximated by:

$$\bar{C}_b = -(\partial v / \partial p_s) \quad (12)$$

The transient characteristics of the pump are assumed to be quasi-steady in Eq. (2), and thus the pump total head rise H is derived from the steady-state characteristics curve and cavitation performance:

$$H = \psi \cdot u^2 / 2g$$

$$\psi = \begin{cases} = \psi_N; & (\text{NPSH} \geq \text{NPSH}_{cr}) \\ = \psi_N + \{\partial \psi / \partial (\text{NPSH})\} (\text{NPSH} - \text{NPSH}_{cr}); & \\ (\text{NPSH} < \text{NPSH}_{cr}) \end{cases}$$

$$\psi_N = h_0 + h_1 \phi + h_2 \phi^2$$

$$\partial \psi / \partial (\text{NPSH}) = h_3$$

$$\text{NPSH}_{cr} = h_4 N + h_5 \phi$$

$$\text{NPSH} = \left(P_1 - p_v - \frac{\rho}{2A_0^2} R_s Q_s^2 - \rho \frac{l_{eqv}}{A_0} \frac{dQ_s}{dt} \right) / \rho g$$

where: ψ_N = head coefficient at noncavitating condition, NPSH_{cr} = critical NPSH based on the conventional 3% head drop, and h_0, h_1, h_2, h_3, h_4 and h_5 are coefficients determined from the steady-state performance of the test pump. The instantaneous rotational speed N_i at pump starting is expressed by the following equation (Tsukamoto and Ohashi, 1982):

$$N_i = N_f \{1 - \exp(-t/T_{na})\} \quad (13)$$

The above simple description of the rotational speed has been chosen because the main interest in the present analysis is the

effect of the acceleration/deceleration rate of the impeller on transient behavior. A more elaborated approach for future study should consider the instantaneous impeller speed of rotation as matching between the hydraulic force exerted by liquid on the impeller and the characteristics of the electrical motor (torque versus speed) and of the shaft.

The basic equations from (1) to (9) with the aid of Eqs. (10) to (13) are solved numerically at each time step to get $p_s, p_d, P_2, p_a, Q_s, Q_d, Q_2, \dot{v}$ and V_a .

Criteria for the Critical Condition Causing Pressure Fluctuations. In order to investigate the critical condition of the occurrence of oscillating cavitation, the above basic equations are linearized. The linearized basic Eqs. (1) to (9) lead to the following set of ordinary differential equation with operator notation D ($\equiv d/dt$):

$$(E_1 D^3 + E_2 D^2 + E_3 D + E_4) Q_s = 0 \quad (14)$$

where, $E_1 = B_1 C_1, E_2 = B_1 C_2 + B_3 C_1, E_3 = B_1 + B_2 + B_3 C_2, E_4 = B_3 + B_4$;

$$B_1 = \rho \left(\frac{L_{eqd}}{A_0} + \frac{l_{eqd}}{A_0} + \frac{l_{eqv}}{A_v} + \frac{l_{eq2}}{A_0} \right),$$

$$B_2 = \rho \left\{ (1 + h_6) \frac{l_{eqs}}{A_0} + \frac{L_{eqs}}{A_0} \right\}, \quad B_3 = \frac{\rho}{2A_0^2} (R_d Q_{df} + R_2 Q_{2f})$$

$$B_4 = \rho \left\{ \frac{R_s}{2A_0^2} (1 + h_6) Q_{sf} - \frac{1}{2\pi^2 b_2^2 d_2^2} h_2 + g h_3 h_5 \right\},$$

$$h_6 = 2g h_3 / u^2$$

$$C_1 = \rho \frac{l_{eqs}}{A_0} C_b, \quad C_2 = \left\{ C_b \left(R_s + \rho \frac{Q_{sf}}{2A_0^2} \right) - M_b \right\}$$

Equation (14) can be rewritten so that the Cardano method can be applied to examine its solution:

$$\xi^3 + 3p\xi + q = 0 \quad (15)$$

where $\xi = D + (E_2/3E_1), E_1 \neq 0$,

$$p = (3E_1 E_3 - E_2^2) / (9E_1^3),$$

$$q = (2E_2^3 - 9E_1 E_2 E_3 + 27E_1^2 E_4) / (27E_1^3)$$

The occurrence of oscillations during transient period can be examined, considering the following three types of equation:

$$-(4p^3 + q^2) > 0 \text{—no fluctuation (three real solutions)}$$

$$-(4p^3 + q^2) = 0 \text{—critical fluctuation (multiple solutions)}$$

$$-(4p^3 + q^2) < 0 \text{—fluctuation}$$

(one real solution and conjugate complex solutions)

In the above calculation for the critical condition causing fluctuations, the time averaged values are used for the resistance of the discharge pipe R_s , the inertia of the ball valve l_{eqv}/A_v and the rotational speed N :

$$\bar{R}_v = \frac{\int_0^{T_v} R_v dt}{T_c}; \quad \text{valve opening case} \quad (16)$$

$$\overline{\left(\frac{l_{eqv}}{A_v} \right)} = \int_0^{T_v} \frac{l_{eqv}(t)}{A_v(t)} dt / T_c; \quad \text{valve opening case} \quad (17)$$

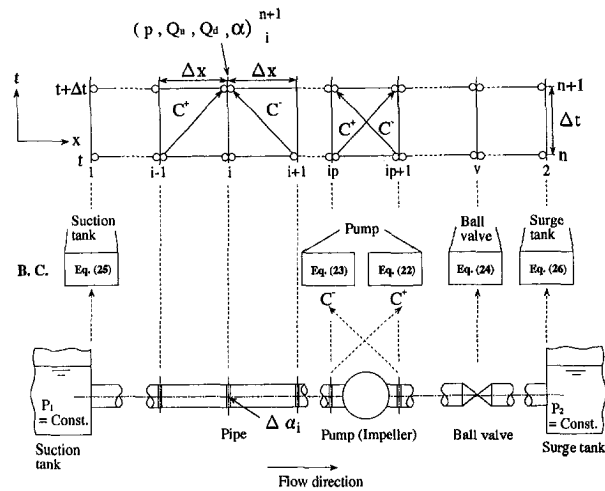


Fig. 2 Model of the pumping system at closure of the discharge valve or pump shutdown

$$\bar{N} = \int_0^{3T_{na}} N_i dt / T_c = \int_0^{3T_{na}} N_f \{1 - \exp(-t/T_{na})\} dt / T_c; \text{ pump startup} \quad (18)$$

where T_c is the time constant of the pumping system, and it indicates the ratio of the inertia to the resistance of the pumping system.

Rapid Discharge Valve Closure and Pump Shutdown Case

Model of Flow. The transient analysis is developed for rapid valve closure or pump shutdown by using the method of characteristics including the effect of water column separation, i.e.,

Discrete Free Gas Model (Wylie, 1984; Yamamoto et al., 1989). Figure 2 describes the schematics of the analytical model, in which an initial condition gives the distributions of gas and vapor volumes at each computing section and their volume change follow the isothermal process of an ideal gas.

The following characteristic equation is derived from the equation of motion for one-dimensional unsteady flow and the equation of continuity:

$$\frac{d}{dt} \left(\frac{Q}{A_0} \pm \frac{1}{\rho a} p \right) + \frac{R}{2dA_0^2} |Q|Q = 0 \quad (19)$$

where a is the wave propagation velocity.

The change rate of the void fraction α with time at each computing section is written by:

$$\frac{d\alpha}{dt} = \frac{Q_d - Q_u}{A_0 \Delta x} \quad (20)$$

where the void fraction α is defined by $\alpha = 4\Delta V / (\pi d^2 \Delta x)$, (ΔV : volume, Δx : abscissa along pipe).

If α_0 is the void fraction at some reference pressure p_0 , the relationship between the void fraction and the static pressure in each section may be expressed by:

$$(p - p_v)\alpha = p_0\alpha_0 \quad (21)$$

The boundary conditions at the pump segment are expressed as:

$$C+: p_{(ip+1)}^{n+1} + \left(\frac{\rho a}{A_0} \right) Q_{u(ip+1)}^{n+1} = p_{(ip)}^n + \left(\frac{\rho a}{A_0} \right) Q_{d(ip)}^n - \rho \frac{R}{2dA_0^2} |Q_{d(ip)}^n| Q_{d(ip)}^n dx + \rho g H(\text{NPSH}, \phi_N, N) \quad (22)$$

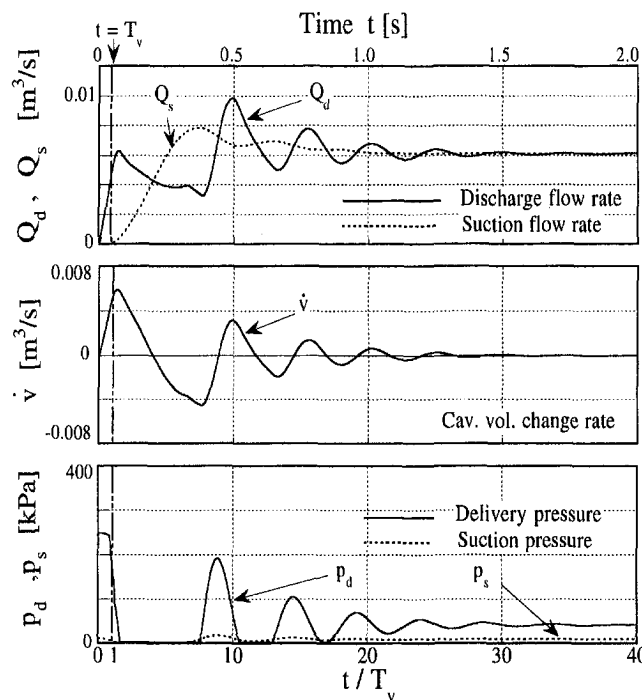


Fig. 3(a) Calculated

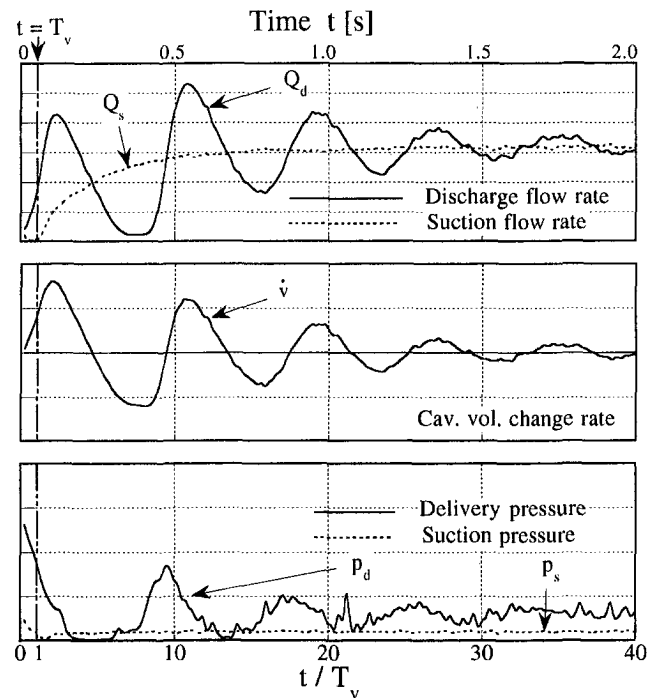


Fig. 3(b) Measured

Fig. 3 Comparisons between calculated and measured time histories of Q_d , Q_s , \dot{v} , p_d and p_s at rapid opening of the discharge valve ($NT_v = 1.6$, $\sigma_r = 0.05$ and $\phi_{Nf}\phi_r = 1.25$). (a) Calculated; $C_b = 2.0 \times 10^{-8}$ [m³/Pa], $M_b = -1.0 \times 10^{-2}$ [s], $A_v = A_0(\theta T)^{1.4}$, time step size $\Delta t = 2.0 \times 10^{-4}$ [s]; (b) Measured: experimental uncertainty in Q_d and $Q_s = \pm 5.5\%$, and in p_d and $p_s = \pm 3.5\%$.

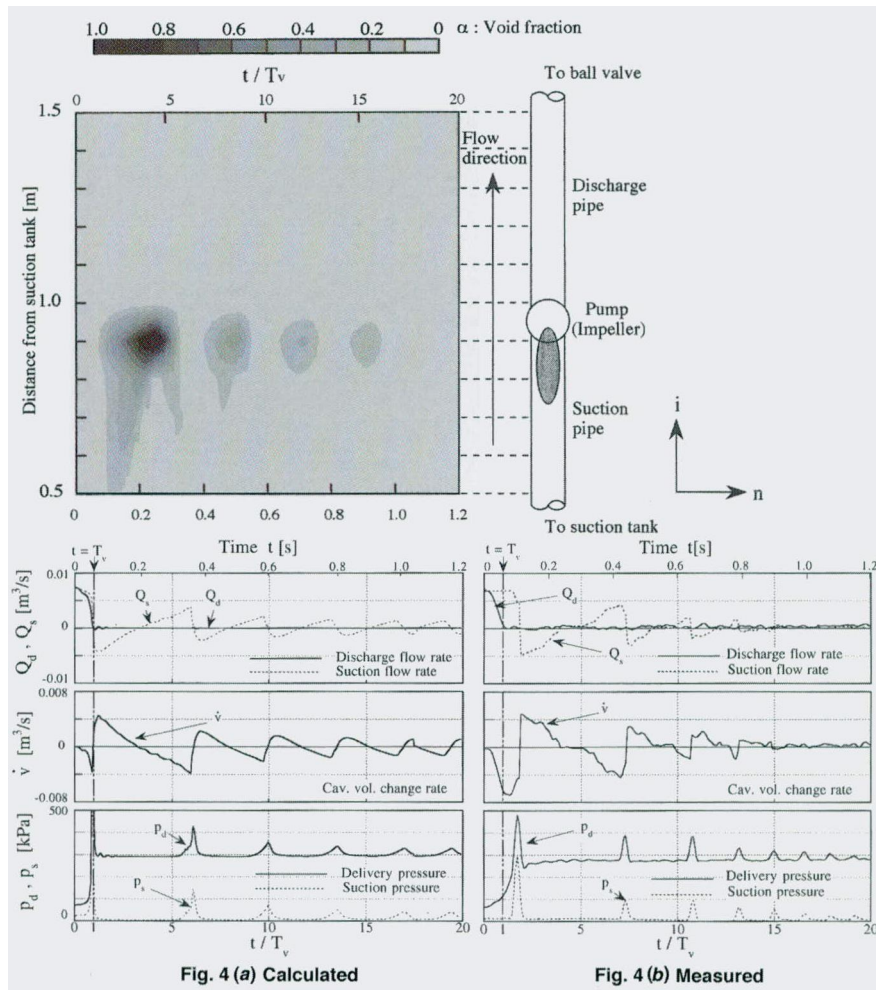


Fig. 4 Comparisons between calculated and measured time histories of Q_d , Q_s , \dot{v} , p_d and p_s at rapid closure of the discharge valve ($NT_v = 1.6$, $\sigma_0 = 0.05$ and $\phi_M/\phi_r = 1.25$). (a) Calculated; $a = 1300$ [m/s], $\alpha_0 = 1.0 \times 10^{-3}$, $\tau = \{1 - (t/T_v)\}^{1.4}$, Courant number $C_r = a\Delta t/\Delta x = 1.0$; (b) measured; experimental uncertainty in Q_d and $Q_s = \pm 5.5\%$, and in p_d and $p_s = \pm 3.5\%$.

$$C-: p_{(ip)}^{n+1} + \left(\frac{\rho a}{A_0}\right) Q_{d(ip)}^{n+1} = p_{u(ip+1)}^n + \left(\frac{\rho a}{A_0}\right) Q_{u(ip+1)}^n + \rho \frac{R}{2dA_0^2} |Q_{u(ip+1)}^n| Q_{u(ip+1)}^n dx - \rho g H(NPSH, \phi_N, N) \quad (23)$$

The above equations indicate the variation of the pressure rise across the pump at the instant when the pressure wave passes through the pump section. Here the total head rise across the pump H is assumed to be quasi-steady.

The boundary condition at the ball valve segment is

$$\frac{Q_{u(v)}^{n+1}}{Q_0} = \tau \sqrt{\frac{p_{(v)}^{n+1}}{\Delta p_0}} \quad (24)$$

in which Δp_0 and Q_0 are the pressure loss and flowrate at the ball valve in a steady-state condition before transient operation, respectively (Wylie and Streeter, 1978), while τ is the nondimensional cross sectional area at the ball valve.

The boundary condition at the suction tank is

$$p_i^{n+1} = \text{const} \quad (25)$$

and at the surge tank

$$p_2^{n+1} = \text{const} \quad (26)$$

The four variables p_i^{n+1} , $Q_{u(i)}^{n+1}$, $Q_{d(i)}^{n+1}$ and α_i^{n+1} are solved numerically at each time step, by using the above fundamental differential equations (19), (20), and (21) with the boundary conditions (22) thru (26). At the same time step, the instantaneous rotating speed N_i at pump shutdown is expressed by the following equation (Tsukamoto et al., 1986):

$$N_i = N_0 \{\exp(-t/T_{nd})\}; \quad \text{pump shutdown} \quad (27)$$

In the present calculations, in which the void fraction α is time dependent, the wave propagation velocity a is supposed to be constant, and the pipe resistance R is assumed to be identical to the quasi-steady value during the transient period.

The critical condition of the occurrence of water column separation is examined by assuming that a water column separation occurs when the void fraction α reaches a critical void fraction, α_{cr} at the pump suction. This is because the static pressure does not reach vapor pressure p_v in the Discrete Free Gas Model, adopted for the theoretical analysis.

Comparison Between Calculated and Experimental Values

Before the comparison between calculated and experimental values, an extensive numerical testing was carried out to validate the computational scheme. The effects of the time step size Δt on the calculated results were examined for the rapid discharge valve opening and pump startup case. The numerical tests with the same

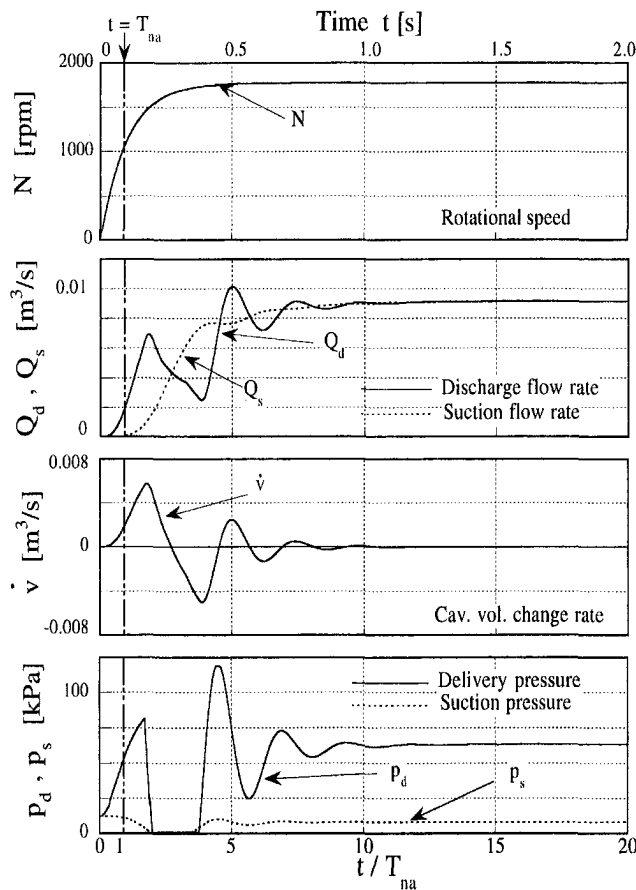


Fig. 5(a) Calculated

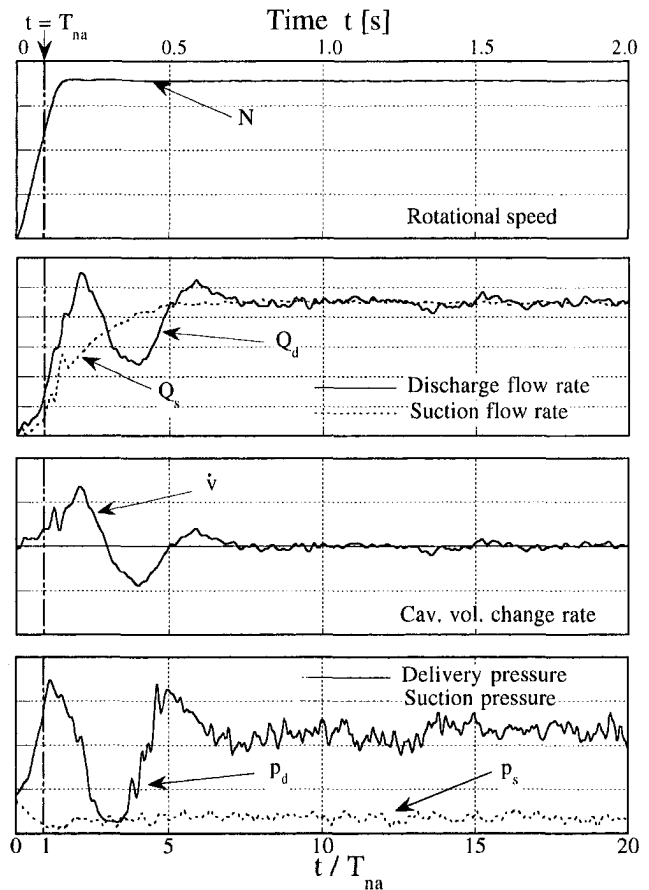


Fig. 5(b) Measured

Fig. 5 Comparisons between calculated and measured time histories of N , Q_d , Q_s , \dot{v} , p_d and p_s at rapid startup of the pump ($N_f T_{na} = 2.8$, $\sigma_f = 0.07$ and $\phi_{Nf}/\phi_r = 1.25$). (a) Calculated; $C_b = 2.0 \times 10^{-8}$ [m³/Pa], $M_b = -1.0 \times 10^{-2}$ [s], $N_t = N_f(1 - \exp(-t/T_{na}))$, time step size $\Delta t = 2.0 \times 10^{-4}$ [s]; (b) Measured; experimental uncertainty in $N = \pm 3.5\%$, in Q_d and $Q_s = \pm 5.5\%$, and in p_d and $p_s = \pm 3.5\%$.

boundary conditions indicated good agreement of the pressure and flowrate fluctuations between $\Delta t = 1.0 \times 10^{-5}$ [s] and 1.0×10^{-3} [s]. Therefore the time step size was chosen to be $\Delta t = 2.0 \times 10^{-4}$ [s] which is identical with the sampling frequency in the experiment. On the other hand, the Courant number C_r ($=a\Delta t/\Delta x$) = 1.0 and x -direction grid size $\Delta x = 0.1$ [m] were chosen for the calculation both at the rapid discharge valve closure and pump shutdown. That is because the effects of the Courant number C_r ($0.8 \leq C_r \leq 1.0$) and the grid size Δx ($\Delta x < 0.1$ [m]) for the same boundary conditions were found to be small in the present calculation using Discrete Free Gas Model.

Time Histories of Fluctuations. Figure 3 shows the calculated and measured time histories of the suction and delivery pressure, p_s and p_d , the suction and discharge flowrate, Q_s and Q_d , and the cavitation volume change rate \dot{v} for a rapid valve opening case at low NPSH ($\sigma_f = 0.05$), very short valve opening time ($NT_v = 1.6$), and large flowrate ($\phi_{Nf}/\phi_r = 1.25$). The present calculation were done for $A_v = A_0(t/T_v)^{1.4}$ [m³], $C_b = 2.0 \times 10^{-8}$ [m³/Pa] and $M_b = -1.0 \times 10^{-2}$ [s]. The cavitation compliance and mass flow gain factor, C_b and M_b , were chosen based on the past works by Watanabe and Kawata (1978), and Brennen and Acosta (1973).

The calculated pressure and flowrate show good qualitative agreement with the experimental ones except for Q_s , which shows a fluctuation with a peak above its final value, whereas the measured Q_s has no fluctuation but a simple rise with asymptotic stabilization. This calculation indicates that the fluctuations of the delivery pressure and the discharge flowrate are dependent from the dynamic behavior of the cavitation volume inside the pump. In other words, the transient phenomena can be described by using

the cavitation compliance C_b and the mass flow gain factor M_b . The time intervals of the calculated pressure and flowrate fluctuations are shorter and decay quicker than the measured ones because the parameters C_b and M_b were maintained constant.

Figure 4 shows the calculated and measured time histories of the suction and delivery pressure, p_s and p_d , the suction and discharge flowrate, Q_s and Q_d , and the cavitation volume change rate \dot{v} for a rapid valve closure case for the same test conditions of the previous case i.e., $\sigma_0 = 0.05$, $NT_v = 1.6$, and $\phi_{Nf}/\phi_r = 1.25$. In the present calculation, the valve closure is assumed to be $\tau = \{1 - (t/T_v)\}^{1.4}$, and the wave propagation velocity $a = 1300$ [m/s] and the initial void fraction $\alpha_0 = 1.0 \times 10^{-3}$.

In Fig. 4, the time history of the calculated void fraction α in the suction pipe line is also presented. The void fraction is maximum near the pump suction at the instant when Q_s turns from negative flow to positive flow. This agrees with the water column separation and the reverse flow in the suction pipe observed with the flow visualization tests. The delivery and suction pressure, p_d and p_s , show impulses with highest peak at the lowest void fraction during the Q_s decreasing process. These phenomena agree with the flow visualization observations which indicated that the impulsive suction and delivery pressure occurred with the collapse of the water column separation. The fluctuations of the suction flowrate and the suction and delivery pressure at rapid closure of the discharge valve are found to be related to the water column separation.

Figure 5 presents the calculated and measured time histories of the rotational speed N , the suction and delivery pressure, p_s and p_d , the suction and discharge flowrate, Q_s and Q_d , and the cavitation volume change rate \dot{v} for a rapid acceleration of the pump at low NPSH ($\sigma_f = 0.07$), very short acceleration time ($N_f T_{na} =$

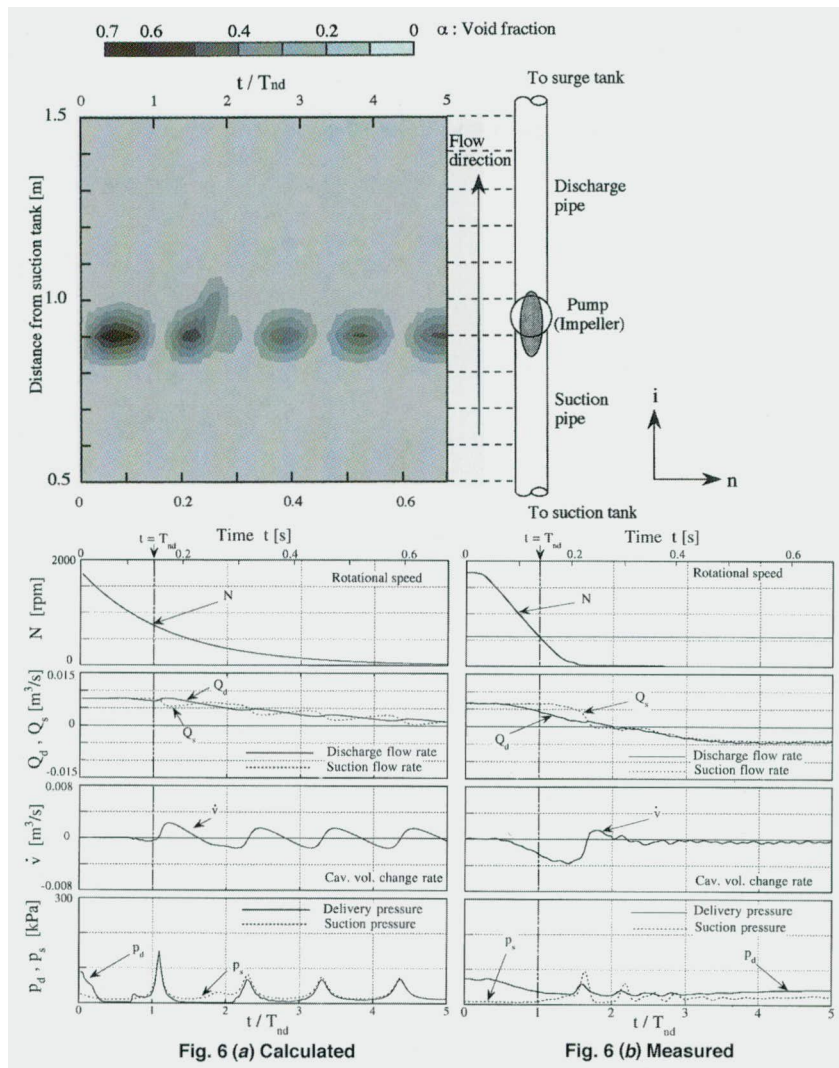


Fig. 6 Comparisons between calculated and measured time histories of N , Q_d , Q_s , \dot{v} , p_d and p_s at rapid shutdown of the pump ($N_0 T_{nd} = 4.2$, $\alpha_0 = 0.05$ and $\phi_{N0}/\phi_r = 1.25$). (a) Calculated; $a = 1300$ [m/s], $\alpha_0 = 1.0 \times 10^{-3}$, $N_i = N_0[\exp(-t/T_{nd})]$, Courant number $C_r = a\Delta t/\Delta x = 1.0$; (b) Measured; experimental uncertainty in $N = \pm 3.5\%$, in Q_d and $Q_s = \pm 5.5\%$, and in p_d and $p_s = \pm 3.5\%$.

2.8), and large flowrate ($\phi_{N0}/\phi_r = 1.25$). This calculation was done for $C_b = 2.0 \times 10^{-8}$ [m³/Pa] and $M_b = -1.0 \times 10^{-2}$ [s]. It is quite evident that all calculated time distributions of pressures and flowrates show acceptable qualitative agreement with the experimental trends. The calculated time intervals of the fluctuating p_d and Q_d are shorter than the measured values. This is because the basic assumptions about instantaneous rotational speed N , and constant level of C_b and M_b during the transient period are not sufficiently accurate.

Figure 6 shows the calculated and measured time histories of the rotational speed N , the suction and delivery pressure, p_s and p_d , the suction and discharge flowrate, Q_s and Q_d and the cavitation volume change rate \dot{v} for the pump shutdown at $\sigma_0 = 0.05$, $N_0 T_{nd} = 4.2$, and $\phi_{N0}/\phi_r = 1.25$. This calculation was made with a wave propagation velocity $a = 1300$ [m/s] and the initial void fraction $\alpha_0 = 1.0 \times 10^{-3}$. The time history of the calculated void fraction α in the pipe line is also presented in Figure 6. The void fraction increases when the suction and delivery pressure decrease (Fig. 6). The delivery and suction pressure, p_d and p_s , show impulses when the void fraction reaches its minimum near the pump suction. This agrees with the pressure pulsations due to the collapse of cavitation bubbles indicated in Part 2.

The calculated time intervals of the pressure and flowrate fluctuations do not agree with the measured values, and the calculated

flowrate Q_s and Q_d do not show the negative values, which were measured in the experimental conditions. These deviations are due to the assumption about the time variation of the rotational speed (Fig. 6(a)—top), which in the latter half of the pump shutdown was chosen larger than the actually measured trend.

Critical Condition for Fluctuation. Figure 7 shows the calculated critical condition of oscillating cavitation. In this figure, the unsteady parameter $K = N_{f,0} T_{v,na,nd} / \phi_{Nf,0}$ at critical oscillation in Eq. (15) is plotted for each cavitation number σ_f with the measured critical condition expressed by $K \cdot \sigma_f = 7.5$. The fluctuations due to oscillating cavitation occur at smaller K and lower σ_f for the calculated critical condition corresponding to each M_b in Fig. 7. Figure 7 indicates that K at critical oscillation increases with decreasing σ_f for each assumed M_b . Also, the range of the oscillating cavitation is found to expand with increasing M_b .

The calculated critical conditions for the occurrence of the water column separation or the cavitation bubble collapse at various σ_f are compared with the measured ones expressed by $K \cdot \sigma_0 = 7.5$ as shown in Fig. 8. The calculation was done for the critical void fraction $\alpha_{cr} = 0.1$. The calculated critical conditions show good agreement with the measured ones, although there is small discrepancy of the slope between the theoretical line and experimental one.

Therefore the occurrence of pressure fluctuations can be pre-

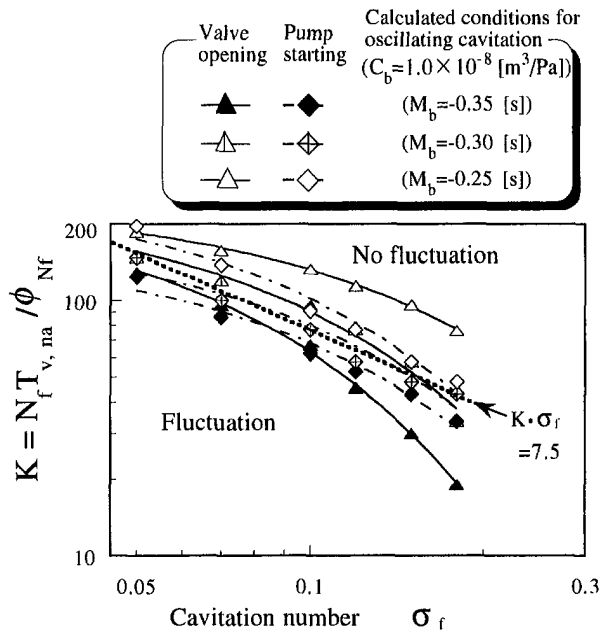


Fig. 7 Critical conditions of oscillating cavitation

dicted by using criteria for the occurrence of either the cavitation or the water column separation, based on one-dimensional analysis using C_b , M_b and the initial void fraction α_0 .

Mechanism of Transient Phenomena

As described above, the transient phenomena of a cavitating pump may be classified into two categories. One is the occurrence of high impulsive pressures due to water column separation at rapid valve closure or bubble collapse at the shutdown of the pump. This phenomenon is a kind of water hammer. The second is the flow fluctuation due to oscillating cavitation at rapid valve opening or pump startup. These fluctuations of the pressure and flowrate with oscillating cavitation are more dominant than water hammer, which may also occur at rapid valve opening or pump startup when the cavitation increases within the pump with increasing Q_s at low cavitation numbers. This is because a cavitating pump may play a similar role to a

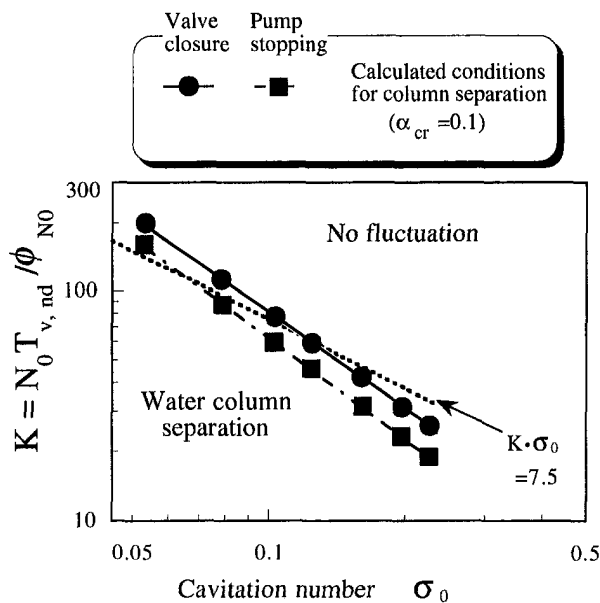


Fig. 8 Critical conditions of water column separation

surge tank in pressure wave propagation (Greitzer, 1981). Then a cavitating pump system becomes susceptible to self-induced vibrations due to the elastic effect, which follows mass conservation, $\dot{v} = Q_d - Q_s$, and affects the pump system as a vibration mass-spring combined element.

These two types of oscillating phenomena can be classified based on the condition of suction flowrate at the beginning of transient operation, i.e., $(\partial Q_s / \partial t)_{0+} > 0$ or < 0 , because the change in cavitation volume depends from both the suction flowrate and the suction pressure, and the growth or shrinkage of the cavitation volume is determining the time derivative of Q_s , $(\partial Q_s / \partial t)_{0+}$. Oscillating cavitation with elastic effect is generated as the cavitation volume increases with decreasing p_s at $(\partial Q_s / \partial t)_{0+} > 0$. Therefore the transient phenomena change from water hammer to oscillating cavitation with decreasing K and σ_f . In other words, transient phenomena shift from wave phenomena to system oscillations, including the contribution of self-induced vibration at rapid valve opening or pump startup in which $(\partial Q_s / \partial t)_{0+} > 0$.

On the other hand, a pressure wave can be propagated, passing through the pump, when the cavitation collapses with increasing p_s at $(\partial Q_s / \partial t)_{0+} < 0$. Therefore the transient phenomena result in water hammer with water column separation when K and σ_0 decrease at rapid valve closure or pump shutdown in which $(\partial Q_s / \partial t)_{0+} < 0$.

Conclusions

An experimental and theoretical study was made on the transient fluid phenomena at the rapid opening/closure of the discharge valve or rapid startup/shutdown of the pump under low NPSH condition. A one-dimensional flow analysis was developed for the transient fluid phenomena at sudden change of the system, either discharge valve opening or pump startup by considering the effect of oscillating cavitation. On the other hand, a water hammer analysis was done for sudden change of the system, either discharge valve closure or pump shutdown by incorporating water column separation. The comparison between calculated and measured transient fluid parameters led to the following conclusions:

(1) The transient behavior in a pump system can be classified into two types: one is characterized by transient phenomena caused by oscillating cavitation at $(\partial Q_s / \partial t)_{0+} > 0$ such as in the cases of the pump startup or the discharge valve opening. The other is due to water hammer with water column separation or collapse of cavitation bubbles at $(\partial Q_s / \partial t)_{0+} < 0$ such as in the cases of the pump shutdown or the discharge valve closure.

(2) The occurrence of pressure and flowrate fluctuations can be predicted by examining the critical conditions for oscillating cavitation or water column separation by using one-dimensional analysis with the aid of assumed C_b , M_b and initial void fraction α_0 .

Acknowledgments

The investigations were carried out in the Department of Mechanical Engineering of Kyushu Institute of Technology and this work was a portion of the first author's dissertation. The authors wish to express their gratitude to Messrs. H. Moritake, H. Nanba, and J. Asakura for their assistance in the experimental work.

References

- Brennen, C. E., and Acosta, A. J., 1973, "Theoretical Quasi-Steady Analysis of Cavitation Compliance in Pump," *Journal of Spacecraft and Rockets*, Vol. 10, No. 3, pp. 175-180.
- Greitzer, E. M., 1981, "The Stability of Pumping Systems," *ASME JOURNAL OF FLUIDS ENGINEERING*, Vol. 103, pp. 193-242.
- Sack, L. E., and Nottage, H. B., 1965, "System Oscillations Associated With Cavitating Inducers," *ASME Journal of Basic Engineering*, Vol. 87, pp. 917-924.
- Tanaka, T., and Tsukamoto, H., 1999a, "Transient Behavior of a Cavitating Centrifugal Pump at Rapid Change in Operating Conditions—Part I: Transient Phenomena at Opening/Closure of Discharge Valve," *ASME JOURNAL OF FLUIDS ENGINEERING*, published in this issue pp. 841-849.
- Tanaka, T., and Tsukamoto, H., 1999b, "Transient Behavior of a Cavitating

Centrifugal Pump at Rapid Change in Operating Conditions—Part 2: Transient Phenomena at Pump Startup/Shutdown," ASME JOURNAL OF FLUIDS ENGINEERING, published in this issue pp. 850–856

Tsukamoto, H., Matsunaga, S., Yoneda, H., and Hata, S., 1986, "Transient Characteristics of a Centrifugal Pump During Stopping Period," ASME JOURNAL OF FLUIDS ENGINEERING, Vol. 108, No. 4, pp. 392–399.

Tsukamoto, H., and Ohashi, H., 1982, "Transient Characteristics of a Centrifugal Pump During Starting Period," ASME JOURNAL OF FLUIDS ENGINEERING, Vol. 104, No. 1, pp. 6–14.

Watanabe, T., and Kawata, Y., 1978, "Research on the Oscillation Cavitating Inducer," *Proceedings of 9th IAHR Symposium*, Vol. 2, Fort Collins, pp. 265–277.

Wylie, E. B., 1984, "Simulation of Vaporous and Gaseous Cavitation," ASME JOURNAL OF FLUIDS ENGINEERING, Vol. 106, No. 3, pp. 307–311.

Wylie, E. B., and Streeter, V. L., 1978, *Fluid Transients*, McGraw-Hill, New York.

Yamamoto, K., Outa, E., Sano, M., Miwa, T., and Okada, K., 1989, "Examination of Discrete Cavity Models for Waterhammer Analysis Including Column Separation in a Horizontal Pipeline," *Trans. of JSME*, Series B, Vol. 55, No. 513, pp. 1296–1301 (in Japanese).

Satoshi Watanabe¹
JSPS Research Fellow.
e-mail: fmnabe@mech.kyushu-u.ac.jp

Kazuhiko Yokota
Research Associate.

Yoshinobu Tsujimoto
Professor.

Osaka University, Graduate School of
Engineering Science,
1-3 Machikaneyama, Toyonaka, Osaka 560-
8531, Japan

Kenjiro Kamijo
Professor,
Tohoku University, Institute of Fluid Science,
2-1-1 Katahira, Aoba, Sendai,
Miyagi 980-8577, Japan

Three-Dimensional Linear Analysis of Rotating Cavitation in Inducers Using an Annular Cascade Model

A three-dimensional linear analysis of rotating cavitation is carried out using an annular cascade model. The purpose is to investigate three-dimensional effects of cavitation, including the radial change of peripheral velocity and the hub/tip ratio of the impeller, on rotating cavitation in inducers. A semi-actuator disk method is employed. It is assumed that the mean stream surface does not radially shift across the impeller. It is shown that there are many modes of instabilities corresponding to rotating cavitation with various radial modes travelling forward and backward. The 0th radial modes are found to correspond to the forward and backward travelling modes predicted by a previous two-dimensional analysis (Tsujimoto et al., 1993). The three-dimensionality of the geometry has the effects of diminishing the amplifying region of these fundamental modes. It is also shown that the amplifying regions of higher radial modes may be larger than those of 0th radial modes. However, it is shown that the three-dimensionality of cavitation does not significantly affect rotating cavitation.

Introduction

Rotating cavitation is one of the most important problems in the development of modern high performance rocket pump inducers (Kamijo et al., 1977; Kamijo et al., 1993). Two-dimensional linear analysis (Tsujimoto et al., 1993) has shown that it is caused by the positive mass flow gain factor (which means that the cavity volume increases/decreases corresponding to the unit decrease/increase of the flow rate) and that it is quite different from rotating stall, which is caused by the positive slope of the pressure performance. This analysis has also shown that there can be two modes of rotating cavitation. One propagates faster than the impeller rotation and the other propagates in the direction opposite to the impeller rotation. The forward rotating mode is generally observed; the backward rotating mode, however, rarely occurs, and there is only one report on it (Hashimoto et al., 1997).

Experimental observations (Kamijo et al., 1993; Goirand et al., 1992; Tsujimoto et al., 1997) show that, under rotating cavitation, large tip cavities occur and oscillate in phase with blade surface cavities. Based on these observations, a 3-D linear analysis of rotating cavitation was carried out using a linear cascade model spanning the space between two parallel rigid walls (Watanabe et al., 1997). The analysis was made for several cases with various spanwise distributions of cavitation compliance K and mass flow gain factor M which represent the three-dimensional effects of cavitation, and the results basically agreed with those of 2-D linear analysis. However, this linear cascade model cannot take into account the radial change of peripheral velocity and the effects of hub ratio which may have greater three-dimensional effects. The present study was designed to facilitate understanding of the 3-D effects of geometry and cavitation under more realistic conditions. It is assumed that the flow is inviscid and incompressible and that the inducer is modelled by an annular cascade in an annular duct.

It is also assumed that the flow in the impeller is perfectly guided by the blades.

Elementary Flow Fields

Analytical Model. We consider an annular cascade with chordlength $l(r)$, pitch $h(r)$, and stagger $\beta(r)$ as shown in Fig. 1. The cascade is rotating in the θ -direction with an angular velocity of Ω . The flow is assumed to be incompressible and inviscid. Even in the case without cavitation, it is difficult and still under the development stage to treat the fully three-dimensional flow theoretically. In the present study focusing on the effect of three-dimensionally developed cavitation, we further assume that the main flow is axial with a constant axial velocity U without swirl, based on the fact that the effect of the main flow deflection on rotating cavitation is small, which is obtained from the two-dimensional linear analysis (Tsujimoto et al., 1993). To extract only the effects of three-dimensionality of cavitation, we neglect the radial shift of the stream surface across the cascade which may occur in real impeller and downstream.

The unsteady flow fluctuations, which are assumed to be small compared with the main flow, are determined by the following linearized momentum and continuity equations.

$$\left(\frac{\partial}{\partial t} + U \frac{\partial}{\partial z} \right) \delta v = - \frac{1}{\rho} \nabla \delta p \quad (1)$$

$$\frac{1}{r} \frac{\partial (r \delta v_r)}{\partial r} + \frac{1}{r} \frac{\partial \delta v_\theta}{\partial \theta} + \frac{\partial \delta u}{\partial z} = 0 \quad (2)$$

Pressure Fluctuations. By eliminating the velocity disturbance from Eqs. (1) and (2), we obtain Laplace's equation for the pressure fluctuation:

$$\nabla^2 \delta p = 0. \quad (3)$$

We assume a mode rotating in the θ -direction with a complex angular velocity, $\omega = \omega_R + j\omega_I$, where ω_R and ω_I are angular velocity and decay rate respectively. It should satisfy the boundary conditions, $\partial p / \partial r = 0$, on the hub and casing ($r = r_H, r_T$), where $v_r = 0$. The pressure should be finite at the upstream and down-

¹ Currently, Lecturer, Kyushu University, Graduate School of Engineering, 6-10-1 Hakozaki, Higashi-ku, Fukuoka 812-8581, Japan.

Contributed by the Fluids Engineering Division for publication in the JOURNAL OF FLUIDS ENGINEERING. Manuscript received by the Fluids Engineering Division February 5, 1998; revised manuscript received July 16, 1999. Associate Technical Editor: C. L. Merkle.

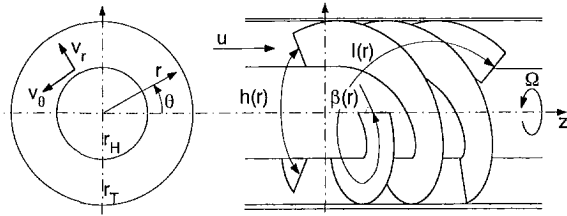


Fig. 1 Annular cascade model

stream infinity. The pressure fluctuation satisfying the above conditions can be expressed as follows.

Upstream of the impeller ($z < 0$),

$$\delta p_1 = \rho U^2 \exp j(\omega t - \theta) \sum_{m=0}^{\infty} A_{1m} Z(\lambda_m r) \exp(\lambda_m z). \quad (4)$$

Downstream of the impeller ($z > 0$),

$$\delta p_2 = \rho U^2 \exp j(\omega t - \theta) \sum_{m=0}^{\infty} A_{2m} Z(\lambda_m r) \exp(-\lambda_m z) \quad (5)$$

where A_{1m} and A_{2m} are normalized complex amplitudes, and λ_m is the wave number in the r -direction. The eigen-function in the r -direction, $Z(\lambda_m r)$, is represented by using the Bessel functions $J_1(\lambda_m r)$ and $Y_1(\lambda_m r)$ as follows:

$$Z(\lambda_m r) = Q_1 J_1(\lambda_m r) + Q_2 Y_1(\lambda_m r). \quad (6)$$

The values of λ_m and Q_2/Q_1 are determined from the boundary conditions $\partial p/\partial r = 0$ on the hub and casing, that is,

$$\begin{bmatrix} J_1(\lambda_m r_H) & \dot{Y}_1(\lambda_m r_H) \\ J_1(\lambda_m r_T) & \dot{Y}_1(\lambda_m r_T) \end{bmatrix} \begin{Bmatrix} Q_1 \\ Q_2 \end{Bmatrix} = \begin{Bmatrix} 0 \\ 0 \end{Bmatrix}. \quad (7)$$

Here, dots on the Bessel functions denote the derivatives in terms of $\lambda_m r$. In the present study, the value of Q_1 is determined so that the value of $Z(\lambda_m r)$ is unity at the tip, $r = r_T$.

Velocity Fluctuations. Velocity fluctuations can be divided into irrotational and rotational components and expressed as follows.

Upstream of the impeller ($z < 0$),

$$\delta u_1 = U \exp j(\omega t - \theta) \sum_{m=0}^{\infty} \frac{-U \lambda_m}{j\omega + U \lambda_m} A_{1m} Z(\lambda_m r) \exp(\lambda_m z),$$

$$r \delta v_{\theta 1} = U \exp j(\omega t - \theta) \sum_{m=0}^{\infty} \frac{jU}{j\omega + U \lambda_m} A_{1m} Z(\lambda_m r) \exp(\lambda_m z),$$

$$\delta v_{r1} = U \exp j(\omega t - \theta) \sum_{m=0}^{\infty} \frac{-U \lambda_m}{j\omega + U \lambda_m} \times A_{1m} Z(\lambda_m r) \exp(\lambda_m z). \quad (8)$$

Downstream of the impeller ($z > 0$),

$$\delta u_2 = U \exp j(\omega t - \theta) \sum_{m=0}^{\infty} \left[\frac{U \lambda_m}{j\omega - U \lambda_m} A_{2m} \exp(-\lambda_m z) + B_{2m} \exp\left(-j \frac{\omega}{U} z\right) \right] Z(\lambda_m r),$$

$$r \delta v_{\theta 2} = U \exp j(\omega t - \theta) \sum_{m=0}^{\infty} \left[\frac{jU}{j\omega - U \lambda_m} A_{2m} \exp(-\lambda_m z) + C_{2m} \exp\left(-j \frac{\omega}{U} z\right) \right] Z(\lambda_m r),$$

$$\delta v_{r2} = U \exp j(\omega t - \theta) \sum_{m=0}^{\infty} \left[\frac{-U \lambda_m}{j\omega - U \lambda_m} A_{2m} \exp(-\lambda_m z) + D_{2m} \exp\left(-j \frac{\omega}{U} z\right) \right] Z(\lambda_m r), \quad (9)$$

where the terms with the complex amplitudes A_{1m} and A_{2m} represent the irrotational components and those with B_{2m} , C_{2m} , and D_{2m} represent the rotational components.

The irrotational component is obtained from the momentum equations (1) by substituting the above-obtained pressure fluctuations into Eq. (1). The continuity equation (2) is satisfied automatically. The rotational component represents the effects of vortices shed from the impeller. It satisfies Eq. (1) with $\delta p = 0$, which

Nomenclature

A = normalized complex amplitude of pressure fluctuation
 B, C, D = normalized complex amplitudes of rotational components of velocity fluctuation
 b = span
 $h(r)$ = pitch of cascade
 $J_1(r), Y_1(r)$ = Bessel functions
 j = imaginary unit
 $K(r)$ = cavitation compliance
 k^* = normalized complex frequency, $= k_R^* + j k_I^*$
 k_R^* = propagation velocity ratio, $= (\text{rotational velocity of fluctuations})/(\text{that of the impeller})$
 k_I^* = decay rate

$l(r)$ = chord length
 $M(r)$ = mass flow gain factor
 p = pressure
 p_v = vapor pressure
 s = circumferential wavelength
 U = mean axial velocity
 u, v_r, v_θ = velocity components in the z -, r -, and θ -directions
 V_c = cavity volume per blade and unit span
 w = relative velocity in a frame rotating with the impeller
 $Z(r)$ = eigen-function in the radial direction
 α = incidence
 β = stagger
 δ = fluctuation
 δv = velocity fluctuation vector, $= (\delta u, \delta v_r, \delta v_\theta)$
 ϕ = relative velocity potential

λ = wave number of fluctuations in the radial direction
 ρ = density
 σ = cavitation number
 Ω = angular velocity of the impeller
 ω = complex angular propagation velocity of disturbance, $= \omega_R + j \omega_I$
 ω_R = angular propagation velocity of disturbance in the stationary frame
 ω_I = decay rate

Subscripts

1, 2 = upstream and downstream of the impeller
 H, T = hub and tip of the impeller
 M = mean radius of the impeller
 m = radial order

means that the rotational disturbance is convected on the main flow. Thus, it has the functional form of $\exp(-j\omega z/U)$ in the z -direction. The radial mode is represented by a series of the eigen-function (6). Both irrotational and rotational components satisfy the boundary conditions on the hub and casing, because the eigen-function satisfies Eq. (7).

As already stated, the irrotational components automatically satisfy the continuity equation. The rotational components should satisfy the following relations obtained by substituting the rotational velocity components into the continuity equation (2) and making use of the orthogonality of the eigen-functions, $Z(\lambda_m r)$,

$$\left(\lambda_m D_{2m} + j \frac{\omega}{U} B_{2m}\right) b_m = \sum_{n=0}^{\infty} \left(\frac{D_{2n}}{\lambda_n} - j C_{2n}\right) a_{mn},$$

$$a_{mn} = \int_{r_H}^{r_T} \frac{1}{r} Z(\lambda_m r) Z(\lambda_n r) dr,$$

$$\text{and } b_m = \int_{r_H}^{r_T} r [Z(\lambda_m r)]^2 dr. \quad (10)$$

Boundary Conditions

Continuity Equation Considering Cavity Volume Change.

We represent the cavity volume per blade and unit span by V_c . We assume that V_c is a function of the local cavitation number, $\sigma(r) = 2[p_1(r) - p_v]/\rho w_1(r)^2$, and of the incidence angle, $\alpha(r)$. Thus, the change of cavity volume due to the change in the inlet condition can be represented as follows:

$$\delta V_c = [-K(r)\delta\sigma + M(r)\delta\alpha] \cdot h(r)^2,$$

$$K(r) = -\frac{1}{h(r)^2} \frac{\partial V_c}{\partial \sigma}, \quad \text{and } M(r) = \frac{1}{h(r)^2} \frac{\partial V_c}{\partial \alpha}, \quad (11)$$

where $K(r)$ and $M(r)$ are termed cavitation compliance and mass flow gain factor, respectively (Brennen and Acosta, 1976; Otsuka et al., 1996), in which the cross-sectional area of cavity at constant radius is normalized by the square of spacing h^2 . As we can see from the definitions of Eq. (11), cavitation compliance K represents the magnitude of cavity volume variation due to the unit cavitation number change. Mass flow gain factor M represents the magnitude of cavity volume variation due to the unit incidence change. Since both factors, K and M , are considered to be dependent on the cavity size, radial distributions of K and M can simulate the three-dimensionality of cavitation.

Since there is no mass transfer in the tangential direction in the frame rotating with the impeller and since we assume that the streamline maintains a constant radial location within the impeller, the continuity relation across the impeller with cavitation can be expressed as follows:

$$\frac{\partial^* V_c}{\partial t^*} = (\delta u_2 - \delta u_1) \cdot h(r) \quad (12)$$

where $\partial^*/\partial t^*$ represents the time-derivative in a frame rotating with the impeller.

Unsteady Bernoulli's Equation. Rotating cavitation occurs under the condition where the pressure performance is not affected by cavitation and the loss has no significant effects on rotating cavitation (Tsujimoto et al., 1993). Thus, we can apply the unsteady version of Bernoulli's equation to the relative flow through the impeller,

$$\frac{\partial^*(\phi_2 - \phi_1)}{\partial t^*} + \frac{p_2 - p_1}{\rho} + \frac{1}{2} (w_2^2 - w_1^2) = 0, \quad (13)$$

Table 1 Analytical conditions

Hub ratio, r_H/r_T	0.5
Stagger angle, β_T [deg.]	81.75
Pitch/radius ratio h_T/r_T	2.09
Chord/radius ratio, l_T/r_T	2.12
Flow coefficient, $\phi = U/r_T \Omega$	0.145
Cavitation number, σ_T	0.04

where ϕ is a relative velocity potential and w is a relative velocity in the rotating frame. Since we neglect the radial shift of the stream surface, the effects of centrifugal force do not appear in the above equation. The 1st term in the above equation can be represented as follows:

$$\frac{\partial^*(\phi_2 - \phi_1)}{\partial t^*} = \frac{l(r)}{\cos \beta(r)} \frac{\partial^* u_2}{\partial t^*} = j(\omega - \Omega) \frac{l(r)}{\cos \beta(r)} \delta u_2. \quad (14)$$

The unsteady Bernoulli's equation (13) is linearized by assuming small disturbances.

Conservation of Momentum in the r -Direction. We assume that the momentum in the r -direction is conserved across the cascade, that is $\rho(U + \delta u_1)\delta v_{r1} = \rho(U + \delta u_2)\delta v_{r2}$. By linearizing the equation, we obtain

$$\delta v_{r1} = \delta v_{r2}. \quad (15)$$

Kutta's Condition. We assume that the flow is tangential to the blade surface at the trailing edge:

$$r\Omega - v_{\theta 2} = u_2 \tan \beta(r).$$

By linearizing the above equation, we obtain the following relation,

$$\delta v_{\theta 2} = -\delta u_2 \tan \beta(r). \quad (16)$$

Analytical Methods and the Conditions for Calculations

We put Eqs. (4), (5), (8), and (9) into the boundary conditions (11)–(16) with Eq. (10). By expanding all linearized terms with the eigen-function, $Z(\lambda_m r)$, we obtain a set of homogeneous linear equations in terms of the complex amplitudes in Eqs. (4), (5), (8), and (9). By equating the determinant of the coefficient matrix of the above linear equations with zero, we obtain a characteristic equation from which we can determine the complex angular frequency, ω . In the present study, we take the radial components of $m \leq 10$ into account for all flow fluctuations.

The complex propagation velocity ratio is defined as follows:

$$k^* = k_R^* + jk_I^* \equiv \frac{\omega}{\Omega}, \quad (17)$$

where k_R^* represents the propagation velocity ratio (rotational velocity of fluctuations/rotational velocity of the impeller) and $k_R^* > 1/k_R^* < 1$ means that the corresponding mode is a forward/backward travelling mode. k_I^* represents the decay rate and $k_I^* > 0/k_I^* < 0$ means that the corresponding mode is decaying/amplifying.

Default values for the example calculations are shown in Table 1. Here, we consider a helical impeller, so the local design parameters of the impeller are given as follows:

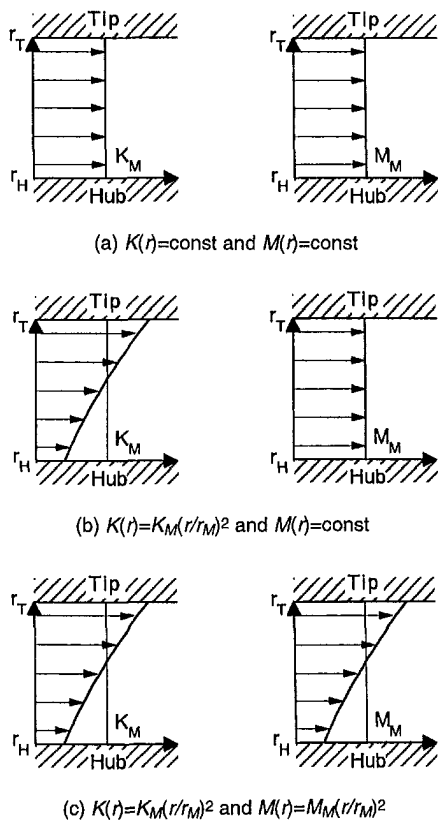


Fig. 2 Radial distributions of cavitation compliance $K(r)$ and mass flow gain factor $M(r)$. (a) $K(r) = \text{const}$ and $M(r) = \text{const}$; (b) $K(r) = K_M(r/r_M)^2$ and $M(r) = \text{const}$; (c) $K(r) = K_M(r/r_M)^2$ and $M(r) = M_M(r/r_M)^2$

$$\tan \beta(r) = \frac{r}{r_T} \tan \beta_T, \quad h(r) = \frac{r}{r_T} h_T, \quad \text{and} \quad l(r) = \frac{r}{r_T} l_T$$

We focus on the effects of the distributions of $K(r)$ and $M(r)$ on the propagation velocity ratio and the amplifying region of rotating cavitation. For this purpose, three cases of distributions of $K(r)$ and $M(r)$ as shown in Fig. 2 are examined. Figure 2(a) corresponds to the case with uniform cavities over the whole span with constant $K(r)$ and $M(r)$. It is known that, as the cavitation number is decreased, the cavitation compliance rapidly increases prior to the increase of mass flow gain factor (Brennen and Acosta, 1976). Figure 2(b) corresponds to the extreme case where only $K(r)$ is unevenly distributed in the r -direction to simulate the condition with smaller cavitation number near the tip region due to larger relative velocity $w(r)$. On the other hand, it is also considered that both $K(r)$ and $M(r)$ are larger near the tip region because large tip cavitation is usually observed in experiments. Figure 2(c) corresponds to that case where both $K(r)$ and $M(r)$ are larger at the tip. To facilitate the mathematical treatment in Eqs. (11) and (12), both $K(r)$ and $M(r)$ are assumed to be proportional to the square of r , specifying the magnitude of $K(r)$ and $M(r)$ with their values at mean radius $r = r_M$, represented as K_M and M_M .

Because there exists no available information on the spanwise distributions of cavitation characteristics $K(r)$ and $M(r)$ obtained both experimentally and theoretically, we assumed the values of K_M and M_M to examine the effects of their radial distributions on rotating cavitation. Results described in this paper are those for the case with $K_M = 1.0$. We obtained the same tendencies for the case with $K_M = 0.1$.

Results and Discussion

Complex Frequency and Modes of Fluctuations. At first, in order to examine the solutions of characteristic equations, calcu-

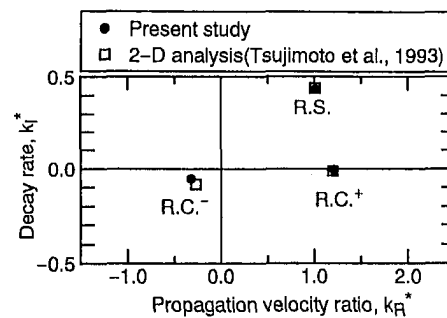


Fig. 3 Solutions of characteristic equation considering only 0th radial component [(K, M) of Fig. 2(c) is used with $(K_M, M_M) = (1.0, 0.5)$]

lations were made with only the 0th radial component of fluctuations. Figure 3 shows an example, i.e., the result under the condition of Fig. 2(c) with $(K_M, M_M) = (1.0, 0.5)$. Figure 3 also shows the result of the 2-D analysis (Tsujimoto et al., 1993), in which three solutions are obtained. One of them has already been identified to be the solution representing rotating stall (R.S.), which is not affected by cavitation and becomes unstable in the region with the positive slope of the cascade pressure performance. The others are solutions representing forward and backward rotating cavitations. It has been shown that the frequencies determined by using the values of K and M from experiments agree reasonably with those in experiments (Tsujimoto et al., 1993; Hashimoto et al., 1996). We have three solutions for the present case and they are close to the solutions of 2-D analysis. Thus, we can identify each of the three solutions as being a forward rotating cavitation (R.C.+), backward rotating cavitation (R.C.-), and rotating stall (R.S.), respectively. The difference between the results of the present analysis and those from the 2-D analysis is small. The difference is considered to be due to the three-dimensional effects of geometry and cavitation, and the radial change of the peripheral velocity.

Figure 4 shows an example of solutions of the present study with the 0th–10th radial components of fluctuations. The condition is the same as that used for the case shown in Fig. 3. We can see that there are not only solutions corresponding to the conventional modes shown in Fig. 3, but also other solutions with a high relative propagation velocity ratio, $|k_R^* - 1|$. Still more solutions with higher relative propagation velocity ratio were obtained out of range of the figure. The modes of the inlet pressure fluctuation and the amplitudes of each radial component, $|A_{1m}|$, are shown in Fig. 5 for four solutions corresponding to rotating cavitation. The ratio of the complex amplitude of each component is determined as the eigen-vector of the set of homogeneous linear equations described in the last section. The amplitudes are then normalized by that of the largest component. Figures 5(a) and (b) show the results of solutions corresponding to the conventional rotating cavitation, and it is shown that the amplitude of the 0th radial component is

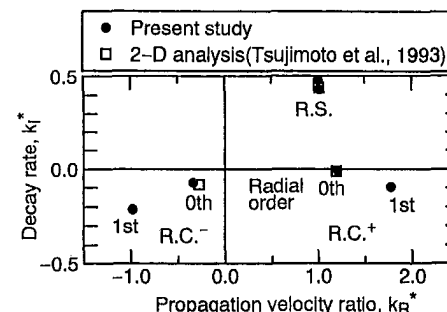


Fig. 4 Solutions of characteristic equation [(K, M) of Fig. 2(c) is used with $(K_M, M_M) = (1.0, 0.5)$]

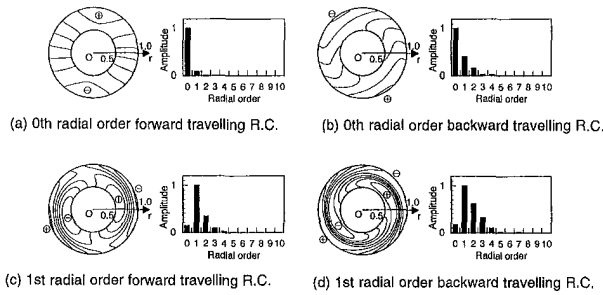


Fig. 5 Inlet pressure perturbation (pressure contours and amplitudes) of 4 modes of R.C. shown in Fig. 4. (a) 0th radial order forward travelling R.C.; (b) 0th radial order backward travelling R.C.; (c) 1st radial order forward travelling R.C.; (d) 1st radial order backward travelling R.C.

significantly larger than the others. Hence, they are herein termed the 0th radial order forward and backward rotating cavitation (denoted by R.C.+₀ and R.C.-₀), respectively. On the other hand, Figs. 5(c) and (d) correspond to the solutions with larger relative propagation velocity ratio. The amplitude of the 1st radial component is the largest; thus, we call them the 1st radial order forward and backward rotating cavitation (denoted by R.C.+₁ and R.C.-₁), respectively. Those modes are also found in the 3-D analysis using the linear cascade model (Watanabe et al., 1997). Although many higher order modes were found in addition to the solutions shown in Fig. 4, we focus on the 0th and 1st radial modes, R.C.+₀, R.C.-₀, R.C.+₁, and R.C.-₁, because their frequencies are closer to that of rotating cavitation observed experimentally. The present result suggests the existence of higher order modes and further experimental efforts are needed to identify them. Similar results were obtained for other cases, showing that many types of rotating cavitation such as R.C.+₀, R.C.-₀, R.C.+₁, and R.C.-₁ generally exist.

It is desirable to show the validity by direct comparison with experiments. However, it is very difficult to determine the values of $K(r)$ and $M(r)$ and only global values (averages over r) are available (Brennen and Acosta, 1976). In the 2-D analysis (Tsujiimoto et al., 1993), the results were plotted in K - M plane and it was found that the propagation velocity ratio determined by using the experimental global values of K and M agrees fairly well with experiments. Since the results of the present 3-D analysis approaches to the 2-D results, the present result is also reasonable as compared with experiments. For example, the value of the propagation velocity ratio $k_R^* = 1.21$ for the 0th radial order mode of forward rotating cavitation in Fig. 4 is close to experimental value $k_R^* = 1.18$ (Hashimoto et al., 1997). The value $k_R^* = -0.40$ for the 0th radial order mode of backward rotating cavitation does not agree well with the experimental value $k_R^* = -1.36$. However, the analytical results with $M = 0.8$ and $K = 0.03$ gives $k_R^* = -1.36$ for backward mode and $k_R^* = 1.20$ for forward mode. These values are quite reasonable. Further experimental efforts are needed to make closer comparisons with experiment and to obtain further knowledge about $K(r)$ and $M(r)$. Under these circumstances, 3-D effects are discussed in the following section based on the present analysis.

Effects of Three-Dimensionality. The effects of the hub/tip ratio of the impeller are shown in Fig. 6. The neutral stability points with $k_R^* = 0$ are shown in the (k_R^*, M_M) plane for various rotating cavitation modes and various hub/tip ratios under the condition shown in Fig. 2(a) with $K_M = 1.0$. Rotating cavitation grows with the values of mass flow gain factor larger than the values shown in the figure. Figure 6 also shows the result of 2-D analysis (Tsujiimoto et al., 1993) and the results of the previous 3-D analysis using a linear cascade model (Watanabe et al., 1997). Although the hub/tip ratio in the 3-D analysis of the linear cascade model corresponds to unity from the view point of the curvature of

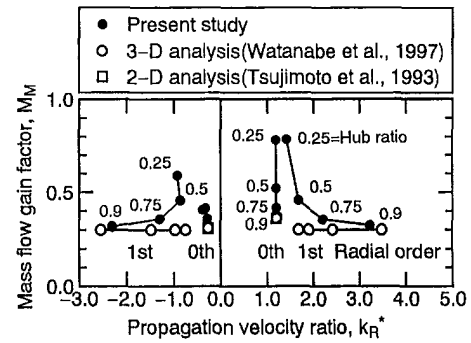


Fig. 6 Neutral stability points of R.C. for various hub/tip ratio $((K, M)$ of Fig. 2(a) is used with $K_M = 1.0$)

hub and shroud, we can relate the span/circumferential wavelength ratio, b/s , to the hub/tip ratio in the present analysis by the following relation

$$\frac{b}{s} = \frac{r_T - r_H}{2\pi r_T} = \frac{1}{2\pi} \left(1 - \frac{r_H}{r_T} \right).$$

The value of r_H/r_T determined from this relation is used for the plot in Fig. 6. The amplifying region of the present calculation is smaller for the case with a smaller hub/tip ratio, whereas the neutral stability point shown by 3-D analysis of the linear cascade model is not affected by the hub/tip ratio determined from the above relation. This shows the necessity of the present treatment for the accurate prediction of rotating cavitation. The results of the two 3-D analyses become closer as the hub/tip ratio is increased. Moreover, the 0th radial modes of the present model approach the results of the previous 2-D analysis if the hub/tip ratio approaches unity. Note that the propagation velocity ratio of the 0th radial mode is not affected by the hub/tip ratio largely. This may be the reason why the 2-D analysis can predict the propagation velocity ratio fairly well.

Figure 7 shows the neutral stability points for the three cases shown in Fig. 2 with $K_M = 1.0$. First, we compare the result for the case with K and M shown in Fig. 2(b) simulating the case with smaller cavitation number near the tip region with the case of Fig. 2(a). We can see that the 0th radial modes are not significantly affected by the three-dimensionality of cavitation. On the other hand, the amplifying regions of the 1st radial modes become slightly larger, and they are more destabilizing than the 0th radial modes. Next, we compare the result for the case with the three-dimensionality of cavitation of Fig. 2(c) simulating larger tip cavitation or larger blade cavitation near the tip region with the case of Fig. 2(a). In this case, the amplifying regions of all modes become slightly larger due to the three-dimensionality of cavitation; among these modes, the 0th radial backward mode is the most

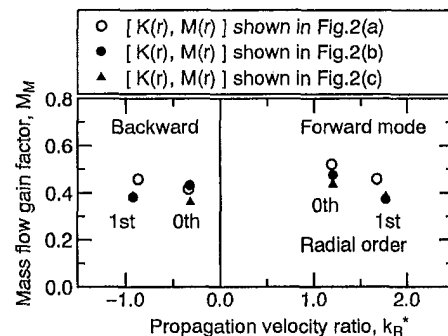


Fig. 7 Neutral stability points of R.C. for various cavitation characteristics shown in Fig. 2(a)-(c) with $K_M = 1.0$

destabilizing. In all cases, the propagation velocity ratio of all modes does not change significantly.

Conclusions

The following results were obtained from the present analysis.

(1) There are many solutions of the characteristic equation, including rotating stall, forward and backward propagating rotating cavitations, with various radial modes.

(2) The 0th radial modes of forward and backward rotating cavitations obtained in the present study correspond to the 0th radial modes of the previous 3-D analysis using a linear cascade model and to the rotating cavitation modes predicted by the previous 2-D analysis.

(3) The 0th radial modes of rotating cavitation are not significantly affected by the three-dimensionality of cavitation.

(4) The amplifying regions of all rotating cavitation modes become smaller for smaller hub/tip ratios of the impeller.

The present analysis provides information regarding some effects of three-dimensionality on rotating cavitation. However, the effects of cavitation are modelled simply by the distributions of K and M and the values of these parameters are assumed in the present study. These parameters should be estimated for various kinds of cavitation such as tip cavitation, blade cavitation, bubble cavitation, etc. The validity of infinitesimal pitch of the semi-actuator disk method should be examined by constructing a finite pitch cascade theory. The authors intend to examine these problems in the near future.

Acknowledgments

This study is partly supported by the Ministry of Education, Science, Sports and Culture through the Grant-in-Aid for Scientific Research.

References

- Brennen, C. E., and Acosta, A. J., 1976, "The Dynamic Transfer Function for a Cavitating Inducer," *ASME JOURNAL OF FLUIDS ENGINEERING*, Vol. 98, pp. 182–191.
- Goirand, B., Mertz, A. L., Jousselein, F., and Rebattet, C., 1992, "Experimental Investigations of Radial Loads Induced by Partial Cavitation with a Liquid Hydrogen Inducer," *IMECHE*, C453/056, pp. 263–269.
- Hashimoto, T., Yoshida, M., Watanabe, M., Kamijo, K., and Tsujimoto, Y., 1997, "Experimental Study on Rotating Cavitation of Rocket Propellant Pump Inducers," *AIAA Journal of Propulsion and Power*, Vol. 13, No. 4, pp. 488–494.
- Kamijo, K., Shimura, T., and Watanabe, M., 1977, "An Experimental Investigation of Cavitating Inducer Instability," *ASME Paper 77-WA/FW-14*.
- Kamijo, K., Yoshida, M., and Tsujimoto, Y., 1993, "Hydraulic and Mechanical Performance of LE-7 LOX Pump Inducer," *AIAA Journal of Propulsion and Power*, Vol. 9, No. 6, pp. 819–826.
- Otuska, S., Tsujimoto, Y., Kamijo, K., and Furuya, O., 1996, "Frequency Dependence of Mass Flow Gain Factor and Cavitation Compliance of Cavitating Inducers," *ASME JOURNAL OF FLUIDS ENGINEERING*, Vol. 118, No. 2, pp. 400–408.
- Tsujimoto, Y., Kamijo, K., and Yoshida, Y., 1993, "A Theoretical Analysis of Rotating Cavitation in Inducers," *ASME JOURNAL OF FLUIDS ENGINEERING*, Vol. 115, No. 1, pp. 135–141.
- Tsujimoto, Y., Yoshida, Y., Maekawa, M., Watanabe, S., and Hashimoto, T., 1997, "Observations of Oscillating Cavitations of an Inducer," *ASME JOURNAL OF FLUIDS ENGINEERING*, Vol. 119, No. 4, pp. 775–781.
- Watanabe, S., Yokota, K., Tsujimoto, Y., and Kamijo, K., 1997, "Three-Dimensional Analysis of Rotating Cavitation in Inducers-Linear Cascade Model Spanning between Two Parallel Plates," (in English), *Proceedings of JSME Centennial Grand Congress*, International Conference on Fluid Engineering, Tokyo, Vol. III, pp. 1377–1382.

Numerical Computation of Shock Waves in a Spherical Cloud of Cavitation Bubbles

Yi-Chun Wang

Assistant Professor,
Department of Mechanical Engineering,
National Cheng Kung University,
Tainan 701, Taiwan

Christopher E. Brennen

Professor,
Division of Engineering and Applied Science,
California Institute of Technology,
Pasadena, CA 91125

The nonlinear dynamics of a spherical cloud of cavitation bubbles have been simulated numerically in order to learn more about the physical phenomena occurring in cloud cavitation. A finite cloud of nuclei is subject to a decrease in the ambient pressure which causes the cloud to cavitate. A subsequent pressure recovery then causes the cloud to collapse. This is typical of the transient behavior exhibited by a bubble cloud as it passes a body or the blade of a ship propeller. The simulations employ the fully nonlinear continuum bubbly mixture equations coupled with the Rayleigh-Plesset equation for the dynamics of bubbles. A Lagrangian integral method is developed to solve this set of equations. It was found that, with strong bubble interaction effects, the collapse of the cloud is accompanied by the formation of an inward propagating bubbly shock wave. A large pressure pulse is produced when this shock passes the bubbles and causes them to collapse. The focusing of the shock at the center of the cloud produces a very large pressure pulse which radiates a substantial impulse to the far field and provides an explanation for the severe noise and damage potential in cloud cavitation.

1 Introduction

Experimental studies have shown that intensive noise and damage potential are associated with the collapse of a cavitating cloud of bubbles (see, for example, Bark and Berlekom, 1978; Shen and Peterson, 1978; Bark, 1985; Franc and Michel, 1988; Kubota et al., 1989; Reisman and Brennen, 1996). Moreover, it has been demonstrated that when clouds of cavitation bubbles collapse coherently, they result in greater material damage (see, for example, Soyama et al., 1992) and greater noise generation (see, for example, Reisman and Brennen, 1996) than would be expected from the cumulative effect of the collapse of the individual bubbles which make up the cloud. However, the precise physical phenomena involved in cloud cavitation have not, as yet, been completely identified. This paper presents numerical studies of the nonlinear dynamics of finite clouds of cavitation bubbles. Some preliminary results were presented earlier in Reisman, Wang and Brennen (1998); here we provide more details and further results. The purpose is to explore the mechanisms for the enhanced noise and damage potential associated with cloud cavitation.

Analytical studies of the dynamics of cavitation clouds can be traced to the work of van Wijngaarden (1964) who proposed a continuum model to study the behavior of a collapsing layer of bubbly fluid next to a flat wall and found higher average pressures at the wall as result of the interactive effects of bubbles. Chahine (1982a, 1982b) explored numerical methods which incorporate the individual bubbles using matched asymptotic expansions. Later, d'Agostino and Brennen (1983, 1989) investigated the linearized dynamics of a spherical cloud of bubbles using a continuum mixture model coupled with the Rayleigh-Plesset equation for the dynamics of the bubbles. They showed that the interaction between bubbles leads to a coherent dynamics of the cloud, including natural frequencies that can be much smaller than the natural frequencies of individual bubbles. Omta (1987) linearized the Biesheuvel-van Wijngaarden homogeneous flow equations for bubbly mixtures (Biesheuvel and Wijngaarden, 1984) and obtained solutions to the flow in a spherical bubble cloud under a number of

simplified assumptions. Thus while the linearized dynamics of clouds of bubbles have been extensively investigated (see also, for example, Prosperetti, 1988), the nonlinear effects in cloud cavitation have received comparatively little attention; in practice, of course, flows with cloud cavitation experience very large pressure perturbations. Both the dynamics of an individual bubble and the bubble/bubble interaction through the hydrodynamics of the surrounding liquid are highly nonlinear. An attempt to understand these nonlinear effects was undertaken in the work of Kumar and Brennen (1991, 1993). They found weakly nonlinear solutions to a number of cloud problems by retaining only the terms that are quadratic in the amplitude. The nonlinear, chaotic behavior of periodically driven bubble clouds have been recently examined by Smereka and Banerjee (1988) and Birnir and Smereka (1990). These studies employed the methods of dynamical systems analysis and reveal a complicated system of bifurcations and strange attractors in the oscillations of bubble clouds. It is clear that much remains to be learned about the massively nonlinear response of a bubble cloud in a cavitating flow.

All the above researches were based on continuum mixture models which were developed using ensemble volume averaging (Biesheuvel and Wijngaarden, 1984) or time averaging (Ishii, 1975). Effects of bubble dynamics, liquid compressibility and relative motion between phases can be included. Such continuum mixture models have been successfully applied to investigate shock wave propagation in liquids containing small gas bubbles (see, for example, Noordzij and van Wijngaarden, 1974; Kameda and Matsumoto, 1995).

Another approach to the modeling of the interaction dynamics of cavities was developed by Chahine and his coworkers (Chahine and Duraiswami, 1992; Chahine et al., 1992). Three-dimensional boundary element methods have been employed to simulate the deformations of the individual bubbles within collapsing clouds in inhomogeneous flow fields or close to solid boundaries. However, most clouds contain many thousands of bubbles, impossible to handle by any high speed computer at this time. It therefore is advantageous to examine the nonlinear behavior of cavitation clouds using continuum mixture models. The recent numerical modeling of unsteady cavitating flows on a two-dimensional hydrofoil by Kubota et al. (1992) is an important step in this direction. Solving the Navier-Stokes equations of the mixture coupled with the Rayleigh equation for bubble dynamics, they reproduced

Contributed by the Fluids Engineering Division for publication in the JOURNAL OF FLUIDS ENGINEERING. Manuscript received by the Fluids Engineering Division September 15, 1997; revised manuscript received August 9, 1999. Associate Technical Editor: C. L. Merkle.

the shedding of cavitation clouds and the generation of vortex cavitation. Unfortunately, there appear to be some limitations in their approach. They artificially prevented the bubbles from collapsing to a size smaller than the initial value. Under these circumstances, the collapse of the bubbles is severely suppressed and highly nonlinear phenomena such as the formation of shock waves are eliminated. Parenthetically, it is shown in this paper that very large pressure pulses can occur due to the violent bubble collapse. In Wang (1996), it was shown that such large pulses cause substantial computational difficulties.

Another perspective on the subject of collapsing clouds was that introduced by Mørch, Hanson and Kedrinskii (Mørch, 1980, 1981, 1982; Hanson et al., 1981). They speculated that the collapse of a cloud of bubbles involves the formation and inward propagation of a shock wave and that the geometric focusing of this shock at the center of a cloud creates the enhancement of the noise and damage potential associated with cloud collapse. However, they assumed that the bubbles are completely annihilated after the shock passing. Fully nonlinear solutions for spherical cloud dynamics were first obtained by Wang and Brennen (1994, 1995). Their computational results show that the continuum models of the cloud indeed manifest the shock wave phenomena and thus confirm the idea put forward by Mørch, Hanson et al. Recently, Reisman et al. (1998) measured very large impulsive pressures on the suction surface of an oscillating hydrofoil experiencing cloud cavitation. They demonstrate that these pressure pulses are associated with the propagation of bubbly shock waves.

2 Basic Equations

Consider a spherical bubble cloud surrounded by an unbounded pure liquid as shown in Fig. 1. The liquid is at rest infinitely far from the cloud. Compared to the large compressibility of the cloud, the pure liquid is assumed incompressible. Although radially symmetric bubble size distribution is allowed in the present model, it is enough for illustration purpose to assume that the initial bubble size is uniform within the cloud. It is also assumed

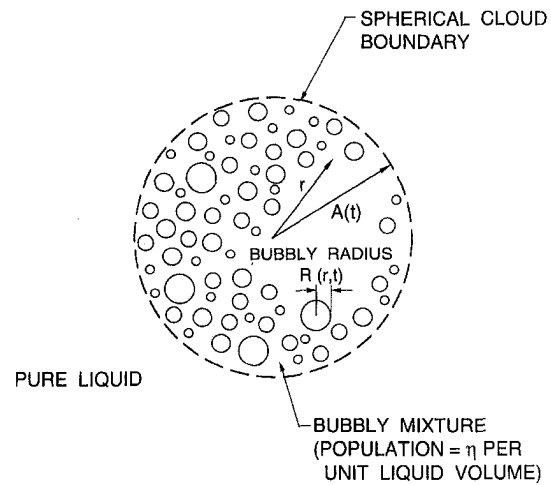


Fig. 1 Schematic of a spherical cloud of bubbles

that the population of bubbles per unit volume of liquid, η , within the cloud, is piecewise uniform initially and that there is no coalescence or break-up of bubbles. Since relative motion between the phases is neglected and the mass of liquid vaporized or condensed is also neglected, it follows that η remains both constant and piecewise uniform within the cloud. The radius of the cloud is represented by $A(t)$, a function of time t . The bubble radius in the cloud is $R(r, t)$, a function of radial coordinate r and time. The bubbles are assumed to be spherical and to contain uniform liquid vapor and residual permanent gas. The problem to be solved is as follows. The cloud and the whole domain of liquid are initially in equilibrium. Starting at $t = 0$, a pressure perturbation, $C_{p\infty}(t)$, is imposed on the pure liquid at infinity and the response of the cloud to this pressure perturbation is sought.

The variables mentioned above and in all the following figures

Nomenclature

A = dimensionless radius of bubble cloud	U^* = reference velocity	t = dimensionless time
A_0 = dimensionless initial cloud radius	V^* = volume of the cloud	t_G = dimensionless duration of the low pressure perturbation
C_p = pressure coefficient	V_{BMAX} = dimensionless maximum total volume of bubbles in the cloud	t^* = time
C_{PMIN} = minimum pressure coefficient at infinity	We = Weber number	u = dimensionless fluid velocity
$C_{p\infty}$ = pressure coefficient at infinity from the cloud, $(p_\infty^* - p_0^*) / \frac{1}{2} \rho_L^* U^{*2}$	c^* = sonic speed in bubbly mixture	u^* = fluid velocity
D = dimensionless length scale of the low pressure perturbation	f = dimensionless frequency	α = void fraction
D^* = length scale of the low pressure perturbation	k = polytropic index for the gas inside the bubbles	α_0 = initial void fraction
I = dimensionless acoustic impulse	p_a = dimensionless far-field acoustic pressure radiated by the cloud	β = cloud interaction parameter, $\alpha_0(1 - \alpha_0)A_0^2/R_0^2$
J = Jacobian of the transformation from Lagrangian coordinates to Eulerian coordinates	p^* = fluid pressure	η = dimensionless bubble population per unit liquid volume, $\eta^* R_0^{*3}$
R = dimensionless bubble radius	p_0^* = fluid pressure at undisturbed reference condition	η^* = bubble population per unit liquid volume
R_0 = dimensionless initial bubble radius	p_a^* = far-field acoustic pressure radiated by the cloud	μ_E^* = effective dynamic viscosity of the liquid
R_0^* = initial bubble radius at undisturbed reference condition	p_v^* = vapor pressure	ω_b^* = natural frequency of bubble pulsation
Re = Reynolds number	p_∞^* = pressure at infinity from the cloud	ρ = dimensionless mixture density
S^* = surface tension of the liquid	r = dimensionless Eulerian radial coordinate measured from the center of cloud, r^*/R_0^*	ρ_0 = dimensionless mixture density at $t = 0$
T_b^* = natural period of bubble pulsation	r_0 = dimensionless Lagrangian radial coordinate measured from the center of cloud and equal to r at the undisturbed reference condition	ρ_L^* = liquid density
T_c^* = time scale of acoustic wave propagation through the cloud	r^* = Eulerian radial coordinate measured from the center of cloud	σ = cavitation number
		Δt = time step

and equations are non-dimensionalized using the initial bubble radius, R_0^* , and a reference flow velocity, U^* . All quantities with superscript * represent dimensional values; without this superscript the quantities are non-dimensional. Thus, the nondimensional bubble radius is $R = R^*/R_0^*$, the nondimensional bubble population per unit liquid volume is $\eta = \eta^*R_0^{*3}$, the nondimensional radial coordinate is $r = r^*/R_0^*$, and the nondimensional time is $t = t^*U^*/R_0^*$.

The basic equations used are those of d'Agostino and Brennen (1983, 1989) except that all the nonlinear convective terms are retained since these are important in the context of the highly nonlinear growth and collapse of the cloud. The dimensionless forms of the continuity and momentum equations for the spherical bubbly flow are:

$$\frac{1}{r^2} \frac{\partial(r^2 u)}{\partial r} = \frac{12\pi\eta R^2}{3 + 4\pi\eta R^3} \frac{DR}{Dt}; \quad r \leq A(t) \quad (1)$$

$$\frac{Du}{Dt} = -\frac{1}{6} (3 + 4\pi\eta R^3) \frac{\partial C_p}{\partial r}; \quad r \leq A(t) \quad (2)$$

where $D/Dt \equiv \partial/\partial t + u\partial/\partial r$ is the Lagrangian derivative, $u(r, t)$ is the mixture velocity, $C_p(r, t) = (p^*(r, t) - p_0^*)/\frac{1}{2}\rho_L^*U^{*2}$ is the mixture pressure coefficient, $p^*(r, t)$ is the mixture pressure, p_0^* is the initial equilibrium pressure, and ρ_L^* is the liquid density. The bubble population per unit liquid volume, η , is related to the void fraction, α , by $\frac{4}{3}\pi R^3\eta = \alpha/(1 - \alpha)$. The interactions of the bubbles with the flow are modeled by the Rayleigh-Plesset equation (Plesset and Prosperetti, 1977) which connects the local mixture pressure coefficient, C_p , to the bubble radius, R :

$$R \frac{D^2 R}{Dt^2} + \frac{3}{2} \left(\frac{DR}{Dt} \right)^2 + \frac{\sigma}{2} (1 - R^{-3k}) + \frac{4}{\text{Re}} \frac{1}{R} \frac{DR}{Dt} + \frac{2}{\text{We}} (R^{-1} - R^{-3k}) + \frac{1}{2} C_p = 0 \quad (3)$$

where $\sigma = (p_0^* - p_v^*)/\frac{1}{2}\rho_L^*U^{*2}$ is the cavitation number and p_v^* is the partial pressure of vapor inside the bubble. The partial pressure of noncondensable gas (it is assumed the mass of gas is constant) does not appear explicitly in (3) because the initial equilibrium condition has been employed to eliminate this quantity. It has been assumed that the noncondensable gas inside the bubbles behaves polytropically with an index k . From the definition of cavitation number, σ , we know that small values of σ imply that the initial equilibrium pressure is close to the vapor pressure and the bubbles therefore cavitate more readily. We define a Reynolds number, $\text{Re} = \rho_L^*U^*R_0^*/\mu_E^*$, where μ_E^* is the effective viscosity of liquid which incorporates the various bubble-damping mechanisms, namely acoustic, thermal, and viscous damping, described by Chapman and Plesset (1971). We also define a Weber number, $\text{We} = \rho_L^*U^{*2}R_0^*/S^*$, where S^* is the surface tension of the liquid.

The Rayleigh-Plesset equation (3) neglects the local pressure perturbations experienced by the individual bubble due to the growth or collapse of its neighbor. d'Agostino and Brennen (1989), Nigmatulin (1991) and Sangani (1991) have shown that, for a mixture with randomly distributing bubbles, the correction factors for local pressure perturbations are of order of the void fraction, α , or higher. While a second-order correction could be incorporated without much difficulty, the void fractions considered in the present work are only few percent so that these higher order effects are neglected.

The boundary condition on the surface of the cloud, $r = A(t)$, is obtained as follows. The spherically symmetric incompressible liquid flow outside the cloud, $r \geq A(t)$, must have a solution of the form:

$$u(r, t) = \frac{C(t)}{r^2}; \quad r \geq A(t) \quad (4)$$

$$C_p(r, t) = C_{p\infty}(t) + \frac{2}{r} \frac{dC(t)}{dt} - \frac{C^2(t)}{r^4}; \quad r \geq A(t) \quad (5)$$

where $C(t)$ is an integration constant to be determined and $C_{p\infty}(t)$ is the imposed pressure perturbation coefficient at infinity which will be described later. By substituting the values of u and r at the boundary of the cloud in (4), $C(t)$ can be determined as

$$C(t) = A^2(t)u(A(t), t) \quad (6)$$

Substituting (6) and $r = A(t)$ into (5), we obtain the time-dependent boundary condition at the surface of the cloud:

$$C_p(A(t), t) = C_{p\infty}(t) + \frac{2}{A(t)} \frac{d[A^2(t)u(A(t), t)]}{dt} - u^2(A(t), t) \quad (7)$$

At the center of cloud, the symmetry of the problem requires

$$u(0, t) = 0 \quad (8)$$

In the context of cavitating flows it is appropriate to assume that, at time $t \leq 0$, the whole flow field is in equilibrium. It is also assumed, for simplicity, that all the bubbles have the same initial size. Therefore, the following initial conditions should be applied:

$$R(r, 0) = 1, \quad \frac{DR}{Dt}(r, 0) = 0, \\ u(r, 0) = 0, \quad C_p(r, 0) = 0 \quad (9)$$

The mathematical model of Eqs. (1), (2), and (3) is complete and, after applying appropriate initial and boundary conditions, can, in theory, be solved to find the unknowns $C_p(r, t)$, $u(r, t)$, and $R(r, t)$ for any bubbly cavitating flow with spherical symmetry. However, the nonlinearities in the Rayleigh-Plesset equation and in the Lagrangian derivative, D/Dt , present considerable computational impediments.

In (7), $C_{p\infty}(t) = (p_\infty^*(t) - p_0^*)/\frac{1}{2}\rho_L^*U^{*2}$ and $p_\infty^*(t)$ is the far-field pressure perturbation experienced by the cloud in a cavitating flow. For the purposes of the present calculations, a simple sinusoidal form is chosen for $C_{p\infty}(t)$ since previous investigations have shown that the results are not very sensitive to the precise functional form of $C_{p\infty}(t)$:

$$C_{p\infty}(t) = \begin{cases} \frac{1}{2} C_{P\text{MIN}} [1 - \cos(2\pi t/t_G)]; & 0 < t < t_G \\ 0 & t < 0 \text{ and } t > t_G \end{cases} \quad (10)$$

where $C_{P\text{MIN}}$ is the minimum pressure coefficient imposed on the cloud and t_G is the nondimensional duration of the pressure perturbation. Consequently, for a cloud flowing with velocity U^* past a body of size D^* , the order of magnitude of t_G will be D^*/R_0^* , and $C_{P\text{MIN}}$ will be the minimum pressure coefficient of the flow.

3 Numerical Method

The natural framework for the present problem is a Lagrangian coordinate system based on the mixture velocity, in which all the nonlinear convective terms in the mixture conservation equations, (1), (2), and Rayleigh-Plesset equation, (3), are eliminated. A Lagrangian integral method based on the integral representation of the continuity and momentum equations in the Lagrangian coordinates, (r_0, t) , has been developed, in which r_0 is the radial distance from the center of the cloud at initial time $t = 0$. The values of other quantities at $t = 0$ are also denoted by a subscript 0. Therefore, the density of a mixture material element, $\rho(r_0, t)$, is related to its initial density, $\rho_0(r_0)$, by

$$\frac{\rho(r_0, t)}{\rho_0(r_0)} = \frac{1}{J} \quad (11)$$

where J is the Jacobian of the coordinate transformation from Lagrangian to Eulerian coordinates: $r_0 \mapsto r(r_0, t)$, and has the following expression in the spherically symmetric configuration:

$$J = \frac{r^2}{r_0^2} \frac{\partial r}{\partial r_0} \quad (12)$$

This also represents the ratio of the current material volume to its initial volume.

The position of a mixture particle can be obtained by integrating (11).

$$r(r_0, t) = \left\{ \frac{3}{3 + 4\pi\eta} \int_0^{r_0} \xi^2 [3 + 4\pi\eta R^3(\xi, t)] d\xi \right\}^{1/3} \quad (13)$$

where ξ is a dummy integration variable and we approximate $\rho(r_0, t)/\rho_0(r_0) \approx [1 - \alpha(r_0, t)]/[1 - \alpha_0(r_0)]$ since the liquid density is very much larger than the vapor density. Note that the boundary condition $r(r_0, t) = 0$ at the center of the cloud has been used to eliminate an integration constant. The mixture velocity can be obtained by differentiating (13):

$$u(r_0, t) = \frac{\partial r(r_0, t)}{\partial t} = \frac{12\pi\eta}{(3 + 4\pi\eta)r^2(r_0, t)} \int_0^{r_0} \frac{\partial R(\xi, t)}{\partial t} R^2(\xi, t) \xi^2 d\xi \quad (14)$$

The mixture momentum equation, (2), and the boundary condition at the surface of the cloud, (7), have the following forms in the Lagrangian coordinate framework:

$$\frac{\partial C_p(r_0, t)}{\partial r_0} = - \frac{6}{3 + 4\pi\eta R^3(r_0, t)} \frac{\partial u(r_0, t)}{\partial t} \frac{\partial r(r_0, t)}{\partial r_0} \quad (15)$$

$$C_p(A_0, t) = C_{p\infty}(t) + \frac{2}{r(A_0, t)} \frac{d}{dt} [r^2(A_0, t)u(A_0, t)] - u^2(A_0, t) \quad (16)$$

After substituting (13) and (14) in the right-hand side of (15) and integrating from r_0 to A_0 using the boundary condition (16), an integral equation for mixture pressure coefficient, $C_p(r_0, t)$, is found:

$$C_p(r_0, t) = \frac{6}{3 + 4\pi\eta} \int_{r_0}^{A_0} \frac{g(\xi, t; C_p) - 2r(\xi, t)u^2(\xi, t)}{r^4(\xi, t)} \xi^2 d\xi + \frac{2g(A_0, t)}{r(A_0, t)} - u^2(A_0, t) + C_{p\infty}(t) \quad (17)$$

where

$$g(\xi, t; C_p) = \frac{12\pi\eta}{3 + 4\pi\eta} \int_0^\xi \left\{ \frac{2}{We} [R^{1-3k}(\zeta, t) - 1] - \frac{4}{Re} \frac{\partial R(\zeta, t)}{\partial t} + \frac{\sigma}{2} R(\zeta, t) [R^{-3k}(\zeta, t) - 1] + \frac{1}{2} R(\zeta, t) \times \left[\left(\frac{\partial R(\zeta, t)}{\partial t} \right)^2 - C_p(\zeta, t) \right] \right\} \zeta^2 d\zeta \quad (18)$$

Here the Rayleigh-Plesset equation, (3), has been used to eliminate the bubble wall acceleration, $\partial^2 R(r_0, t)/\partial t^2$.

These equations form the basis of the present method for solving for these flows. More explicitly, a complete integration time step proceeds as follows:

1. At each Lagrangian node, r_0 , $R(r_0, t + \Delta t)$ and $\partial R(r_0, t + \Delta t)/\partial t$ are calculated using an explicit time marching scheme (an Euler scheme) based on the known solution at the previous time step, $R(r_0, t)$, $\partial R(r_0, t)/\partial t$ and $\partial^2 R(r_0, t)/\partial t^2$.
2. With $R(r_0, t + \Delta t)$ and $\partial R(r_0, t + \Delta t)/\partial t$, Eqs. (13) and (14) can be integrated to obtain $r(r_0, t + \Delta t)$ and $u(r_0, t + \Delta t)$.
3. With the results of steps 1 and 2, we can iterate upon equation (17) to find $C_p(r_0, t + \Delta t)$. Then the Rayleigh-Plesset equation (3) can be used to find $\partial^2 R(r_0, t + \Delta t)/\partial t^2$. Under-relaxation was necessary to make this iterative process converge. This and other numerical difficulties are discussed in Wang (1996).
4. Proceed to next time step.

The interval of each time step is automatically adjusted during the computation to ensure that the maximum fractional change of bubble radius in the cloud between any two consecutive times does not exceed some specific value (typically, 5%). This is essential for time marching through a violent bubble collapse. The number of Lagrangian nodes is 100 in all the computational results presented here. Nodal numbers of 200 and 400 were used to check the grid independence of the results.

4 Results and Discussion

The following typical flow variables were chosen to illustrate the calculated results. A cloud of nuclei, composed of air bubbles of initial radius $R_0^* = 100 \mu\text{m}$ in water at 20°C ($\rho_L^* = 1000 \text{ kg/m}^3$, $S^* = 0.0728 \text{ N/m}$) flows with velocity $U^* = 10 \text{ m/s}$ through a region of low pressure characterized by Eq. (10). The computation is performed for different combinations of the following parameters: the minimum pressure coefficient, $C_{p\text{MIN}}$, of -0.7 and -0.75 ; a nondimensional duration of the pressure perturbation, t_G , ranging from 50 to 1000; an initial void fraction, α_0 , ranging from 0.02% to 5%; a cavitation number, σ , ranging from 0.4 to 0.65; a nondimensional cloud radius, A_0 , of 32, 100, and 312. These ranges of values of A_0 and t_G correspond to the ratio of the length-scale of the pressure perturbation to the initial radius of the cloud, D/A_0 , of 0.5 to 31.25, values which cover the range of experimental observations. The value of bubble radius, R_0^* , and the range of values of void fraction result in the bubble population, η^* , ranging approximately from 50 to 12600 $1/\text{cm}^3$. Although bubble population is strongly dependent on facility, the above range is reasonable compared to the observation in realistic cavitating flows (see, for example, Maeda et al., 1991). The Reynolds number, based on the reference flow velocity, initial bubble radius, the liquid density, and the effective viscosity, is 28.6 in all the cases presented. Recall that an effective liquid viscosity, $\mu_E^* = 0.035 \text{ Ns/m}^2$, is used in place of actual liquid viscosity to incorporate the various bubble damping mechanisms (Chapman and Plesset 1971).

4.1 Cloud Interaction Parameter. One of the complexities of multiphase flows is the existence of different characteristic time or length scales and the interactions between them. In cloud cavitation one of the most important factors is the effect of the bubble dynamics on the global flow fields. The parameter controlling this effect is $\beta \equiv \alpha_0(1 - \alpha_0)A_0^2/R_0^2$, which will be termed the "cloud interaction parameter." Here, α_0 is the initial void fraction of the cloud, A_0 is the initial cloud radius and R_0 is the initial bubble radius. In the present study, we will show that the nonlinear cloud dynamics were strongly dependent on this parameter. Earlier linear and weakly nonlinear studies of cloud dynamics (d'Agostino and Brennen, 1983, 1989; Kumar and Brennen, 1991, 1993) showed that the cloud natural frequency is strongly dependent on this parameter. If β is small, the natural frequency of the cloud is close to that of the individual bubbles in the cloud. In other words, the bubbles in the cloud tend to behave as individual units in an infinite fluid and the bubble/bubble interaction effects are minor. Then the dynamic effects of the cloud are approximately the sum

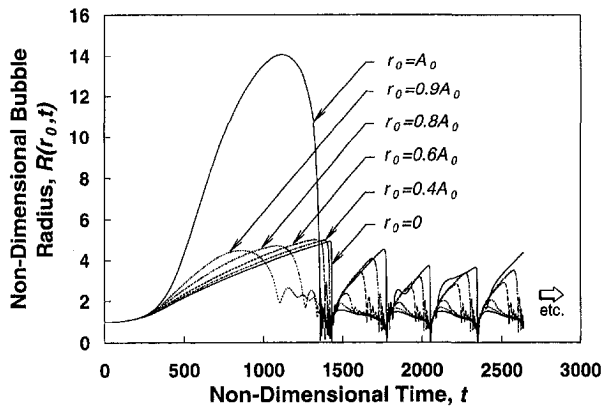


Fig. 2 The time history of the dimensionless bubble size at six different Lagrangian positions in the cloud for $\sigma = 0.4$, $C_{P\text{MIN}} = -0.7$, $\alpha_0 = 5\%$, $A_0 = 100$, and a ratio of the low pressure perturbation length-scale to initial cloud radius, $D/A_0 = 10$ (corresponds to $t_G = 1000$). The cloud interaction parameter, β , is 475 in this case.

of the effects of the individual bubbles in the cloud. On the other hand the bubble interaction effects in the cloud are dominant when the value of β is greater than order one. Then the collective oscillation of bubbles in the cloud results in a cloud natural frequency which is lower than the natural frequency of individual bubbles.

In the expression of β , A_0 is the macroscopic length-scale in the flow, R_0 characterizes the microscale, and $\alpha_0(1 - \alpha_0) \approx \alpha_0$ represents the concentration of the dispersed phase. It is useful to mention one physical interpretation of β . The sonic speed in a bubbly mixture of void fraction α_0 without viscosity and surface tension effects is approximately (see, for example, Brennen, 1995)

$$c^* = \left[\frac{kp^*}{\alpha_0(1 - \alpha_0)\rho_L^*} \right]^{1/2} \quad (19)$$

where p^* is the mixture pressure and k is the polytropic index of the gas inside the bubble. The natural frequency of bubbles in the mixture is approximately

$$\omega_B^* = \left(\frac{3kp^*}{\rho_L^* R_0^{*2}} \right)^{1/2} \quad (20)$$

where R_0^* is the bubble radius. But the characteristic global dimension of the flow is the radius of the cloud, A_0^* , and, consequently, there are two dynamic time-scales in the flow: the time-scale of bubble dynamics, $T_B^* \equiv 1/\omega_B^*$, and the time-scale of wave propagation through the cloud, $T_c^* \equiv 1/\omega_c^* = A_0^*/c^*$. The ratio of these two characteristic times is

$$\frac{T_c^*}{T_B^*} \approx \left[\frac{\alpha_0(1 - \alpha_0)A_0^{*2}}{R_0^{*2}} \right]^{1/2} = \sqrt{\beta} \quad (21)$$

Therefore, β determines the ratio of the two characteristic times in the flow. If β is small, the bubbles are little affected by the global perturbations in the flow and the global interactions are weak. On the other hand, if β is much larger than order one, the bubble dynamics can effectively influence the large scale perturbations and contribute to the global dynamics of the cloud.

4.2 Nonlinear Growth and Collapse of the Cloud With Various Cloud Interaction Parameters, β . For the case of a large value of β , Fig. 2 ($\beta = 475$) presents typical time histories of bubble radius for six different Lagrangian locations, r_0 , within the cloud, from the surface, $r_0 = A_0$, to the center, $r_0 = 0$. It is clear that the bubble growth rate decreases greatly with increasing distance from the cloud surface. This is due to bubble/bubble interaction in the cloud. The bubbles in the interior are shielded by the surface shell of bubbles and grow to a smaller maximum size.

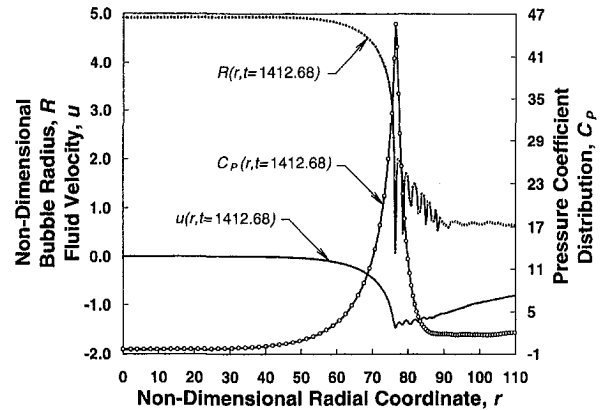


Fig. 3 Bubble size, fluid velocity, and pressure distributions in the inward propagating shock wave at a sample moment in time, $t = 1412.68$. Parameters as in Fig. 2.

This shielding effect is typical of the bubble interaction phenomenon appearing in the earlier investigations of cloud dynamics (see, for example, d'Agostino and Brennen, 1983, 1989; Omta, 1987; Smereka and Banerjee, 1988; Chahine and Duraiswami, 1992).

After the recovery of the ambient pressure, bubbles near the surface (at $r_0 = 0.9A_0$ in the present case) of the cloud start to collapse first and the collapse propagates inward. Meanwhile, bubbles on the surface of the cloud keep growing due to their large growth rate and collapse later. If the duration of the pressure perturbation, t_G , is sufficiently short (say, $t_G = 500$), the collapse is forced to start from the surface of the cloud (see Wang and Brennen, 1995). Note that the shielding effect causes the bubbles in the interior region to continue to grow even after the surface-layer bubbles have collapsed.

As a result of the inward propagating collapse, a bubbly shock wave develops. To illustrate a typical transient structure of this shock wave, Fig. 3 shows spatial distribution of bubble radius, fluid velocity, and fluid pressure coefficient at one moment in time. The shock wave has progressed inward to a Eulerian position, $r \approx 76$. The wave front of the shock can be easily identified by the bubble collapse front. Unlike gas dynamic shock waves, the bubbly shock has an oscillatory structure behind the shock front which involves a series of rebounds and secondary collapses. This structure is very similar to that of the gas/liquid shocks investigated by Noordzij and van Wijngaarden (1974) (see also Brennen, 1995, Section 6.9). The locations with small bubble size represent regions of low void fraction and higher pressure due to the local bubble collapse. It is clear that the collapse of bubbles induces inward flow acceleration which creates a local pressure gradient and promotes more violent collapse of the neighboring bubbles. As the shock front passes bubbles and causes them to collapse, a very large pressure pulse can be produced, as shown in Fig. 3. The dimensional magnitude of the peak is about 46 atm in this case. Oscillations in the pressure resulting from secondary collapses do occur but are dwarfed by the primary pressure pulse and are not therefore seen in Fig. 3.

The shock wave strengthens considerably as it propagates into the cloud primarily because of the focusing effect of the spherical configuration. The strengthening of the shock can be seen in Fig. 2; the closer the bubbles are to the cloud center, the smaller the size to which they collapse. Very complicated bubble-bubble interactions are observed when the focusing shock reaches the center of the cloud (at $t \approx 1430$ in the case shown). Very high pressures are generated which cause a rebound of the cloud. Then a spreading expansion wave causes all bubbles to grow and starts another cycle of cloud oscillation.

In the case of small β , the cloud exhibits very different dynamics, as shown in Fig. 4 ($\beta \approx 2$). The bubbles in the cloud now have

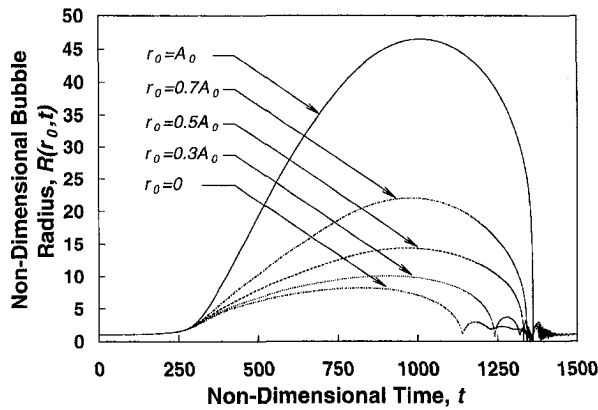


Fig. 4 The time history of the dimensionless bubble size at five different positions in the cloud for $\alpha_0 = 0.02\%$ and $D/A_0 = 10$ (corresponds to $t_G = 1000$). Other parameters as in Fig. 2. The cloud interaction parameter, $\beta \approx 2$.

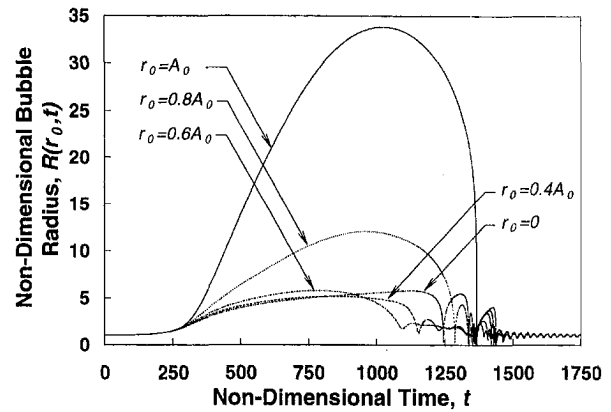


Fig. 6 The time history of the dimensionless bubble size at five different positions in the cloud for $\alpha_0 = 0.1\%$ and $D/A_0 = 10$ (corresponds to $t_G = 1000$). Other parameters as in Fig. 2. The cloud interaction parameter, $\beta \approx 10$.

weaker interactions and, therefore, grow to a larger size. However, the inner bubbles still have a smaller growth rate than that of the outer bubbles. As a result, the inner bubbles grow to a size which is an order of magnitude smaller than that of the surface bubbles. But, more importantly, the inner bubbles collapse first. The collapse then spreads outward and results in an outward propagating shock, as shown in Fig. 5. Obviously, no geometric focusing occurs and the pressure and noise generated by the collapse are much smaller than when $\beta \gg 1$.

When β has an intermediate order of magnitude, as illustrated in Fig. 6, the collapse starts at mid-radius ($0.6A_0$ in the case of Fig. 6) and spreads inward and outward from this location. The outward moving collapse tends to cancel the inward acceleration of the flow caused by the collapse of the bubbles on the cloud surface. The inward moving collapse has a structure similar to the shock wave described in Fig. 3. However, the shock-enhancing effect is weaker than in the case of large β due to the reduced "effective collapse size" of the cloud.

We note that Mørch, Hanson and Kedrinskii (Mørch, 1980, 1981, 1982; Hanson et al., 1981) first suggested that the collapse of a cloud of bubbles involves an inwardly propagating shock wave. Results of the present analysis confirm the formation of the shock waves which, however, can propagate in either direction, depending on the value of β in the cloud.

4.3 Far-Field Noise Generated by the Cloud. In this section, we examine the far-field noise generated by typical cloud dynamics. If $V^*(t^*)$ denotes the time-varying volume of the cloud,

then the far-field acoustic pressure produced by the volumetric acceleration of the cloud is given by (Dowling and Ffowcs-Williams, 1983; Blake, 1986)

$$p_a^*(t^*) = \frac{\rho_L^*}{4\pi r^*} \frac{d^2 V^*(t^*)}{dt^{*2}}, \quad (22)$$

where p_a^* is the dimensional radiated acoustic pressure and r^* is the distance from the cloud center to the point of measurement. We have neglected the acoustic contributions from individual bubbles since they are minor in the far field. For present purposes a normalized far-field acoustic pressure is defined as

$$p_a(t) = \frac{p_a^* r^*}{\frac{1}{2} \rho_L^* U^{*2} D^*} = \frac{2R_0}{D} \left[A^2(t) \frac{d^2 A(t)}{dt^2} + 2A(t) \left(\frac{dA(t)}{dt} \right)^2 \right] \quad (23)$$

where the normalizing length-scale was chosen to be D^* , the typical length of the pressure perturbation experienced by the cloud. In practice, D^* will be comparable to the size of the body, for example, the chord of a propeller blade. A typical example of the time history of the cloud radius and the far-field acoustic pressure is given in Fig. 7. Here, the ratio of the pressure perturbation length-scale to initial size of the cloud, D/A_0 , is chosen as 2 (which corresponds to the duration of the pressure perturbation, $t_G = 200$), small enough to cause the collapse to start from the

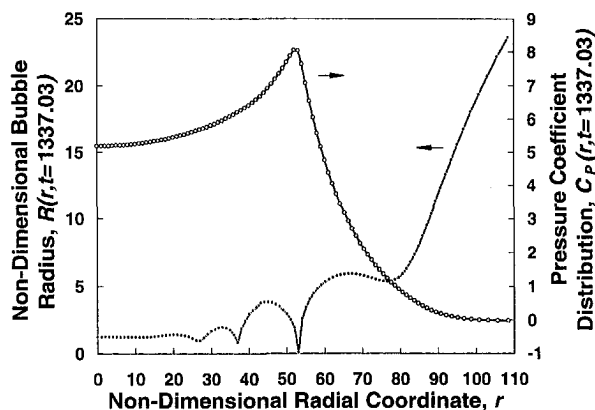


Fig. 5 Bubble size and pressure distributions in the outward propagating shock wave at a sample moment in time, $t = 1337.03$. Parameters as in Fig. 4.

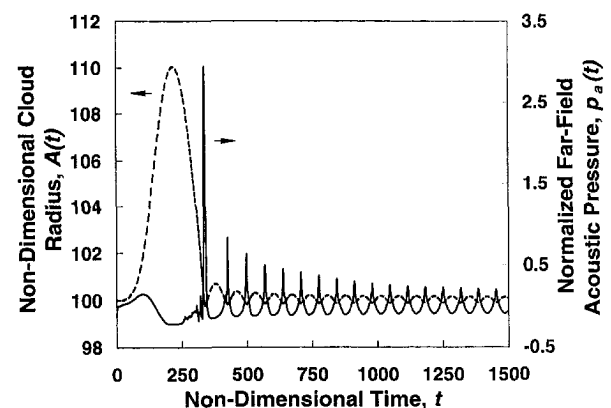


Fig. 7 The time history of the dimensionless cloud radius and the resulting far-field noise for $\alpha_0 = 0.8\%$ and $D/A_0 = 2$ (corresponds to $t_G = 200$). Other parameters as in Fig. 2.

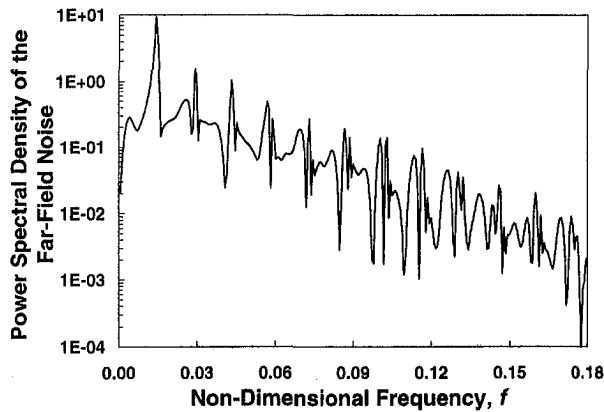


Fig. 8 The nondimensional power spectral density of the far-field noise in Fig. 7 as a function of dimensionless frequency. The lowest cloud natural frequency is about 0.015. The natural frequency of single bubbles in the cloud is 0.158.

cloud surface and, therefore, to result in coherent oscillation of the cloud. It is interesting that, unlike single bubbles, the cloud only collapses to a size marginally smaller than its equilibrium size. However, the void fraction within the cloud undergoes large changes. This is consistent with the recent experimental observations of unsteady cloud collapse by Reisman et al. (1998).

As illustrated in Section 4.2, an inward propagating shock wave develops during the collapse process. When the enhanced shock wave reaches to the center of the cloud, large impulsive noise is generated, as shown in Fig. 7. The first collapse is followed by successive rebounds and collapses which also produce radiated pulses. The magnitudes of the subsequent pulses decay with time due to the attenuation from bubble damping mechanisms. After several cycles, the cloud begins to oscillate at its natural frequency.

Figure 8 presents the power spectral density of the far-field noise in Fig. 7 as a function of dimensionless frequency, f , which is nondimensionalized by the time scale, R_0^*/U^* . This spectrum exhibits an average f^{-2} decay over the frequency range used. This behavior is typical of the cavitation noise associated with cavitating bodies or hydrofoils (see, for example, Blake et al., 1977; Arakeri and Shangumanathan, 1985; Ceccio and Brennen, 1991; Reisman et al., 1998). Other computational cases exhibited an average f^{-n} behavior with n in the range of 0.5 to 2.

The first and highest peak in Fig. 8 corresponds to the first natural frequency of the cloud, $f = 0.015$ (or 1.5 kHz in dimensional terms), in the present case. Higher harmonics of the first cloud natural frequency are also present in the spectrum and reflect the high degree of nonlinearity in the cloud dynamics. Another significant feature of the spectrum is that most of the energy is in the lower frequency range and is due to the coherent dynamics of the cloud. Note that in their cavitation experiments both Marboe et al. (1986) and Arakeri and Shangumanathan (1985) observed a tendency for the noise spectrum to shift towards lower frequencies at higher bubble densities. Bubble interactions were speculated to be the cause and this conjecture is strengthened by the present results.

To determine the magnitude of noise, the far-field acoustic impulse, I , is defined as the area under the largest pulse of the pressure signal or

$$I = \int_{t_1}^{t_2} p_a(t) dt, \quad (24)$$

where t_1 and t_2 are times before and after the pulse at which the acoustic pressure, p_a , is zero. Figure 9 presents the acoustic impulse as a function of the cloud interaction parameter, β , for flows with different cavitation numbers, σ , and different ratios of the pressure perturbation length-scale to initial cloud size, D/A_0 . In

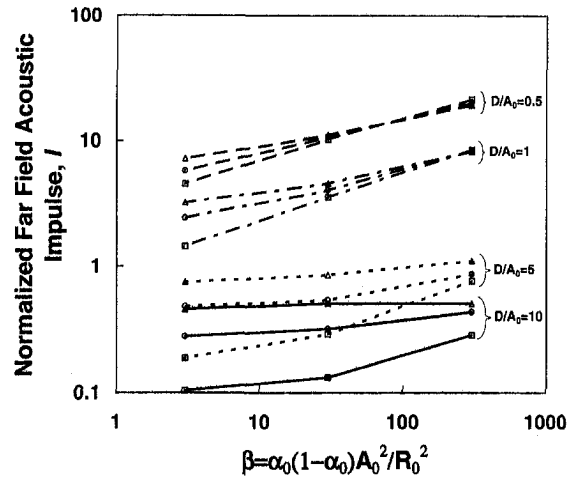


Fig. 9 The impulse of the normalized far-field noise, I , as a function of the cloud interaction parameter, β , for different values of D/A_0 and three cavitation numbers, σ (0.45 = Δ , 0.55 = \circ , 0.65 = \square). Other parameters are $C_{MIN} = -0.75$ and $A_0/R_0 = 100$.

all cases, the impulse increases with increasing β . Moreover, for larger D/A_0 , there is a larger difference in different cavitation numbers. This is because the recovery of the ambient pressure of the cloud is slower and, therefore, the bubbles have more time to cavitate. Under these circumstances the degree of cavitation in the cloud and the resulting acoustic impulse increases with decreasing cavitation number. On the other hand, if D/A_0 is small, the cloud will not have cavitated much before the recovery of the ambient pressure. Therefore, the influence of the cavitation number is smaller.

To investigate the relationship of the acoustic impulse to various parameters of the flow, calculations using a wide variety of parameter choices (45 permutations) were performed. It was found that the acoustic impulse is linearly correlated with the maximum total volume of the bubbles in the cloud normalized by the pressure perturbation length-scale, $V_{BMAX}/(0.5D)^3$, as shown in Fig. 10. Moreover, as illustrated in Fig. 11, this total volume decreases with increasing cavitation number and with increase in initial void fraction. It also varies with D/A_0 .

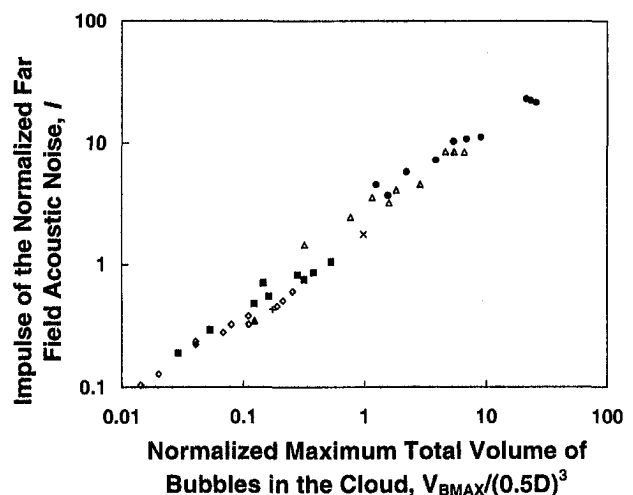


Fig. 10 The impulse of the normalized far-field noise as a function of the normalized maximum total volume of bubbles in the cloud at different values of D/A_0 (31.25 = solid Δ , 15.625 = +, 10 = \diamond , 5 = solid \square , 3.125 = \times , 1 = Δ , 0.5 = \bullet). Three different cavitation numbers, σ , of 0.45, 0.55, and 0.65, and three different initial void fractions, α_0 , of 0.03%, 0.3%, and 3% are used. Other parameters are $C_{MIN} = -0.75$ and three different initial cloud radii, A_0/R_0 , of 31, 100, and 312.

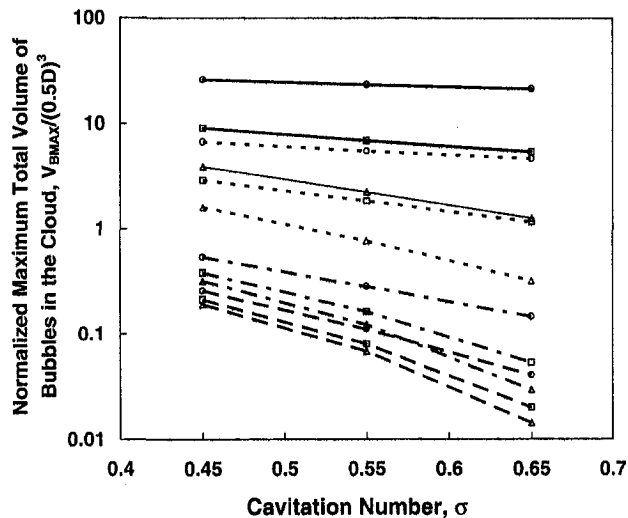


Fig. 11 The normalized maximum total volume of bubbles in the cloud as a function of cavitation number. Data is shown for $C_{P\text{MIN}} = -0.75$, four different values of D/A_0 (0.5 = solid lines, 1.0 = dotted lines, 5.0 = dash-dot lines, 10 = dashed lines) and three initial void fractions, α_0 (3% = \circ , 0.3% = \square , 0.03% = \triangle). Other parameters as in Fig. 4.

4.4 Shock Speed. Figure 12 shows the inward propagation speed of the spherical bubbly shock wave (normalized by U^*) as a function of the location of the shock front for three different initial void fractions, α_0 , of 0.03%, 0.3%, and 3%. In each case, the speed of the shock when it is initially formed at the outer radii in the cloud is of the order of 10 m/s, a little larger than the local sonic speed. The local sonic speed can be estimated using Eq. (19) in which the fluid pressure and the void fraction upstream of the shock should be employed. For example, the sonic speed upstream of the shock in Fig. 3 is approximately 8 m/s (assuming $p_0^* = 1$ atm). The shock speed increases considerably as the strengthening shock propagates into the cloud. The increase in the speed is very pronounced over the last 20% of the collapse so that the shock speed near the center of the cloud is an order of magnitude larger than that in the outer region. The speed is $O(10^2$ m/s) for the larger void fractions used here and can reach $O(10^4$ m/s) for the smallest void fraction ($\alpha_0 = 0.03\%$). If these shock pulses passed over a pressure transducer in a cavitating flow, the typical durations of the output signals would range from 10^{-4} s to 10^{-6} s.

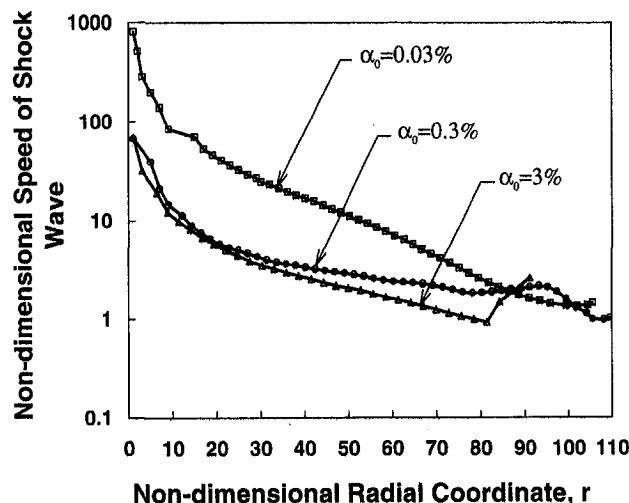


Fig. 12 The speed of the inward propagating bubbly shock wave as a function of shock front position in the cloud for three different initial void fractions. Other parameters are $C_{P\text{MIN}} = -0.75$, $\sigma = 0.45$, $D/A_0 = 5$, and $A_0/R_0 = 100$.

4.5 Comparison With Experimental Observations. Earlier measurements of the noise produced by cloud cavitation are characterized by pressure pulses of very short duration and large magnitude (see, for example, Bark and Berlekorn, 1978; Shen and Peterson, 1978; Bark, 1985; Reisman and Brennen, 1996). However, the basic mechanism for the production of these pulses was not clear. The present theory suggests that the formation and concentration of the bubbly shock waves could be responsible. Recently, experimental investigations of the large unsteady and impulsive pressures which are experienced on the suction surface of an oscillating hydrofoil as a result of cloud cavitation were conducted (Brennen et al., 1996; Reisman et al., 1998). The experiments used piezo-electric transducers to measure the unsteady pressures at four locations along the chord of the foil and at two locations along the walls of the tunnel test section. The transducers on the foil surface registered very large positive pressure pulses with amplitudes of $O(10$ bar) with durations of $O(10^{-4}$ sec). These orders of magnitudes are in the same range as the present calculations. Moreover, it was found that the pressure pulses moved with speeds of $O(10-100$ m/sec) in agreement with the range predicted by the present theory.

5 Concluding Remarks

The nonlinear growth and collapse of a spherical cloud of cavitation bubbles has been computed using fully nonlinear continuum mixture equations coupled with the Rayleigh-Plesset equation for the dynamics of the bubbles. This system is solved numerically using a Lagrangian integral method. It is shown that a bubbly shock wave develops as part of the nonlinear collapse of the bubble cloud. The dynamics and acoustic consequences of the shock wave are strongly dependent on the cloud interaction parameter, $\beta = \alpha_0(1 - \alpha_0)A_0^2/R_0^2$, where, α_0 is the initial void fraction of the cloud, A_0 is the initial cloud radius and R_0 is the initial bubble radius. For a cloud with large β , the shock wave forms near the surface of the cloud and propagates inward. The strength and the speed of the shock increase considerably due to the geometric focusing. Very high pressure pulses are produced when the shock wave passes the bubbles in the cloud and causes them to collapse. Moreover, the enhanced shock produces very high pressures at the center of the cloud and then causes the rebound of the cloud. The volumetric acceleration of the cloud induces a large pulse in the far-field noise.

When β is small, shock enhancement does not occur. Rather bubble collapse first occurs in the center of the cloud and results in an outward propagating shock wave. At intermediate β the collapse starts at mid-radius and propagates inward and outward simultaneously. These shock wave dynamics, however, also depend on the duration of the pressure perturbation imposed on the cloud. If the cloud experiences a short period of depressurization, bubble collapse will start at the cloud surface.

Understanding such bubbly flow and shock wave processes is important because these flow structures propagate the noise and produce the impulsive loads on nearby solid surfaces in a cavitating flow. The results of this research suggest that large value of β promotes the formation and focusing of a bubbly shock wave which is one of the major mechanisms for the enhanced noise and damage potential associated with cloud cavitation. Parenthetically, this requires either the initial void fraction or the ratio of cloud size to bubble size be sufficiently large and this, in turn, is qualitatively in accord with the observation that cavitation must be quite extensive for the cloud phenomenon to be manifest. Furthermore, this implies that bubble/bubble interaction effects play a crucial role in cloud cavitation noise and damage.

The theoretical results shed some light on previous experimental observations of cloud cavitation (Bark and Berlekorn, 1978; Shen and Peterson, 1978; Bark, 1985; Franc and Michel, 1988; Kubota et al., 1989; Reisman and Brennen, 1996; Reisman et al., 1998). Experimental measurements of the noise produced by cloud cavitation all exhibit pressure pulses of very short duration and large

amplitude. These pulses have magnitudes on the order of tens of atmospheres with typical durations of the order of tens of milliseconds (see, for example, Reisman et al., 1998). Moreover, these pulses appear to propagate through the bubbly cloud with speeds ranging from $O(10)$ m/s to $O(100)$ m/s (Brennen et al., 1996; Reisman et al., 1998). These magnitudes are consistent with the present calculations.

It also appears that an understanding of the collapse shock dynamics and acoustics has important consequences and implications for the scaling of cloud cavitation noise and damage. For example, the β values could be very different for the model and the prototype; frequently, α_0 and R_0 will be similar but A_0 will be quite different. This could cause severe cloud cavitation in the prototype which might not show up in the model if the model values of β were small.

Finally we should note that, of course, most clouds are not spherical. Nevertheless the collapse of all or part of non-spherical clouds will produce points at which shock waves focus to produce large local and radiated pulses. Sturtevant and Kulkarny (1976) present a useful review of the various gasdynamic shock wave focusing phenomena including the effects of inhomogeneous media. However, it is not currently clear what three-dimensional forms the propagating bubbly shock waves might take in the highly non-uniform bubbly environments which occur in real cavitating flows.

Acknowledgments

The authors are very grateful for the support for this research provided by National Science Council, Taiwan, R.O.C., under Contract NSC 87-TPC-E-006-009 and by the Office of Naval Research under Contract N00014-91-J-1295.

References

Arakeri, V. H., and Shangumanathan, V., 1985, "On the Evidence for the Effect of Bubble Interference on Cavitation Noise," *Journal of Fluid Mechanics*, Vol. 159, pp. 131–150.

Bark, G., 1985, "Developments of Distortions in Sheet Cavitation on Hydrofoils," *Proceedings of the ASME International Symposium on Jets and Cavities*, pp. 470–493.

Bark, G., and Berlekom, W. B., 1978, "Experimental Investigations of Cavitation Noise," *Proceedings of the 12th ONR Symposium on Naval Hydrodynamics*, pp. 470–493.

Biesheuvel, A., and van Wijngaarden, L., 1984, "Two Phase Flow Equations for a Dilute Dispersion of Gas Bubbles in Liquid," *Journal of Fluid Mechanics*, Vol. 148, pp. 301–318.

Birnir, B., and Smereka, P., 1990, "Existence Theory and Invariant Manifolds of Bubble Cloud," *Communications on Pure and Applied Mathematics*, Vol. 43, pp. 363–413.

Blake, W. K., 1986, *Mechanics of Flow-Induced Sound and Vibration*, Academic Press.

Blake, W. K., Wolpert, M. J., and Geib, F. E., 1977, "Cavitation Noise and Inception As Influenced by Boundary-Layer Development on a Hydrofoil," *Journal of Fluid Mechanics*, Vol. 80, pp. 617–640.

Brennen, C. E., 1995, *Cavitation and Bubble Dynamics*, Oxford University Press, New York.

Brennen, C. E., Reisman, G. E., and Wang, Y.-C., 1996, "Shock Waves in Cloud Cavitation," *Proceedings of the 21th ONR Symposium on Naval Hydrodynamics*, Trondheim, Norway.

Ceccio, S. L., and Brennen, C. E., 1991, "Observations of the Dynamics and Acoustics of Travelling Bubble Cavitation," *Journal of Fluid Mechanics*, Vol. 233, pp. 633–660.

Chahine, G. L., 1982a, "Pressure Field Generated by the Collective Collapse of Cavitation Bubbles," *IAHR Symposium on Operating Problems of Pump Stations and Power Plants*, Amsterdam, The Netherlands, Vol. 1(2), pp. 1–12.

Chahine, G. L., 1982b, "Cloud Cavitation: Theory," *Proceedings of the 14th ONR Symposium on Naval Hydrodynamics*, National Academy Press, pp. 165–194.

Chahine, G. L., and Duraiswami, R., 1992, "Dynamical Interactions in a Multibubble Cloud," *ASME JOURNAL OF FLUIDS ENGINEERING*, Vol. 114, pp. 680–686.

Chahine, G. L., Duraiswami, R., and Rebut, M., 1992, "Analytical and Numerical Study of Large Bubble/Bubble and Bubble/Flow Interactions," *Proceedings of the 19th ONR Symposium on Naval Hydrodynamics*, Seoul, South Korea.

Chapman, R. B., and Plesset, M. S., 1971, "Thermal Effects in the Free Oscillation of Gas Bubbles," *ASME Journal of Basic Engineering*, Vol. 93, pp. 373–376.

d'Agostino, L., and Brennen, C. E., 1983, "On the Acoustical Dynamics of Bubble Clouds," *ASME Cavitation and Multiphase Flow Forum*, Houston, TX, pp. 72–75.

d'Agostino, L., and Brennen, C. E., 1989, "Linearized Dynamics of Spherical Bubble Clouds," *Journal of Fluid Mechanics*, Vol. 199, pp. 155–176.

Dowling, A. P., and Ffowcs-Williams, J. E., 1983, *Sound and Sources of Sound*, Ellis Horwood Ltd. and John Wiley.

Franc, J. P., and Michel, J. M., 1988, "Unsteady Attached Cavitation on an Oscillating Hydrofoil," *Journal of Fluid Mechanics*, Vol. 193, pp. 171–189.

Hanson, I., Kedrinskii, V. K., and Mørch, K. A., 1981, "On the Dynamics of Cavity Clusters," *Journal of Applied Physics*, Vol. 15, pp. 1725–1734.

Ishii, M., 1975, *Thermo-Fluid Dynamic Theory of Two-Phase Flow*, Eyrolles.

Kameda, M., and Matsumoto, Y., 1995, "Structure of Shock Waves in a Liquid Containing Gas Bubbles," *IUTAM Symposium on Waves in Liquid/Gas and Liquid/Vapour Two-Phase Systems*, Morioka, S., and van Wijngaarden, L., eds., Kluwer Academic Publishers, Dordrecht, The Netherlands, pp. 117–126.

Kubota, A., Kato, H., Yamaguchi, H., and Maeda, M., 1989, "Unsteady Structure Measurement of Cloud Cavitation on a Foil Section Using Conditional Sampling," *ASME JOURNAL OF FLUIDS ENGINEERING*, Vol. 111, pp. 204–210.

Kubota, A., Kato, H., and Yamaguchi, H., 1992, "A New Modelling of Cavitating Flows: A Numerical Study of Unsteady Cavitation on a Hydrofoil Section," *Journal of Fluid Mechanics*, Vol. 240, pp. 59–96.

Kumar, S., and Brennen, C. E., 1991, "Non-linear Effects in the Dynamics of Clouds of Bubbles," *Journal of the Acoustical Society of America*, Vol. 89, pp. 707–714.

Kumar, S., and Brennen, C. E., 1993, "Some Nonlinear Interactive Effects in Bubbly Cavitating Clouds," *Journal of Fluid Mechanics*, Vol. 253, pp. 565–591.

Maeda, M., Yamaguchi, H., and Kato, H., 1991, "Laser Holography Measurement of Bubble Population in Cavitation Cloud on a Foil Section," *ASME Cavitation and Multiphase Flow Forum*, Portland, Oregon, FED Vol. 116, pp. 67–75.

Marboe, R. C., Billet, M. L., and Thompson, D. E., 1986, "Some Aspects of Traveling Bubble Cavitation and Noise," *Proceedings of the ASME International Symposium on Cavitation and Multiphase Flow Noise*, FED Vol. 45, pp. 119–126.

Mørch, K. A., 1980, "On the Collapse of Cavity Cluster in Flow Cavitation," *Proceedings of the 1st International Conference on Cavitation and Inhomogeneities in Underwater Acoustics*, Lauterborn, W., ed., Springer Series in Electrophysics, Vol. 4, pp. 95–100.

Mørch, K. A., 1981, "Cavity Cluster Dynamics and Cavitation Erosion," *Proceedings of the ASME Cavitation and Polyphase Flow Forum*, pp. 1–10.

Mørch, K. A., 1982, "Energy Considerations on the Collapse of Cavity Cluster," *Applied Scientific Research*, Vol. 38, p. 313.

Nigmatulin, R. I., 1991, *Dynamics of Multiphase Media*, Hemisphere, New York.

Noordzij, L., and van Wijngaarden, L., 1974, "Relaxation Effects, Caused by Relative Motion, on Shock Waves in Gas-Bubble/Liquid Mixtures," *Journal of Fluid Mechanics*, Vol. 66, pp. 115–143.

Omta, R., 1987, "Oscillations of a Cloud of Bubbles of Small and Not So Small Amplitude," *Journal of the Acoustical Society of America*, Vol. 82, pp. 1018–1033.

Plesset, M. S., and Prosperetti, A., 1977, "Bubble Dynamics and Cavitation," *Annual Review of Fluid Mechanics*, Vol. 9, pp. 145–185.

Prosperetti, A., 1988, "Bubble-Related Ambient Noise in the Ocean," *Journal of the Acoustical Society of America*, Vol. 84, pp. 1042–1054.

Reisman, G. E., and Brennen, C. E., 1996, "Pressure Pulses Generated by Cloud Cavitation," *ASME Symposium on Cavitation and Gas-Liquid Flows in Fluid Machinery and Devices*, San Diego, California, FED Vol. 236, pp. 319–328.

Reisman, G. E., Wang, Y.-C., and Brennen, C. E., 1998, "Observations of Shock Waves in Cloud Cavitation," *Journal of Fluid Mechanics*, Vol. 355, pp. 255–283.

Sangani, A. S., 1991, "A Pairwise Interaction Theory for Determining the Linear Acoustic Properties of Dilute Bubbly Liquids," *Journal of Fluid Mechanics*, Vol. 232, pp. 221–284.

Shen, Y., and Peterson, F. B., 1978, "Unsteady Cavitation on an Oscillating Hydrofoil," *Proceedings of the 12th ONR Symposium on Naval Hydrodynamics*, pp. 362–384.

Smereka, P., and Banerjee, S., 1988, "The Dynamics of Periodically Driven Bubble Clouds," *Physics of Fluids*, Vol. 31(12), pp. 3519–3531.

Soyama, H., Kato, H., and Oba, R., 1992, "Cavitation Observations of Severely Erosive Vortex Cavitation Arising in a Centrifugal Pump," *Proceedings of the Third IMechE International Conference on Cavitation*, pp. 103–110.

Sturtevant, B., and Kulkarny, V. J., 1976, "The Focusing of Weak Shock Waves," *Journal of Fluid Mechanics*, Vol. 73, pp. 651–680.

Wade, R. B., and Acosta, A. J., 1966, "Experimental Observations on the Flow Past a Plano-Convex Hydrofoil," *ASME Journal of Basic Engineering*, Vol. 88, pp. 273–283.

Wang, Y.-C., 1996, "Shock Waves in Bubbly Cavitating Flows," Ph.D. thesis, California Institute of Technology, Pasadena, CA.

Wang, Y.-C., and Brennen, C. E., 1994, "Shock Wave Development on the Collapse of a Cloud of Bubbles," *ASME Cavitation and Multiphase Flow Forum*, Furuya, O., and Katz, J., eds., FED Vol. 194, pp. 15–19.

Wang, Y.-C., and Brennen, C. E., 1995, "The Noise Generated by the Collapse of a Cloud of Cavitation Bubbles," *ASME/JSM Symposium on Cavitation and Gas-Liquid Flow in Fluid Machinery and Devices*, Ceccio, S. L., Furukawa, A., and Kim, J. H., eds., FED Vol. 226, pp. 17–29.

van Wijngaarden, L., 1964, "On the Collective Collapse of a Large Number of Gas Bubbles in Water," *Proceedings of the 11th International Congress on Applied Mechanics*, Springer-Verlag, Berlin, pp. 854–861.

Effects of Nuclei Size Distribution on the Dynamics of a Spherical Cloud of Cavitation Bubbles

Yi-Chun Wang

Assistant Professor,
Department of Mechanical Engineering,
National Cheng Kung University,
Tainan 701, Taiwan

The nonlinear dynamics of a spherical bubble cloud with nuclei size distribution are studied numerically. The spectrum of nuclei is assumed uniform initially. The simulations employ a nonlinear continuum bubbly mixture model with consideration of the presence of bubbles of different sizes. This model is then coupled with the Rayleigh-Plesset equation for the dynamics of bubbles. A numerical method based on the integral representation of the mixture continuity and momentum equations in the Lagrangian coordinates is developed to solve this set of integro-differential equations. Computational results show that the nuclei size distribution has significant effects on the cloud dynamics in comparison to the results for a single bubble size. One important effect is that the bubble collapse is always initiated near the surface of the cloud, even if the cloud has a very small initial void fraction. This effect has an important consequence, namely that the geometric focusing of the bubbly shock wave is always a part of the nonlinear dynamics associated with the collapse of a spherical cloud with nuclei size distribution. The strength of the shock and the oscillation structure behind the shock front are suppressed due to the effects of multiple bubble sizes.

Far-field acoustic pressures radiated by two bubble clouds, one of equal-size bubbles and the other with bubble size distribution, are also compared. It is found that the cloud containing bubbles of different sizes emits a larger noise than the cloud of identical bubbles. Explanations for this effect are also presented.

Introduction

The dynamics of cloud cavitation have attracted much attention during the last few decades. Numerous experimental observations have demonstrated the intensive noise and erosion produced by collapse of clouds of cavitation bubbles (see, for example, Bark and Berlekom, 1978; Shen and Peterson, 1978, 1980; Bark, 1985; Soyama et al., 1992; Le et al., 1993; Reisman et al., 1994). However, there is no clear explanation for the enhancement of these deleterious effects. Recently Wang, Brennen, and Reisman (see, Wang and Brennen, 1995, 1999; Reisman et al., 1998) have conducted numerical and experimental investigations for the dynamics and acoustics of cloud cavitation. They suggested that the formation and focusing of bubbly shock waves, which are formed during the collapse of a cloud, are responsible for the severe noise and damage potential associated with this form of cavitating flows. The present work is an extension of the previous work of Wang and Brennen (1995, 1999) on the nonlinear dynamics of a spherical cloud of cavitation bubbles. The main objective is to study the effects of nuclei size distribution on the spherical cloud dynamics, especially on the formation and the structure of the bubbly shock waves associated with the cloud collapse.

Any bubbly mixture contains bubbles of different sizes. It is well acknowledged that the size distribution of the upstream microbubbles can significantly affect the flows of cavitation of various types (see, for example, Keller, 1972; Ceccio and Brennen, 1991; Tanger et al., 1992; Gindroz et al., 1992). Commander and Prosperetti (1989) and Hawkins and Bedford (1992) derived continuum mixture models for the pressure wave propagation in bubbly liquids including the effects of multiple bubble sizes. Gavriluk and Fil'ko (1991) and Gavriluk (1993) proved math-

ematically the existence and uniqueness theorems of traveling pressure waves in a bubbly liquid with a discrete and a continuous bubble size distribution. Kameda and Matsumoto (1996) found that the spatial distribution of bubbles greatly affects the structure of shock waves in a bubbly liquid. All of these investigations suggest that the existence of a bubble size spectrum can significantly influence the wave propagation in bubbly liquids, both in the linear (at frequencies close to the resonance frequencies of the individual bubbles) and in the nonlinear regimes.

In the content of bubbly clouds, recent interest in the effects of bubble dynamics on cavitating flows and in the sources of low frequency ambient noise in the ocean have led to extensive study of the acoustic behavior of bubble clouds and a few references will be sufficient in this respect (d'Agostino and Brennen, 1988, 1989; Prosperetti, 1988; Yoon et al., 1991; Prosperetti et al., 1993). The number density distribution of bubbles is shown to be a minor effect in the emission and scattering of sound from bubble clouds at frequencies much lower than the resonance frequency of bubbles (Prosperetti et al., 1993). This, however, may be very important as the clouds behave nonlinearly. Kumar and Brennen (1991, 1992, 1993) employed a weakly nonlinear model to study the interactive effects of nuclei of different sizes in a bubbly layer. A nonlinear phenomenon called harmonic cascading was identified as a result of the harmonic interactions between the bubbles of different sizes. It is clear that a bubble cloud can behave in a highly nonlinear manner in a massive cavitating flow. The purpose of the present research is to understand the fully nonlinear effects of bubble size distribution by studying an amenable model problem.

Basic Equations

The problem addressed here is the same as in Wang and Brennen (1995, 1999) except for the presence of a bubble size distribution in the cloud. As shown in Fig. 1, consider a spherical bubble cloud surrounded by an unbounded pure liquid. The liquid phase is

Contributed by the Fluids Engineering Division for publication in the JOURNAL OF FLUIDS ENGINEERING. Manuscript received by the Fluids Engineering Division July 28, 1998; revised manuscript received July 6, 1999. Associate Technical Editor: J. Katz.

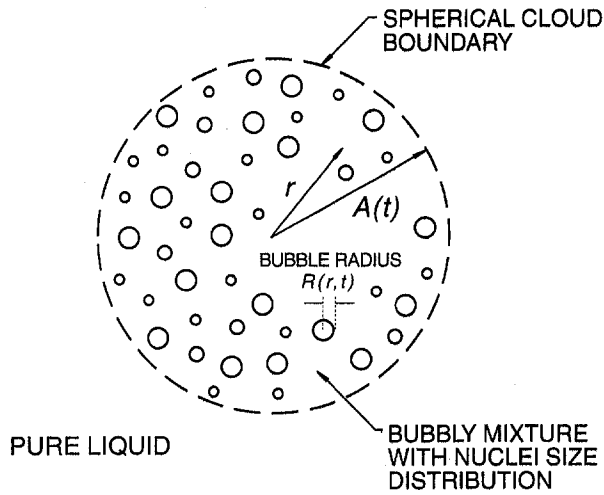


Fig. 1 Schematic of a spherical cloud of bubbles

assumed incompressible and has no relative motion with respect to the vapor phase. Both were found by d'Agostino and Brennen (1989) to have minor effects on the dynamics of the cloud. The radius of the cloud is represented by $A(t)$, a function of time t . The radius of bubbles with initial equilibrium size, R_0 , is represented by $R(r, t; R_0)$, where r is the radial coordinate. The bubble is assumed to contain vapor and residual permanent gas and to be spherical. Coalescence and break-up of bubbles are not considered.

The initial bubble size distribution within the cloud is represented by a nuclei number density distribution function, $\chi(R_0)$, which is assumed uniform for simplicity. The number of bubbles per unit liquid volume with initial size between R_0 and $R_0 + dR_0$ is $\chi(R_0)dR_0$ and the gas void fraction is then given by

$$\alpha(r, t) = \frac{\int_{R_{0MIN}}^{R_{0MAX}} \tau(r, t; R_0) \chi(R_0) dR_0}{1 + \int_{R_{0MIN}}^{R_{0MAX}} \tau(r, t; R_0) \chi(R_0) dR_0} \quad (1)$$

Nomenclature

A = dimensionless radius of bubble cloud
 A_0 = dimensionless initial cloud radius
 C_p = mixture pressure coefficient, $(p^* - p_0^*) / \frac{1}{2} \rho_L^* U^{*2}$
 C_{pMIN} = minimum pressure coefficient at infinity
 $C_{p\infty}$ = pressure coefficient at infinity from the cloud, $(p_\infty^* - p_0^*) / \frac{1}{2} \rho_L^* U^{*2}$
 D^* = length scale of the pressure perturbation
 N = proportional constant in the expression of nuclei number density distribution function
 R = dimensionless bubble radius, R^*/R_{0MIN}^*
 R_0 = dimensionless initial bubble radius
 R_{0MAX} = dimensionless maximum initial bubble radius

R_{0MIN}^* = minimum initial bubble radius
 R_{0MAX}^* = maximum initial bubble radius
 R_{0s}^* = initial bubble radius for the case of single bubble size
 Re = Reynolds number
 S^* = surface tension of the liquid
 U^* = reference velocity
 We = Weber number
 k = polytropic index for the gas inside the bubbles
 p_a = dimensionless far-field acoustic pressure
 p^* = mixture pressure
 p_v^* = vapor pressure
 p_0^* = mixture pressure at undisturbed reference condition
 p_∞^* = pressure at infinity from the cloud
 r = dimensionless Eulerian radial coordinate measured from the center of cloud

r_0 = dimensionless Lagrangian radial coordinate measured from the center of cloud and equal to r at the undisturbed reference condition
 t = dimensionless time
 t_G = dimensionless duration of the pressure perturbation
 u = dimensionless mixture velocity
 α = void fraction
 α_0 = initial void fraction
 χ = nuclei number density distribution function
 μ_E^* = effective dynamic viscosity of the liquid
 ρ_L^* = liquid density
 σ = cavitation number, $(p_0^* - p_v^*) / \frac{1}{2} \rho_L^* U^{*2}$
 τ = volume of individual bubble
 Δt = time step

Superscripts

* = dimensional quantities

where R_{0MIN} and R_{0MAX} are minimum and maximum initial bubble radii present in the cloud and $\tau(r, t; R_0)$ is the volume of the individual bubbles with initial radius of R_0 . In the present work, it is assumed that the cloud contains a finite number of sizes of bubbles and therefore the integration over the size spectrum can be replaced by a summation. Several researchers have measured the distribution functions of free-stream nuclei in different water tunnels (see, for example, Peterson et al., 1975; Gates and Bacon, 1978; Katz, 1978; Gates and Acosta, 1978) and in the ocean (O'Hern et al., 1985). The sizes of nuclei have a typical range from 10 μm to 200 μm with a distribution approximately fit by

$$\chi(R_0) = N/R_0^4 \quad (2)$$

The bubble population in a cavitating cloud measured by Maeda et al. (1991) can also be described by (2). The value of N relates to the degree of air content and can be obtained by matching the prescribed value of the initial void fraction, α_0 , by substituting (2) into (1):

$$N = \frac{3\alpha_0}{4\pi(1 - \alpha_0) \ln(R_{0MAX}/R_{0MIN})} \quad (3)$$

The variables in all the following figures and equations are nondimensionalized using the minimum initial bubble radius, R_{0MIN}^* , a reference flow velocity, U^* , and the dynamic pressure, $\frac{1}{2} \rho_L^* U^{*2}$, where ρ_L^* is the liquid density. All quantities with superscript * represent dimensional values; without this superscript the quantities are nondimensional. Thus, the nondimensional bubble radius is $R = R^*/R_{0MIN}^*$ (and $R_{0MIN} = 1$), the nondimensional radial coordinate is $r = r^*/R_{0MIN}^*$, the nondimensional time is $t = t^* U^*/R_{0MIN}^*$, and so on.

The problem to be solved is as follows. The cloud and the whole domain of liquid are initially in equilibrium. Starting at $t = 0$, a pressure perturbation, $C_{p\infty}(t)$, is imposed on the pure liquid at infinity and the response of the cloud to this pressure perturbation is sought. Following the same approach described in a separate study (Wang and Brennen, 1999) the mixture continuity equation can be used to obtain the integral expressions of the Eulerian position of a fluid particle, r , and of the mixture velocity, u , in a Lagrangian framework:

$$r(r_0, t) = \left\{ (1 - \alpha_0) \int_0^{r_0} \xi^2 d\xi \left[3 + 4\pi \int_1^{R_{\text{MAX}}} R^3(\xi, t; R_0) \chi(R_0) dR_0 \right] \right\}^{1/3} \quad (4)$$

$$u(r_0, t) = \frac{4\pi(1 - \alpha_0)}{r^2(r_0, t)} \int_0^{r_0} \xi^2 d\xi \int_1^{R_{\text{MAX}}} \dot{R}^2(\xi, t; R_0) \dot{R}(\xi, t; R_0) \chi(R_0) dR_0 \quad (5)$$

where a dot denotes the partial time derivative, (r_0, t) is the Lagrangian coordinates, r_0 is the radial distance from the center of the cloud at initial time $t = 0$, and ξ is a dummy variable. The mixture momentum equation is then integrated with respect to r_0 to produce an integral equation of the pressure coefficient, $C_p = (p^* - p_0^*) / \frac{1}{2} \rho_L^* U^{*2}$, where p^* is the mixture pressure and p_0^* is the initial equilibrium pressure:

$$C_p(r_0, t) = 2(1 - \alpha_0) \int_{r_0}^{A_0} \frac{g(\xi, t; C_p) - 2r(\xi, t)u^2(\xi, t)}{r^4(\xi, t)} \times \xi^2 d\xi + \frac{2g(A_0, t; C_p)}{r(A_0, t)} - u^2(A_0, t) + C_{p\infty}(t) \quad (6)$$

where

$$g(\xi, t; C_p) = -2\pi(1 - \alpha_0) \int_0^\xi \xi'^2 d\xi' \int_1^{R_{\text{MAX}}} \left\{ RC_p(\xi', t) + \sigma R \left[1 - \left(\frac{R_0}{R} \right)^{3k} \right] + \frac{8\dot{R}}{\text{Re}} - R\dot{R}^2 + \frac{4}{\text{We}} \left[1 - \left(\frac{R_0}{R} \right)^{3k-1} \right] \right\} \chi(R_0) dR_0 \quad (7)$$

in which $R = R(\xi, t; R_0)$, $\sigma = (p_0^* - p_v^*) / \frac{1}{2} \rho_L^* U^{*2}$ is the cavitation number, p_v^* is the partial pressure of vapor inside the bubble. Note that the Reynolds number, $\text{Re} = \rho_L^* U^* R_{\text{MIN}}^* / \mu_E^*$, is a function of initial equilibrium bubble radius since the effective viscosity, μ_E^* , which incorporates the various bubble-damping mechanisms, namely acoustic, thermal, and viscous damping, can be quite different for different R_0 (Chapman and Plesset, 1971). The Weber number is given by $\text{We} = \rho_L^* U^{*2} R_{\text{MIN}}^* / S^*$ where S^* is the surface tension. The polytropic index of the noncondensable gas inside the bubbles is denoted by k .

In deriving (6), the Rayleigh-Plesset equation (Knapp et al., 1970; Plesset and Prosperetti, 1977) for the individual bubbles

$$R\ddot{R} + \frac{3}{2} \dot{R}^2 + \frac{\sigma}{2} \left[1 - \left(\frac{R_0}{R} \right)^{3k} \right] + \frac{4}{\text{Re}} \frac{\dot{R}}{R} + \frac{2}{\text{We} R} \left[1 - \left(\frac{R_0}{R} \right)^{3k-1} \right] + \frac{1}{2} C_p = 0 \quad (8)$$

and the boundary condition on the surface of the cloud (see Wang and Brennen, 1995, 1999)

$$C_p(A_0, t) = C_{p\infty}(t) + \frac{2}{r(A_0, t)} \frac{d}{dt} [r^2(A_0, t)u(A_0, t) - u^2(A_0, t)] \quad (9)$$

have been employed. Equation (8) assumes the bubble interior to be uniform and neglects the mass of liquid vaporized or condensed in view of the fact of large density difference between the phases. The partial pressure of noncondensable gas (it is assumed the mass of gas is constant) does not appear explicitly in (8) because the

initial equilibrium condition has been used to eliminate this quantity. Heat transfer between the bubbles and the surrounding liquid is also neglected. Therefore, the value of k is to be taken as the ratio of specific heats of the gas. It has been clarified by many investigators (see, for example, Nigmatulin, 1991; Watanabe and Prosperetti, 1994; Kameda and Matsumoto, 1996) that the thermal effects may be very important in the shock dynamics. However, if the shock strength is strong, Watanabe and Prosperetti (1994, §4.3) showed that the bubble content is nearly adiabatic and it is appropriate to use a simplified model like the Rayleigh-Plesset equation. The validity of this simplification in the present study is to be demonstrated below. Finally, at the center of the cloud, geometric symmetry requires

$$u(0, t) = 0 \quad (10)$$

In the context of cavitating flows it is appropriate to assume that, at time $t \leq 0$, the whole flow field is in equilibrium. Therefore, the following initial conditions should be applied:

$$r(r_0, 0) = r_0, \quad u(r_0, 0) = 0, \quad C_p(r_0, 0) = 0, \\ R(r_0, 0; R_0) = R_0, \quad \dot{R}(r_0, 0; R_0) = 0 \quad (11)$$

In (9), $C_{p\infty}(t) = (p_\infty^*(t) - p_0^*) / \frac{1}{2} \rho_L^* U^{*2}$ and $p_\infty^*(t)$ is the far-field pressure perturbation experienced by the cloud. For the purposes of the present calculations, a simple sinusoidal form is chosen for $C_{p\infty}(t)$ since previous investigations have shown that the results are not very sensitive to the precise functional form of $C_{p\infty}(t)$:

$$C_{p\infty}(t) = \begin{cases} \frac{1}{2} C_{P\text{MIN}} [1 - \cos(2\pi t/t_G)]; & 0 < t < t_G \\ 0; & t < 0 \text{ and } t > t_G \end{cases} \quad (12)$$

where $C_{P\text{MIN}}$ is the minimum pressure coefficient imposed on the cloud and t_G is the nondimensional duration of the pressure perturbation and therefore controls the residence time of bubble growth. Consequently, for a cloud flowing with velocity U^* past a body of size D^* , the order of magnitude of t_G will be D^*/R_{MIN}^* , and $C_{P\text{MIN}}$ will be the minimum pressure coefficient of the flow.

Numerical Method

The numerical method applied in the present work is based on the integral equations, (4), (5), and (6), and a complete time step of integration proceeds as follows:

1. At each Lagrangian node, r_0 , and for each initial bubble size, $R_0 \in [1, R_{\text{MAX}}]$, $R(r_0, t + \Delta t; R_0)$ and $\dot{R}(r_0, t + \Delta t; R_0)$ are calculated using Taylor's series expansion based on the known solution at the previous time step, $R(r_0, t; R_0)$, $\dot{R}(r_0, t; R_0)$ and $\ddot{R}(r_0, t; R_0)$.
2. With $R(r_0, t + \Delta t; R_0)$ and $\dot{R}(r_0, t + \Delta t; R_0)$, Eqs. (4) and (5) can be integrated to obtain $r(r_0, t + \Delta t)$ and $u(r_0, t + \Delta t)$.
3. With the results of steps 1 and 2, we can iterate upon equation (6) to find $C_p(r_0, t + \Delta t)$. Then the Rayleigh-Plesset equations (8) for each R_0 can be used to find $\dot{R}(r_0, t + \Delta t; R_0)$. Under-relaxation was necessary to make this iterative process converge. This and other numerical difficulties are discussed in Wang (1996).
4. Proceed to next time step.

The interval of each time step is automatically adjusted during the computation to ensure that the maximum fractional change of bubble radius in the cloud between any two consecutive times does not exceed some specific value (typically, 5%). This is essential for time marching through a violent bubble collapse. The number of Lagrangian nodes is 100 in all the following computational results. Nodal numbers of 200 and 400 were used to check the grid independence of the results. The number of bubbles sizes present

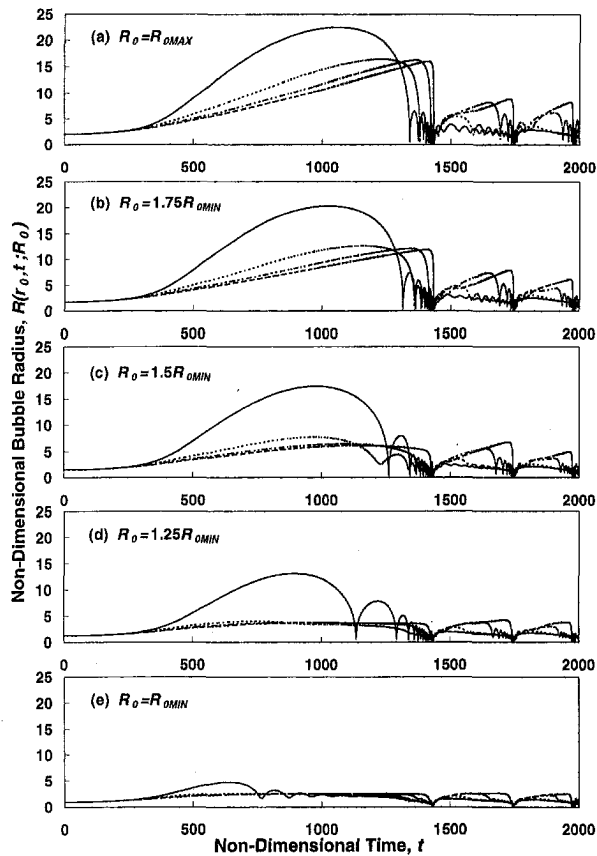


Fig. 2 The typical time history of the radius of bubbles of different initial sizes in a cloud: (a) $R_0 = R_{0MAX}$, (b) $R_0 = 1.75R_{0MIN}$, (c) $R_0 = 1.5R_{0MIN}$, (d) $R_0 = 1.25R_{0MIN}$, and (e) $R_0 = R_{0MIN}$. Four different Lagrangian positions are shown in each figure; $r_0 = A_0$ (solid line), $r_0 = 0.8A_0$ (dotted line), $r_0 = 0.5A_0$ (dash-dot-dot line), and $r_0 = 0$ (dashed line). Parameters are $\sigma = 0.4$, $\alpha_0 = 3\%$, $R_{0MIN}^* = 100 \mu\text{m}$, $R_{0MAX}^* = 200 \mu\text{m}$, $C_{PMIN} = -0.7$, and $t_G = 1000$.

in the nuclei spectrum is 21 in all cases. This number was found not critical on the important features of the cloud dynamics.

Results and Discussion

In order to compare the present results with those of single bubble size (see Wang and Brennen, 1999), the following typical flow variables were chosen: a bubble cloud of radius of 1 cm, composed of air bubbles ($k = 1.4$) of initial radii between 50 and 200 μm in water at 20°C ($\rho_L^* = 1000 \text{ kg/m}^3$, $S^* = 0.0728 \text{ N/m}$) flows with velocity $U^* = 10 \text{ m/s}$ through a region of low pressure characterized by Eq. (12) with $C_{PMIN} = -0.7$ and different values of t_G , ranging from 400 to 2000. The cavitation number, σ , is set as 0.4 in all cases and an initial void fraction, α_0 , ranging from 0.02%, to 3% is assigned. Values of the effective liquid viscosity, μ_E^* , for bubbles with different equilibrium sizes were obtained using the data taken from Chapman and Plesset (1971) to incorporate the various bubble damping mechanisms. As a result, the Reynolds number defined previously ranges between 16.2 and 39.6. Finally, it should be noticed in the following figures that some of the nondimensional quantities are normalized by a factor, R_{0MIN}^*/R_{0S}^* , in order to present a consistent scale with the results from the case of equal bubble size, in which R_{0S}^* is the initial bubble radius.

Figure 2 presents typical time histories of bubble radius for four different Lagrangian locations, r_0 , from the cloud surface, $r_0 = A_0$, to the center, $r_0 = 0$. Five initial sizes of bubbles were chosen for illustration. It is clear that the growth rate of the bubbles is not only a function of the location within the cloud but also a function of their initial size. The bubbles in the interior region are shielded

by the outer bubbles and have a smaller growth rate. The shielding effect also appeared in the case of single bubble size and is typical of the bubble interaction phenomenon in cloud dynamics (see d'Agostino and Brennen, 1989; Wang and Brennen, 1999). For bubbles with larger initial sizes, as shown in Fig. 2(a) and 2(b), the inner bubbles can still gain a sufficient growth rate and continue to grow after the bubbles on the surface have collapsed. However, for small R_0 , the bubbles, except those on the surface of the cloud, react passively and even do not really cavitate. This result suggests that, as far as cavitation is concerned, nuclei of larger sizes play a critical role. This is not unexpected indeed in view of the fact that the susceptibility of bubbles to a tensile stress is a function of their equilibrium size.

As in the case of single bubble size, a bubbly shock wave develops as part of the collapse of the cloud. A typical structure of this shock wave is included in Fig. 3(b) together with the results for single bubble size (Fig. 3(a)). The distribution of void fraction clearly shows that the oscillation structures behind the shock front (at $rR_{0MIN}^*/R_{0S}^* \approx 80$) is diminished due to the effects of bubble size distribution. The thickness of the shock (≈ 40 in terms of the normalized radial coordinate) becomes much larger in Fig. 3(b) than in 3(a). Also the shock strength is mitigated as illustrated by the distribution of pressure coefficient. The strength of the shock, which can be defined as the pressure ratio across the shock, is found as 1.7 in Fig. 3(b), larger than the ratio of specific heats, and, therefore, is strong (see Watanabe and Prosperetti, 1994). The shock strengthens considerably as it propagates inward primarily because of geometric focusing.

Another major effect of bubble size distribution can be seen in Fig. 4. Figures 4(b) and 4(c) present the time history of the normalized radius of the bubbles of maximum initial size at different Lagrangian positions for clouds with different ranges of initial bubble radius. The results of the single bubble size are also shown in Fig. 4(a) for comparison. Each case uses the same values of the initial void fraction and the imposed pressure perturbation. It is obvious that the asymptotic growth rate of bubbles is much larger for the case of multiple bubble sizes than that of single size. Therefore the interior bubbles in Fig. 4(b) and 4(c) can grow to a larger size than those in Fig. 4(a) and the bubble collapse always starts from the surface of the cloud. This phenomenon has important consequences in the cloud dynamics, as illustrated in Fig. 5.

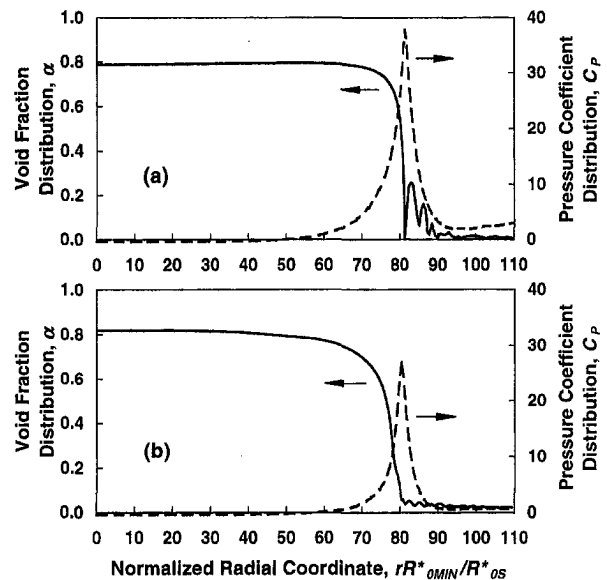


Fig. 3 A comparison of the structure of bubbly shock wave in clouds with and without bubble size distribution: (a) single bubble size, $R_{0S}^* = 100 \mu\text{m}$, and (b) $R_{0MIN}^* = 50 \mu\text{m}$ and $R_{0MAX}^* = 100 \mu\text{m}$. Both clouds experience the same pressure perturbation ($C_{PMIN} = -0.7$ and $t_G = 1000$ in (a) and 2000 in (b) due to the difference of R_{0S}^* and R_{0MIN}^*). Other parameters as in Fig. 2.

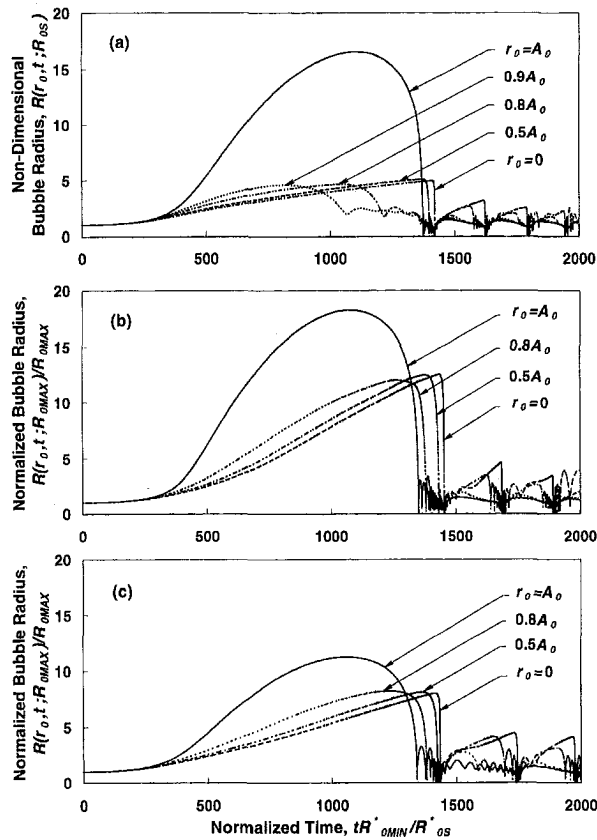


Fig. 4 The time history of the radius of bubbles of maximum initial size at different Lagrangian positions in the cloud for: (a) single bubble size, $R_{0S} = 100 \mu\text{m}$ ($R_{0S} = 1$), (b) $R_{0MIN} = 50 \mu\text{m}$ and $R_{0MAX} = 100 \mu\text{m}$, and (c) $R_{0MIN} = 100 \mu\text{m}$ and $R_{0MAX} = 200 \mu\text{m}$. The same pressure perturbation ($C_{PMIN} = -0.7$ and $t_G = 1000$ in (a) and (c), and 2000 in (b)) is employed in each case. In (b) and (c), the bubble radius are normalized by R_{0MAX} . Other parameters are $\sigma = 0.4$ and $\alpha_0 = 3\%$.

Figure 5(a) is taken from Wang and Brennen (1999) for a cloud of single bubble size and Fig. 5(b) is obtained from present compu-

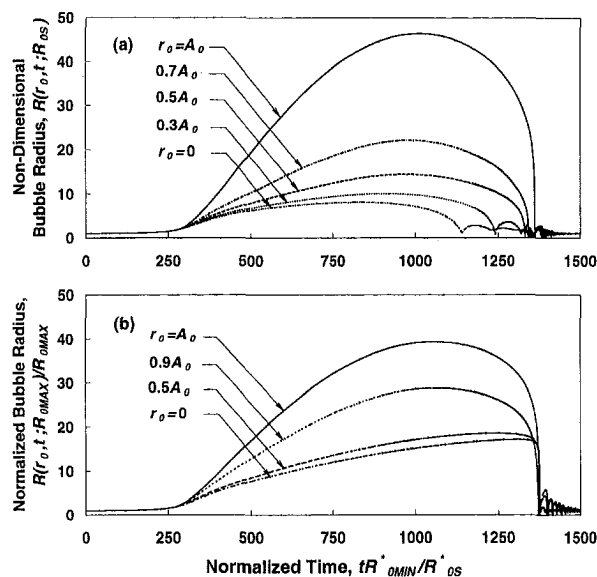


Fig. 5 The time history of the radius of bubbles of maximum initial size at different Lagrangian positions in the cloud for: (a) single bubble size, $R_{0S} = 100 \mu\text{m}$, and (b) $R_{0MIN} = 50 \mu\text{m}$ and $R_{0MAX} = 100 \mu\text{m}$. The initial void fraction, $\alpha_0 = 0.02\%$. Other parameters as in Fig. 2.

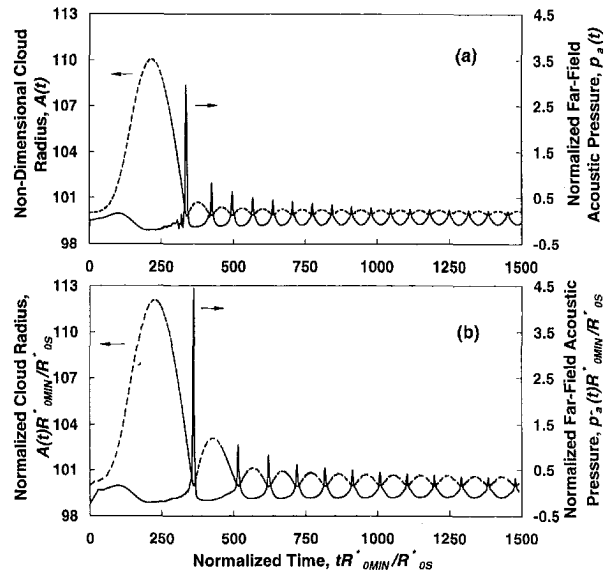


Fig. 6 A comparison of the time history of the cloud radius and the resulting far-field acoustic pressure between (a) single bubble size, $R_{0S} = 100 \mu\text{m}$, and (b) $R_{0MIN} = 50 \mu\text{m}$ and $R_{0MAX} = 200 \mu\text{m}$. Both clouds have the same pressure perturbation ($C_{PMIN} = -0.7$ and $t_G = 200$ in (a) and 400 in (b)) and the initial void fraction, $\alpha_0 = 0.8\%$. The cavitation number, $\sigma = 0.4$.

tation for the same problem except for the presence of bubble size distribution in the cloud. As shown in Fig. 5(b), increase of the bubble growth rate inside the cloud causes the collapse to start near the cloud surface ($0.9A_0$) instead of at the center of the cloud (Fig. 5(a)). Collapse beginning in the center was found by Wang and Brennen (1999) to occur only for a cloud with a small value of the cloud interaction parameter, $\alpha_0(1 - \alpha_0)A_0^2/R_0^2$. (≈ 2 in Fig. 5(a)). Results from the present analysis suggest that the effects of bubble size distribution could change the collapse of the cloud from an outward propagating mode to an inward mode. In other words, the geometric focusing of the bubbly shock wave is a genuine part of the nonlinear dynamics associated with the collapse of a spherical cloud with bubble size distribution.

A typical time history of the far-field acoustic pressure, p_a , produced by the volumetric acceleration of the clouds is shown in Fig. 6. The corresponding time history of the cloud radius, $A(t)$, is also presented. Figure 6(a) is taken from Wang and Brennen (1999) and an exact definition of p_a can be found therein. It is clear that the volumetric motion of the cloud and the resultant far-field noise are magnified due to the existence of bubble size distribution. The cloud in Fig. 6(b) can reach a larger maximum size and has a series of rebounds after each collapse which are larger than in Fig. 6(a). Increase of the bubble growth rate described above is responsible for this magnification effect.

Concluding Remarks

The effects of bubble size distribution on the nonlinear growth and collapse of a spherical cloud of cavitation bubbles have been computed using a fully nonlinear continuum bubbly mixture model coupled with the Rayleigh-Plesset equation for the dynamics of the bubbles. The comparison with the case of single bubble size shows that the size distribution can significantly affect the cloud dynamics, including the increase of bubble growth rate inside the cloud. It has been shown that this effect can change the starting point for the collapse of the cloud from the cloud center to the surface region even when the initial void fraction is as small as 0.02%. In other words, the shock wave dynamics are changed from the outward expanding mode to the inward focusing mode. Larger impulsive pressures are associated with the inward focusing mode.

It is also shown that the bubble size distribution smooths out the

trailing oscillations and weakens the strength of the shock wave. However, the far-field noise emitted by the cloud is amplified as a result of the increase of the bubble growth rate during the cloud rebound. Note that this result is obtained for the idealized case of spherical cloud motion and is hardly applicable to the collapse of the nonspherical clouds which occur in real cavitating flows. Extension of the present one-dimensional solver to a higher dimensional form is clearly an important step in the future.

Acknowledgments

The author is very grateful to Professor Christopher E. Brennen for his encouragement and helpful suggestions on the subject of this paper. This research has been supported by National Science Council, Taiwan, R.O.C., under grant number NSC 88-2212-E-006-032.

References

- Bark, G., 1985, "Developments of Distortions in Sheet Cavitation on Hydrofoils," *Proceedings of the ASME International Symposium on Jets and Cavities*, pp. 470–493.
- Bark, G., and Berlekom, W. B., 1978, "Experimental Investigations of Cavitation Noise," *Proceedings of the 12th ONR Symposium on Naval Hydrodynamics*, pp. 470–493.
- Ceccio, S. L., and Brennen, C. E., 1991, "Observations of the Dynamics and Acoustics of Travelling Bubble Cavitation," *Journal of Fluid Mechanics*, Vol. 233, pp. 633–660.
- Chapman, R. B., and Plesset, M. S., 1971, "Thermal Effects in the Free Oscillation of Gas Bubbles," *ASME Journal of Basic Engineering*, Vol. 93, pp. 373–376.
- Commander, K. W., and Prosperetti, A., 1989, "Linear Pressure Waves in Bubbly Liquids: Comparison between Theory and Experiments," *Journal of the Acoustical Society of America*, Vol. 85, pp. 732–746.
- d'Agostino, L., and Brennen, C. E., 1988, "Acoustical Absorption and Scattering Cross-Sections of Spherical Bubble Clouds," *Journal of the Acoustical Society of America*, Vol. 84, pp. 2126–2134.
- d'Agostino, L., and Brennen, C. E., 1989, "Linearized Dynamics of Spherical Bubble Clouds," *Journal of Fluid Mechanics*, Vol. 199, pp. 155–176.
- Gates, E. M., and Acosta, A. J., 1978, "Some Effects of Several Free Stream Factors on Cavitation Inception on Axisymmetric Bodies," *Proceedings of the 12th ONR Symposium on Naval Hydrodynamics*, Washington DC, 86–108.
- Gates, E. M., and Bacon, J., 1978, "Determination of Cavitation Nuclei Distribution by Holography," *Journal of Ship Research*, Vol. 22(1), pp. 29–31.
- Gavrilyuk, S. L., and Fil'ko, S. A., 1991, "Shock Waves in Polydisperse Bubbly Media with Dissipation," (Translated from *Zhurnal Prikladnoi Mekhaniki i Tekhnicheskoi Fiziki*, No. 5, pp. 26–34.)
- Gavrilyuk, S. L., 1993, "Travelling Waves in Bubbly Liquid with Continuous Bubble Size Distribution," UMPA-93-n°113, Ecole Normale Supérieure de LYON, France.
- Gindroz, B., Henry, P., and Avellan, F., 1992, "Francis Cavitation Tests with Nuclei Injection: A New Test Procedure," *Proceedings of the 16th IAHR*, Sao Paulo.
- Hawkins, J. A., and Bedford, A., 1992, "Variational Theory of Bubbly Media with a Distribution of Bubble Sizes—I. Liquids," *International Journal of Engineering Science*, Vol. 30(9), pp. 1161–1176.
- Kameda, M., and Matsumoto, Y., 1996, "Shock Waves in a Liquid Containing Small Gas Bubbles," *Physics of Fluids*, Vol. 8(2), pp. 322–335.
- Katz, J., 1978, "Determination of Solid Nuclei and Bubble Distributions in Water by Holography," Report No. 183-3, Division of Engineering and Applied Science, California Institute of Technology, Pasadena, CA.
- Keller, A. P., 1972, "The Influence of the Cavitation Nucleus Spectrum on Cavitation Inception, Investigated with a Scattered Light Counting Method," *ASME Journal of Basic Engineering*, Vol. 94, pp. 917–925.

- Knapp, R. T., Daily, J. W., and Hammit, F. G., 1970, *Cavitation*, McGraw-Hill, New York.
- Kumar, S., and Brennen, C. E., 1991, "Non-linear Effects in the Dynamics of Clouds of Bubbles," *Journal of the Acoustical Society of America*, Vol. 89, pp. 707–714.
- Kumar, S., and Brennen, C. E., 1992, "Harmonic Cascading in Bubble Clouds," *Proceedings of the International Symposium on Propulsors and Cavitation*, pp. 171–179.
- Kumar, S., and Brennen, C. E., 1993, "Some Nonlinear Interactive Effects in Bubbly Cavitating Clouds," *Journal of Fluid Mechanics*, Vol. 253, pp. 565–591.
- Le, Q., Franc, J. M., and Michel, J. M., 1993, "Partial Cavities: Global Behaviour and Mean Pressure Distribution," *ASME JOURNAL OF FLUIDS ENGINEERING*, Vol. 115, pp. 243–248.
- Maeda, M., Yamaguchi, H., and Kato, H., 1991, "Laser Holography Measurement of Bubble Population in Cavitation Cloud on a Foil Section," 1st ASME/JSME Conference, Portland, OR, FED Vol. 116, pp. 67–75.
- Nigmatulin, R. I., 1991, *Dynamics of Multiphase Media*, Hemisphere, New York.
- O'Hern, T. J., Katz, J., and Acosta, A. J., 1985, "Holographic Measurements of Cavitation Nuclei in the Sea," *Proceedings of ASME Cavitation and Multiphase Flow Forum*, pp. 39–42.
- Peterson, F. B., Danel, F., Keller, A. P., and Lecoffre, Y., 1975, "Comparative Measurements of Bubble and Particulate Spectra by Three Optical Methods," *Proceedings of the 14th International Towing Tank Conference*, Vol. 2, pp. 27–52, Ottawa, Canada.
- Plesset, M. S., and Prosperetti, A., 1977, "Bubble Dynamics and Cavitation," *Annual Review of Fluid Mechanics*, Vol. 9, pp. 145–185.
- Prosperetti, A., 1988, "Bubble-Related Ambient Noise in the Ocean," *Journal of the Acoustical Society of America*, Vol. 84, pp. 1042–1054.
- Prosperetti, A., Lu, N. Q., and Kim, H. S., 1993, "Active and Passive Acoustic Behavior of Bubble Clouds at the Ocean's Surface," *Journal of the Acoustical Society of America*, Vol. 93, pp. 3117–3127.
- Reisman, G. E., McKenney, E. A., and Brennen, C. E., 1994, "Cloud Cavitation on an Oscillating Hydrofoil," *Proceedings of the 20th ONR Symposium on Naval Hydrodynamics*, pp. 78–89.
- Reisman, G. E., Wang, Y.-C., and Brennen, C. E., 1998, "Observations of Shock Waves in Cloud Cavitation," *Journal of Fluid Mechanics*, Vol. 355, pp. 255–283.
- Shen, Y., and Peterson, F. B., 1978, "Unsteady Cavitation on an Oscillating Hydrofoil," *Proceedings of the 12th ONR Symposium on Naval Hydrodynamics*, pp. 362–384.
- Shen, Y., and Peterson, F. B., 1980, "The Influence of Hydrofoil Oscillation on Boundary Layer Transition and Cavitation Noise," *Proceedings of the 13th ONR Symposium on Naval Hydrodynamics*, pp. 221–241.
- Soyama, H., Kato, H., and Oba, R., 1992, "Cavitation Observations of Severely Erosive Vortex Cavitation Arising in a Centrifugal Pump," *Proceedings of the Third IMechE International Conference on Cavitation*, pp. 103–110.
- Tanger, H., Streckwall, H., Weitendorf, E.-A., and Mills, L., 1992, "Recent Investigations of the Free Air Content and its Influence on Cavitation and Propeller-Excited Pressure Fluctuations," *Proceedings of the International Symposium on Propulsors and Cavitation*, Hamburg.
- Wang, Y.-C., 1996, "Shock Waves in Bubbly Cavitating Flows," Ph.D. thesis, California Institute of Technology, Pasadena, CA.
- Wang, Y.-C., and Brennen, C. E., 1995, "The Noise Generated by the Collapse of a Cloud of Cavitation Bubbles," *ASME/JSME Symposium on Cavitation and Gas-Liquid Flow in Fluid Machinery and Devices*, Ceccio, S. L., Furukawa, A., and Kim, J. H., ed., FED Vol. 226, pp. 17–29.
- Wang, Y.-C., and Brennen, C. E., 1999, "Numerical Computation of Shock Waves in a Spherical Cloud of Cavitation Bubbles," *ASME JOURNAL OF FLUIDS ENGINEERING*, Vol. 121, pp. 872–880.
- Watanabe, M., and Prosperetti, A., 1994, "Shock Waves in Dilute Bubbly Liquids," *Journal of Fluid Mechanics*, Vol. 274, pp. 349–381.
- Yoon, S. W., Crum, L. A., Prosperetti, A., and Lu, N. Q., 1991, "An Investigation of the Collective Oscillations of a Bubble Cloud," *Journal of the Acoustical Society of America*, Vol. 89, pp. 700–706.

J. Ruud van Ommen

Ph.D. Student,
Delft University of Technology,
Faculty of Applied Sciences,
Chemical Reactor Engineering Section,
Julianalaan 136, 2628 BL Delft,
The Netherlands
e-mail: J.R.vanOmmen@stm.tudelft.nl

Jaap C. Schouten

Professor,
Eindhoven University of Technology,
Laboratory of Chemical Reactor Engineering,
P.O. Box 513, 5600 MB Eindhoven,
The Netherlands
e-mail: J.C.Schouten@tue.nl

Cor M. van den Bleek

Professor,
Delft University of Technology,
Faculty of Applied Sciences,
Chemical Reactor Engineering Section,
Julianalaan 136, 2628 BL Delft,
The Netherlands
e-mail: C.M.vandenBleek@stm.tudelft.nl

Monitoring Fluidization Dynamics for Detection of Changes in Fluidized Bed Composition and Operating Conditions

In many industrial applications of gas-solids fluidized beds, it is worthwhile to have an on-line monitoring method for detecting changes in the hydrodynamics of the bed (due for example to agglomeration) quickly. In this paper, such a method, based on the short-term predictability of fluidized bed pressure fluctuations, is examined. Its sensitivity is shown by experiments with small step changes in the superficial gas velocity and by experiments with a gradual change in the particle size distribution of the solids in the bed. Furthermore, it is demonstrated that the method is well able to indicate if a stationary hydrodynamic state has been reached after a change in the particle size distribution (a 'grade change').

Introduction

Gas-solids fluidized beds are often applied in the chemical industry for physical processes (e.g., particle drying) as well as for chemical processes (e.g., catalyzed gas phase reactions). In both types of processes, particles can stick together and form agglomerates; this can lead to a decreasing fluidization quality and even to defluidization of (parts of) the bed. Therefore, it is worthwhile to be able to detect agglomeration in an early stage, so measures can be taken to prevent the bed from becoming defluidized. Such a method could also be employed for on-line monitoring of changes in the fluidized bed dynamics due to imposed alterations in the hydrodynamically-relevant particle properties, for example when switching from one particle feed stream to another (a 'grade' change).

Since a fluidized bed can be regarded as a chaotic system, signals measured in a fluidized bed will have a nonlinear nature (see e.g., Vander Stappen, 1996). The last years, a number of methods have been proposed to detect non-stationarities in nonlinear time-series. Kantz (1994) introduced a cross-correlation integral for this purpose. Albano et al. (1995) proposed to use the Kolmogorov-Smirnov test to compare correlation integrals from different time-series. Diks et al. (1996) developed a statistical test based on the distance between multi-dimensional distributions. Wright (1995) used the Fourier transform of the probability densities to distinguish fluidized bed pressure time-series measured in different fluidization regimes. Kennel (1997) proposed a statistical test for detecting non-stationarity based on a nearest-neighbour approach; he showed for fluidized bed data that this method is able to detect a change of 5% in the superficial gas velocity.

Recently, Schouten and Van den Bleek (1998) have proposed a method for monitoring the fluidization quality using the short-term predictability of pressure fluctuations. This monitoring method distinctly differs from the previously mentioned methods since it makes use of the limited predictability of the signals, a typical

feature of a chaotic system. The method is based on a comparison of a reference time-series of pressure fluctuations (a time-series representing the desired fluidization behaviour) with successive time-series measured during operation of the bed. For this comparison a discriminating statistic is used; the null hypothesis that the reference and successive time-series are similar is rejected if the discriminating statistics of both time-series differ significantly.

Schouten and Van den Bleek (1998) have tested their method with experiments in which plastic particles, fluidized at elevated temperature, agglomerated. These experiments showed that the method detects the formation of agglomerates in an early stage, whereas the average pressure drop over the bed only indicates late that defluidization of the bed has occurred. However, it was not possible to determine the sensitivity of the monitoring method by these experiments, since agglomeration is an uncontrolled, random-like process.

The objective of the current paper is to determine the sensitivity of the monitoring method. Hence, two types of experiments have been carried out in which the hydrodynamics was affected in a controlled way: experiments with small step changes in superficial gas velocity and experiments with a gradual change in the particle size distribution. In the first type of experiment the excess gas velocity (i.e., the difference between the superficial gas velocity and the minimum fluidization velocity) varies due to changes in the superficial gas velocity and in the second type of experiment due to changes in the minimum fluidization velocity. Both types of experiments mimic the cases of particle agglomeration and grade changes, where the excess gas velocity changes as well. The excess gas velocity is an important parameter for the fluidized bed hydrodynamics, since it is proportional to the bubble flow rate, which determines the hydrodynamics to a large extent.

Theory

The method of Schouten and Van den Bleek (1998) is based on a comparison of a reference time-series of pressure fluctuations, reflecting a certain required or accepted state of the fluidization dynamics, with successive time-series measured during operation of the bed. The length of the reference and successive time-series should be chosen such that a good representation of the actual bed

Contributed by the Fluids Engineering Division for publication in the JOURNAL OF FLUIDS ENGINEERING. Manuscript received by the Fluids Engineering Division September 24, 1998; revised manuscript received July 6, 1999. Associate Technical Editor: M. Sommerfeld.

dynamics is obtained. In practice this implies that the time-series should be of the order of one minute, which for a bubbling bed corresponds to the passage of several tens, up to a few hundreds of bubbles through the bed.

The comparison is based on some discriminating statistic that is computed for the original time series as well as for each of the successive time-series. Schouten and Van den Bleek (1998) have chosen a measure quantifying the time-series' short-term predictability, since it is a sensitive measure of the fluidized-bed dynamical state and it includes the signal's intensity (viz., average absolute deviation) as well as a typical time scale (viz., average cycle time); this will be explained below. Because of the inclusion of the signal's intensity, one has to make sure that the transducer sensitivity will not change (e.g., due to solids blocking the pressure probe) during the measurements. For a discussion of the separate influences of these three elements (short-term predictability, average absolute deviation, and average cycle time), the reader is referred to Van Ommen et al. (1999). An important advantage over classical analysis methods, like spectral analysis or calculation of the standard deviation of the signal, is, that the proposed method gives a statistically founded result.

Attractor Reconstruction. The state of the fluidized bed at a certain time can be obtained by projecting all variables governing the system in a multidimensional space (the 'state space'); the collection of the successive states of the system during its evolution in time is called the 'attractor.' However, it is unknown which are the independent variables governing the system. Moreover, even if these variables were all known, the measuring of many of those variables (e.g., voidage, gas and solids velocity components) is at least very impractical, especially in industrial facilities, and often even impossible. Therefore, this is not a very sensible way of obtaining the system's dynamical state.

Takens (1981) proved that the dynamical state of a system can be reconstructed from the time-series of only one characteristic variable (e.g., the local pressure in the fluidized bed). Using so-called time-delay coordinates, one can convert a pressure time-series (p_1, p_2, \dots, p_N) consisting of N values into a set of $N - m$ vectors \mathbf{P}_i with m elements, where $\mathbf{P}_i = (p_i, p_{i+1}, \dots, p_{i+m-1})^T$. As an example for $m = 3$ (normally a much larger value of m is used): $\mathbf{P}_1 = (p_1, p_2, p_3)$, $\mathbf{P}_2 = (p_2, p_3, p_4)$, etc. The subsequent vectors can be regarded as points in an m -dimensional state space yielding a reconstructed attractor, of which Takens (1981) has proven that it shows the same characteristics as the 'true' attractor obtained from all variables governing the system.

Two choices have to be made when applying this reconstruction procedure: (1) the embedding dimension m (viz., the number of

elements of the state vector), and (2) the time-step between two successive vector elements. The embedding dimension should be large enough to give a smooth description of the signal; it has been found (Schouten et al., 1994; Vander Stappen, 1996) that a value of the order of 100 suffices well. Furthermore, good results are obtained when the time between the first and the last element of the reconstruction vector is taken equal to a characteristic time scale of the pressure signal, the average cycle time (T_c), defined by:

$$T_c = \frac{\text{length of time series [units of time]}}{(\text{number of crossings of average of time series})/2} \quad (1)$$

A time difference between the first and the last vector element that is equal to T_c , together with the criterion of m equal to about 100 points per vector, yields a time-step of $T_c/100$. Alternatively, the sampling frequency f_s of data points in the time-series is given by:

$$f_s = \frac{m}{T_c} \quad (2)$$

Short-Term Predictability. One of the features of a chaotic system like a fluidized bed is the divergence, in the state space, of initially nearby points. The development of the distance between two points in the reconstructed state space that are initially close, is used to characterize the system. Two points are called initially close when their distance is smaller than a length l_0 . It has previously been shown (Schouten et al., 1994; Vander Stappen, 1996) that the average absolute deviation of the original time-series is a good choice for this length. This means that l_0 can be calculated as

$$l_0 = \frac{1}{N} \sum_{i=1}^N |p_i - \bar{p}| = \frac{1}{N} \sum_{i=1}^N \left| p_i - \frac{1}{N} \sum_{j=1}^N p_j \right| \quad (3)$$

To obtain a fast algorithm, the distance between two points in the state space is not calculated using the Euclidian distance, but using the so-called supremum norm, i.e., the maximum difference between the co-ordinates of the two points. The requirement for a (randomly chosen) pair of points on the reconstructed attractor to be regarded close is thus:

$$\max_{0 \leq s \leq m-1} |p_{i+s} - p_{j+s}| \leq l_0 \quad (4)$$

If the distance between the two points meets this requirement, it is followed during a certain period of time, the prediction horizon.

Nomenclature

A = set of distances on the reconstructed attractor
 B = set of distances on the reconstructed attractor
 d = particle diameter [m]
 d_{10} = 10% volume percentile of particle diameter [m]
 d_{50} = median particle diameter [m]
 d_{90} = 90% volume percentile of particle diameter [m]
 $d_{50,t}$ = median particle diameter based on volume fraction at time t [m]
 f_s = sampling frequency [Hz]
 g = acceleration due to gravity [m/s^2]
 l_0 = average absolute deviation of the pressure time-series [Pa]

$l_{i,j}$ = distance between point i and j on the reconstructed attractor [Pa]
 m = embedding dimension
 N = number of values in the pressure time series [—]
 N_A = number of distances in set A [—]
 N_B = number of distances in set B [—]
 \mathbf{P}_i = point in the m -dimensional state space at time i
 p_i = pressure at time i [Pa]
 \bar{p} = average value of the pressure time-series [Pa]
 T_c = average cycle time [s]
 t = time [s]
 U = rank-sum of all elements of set A compared to set B [—]
 u_0 = superficial gas velocity [m/s]

u_E = excess gas velocity, i.e., $u_0 - u_{mf}$ [m/s]
 u_{mf} = minimum fluidization velocity [m/s]
 Z = normalized value of U [—]
 η = dynamic viscosity of the gas [Pa s]
 $\Theta(x)$ = Heaviside step-function, defined as: $\Theta(x) = 1$ for $x > 0$;
 $\Theta(x) = 0$ for $x \leq 0$ [—]
 μ_U = estimated average of U [—]
 ρ_g = gas density [kg/m^3]
 ρ_s = solids density [kg/m^3]
 σ_U = estimated standard deviation of U [—]
 τ = solids residence time in one compartment of the twin-fluidized-bed [s]

Subsequently, the distance between the points after this time period,

$$l_{i,j} = \max_{0 \leq s \leq m+m_d-1} |p_{i+s} - p_{j+s}| \quad (5)$$

is calculated. On the one hand, we want to focus on the *initial* growth of the distance between the points, and therefore the prediction horizon should be chosen small compared to the typical time-scale of the attractor, T_c . On the other hand, the prediction horizon should contain a sufficient number of time steps to be able to observe a certain growth. A prediction horizon of 10% of the average cycle time was chosen by Schouten and Van den Bleek (1998); this corresponds to about 10 sample time steps, since the sample frequency was chosen such that T_c corresponded to about 100 points.

From the reference time-series, a large number (N_A) of distances fulfilling the requirement given by Eq. (4) is randomly drawn; by calculating their growth according to Eq. (5) we obtain a set A of N_A distances $l_{i,j}$. The same procedure is followed for each of the successive time-series to be evaluated, yielding a set B of N_B distances for each successive time-series.

Discriminating Statistic. To examine if the fluidization dynamics is different for the reference time-series and the successive time-series, it should be tested if the two sets of distances A and B are generated by the same mechanism, or, to state it more precisely, originate from the same underlying distribution function. Because we have no prior knowledge about this distribution, we need a so-called non-parametric test like the Mann-Whitney rank-sum test, also known as the Wilcoxon test. The Mann-Whitney rank-sum U counts the number of times an element of the set A is larger than an element of the set B :

$$U = \sum_{i=1}^{N_A} \sum_{j=1}^{N_B} \Theta(A_i - B_j) \quad (6)$$

where Θ is the Heaviside step function, which is defined as: $\Theta(x) = 1$ for $x > 0$, and $\Theta(x) = 0$ for $x \leq 0$. If N_A and N_B are large enough (at least equal to 8 (Spiegel, 1988); we will use 200), U is normally distributed with mean

$$\mu_U = \frac{N_A N_B}{2} \quad (7)$$

and variance

$$\sigma_U^2 = \frac{N_A N_B (N_A + N_B + 1)}{12} \quad (8)$$

Consequently, the quantity

$$Z = \frac{U - \mu_U}{\sigma_U} \quad (9)$$

is normally distributed with zero mean and unit variance under the null hypothesis that the two sets A and B originated from the same distribution. If the absolute value of Z is larger than 3, the null hypothesis can be rejected at a more than 99% confidence level.

If the two sets A and B are completely different (i.e., the largest element of the one is smaller than the smallest element of the other), then the absolute value of Z is maximal. This maximum value depends on the number of elements in the two sets and can be calculated by

$$|Z|_{\max} = \sqrt{\frac{3N_A N_B}{N_A + N_B + 1}} \quad (10)$$

For example, for $N_A = 200$ and $N_B = 200$, the value of $|Z|_{\max}$ is 17.3. The sign of Z_{\max} depends on which of the two sets has the smaller elements.

The validity of the Mann-Whitney rank-sum test depends on the

Table 1 Particle size distributions (based on volume fraction) of the three types of sand

Type of sand	d_{10} [μm]	d_{50} [μm]	d_{90} [μm]
S1	255	388	564
S2	313	435	628
S3	403	471	684

samples in each set being uncorrelated. Since we use successive time-series consisting of 4000 values (the reference time-series are even larger), there are approximately 3900 m -dimensional points in the state space (assuming an embedding dimension of about 100). Consequently, approximately $7.6 \cdot 10^6$ combinations are possible yielding the same number of distances, from which we draw 200 distances randomly, with exclusion of the previously drawn samples. It can thus be seen that the requirement of the samples being uncorrelated will practically speaking be fulfilled.

Experimental

Two types of experiments were carried out in which the hydrodynamics was affected in a controlled way:

- experiments with small step changes in superficial gas velocity;
- experiments with a gradual change in the particle size distribution.

Experiments of type A were carried out in a laboratory-scale fluidized bed as well as in a bench-scale fluidized bed; experiments of type B were carried out in a laboratory-scale twin-fluidized-bed (i.e., two interconnected fluidized beds).

Experimental Facilities and Operating Conditions. The experiments with varying superficial gas velocity were carried out in fluidized bed columns with a circular cross-section and an internal diameter of, respectively, 10 and 80 cm. In both columns a distributor plate made of sintered bronze particles is used; pore diameters are typically 30 μm . In both facilities, the bed material used is sand with a median diameter of 471 μm and a density of 2700 kg/m^3 (Geldart type B); the minimum fluidization velocity of this sand is 0.14 m/s. This sand is indicated with code S3; its size range is given in Table 1. The 10 cm ID bed was filled with S3 sand to a settled bed height of 20 cm; in the 80 cm ID bed, a settled bed height of 81 cm has been applied. The 10 cm ID bed was operated at a superficial gas velocity ranging from 0.12 to 0.38 m/s; in the 80 cm ID bed the superficial gas velocity was varied between 0.20 and 0.30 m/s.

Experiments of type B were carried out in a twin-fluidized-bed: two compartments with a rectangular cross-sectional area of 10 \times 10 cm, connected by a circular orifice of 20 mm diameter at 9 cm above the distributor. Figure 1 shows a schematic picture of the twin-bed facility. A constant solids flow of 0.5 kg/min was supplied to the first compartment, leading to a similar solids flow from the first to the second compartment through the orifice. A continuous solids flow was leaving the second compartment over an overflow weir; in this way the total mass in the system remained constant. In both twin-bed compartments the superficial gas velocity was 0.20 m/s. The bed height in both compartments was approximately 20 cm; due to small fluctuations in the solids feed, the bed height fluctuated with approximately 2 cm. In all experiments, the solids feed consisted of S3 sand; S1, S2, and S3 sand were used as starting material in both compartments of the twin-bed. The size ranges of the sand types are given in Table 1; all three types are Geldart B powders.

Pressure Measurements. Local pressure measurements in the bed were performed in all experiments. In the A type experiments the pressure drop over a part of the bed was measured as well.

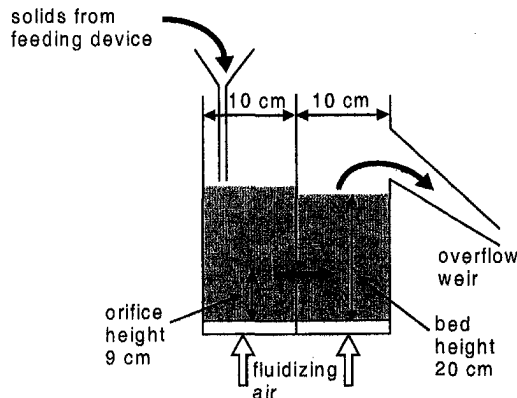


Fig. 1 A schematic overview of the twin-fluidized-bed used for the grade change (type B) experiments

Table 2 gives the positions of the pressure probes for the different facilities; 4 mm ID tubes of 10 to 40 cm long were used as pressure probes. The end of each probe was located at the fluidized bed wall and was covered by a wire gauze to prevent particles from intruding and blocking the probe.

Piezo-electric pressure sensors of Kistler type 7261 connected to the probes were used to measure the local pressure fluctuations. The charge from the piezo element is amplified and converted to a DC voltage signal using a Kistler amplifier type 5011. The sensitivities of amplification of the pressure signals were varied from 100 Pa/V to 400 Pa/V to utilize the sensor output range as optimal as possible. Due to a time constant that can be set in the amplifier, the lowest frequencies are high-pass filtered with a cut-off frequency of 0.16 Hz. By this filtering action the fluctuations of the pressure are measured relative to the local average pressure, i.e., the off-set of the signal is zero.

The sensor used for the pressure drop measurements is a diaphragm type differential pressure sensor, Validyne DP15. For the experiments in the 10 cm ID bed, a 0–3.5 kPa diaphragm has been employed; a 0–5.5 kPa diaphragm has been used for the 80 cm bed experiments. The sensor signal is amplified by a Validyne CD23 amplifier.

Data Acquisition and Analysis. The signals were transferred to a Scadas II data acquisition system (Difa Measuring Systems, The Netherlands) connected to a personal computer, controlled by the software package D_TAC. In the 10 cm ID bed experiments and in the twin-bed experiments, a sample frequency of 400 Hz was used to fulfill the requirement given by Eq. (2). For the 80 cm ID bed experiments, the average cycle time is lower; a sample frequency of 200 Hz sufficed in that case. The signals were low-pass filtered with a cut-off frequency of one third of the sample frequency, satisfying the Nyquist criterion. Subsequently, 16 bits analogue-to-digital conversion was applied to the signal. For the A type experiments, time-series of 240,000 points were recorded, i.e., a measurement time of 10 minutes for the 10 cm ID bed and 20 minutes for the 80 cm ID bed. For the B type experiments, which were carried out in the twin-bed, the time-series contained 1,920,000 points, corresponding to a time period of 80 minutes.

Table 2 Probe positions (height above the distributor) for the three facilities

Facility	Vertical probe position [cm]	
	Local pressure measurements	Pressure drop measurements
10 cm ID bed	3.6; 7.9; 16.5	3.0 - 12.7
80 cm ID bed	24; 44; 64	34 - 54
twin-bed	7.5; 17.5	-

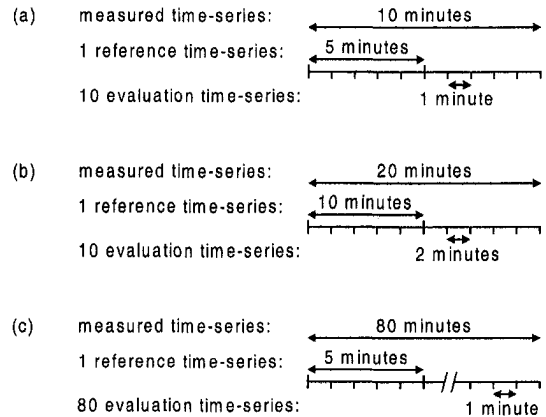


Fig. 2 A schematic representation of the division of the experimentally obtained time-series in reference and evaluation time-series for (a) the laboratory-scale fluidized bed, (b) the bench-scale fluidized bed, and (c) the twin-fluidized-bed

The hydrodynamic state of the bed with which other states are compared over time is called the reference state. A time-series of 120,000 points (viz., 10 minutes measuring time for the 80 cm ID bed and 5 minutes for the two other facilities) sampled at the reference state of the bed will be used as reference time-series. Since the time-series obtained in the experiments contain more than 120,000 points, only a part of these time-series is used. In the case of the A type experiments, this is the first half of the time-series measured at the reference state. For the B type experiments it is either the first five minutes or the last five minutes of the complete time-series.

For evaluation by the monitoring method, the complete time-series were divided in partial time-series of 24,000 points each (2 minutes for the 80 cm ID bed, 1 minute for the two other facilities), which will be called the evaluation time-series. For each evaluation time-series, the Z-value was calculated with the use of the reference time-series. The division of the measured time-series in reference and evaluation time-series is schematically depicted in Fig. 2.

Results and Discussion

Laboratory-Scale Fluidized Bed; Type A Experiments. In Fig. 3 the Z-value as a function of time is shown as calculated from the local pressure fluctuations measured in the 10 cm ID bed at 7.9 cm above the distributor. As reference time-series, the first half has been taken from a pressure time-series measured at a superficial gas velocity of 0.20 m/s (i.e., an excess gas velocity of 0.06 m/s). With this reference time-series, both the time-series from which it originates and a duplicate time-series, measured at the same operating conditions, have been evaluated. In both cases the complete time-series are divided in 10 evaluation time-series of one minute; for each evaluation time-series the Z-value is calculated.

Figure 3 shows that for both cases the Z-value stays within the $-3/3$ region, indicating that no statistically significant change in the bed hydrodynamics takes place. A certain variation in Z is found, since it is a statistic, implying it has a certain spread also if the system for which it is calculated is completely stationary. Moreover, it is practically impossible to fully eliminate external influences, like slight variations of the gas supply. Still, the variations in Z mostly stay inside the $-3/3$ region. However, when the superficial gas velocity is reduced to 0.19 m/s, the Z-value clearly leaves the $-3/3$ region, thus indicating a hydrodynamic behaviour significantly different from the reference state.

Figure 4 gives the average Z-value as a function of the excess gas velocity. Each value is the average of ten Z-values; the error bars indicate the standard deviation. As in the previous example, the employed pressure time-series have been sampled at 7.9 cm

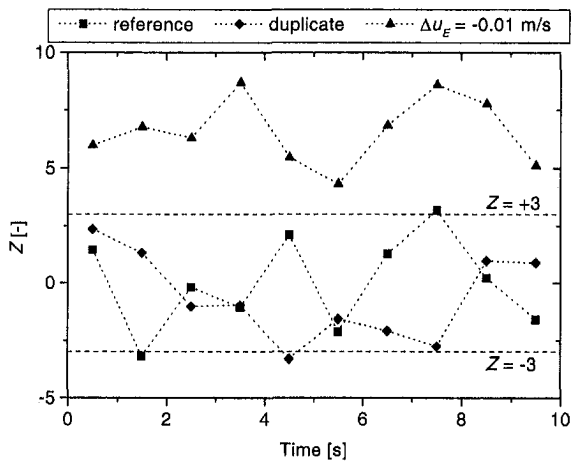


Fig. 3 The Z-value as a function of time for local pressure fluctuation measurements in the 10 cm ID bed at 7.9 cm above the distributor. The dashed lines at $Z = -3$ and $Z = 3$ mark the limits for a statistically significant difference in the hydrodynamics. The bed is initially operated at an excess gas velocity of 0.06 m/s. Both for the complete time-series from which the reference time-series has been taken (squares) and for the duplicate time-series (circles), the Z-value mainly stays within the $-3/3$ region. The Z-value for a time-series measured at an excess gas velocity of 0.05 m/s (triangles) clearly shows a significantly different hydrodynamical behaviour.

above the distributor; the reference time-series has been measured at an excess gas velocity of 0.06 m/s. The figure convincingly shows the Z-value to indicate not only that a change has taken place, but also how much the state of the bed deviates from a certain intended state: the larger the deviation from the reference state, the larger the absolute value of Z. Moreover, it is exhibited that a change in the excess gas velocity as small as 0.01 m/s, as well upward as downward, is detected as a significant change in the hydrodynamics.

Figure 5 shows the Z-values for the local pressure fluctuations measured at three positions in the bed and for the *fluctuations* in the pressure drop across a part of the bed. As indicated by the error bars, the standard deviations for all positions are of comparable magnitude as to those for a probe height of 7.9 cm shown in Fig. 4. It can be seen that there is no substantial difference between the Z-values for the different measurement positions; all three absolute pressure measurements as well as the pressure drop measurements clearly show the change in the hydrodynamics reflected in Z with varying the excess gas velocity.

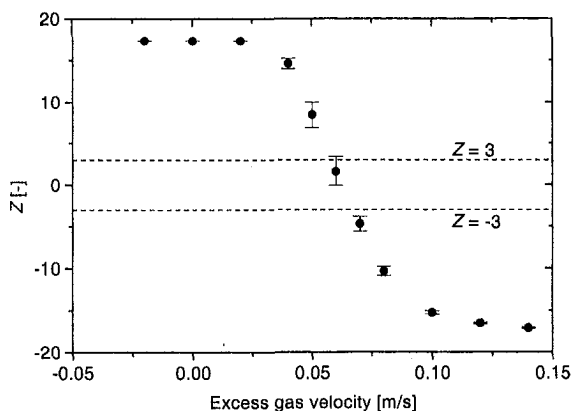


Fig. 4 The Z-value (averaged over 10 minutes) as a function of the excess gas velocity for local pressure fluctuations in the 10 cm ID bed at 7.9 cm above the distributor. The error bars give the standard deviation; the dashed lines mark the limits for a significant difference. The time-series measured at an excess gas velocity of 0.06 m/s is used as the reference state.

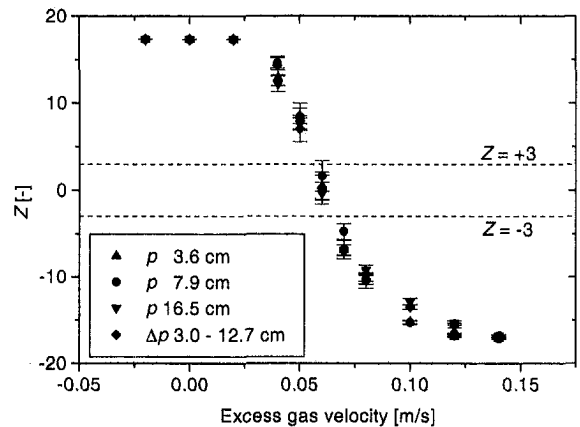


Fig. 5 The Z-value (averaged over 10 minutes) as a function of the excess gas velocity for local pressure fluctuations in the 10 cm ID bed at three heights above the distributor and for pressure drop fluctuations over a part of the bed. The error bars give the standard deviation; the dashed lines mark the limits for a significant difference. The time-series measured at an excess gas velocity of 0.06 m/s are used as the reference state for each respective signal.

Figures 4 and 5 show the Z-value to change most steeply with the excess gas velocity around the reference state, i.e., it is most sensitive close to the state which is chosen as the target state. This is alternatively shown by the standard deviations depicted in Fig. 3. Around the reference state, the standard deviations are largest: in that region, the monitoring method is most sensitive to small variations in the pressure time-series. This is because Z saturates for an excess gas velocity very different from the reference state. When Z reaches its minimum or maximum value (cf., Eq. (10)), it does not change anymore when moving further away from the reference state and its standard deviation drops to zero. So when two evaluated time-series give the same Z-values which are close to the maximum or minimum Z-value, one may not conclude that the two situations, from which those time-series originate, show the same behaviour, but one should choose a new reference state.

The effect of the choice of a new reference state is demonstrated in Fig. 6: now the bed behaviour at an excess gas velocity of 0.16 m/s is chosen as the reference state. The picture shows a dependence of Z on the excess gas velocity that is qualitatively similar to that depicted in Fig. 5, but the slope of the curve is now somewhat more moderate. This is reasonable, since we are now further away from the point of minimum fluidization, so that a change in the excess gas velocity u_E with the same absolute quantity will have a smaller influence on the hydrodynamics. Alternatively said, since the gas bubbles—of which the dynamic

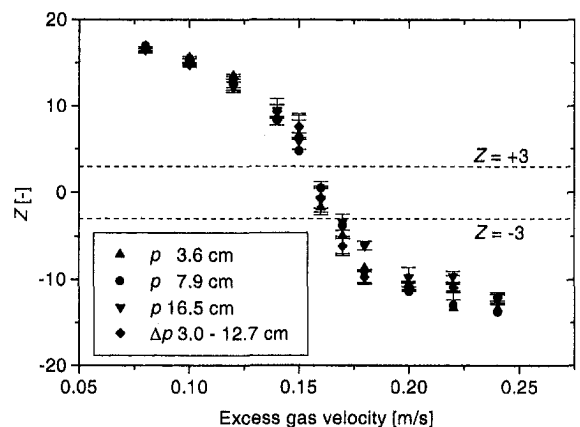


Fig. 6 Idem as Fig. 5, but now the time-series measured at an excess gas velocity of 0.16 m/s are used as the reference state

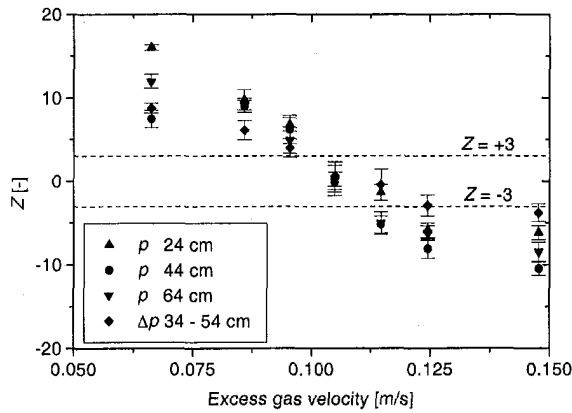


Fig. 7 The Z-value (averaged over 20 minutes) as a function of the excess gas velocity for local pressure fluctuations in the 80 cm ID bed at three heights above the distributor and for pressure drop fluctuations over a part of the bed. The error bars give the standard deviation; the dashed lines mark the limits for a significant difference. The time-series measured at an excess gas velocity of 0.105 m/s are used as the reference state for each respective signal.

behaviour is reflected in the pressure fluctuation signal—are larger, the influence of adding the same extra amount of gas will be smaller than for the case of smaller bubbles. Consequently, we expect that for higher values of u_E/u_{mf} the method will need a larger change in u_E to indicate a significantly different hydrodynamic state. For this particular situation where u_E/u_{mf} is 1.1, the monitoring method however still detects a change in the excess gas velocity of 0.01 m/s. The performance of the monitoring method at higher excess gas velocities is currently being investigated by the authors. The preliminary results show that the sensitivity of the method to changes in excess gas velocity and in particle size distribution further decreases at increasing gas velocity. When the method is for example used to detect agglomeration, this means that it will take longer before agglomeration is noticed. However, at higher gas velocity it will also take longer before agglomeration has a negative effect on the hydrodynamics: the ‘resistance’ of the bed to agglomeration is larger at higher gas velocities. Therefore, we expect the reduced sensitivity at higher gas velocities not to be a crucial problem.

Bench-Scale Fluidized Bed; Type A Experiments. In the case of the bench-scale fluidized bed of 80 cm ID, the pressure time-series are divided in ten time-series of 2 minutes each. A reference time-series of 10 minutes is taken from a pressure time-series measured when the bed was operated at an excess gas velocity of 0.105 m/s. The dependence of Z on the excess gas velocity is shown in Fig. 7 for three different local pressure measurement positions and for the pressure drop across a part of the bed. Unlike the case of the 10 cm ID bed, in the larger 80 cm ID bed the trend in the Z-value much more depends on the pressure sampling position for which it is calculated. Especially the pressure drop gives poorer results regarding the sensitivity of Z for changes in the gas velocity compared to the local pressure measurements. This is possibly due to the fact that in pressure drop fluctuations fast pressure waves traveling through the bed are filtered out, while the fast pressure waves also reflect an important part of the bed hydrodynamics (Van der Schaaf et al., 1998). The Z-values calculated from the local pressure signals sampled in the upper part of the bed (at 44 and at 64 cm above the distributor) still show a significant change in the hydrodynamics when the excess gas velocity differs only 0.01 m/s from the reference state.

While in the laboratory-scale 10 cm ID fluidized bed, the sampling position does not remarkably influence the results obtained with the monitoring method (cf., Figs. 5 and 6), in the 80 cm ID bed it clearly does. For a change in the excess gas velocity caused by altering the superficial gas velocity, the whole bed is affected

and one optimum measurement position can be chosen for evaluation. However, when one also wants to monitor phenomena in a large scale fluidized bed that (initially) take place locally, like agglomeration of particles or clogging of the distributor, one will have to measure at different vertical positions and possibly also at different horizontal positions. Furthermore, in a larger fluidized bed independent hydrodynamic ‘cells’ can be distinguished beside each other (Kunii and Levenspiel, 1991), necessitating measuring at multiple positions in the horizontal plane for conscientiously monitoring the process. In a small laboratory-scale bed one measurement position will normally suffice, since all parts of the bed are strongly coupled: the pressure fluctuations at one point in the bed reflect the complete bed behaviour.

Twin-Fluidized-Bed; Type B Experiments. In the first twin-bed experiment, S3 sand is used as starting material in the two compartments; the solids feed to the first compartment also consists of S3 sand. Accordingly, the particle size distribution in the two twin-bed compartments remains unaltered and no change in the hydrodynamics is expected. Figure 8 shows the Z-value as a function of time for pressure fluctuations measured at 7.5 cm (solid lines) and 17.5 cm (dotted lines) above the distributor in the second twin-bed compartment. The thin lines give the Z-value for each separate time-series of 1 minute. It can be seen that the Z-value mainly stays within the $-3/3$ region. However, small temporary changes, like fluctuations in the solids feed flow giving variations in the bed height, will sometimes push the Z-value somewhat further away from zero. The effect of these momentary variations can be reduced by applying a moving-average-filter; the thick lines in Fig. 8 give the moving average of Z over a period of five minutes.

Furthermore, Fig. 8 shows that the pressure signal for the pressure probe at 17.5 cm height is less stationary than the pressure signal for 7.5 cm height; this is due to the fact that the 17.5 cm probe is only 2.5 cm away from the bed surface and is therefore much more sensitive for fluctuations in the bed surface. In the twin-bed experiments we want to focus on changes in the particle size distribution and not on variations in the bed height; the measurements at 7.5 cm seem more suitable for that purpose. However, in industrial practice this difference between the probe positions can be exploited. Whereas the Z-value for one position does only indicate if the hydrodynamics changes and does not give information about the nature of a change, combining the information from multiple probe positions may enable identification of the cause of the change in hydrodynamics.

Subsequently, a ‘grade change’ from S1 sand to S3 sand was carried out: both twin-bed compartments were filled with S1 sand and at $t = 0$ the solids feed of S3 sand was started. In Fig. 9 the

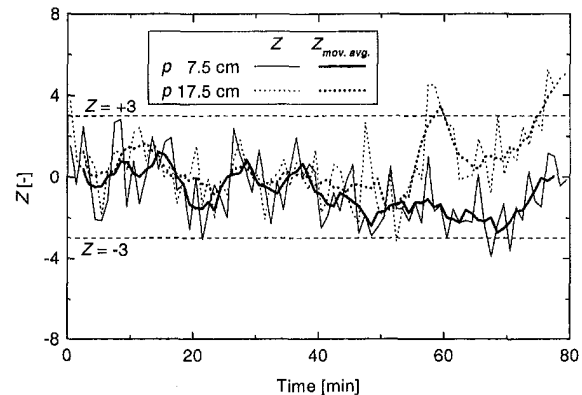


Fig. 8 The Z-values (thin lines) and their moving average (thick lines) calculated for local pressure fluctuations at two pressure probe positions in the second twin-bed compartment. The bed material is S3 sand; a constant flow of this sand is added to the first twin-bed compartment and removed from the second compartment. The first five minutes of the pressure fluctuation measurements are used as reference time-series.

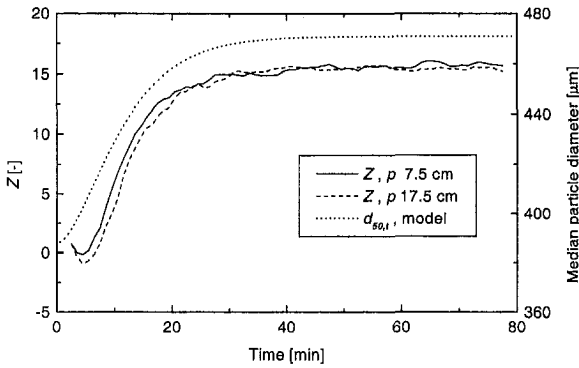


Fig. 9 The moving average of the Z -value calculated for local pressure fluctuations at two pressure probe positions in the second twin-bed compartment; a grade change from S1 sand to S3 sand is shown. The first five minutes of the pressure fluctuation measurements are used as reference time-series. The dotted curve gives the median particle diameter calculated using Eq. (11).

averaged Z -value (moving average over 5 minutes) as a function of the time is shown. When the experiment is started, the bed level varies because of the starting of the particle feed. As stated before, this less influences the starting of the probe at 7.5 cm above the distributor than the one at 17.5 cm.

To compare the calculated Z -value to the change in particle size distribution in the fluidized bed, we use a simple model for predicting the median particle diameter in the bed. Since it is shown by Stellema et al. (1997) that each well-fluidized compartment of the twin-bed can be considered as an ideal mixer for the particle phase, the twin-bed can be modeled as two equally sized ideal mixers in series. When $d_{50,0}$ is the median particle diameter of the starting material and $d_{50,\infty}$ the median diameter of the added sand (i.e., the median diameter in the bed in the final situation), the median particle diameter $d_{50,t}$ in the bed at time t is given by

$$d_{50,t} = d_{50,\infty} - (d_{50,\infty} - d_{50,0}) \frac{t + \tau}{\tau} e^{-t/\tau} \quad (11)$$

where τ is the residence time of one twin-bed compartment. From the mass in one compartment and the solids feed, it can be calculated that τ is 6 minutes. In Fig. 9 the dotted curve shows the median particle diameter calculated using Eq. (11); it can be seen that there is a clear relationship between the Z -value and the calculated particle diameter.

The Z -curve in Fig. 9 is calculated using the first five minutes of the pressure time-series as the reference state. On the one hand, this curve shows a strong resemblance with the particle diameter curve; this may seem to justify choosing the first five minutes of the experiment as the reference state. On the other hand, the experiments with varying gas velocity in the 10 cm bed already showed that the monitoring method is rather insensitive near the maximum and minimum values. The final Z -value in Fig. 9 (about 16) comes close to the maximal possible Z -value (17.3). Therefore, if one wants to monitor if the fluidized bed hydrodynamics has reached a stationary state after applying a grade change, it is better to take a time-series at the final stage as the reference state. The resulting curve when taking the last 5 minutes as the reference state is shown in Fig. 10: in this case the Z -value rises much more gradual. After about 40 minutes the Z -curve shows that a stationary situation (i.e., $|Z| < 3$) is reached. This corresponds to reaching 99% of the final value in the residence time model, which shows that the method is a useful tool for indicating if the fluidized bed hydrodynamics has reached a stationary situation. When using the method for on-line monitoring, it is of course impossible to take a future time-series as the reference state. Alternatively, measurements of the stationary situation one wants to reach obtained in a previous run can be used as reference state.

To focus on the sensitivity of the monitoring method, a grade

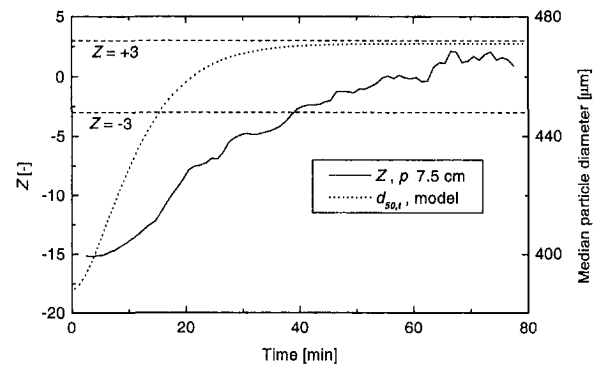


Fig. 10 The moving average of the Z -value calculated for local pressure fluctuations at 7.5 cm above the distributor in the second twin-bed compartment; a grade change from S1 sand to S3 sand is shown. The last five minutes of the pressure fluctuation measurements are used as reference time-series. The dotted curve gives the median particle diameter calculated using Eq. (11).

change from S2 sand to S3 sand is executed; the median particle diameters of these two sand types are rather close (respectively, 435 and 471 μm). During this experiment, samples have been taken from the sand leaving the second twin-bed compartment by the overflow weir to test if the two-ideal-mixers-in-series model is correct. The result is shown in Fig. 11: the experimentally determined median particle diameters lie close to the model curve. Only in the beginning some deviations are shown; this is likely due to fluctuations in the bed height when starting the experiment, which are also shown by the Z -curve which first declines before rising. Like for the S1 sand to S3 sand grade change, the stationary situation ($|Z| < 3$) is reached after 40 minutes. This is reasonable since the only difference with the previous experiment is the type of sand used as starting material; the residence time of the sand in both compartments is the same for both experiments.

To compare our method to a more classical tool for analysing pressure fluctuations, Fig. 12 shows the power spectral densities for two parts of the pressure time-series measured during the grade change from S2 sand to S3 sand: the part measured between 20 and 25 minutes and the part measured between 75 and 80 minutes after the start of the experiment. Whereas our 'Z-method' clearly indicates a statistically significant difference between these two parts of the time-series (see Fig. 11), the power spectral densities do not show this difference. This illustrates that the power spectral density of pressure fluctuations is less sensitive to changes in the fluidized bed hydrodynamics than our Z -method.

Figure 11 shows that 20 minutes after the start of the experiment the Z -value clearly indicates that the hydrodynamic state is still significantly different from the target state. Both the model calculation and the particle size measurements give a median particle

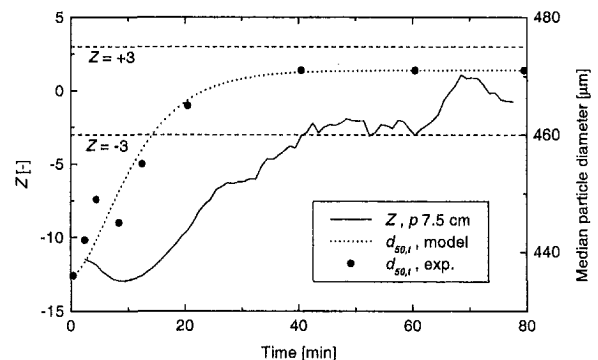


Fig. 11 Idem as Fig. 10, but now for a grade change from S2 sand to S3 sand. The circles give the measured median particle diameters, determined from samples of the outflowing sand.

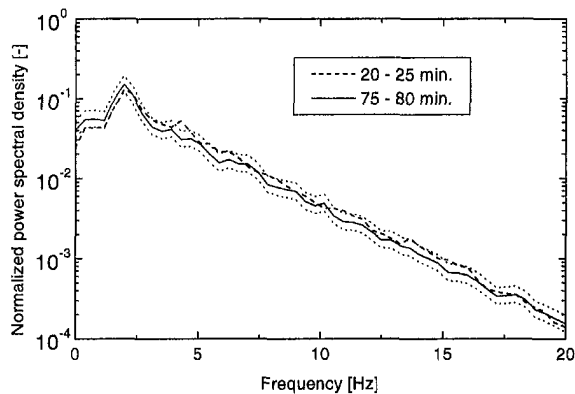


Fig. 12 The power spectral densities for a grade change from S2 sand to S3 sand, normalized with respect to the standard deviation. The dashed curve gives the power spectral density for the pressure signal measured between 20 and 25 minutes after the start of the experiment and the solid curve for the pressure signal measured between 75 and 80 minutes. The dashed curves give the 99% confidence region of the solid curve.

diameter of about $465 \mu\text{m}$ at that moment. This illustrates the sensitivity of the monitoring method, since the final median particle diameter is $471 \mu\text{m}$ (sand type S3). Using the Wen and Yu (1966) correlation for the minimum fluidization velocity, u_{mf} , giving

$$u_{mf} = \frac{\eta}{d\rho_g} \left[-33.7 + \sqrt{(33.7)^2 + 0.0408 \frac{d^3\rho_g(\rho_s - \rho_g)g}{\eta^2}} \right] \quad (12)$$

and knowing that u_{mf} of S3 sand is experimentally determined to be 0.14 m/s, it can be estimated that u_{mf} of the mixture is 0.13 m/s at $t = 20$ minutes. Consequently, it can be concluded that the grade change experiments show that the method is able to detect a change as small as 0.01 m/s in the minimum fluidization velocity, which also means a change of 0.01 m/s in the excess gas velocity. This agrees well with the results obtained for the variation of the superficial gas velocity in the 10 and 80 cm ID bed (cf., Figs. 5, 6, and 7).

Conclusions

1. The monitoring method using the short-term predictability of pressure fluctuations (Schouten and Van den Bleek, 1998) is a sensitive method for detecting changes in fluidized bed hydrodynamics caused by variations in the excess gas velocity, due to either changing superficial gas velocity or changing particle size distribution. In both cases, experiments with u_E/u_{mf} ranging from 0 to about 1 showed that the monitoring method is able to detect changes in the excess gas velocity as small as 0.01 m/s.

2. It has been shown that the Z-value does not only indicate if the hydrodynamic state in the fluidized bed significantly differs from a reference state; it also gives an indication how much the situation differs from the reference state. However, there are restrictions to this quantitative use of the Z-value, since there are a minimum and a maximum Z-value; near these limits the method is insensitive to changes. Therefore, the reference state should be chosen at the hydrodynamic state one wants to reach or maintain, since the Z-value is most sensitive around this reference state.

3. For the case of a 'grade change' (e.g., changing particle size distribution), it has been shown that the Z-value accurately shows the point at which a stationary situation is reached. This is substantiated by model calculations as well as by particle size measurements. Applying a moving-average-filter is useful in this case to suppress the effect of small temporary variations, e.g., in solids feed flow or superficial gas velocity.

4. In many practical situations, the choice of the pressure probe positions will be important for the performance of the monitoring method. In the small 10 cm ID bed used in this study, all probe positions give the same information, while in the bench-scale 80 cm ID bed the results obtained at the higher probe positions are more sensitive for changes in the superficial gas velocity. When changes in the bed height occur, the pressure signal from probes near the bed level will be dominated by these bed level variations at the cost of decreased sensitivity for other changes in the bed. If one is interested in those other changes, like changing particle size distribution, it is advisable to measure also at lower positions in the bed.

5. The Z-value, calculated for a single pressure measurement position, does not give information about what the nature of the change is, but only indicates that some, statistically significant change has occurred. However, by comparing the Z-values calculated for multiple positions, one can deduce information about the cause of the change in hydrodynamics. By choosing a good measurement configuration, one could for example discriminate changes in the hydrodynamics caused by changing particle size distribution from those caused by bed level variations.

References

- Albano, A. M., Rapp, P. E., and Passamante, A., 1995, "Kolmogorov-Smirnov Test Distinguishes Attractors With Similar Dimensions," *Physical Review E*, Vol. 52, pp. 196–206.
- Diks, C., Van Zwet, W. R., Takens, F., and DeGoede, J., 1996, "Detecting Differences Between Delay Vector Distributions," *Physical Review E*, Vol. 53, pp. 2169–2176.
- Kantz, H., 1994, "Quantifying the Closeness of Fractal Measures," *Physical Review E*, Vol. 49, pp. 5091–5097.
- Kennel, M. B., 1997, "Statistical Test for Dynamical Nonstationarity in Observed Time-Series Data," *Physical Review E*, Vol. 56, pp. 316–321.
- Kunii, D., and Levenspiel, O., 1991, *Fluidization Engineering*, 2nd edition, Butterworth-Heinemann, Stoneham.
- Schouten, J. C., Takens, F., and Van den Bleek, C. M., 1994, "Estimation of the Dimension of a Noisy Attractor," *Physical Review E*, Vol. 50, pp. 1851–1861.
- Schouten, J. C., and Van den Bleek, C. M., 1998, "Monitoring the Quality of Fluidization Using the Short-Term Predictability of Pressure Fluctuations," *AIChE Journal*, Vol. 44, pp. 48–60.
- Spiegel, M. R., 1988, "Schaum's Outline of Theory and Problems of Statistics," *Schaum's Outline Series*, McGraw-Hill, New York.
- Stellema, C. S., Kolar, Z. I., de Goeij, J. J. M., Schouten, J. C., and Van den Bleek, C. M., 1997, "Solids Residence Time Distribution in Interconnected Fluidized Beds," *AIChE Symposium Series*, Vol. 93, No. 317, pp. 40–45.
- Takens, F., 1981, "Detecting Strange Attractors in Turbulence," *Lecture Notes in Mathematics*, Vol. 898, Dynamical Systems and Turbulence, D. A. Rand and L.-S. Young, eds., Springer-Verlag, Berlin, Germany, pp. 366–381.
- Van der Schaaf, J., Schouten, J. C., and Van den Bleek, C. M., 1998, "Origin, Propagation and Attenuation of Pressure Waves in Gas-Solids Fluidized Beds," *Powder Technology*, Vol. 95, pp. 220–233.
- Vander Stappen, M. L. M., 1996, "Chaotic Hydrodynamics of Fluidized Beds," Ph.D. thesis, Delft University of Technology, Delft, The Netherlands.
- Van Ommen, J. R., Schouten, J. C., and Van den Bleek, C. M., 1999, "An Early-Warning-Method for Detecting Bed Agglomeration in Fluidized Bed Combustors," *Proceedings of the 15th International Conference on Fluidized Bed Combustion*, R. B. Reuther, ed., ASME, New York, Paper No. FBC99-0150.
- Wen, C. Y., and Yu, Y. H., 1966, "A Generalized Method for Predicting the Minimum Fluidization Velocity," *AIChE Journal*, Vol. 12, pp. 610–612.
- Wright, J., 1995, "Monitoring Changes in Time of Chaotic Nonlinear Systems," *Chaos*, Vol. 5, pp. 356–366.

Flow Pattern Transition During Gas Liquid Upflow Through Vertical Concentric Annuli— Part I: Experimental Investigations

G. Das

Research Associate,
Department of Chemical Engineering.

P. K. Das

Associate Professor,
Department of Mechanical Engineering,
pkd@mech.iitkgp.ernet.in

N. K. Purohit

Former Professor,
Department of Chemical Engineering.

A. K. Mitra

Former Professor,
Department of Chemical Engineering.

Indian Institute of Technology,
Kharagpur - 721 302, India

In the present work, extensive experiments have been carried out on air-water upflow through concentric annuli to identify the distribution of the two phases in the bubbly, slug, and churn flow regimes. A parallel plate type conductivity probe has been indigenously designed and constructed from a unique material for this purpose. The probability density function analysis of the probe signals has been performed for a better appraisal of the flow situation. The unique design of the probe and its extensive use at different axial and azimuthal positions have enabled us to note the asymmetric phase distribution in the slug flow regime. Based on the experimental results, an insight has been obtained into the physical mechanism underlying the transitions between different flow regimes. This has enabled the development of mechanistic models for the transition boundaries between the bubbly-slug and the slug-churn flow regimes. They have been reported in a subsequent paper.

Introduction

The simultaneous flow of gas and liquid through an annular passage is encountered during the flow of oil and gas through risers in petroleum industries, the flow of complex mixtures in boring operation and in process equipment like heat exchangers, serpentine boilers, and internal loop air lift reactors. In addition, a study of the flow through this doubly connected geometry provides a stepping stone for investigations of the flow through complex multiply connected geometries like the shell side of a shell and tube heat exchanger, the rod bundle of a nuclear reactor, and the tubing string in oil wells. In all these applications, the two phases exhibit a variety of interfacial configurations. The distribution of the two phases depends on the flow rates and properties of the two fluids, conduit shape, and the presence of any body force field. Based on the extensive studies on cocurrent upflow of gas-liquid mixture through vertical circular tubes, the past researchers (Hewitt and Hall Taylor, 1970; Jones and Zuber, 1975, etc.) have been successful in delineating the interfacial distributions into four major flow regimes or flow patterns. They are bubbly, slug, churn, and annular flow. Elaborate efforts (Taitel et al., 1980; Weisman and Kang, 1981; Mishima and Ishii, 1984; Mc Quillan and Whalley, 1985; Billicki and Kestin, 1987, etc.) have also been made to develop mechanistic models for predicting the transitions between different flow patterns. As the flow patterns and their transition criteria depend on the conduit shape, there is no guarantee that the information already available for circular tubes can be extended to a concentric annulus. The very few studies on gas-liquid upflow through an annulus have revealed that although similar flow patterns exist in this conduit, there are subtle differences between the phase distributions characterizing the different regimes in the two geometries.

Sadatomi et al. (1982) have identified the bubbly, slug, and annular flow patterns in a concentric annulus. Venkateswarao et

al. (1982) in their experiments on rod bundles have also identified the bubbly, slug, churn, and annular flow regimes and reported the existence of two types of Taylor bubbles, the shroud and cell Taylor bubbles in slug flow. Ferukawa and Sekoguchi (1986) also observed the aforementioned flow regimes in an annulus by visual observations and photographic techniques. They noted the difference between slug flow in a circular tube and an annulus due to the presence of asymmetric Taylor bubbles in the later case. Caetano et al. (1989a) have reported the existence of asymmetric Taylor bubbles in slug flow, but have not incorporated asymmetry in their analysis. Kelessidis and Dukler (1989) have employed point electrode type conductivity probes and the PDF analysis of the probe signals to identify the flow regimes as well as the transitions between them. Their studies in a concentric and an eccentric annulus have mentioned the asymmetric structure of the Taylor bubbles and negligible effect of eccentricity on the flow regimes. However, they have neither undertaken a detailed study of this unique feature of two-phase flow in a concentric annulus nor incorporated asymmetry in their transition criteria. Nakoryakov et al. (1992) noted altogether different flow distribution in a narrow vertical annulus with a gap thickness less than the capillary constant.

The literature survey shows that the limited studies on two-phase flow through an annulus have identified the flow regimes by visual observations in most of the cases. As a consequence, they could neither provide an insight into the intrinsic details of the flow characteristics nor the development of one flow regime from the other with changes in operating conditions. Moreover, the transition criteria proposed by them were mere extensions of the theory suggested by Taitel et al. (1980). This leaves a scope for an in-depth study of the phase distribution over a cross-sectional plane as well as along the axial length to understand the exact mechanisms underlying the transitions.

With these considerations, extensive experimentation has been carried out in the present work to investigate the local phase distribution characterizing each flow regime and the changes in the distribution marking the transitions from one regime to another. Considering the uniqueness of the slug flow pattern in this geometry and the scarce literature in this field, the work has been

Contributed by the Fluids Engineering Division for publication in the JOURNAL OF FLUIDS ENGINEERING. Manuscript received by the Fluids Engineering Division February 6, 1997; revised manuscript received October 6, 1998. Associate Technical Editor: M. Sommerfeld.

confined in and around the slug flow regime. It focuses on the mechanisms of the bubbly-slug and the slug-churn transitions. The conductivity probe technique has been adopted for this purpose. Indigenously designed unique probes positioned at different axial and azimuthal locations have enabled us to understand the asymmetry in flow situation over a wide variety of operating conditions.

Experiments

The test facility consists of a vertical test section, the fluid handling systems, and the instrumentation scheme. The test section is a concentric annulus. It is preceded by an entry section which is a circular tube with the same inside diameter as the outer tube of the corresponding annulus. The two phases are introduced at the base of the entry section through two openings (dia = 12.7 mm) positioned diametrically opposite to each other. It has been observed that this arrangement ensures thorough mixing of the two fluids prior to the annular test passage for the entire range of phase velocities used in the investigation. The annulus is constructed by inserting galvanized iron pipes concentrically into acrylic (poly-methyl methacrylate) columns by means of specially designed flanges at the lower and upper end of the outer tube. The transparent outer tube enables visual observation of the flow phenomena occurring throughout the test length. Three annuli A, B, and C of outside diameters 0.0508 m, 0.0381 m, 0.0254 m and inside diameters 0.0254 m, 0.0127 m, 0.0127 m, respectively, have been constructed to investigate the effect of annulus dimensions on phase distribution. Air and water have been selected as the test fluids. The two phases are gravity separated in the separator after flowing through the entry section and the annular passage.

Apart from the visual observations of the flow phenomena, the phase distribution during different flow regimes and the changes in flow structure during the bubbly-slug and the slug-churn transitions have been studied in details using conductivity probes. The widely different electrical conductivities of the test fluids have enabled this selection. Although the conductivity probes of different designs have widely been used in circular tubes, they have rarely been adopted in an annulus. Only two studies by Kelessides and Dukler (1989, 1990) have so far reported the use of point electrode probes in an annulus. This is mainly due to the difficulty of installing probes of conventional designs in this doubly connected geometry.

In the present work, a specially designed parallel plate type conductivity probe has been indigenously constructed from a unique material. They have been made of 1 mm wide strips cut out from 1 mm thick plates generally used as double sided printed circuit boards. The copper claddings on the two external faces, placed perpendicular to the direction of flow serve as the two electrodes of the probe. The filler between them being a perfect insulator ensures that the current path is provided only by the surrounding fluid when the probe is dipped in it. The probe is inserted in the annular passage through the outer tube and is held normal to the wall. It spans the annular gap radially and gives an idea regarding the phase distribution along its length. Readings obtained simultaneously from two probes inserted at diametrically opposite points in the same cross-sectional plane helps to assess the asymmetry in phase distribution. The construction of the PCB ensures sufficient rigidity of the probe so that it is not deflected by the flowing mixture when it is held by the outer wall only. It also provides uniformity of the electrodes and a constant gap between them. Although the probe is not nonintrusive, it offers a small obstruction to the flow passage and negligible wake formation at its downstream. The area blockage in a diametral plane has been calculated as 1.2 percent in the smallest annulus. Since the cost of the probe is not prohibitive, an elaborate arrangement of eight conductivity probes have been installed at different measuring stations to investigate the axial development of flow as well as the azimuthal phase distribution. Two pairs of probes (P_1 - P_4) have been inserted at the lower end of the test section and the other four probes (P_5 - P_8) have been located far downstream where the flow

can be assumed as further developed. The probes designated by odd numbers have been located at one side of the annulus and the consecutive even numbered ones on the diametrically opposite side.

To increase the sensitivity of the probe, it is connected in parallel to one of the arms of a Wheatstone bridge. The voltage signal across the bridge is amplified, rectified, filtered, and recorded in a multichannel recorder. The resistances of the bridge are so adjusted that the bridge is balanced when the probe is totally submerged in water. On the other hand, the unbalanced voltage across the bridge during the passage of an air bubble results in a peak in the output signal.

Identification of the Flow Regimes

A knowledge regarding the instantaneous distribution of the two phases along the probe length can be obtained from the physical appearance of the probe signals under different flow rates of the two phases. A typical probe signal obtained under the operating conditions of the present work is shown in Fig. 1(a). It exhibits fluctuations between the two extreme values of voltage. The valleys at zero voltage (period A) show water to be the continuous phase and the peaks to positive voltage values (periods B and C) show the passage of air bubbles of different sizes. Besides direct readout of the trace, an effort has also been made to quantitatively evaluate the ratio of the peaks and the valleys in order to obtain a measure of the relative volumes of the two phases contacting the probe for the pulsating nature of the flow phenomenon. This has been achieved by determining the gas time ratio t_g of the signals, where t_g at a point in the conduit has been defined by Akagawa (1964) as the ratio of the existence of gas phase ($\sum t_a$) to the entire time during which the test run was executed ($\sum(t_a + t_w)$). In this case t_a and t_w are the time intervals during which the predominant phase around the probe is air and water respectively. A threshold value of 1.5 mV distinguishes the signals indicating random fluctuations in the valleys from those signifying the passage of air bubbles. This is based on our observations that the output at zero voltage is more or less steady with a maximum fluctuation of 1 mV during the flow of water through the test passage and a peak of at least 2 mV is produced at the minimum air velocity when very small bubbles are occasionally observed in the water stream.

While the probe signals provide an idea of the local phase distribution, the probability density function (PDF) analysis of the signals is performed for an effective identification of the flow regimes. A detailed description of this analysis has been presented by Jones and Zuber (1975) and Kelessidis and Dukler (1989). A typical PDF curve corresponding to the trace of Fig. 1(a) is shown in Fig. 1(b) where the PDF values corresponding to the voltage values have been plotted against the ratio of voltage to maximum voltage (V/V_{max}) as the ordinate following the methodology of Kelessidis and Dukler (1989). V_{max} is the maximum voltage for which a non zero PDF value is estimated. Therefore, the peaks at zero and maximum voltage indicate the respective presence of water and air as the continuous phase around the probe. The area between the two peaks depict the presence of air bubbles in the continuous water phase and the liquid films surrounding the elongated bubbles. An additional effort has been made to calculate the ratio of the heights of the peaks at the two extreme values of voltage (designated as the peak ratio) to pinpoint the flow regime transitions.

In order to ensure reliable values of PDF curves and gas-time

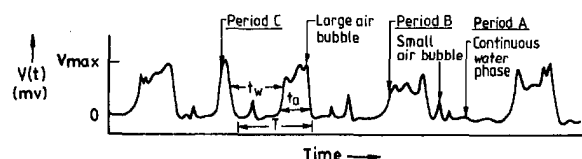


Fig. 1(a) Typical probe signal representing the pulsating flow phenomena

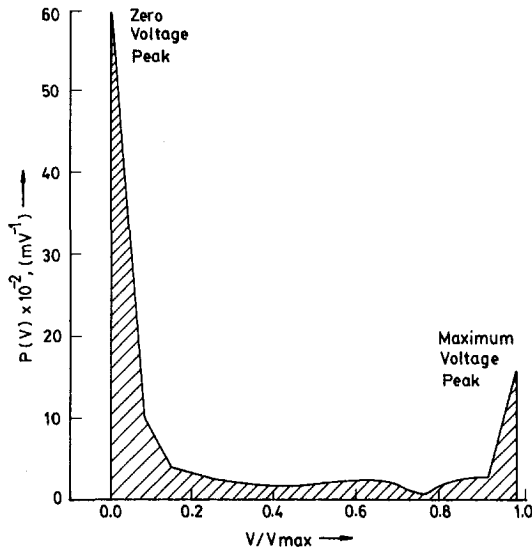


Fig. 1(b) The corresponding PDF curve

ratios for a particular set of operating conditions, the signals need to be recorded for a sufficiently long time. Our initial test runs have revealed that a period of 1 minute is adequate for this purpose. The reproducibility of the results was checked by recording the probe signals for longer time periods under different combinations of phase velocities in the three flow regimes. Different windows of time span 1 minute have been selected from the same continuous signals for the construction of PDFs and calculation of t_g . Both the parameters exhibited good repeatability for all the cases. The

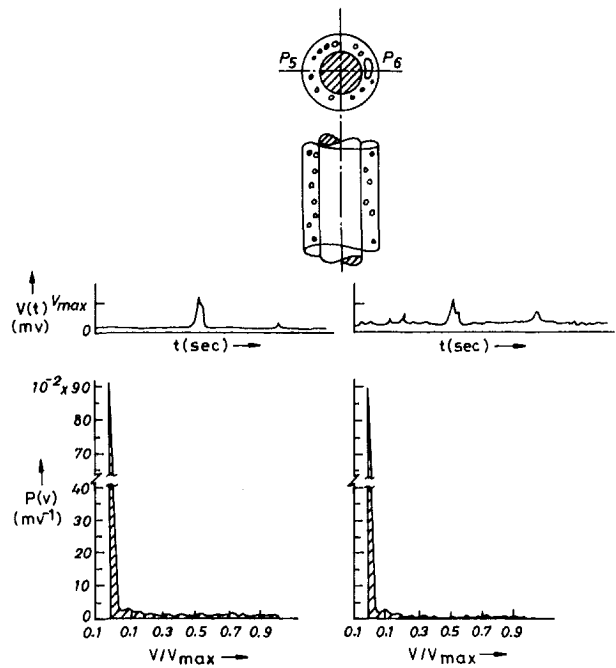


Fig. 3 Bubbly flow through annulus B, $U_{LS} = 0.14$ m/s, $U_{GS} = 0.082$ m/s

gas-time ratio and the peak values of the different PDFs thus constructed agreed within 5 percent whereas the total area under the PDF curve varied within 10 percent.

The typical probe signals and the corresponding PDF curves representing the phase distribution of fully developed bubbly, dispersed bubbly, slug and the churn flow regimes have been presented in Fig. 2 where the quantitative measures indicating the limits of the different regimes have also been tabulated. Bubbly flow regime comprising of discrete cap and spherical bubbles dispersed in the continuous water phase is indicated by a steady output at zero voltage with occasional peaks of varying widths and amplitudes in the probe signals and a single peaked PDF at zero voltage. On the other hand, the homogeneous distribution of spherical bubbles characterising the dispersed bubbly flow regime is denoted by the uniform oscillations about the zero voltage in the probe signals and a unimodal PDF curve with a large area beyond the peak till $V/V_{max} = 0.3$. Although the two bubbly flows existing at different water velocities can not always be distinguished by visual observations, the objective methods of flow pattern detection bring out the subtle differences. The value of t_g exceeding 0.2 for many cases indicate that the dispersed bubbly flow can exist at higher void fractions as compared to ordinary bubbly flow. The small width and amplitude of the crowded pulses in the signals and the negligible area at higher voltage values in the PDF curve is indicative of the dense distribution of the small sized bubbles characterising this flow pattern. The intermittent character of the slug flow regime with the Taylor bubbles and the liquid slugs alternating one another is obvious from the pulsating nature of the trace and the bimodal PDF curve. Fig. 2 shows the typical asymmetric shape of the Taylor bubble in an annular geometry. They enclose the inner tube only partially and the peripheral area between the two edges of the bubble is occupied by a liquid bridge. The chaotic nature of the churn flow regime is brought out by the random oscillations in the probe signals where no separate peaks and valleys can be identified. On the other hand, a large area under the PDF curve over the entire range of voltage values highlights the well mixed nature of this flow pattern.

Although experiments have been performed in all the three annuli over a wide range of phase velocities, only a few representative results in annulus B have been presented here to avoid repetition. Signals recorded simultaneously from P_5 and P_6 have been selected to highlight the phase distribution in a diametral plane while the same from P_2 and P_8 denote the development of

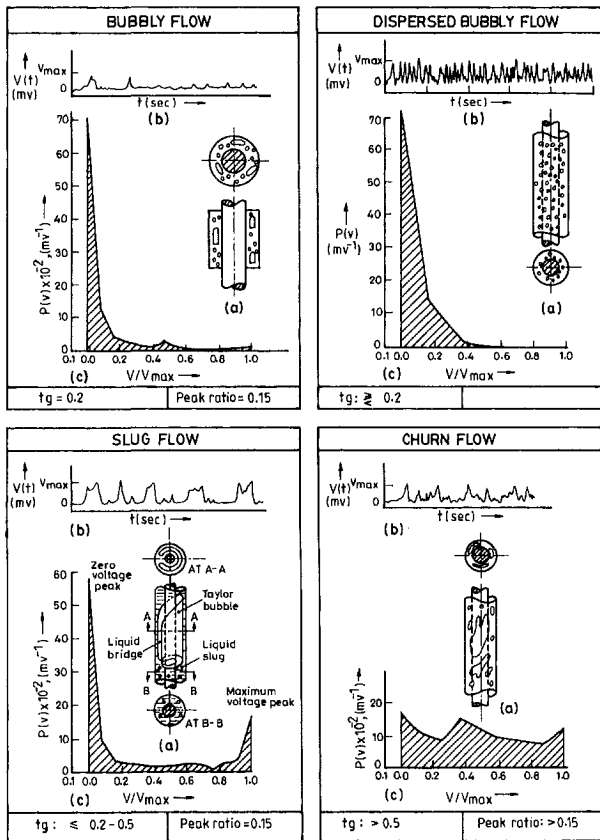


Fig. 2 Characteristics of the different flow regimes as observed in the present work

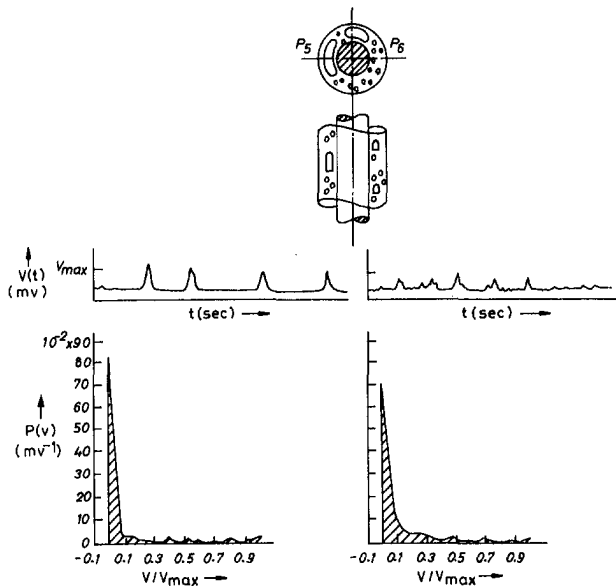


Fig. 4 Bubbly flow through annulus B, $U_{LS} = 0.14$ m/s, $U_{GS} = 0.123$ m/s

flow along the test length. Figs. 3 to 8 depicting the phase distribution at a diametral plane contains three parts. The pictorial representation of the flow regime along with the location of the probes has been placed at the top of the figure. The probe signals and the corresponding PDF curves obtained from a particular probe have been shown below the pictorial representation at the side of the respective probe. Figs. 9 and 10 represent the axial development of flow regime as seen visually and conceived from the signals and corresponding PDF curves of the probes P_5 (lower) and P_6 (upper). It has been observed that a better appraisal of the phase distribution may be obtained from a quantitative comparison of the parametric values of the probe signals and the PDF curves depicted in Figs. 3 to 7. For this purpose, the relevant details have been provided in Table 1.

Bubbly-Slug Transition

At low phase velocities, the bubbly flow is indicated by a steady output at zero voltage and a few spikes to positive voltage values in the probe signal and a small area beyond the zero voltage peak in the PDF curve. One such instance is depicted in Fig. 3. The

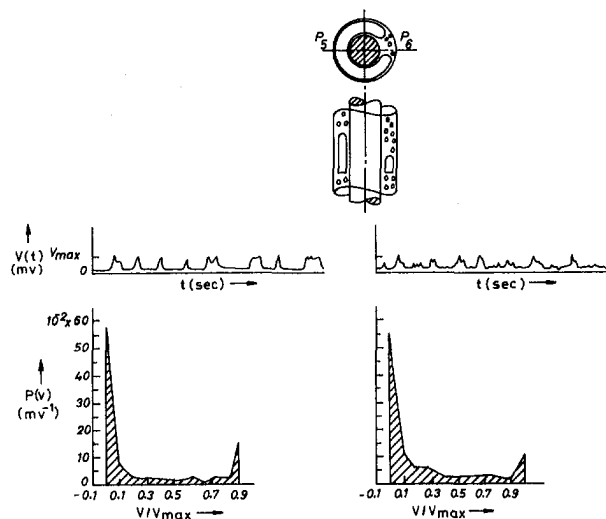


Fig. 5 Slug flow through annulus B, $U_{LS} = 0.14$ m/s, $U_{GS} = 0.244$ m/s

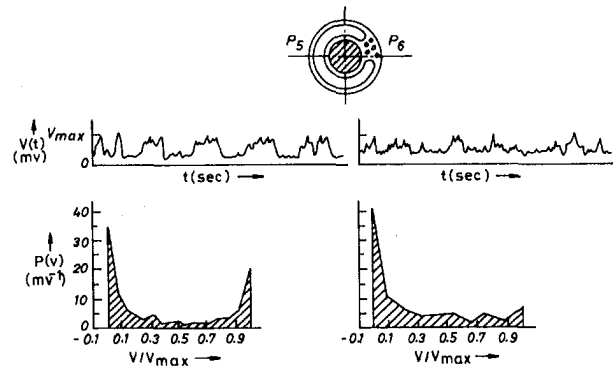


Fig. 6 Slug flow through annulus B, $U_{LS} = 0.14$ m/s, $U_{GS} = 0.37$ m/s

small values of t_g and the area beyond the peak becoming zero after $V/V_{max} = 0.3$ also signifies the low frequency and size of the bubbles dispersed in the water phase.

The change in the flow situation at a higher air and the same water velocity is shown in Fig. 4. An increase in the frequency and size of the bubbles is evident from an increase in the number and size of the pulses in both the probe signals and an extension of the area under the PDF curves beyond the zero voltage peak. An additional feature accompanying bubbly flow at the higher air velocity is the onset of asymmetry at a diametral plane. The larger size of the peaks in Fig. 4.2(a) as compared to Fig. 4.2(b) and a small peak like appearance at the maximum voltage of Fig. 4.3(a) with the absence of the same in Fig. 4.3(b) is indicative of the fact. This arises due to the appearance of oblate spheroidal cap bubbles which partially wrap the inner tube and prefer to rise across P_5 , while the smaller sized bubbles traverse probe P_6 .

The increase in the number and size of the bubbles with an increase in the air velocity continues till the cap bubbles become large enough to form the Taylor bubbles and the bubbly flow regime transforms into slug flow. This is manifested not only by an increase in the peaks and t_g values in the trace but also by an increase in the maximum voltage peak and the peak ratio in the PDF curve. Figure 5 shows such a flow situation. Here the formation of Taylor bubbles from the cap shaped ones have resulted in the intermittent appearance of the probe signals and the bimodal PDF curve with a peak ratio exceeding 0.15.

An increase in the maximum voltage peak rather than an increase in the area between the two peaks in the PDF curve

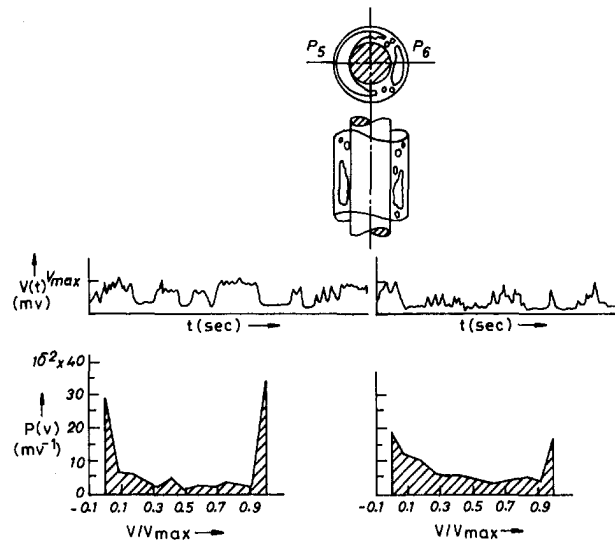


Fig. 7 Slug-churn flow through annulus B, $U_{LS} = 0.14$ m/s, $U_{GS} = 0.6$ m/s

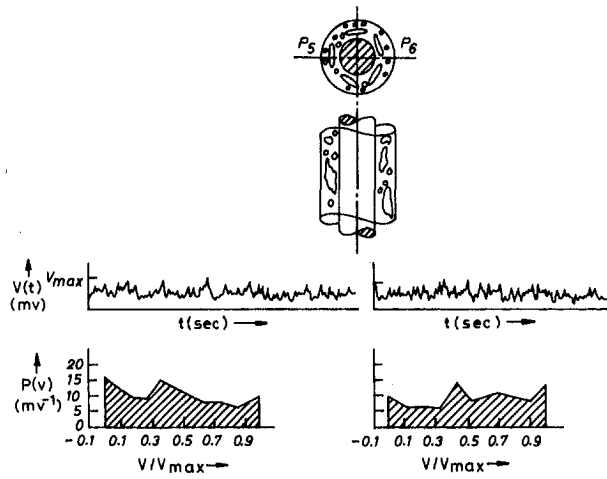


Fig. 8 Churn flow through annulus B, $U_{LS} = 0.14$ m/s, $U_{GS} = 2.12$ m/s

indicates that the coalescence of the cap and not the spherical bubbles causes the bubbly-slug transition. A growth in asymmetry of the phase distribution with increase in air velocity both in the bubbly-slug and the slug flow regimes further justifies the fact. This arises because the Taylor bubbles formed from the cap bubbles are also open annular rings never enclosing the inner tube completely. The mechanism has been verified at other water velocities and in all the three annuli. It may be noted that the previous researchers (Taitel et al. 1980 for circular tubes and Kelessides and Dukler, 1989 for annular geometry) have also postulated this transition to occur from an increased rate of bubble collision and coalescence but they did not distinguish between the two types of coalescing bubbles.

Slug-Churn Transition

A survey of the past literature shows that the physical mechanism underlying the slug-churn transition is not fully understood

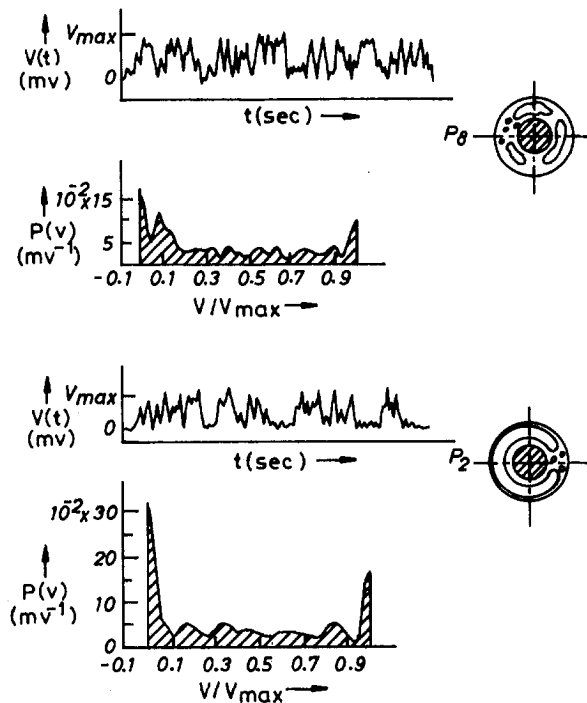


Fig. 9 Transition of slug-churn flow into churn flow with axial distance in annulus B, $U_{LS} = 0.14$ m/s, $U_{GS} = 0.955$ m/s

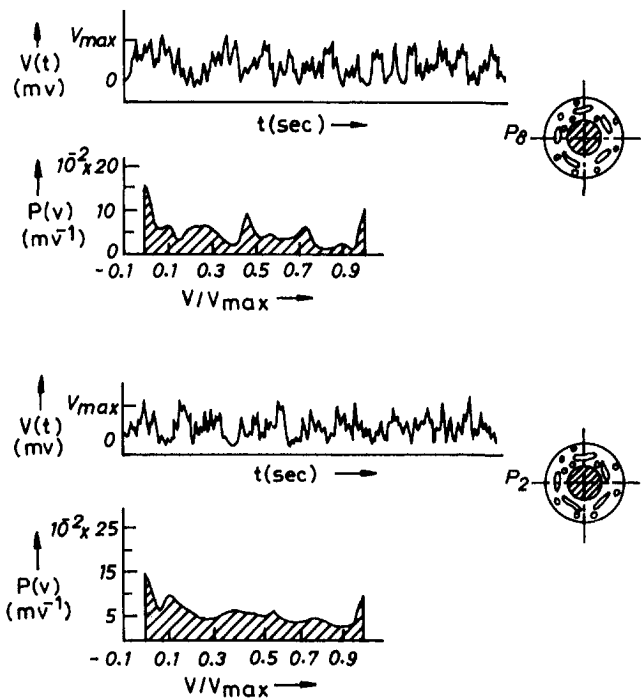


Fig. 10 Churn flow throughout the test length in annulus B, $U_{LS} = 0.14$ m/s, $U_{GS} = 2.11$ m/s

even in circular tubes. The reason behind this can be attributed to the inherent random and chaotic nature of the churn flow regime. The researchers have suggested four different mechanisms namely the entrance effect (Taitel et al., 1980), flooding (McQuillan and Whalley, 1985), wake effect of Taylor bubbles (Mishima and Ishii, 1984), and liquid slug collapse due to bubble coalescence (Barnea and Brauner, 1986). Jayanti and Hewitt (1992) have suggested flooding to govern this transition in their comparative study of the four mechanisms. On the other hand, almost no work has been carried out on this aspect in an annular geometry. The work by Kelessides and Dukler (1989) have adopted the entry length effect suggested by Taitel et al. (1980). However, based on the observations in the present work, a different approach has been adopted to predict the inception of churn flow.

Our experiments have revealed that an increase in air velocity in

Table 1 Quantitative measures depicting the flow situation under different operating conditions

Fig. No.	U_{LS} m/s	U_{GS} m/s	Probes	T_g	Peak at zero voltage (m_v^{-1})	Peak at $V/V_{max} = 1$ (m_v^{-1})	Peak ratio	% area between the peak
3	0.14	0.082	P_5	0.054	0.902	-	-	-
			P_6	0.057	0.8875	-	-	-
4	0.14	0.123	P_5	0.142	0.852	0.0316	0.03708	14
			P_6	0.106	0.71	0.01	0.0141	19.7
5	0.14	0.244	P_5	0.3168	0.5752	0.1504	0.2615	25.63
			P_6	0.306	0.5358	0.1043	0.1946	35.8
6	0.14	0.37	P_5	0.423	0.346	0.2055	0.594	23.34
			P_6	0.3533	0.4045	0.0635	0.157	47.675
7	0.14	2.12	P_5	-	0.27	0.355	1.3148	36.28
			P_6	-	0.185	0.165	0.8918	50.32

the slug flow regime is manifested primarily by an increase in the width of the peaks in the probe signals and an increase in the maximum voltage peak in the PDF curves obtained from both the probes. The area between the PDF peaks remains relatively unaffected. Moreover, the differences in the probe signals and PDF curves obtained from probes P_5 and P_6 for the entire range of slug flow depict that the increased air velocity, while increasing the lengths of the Taylor bubbles, does not influence their typical asymmetric shape. The bubbles never assume a nice rotationally symmetric shape during slug flow.

An interesting feature arises at higher air velocities. This can be appreciated by a comparison between Figs. 5 and 6. In the previous cases, an increase in air velocity resulted in PDFs with a lower zero voltage peak and a higher maximum voltage one whereas the PDF of Fig. 6 exhibits a reduction in both the peaks as compared to Fig. 5 and an increase in the area between them. On the other hand, the traces and PDF curves as obtained from probe P_5 [Figs. 6.2(a) and 6.3(a)] denote typical slug flow with the passage of longer Taylor bubbles as compared to Fig. 5. This shows that at higher gas velocities, an increase in air flow rate results in longer Taylor bubbles as well as an increase of the bubble concentration in the liquid bridge.

The observations with a further increase in air velocity is presented in Fig. 7. Table 1 shows the flow to be in the slug-churn regime. Although the random oscillations observed in Fig. 6 have become more pronounced in this case, their effect is relatively prominent at P_6 compared to P_5 as can be seen from Fig. 7. This once more proves an earlier termination of the slug flow characteristics at P_6 (liquid bridge) while still retaining it at P_5 . The asymmetry in phase distribution continues in the entire range of slug-churn flow pattern and the intermittent character finally breaks down at both the probes (Fig. 8) with further increase in air velocity. In this case, the signals from both the probes exhibit a continuously oscillating and random output which assumes neither 0 nor V_{max} but altogether shifts toward V_{max} and have yielded PDF curves characteristic of churn flow. Interestingly, the similar nature of the signals and PDF curves obtained from diametrically opposite probes depict that the symmetric phase distribution which existed during bubbly flow (Fig. 2) has been restored with the onset of the churn flow regime.

The experiments thus indicate that slug flow transforms into the churn flow regime with increase in air velocity. The feature which marks this transition is the collapse of the asymmetric nature of slug flow and the restoration of symmetry in phase distribution. This indicates that the slug-churn transition initiates in the Taylor bubble region and bubble coalescence as well as wake effect in the liquid slug can not be used for explaining the physical mechanism. The entrance effect is also not suitable for the present case since it has been observed that slug flow at the entry produces churn flow far downstream (Fig. 9) whereas churn flow at the entry remains unchanged throughout the test length (Fig. 10). Moreover, our observations that an increase in the lengths of the Taylor bubbles with the increase in air velocity throughout the slug flow regime and the collapse of these bubbles at the onset to churn flow suggest flooding in the Taylor bubble region as the transition criterion. The opposing direction of flow of the Taylor bubbles and the liquid films as well as the oscillatory nature of the churn flow pattern further emphasises the fact.

Flow Pattern Map

The experimental data were recorded over a range of gas velocities from 0.04 m/s to 9.0 m/s and liquid velocities from 0.08 m/s to 2.8 m/s in the three annuli and classified into the flow patterns using the criteria discussed in Fig. 1. The typical results have been presented in Fig. 11 for probes P_5 and P_6 . The figure indicates that except for a few data points, the experimental results can be clearly divided into the three flow regimes and the transitions between them can be represented by bands lying between the respective patterns.

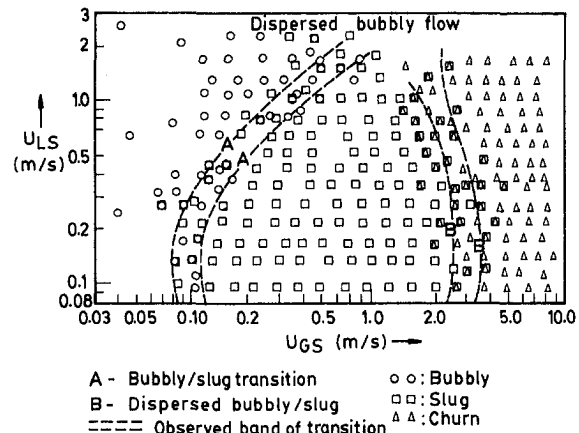


Fig. 11 Experimental flow pattern map

Conclusions

Considering the uniqueness of the slug flow regime in a concentric annulus, a detailed experimental investigation has been undertaken to understand the inception, development and termination of the slug flow pattern. For this, the phase distribution in the bubbly, dispersed bubbly, slug and churn flow regimes have been investigated from the signals obtained from a number of conductivity probes at different locations in the annular passage and the probability density function analysis of these signals. Indigenously designed parallel plate type conductivity probes specially suited for an annular geometry have been used in the present work. The use of two such probes at a particular cross-section could provide an assessment of the asymmetry in phase distribution at a diametral plane. The study has shown that the bubbly-slug transition is marked by an increase in the peaks in the probe signals and the maximum voltage peak in the PDF curve rather than the area between the two peaks. This signifies that the growth of cap bubbles rather than the coalescence of the spherical ones at an increased air velocity results in the slug flow regime from the bubbly flow pattern. On the other hand, the growth of the Taylor bubbles throughout the slug flow regime and their collapse on the onset to the churn flow pattern indicates flooding in the Taylor bubble region to govern the slug-churn transition. This has been indicated by dissimilar probe signals and PDF curves from diametrically opposite probes in the slug flow regime and the symmetric phase distribution in churn flow. Mathematical models based on these physical mechanisms have been reported in a subsequent paper.

Acknowledgment

We acknowledge all the reviewers for their valuable suggestions. Help and encouragement received from Prof. Demetri P. Telenois of Virginia Polytechnic Institute is gratefully acknowledged. One of the authors (G. Das) is grateful to the Council of Scientific and Industrial Research, India for their financial support.

References

- Akagawa, K., 1964, "Fluctuations of Void Ratio in Two Phase Flow, 1st Report, The Properties in a Vertical Upward Flow," *Bulletin of JSME*, Vol. 7, No. 25, pp. 122-128.
- Barnea, D., and Brauner, N., 1986, "Slug Churn Transition in Upward Gas-Liquid Flow," *Chemical Engineering Science*, Vol. 41, No. 1, pp. 159-163.
- Billicki, Z., and Kestin, J., 1987, "Transition Criteria for Two Phase Flow Patterns in Vertical Upward Flow," *International Journal of Multiphase Flow*, Vol. 13, pp. 283-294.
- Caetano, E. F., Shoham, O., and Brill, J. P., 1989a, "Upward Vertical Two Phase Flow Through an Annulus—Part I: Single Phase Friction Factor, Taylor Bubble Rise Velocity and Flow Pattern Prediction, Multiphase Flow," *Proceedings of 4th International Conference*, pp. 301-330, BHRA, Cranfield, England.

- Ferukawa, T., and Sekoguchi, K., 1986, "Phase Distribution for Air-Water Two Phase Flow in Annuli," *Bulletin of JSME*, Vol. 29, No. 225, pp. 3007-3014.
- Hewitt, G. F. and Hall-Taylor, N. S., 1970, *Annular Two Phase Flow*, Pergamon Press, New York, pp. 4-18.
- Jayanti, S., and Hewitt, G. F., 1992, "Prediction of the Slug to Churn Flow Transition in Vertical Two-Phase Flow," *International Journal of Multiphase Flow*, Vol. 18, No. 6, pp. 847-860.
- Jones, O. C., and Zuber, N., 1975, "The Interrelation between Void Fraction Fluctuations and Flow Patterns in Two Phase Flow," *International Journal of Multiphase Flow*, Vol. 2, pp. 273-306.
- Kelessidis, V. C., and Dukler, A. E., 1989, "Modeling Flow Pattern Transitions for Upward Gas-Liquid Flow in Vertical Concentric and Eccentric Annuli," *International Journal of Multiphase Flow*, Vol. 15, No. 2, pp. 173-191.
- Kelessidis, V. C., and Dukler, A. E., 1990, "Motion of Large Gas Bubbles through Liquids in Vertical Concentric and Eccentric Annuli," *International Journal of Multiphase Flow*, Vol. 16, No. 3, pp. 375-390.
- McQuillan, K. W., and Whalley, P. B., 1985, "Flow Patterns in Vertical Two-Phase Flow," *International Journal of Multiphase Flow*, Vol. 11, pp. 161-175.
- Mishima, K., and Ishii, I., 1984, "Flow Regime Transition Criteria for Two-Phase Flow in Vertical Tubes," *International Journal of Heat and Mass Transfer*, Vol. 27, pp. 723-734.
- Nakoryakov, V. E., Keiznetsov, V. V., and Vitovsky, O. V., 1992, "Experimental Investigations of Upward Gas-Liquid Flow in a Vertical Narrow Annulus," *International Journal of Multiphase Flow*, Vol. 18, No. 3, pp. 313-326.
- Sadatomi, M., Sato, Y., and Saruwatari, S., 1982, "Two Phase Flow in Vertical Non-Circular Channels," *International Journal of Multiphase Flow*, Vol. 8, pp. 641-655.
- Taitel, Y., Barnea, D., and Dukler, A. E., 1980, "Modeling Flow Pattern Transitions for Steady Upward Gas-Liquid Flow in Vertical Tubes," *AIChE Journal*, Vol. 26, No. 3, pp. 345-354.
- Venkateswararao, P., Semiat, R., and Dukler, A. E., 1982, "Flow Pattern Transition for Gas-Liquid Flow in a Vertical Rod Bundle," *International Journal of Multiphase Flow*, Vol. 8, No. 5, pp. 509-524.
- Weisman, J., and Kang, S. Y., 1981, "Flow Pattern Transitions in Vertical and Upwardly Inclined Lines," *International Journal of Multiphase Flow*, Vol. 7, pp. 271-291.

G. Das

Research Associate,
Department of Chemical Engineering.

P. K. Das

Associate Professor,
Department of Mechanical Engineering,
pkd@mech.iitkgp.ernet.in

N. K. Purohit

Former Professor,
Department of Chemical Engineering.

A. K. Mitra

Former Professor,
Department of Chemical Engineering.

Indian Institute of Technology,
Kharagpur - 721 302, India

Flow Pattern Transition During Gas Liquid Upflow Through Vertical Concentric Annuli— Part II: Mechanistic Models

In this paper the transition boundaries between different flow regimes during cocurrent upflow of gas liquid two-phase mixture through concentric annuli has been predicted theoretically. On the basis of the experimental observations (Das et al., 1999), mechanistic models have been proposed to formulate mathematical equations of the regime boundaries as functions of the annulus dimensions, the physical properties, and velocities of the two phases. The analysis has yielded the bubbly-slug transition to occur at a limiting void fraction of 0.2, and the slug-churn transition to occur due to flooding of the liquid films by the Taylor bubbles. A comparison of the model predictions with experimental data corroborate the suitability of the proposed mechanisms.

Introduction

The flow patterns during the simultaneous flow of gas and liquid through a conduit, have a profound influence on all the two-phase transport processes. This has encouraged a large number of studies for the identification of flow regimes and the prediction of the transition boundaries. Conventionally, the transition boundaries are represented on a two-dimensional plane termed as flow pattern map. The early flow pattern maps, constructed purely from experimental observations, suffered from limited applicability. This has motivated the researchers to predict the transition criteria based on mechanistic models and to validate them against experimental data. The majority of the investigations in this field have been confined to circular tubes (Taitel et al., 1980; Weisman and Kang, 1981; Mishima and Ishii, 1984; Mc Quillan and Whalley, 1985; Billicki and Kestin, 1987, etc.). Taitel et al. (1980) used the superficial phase velocities as the coordinate axes of their flow pattern map for a convenient representation of all the regime boundaries. Henceforth, several researchers have adopted this methodology for construction of flow pattern maps in circular tubes. In recent years, some endeavours have been made toward the development of such flow pattern maps in noncircular geometries including the concentric annulus. Sadatomi et al. (1982) have investigated the flow regime transitions in seven different noncircular passages. Their studies in a concentric annulus have shown the regime boundaries to be functions of the hydraulic diameter. Venkateswararao et al. (1982) have proposed analytical models based on the model of Taitel et al. (1980) for predicting the flow regime transitions in rod bundles. Ferukawa and Sekoguchi (1986) have noted the difference between slug flow in a circular tube and an annulus due to the presence of asymmetric Taylor bubbles in the later case. They postulated the transitions between the bubbly-slug and the froth-annular flows to occur at an equivalent bubble diameter of 6 mm and 200 mm, respectively. Such asymmetric Taylor bubbles have also been observed by Caetano et al. (1989a) and Kelessidis and Dukler (1989). However, the models suggested by them to predict the transitions between the flow regimes were primarily based on the mechanistic models proposed

by Taitel et al. (1980) for circular tubes. The typical phase distribution characterizing the different flow regimes in a concentric annulus have rarely been incorporated in the analysis. For example, the slug flow in an annulus is markedly different from that observed in circular tubes due to the presence of asymmetric Taylor bubbles in the former geometry. However, the effect of asymmetry has not been considered in the available models. Considering the uniqueness of slug flow in an annulus, the criteria for bubbly-slug and slug-churn transitions have been developed in the present work. The mechanistic models have been formulated as predictive tools for the above transition boundaries on the basis of the insight gained from experimental observations (Das et al., 1999). The model predictions have been represented in the form of a flow pattern map where the transition boundaries have been observed to agree well (by the present standards of the topic) with the experimental data.

Mathematical Models for Predicting the Regime Boundaries

(a) **Bubbly-Slug Transition.** The previous researchers (Taitel et al., 1980; McQuillan and Whalley, 1982, etc.) had postulated the bubbly-slug transition in circular tubes to occur at low liquid flow rates for a limiting void fraction. They suggested that under this condition, the dispersed bubbles become so closely packed that many collision occur and the rate of agglomeration to large Taylor bubbles increases sharply. On the basis of maximum allowable bubble packing, Taitel et al. (1980) have obtained the limiting void fraction as 0.25 for circular tubes. They have substituted this value in the general equation for gas-liquid two phase flow viz.,

$$U_G = U_L + U_o \quad (1)$$

where U_o , the bubble rise velocity with respect to the average liquid velocity has been expressed by Harmathy (1960) as

$$U_o = 1.53 \left[\frac{\sigma g (\rho_L - \rho_G)}{\rho_L^2} \right]^{1/4} (1 - \epsilon_g)^{1/2} \quad (2)$$

This equation expresses rise velocity for a bubble swarm comprising of spherical and cap shaped bubbles which characterises bubbly flow near the transition.

Thus the past researchers have obtained the equation for bubbly-

Contributed by the Fluids Engineering Division for publication in the JOURNAL OF FLUIDS ENGINEERING. Manuscript received by the Fluids Engineering Division February 6, 1997; revised manuscript received October 6, 1998. Associate Technical Editor: M. Sommerfeld.

slug transition in terms of the phase superficial velocities by substituting the expression of U_o in Eq. (1) which yields

$$U_{LS} = \frac{1 - \epsilon_g}{\epsilon_g} U_{GS} - 1.53(1 - \epsilon_g) \left[\frac{\sigma g (\rho_L - \rho_G)}{\rho_L^2} \right]^{1/4} (1 - \epsilon_g)^{1/2} \quad (3)$$

and putting the value of ϵ_g as 0.25. Kelessides and Dukler (1989) have also adopted a similar approach and assumed a value of ϵ_g as 0.25.

On the other hand, it has been clearly observed by Das et al. (1999) that the bubbly-slug transition is marked by an onset of asymmetric phase distribution from the symmetry prevailing in bubbly flow at low phase flow rates. This asymmetry persists in the entire range of slug flow and occurs due to the typical shape of cap and Taylor bubbles. They are open annular rings never enclosing the inner tube completely. An increase in air velocity merely increases their length but never forms a nice rotationally symmetric bubble. This observation as brought out by the probe signals and PDF curves of Das et al. (1999) clearly reveals the fact that the coalescence of the cap bubble rather than the spherical ones result in the bubbly-slug transition. Therefore, instead of the concept of maximum allowable bubble packing, this transition in the present case has been postulated to occur when the elongated bubbles formed from coalescence of the cap bubbles have attained the nose dimensions of the Taylor bubble. An idealized representation of the flow situation is depicted in Fig. 1 and the average void fraction of the flowing mixture has been calculated considering the cellular approach of Fernandes et al. (1983) for circular tubes. He suggested the voidage of such a mixture to be equal to the

$$\epsilon_g^* = \epsilon_{g \text{ cap bubble}} \frac{l_{\text{cap bubble}}}{l_T} + \epsilon_{GLS} \frac{l_{LS}}{l_T} \quad (4)$$

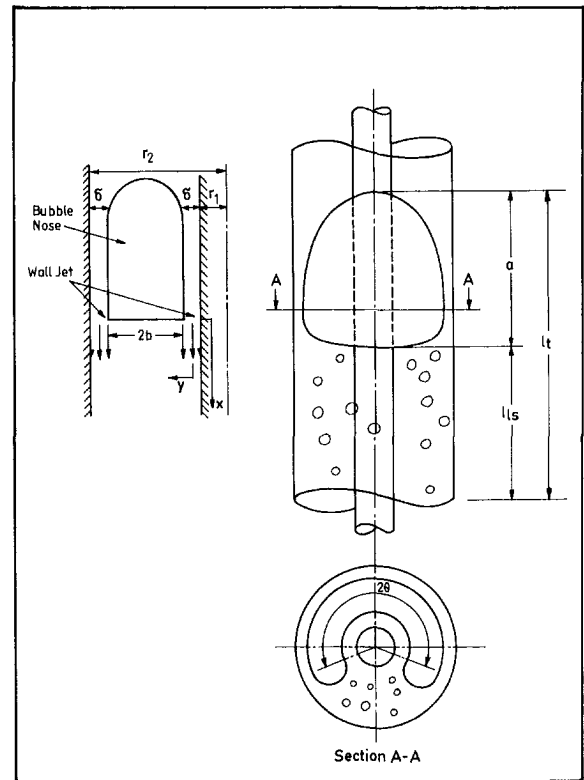


Fig. 1 Idealized representation of bubbly-slug transition

An evaluation of ϵ_g^* from Eq. (4) has then been done by determining the individual parameters in the right-hand side of the equation. The adopted procedure is as follows:

Nomenclature

a = semi-major axis of the elliptic cap (m)	U = local axial velocity at any point in the wall jet (m/s)	U_o = bubble rise velocity with respect to average liquid velocity (m/s)
A = cross-sectional area of the annular passage (m ²)	U_f = velocity of the liquid film (m/s)	x = vertical axis as shown in Fig. 5 (m)
A_f = cross-sectional area occupied by the liquid films (m ²)	U_{fs} = superficial velocity of the liquid film (m/s)	y = horizontal axis, shown in Fig. 5 (m)
A_{TB} = cross-sectional area occupied by the Taylor bubble (m ²)	U_{fs}^* = dimensionless superficial velocity of the liquid film (dimensionless)	γ = constant in Eq. (7)
b = semi-minor axis of the elliptic cap (m)	U_G = gas velocity at a point averaged across the flow direction (m/s)	δ = liquid film thickness at the two walls of the annulus (m)
C = Wallis constant in Eq. (11) (dimensionless)	U_{GS} = superficial gas velocity (m/s)	ϵ_g = void fraction (dimensionless)
D_1 = inside diameter of annulus (m)	U_{GS}^* = dimensionless superficial gas velocity (dimensionless)	ϵ_g^* = void fraction of a unit cell during bubbly-slug transition (dimensionless)
D_2 = outside diameter of annulus (m)	U_{jmax} = maximum velocity of the wall jet (m/s)	$\epsilon_{g \text{ cap bubble}}$ = void fraction in the cap bubble region during bubbly-slug transition (dimensionless)
D_e = characteristic dimension of the test geometry (m)	U_L = liquid velocity at a point averaged across the flow direction (m/s)	ϵ_{GLS} = void fraction in the liquid slug region (dimensionless)
g = acceleration due to gravity (m/s ²)	U_{LS} = superficial liquid velocity (m/s)	ρ_G = gas density (kg/m ³)
$l_{\text{cap bubble}}$ = length of the cap bubble during bubbly-slug transition (m)	U_{LS}^* = dimensionless superficial liquid velocity (dimensionless)	ρ_L = liquid density (kg/m ³)
l_{LS} = length of the liquid slug in a slug unit (m)	U_M = mixture velocity (m/s)	$\Delta\rho = (\rho_L - \rho_G)$ (kg/m ³)
l_T = total length of slug unit (m)	U_{TB} = velocity of the Taylor bubble (m/s)	σ = surface tension of liquid (N/m)
r_1 = inside radius of annulus (m)	U_{TBS} = superficial velocity of the Taylor bubble (m/s)	μ_L = liquid viscosity (poise)
r_2 = outside radius of annulus (m)	U_{TBS}^* = dimensionless superficial velocity of the Taylor bubble (dimensionless)	Γ = mass flow rate of the film per unit wetted perimeter (kg/m · s)
Re_F = film Reynolds number, dimensionless		ν_L = kinematic viscosity of the liquid (m ² /s)

Table 1 Bubble geometry in the three annuli

Annulus No.	a (m)	b (m)	δ (m)
A	8.948×10^{-2}	4.562×10^{-2}	7.25×10^{-4}
B	5.9125×10^{-2}	3.12×10^{-2}	6.79×10^{-4}
C	6.54×10^{-2}	1.045×10^{-2}	5.02×10^{-4}

(1) Considering the nose to be a semi-ellipse with its major axis oriented vertically (Kelessidis and Dukler, 1990), the minimum length of a stable elongated bubble is the semi-major axis of the ellipse

$$l_{\text{cap bubble}} = a \quad (5)$$

(2) $\epsilon_{g, \text{cap bubble}}$ has been obtained from a knowledge of the cap dimensions of a Taylor bubble rising in a particular annulus on the basis of the assumption that the dimensions are equal for Taylor bubbles rising in stagnant water and in slug flow. It has been observed from experimental investigations that the nose dimensions are insensitive to bubble length and function of annulus dimensions only in liquid filled annuli. They can, therefore, be obtained by considering the geometry of the rising semi-ellipse in the annular passage, viz.,

$\epsilon_{g, \text{cap bubble}}$

$$= \frac{\left(\frac{\pi ab}{2}\right)(r_2 - r_1 - 2\delta) + \left(\frac{\pi^2}{16}\right)(a + b)(r_2 - r_1 - 2\delta)^2}{\left(\frac{\pi}{4}\right)(D_2^2 - D_1^2)a} \quad (6)$$

for identical thickness of the liquid films on either side of the bubble (Das, 1995). The values of a and b for the three annuli of the present work have been calculated by the analysis of Das et al. (1998) and presented in Table 1.

(3) l_{ls} , the length of the liquid slug has to be greater than the wake of the preceding Taylor bubble formed by collision of the falling liquid film with the rising liquid slug. This ensures that the effect of the falling liquid film is completely absorbed before the next bubble appears and the bubbles have no tendency to overtake one another. Following the procedure of Taitel et al. (1980) for the estimation of l_{ls} , the liquid films have been considered as two-dimensional free jets entering a stagnant pool of liquid at a uniform velocity ($U_f + U_G$). This yields the local axial velocity U induced in the liquid by the jet as

$$\frac{U}{U_{j \max}} = 1 - \tanh^2\left(\gamma \frac{y}{x}\right) \quad (7)$$

where γ a universal constant is equal to 7.67. The solution of Eq. (7) by using the boundary condition viz.,

$$\frac{U}{U_{j \max}} \geq 0.95 \quad \text{at} \quad y = \frac{D_2 - D_1}{4}$$

gives the minimum length of the liquid slug in an annulus as

$$l_{ls} = 8.33(D_2 - D_1) \quad (8)$$

It may be noted that Taitel et al. (1980) had made this analysis for modeling the churn-slug transition. Since the condition of existence of stable slug flow is same for both the cases, we have adopted their procedure for the present case.

(4) ϵ_{GLS} , has to be low enough to suppress any tendency of coalescence. According to Radovich and Moissis (1962), this occurs at a voidage close to 0.1 where the collision frequency is very low and it increases drastically at a void fraction between 0.2–0.3. ϵ_{GLS} has, therefore, been assumed as 0.1 in the present work. On substituting Eqs. (5), (6), and (8) in Eq. (4), the limiting value of the void fraction at the bubbly-slug transition has been

calculated as 0.21, 0.199, and 0.19 for annuli A, B, and C of the present work, respectively. The overall voidage for the initiation of slug flow has, therefore, been considered as 0.2. This is also in agreement with the value assumed by Caetano et al. (1989a). Substituting the value of ϵ_g as 0.2 in Eq. (3) yields the equation describing the bubbly-slug transition as

$$U_{LS} = 4.0U_{GS} - 1.1 \left[\frac{\sigma g(\rho_L - \rho_G)}{\rho_L^2} \right]^{1/4} \quad (9)$$

Dispersed Bubbly-Slug Transition. Since the dispersed bubbly flow is marked by the total absence of cap bubbles, the coalescence mechanism postulated above is unsuitable for predicting this transition. However, a detailed investigation could not be undertaken in the present work due to paucity of experimental data. It has only been observed that the size of the spherical bubbles appear to be the factor governing the transition. Once the largest stable size of the bubble in the turbulent field exceeds the critical bubble diameter, increased collision and coalescence initiates slug flow. Taitel et al. (1980) had suggested a similar criterion for the transition in circular tubes. Since the proposed mechanism was governed by the bubble size only and not by the conduit geometry, the same methodology has been adopted in the present work. This has yielded the equation describing the transition as,

$$\frac{\left[\frac{\rho_L}{(\rho_L - \rho_G)g} \right]^{1/2} \gamma_L^{0.08}}{\left(\frac{\sigma}{\rho_L} \right)^{0.1} (D_2 - D_1)^{0.48}} U_M^{1.12} = 3.0 \quad (10)$$

Further, the upper limit for the existence of dispersed bubbly flow has also been taken as $\epsilon_g = 0.52$ from the value suggested by Taitel et al. (1980) for circular tubes.

(b) Slug-Churn Transition. In the present work, it has been observed that the churn flow regime occurs from the slug flow pattern at an increased air velocity. The probe signals and PDF curves have shown that this transition is marked by a breakdown of the asymmetric structure of slug flow and restoration of symmetric phase distribution. This can occur if the slug-churn transition results from the collapse of the Taylor bubbles. On the basis of experimental results, the flooding in the Taylor bubble region has been postulated as the criteria underlying the slug-churn transition. The equation governing this transition has been obtained from the most commonly used correlation for flooding (Wallis, 1969) viz.,

$$(U_{LS}^*)^{1/2} + (U_{GS}^*)^{1/2} = C \quad (11)$$

where U_{LS}^* and U_{GS}^* , the dimensionless superficial velocities, can be expressed as:

$$U_{LS}^* = U_{LS} \left[\frac{\rho_L}{(\rho_L - \rho_G)gD_e} \right]^{1/2} \quad (12)$$

$$U_{GS}^* = U_{GS} \left[\frac{\rho_G}{(\rho_L - \rho_G)gD_e} \right]^{1/2} \quad (13)$$

and the constant C is a function of tube length and entrance conditions with its value being close to unity for most of the cases.

For using Eq. (11) to predict the slug-churn transition, the dimensionless superficial velocities U_{LS}^* and U_{GS}^* have been replaced by the corresponding velocities of the liquid film (U_{fs}^*) and Taylor bubble (U_{TBS}^*), respectively. This requires a proper definition of D_e in Eqs. (12) and (13). The previous researchers (Richter, 1981) investigating flooding in an annular geometry proposed the average circumference as the characteristic dimension. However, the characteristic diameter of an annulus in Froude number has been obtained as $(D_2 + D_1)$ by Das et al. (1998). This gives the definitions of U_{fs}^* and U_{TBS}^* as

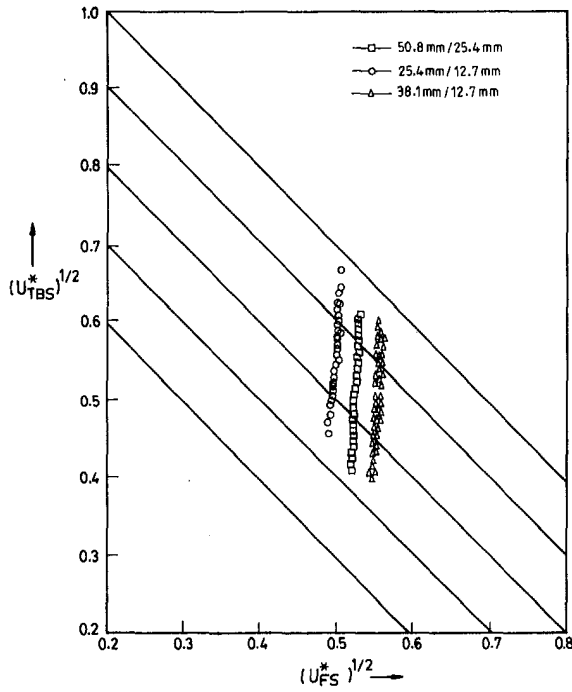


Fig. 2 $(U_{TBS}^*)^{1/2}$ versus $(U_{FS}^*)^{1/2}$ for slug churn transition

$$U_{fs}^* = U_{fs} \left[\frac{\rho_L}{(\rho_L - \rho_G)g(D_1 + D_2)} \right]^{1/2} \quad (14)$$

$$U_{TBS}^* = U_{TBS} \left[\frac{\rho_G}{(\rho_L - \rho_G)g(D_1 + D_2)} \right]^{1/2} \quad (15)$$

and the definitions of U_{fs} and U_{TBS} as

$$U_{fs} = U_f \frac{A_f}{A} \quad (16)$$

and

$$U_{TBS} = U_{TB} \frac{A_{TB}}{A} \quad (17)$$

Since the inception of flooding occurs by the collapse of the liquid bridge, the asymmetry in the Taylor bubble region has been assumed as negligible. The formation of ring like Taylor bubbles in the churn flow regime has also been reported by Ferukawa and Sekoguchi (1986). A_f and A_{TB} can be expressed as follows:

$$\frac{A_f}{A} = \frac{2\delta}{(r_2 - r_1)} \quad (18)$$

and

$$\frac{A_{TB}}{A} = \frac{(r_2 - r_1 - 2\delta)}{(r_2 - r_1)} \quad (19)$$

Jayanti and Hewitt (1992) suggest Brotz (1954) equation for evaluation of the film thickness over a wide range of Reynolds number.

$$\delta \left[\frac{g\Delta\rho}{v_L^2\rho_L} \right]^{1/3} = 0.1719 Re_f^{2/3} \quad (20)$$

where

$$Re_f = \frac{\Gamma}{\mu_L} \quad (21)$$

The velocity of the rising Taylor bubble can be expressed (Das, 1995) as

$$U_{TB} = 1.2U_M + 0.323 \sqrt{g(D_1 + D_2)} \quad (22)$$

Finally, the continuity equation for the Taylor bubble region is used as the closure:

$$U_{fs} = U_{TBS} - (U_{LS} - U_{GS}) \quad (23)$$

The iterative solution of the above-mentioned equations gives the dimensionless superficial bubble and film velocities and the value of C at the transition from a knowledge of the inlet velocities and annulus dimensions.

The calculations for all the experimental data on slug-churn transition in the three annuli show that the value of C lies between 0.8–0.9 for the majority of the cases. They further show that contradictory to the results of ordinary flooding, the transition occurs at a higher superficial gas velocity for a higher liquid velocity. The same has been reported by Jayanti and Hewitt (1992) for circular tubes and occurs because lower flooding velocities are required for longer Taylor bubbles which exist at low superficial liquid velocities. The graphical representation of the results in Fig. 2 show that the data on $(U_{fs}^*)^{1/2}$ and $(U_{TBS}^*)^{1/2}$ fall in a vertical line for a particular annulus and the data are correlated by different vertical lines for different annular dimensions. The spread of C can be converged to a single point for all operating conditions by expressing C as a function of annulus dimensions and phase superficial velocities. In the absence of such information, the mean value of C has been taken as 0.85. The lower value of C as compared to ordinary flooding experiments is due to the fact that the increase in gas velocity is accompanied by an increase in the length of the Taylor bubbles. The value is also lower than the value obtained by the previous researchers in circular tubes probably due to the additional factor of liquid bridge collapse which is absent in the later case.

Comparison of the Theoretical With Experimental Data.

The solution of Eqs. (9), (10), and (11) give the loci of the points denoting the bubbly-slug, the dispersed bubbly-slug and the slug-churn transitions. The curves obtained from theoretical considerations have been represented in the form of a flow pattern map in Fig. 3. Curve A representing bubbly-slug transition terminates in curve B above which the flow is dispersed bubbly with the absence of cap bubbles. Curve B extends till its intersection with curve C which relates the phase superficial velocities for $\epsilon_g = 0.52$. This indicates that the dispersed bubbly flow can not exist beyond curve C. Curve D in the figure marks the termination of the slug flow pattern and the onset to the churn flow regime.

Although the theoretical models have yielded single curves for the different transition boundaries, the experimental data of the

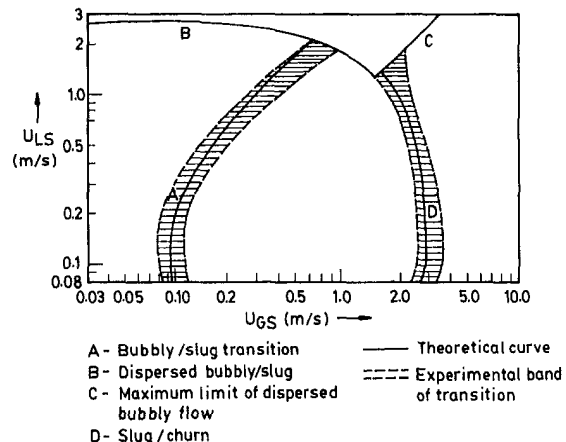


Fig. 3 Flow pattern map—comparison with present experiments

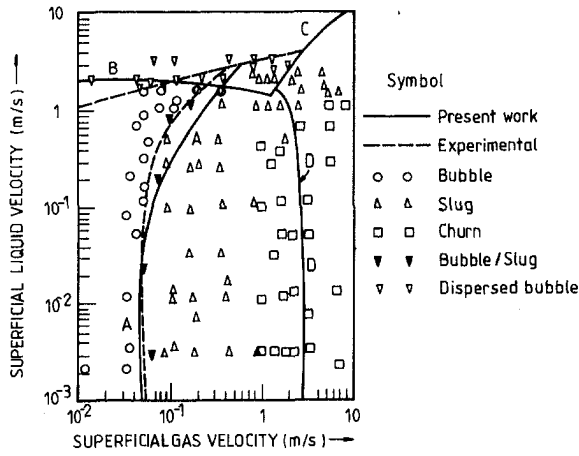


Fig. 4 Comparison of theoretical flow pattern map with data of Caetano et al. (1989a)

present work clearly indicate that the transitions from one regime to the other are gradual and occur over a range of phase flow rates. This has also been reported by the previous researchers both in circular tubes (Taitel et al., 1980; Mc Quillan and Whalley, 1985; etc.) and in annular geometry (Kelessidis and Dukler, 1989). Therefore, in order to compare the experimental and the theoretical predictions of the regime boundaries, experimental data of the transitions have been represented as bands in Fig. 3. The theoretical curves lie within the experimental zones for all the cases. This justifies the validity of the proposed mechanisms and indicates that the theoretical models have been successful in denoting the most probable positions of transition as functions of the phase superficial velocities and annulus dimensions.

A further attempt has been made to superimpose the curves obtained in the present work on the experimental maps reported in literature by Caetano et al. (1989a) and Kelessidis and Dukler (1989). The results are evident from Figs. 4 and 5 respectively. Figure 4 shows that the equations for the bubbly-slug and the dispersed bubbly-slug transitions agree well with the experimental curves. However, they have not indicated the slug-churn transition in their map. The transition obtained by us when drawn in the figure passes through the middle of their churn flow regime. The primary reason behind this is the difference of the definition of churn flow as proposed by us and by them. They have described churn flow as "somewhat similar to slug flow with the Taylor bubbles becoming narrow and its shape being destroyed." This shows that they have identified churn flow in a region where our probe signals denote the initiation of the slug-churn transition. Due to this, they could successfully extend their holdup model formulated for the slug flow regime to predict the same in churn flow. On the other hand, we have identified the churn flow regime with altogether different phase distribution which occurs at much higher phase velocities.

Figures 5(a) and (b) represent the comparisons between the experimental bands of transitions as obtained by Kelessidis and Dukler (1989) with our theoretical models for measuring stations 1 and 2. The bubbly-slug curve as obtained from Eq. (9) lies within the experimental transition zone obtained by them for both the cases. On the other hand, the slug-churn curve lies outside their transition band at lower phase velocities for MS#1 while it predicts the experimental region better than their model at higher phase velocities for MS#2. They have also described churn flow as "somewhat similar to slug flow" due to which the theoretical curves probably predict higher velocities for transition as compared to their experimental data.

The poor prediction of the slug-churn transition along with a success in predicting the other regime boundaries have also been reported by Mc Quillan and Whalley (1985) for circular tubes. They have attributed the reason behind this to the different interpretations of the churn flow regime and the difficulty in identifying this transition.

Nevertheless, considering the subjectivity of the researchers in identifying the transition zones and the discrepancies in recognizing the flow patterns, the agreement between experiment and theory can be considered as good. Thus, all the figures indicate that the theoretical predictions of the bubbly-slug, the dispersed bubbly-slug and the slug-churn transitions are successful in denoting the most likely loci of the points under which the flow regimes change their characteristics and transform into the next one.

Conclusions

Based on an understanding of the physical mechanisms underlying the bubbly-slug and the slug-churn transitions by Das et al. (1999), mathematical models have been formulated to identify the regime boundaries as functions of the annulus dimensions and phase superficial velocities. The bubbly-slug transition has been postulated to occur when the bubbles formed by the coalescence of the cap bubbles attain the nose dimensions of the Taylor bubbles. The limiting void fraction for the transition has been obtained as 0.2. The termination of the slug flow pattern has been observed to occur due to a collapse of the Taylor bubbles. The mechanism of the slug-churn transition has

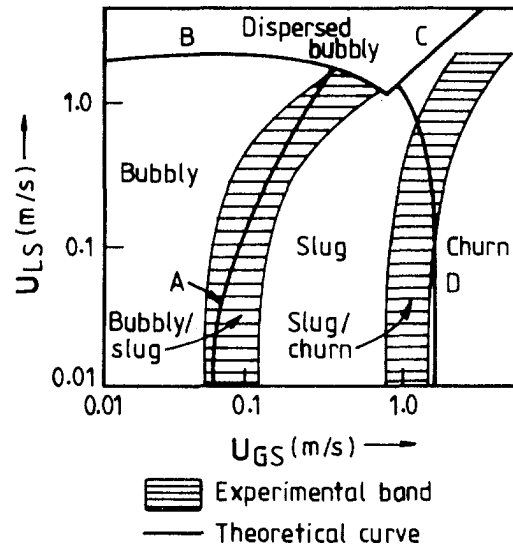


Fig. 5(a) For MS#1

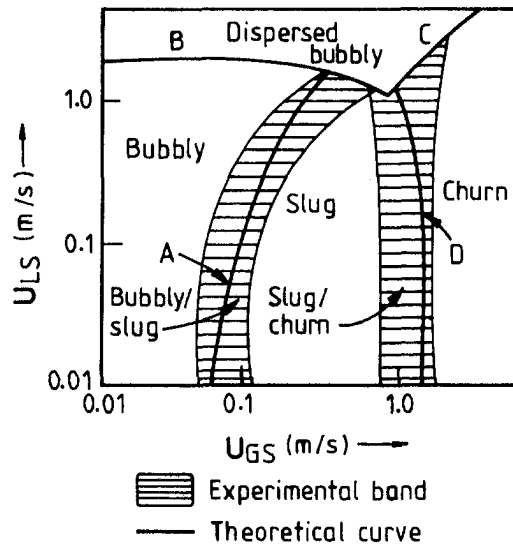


Fig. 5(b) For MS#2

Fig. 5 Comparison of theoretical flow pattern map with data of Kelessidis and Dukler (1989)

been postulated as flooding in the Taylor bubble region. A comparison of the mathematical models with the experimental data emphasises the suitability of the proposed mechanisms.

Acknowledgment

We acknowledge all the reviewers for their valuable suggestions. Help and encouragement received from Prof. Demetri P. Telenois of Virginia Polytechnique Institute is gratefully acknowledged. One of the authors (G. Das) is grateful to the Council of Scientific and Industrial Research, India for their financial support.

References

- Billicki, Z., and Kestin, J., 1987, "Transition Criteria for Two Phase Flow Patterns in Vertical Upward Flow," *International Journal of Multiphase Flow*, Vol. 13, pp. 283–294.
- Brotz, W., 1954, "Über die Vorausberechnung der Absorptionsgeschwindigkeit von Gasen in Stromenden Flüssigkeitsschichten," *Chemical Engineering Technik*, Vol. 26, p. 470.
- Caetano, E. F., Shoham, O., and Brill, J. P., 1989a, "Upward Vertical Two Phase Flow through an Annulus—Part I: Single Phase Friction Factor, Taylor Bubble Rise Velocity and Flow Pattern Prediction," *Multiphase Flow—Proceedings of 4th International Conference*, pp. 301–330, BHRA, Cranfield, England.
- Das, G., 1995, "Some Hydrodynamic Aspects of Two Phase Gas-Liquid Upflow through Concentric Annulus," Ph.D. thesis, Department of Chemical Engineering, Indian Institute of Technology, Kharagpur, India, pp. 138–245.
- Das, G., Das, P. K., Purohit, N. K., and Mitra, A. K., 1998, "Rise of Taylor Bubbles Through Concentric Annuli," *Chemical Engineering Science*, Vol. 53, No. 5, pp. 977–995.
- Das, G., Das, P. K., Purohit, N. K., and Mitra, A. K., 1999, "Flow Pattern Transition during Gas Liquid Upflow Through Vertical Concentric Annuli—Part I: Experimental Investigations," *ASME JOURNAL OF FLUIDS ENGINEERING*, published in this issue, pp. 895–901.
- Fernandes, R. C., Semiat, R., and Dukler, A. E., 1983, "Hydrodynamic Model for Gas-Liquid Slug Flow in Vertical Tubes," *AIChE Journal*, 29, No. 6, pp. 981–989.
- Ferukawa, T., and Sekoguchi, K., 1986, "Phase Distribution for Air-Water Two Phase Flow in Annuli," *Bulletin of JSME*, Vol. 29, No. 225, pp. 3007–3014.
- Harmathy, T. Z., 1960, "Velocity of Large Drops and Bubbles in Media of Infinite or Restricted Extent," *AIChE Journal*, Vol. 6, No. 2, pp. 281–288.
- Jayanti, S., and Hewitt, G. F., 1992, "Prediction of the slug to churn flow transition in vertical two-phase flow," *International Journal of Multiphase Flow*, Vol. 18, No. 6, pp. 847–860.
- Kelessidis, V. C., and Dukler, A. E., 1989, "Modeling Flow Pattern Transitions for Upward Gas-Liquid Flow in Vertical Concentric and Eccentric Annuli," *International Journal of Multiphase Flow*, Vol. 15, No. 2, pp. 173–191.
- Kelessidis, V. C., and Dukler, A. E., 1990, "Motion of Large Gas Bubbles through Liquids in Vertical Concentric and Eccentric Annuli," *International Journal of Multiphase Flow*, Vol. 16, No. 3, pp. 375–390.
- McQuillan, K. W., and Whalley, P. B., 1985, "Flow Patterns in Vertical Two-Phase Flow," *International Journal of Multiphase Flow*, Vol. 11, pp. 161–175.
- Mishima, K., and Ishii, I., 1984, "Flow Regime Transition Criteria for Two-Phase Flow in Vertical Tubes," *International Journal of Heat and Mass Transfer*, Vol. 27, pp. 723–734.
- Radovich, N. A., and Moissis, R., 1962, "The Transition from Two Phase Bubble Flow to Slug Flow," MIT Report, 7-7673-22.
- Richter, H. J., 1981, "Flooding in Tubes and Annuli," *International Journal of Multiphase Flow*, Vol. 7, No. 6, pp. 647–658.
- Sadatomi, M., Sato, Y., and Saruwatari, S., 1982, "Two Phase Flow in Vertical Non-Circular Channels," *International Journal of Multiphase Flow*, Vol. 8, pp. 641–655.
- Taitel, Y., Barnea, D., and Dukler, A. E., 1980, "Modeling Flow Pattern Transitions for Steady Upward Gas-Liquid Flow in Vertical Tubes," *AIChE Journal*, Vol. 26, No. 3, pp. 345–354.
- Venkateswararao, P., Semiat, R., and Dukler, A. E., 1982, "Flow Pattern Transition for Gas-Liquid Flow in a Vertical Rod Bundle," *International Journal of Multiphase Flow*, Vol. 8, No. 5, pp. 509–524.
- Wallis, G. B., 1969, *One Dimensional Two Phase Flow*, McGraw-Hill, New York, pp. 336–345.
- Weisman, J., and Kang, S. Y., 1981, "Flow Pattern Transitions in Vertical and Upwardly Inclined Lines," *International Journal of Multiphase Flow*, Vol. 7, pp. 271–291.

O. Igra
Professor.

I. Elperin
Researcher.

G. Ben-Dor
Professor.

The Pearelstone Center for
Aeronautical Studies,
Department of Mechanical Engineering,
Ben-Gurion University of the Negev,
Beer-Sheva, Israel

Dusty Gas Flow in a Converging-Diverging Nozzle

The flow in a converging-diverging nozzle is studied numerically. The flowing medium is a suspension composed of gas seeded with small, spherical, solid particles. The solution covers the entire flow history, from its initiation and until a steady state flow is reached. The covered flow domain includes both the flow field inside the nozzle and part of the free jet flow outside of the nozzle exit plane. The solution is repeated for different solid particle diameters, ranging from 0.5 μm to 50 μm , and different dust loading ratios. It is shown that the presence of solid particles in the flow has a significant effect on the developed flow field, inside and outside the nozzle. In particular, by a proper choice of particles diameter lateral pressure waves and the secondary shock wave can be significantly attenuated. The solid particles size has also a marked effect on the position and size of the Mach disk appearing in the free jet flow. It is also shown that in a suspension case a steady state flow is reached faster than in a similar pure gas flow.

Introduction

Two phase flow in nozzles appears in many engineering applications, for example in nozzles of solid propellant rockets and/or in nozzles of jet engines which are operated over a dusty terrain. Even for the simple case of a pure gas flow, solving the flow field through a converging-diverging nozzle is not a simple task since such flows are, at least, two-dimensional and time dependent (until a steady flow is reached). As a result, past studies of two phase flows in nozzles assumed the flow field to be quasi-one-dimensional, e.g., Hoglund (1962) and Kliegel (1963). However, assuming the flow field to be quasi-one-dimensional is unrealistic since in most nozzles used for propulsion large area ratios are encountered in a relatively short nozzles, to result in significant lateral gradients. Furthermore, as pointed out by Regan et al. (1971) the assumption of quasi-one-dimensional flow is particularly weak near the nozzle wall where, unlike the gaseous phase, the solid phase flow (particles) detaches from the nozzle wall. Chang (1980) studied numerically the flow of a gas-dust suspension through a converging-diverging nozzle. He formulated the conservation equations, in a two-dimensional flow, for the two components of the suspension and solved them for three different nozzle geometries. The solution was conducted for both, a pure gas flow and a suspension. The solution obtained for the pure gas case served as a first approximation in the two-phase flow solution. More recently, Ishii and Kawasaki (1982) studied analytically a suspension flow through an axisymmetric nozzle assuming that the velocity and temperature differences between the two phases of the suspension are very small. Emphasis was placed in this study on reconstructing streamlines in the solid phase. Later, Ishii et al. (1987) studied suspension flows through a JPL nozzle using a homogeneous flow mixture model, which was solved numerically using a second order accurate scheme. Like Chang's (1980) solution, theirs too was limited to the flow inside the nozzle, and to a steady state flow. Unlike in the above-mentioned papers, the present solution covers the flow field inside and outside of the nozzle; from its initiation and until a steady state flow field is reached.

The analysis of the flow in the axisymmetric nozzle and the free jet developed behind the nozzle is based on the following assumptions.

1. Both the gaseous and the solid phases can be treated as continuous media.
2. Excluding the interaction between the two phases, the gaseous phase is assumed to be inviscid and non-conductive.
3. The gaseous phase can be treated as an ideal gas, i.e., it has a simple equation of state ($p = \rho RT$) and constant thermal heat capacities (c_p and c_v). This is a reasonable assumption in the range of Mach numbers covered in the present study.
4. The solid phase is composed of inert, rigid small spheres of identical radius, which initially are uniformly distributed in the suspension.
5. The volume occupied by the solid phase is negligibly small in comparison with the suspension volume. This is a reasonable assumption as long as the solid particles radius and the dust loading ratio are small; as is the case in the present study. Due to this assumption, collisions between solid particles can be ignored.
6. Due to the particle's small diameter, at any given time one temperature represents the entire solid particle. (No temperature variations inside a particle.)
7. The only force acting on solid particles is the drag force. Gravity, buoyancy and other forces are negligibly small in comparison with the drag force.
8. Radiative heat transfer is negligibly small. This is a reasonable assumption for the temperature range covered in the present study.

Based on the above assumptions the governing equations for the suspension are as follows (for detailed derivation see Elperin, 1996):

For the gaseous phase,

$$\frac{\partial \rho}{\partial t} + \frac{\partial}{\partial x}(\rho u) + \frac{\partial}{\partial r}(\rho v) = -\frac{\rho v}{r} \quad (1)$$

$$\begin{aligned} \frac{\partial}{\partial t}(\rho u) + \frac{\partial}{\partial x}(\rho u^2 + p) + \frac{\partial}{\partial r}(\rho u v) \\ = -\frac{\rho u v}{r} - \rho_p A(u - u_p) \end{aligned} \quad (2)$$

$$\begin{aligned} \frac{\partial}{\partial t}(\rho v) + \frac{\partial}{\partial x}(\rho u v) + \frac{\partial}{\partial r}(\rho v^2 + p) \\ = -\frac{\rho v^2}{r} - \rho_p A(v - v_p) \end{aligned} \quad (3)$$

Contributed by the Fluids Engineering Division for publication in the JOURNAL OF FLUIDS ENGINEERING. Manuscript received by the Fluids Engineering Division May 22, 1998; revised manuscript received September 10, 1999. Associate Technical Editor: J. K. Eaton.

$$\frac{\partial e}{\partial t} + \frac{\partial}{\partial x} u(e+p) + \frac{\partial}{\partial r} v(e+p) = -\frac{v}{r}(e+p) - \rho A [u_p(u-u_p) + v_p(v-v_p)] - \rho_p c B (T - T_p) \quad (4)$$

And for the solid phase,

$$\frac{\partial \rho_p}{\partial t} + \frac{\partial}{\partial x} (\rho_p u_p) + \frac{\partial}{\partial r} (\rho_p v_p) = -\frac{\rho_p v_p}{r} \quad (5)$$

$$\frac{\partial u_p}{\partial t} + u_p \frac{\partial u_p}{\partial x} + v_p \frac{\partial u_p}{\partial r} = A(u - u_p) \quad (6)$$

$$\frac{\partial v_p}{\partial t} + u_p \frac{\partial v_p}{\partial x} + v_p \frac{\partial v_p}{\partial r} = A(v - v_p) \quad (7)$$

$$\frac{\partial T_p}{\partial t} + u_p \frac{\partial T_p}{\partial x} + v_p \frac{\partial T_p}{\partial r} = B(T - T_p) \quad (8)$$

where ρ , p , T , and e are density, pressure, temperature and total internal energy per unit volume, respectively. Index 'p' refers to the solid phase (no index refers to the gaseous phase); $e = p/(\gamma - 1) + \rho(u^2 + v^2)/2$. u and v are the velocity components in the x and r directions, respectively. $A = \frac{3}{2}(\rho C_p / \rho_m d) |V - V_p|$ and $B = (6k \text{Nu} / \rho_m c d^2)$ where ρ_m is the material density of a solid particle ($m_p = \rho_m \pi d^3 / 6$) and for the drag coefficient C_D , the correlations proposed by Ivandeev et al. (1981) and by Gonor and Rivkind (1982) were used; for the Nusselt number Nu , the following correlation was used: $\text{Nu} = 2 + 0.6 \text{Pr}^{1/3} \text{Re}^{1/2}$. The Reynolds number, Re , is based on the relative velocity between the two phases of the suspension, and the Prandtl number, Pr , was set at 0.71. d and c are the solid particles diameter and specific heat capacity, respectively. k is the gas phase thermal conductivity. It should be noted that the spatial dust density, ρ_p , is related to the dust material density ρ_m as follows: $\rho_p = N \rho_m \pi d^3 / 6$ where N is the number of dust particles per unit volume.

Equations (1) to (8) are a set of eight, nonlinear, partial differential equations containing the following dependent variables: ρ , ρ_p , u , u_p , v , v_p , T and T_p (the suspension pressure p , can be evaluated from the equation of state for an ideal gas, i.e., $p = \rho RT$; R is the gas constant). This set of nonlinear partial differential equations, Eqs. (1) to (8), was solved numerically using a second order modification of the Godunov's scheme described in Vasiliev (1996). Essentially, this modification employs the evaluation of corrections at the two-dimensional stencil. The corrections are calculated using the governing equations in a nonconservative form. Corrections are constant over a cell in the computational domain and are added to the main parameters before calculating fluxes through the cell boundaries. The second order accurate in space and time W -modification of the Godunov's scheme was used only for gaseous phase. The numerical scheme employed for the solid phase comprises two stages. At the first stage an upwind scheme is applied to Eqs. (6)–(8) for finding the particles velocity components and temperature. These equations do not contain the particle density explicitly. At the second stage, a conservative upwind difference scheme is applied to update the particle density when the particle velocity obtained in the first stage is used. Thus the same approach was applied to obtain a second order accuracy in the parameters of gaseous and solid phases (for details see, Vasiliev, 1996 and Elperin, 1996).

For testing the accuracy of the numerical scheme used in the present study a few well known flows were solved; for example the case of an ideal shock tube, where an analytical solution is available. Our numerical simulation of these flows yields excellent agreement with the analytical solutions. In addition, the present solution was compared, for the case of equilibrium flow, with the solution of Chang (1980) and Ishii et al. (1987) and excellent agreement was obtained between their and our results.

For examination of numerical convergence calculations were performed for a suspension having dust loading ratio of $\eta = 0.5$

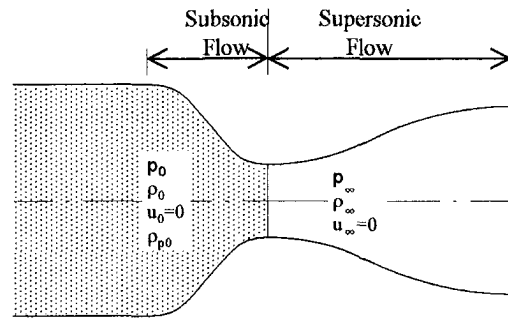


Fig. 1 Initial conditions in the studied flow field

and particles diameter of $d = 8 \mu\text{m}$ using three different grids. The first one was $(100 + 80) \times 40$, i.e., 100×40 mesh inside the nozzle and 80×40 mesh in the space outside the nozzle. The second one was $(120 + 120) \times 60$ and the third grid was $(200 + 200) \times 100$. Comparison between the gas phase isopycnics shows very good agreement for steady-state flow inside the nozzle, and the free jet outside the nozzle, for all three grids.

The geometry of the flow field to be solved is shown schematically in Fig. 1. The converging-diverging nozzle is connected to a long duct (reservoir) whose cross-section is identical to that of the nozzle inlet. The flow discharges from the nozzle outlet into a quiescent gas at ambient condition (p_∞). Initially ($t < 0$) a diaphragm is placed at the nozzle throat; it separates between two quiescent gases. On its left the gas pressure, density and temperature are higher than those prevailing on its right side (see Fig. 1). The gas placed on the left side of the diaphragm contains particles. The diaphragm is suddenly ruptured at $t = 0$ to result in a shock wave propagation into the low pressure section of the nozzle and a rarefaction wave propagation in the opposite direction. For solving the flow field generated after the diaphragm's rupture the grid shown in Fig. 2 was used. It contains the entire nozzle space and some of the free jet flow emerging from the nozzle outlet. A 40×100 mesh inside the nozzle and a 40×80 mesh in the space outside the nozzle were used for calculating the results to be discussed subsequently. The boundaries of the computation range are marked by numbers in Fig. 2. They contain the subsonic inflow of thermodynamic equilibrium suspension (1), axis of nozzle symmetry (2), the boundary outside the nozzle (3) with smooth non-reflection boundary condition, and the nozzle wall (4) meaning non-penetration boundary condition for gas and free penetration for particle. For the present study a JPL nozzle was used, its geometry is shown in Fig. 3 in Igra et al. (1997). This nozzle geometry was also used in the numerical solutions of Chang (1980), Ishii et al. (1987) and by Nishida and Ishimura (1990); however, in the above-mentioned studies, numerical solutions were limited to the nozzle space only, no external flow. Furthermore, these studies treated steady flow only. In practice, a boundary layer is present on the nozzle wall. However, in the considered

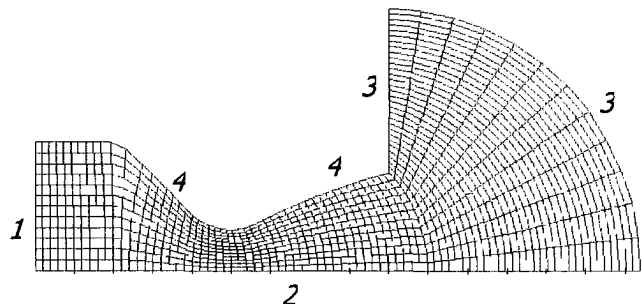


Fig. 2 Schematic description of the grid used for the present solution and boundaries of the computational domain

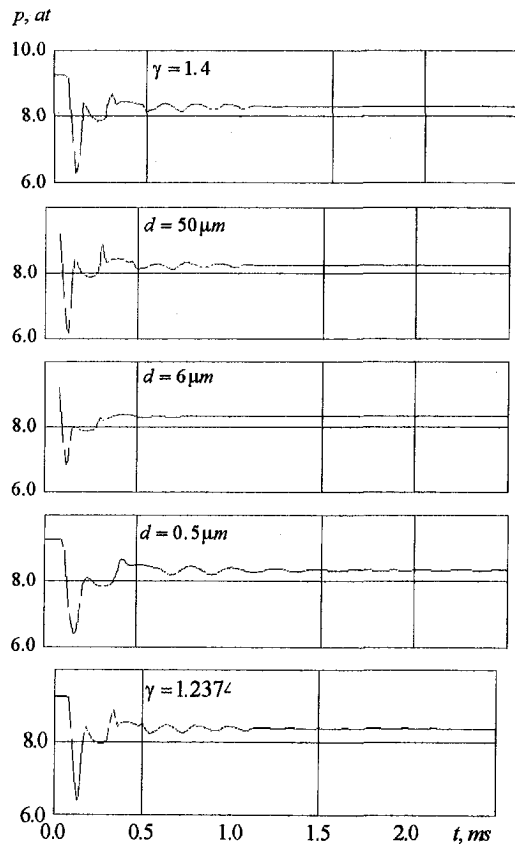


Fig. 3 Pressure along the nozzle axis of symmetry, at $x = 0.2$ m, for a suspension in which $\rho_{p0} = 0.3$ kg/m³

flow the thickness of the boundary layer will be relatively small. For the considered flow conditions, the thickness of the boundary layer at $x = L/2$ (L is the nozzle length) is 4×10^{-4} m. This is less than 5% of the nozzle throat diameter. It should be noted that in previous studies (Chang (1980), Ishii and Kawasaki (1982), Ishii et al. (1987), and Nishida and Ishimura (1990)) the boundary layer presence on the nozzle inner walls was also ignored. The subsequently shown numerical results were obtained for the following initial and boundary conditions: For the gaseous phase (air); $\gamma = 1.4$, $c_p = 1034$ J/(kgK), $\mu = 7.974 \times 10^{-5}$ kg/(ms), $Pr = 0.71$. For the solid phase; $c = 1686$ J/(kgK), $\rho_m = 3990$ kg/m³, $d = 0.5, 1, 2, 4, 6, 8, 10$ or $50 \mu\text{m}$. In the feeding reservoir: $p_0 = 945$ kPa, $T_0 = 3200$ K, $\rho_0 = 1.0$ kg/m³ and $\rho_{p0} = 0, 0.3, 0.5$, or 0.7 kg/m³. The ambient conditions were; $p_\infty = 102$ or 153 kPa and $T_\infty = 300$ K.

Results and Discussion

The flow through a relatively short, axisymmetric, converging-diverging nozzle and in the free jet developed outside of the nozzle outlet is a complex two-dimensional, time dependent flow field. The resulting flow field will be more complex when the flowing medium is not a homogeneous gas, but a suspension. Therefore, the present solution is conducted in two stages. In the first, the flow of a pure gas through a converging-diverging nozzle is studied. Results obtained for the pure gas case can be found in Elperin (1996) and in Igra et al. (1997). Due to lack of space these results are not shown here. In the following, results obtained in the second stage, for suspension flows, are given.

The dust present in the feeding reservoir affects the flow field generated in the nozzle, and in the free jet, after the diaphragm rupture. This is expected due to the large difference in kinematic and thermal inertias existing between the gas and the solid particles. Dust parameters that have the strongest contribution to the

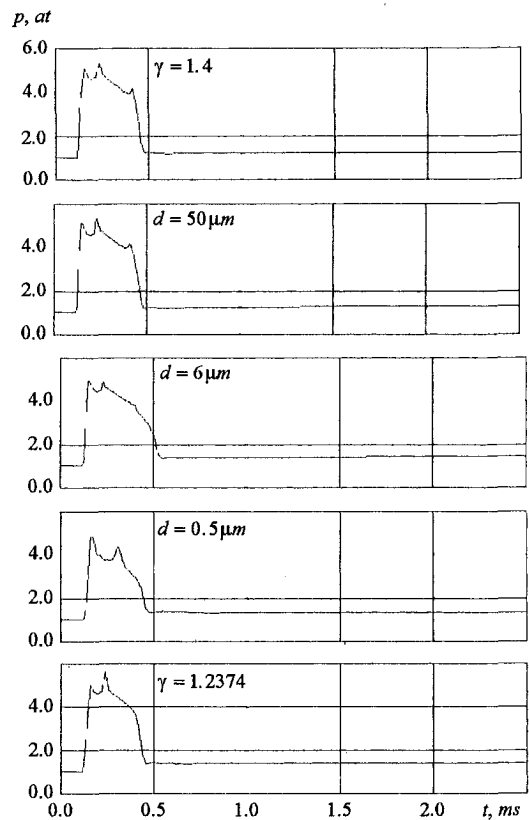


Fig. 4 Pressure along the nozzle axis of symmetry, at $x = 0.4$ m, for a suspension in which $\rho_{p0} = 0.3$ kg/m³

dust kinematic and thermal inertias are the particle diameter (d) and the dust initial spatial density (ρ_{p0}); or the dust loading ratio η ($\eta = \rho_{p0}/\rho_0$) where ρ_0 is the gaseous phase initial density. These parameters were changed within the ranges specified at the end of the previous section.

For examining the effects of the dust presence on the flow evolution in the nozzle (the initial nonsteady flow) pressure variations, with time, were computed at two different locations inside the nozzle. Both were placed on the nozzle axis of symmetry; one at a distance of 0.1 m upstream of the nozzle throat, the second at 0.1 m downstream of the nozzle throat. The results for pressure variations at $x = 0.1$ m upstream of the nozzle throat are shown in Fig. 3 while those for $x = 0.1$ m downstream of the nozzle throat are shown in Fig. 4. The first and the last plots in Figs. 3 and 4 represents extreme cases of frozen and equilibrium suspension flows, respectively. A frozen suspension flow is characterized by a very slow relaxation and therefore, the dust presence has practically no effect on the flow. In the other extreme, an equilibrium flow, momentum and heat exchanges between the two phases are very fast and as a result both phases have equal velocity and temperature. For the case of equilibrium flow the suspension was replaced by an equivalent pure gas whose specific heats ratio γ is given by:

$$\gamma = \frac{c_p \rho_0 + c_p \rho_{p0}}{c_v \rho_0 + c_v \rho_{p0}} = \frac{c_p + c \eta}{c_v + c \eta}$$

The results shown between these two extreme cases, frozen and equilibrium flows, indicate pressure variations in suspensions with solid particles whose diameter is within the range of $0.5 \mu\text{m}$ and $50 \mu\text{m}$ as indicated on each plot. In all plots shown in Fig. 3 the sudden pressure drop through the rarefaction wave generated immediately after the diaphragm rupture is clearly noticed. The cyclic pressure changes observed thereafter are due to lateral flow disturbances, moving back and forth between the nozzle wall and its

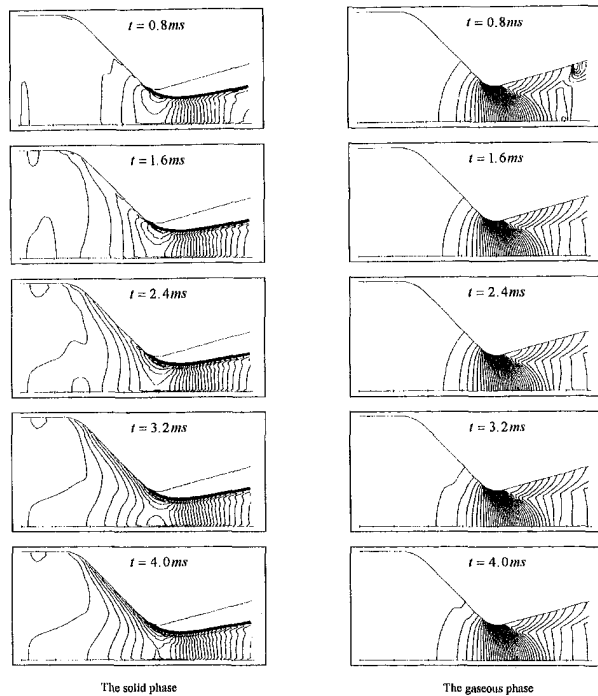


Fig. 5 Isopycnics in a suspension at which $\eta = 0.5$ and $d = 8 \mu\text{m}$

axis of symmetry. It is apparent from Fig. 3 that very similar pressure variations are obtained in both the frozen and the equilibrium flows. The small difference in time periods of pressure cycles results from the different speed of sound. In the frozen case $\gamma = 1.4$ while in the equilibrium case, $\gamma = 1.2374$. Pressure variations obtained for the different dust particles diameter, in the dusty cases, changes in a non-monotonic way. The pressure signature obtained for the largest particles ($d = 50 \mu\text{m}$) is similar to the that observed in the frozen flow case. Reducing the particles diameter results in a clear change in the pressure signatures.

As expected, the pressure signatures obtained at $x = 0.1 \text{ m}$ downstream of the nozzle throat (shown in Fig. 4) are very different from those shown in Fig. 3. In the present pressure plots a large pressure jump through the incident shock wave is clearly noticeable. A second, smaller, pressure peak represents the arrival of a lateral compression wave at the observation point. The last, large pressure jump (shown on pressure traces in Fig. 4) is through the secondary, upstream facing, shock wave. This shock wave appears strongest in the frozen flow case. It approaches a compression wave in the case of suspension with particles having $d = 6 \mu\text{m}$. As in the previously discussed case, here too, the pressure signature obtained for the largest particles ($d = 50 \mu\text{m}$) is very similar to that observed for a frozen flow, while the pattern obtained for the smallest particles ($d = 0.5 \mu\text{m}$) is similar to the equilibrium flow case. It is clear from Figs. 3 and 4 that the dust presence has significant effect on the lateral pressure disturbances and the secondary shock wave. By a proper choice of particle diameter the secondary shock wave can be reduced to a compression wave.

In Fig. 5, the flow field inside the nozzle is shown via isopycnics (lines of constant density) maps in the two phases of the suspension, at a few different times. The plots appearing in this figure are helpful in assessing the approach to a steady flow in the two phases; it also reveals the different flow behavior in the two phases. It is apparent from Fig. 5 that the solid phase approaches a steady state at about 3.2 ms after flow initiation. At earlier times the solid phase spatial density experiences meaningful variations with time, especially near the nozzle wall, at its subsonic flow regime. The approach to equilibrium in the gaseous phase is much faster; starting from $t = 1.6 \text{ ms}$ the gaseous phase exhibits almost

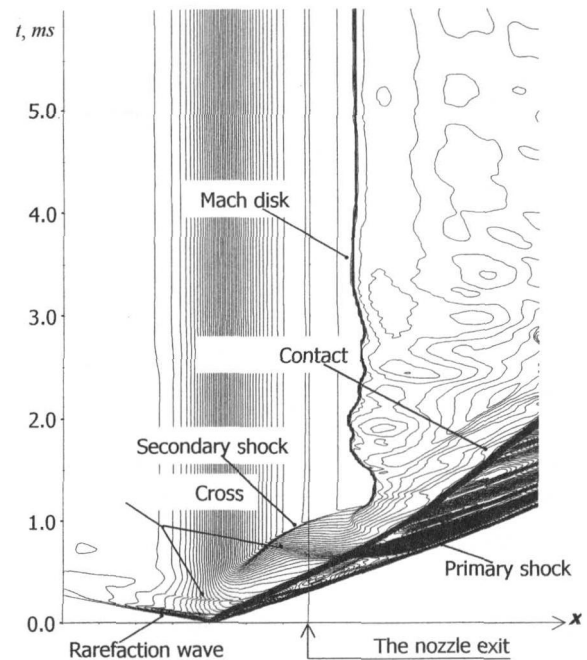


Fig. 6(a) Propagation of flow disturbances along the nozzle axis of symmetry in a suspension with $\eta = 0.3$ and $d = 4 \mu\text{m}$

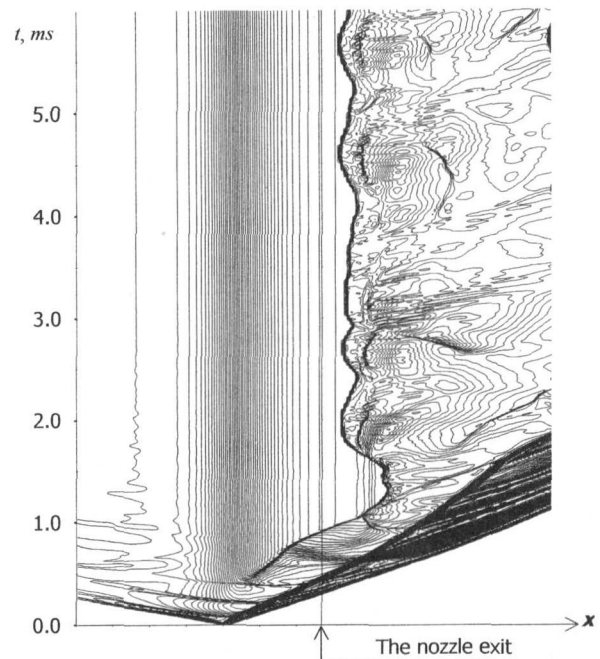


Fig. 6(b) Propagation of flow disturbances along the nozzle axis of symmetry in a case of a pure gas

a steady flow behavior. It is also clear from Fig. 5 that unlike the gaseous phase, the solid particles are unable to follow the nozzle contour downstream of its throat. Just ahead of the nozzle throat they detach from the wall creating a dust free zone in the nozzle's supersonic flow regime, near the nozzle wall.

The effect of the dust presence on the rate at which a steady flow is reached can also be seen by comparing Fig. 6(a) with its pure gas equivalent, Fig. 6(b). In the pure gas case the flow field in the free jet does not reach a steady state throughout the investigated time. It is apparent from Fig. 6(b) that the flow behind the Mach disk is time dependent and the position of the Mach disk changes with time; from $t = 4 \text{ ms}$ its position follows a cyclic pattern. This is not the case when dust particles are present in the flow (see Fig.

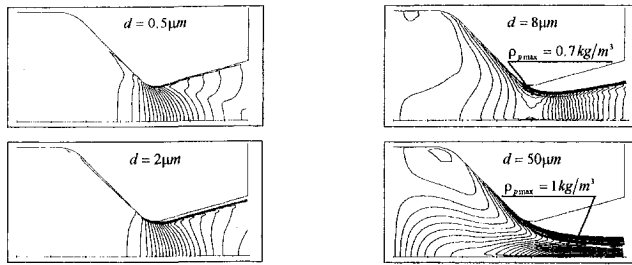


Fig. 7 Isopycnics in the solid phase of a suspension at which $\rho_{p0} = 0.5 \text{ kg/m}^3$

6(a)). Now the Mach disk position becomes stationary from about $t = 3 \text{ ms}$ and so is the flow behind it. Furthermore, the dust particles reduce the intensity of the secondary shock wave and attenuate the lateral waves inside the nozzle. This helps in reaching a steady state flow faster than in a similar pure gas case.

In the following, the flow field inside the nozzle, after a steady flow is reached, is investigated for initial dust spatial density of $\rho_{p0} = 0.5 \text{ kg/m}^3$ and dust particle diameter of $d = 0.5 \mu\text{m}$, $2 \mu\text{m}$, $8 \mu\text{m}$ and $50 \mu\text{m}$. The results are summarized in Fig. 7 as isopycnics in the solid phase flow field. It is apparent from this figure that for the smallest particles ($d = 0.5 \mu\text{m}$) the isopycnics are very similar to those observed in a similar pure gas case (see Fig. 5(d) in Igra et al., 1997). Small differences are noticed only close to the nozzle wall and they result from different boundary conditions used for the pure gas and the suspension cases (non-penetration boundary condition for gas and free penetration for particles). Increasing the particles diameter changes this pattern. Increasing the particle diameter increases its inertia and as a result the solid particles are unable to follow the nozzle contour, in the expansion region downstream of the nozzle throat, and detach from it. Starting from particle diameter of $2 \mu\text{m}$ this detachment is very clear. Now the isopycnics in the solid phase flow field differ from those obtained for a similar pure gas case as was already noticed earlier (in Fig. 5). In the dusty gas case, for $d \geq 2 \mu\text{m}$ a dust free zone near the nozzle wall is evident. The larger the dust particle diameter is, the larger is the dust free zone. Close to the limiting line for the dust cloud there exists a maximum in the dust spatial density. For $d = 8 \mu\text{m}$ this maximum is reached close to the nozzle throat and it is $\rho_{p,max} = 0.7 \text{ kg/m}^3$. This is higher than the initial dust spatial density. As seen in Fig. 7 this maximum moves downstream with increase in the dust particle diameter. For the case of $d = 50 \mu\text{m}$ the maximum dust spatial density is placed further downstream and now it doubled its initial value. Also, in the present case the dust free zone covers the largest area; see Fig. 7. It is of interest to note that the detachment of the solid particles (of all diameters) from the nozzle wall starts close to the place where the nozzle straight wall experiences a circular bending, in the subsonic part of the nozzle. A comparison between the present results and those reported by Ishii et al. (1987) regarding the limiting solid particles streamlines are shown in Fig. 8. It is

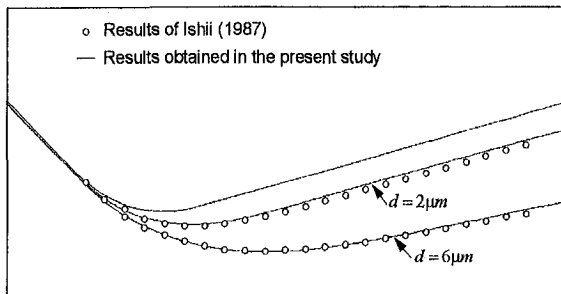


Fig. 8 Limiting solid particles streamlines

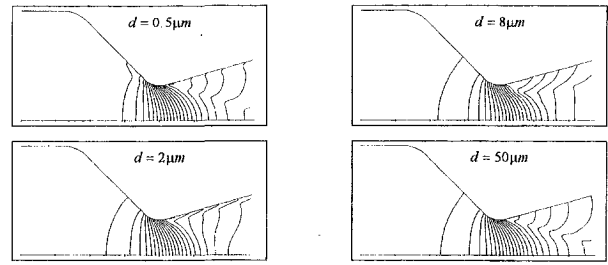


Fig. 9 Isopycnics in the gaseous phase of a suspension at which $\rho_{p0} = 0.5 \text{ kg/m}^3$

apparent that good agreement is found between these two solutions.

In order to further check the accuracy of the present results, the calculations obtained for the fine mesh were compared with the calculations carried out for a 24×60 mesh inside the nozzle and a 24×40 mesh in the space outside the nozzle. No appreciable difference was found between the results for the location of the limiting particle streamlines.

The effects of the dust presence on the gaseous phase of the suspension are shown in Fig. 9 where isopycnics, in the gaseous phase, are shown for $\eta = 0.5$ and $d = 0.5 \mu\text{m}$, $2 \mu\text{m}$, $8 \mu\text{m}$, and $50 \mu\text{m}$. A clear bending in the isopycnics, at the boundary of the dust free zone, is detectable in this figure. This bending (shift) is a direct result of changes in the gaseous phase density experienced while crossing the dust free zone. In the dusty gas region, density changes take place due to momentum and energy transfer between the two phases.

The flow field in the free jet outside of the nozzle is shown in Figs. 10 to 12. Figures 10 and 11 show isopycnics in the gaseous phase for $p_\infty = 1$ atmosphere at $t = 6 \text{ ms}$; a time at which the flow field reached a steady state. In all cases shown in these two figures the pressure at the nozzle exit plane is smaller than p_∞ , i.e., the flow is overexpanding. In Fig. 10 isopycnics are shown for two extreme cases; a frozen flow ($\gamma = 1.4$) and an equilibrium flow ($\gamma = 1.1868$). In both plots the free jet boundaries are clearly noticed. Above this boundary a slow moving gas is present; it

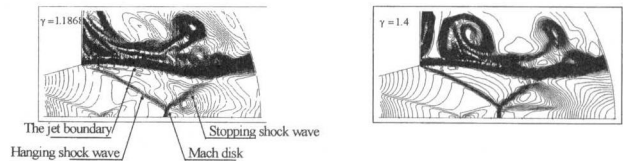


Fig. 10 Isopycnics in the free jet flow for pure gas case

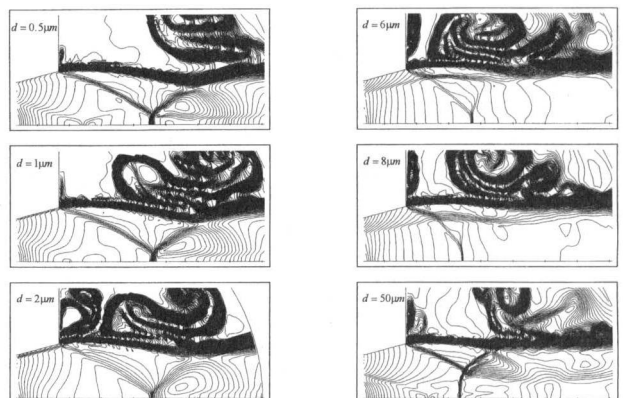


Fig. 11 Isopycnics in the gaseous phase of a suspension at which $\rho_{p0} = 0.5 \text{ kg/m}^3$

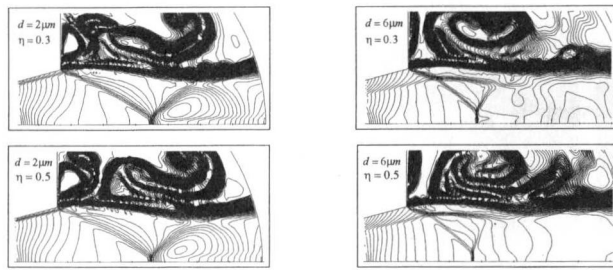


Fig. 12 Isopycnics in the gaseous phase for four different suspensions

contains layers of different density gases which resulted from the contact surface diffraction while leaving the nozzle. In the over-expanding jet a triple shock wave structure is evident. It composes of an hanging shock wave, a Mach disk and a stopping shock wave. Comparing between the two plots shown in Fig. 10 reveals that in the equilibrium case ($\gamma = 1.1868$), the Mach disk is shorter and it appears further downstream than its position in the frozen case ($\gamma = 1.4$). In Fig. 11 isopycnics in the gaseous phase of the suspension are shown for six different particle diameters. As observed previously for the flow inside the nozzle, the flow field obtained for the free jet in which $d = 0.5 \mu\text{m}$ is similar to that obtained for the equilibrium flow, i.e., for $\gamma = 1.1868$. Increasing the particles diameter up to $8 \mu\text{m}$ results in a considerable weakening of the triple shock wave configuration; part of this structure is hardly noticeable in the $d = 8 \mu\text{m}$ case. For $d = 6$ and $8 \mu\text{m}$ the flow in the core of the free jet is almost one-dimensional (see Fig. 11). When the solid particle diameter is increased, to $d = 50 \mu\text{m}$, the flow behavior changes. Now all three shocks of the triple configuration are clearly visible. However, unlike the flow observed inside the nozzle, in the free jet flow there is no similarity between isopycnics obtained for the largest particle diameter ($d = 50 \mu\text{m}$) and the frozen flow case ($\gamma = 1.4$). In summary, increasing the dust particle diameter first attenuates the triple shock complex to result in weaker waves, however, for large diameter particles ($d = 50 \mu\text{m}$) the triple wave configuration regains its strength. Increasing the particles diameter causes the Mach disk to move upstream and to cover a larger area. In Fig. 12 isopycnics in the gaseous phase of the suspension are shown for different dust particles diameter and dust loading ratios. It is apparent from this figure that increasing the dust loading in the suspension results in weakening the triple shock configuration. For the $6 \mu\text{m}$ diameter particles it also causes the Mach disk to move upstream. Such an upstream movement, due to increase in the dust loading, was observed experimentally by Sommerfeld (1994). For the smaller diameter particles ($2 \mu\text{m}$) a small opposite movement is observed.

Summary and Conclusions

The two-phase flow field developed inside and outside of a converging-diverging nozzle was studied numerically. First, the flow development until a steady state is reached was studied for a pure gas case. Thereafter, the two-phase flow case was analyzed. The following are the main conclusions reached in the present study.

(a) In the pure gas case the flow evolution in a converging-diverging nozzle contains flow discontinuities. The lateral ones

results from changes in the nozzle cross-section. Some of the flow discontinuities subside with time; the major ones, like the incident shock wave, the contact surface and the secondary shock wave, are eventually emitted from the nozzle.

(b) The prevailing back-pressure, to which the nozzle flow discharges, is an important parameter affecting the approach to a steady flow in the nozzle and in the free jet.

(c) In a case of a two phase flow, the presence of solid particles effects the developed flow in two opposite ways. They either weaken or enhance the flow discontinuities in comparison with a similar pure gas case. Weakening or enhancing depends on the solid particles size. In the analyzed flows, particles of $d = 2, 6 \mu\text{m}$ weakened the lateral disturbances in the nozzle and the secondary shock wave. However, very large particles ($d = 50 \mu\text{m}$) or very small particles ($d = 0.5, 1 \mu\text{m}$) caused an opposite phenomenon.

(d) In a suspension flow, a dust free zone is observed near the nozzle wall in the supersonic flow field. The larger the dust particle diameter is, the larger is the dust free zone.

(e) For very large particles ($d = 50 \mu\text{m}$) the observed flow in the nozzle is similar to a frozen flow. Indicating that in such a case all relaxation processes are relatively slow and the presence of large solid particles hardly affects the flow in the nozzle. On the other hand, for very small particles ($d = 0.5 \mu\text{m}$) the observed flow field in the nozzle is similar to an equilibrium flow, indicating that in such a case relaxation processes are relatively fast.

(f) The solid particle diameter affects the location and extend of the Mach disk appearing in the free jet outside of the nozzle. It also has an effect on the strength of the triple shock wave configuration in the free jet.

References

- Chang, I. S., 1980, "One- and Two-Phase Nozzle Flows," *AIAA Journal*, Vol. 18, pp. 1455–1461.
- Elperin, I., 1996, "Dusty Gas Flow Through a Converging-Diverging Nozzle," Ph.D. thesis, Dept. Mech. Eng., Ben-Gurion University of the Negev, Israel (in Hebrew).
- Gonor, A. L., and Rivkind, V. Y., 1982, "Dynamics of a Drop," M.: VINITI, Ser. MJG, Vol. 17, p. 86 (In Russian).
- Hoglund, R. F., 1962, "Recent Advances in Gas-Particle Nozzle Flow," *ARS Journal*, Vol. 32, pp. 662–671.
- Igra, O., Elperin, I., and Ben-Dor, G., 1997, "Dusty Gas Flow in a Nozzle," The annual ASME Fluids Engineering Conference & Exhibition, Vancouver, Canada.
- Ivandeev, A. I., Kutashv, A. G., and Nigmatulin, R. I., 1981, "Gas Dynamics of Multiphase Flows," M.: VINITI, Ser. MJG, Vol. 16, pp. 209. (In Russian).
- Ishii, R., and Kawasaki, K., 1982, "Limiting Particle Streamline in the Flow of a Gas-Particle Mixture Through an Axially Symmetric Nozzle," *Physics of Fluids*, Vol. 25, pp. 959–966.
- Ishii, R., Umeda, Y., and Kawasaki, K., 1987, "Nozzle Flow of Gas-Particles Mixtures," *Physics of Fluids*, Vol. 30, pp. 752–760.
- Kliegel, J. R., 1963, "Gas Particle Nozzle Flow," *Proceedings, 9th International Symposium on Combustion*, Pittsb, PA, pp. 811–828.
- Nishida, M., and Ishimura, S., 1990, "Numerical Analysis of Gas-Solid Two-Phase Nonequilibrium Nozzle Flows," *JSME International Journal*, Ser. II, Vol. 33, pp. 494–500.
- Regan, J. F., Thompson, H. D., and Hoglund, R. F., 1971, "Two-Dimensional Analysis of Transonic Gas-Particle Flows in Axisymmetrical Nozzles," *Journal Spacecraft and Rockets*, Vol. 8, pp. 346–351.
- Sommerfeld, M., 1994, "The Structure of Particle-Laden, Underexpanded Free Jets," *Shock Waves Journal*, Vol. 3, pp. 299–311.
- Vasiliev, E. I., 1996, "A W-Modification of Godunov's Method and Its Application for Two-Dimensional Non-Stationary Flows of Dusty Gas," *Computational Mathematics and Mathematical Physics*, Vol. 36, pp. 101–112.

Aerodynamic Torque Acting on a Butterfly Valve. Comparison and Choice of a Torque Coefficient

C. Sollic¹ and F. Danbon¹

Most technological devices use butterfly valves to check the flow rate and speed through piping. Their main advantages are their low cost, their mechanical suitability for fast operation, and their small pressure drops when they are fully open. The fluid dynamic torque about the axis of large valves has to be considered as the actuator could be overstrained. This torque is generally defined using a nondimensional coefficient K_T , in which the static pressure drop created by the valve is used for normalization. When the valve is closed downstream of an elbow, the valve pressure drop is not well defined. Thus, the classic normalization method gives many ambiguities. To avoid the use of the pressure drop, we define another torque coefficient C_T in which the dynamic pressure of the flow is the normalization factor instead of the pressure drop. Advantages and drawbacks of each normalization method are described in the following.

Nomenclature

- C_T = torque coefficient, normalized with the dynamic pressure []
 D = inlet duct diameter [m]
 K_T = torque coefficient normalized with the pressure drop []
 Q = flow rate [$\text{m}^3 \text{s}^{-1}$]
 R_c = radius of curvature of the elbow [m]
 Re = pipe Reynolds number []
 S = cross section area [m^2]
 T = aerodynamic torque [Nm]
 V_d = flow rate velocity [ms^{-1}]
 ρ = air density [kg m^{-3}]
 ξ = pressure drop coefficient []
 α = valve opening angle [$^\circ$]
 ΔP = pressure drop of the system [Pa]

¹ Associate Professor and Research Scientist, respectively, Ecole des Mines de Nantes, Département Systèmes Energétiques et Environnement, Division Dynamique des Fluides et Procédés, 4, rue A. Kastler, B.P. 20 722 F 44 307 Nantes, France. e-mail: camille.sollic@emn.fr

Contributed by the Fluids Engineering Division of THE AMERICAN SOCIETY OF MECHANICAL ENGINEERS. Manuscript received by the Fluids Engineering Division January 21, 1999; revised manuscript received September 1, 1999. Associate Technical Editor: D. R. Williams.

Subscript

- T = relative to torque
max = maximum value
ref = reference configuration (straight pipe)

1 Introduction

Butterfly valves are common industrial piping components which are used for flow check-up in a variety of processes, Eom (1988). Because of their simple mechanical assembly, and the small flow resistance of their disks in the fully open position, butterfly valves provide a relatively high flow capacity. More recently, the fluid torque has received attention for on/off applications in which quick closure is essential.

The aero or hydrodynamic torque is generally defined by a nondimensional coefficient K_T , in which the static pressure drop through the valve system is used for normalization. Most authors such as Silvester (1982) and Morris et al. (1987) apply this normalization. This approach is suitable for basic geometries in which the butterfly valve is located in a straight section of pipe. In this case, the pressure drop is easily obtained but nonetheless presents a real ambiguity when the piping circuitry contains an elbow, a branching or a variation of section near the valve.

However, in spite of its fundamental interest, this straight pipe configuration is uncommon in industry. Moreover, for reasons of economy and convenience the valve is generally set in critical spots near a bifurcation, an elbow, a tank or a centrifugal pump. As noted by Morris (1987), many of these piping geometries have an influence on the operating characteristics, especially on the pressure drop.

Thus, in order to perform comparisons on the fluid torque of a butterfly valve used in complex industrial circuits, we decided to use a different approach. We defined another dimensionless torque coefficient, C_T . This coefficient is based on a classic normalization, like the well-known drag coefficient. It uses the dynamic pressure based on the approach velocity (the dynamic pressure of the flow) as the normalization factor instead of the pressure drop.

We compare the two approaches and present the respective advantages and drawbacks of each one.

2 Experimental Facilities and Methodology

2.1 Wind Tunnel Facility. The tests were conducted in an open air circuit driven by a 10,000 m^3/h centrifugal fan. The circular test section is 0.3 m in diameter. The butterfly valve tested is a scaled down model ($\frac{1}{6}$) of an actual valve used in power or water distribution plants. A schematic view of the experimental facility is depicted in Fig. 1.

The valve disk angle, α , can be continually set from the fully open position $\alpha = 0$ deg to the closure $\alpha = 90$ deg. The flow rate is measured by a Wilson cross flowmeter. The inlet duct Reynolds number, based on the approach velocity, can be set through the range $5.0 \times 10^4 < Re < 10^6$.

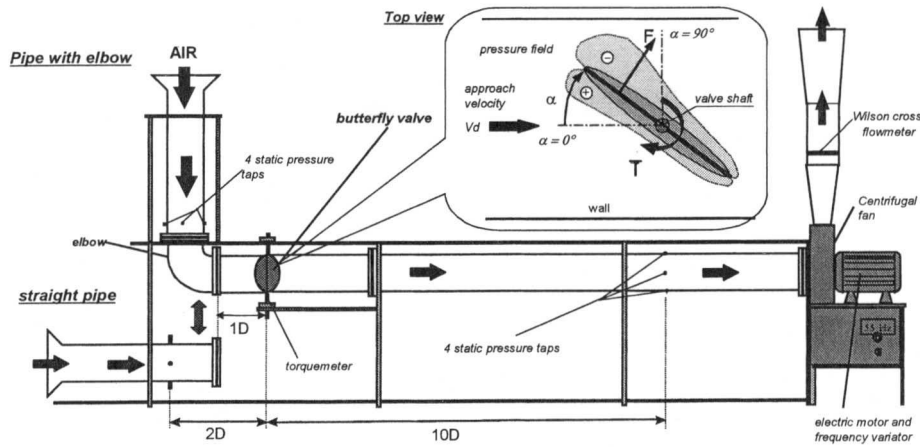


Fig. 1 Schematic view of the test bench and nomenclature

2.2 Torque and Pressure Drop Measurements. The shaft of the model is supported by ball bearings. Therefore, as soon as the valve is sufficiently opened, the bearing and seating torques are insignificant in comparison to the aerodynamic torque. As the working fluid is air, the hydrostatic torque can also be neglected.

The method used to measure the aerodynamic torque T is based on a strain gauge torquemeter which has a range from 0 to 12 Nm. The measurement principle is based on the torsion of a cantilever beam attached to the valve shaft at one end and held at the other one by a ball bearings. The sensitivity of the torquemeter given by the manufacturer is 2 mV/V. Thus, for 10 V full scale output and an operating range of 0–12 Nm, the sensitivity is 0.6448 Nm/mV \pm 0.0017 Nm/mV with 95% of confidence. We have checked the manufacturer calibration, by placing the torquemeter in pure torsion, on a specific test bench. We find a sensitivity very close to that reported. The torquemeter has been installed very carefully in situ in order to eliminate the mechanical friction.

The total pressure drop was measured with a Furness differential manometer (range 0–2,000 Pa, precision 0.1% FS). The pressure taps are placed between two cross sections located at 2 diameters upstream and 10 diameters downstream from the valve, see Fig. 1. Thus the measurements include regular and singular (valve and elbow) pressure drops. This length of 10 diameters corresponds to the re-establishment of the flow, required to obtain an accurate pressure drop measurement.

3 Torque Coefficient Definitions

3.1 Definitions. For full-scale extrapolation, we need to present the torque in a nondimensional form. We used two quite different normalization methods. In the classic approach, used in most hydraulic design departments, the coefficient torque $K_T(\alpha)$ is presented as:

$$K_T(\alpha) = \frac{T(\alpha)}{\Delta P(\alpha) D^3} \quad (1)$$

The pressure used for torque normalization is the total pressure drop, $\Delta P(\alpha)$, induced by the valve, the pipe and the elbow when it is present. It includes regular and singular pressure drops.

The other approach, which is of common use for aerodynamic problems, defines the dimensionless coefficient $C_T(\alpha)$ as in Eq. (2). Note that the pressure drop does not appear in this definition.

$$C_T(\alpha) = \frac{T(\alpha)}{\frac{1}{2} \rho V_d^2 D^3} \quad (2)$$

4 Torque of a Butterfly Valve Located in a Straight Pipe Section and Downstream of a 90 Deg Elbow

4.1 Mean Torque. Except for the work of Morris and Dutton (1991), who conducted an experimental investigation on a butterfly valve downstream of a 90 deg elbow, no extensive studies of fluid torque acting on butterfly valves located in an industrial piping system have been done. Like them, we focused our attention on the influence of a 90 deg elbow on the aerodynamic torque. But this elbow was placed nearer to the valve, at a distance of 1 diameter.

We studied two different elbows, see Fig. 2. As in most industrial plants, the valve shaft is in the elbow plane.

The mean torque T , normalized by its highest value $T_{\max} = T(30^\circ)$, is plotted in Fig. 3 for three types of geometry (straight pipe, elbows n°1 and n°2). The curve gives the magnitude of the mean torque with the valve angle opening position. As indicated by Bryer and Walshe (1969), the maximum value of the torque is strongly influenced by the valve and the trailing and leading edge shapes. For this particular valve, the maximum torque occurs at 30 deg.

The mean torque T is weakly influenced by the elbow shape. The deviation from the reference is less than 7%.

4.2 Mean Torque Coefficient

- Influence of the Reynolds number on the Torque Coefficients

So as to extrapolate our results to full-scale installations, we studied the evolution of the torque coefficients C_T and K_T versus the Reynolds number for the critical opening of 30 deg where the

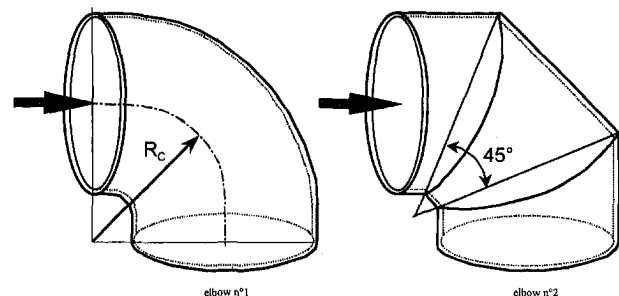


Fig. 2 Cross section of the two 90 deg elbows

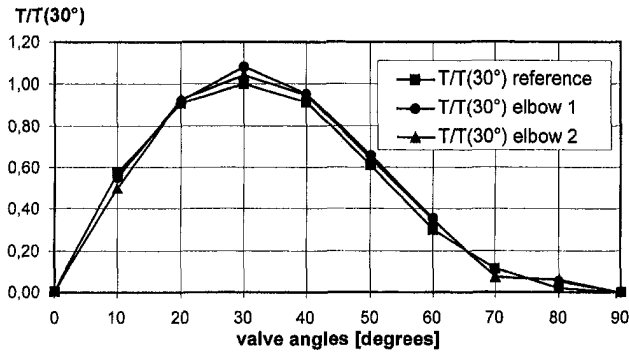


Fig. 3 Mean normalized torque for three geometrical arrangements (statistical uncertainty in $T = \pm 2\%$ and in $\alpha = \pm 1$ deg)

maximum torque occurred. As shown in Fig. 4, both C_T and K_T reach constant values at $Re > 6 \cdot 10^5$. Thus, the extrapolation to greater Reynolds numbers, for other diameters or other working fluids or flow rates, is possible.

• Results

In Figs. 5 and 6, time average values of K_T are compared to C_T . According to the results given in the literature, Morris and Dutton (1987, 1989), K_T reaches a maximum value between 10 and 20 deg. The design of each elbow leads to quite a different pressure

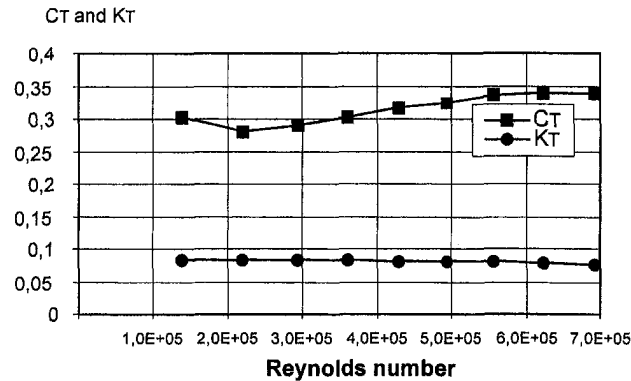


Fig. 4 Mean torque coefficients versus Reynolds number for the critical angle of 30 deg (uncertainty in $T = \pm 2\%$, in $Q = \pm 2\%$)

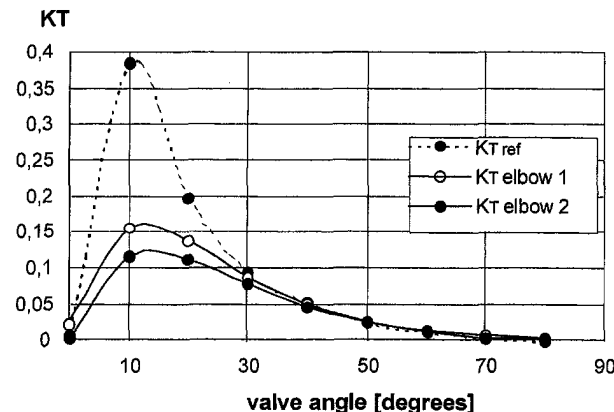


Fig. 5 Influence of the piping geometry on K_T (uncertainty in $T = \pm 2\%$, in $\alpha = \pm 1$ deg and in $\Delta P = \pm 2\%$)

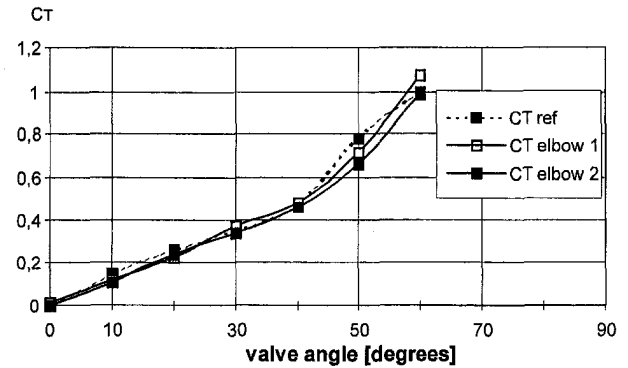


Fig. 6 Influence of the piping geometry on C_T (uncertainty in $T = \pm 2\%$, in $\alpha = \pm 1$ deg, and in $Q = 2\%$)

drop. Thus, the coefficient K_T is different in each case, in contrast to the real torque which remains unchanged, see Fig. 3.

C_T is a quasi-linear function of α and unchanged by the geometry like the torque T , see Fig. 3. As the flow rate near the valve closure is very small, the values obtained for these angles are not of any design interest. For this reason, the torque coefficient C_T is not given near the closure of the valve.

5 Discussion of the Torque Normalization Methods and on the Results

5.1 Comparison Between the Methods of the Torque Coefficient Normalization. The actual aerodynamic torque $T(\alpha)$ could be calculated when $K_T(\alpha)$ has been determined on a testing bench:

$$T(\alpha) = K_T(\alpha) \Delta P(\alpha) D^3 \quad (3)$$

In expression (3) the pressure drop could be written as a function of the nondimensional pressure drop coefficient $\xi(\alpha)$, and the approach velocity V_d :

$$\Delta P(\alpha) = \xi(\alpha) \frac{1}{2} \rho V_d^2 \quad (4)$$

The flow rate velocity in the pipe is:

$$V_d = 4Q/\pi D^2 \quad (5)$$

Combining Eqs. (1), (3), (4), and (5), the aerodynamic torque is shown to vary as the square of the flow rate Q . The aerodynamic torque can be expressed by the two following expressions:

$$T(\alpha) = 8\rho C_T(\alpha) Q^2 / \pi^2 D \quad (6)$$

$$T(\alpha) = 8\rho \xi(\alpha) K_T(\alpha) Q^2 / \pi^2 D \quad (7)$$

So that:

$$K_T(\alpha) = \frac{C_T(\alpha)}{\xi(\alpha)} \quad (8)$$

The K_T coefficient is a combination of effects due to the aerodynamic torque $C_T(\alpha)$ and pressure drop $\xi(\alpha)$ induced by the hydraulic singularities. Knowing the flow rate V_d in full scale pipes and $K_T(\alpha)$ by experimentations, it is necessary to estimate $\xi(\alpha)$ so as to calculate $\Delta P(\alpha)$ and finally the actual torque $T(\alpha)$.

Using the C_T definition, the only variables which need to be known for full scale extrapolation are C_T and V_d or Q . In most applications, the flow rate, which is generally one of the control parameters of the process, is inevitably known or dictated. So, the C_T method is more suitable for designing.

5.2 Discussion on the Results. Figures 5 and 6 demonstrate the importance of the normalization used. Unlike the torque, K_T is strongly influenced both by the shape and the arrangement of the

A Model for Flows With Massive Separation

K. Sanjeev Rao¹

pipng circuitry. Because of its dependence on the pressure drop, which is greater for the valve-elbow system, the maximum value of K_T obtained at 10° is really lower than that for the straight pipe. In each circumstance, the pressure drop of each piece of the piping system must be defined exactly. When the piping design is particularly complex, it is advisable to include all the geometry effects in the torque coefficient as is done by C_T .

It is important when assessing results presented in the above manner to appreciate that the maximum aerodynamic torque will occur at the value of α for maximum K_T only when the pressure difference across the valve is kept constant for all angles. In practice, this is seldom the case, because the pressure drop usually increases with α . It follows that quite small values of K_T , obtained when the valve is near the open position, could give rise to unacceptably high values of torque. In contrary, an higher accuracy will be obtained with the coefficient C_T near the critical angles (0–45 deg) because the measurement of the flow Q is more accurate when the valve is close to full opening.

Like $T(\alpha)$, C_T does not show great differences between each of the three geometries we have tested, thus it is easier to compare the influence of the pipe and valve design with the C_T approach. That is why the torque coefficient C_T is more representative of the real torque in most piping configurations.

6 Conclusion

Torque measurements of a butterfly valve were performed on a scaled down model of actual devices installed on a special test bench. Several piping configurations were tested to analyze the influence of the piping geometry on the mean torque and on the dimensionless coefficients K_T and C_T .

These investigations have shown that the results are very sensitive to the normalization method of the torque coefficient used. The classic approach, which consists of normalizing the torque with the pressure drop created by the valve, is only suitable in the basic configuration, i.e., in a straight pipe. When an hydraulic singularity is added close to the valve, the use of the C_T coefficient is preferable and more general and representative.

The influence of the opening angle and the upstream piping configuration on K_T and C_T are reported and compared to each other. It appears that the influence of an elbow installed at one diameter spacing upstream of the valve has no significant effect on the mean torque.

Acknowledgments

This work is supported by the K. S. B-Amri compagny, Design Department, Parc Rémorea-33 170 Gradignan, France. The authors are very grateful to Dr. Pascal L'Hôte who initiated this research.

References

- Bryer, D. W., and Walshe, D. E., 1969, "Devices for Reducing the Fluid-Dynamic Torque on Butterfly-Valve Discs," National Physical Laboratory Aerodynamics Division, Report 1298.
- Eom, K., 1988, "Performance of Butterfly-Valves as a Flow Controller," ASME JOURNAL OF FLUIDS ENGINEERING, Vol. 110, pp. 16–19.
- Morris, M. J., Dutton, J. C., and Addy, A. L., 1987, "Peak Torque Characteristics of Butterfly-Valves," *Proceedings of the Forum on Industrial Applications of Fluids Mechanics*, ASME FED-Vol. 54, pp. 63–66.
- Morris, M. J., and Dutton, J. C., 1989, "Compressible Flow Field Characteristics of Butterfly-Valves," ASME JOURNAL OF FLUIDS ENGINEERING, Vol. 111, pp. 399–407.
- Morris, M. J., and Dutton, J. C., 1991, "An Experimental Investigation of Butterfly-Valve Performance Downstream of an Elbow," JOURNAL OF FLUIDS ENGINEERING, Vol. 113, pp. 81–85.
- Morris, M. J., and Dutton, J. C., 1989, "Aerodynamic Torque Characteristics of Butterfly-Valves in Compressible Flow," ASME JOURNAL OF FLUIDS ENGINEERING, Vol. 111, pp. 392–399.
- Morris, M. J., 1987, "An Investigation of Compressible Flow Through Butterfly-Valves," Ph.D. thesis, Department of Mechanical and Industrial Engineering, University of Illinois at Urbana-Champaign.
- Silvester, R. S., 1982, "Torque Induced by Butterfly-Valve Carrying a Compressible Flow," *IMEchE, Proc. Instn. Mech. Engrs.*, Vol. 196, pp. 229–237.

1 Introduction

The objective of this technical brief is to present a simple inviscid model for separated flow past two or three-dimensional objects. Given the points/lines of separation and the base pressure as inputs, the pressure distribution on the wetted surface can be computed. As the full viscous problem including the unsteady wake is intractable at present, an engineering model such as the present one is of interest.

All the present methods that work for high Reynolds number flows past aerodynamically well shaped bodies do so only at small angles of attack. At slightly larger angles of attack there is separation. The effects of viscosity are confined to the thin boundary layer on the wetted surface, thin shear layers along the separation streamlines, and the wake. Outside these regions, the flow is inviscid and irrotational. Hence it is possible to treat the flow as inviscid, with viscous effects in the neighborhood of solid surfaces being obtained by standard boundary layer methods. This generally works if there is a mild separation. On the other hand, if the separation is massive, these methods fail completely. The flow behind the body is known to be unsteady and highly complex, and possibly contains organized vortex systems. The link between the wake and the separation conditions is not well understood. In spite of this, the unsteadiness in the wake has little effect on the flow upstream of the separation points. Thus, well-defined mean values of the pressure distribution are observed on the wetted surface. It is seen experimentally that the base pressure is almost constant.

A general theory of bluff body potential flows is given in Woods (1961), while Wu (1968) develops a model in which the pressure in the near wake remains constant. These methods use hodograph techniques, and involve the solution of complicated integral or functional integral equations. Parkinson and Jandali (1970) develop a wake source model for separated flows using a conformal mapping technique, and hence are restricted to the two-dimensional analytical cases. Potential flow on an arbitrary three-dimensional body can be solved by the panel methods. The present model, based on the ideas of Parkinson and Jandali (1970), is coupled with a lower order panel code (see Ahmed, 1973 for details) to solve the separated flow around an arbitrary body, given the points/lines of separation and the base pressure. The model is discussed in the next section and applied to a circular cylinder and a sphere.

2 Model

Consider the separated flow past a bluff body, in general, at an angle of attack (Fig. 1). Uniform panels are introduced on the body from the stagnation point to the separation points S_1 and S_2 . Parkinson and Jandali consider sources in the wake to solve this problem. In the same spirit, an extra panel(s) is taken on the bluff body, beyond each of the points of separation S_1 and S_2 . The edges of these typical panels are shown as dots in Fig. 1. The pressure on the points of separation are assumed to be equal to the base pressure p_b . Further, it is assumed that the base pressure in the wake is constant, the flow leaves the body tangentially after

¹ Scientist, Computational and Theoretical Fl. Dy. Division, NAL, Bangalore 560017, India.

Contributed by the Fluids Engineering Division of THE AMERICAN SOCIETY OF MECHANICAL ENGINEERS. Manuscript received by the Fluids Engineering Division July 28, 1998; revised manuscript received July 13, 1999. Associate Technical Editor: P. W. Bearman.

pipng circuitry. Because of its dependence on the pressure drop, which is greater for the valve-elbow system, the maximum value of K_T obtained at 10° is really lower than that for the straight pipe. In each circumstance, the pressure drop of each piece of the piping system must be defined exactly. When the piping design is particularly complex, it is advisable to include all the geometry effects in the torque coefficient as is done by C_T .

It is important when assessing results presented in the above manner to appreciate that the maximum aerodynamic torque will occur at the value of α for maximum K_T only when the pressure difference across the valve is kept constant for all angles. In practice, this is seldom the case, because the pressure drop usually increases with α . It follows that quite small values of K_T , obtained when the valve is near the open position, could give rise to unacceptably high values of torque. In contrary, an higher accuracy will be obtained with the coefficient C_T near the critical angles (0–45 deg) because the measurement of the flow Q is more accurate when the valve is close to full opening.

Like $T(\alpha)$, C_T does not show great differences between each of the three geometries we have tested, thus it is easier to compare the influence of the pipe and valve design with the C_T approach. That is why the torque coefficient C_T is more representative of the real torque in most piping configurations.

6 Conclusion

Torque measurements of a butterfly valve were performed on a scaled down model of actual devices installed on a special test bench. Several piping configurations were tested to analyze the influence of the piping geometry on the mean torque and on the dimensionless coefficients K_T and C_T .

These investigations have shown that the results are very sensitive to the normalization method of the torque coefficient used. The classic approach, which consists of normalizing the torque with the pressure drop created by the valve, is only suitable in the basic configuration, i.e., in a straight pipe. When an hydraulic singularity is added close to the valve, the use of the C_T coefficient is preferable and more general and representative.

The influence of the opening angle and the upstream piping configuration on K_T and C_T are reported and compared to each other. It appears that the influence of an elbow installed at one diameter spacing upstream of the valve has no significant effect on the mean torque.

Acknowledgments

This work is supported by the K. S. B-Amri compagny, Design Department, Parc Rémorea-33 170 Gradignan, France. The authors are very grateful to Dr. Pascal L'Hôte who initiated this research.

References

- Bryer, D. W., and Walshe, D. E., 1969, "Devices for Reducing the Fluid-Dynamic Torque on Butterfly-Valve Discs," National Physical Laboratory Aerodynamics Division, Report 1298.
- Eom, K., 1988, "Performance of Butterfly-Valves as a Flow Controller," ASME JOURNAL OF FLUIDS ENGINEERING, Vol. 110, pp. 16–19.
- Morris, M. J., Dutton, J. C., and Addy, A. L., 1987, "Peak Torque Characteristics of Butterfly-Valves," *Proceedings of the Forum on Industrial Applications of Fluids Mechanics*, ASME FED-Vol. 54, pp. 63–66.
- Morris, M. J., and Dutton, J. C., 1989, "Compressible Flow Field Characteristics of Butterfly-Valves," ASME JOURNAL OF FLUIDS ENGINEERING, Vol. 111, pp. 399–407.
- Morris, M. J., and Dutton, J. C., 1991, "An Experimental Investigation of Butterfly-Valve Performance Downstream of an Elbow," JOURNAL OF FLUIDS ENGINEERING, Vol. 113, pp. 81–85.
- Morris, M. J., and Dutton, J. C., 1989, "Aerodynamic Torque Characteristics of Butterfly-Valves in Compressible Flow," ASME JOURNAL OF FLUIDS ENGINEERING, Vol. 111, pp. 392–399.
- Morris, M. J., 1987, "An Investigation of Compressible Flow Through Butterfly-Valves," Ph.D. thesis, Department of Mechanical and Industrial Engineering, University of Illinois at Urbana-Champaign.
- Silvester, R. S., 1982, "Torque Induce by Butterfly-Valve Carrying a Compressible Flow," *IMEchE, Proc. Instn. Mech. Engrs.*, Vol. 196, pp. 229–237.

A Model for Flows With Massive Separation

K. Sanjeev Rao¹

1 Introduction

The objective of this technical brief is to present a simple inviscid model for separated flow past two or three-dimensional objects. Given the points/lines of separation and the base pressure as inputs, the pressure distribution on the wetted surface can be computed. As the full viscous problem including the unsteady wake is intractable at present, an engineering model such as the present one is of interest.

All the present methods that work for high Reynolds number flows past aerodynamically well shaped bodies do so only at small angles of attack. At slightly larger angles of attack there is separation. The effects of viscosity are confined to the thin boundary layer on the wetted surface, thin shear layers along the separation streamlines, and the wake. Outside these regions, the flow is inviscid and irrotational. Hence it is possible to treat the flow as inviscid, with viscous effects in the neighborhood of solid surfaces being obtained by standard boundary layer methods. This generally works if there is a mild separation. On the other hand, if the separation is massive, these methods fail completely. The flow behind the body is known to be unsteady and highly complex, and possibly contains organized vortex systems. The link between the wake and the separation conditions is not well understood. In spite of this, the unsteadiness in the wake has little effect on the flow upstream of the separation points. Thus, well-defined mean values of the pressure distribution are observed on the wetted surface. It is seen experimentally that the base pressure is almost constant.

A general theory of bluff body potential flows is given in Woods (1961), while Wu (1968) develops a model in which the pressure in the near wake remains constant. These methods use hodograph techniques, and involve the solution of complicated integral or functional integral equations. Parkinson and Jandali (1970) develop a wake source model for separated flows using a conformal mapping technique, and hence are restricted to the two-dimensional analytical cases. Potential flow on an arbitrary three-dimensional body can be solved by the panel methods. The present model, based on the ideas of Parkinson and Jandali (1970), is coupled with a lower order panel code (see Ahmed, 1973 for details) to solve the separated flow around an arbitrary body, given the points/lines of separation and the base pressure. The model is discussed in the next section and applied to a circular cylinder and a sphere.

2 Model

Consider the separated flow past a bluff body, in general, at an angle of attack (Fig. 1). Uniform panels are introduced on the body from the stagnation point to the separation points S_1 and S_2 . Parkinson and Jandali consider sources in the wake to solve this problem. In the same spirit, an extra panel(s) is taken on the bluff body, beyond each of the points of separation S_1 and S_2 . The edges of these typical panels are shown as dots in Fig. 1. The pressure on the points of separation are assumed to be equal to the base pressure p_b . Further, it is assumed that the base pressure in the wake is constant, the flow leaves the body tangentially after

¹ Scientist, Computational and Theoretical Fl. Dy. Division, NAL, Bangalore 560017, India.

Contributed by the Fluids Engineering Division of THE AMERICAN SOCIETY OF MECHANICAL ENGINEERS. Manuscript received by the Fluids Engineering Division July 28, 1998; revised manuscript received July 13, 1999. Associate Technical Editor: P. W. Bearman.

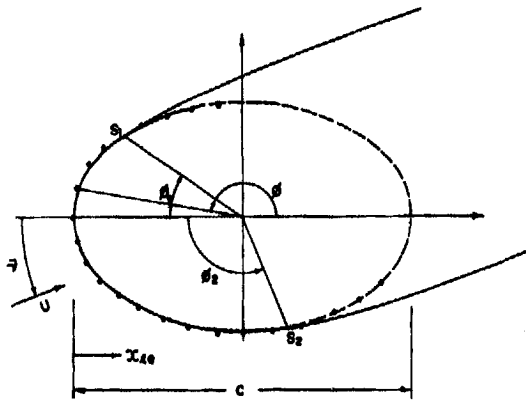


Fig. 1 Separated flow past a bluff body at an angle of attack

separation and the separating streamline is straight (for simplicity, even though this is not essential). As a result, Bernoulli's equation fixes the tangential velocities at these points. The model solves for the separated flow around this arbitrary body, given the point/line of separation and the base pressure, as mentioned earlier.

One velocity component has to be specified on each panel initially to solve for the flow using the panel code. The normal velocity at each panel is chosen for this purpose. For all the panels on the wetted surface and those on the separation points, this velocity component vanishes. But for the panels beyond S_1 and S_2 this is nonzero and has to be determined. Here, we make use of the assumption that the pressure in the entire wake is constant and is equal to the base pressure p_b . The projection of the velocity at the separation point on the normal of each panel is taken to be the normal velocity.

All the panels chosen are uniform and are on the body. Panels cover the body from the leading edge up till separation and beyond. The number of additional panels taken beyond separation depends on the angle of separation. When this angle is small (less than 90 degrees), only one additional panel is taken beyond separation, and is of the same size as the remaining ones. But when the separation is large, uniform panels are taken all over the body. This is discussed further below. Computations reveal that as the panels are made finer in the latitudinal and longitudinal directions, the pressure distributions quickly converge to the experimental value, as seen in Figs. 2 and 3. Here the experimental results and previous computations are taken from Bearman and Fackrell (1975). Figure 2 shows the pressure distribution on a circular cylinder, where as Fig. 3 shows the corresponding quantities on a sphere. The separation angle in both of them is 80 degrees.

The effect of adding additional panels on the body beyond S_1 and S_2 was studied. The normal velocity was again prescribed by projecting the velocity at S_1 (S_2 in the lower part) on the normal

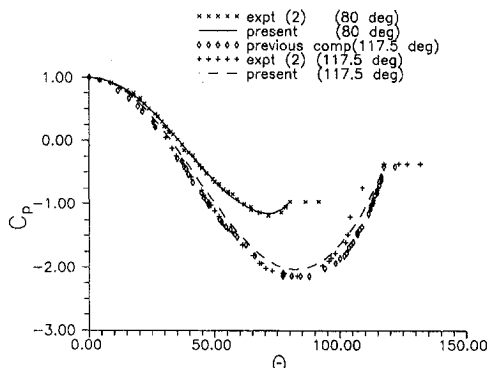


Fig. 2 Pressure distribution on a circular cylinder. Upper curve: separation at 80 deg; lower curve: separation at 117.5 deg.

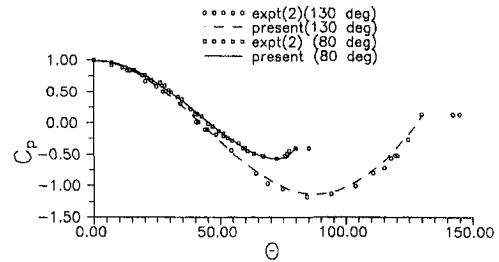


Fig. 3 Pressure distribution on a sphere. Upper curve: separation at 80 deg; lower curve: separation at 130 deg.

of these panels. It was seen that the maximum variation in the C_p was at the bottom, and it was less than 5%. For small angles of separation it is seen that one additional panel beyond separation gives best results. The effect caused by reducing the size of the last panel beyond separation was studied. The corresponding pressure distribution for the flow over a circular cylinder separating at 80 degrees is shown in Fig. 4. It is seen that the change is noticeable only near the suction peak, and is very small everywhere. It should be pointed out here that when the panels are taken only up till the point/line of separation, the resulting pressure distribution still compares reasonably well with the experiments.

The behavior is different when the separation angle is large. As the additional panels beyond the separation points are increased, the pressure distribution curve gradually comes down and approaches the experimental curve from above. Hence, panels are taken all over the body to get the best results. The bottom curve of Fig. 2 shows the pressure distribution on a circular cylinder when the separation angle is 117.5 degrees. It can be seen that the present model is in better agreement with the experiments than the previous computations. Similar computations for elliptical cylinders at different angles of attack (results not presented here) show good comparison with previous theories and experiments.

The effect and necessity of additional panels is seen in Fig. 5, where the number of these panels beyond the separation point is varied. In the first case shown, 12 additional panels are taken right up till the trailing edge, so that the entire body is covered by panels. It is seen that the additional panels bring the suction peak to the experimental value. The assumption that the separating streamline is straight may be questioned here. This assumption is certainly valid locally near the point of separation. Away from it, the effect outside the wake starts diminishing. Hence, the actual shape of the separating streamline should not affect the results outside the wake considerably. For the same reason, it should be possible in principle to use the actual streamline in this model.

The bottom curve of Fig. 3 shows the pressure distribution on a sphere when the separation is at 130 degrees. Note that the geometry here is three dimensional and the separation angle is greater than the corresponding value on the cylinder. In spite of this, the

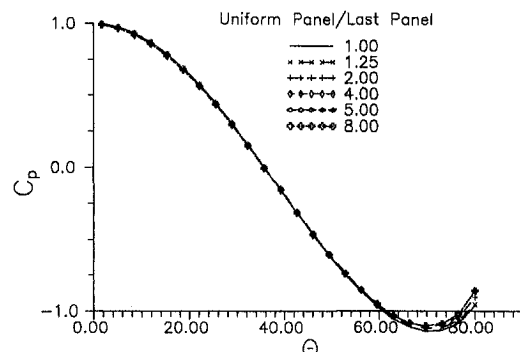


Fig. 4 Computed pressure distribution on a circular cylinder as the size of the last panel is varied. Separation at 80 deg.

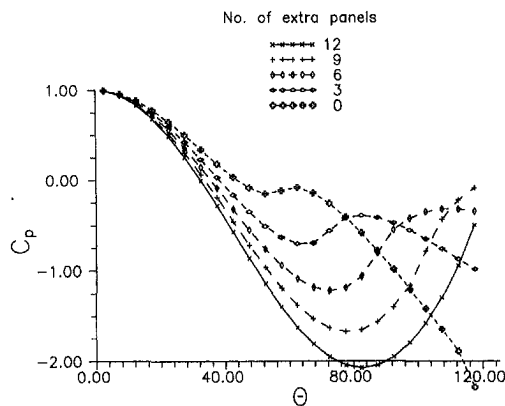


Fig. 5 Effect of extra panels on the pressure distribution on a circular cylinder. Separation at 117.5 deg.

agreement with the experiments is better, even though the results for the cylinder are still of engineering importance.

3 Conclusion

Thus, the wake source model has been implemented using a panel code, for certain two and three dimensional configurations. The physical inputs are the two separation points or lines and the base pressure. These computations involve simple algebraic eval-

uations, unlike the hodograph techniques, which require iterative solutions of functional or integral equations in general. Given the fact that there are no other methods to handle this high Reynolds number situation, this should be looked upon as an adjunct to experiments to reduce the data that needs to be determined. Kumar and Shankar (1980) apply this wake source model to lifting separated flows. In a similar manner, it is possible to apply the present model to aerofoils, wings and other practical aerodynamic configurations if the panel code is generalized to handle vorticity distributions.

Acknowledgment

The author thanks Dr. C. L. Narayana for help in using the panel code, and Dr. P. N. Shankar for suggesting this problem.

References

- Ahmed, S. R., 1973, "Calculation of the Inviscid Flow Field Around Three Dimensional Wings, Fuselages and Wing-Fuselage Combinations Using the Panel Method," DLR-FB 73-102.
- Bearman, P. W., and Fackrell, J. E., 1975, "Calculation of Two-Dimensional and Axisymmetric Bluff-Body Potential Flow," *Journal of Fluid Mechanics*, Vol. 72, pp. 229-241.
- Kumar, A., and Shankar, P. N., 1980, "A Potential Flow Model for Lifting Separated Flows," ASME paper 80-FE-4.
- Parkinson, G. V., and Jandali, T., 1970, "A Wake Source Model for Bluff Body Potential Flow," *Journal of Fluid Mechanics*, Vol. 40(3), pp. 577-594.
- Woods, L. C., 1961, *The Theory of Sub-Sonic Plane Flow*, Cambridge University Press, Cambridge.
- Wu, T. Y., 1968, *Inviscid Cavity and Wake Flows, Basic Developments in Fluid Mechanics*, Vol. 2, Academic Press, New York.